Novel btp [2,6-bis(1,2,3-triazol-4-yl)pyridine] systems: a versatile motif for the formation of supramolecular self-assembly structures

Joseph P. Byrne, B. Sc.

May 2015

University of Dublin

Trinity College

Based on research carried out under the direction of

Prof. Thorfinnur Gunnlaugsson

A thesis submitted to the School of Chemistry,

University of Dublin, Trinity College for the degree of

Doctor of Philosophy

Declaration

I declare that this thesis for the degree of Doctor of Philosophy has not been submitted as an exercise for a degree at this or any other university. Except where duly acknowledged, all work described herein is original has been carried out by the author. I agree to deposit this thesis in the University's open access institutional repository or allow the library to do so on my behalf, subject to Irish Copyright Legislation and Trinity College Library conditions of use and acknowledgement.

_____

Joseph P. Byrne

Abstract

This thesis, entitled "Novel **btp** [2,6-bis(1,2,3-triazol-4-yl)pyridine] systems: a versatile motif for the formation of supramolecular self-assembly structures" describes the synthesis and characterisation of a range of new ligands containing the **btp** binding motif and their various supramolecular self-assembly formations, particularly with metal ions.

Chapter 1 introduces the **btp** motif, comparing it to other terdentate binding motifs and describing synthetic routes for its formation *via* the Cu(I)-catalysed azide–alkyne 'click' reaction, as well as some key features of these systems. All of the literature concerning **btp** is summarised, with particular interest paid to *d*- and *f*-metal coordination chemistry and anion binding. Some specific applications and the formation of polymeric and supramolecular systems are presented as well. Prior studies of Ln(III)-directed self-assembly studies in the Gunnlaugsson laboratory are also summarised.

Chapter 2 describes the design and synthesis of two new **btp** ligands, by means of a one pot 'click' reaction, and their coordination chemistry with *d*-metal ions Ru(II), Ni(II), Ir(III) and Pt(II). X-ray crystal structures of a number of these compounds were obtained. All complexes display non-classical triazolyl C–H···Cl^- hydrogen bonding. Photophysical studies of the Ru(II), Ir(III) and Pt(II) complexes at room temperature are described, where all but one complex showed only ligand-centred fluorescence; measurements at 77K gave more interesting emission properties. Electrochemical properties of the Ru(II) systems are reported and the formation of a metallo-supramolecular gel is described, which was imaged by scanning electron and helium ion microscopy (SEM and HIM).

Chapter 3 principally focusses on *f*-metal ions and the formation of Ln(III)-directed self-assemblies of ligands, including an allyl amide **btp** derivative and a range of amino acid derivatives. These complexes are luminescent, with modest to very high quantum yields (Φ_{Eu} = 0.4–3.0 %, Φ_{Tb} = 6.3–70 %). Self-assembly was monitored by various spectroscopic titration techniques and global stability constants for the assemblies determined by fitting the data to models ($\log\beta_{1:3}$ = 18.9–23.0). This chapter also describes the formation of a self-templated [2]catenane through olefin ring-closing metathesis and supramolecular pre-organisation, confirmed by single crystal X-ray diffraction. This elegant structure shows promise for selective anion binding.

Chapter 4 details the design and synthesis of a number of chiral **btp** ligands from either carbohydrate azide, or chiral amine starting materials, the latter through a one-pot diazo-

transfer–deprotection–'click' protocol. Three of the ligand were characterised by X-ray crystallography. These ligands all form luminescent Eu(III)-directed self-assemblies (Φ_{Eu} = 0.5–1.9 %) and one enantiomeric pair forms very emissive Tb(III)-directed self-assemblies (Φ_{Tb} = 56–67 %). These complexes possess chiroptical properties (namely circular dichroism and circularly polarised luminescence). Self-assembly in solution was monitored by means of various spectroscopic titrations as in the previous chapter, and also, by virtue of the chiroptical properties of these assemblies, by CD titration. Determination of stability constants from CD titrations is not commonly reported; here such values are comparable to those determined by fitting absorbance and emission titration data ($\log\beta_{1:3}$ = 19.0–23.2).

Finally, Chapter 5 gives experimental details and procedures for the work carried out in the other chapters. Supplementary spectra and data are provided in the Appendices.

Acknowledgements

First and foremost, I have to thank Professor Thorri Gunnlaugsson for his guidance, support and advice over the past four years, for welcoming me to Trinity, challenging me and always convincing me not to sell myself short.

Many of the results in this thesis could not have been gathered without the help of others. I thank Professor Martin Albrecht and his colleagues Dr Vivienne Leigh and Bryan Hogan at University College Dublin for carrying out CV measurements in Chapter 2; Dr Alan Bell and Professor John Boland in CRANN for SEM and HIM in Chapter 2; Dr Ann Connolly (University College Dublin) for elemental analysis measurements throughout; Dr Martin Feeney and Dr Gary Hessman for HRMS measurements (even those pesky lanthanide complexes); Dr Robert Peacock (University of Glasgow) for CPL measurements and useful discussion about these results, particularly those discussed in Chapter 4; and of course, the omnipresent Dr John O'Brien and Dr Manuel Reuther for many, many NMR measurements, as well as technical assistance, advice and enthusiasm.

The TG Group has always been blessed with good postdocs. I also owe a particular debt of gratitude to Dr Jonathan Kitchen for setting me on the path to 'click' chemistry. Our many useful discussion, ideas and work together while he was in Dublin formed the seed from which this thesis crystallised. Thanks, Jon, for that and indeed the many beautiful crystal structures which you resolved scattered throughout these pages (persistence paid off). Dr Oxana Kotova, always willing to give your time to discuss science, and Dr Steve Comby, a man whose first answer is 'No', always followed by a detailed discussion. Dr Miguel Martínez-Calvo, you always kept things fun (particular thanks for the various X-ray crystal structures in Chapters 2 and 4) and Dr Salvador Blasco for some last minute X-ray results and the biological studies mentioned in Chapter 3 and much useful advice about his many topics of expertise; *¡Gracias, señors!* Dr Jenn Jones tried to keep me sane and taught me an awful lot, while Dr Rob Elmes introduced me to ruthenium. My thanks too to Dr Emma Veale, Dr Komala Pandurangan and Dr Sankarasekaran "Raju" Shanmugaraju for sharing your expertise and experience freely. Not forgetting our semi-detached expert Dr Ciaran O'Reilly for many long synthetic discussions and for synthesis of carbohydrate azide precursors used in Chapter 4.

To those I watched pass through the lab before me: Dr Brian McMahon, Dr Samantha Murphy, Dr Elaine Boyle, Dr Laura Truman and Dr Swagata Banerjee; thanks for the memories. To those who walked most of the way with me: Dr David Caffrey and Dr Dawn

Barry; thanks for the solidarity – ye were a pleasure to persevere with. And to those who follow: Fergus Poynton, Esther Surender, Savyasachi "Sachi" Aramballi Jayant, Helen Burke, Eoin McCarney, Bjørn la Cour Poulsen, Anna Aletti, Amy Lynes, Elena Calatrava and Dermot Gillen; you make it a pleasure to come to the lab and are willing to read anything. Sam Bradberry deserves a special mention for the long hours we have spent theorising, debating and thinking outside the box, as well as for introducing me to materials; thanks $\times 10^6$.

Our many and varied visitors have added colour to our lunchtime discussions; to name a few: Anna, Rebecca, Lisa, Audric, Stefano, Valeria, Doria, Devis and Agostino kept the lab constantly-changing. Senior sophistor students Eoin McCarney and Danielle Bruen for listening to my mad ideas for projects and still managing to go on to do PhD studies themselves; thanks for your patience.

I cut my research teeth with the UREKA crowd in Maynooth: Ursula Sheridan, Damien Carr, Elizabeth Jennings, Colm Duffy, Aisling Ní Cheallaigh, we're all now approaching the end; thanks for all the inter-university conversations, introductions and fun over the years.

The work couldn't have been done without the generous financial support of the Irish Research Council *Embark* Initiative (2010–2013) and Trinity School of Chemistry (2013–2014).

Massive thanks to my friends in Dublin over the 4 years, some of whom have been with me since my schooldays, many of whom I picked up along the way in Maynooth, others who are more recent additions and even those who are now flung around the world; you've kept me constantly distracted from my studies, given me things outside the lab to look forward to and always understood the value of brunch.

Finally I thank my family, who unconditionally support me in everything I do. My parents Pat and Eithne have given me everything I ever needed for the last quarter century and I can't thank them enough, nor my brothers Kevin (for his solid advice, opinions and company), Noel (for keeping me grounded and aware of the real world) and Owen (for always being one step ahead of me and looking after me). Thanks too to the ladies of the family: Liz, Sophie and Olivia.

No work is done in a vacuum, so I sincerely thank all those who filled the spaces around me as I undertook this project and made the journey fulfilling and interesting.

Go raibh míle maith agaibh go léir as ucht gach rud

List of abbreviations

Å	angstrom (1×10^{-10} m)
AIBN	azobisisobutyronitrile
Ala	alanine
app	apparent
ar	aromatic (IR)
β	global stability constant
bipy	2,2′-bipyridine
bpp	2,6-bis(pyrazolyl)pyridine
btp	2,6-bis(1,2,3-triazol-4-yl)pyridine
btp′	2,6-bis(1,2,4-triazolyl)pyridine
br s	broad singlet
CD	circular dichroism
cod	cyclooctadiene
COSY	correlation spectroscopy
CPL	circularly polarised luminescence
CuAAC	copper(I)-catalysed alkyne–azide ‘click’ reaction
CV	cyclic voltammetry
cyclen	1,4,7,10-tetraazacyclododecane
δ	chemical shift (NMR)
d	doublet
DEPT	distortionless enhancement by polarization transfer
DFT	density functional theory
DIC	*N*,*N*′-diisopropylcarbodiimide
DMAP	4-dimethylaminopyridine
DMSO	dimethylsulfoxide
DMF	*N*,*N*-dimethylformamide
dpa	dipicolinic acid; pyridine-2,6-dicarboxylic acid
DSSC	dye-sensitised solar cell
EDTA	ethylenediaminetetraacetic acid
EET	excitation energy transfer
equiv.	equivalent(s)
ESI+/ESI−	electrospray ionisation (positive/negative mode)

EtOAc	ethyl acetate
Fc	ferrocene; bis(η^5-cyclopentadienyl)iron
FESEM	field emission scanning elctron microscopy
FT-IR	Fourier-transform infrared spectrometry
γ	skeletal vibration (IR)
Gly	glycine
h	hour
HEMA	(hydroxyethyl)methacrylate
HIM	scanning helium ion microscopy
HMBC	heteronuclear multiple-bond correlation spectroscopy
HOMO	highest occupied molecular orbital
HRMS	high resolution mass spectrometry
HSQC	heteronuclear single quantum coherence spectroscopy
IR	infrared
IC	internal conversion
ISC	inter-system crossing
ITC	isothermal titration calorimetry
J	NMR coupling constant
K	Formation equilibrium constant
λ	wavelength
LC	ligand-centred
LMCT	ligand-to-metal charge transfer
Ln(III)	trivalent lanthanide(III) ion
LUMO	lowest unoccupied molecular orbital
m	multiplet
MALDI	matrix-assisted laser desorption/ionisation
MLCT	metal-to-ligand charge transfer
ML*n*	1:*n* metal-to-ligand assembly, where *n* = 1,2,3.
MC	metal-centred
MRI	magnetic resonance imaging
m/z	mass-to-charge ratio
NHC	*N*-heterocyclic carbene
NMR	nuclear magnetic resonance
NOE	nuclear Overhauser effect

Φ	total luminescence quantum yield
PET	photoinduced electron transfer
Phe	phenylalanine
ppm	parts per million
Ph	phenyl
pybox	2,6-bis(oxazoline)pyridine
pyr	pyridyl
pytz	2,6-bis(1,2,4-triazol-3-yl)pyridine
q	quartet
q	metal-bound water molecules, i.e. ‘hydration state’
qt	quaternary (carbon)
quin	quintet
RAFT	reversible addition fragmentation chain transfer
RCM	ring-closing metathesis
ROESY	rotational Overhauser effect spectroscopy
rt	room temperature
s	singlet
S_0	singlet ground state
S_1	singlet excited state
SEM	scanning electron microscopy
st	stretching vibration mode (IR)
τ	lifetime
t	triplet
T_1	triplet excited state
TBA	tetrabutylammonium
TEM	transmission electron microscopy
Tg	3,6,9-trioxadec-1-yl
THF	tetrahydrofuran
TMS	trimethylsilane/trimethylsilyl
TOCSY	total correlation spectroscopy
Tris	tris(hydroxymethyl)aminomethane
Trp	tryptophan
terpy	2,2':6',2''-terpyridine
UV-Vis	ultra-violet–visible

Note on publications

Much of the work presented in this thesis has been either published or submitted for publication. A brief description of the relationship between the chapters of the thesis and these articles follows:

Chapter 1, the Introduction, contains most of the material from a review entitled "*The **btp** [2,6-bis(1,2,3-triazol-4-yl)pyridine] binding motif: A new versatile terdentate ligand for applications in coordination, supramolecular and material chemistry*" co-authored with Dr Jonathan A. Kitchen and Prof Thorfinnur Gunnlaugsson, which was published by *Chemical Society Reviews* in May 2014 (*Chem. Soc. Rev.*, 2014, **43**, 5302).

Chapter 2 is based closely on work published in *Dalton Transactions* (Joseph P. Byrne, Jonathan A. Kitchen, Oxana Kotova, Vivienne Leigh, Alan P. Bell, John J. Boland, Martin Albrecht and Thorfinnur Gunnlaugsson, *Dalton Trans.*, 2014, **43**, 196; published online October 2013) with the title "*Synthesis, structural, photophysical and electrochemical studies of various d-metal complexes of **btp** [2,6-bis(1,2,3-triazol-4-yl)-pyridine] ligands that give rise to the formation of metallo-supramolecular gels*".

A significant amount of Chapter 3, namely all of the work related to the lanthanide(III)-directed self-assembly of amino acid derivatives, is published in *Inorganic Chemistry* with the title *"Lanthanide directed self-assembly of highly luminescent supramolecular 'peptide' bundles from α-amino acid functionalized 2, 6-bis (1, 2, 3-triazol-4-yl) pyridine (**btp**) ligands"* (*Inorg. Chem.*, 2015, **54**, 1426). This manuscript was co-authored with Dr Jonathan A. Kitchen, Dr Robert Peacock and Prof Thorfinnur Gunnlaugsson.

Table of Contents

1. Introduction

1.1 Supramolecular chemistry

Supramolecular chemistry encompasses the design and development of complex architectures from simpler subunits utilising various non-covalent and covalent interactions between molecules, such as hydrogen bonding, π–π stacking and metal–ligand coordination interactions.[1] In the field of supramolecular chemistry, 'self-assembly' describes processes whereby a system of pre-existing components becomes organised or forms a pattern, as a result of local interactions between the components. Self-assembly may be templated through the use of metal coordination to pre-organise components into a desired geometry.[1] Examples of this which are of particular interest are the lanthanide ions[2] and transition metals such as ruthenium[3], iridium, nickel and platinum which have various desirable properties: photophysical, magnetic and electrochemical, for example. Transition metal (*d*-block) ions display various geometries, such as tetrahedral, *e.g.* Cu(I), square planar, *e.g.* Pt(II), and octahedral, *e.g.* Ru(II), allowing for templating different kinds of self-assembly around the metal ion centre; lanthanide (*f*-block) metal ions have high coordination numbers of 9–12, allowing for more complex geometries, such as trigonal prismatic and trigonal antiprismatic.

In recent years, the Gunnlaugsson research group have developed a diverse range of unique architectures *via* lanthanide-directed self-assembly of appropriately designed ligands, such as bundles,[4] helicates,[5] half-helicates,[6] and interlocked systems[7] with dipicolinic acid derivatives, as well as luminescent Langmuir–Blodgett films[8,9] and mechanically interlocked systems including [n]catenanes,[7] which are a particularly elegant self-assembly system. Such metal-based luminescent systems have potential applications in fields including sensing[10], imaging[11], MRI contrast agents[12] as well as physical applications such as gas storage.[13] The lanthanide ions, as a result of their high coordination numbers may provide interesting template geometries, as well as fascinating photophysical properties, which will be discussed in detail in Chapter 3.

The objective of this Ph.D. project was to develop a number of novel ligands based on the **btp** [2,6-bis(1,2,3-triazol-4-yl)pyridine] framework, which can self-assemble around *d*- and *f*-metal ion centres, study these self-assembly processes in the solid-state and in solution (in the case of the lanthanide-directed systems) and understand the properties of these systems, principally with regard to their photophysical behaviour.

1.2 Terdentate ligands

Terdentate pyridine-centred heteroaromatic ligands represent a privileged class of coordination frameworks that is used in a wide range of research fields, such as in coordination chemistry and supramolecular self-assembly, in photochemical and optoelectronic applications and in the development of catalysts and magnetic materials. A variety of terdentate coordinating motifs have been reported in the literature to date; including (but not limited to) derivatives of dipicolinic acid (**dpa**), 2,6-bis(oxazoline)-pyridine (**pybox**), 2,6-di(pyrazolyl)pyridines (**bpp**), bis(1,2,4-triazolyl)pyridines (**btp′**), 2,6-bis(tetrazol-4-yl)pyridines (**pytz**), and most importantly 2,2';6',2"-terpyridine (**terpy**), Scheme 1.1. All of these have been exploited for a host of applications.

Of these, the **dpa** ligand and its derivatives are well studied by researchers such as Bünzli, Piguet and Chauvin and their co-workers, predominantly for their use in the formation of luminescent supramolecular self-assemblies with Ln(III) ions.[14-20] Chauvin *et al.* have proposed the use of $Cs_3[Ln\cdot(\mathbf{dpa}-2H)_3]$ complexes as secondary standards for luminescent quantum yield determination.[21,22] **Dpa** ligands have also been studied for their interactions with transition metal ions,[23] and in particular amide derivatives of **dpa** have been studied extensively, including for use in the formation of transition metal templated interlocked systems, such as Pd·(**1**−2H) (Scheme 1.2 shows this molecule and a related hydrogen bonding templated rotaxane **1**),[24-26] as a ligand in Cu(II)-promoted hydroxylation of THF[27] as well as coordination chemistry with Ln(III) ions.[28] Muller and co-workers reported isostructural complexes of chiral ligand **2** with a range of Ln(III) ions, all of which were luminescent. Complex $[Eu\cdot(\mathbf{2})_3]^{3+}$, Scheme 1.3, was shown to exhibit circularly polarised luminescence (CPL) as a result of its chirality.[29] Some examples of Ln(III) interactions with this motif reported in the Gunnlaugsson laboratory recently will be presented in Section 1.9 below.

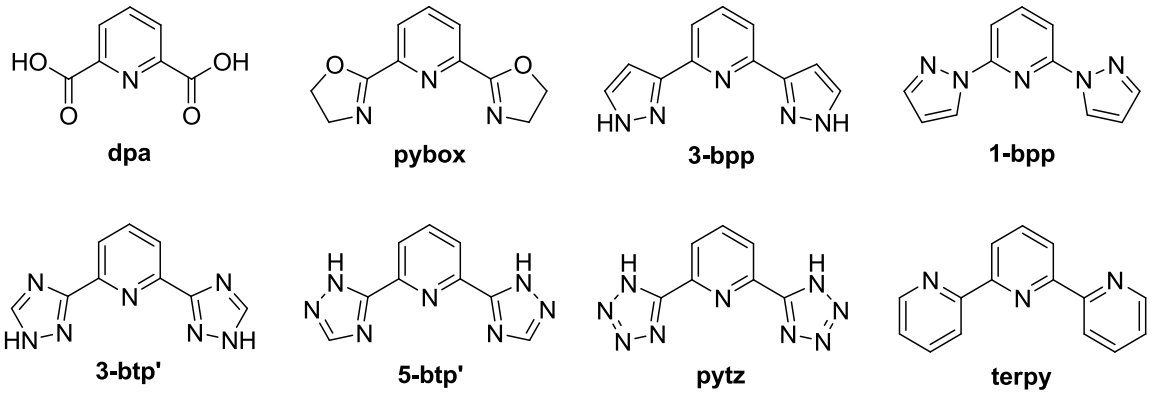

Scheme 1.1 A selection of pyridine-centred terdentate binding motifs attested in the literature.

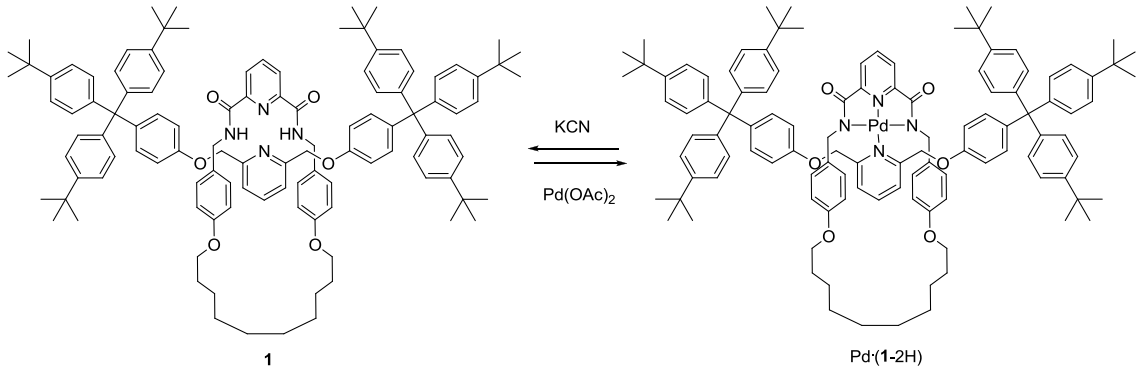

Scheme 1.2 Examples of **dpa**-containing [2]rotaxanes templated by hydrogen bonding, **1**, and Pd(II), Pd·(**1**−2H).[24–26]

Related to the **dpa** ligands are the **pybox** ligands, Figure 1.1, which can in fact be prepared from **dpa**. **Pybox** ligands have been investigated as suitable ligands in asymmetric catalysis (for a useful review of **pybox** in this context, see Desimoni *et al.*[30]). As with **dpa** these ligands have been employed as sensitisers for Ln(III) ions, including **3**, which was a very efficient sensitiser for Eu(III) and Tb(III) (Φ = 76% and 59% respectively in CH_3CN);[31] chiral ligand **4**, which formed isomorphic solid state 1:2 structures across the entire Ln(III) series;[32] and 4-pyridyl derivatised ligands **5**, containing electron-withdrawing bromo or electron-donating methoxy groups, which give Eu(III) and Tb(III) complexes with quantum efficiencies in CH_3CN of 21–36%.[33] More recently, the group of de Bettencourt-Dias has reported the preparation of a water-soluble **pybox** sensitiser for Ln(III) luminescence, **6**, forming luminescent compounds, such as [Eu·(**6**)]$(NO_3)_3$, which had an aqueous quantum yield of 30%.[34] Stability constants were determined for a number of the aforementioned compounds, with the binding of the 1:3 complex (log$\beta_{1:3}$) ranging from 12–15.

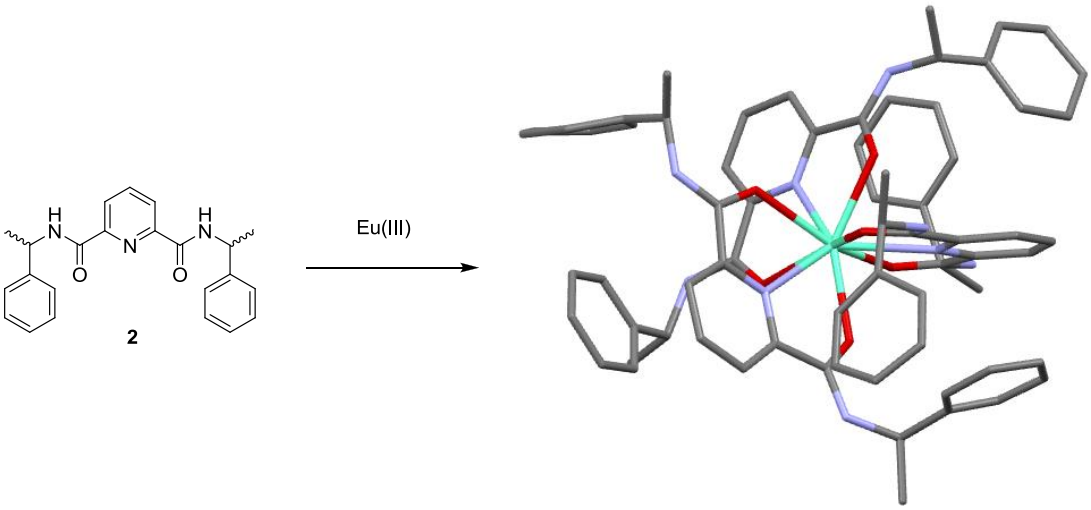

Scheme 1.3 Formation of $[Eu\cdot(\mathbf{2})_3]^{3+}$. In the molecular structure, hydrogen atoms, solvent molecules and counterions have been omitted.[29]

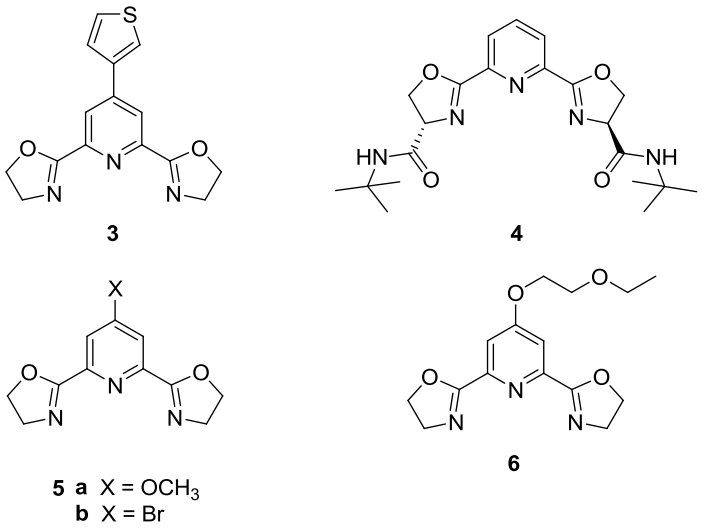

Figure 1.1 Some examples of **pybox** ligands.

Bpp ligands have been reported as synthetically versatile planar terdentate ligands.[35] Two recent reviews by Halcrow concern the coordination properties of **bpp** and related ligands, particularly with respect to their spin-crossover, self-assembly and catalytic applications.[36,37]

The **3-** and **5-btp′** ligands, Scheme 1.1, have been employed as coordination ligands for transitional metal ions with different applications in mind, *e.g.* determining structural and electronic properties of Ni(II) and Fe(II) complexes, Figure 1.2;[38] enhancing the luminescence properties of Ru(II) complexes;[39,40] forming highly emissive Pt(II) complexes and fibres, such as **7**;[41,42] as well as for the preparation of Os(II)-based light absorbing complexes, including **8**, for solar cell applications, Figure 1.3.[43] Formation of Ln(III) based complexes was also reported.[44] Structural isomers prepared from 2,6-azidopyridines have also been attested,[45-48] recently showing some promise as anion receptors.[49] The 1,2,3-triazol-4-yl structural isomers, **btp**, will be discussed at length in the following sections.

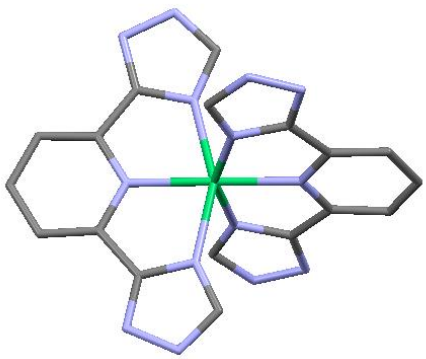

Figure 1.2 Molecular structure of $[Ni{\cdot}(\mathbf{btp'}{-}2H)_2]Cl_2{\cdot}3H_2O$. Hydrogen atoms, counterions and solvent molecules have been omitted for clarity.[38]

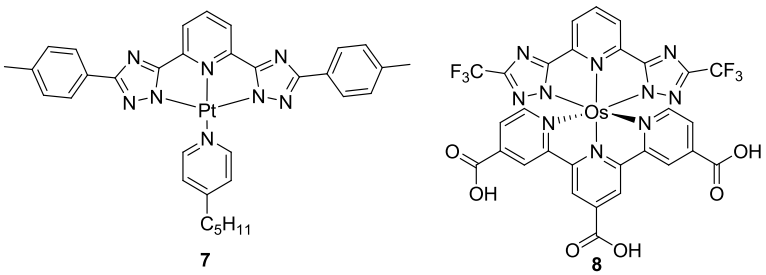

Figure 1.3 Some examples of **btp′** complexes.

Related to these ligands are the **pytz** systems, Figure 1.4, a pyridine-containing binding unit flanked by five-membered tetrazole rings at the 2- and 6-postions, which is synthesised *via* 'click' chemistry. Such ligands have been reported as potential sites of transition metal coordination, for example **9**, **10** and **11**. [50,51] In its deprotonated form, **pytz** has been used as a ligand in Pt(II) complexes, which, upon aggregation, yielded highly luminescent gels and films,[52,53] as well as 'antennae' for sensitising the excited states of Ln(III) ions.[54,55]

The final terdentate motif to be discussed here is **terpy**, which is ubiquitous in the literature, chiefly with respect to the photophysical applications of its Ru(II) complexes,[56,57] but also in other areas, such as materials research,[58] fabrication of dye-sensitised solar cells,[59] formation of metal complex wires for electron transport,[60] DNA and protein binding,[61,62] formation of metallo-supramolecular coordination polymers[63] luminescent supramolecular gels,[64] and in ion sensing.[65-67] In the Gunnlaugsson group, **terpy** ligands have been employed as an appendant arm on Ln(III)-complexed cyclen structures for the formation of mixed supramolecular *f–d* metal ion hybrids, as well as in an *f–d* metal ion hybrid strategy for the recognition of nucleic acids.[67,68]

All of the above terdentate frameworks have been explored at length, however a relatively new terdentate motif exists, which has been less explored, particularly with regard to Ln(III) self-assembly. This motif is at the core of the new molecules synthesised in the course of the work described in this thesis. The **btp** motif will now be introduced and discussed in detail in the following sections.

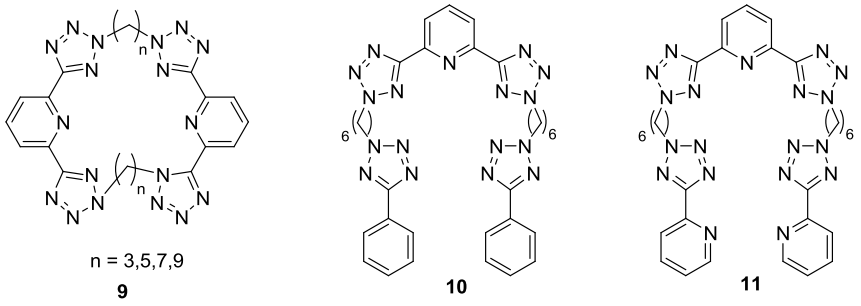

Figure 1.4 Some examples of **pytz** ligands.

1.3 A versatile new motif: 2,6-bis(triazol-4-yl)pyridine (btp)

The **btp** [†] binding motif [2,6-bis(1,2,3-triazol-4-yl)pyridine], Figure 1.5, has recently garnered increasing interest and has the potential to acts as an efficient ligand for metal ion coordination. In the following sections, a comprehensive overview of the chemistry of **btp** will be given. The material in these sections has, for the most part, been published as a review article.[69]

Btp is chiefly employed as a terdentate ligand, but also displays interactions with anions and has been demonstrated to act as a C^N^C chelate upon alkylation. Given the range of fields and the potentially wide-ranging applications that this versatile class of ligand has to offer, there has been a surprising paucity of publications reporting the synthesis of such ligands and complexes to date. To the best of our knowledge, between 2004 and 2014, only 55 articles have been published that focus on the use of **btp**-based systems, with nearly a third of those examples published since 2013. There is vast potential in the study of these systems, which has grown significantly in recent years and will certainly continue apace. Hence, given the important role this motif will play as a building block in the compounds discussed in the following chapters, and the fact that its application will certainly grow steadily in the years to come, **btp** will now be discussed comprehensively.

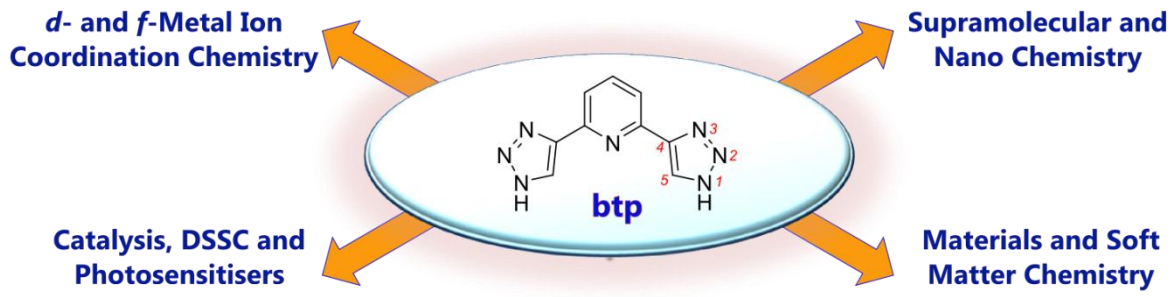

Figure 1.5 Some of the fields in which **btp** systems have been utilised. Triazole numbering convention is indicated in red.

1.3.1 Btp as a terdentate ligands

Btp is a relatively recent addition to the family of pyridine-centred terdentate ligands. Being a highly synthetically versatile building block, it complements the ligands mentioned in Section 1.2 above, with respect to shape/structure, physical, and coordination properties. However, in contrast to the aforementioned systems, **btp** ligands can be easily

[†] The **btp** motif has also been called by other names in the literature, such as '**tripy**' (by Professor Ulrich Schubert and co-workers) and '**bitapy**' (in work by Professor Toyoji Kakuchi and co-workers). The term 'clickate' has also been used by Professor Stefan Hecht and co-workers to describe such systems.

synthesised in relatively high yielding and facile reactions by exploiting Cu(I)-catalysed azide–alkyne cycloaddition (CuAAC) chemistry. Therefore the synthesis is amenable to a wide range of functional groups as will be discussed below, making derivatives of this ligand highly attractive targets for supramolecular and materials applications. Consequently, it offers a new means to generate both structurally simple coordination complexes as well as more complex and novel supramolecular self-assembled architectures, and materials.

It is worthwhile to consider how well the **btp** ligand compares to the classical examples listed above. Flood *et al.* pointed out, when first investigating the **btp** motif, that **btp′** (containing 1,2,4-triazoles, *vide supra*) had been extensively studied as a coordination ligand.[70] For instance, Vos and co-workers incorporated such a **btp′** ligand as a heteroligand into a complex of the form $[Ru(\mathbf{terpy})(\mathbf{btp'}-2H)]^{2+}$ and saw a 300-fold increase of the lifetime of this complex relative to $[Ru\cdot(\mathbf{terpy})_2]^{2+}$ as a result of raising the ^{3}MC states following the replacement of the weak field **terpy** ligand by a strong σ-donor ligand.[39]

It has also been shown that the **btp** motif has very similar binding properties to **terpy**, with similar bond angles and lengths determined for Ru(II) complexes by X-ray diffraction; as illustrated in Figure 1.6. Therefore study of systems such as these is highly valuable; there is still a need in coordination chemistry to explore the development of novel ligands as **terpy** analogues, for a variety of applications. Given the fact that the **btp** ligand can be readily derivatised at the 1-position of the triazole units, this ligand is an excellent candidate for such endeavours.[71,72] This is further fuelled by the rapid developments that have occurred within the field of metallo-supramolecular chemistry. Here, most architectural shapes and topologies have been accessed; hence, the focus has increasingly moved towards developing new methods for functionalising ligands, and synthesis that is modular, facile and high-yielding. The CuAAC reaction, yielding 1,2,3-triazoles, is an obvious candidate which fulfils these criteria. Being central to the synthesis of the structures presented in this thesis, some of the key features of this reaction are highlighted in the following section. The development of triazole-based structures using 'click' chemistry has recently been reviewed in detail by Schubert *et al.* and more detailed discussion than will be embarked upon here about its application can be found in that comprehensive review.[73]

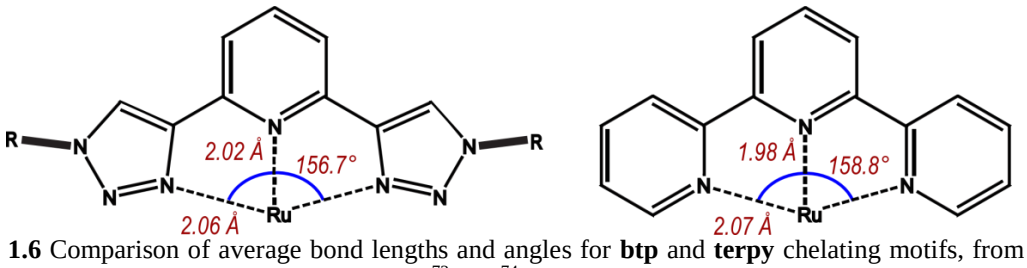

Figure 1.6 Comparison of average bond lengths and angles for **btp** and **terpy** chelating motifs, from X-ray crystal structure analysis. Data from references [72] and [74] respectively.

1.3.2 1,2,3-Triazoles and the CuAAC 'click' reaction

A challenge for the synthesis of metal-coordinating compounds, identified by Schibli *et al.* in a recent perspective article, is to discover strategies which can give access to wide ranges of ligands with reduced synthetic complexity and preparation, allowing modular synthesis of diverse metal-chelators.[75] Clearly, 'click' reactions are ideal candidates to fulfil these criteria.

'Click chemistry' is a term first coined by Sharpless and co-workers[76,77] to describe modular, high-yielding reactions which are ideally insensitive to the presence of oxygen and water. The azide–alkyne 1,3-dipolar cycloaddition (or the 1,3-Huisgen reaction[78]) was identified as the 'cream of the crop' of 'click' reactions. Despite this reaction being first reported in 1893[79], the non-selective formation of both 1,4- and 1,5-substituted 1,2,3-triazoles led to minimal applications of these compounds. This setback was largely overcome by the development of the CuAAC reaction[77,80] which is a regioselective, high yielding and tolerant reaction, exclusively giving 1,4-disubstituted 1,2,3-triazole products.[81,82] Both the azide and alkyne groups, which form the substrates for the CuAAC reaction, have a wide range of advantages. Both are stable in the presence of nucleophiles, electrophiles, solvents and molecular oxygen, which are common under standard reaction conditions. In addition, both functionalities can be easily introduced into organic compounds,[83] the azide upon reaction of sodium azide with organic halides, or by converting primary amines into azides (allowing for the use of chiral amines in synthesis), while the alkyne moiety can be introduced, for instance, *via* Sonogashira coupling reactions.

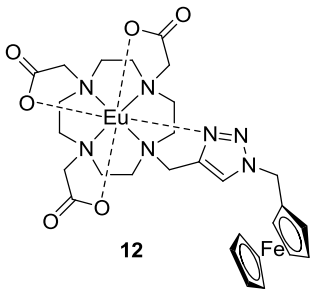

12

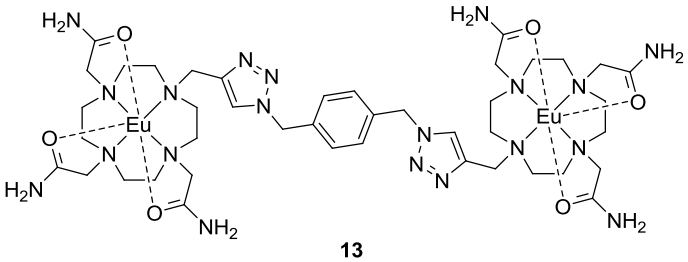

13

The majority of reported uses of the CuAAC reaction have not taken advantage of the coordinative abilities of the 1,2,3-triazole motif, rather employing it as a linker between other functional building blocks, such as their use in coupling Ln(III) cyclen complexes to redox-active motifs such as ferrocene, **12**,[84] carbohydrate building blocks[85] or another Ln(III) cyclen complex, **13**,[86] an area of research developed by Faulkner *et al.*, Hudson and co-workers and the Gunnlaugsson research group, respectively, for application in sensing and imaging. The 'active metal template' strategy was pioneered by David Leigh and co-workers; CuAAC was utilised in this approach by Goldup, Watkinson and co-workers of [2]catenanes, where the Cu(I) ion simultaneously templates two molecules in place and also closes one molecule into a macrocycle *via* the formation of a 1,2,3-triazole,[87,88] or [2]rotaxanes, such as **14**·H and **14**·Cu, where the 1,2,3-triazole–containing 'axle' is formed *in situ* by Cu(I) localised within a macrocyle, Figure 1.7.[88-90] The CuAAC reaction has also been used to 'click' modifications onto the 4-pyridyl position of terdentate ligands, such as **dpa** derivatives in order to synthesise metal chelators, such as **15**,[91] form Ln(III) luminescent probes, such as **16**,[92] and to graft such probes onto silica nanoparticles.[93]

There are many review articles covering this area, such as the use of the CuAAC reaction in construction of dendrimers and polymeric architectures,[94] modification of peptidomimetic oligomers,[95] and construction of higher order interlocked supramolecular structures.[96] Schibli *et al.* described the installation of triazolyl metal chelating sites into molecules in a single step using the CuAAC reaction as the 'click to chelate' approach.[97] It is worth noting that due to its relative planarity and strong dipole moment, the 1,2,3-triazole has a physicochemical resemblance to the amide bond, explaining its use as a linker in biological, biochemical and carbohydrate research,[98] as well as interest in 1,2,3-triazole hydrogen bonding behaviour in anion supramolecular chemistry, which has been reviewed by Hua and Flood.[99]

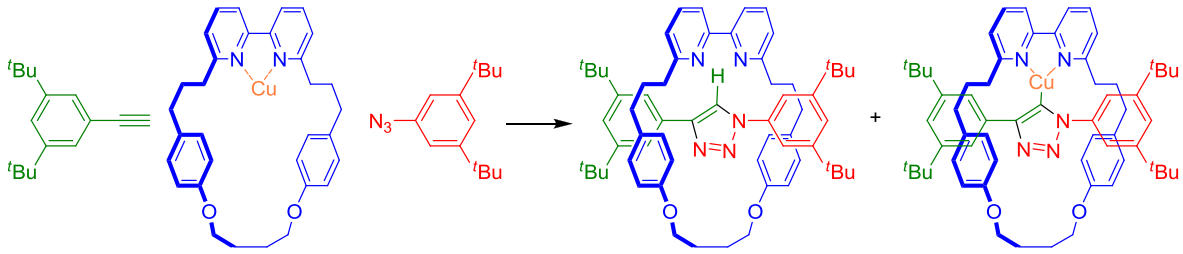

Figure 1.7 Schematic representation of the formation of [2]rotaxanes **14**·H and **14**·Cu by 'active metal template' CuAAC reaction.[87]

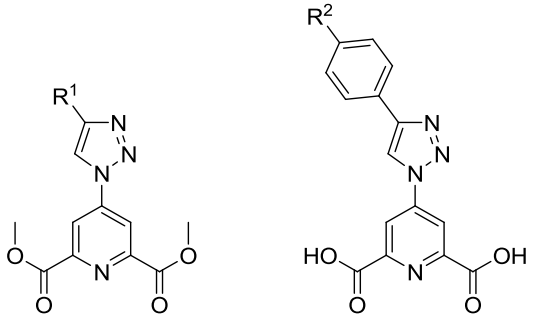

15 a $R^1 = C_2H_4OH$
b $R^1 = C_2H_4Br$
c $R^1 = Ph$

16 a $R^2 = H$
b $R^2 = OCH_3$
c $R^2 = NO_2$

Although there have been a number of recent overviews of metal-chelating systems synthesised using the CuAAC reaction,[75,100,101] as a result of the rapid and recent explosion of interest in the terdentate **btp** motif, only limited examples of ligands containing this motif have been included.[70,82,102,103] The objective of the review article upon which the following sections are based[69] was, as stated above, to address this deficit, detailing the chemistry and the applications of **btp** ligands which have been reported in the literature over the last few years.

1.3.3 Preparation and properties of the btp motif

The **btp** motif combines the favourable features of a pyridine-centred terdentate binding site with the coordinating ability of the 1,2,3-triazole, along with its ease of preparation *via* CuAAC chemistry. The first instance in the literature of the **btp** motif, ligand **17**, was presented in work by Fokin and co-workers in 2004 as part of a library of 1,2,3-triazole–containing ligands designed to stabilise Cu(I) and increase the rate of the CuAAC reaction,[104] the very reaction that was used to prepare these ligands (a number of 1,2,3-triazole–containing ligands had previously been reported for stabilising various metal ions for catalysis[75]). The benzyl-substituted ligand **17** was reported as facilitating increased yields in the reaction, however, **TBTA** performed better. In the same year, another **btp**-containing structure **18**, reported by Abarca and co-workers, was designed to act as a polynitrogenated potential helicating ligand.[105] The proposed structure of a fused aromatic system, however, was not synthesised *via* the CuAAC reaction (*vide infra*).

In 2007, Flood and co-workers reported the interactions of **btp**-containing ligands **19** with metal ions, including Fe(II), Ru(II) and Eu(III), and showed that that these ions could form stable coordination compounds with **19**.[70] This research demonstrated that synthesis of the **btp** based ligand provided easy access to a class of terdentate ligands, possessing a **terpy**-like coordination environment, but with distinctive differences such as the broad

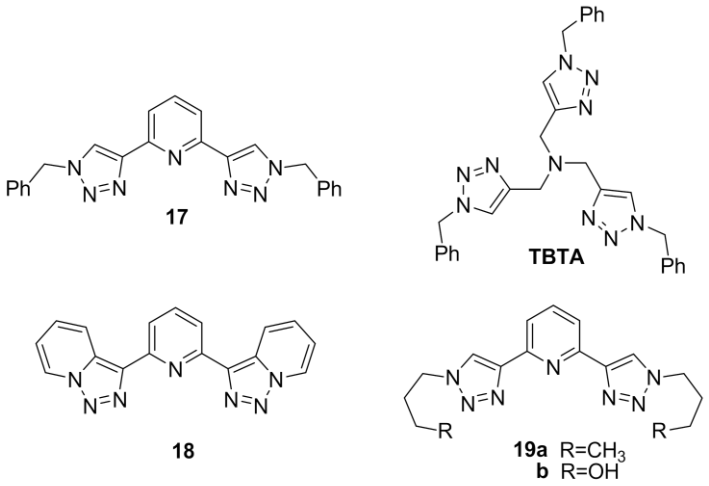

scope of functionalisation available *via* the CuAAC reaction and size differential between the heterocyclic rings. Hence, **btp** provides a promising method of introducing **terpy**-like functionality to macromolecules because of the excellent feasibility of azide substitution and 'click' chemistry.[71]

1.3.3.1 Synthetic strategies

As discussed above, the CuAAC reaction is versatile and tolerant to a wide range of substrates and solvents. Reported syntheses of **btp**-containing molecules are almost all performed by undertaking such a reaction or a variant of it, with a range of substrates and solvent systems. Generally, the synthesis is achieved upon reaction of an organic azide with a 2,6-diethynylpyridine (either protected or not, as discussed below) in the presence of Cu(I), obtained from either a Cu(I) salt (*e.g.* CuI) but more commonly from a Cu(II) salt reduced *in situ*, (*e.g.* $CuSO_4 \cdot 5H_2O$). Fletcher *et al.* found a one-pot deprotection/'click' synthesis, such as that shown in Scheme 1.4 was ideal for formation of ligands such as **20** in near quantitative yields from protected alkyne **21**.[106] The scope of azides and alkynes used as substrates for these reactions are discussed in the following sections, as well as methods for obtaining **btp** ligands derivatised at the 4-pyridyl position and asymmetrical ligands. The versatility of triazolyl substituents reported is remarkable, with alkyl chains of various lengths, aryl groups and even motifs such as ferrocenes[107] and porphyrins[82] being introduced. **Btp** ligands have even been attached directly to surfaces, such as polystyrene,[71] and bound to TiO_2 surfaces;[108] clearly demonstrating the wide scope such ligands have in modern coordination and supramolecular chemistry.

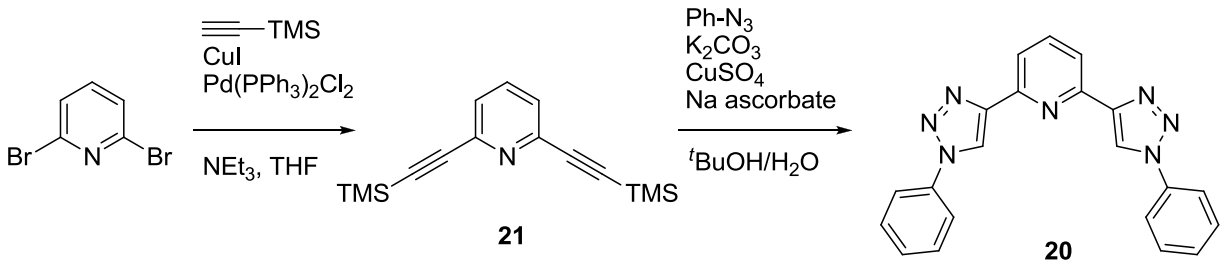

Scheme 1.4. CuAAC synthesis of ligand **20** *via* the one-pot deprotection/'click' paradigm.[106]

1.3.3.2 Azides

The chemistry of azides is well-established and an endless number of variants can be synthesised according to the requirements of the research. Azide compounds, however, particularly low-weight organic azides, can be hazardous to handle when isolated, due to the potential explosive nature of compounds where $(N_C + N_O)/N_N \leq 3$ (N_X being the number of a given atom X in the molecule) and hence appropriate care should be taken. A number of research groups have, therefore, developed protocols to generate the azide substrate for the CuAAC reaction *in situ* from the halide precursor and use it immediately. For example, Crowley *et al.* have reported a number of compounds, such as **17**, **20**, **22** and **23**, that can be synthesised by a 'one pot multi-component CuAAC "click" approach'.[107] Here, the authors have taken advantage of the convenience of introducing azide functionality into organic halides upon stirring with sodium azide in order to introduce a diverse range of groups, such as alkyl chains, ferrocenyl groups and aryl groups. While compounds **17**, **22** and **23** can all be prepared under the same conditions and at room temperature in a DMF–water (4:1) mixture, the aryl azide **20** required more forcing conditions by refluxing in an aqueous ethanol mixture.

1.3.3.3 Alkynes

Of necessity, to form **btp** systems, the alkyne substrate for these reactions must be some derivative of 2,6-diethynylpyridine. For most **btp** ligands discussed herein, which do not contain a substituent in the 4-position of the pyridine ring, the 2,6-diethynylpyridine substrate was prepared upon performing a Sonogashira coupling between 2,6-dibromopyridine and (trimethylsilyl)ethyne furnishing the protected species **21** (other silylethynes, such as triisopropylsilyl groups, have also been reported[82]). The protected

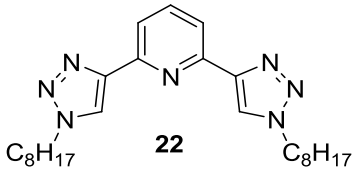

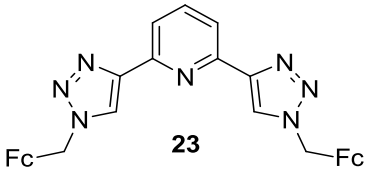

alkyne can either be deprotected before use (treating with a base, *e.g.* K_2CO_3,[106,109] KF,[110] or KOH[102,111]) or used directly in the CuAAC reaction, as shown in Scheme 1.4.

Fletcher *et al.* reported a one-pot deprotection/'click' paradigm for the synthesis of a range of triazole-ligands, which provided near quantitative and selective transformation of trimethylsilyl-protected terminal alkynes and organic azides to the desired 1,2,3-triazole-containing products.[106] K_2CO_3 was included with the substrates in the reaction and the *in situ* deprotection step was reported to be the rate-determining step, since only triazole products and trimethylsilyl-protected alkynes were observed in reaction mixtures, never free terminal alkyne intermediates. This paradigm removes the necessity for purification of the intermediate terminal alkyne, and hence, in the pursuit of new **btp**-derivatives, it would be expected that this methodology would be incorporated into an optimised synthetic approach.

1.3.3.4 Solvents and workup

Another great advantage of 'click' reactions is that they can be carried out under aqueous conditions, which is convenient, cheap and environmentally preferable. As such, it is no surprise that the vast majority of CuAAC reactions reported for the synthesis of **btp**-ligands were carried out in aqueous media. Solvent choice has relatively little effect on yields, and it appears to be a matter of preference and, sometimes, solubility of starting materials that determines the choice of solvent systems. Alcohols like ethanol[102,110,112,113] and *tert*-butyl alcohol[106,109,111] mixed with water are most common in the literature, while the use of DMSO (with[114] or without[115] water), THF,[71] CH_3CN[116] and DMF[81,107] is also attested.

Reviewing the literature shows a few common approaches to purifying the **btp** products. If the product precipitates from the reaction mixture it is simply isolated by filtration and purified by chromatography, otherwise the reaction mixture was concentrated and then purified upon use of chromatography. Alternatively, the treatment of the crude reaction mixture with a basic solution of an EDTA salt, in order to scavenge Cu(I) ions, has also been demonstrated, resulting in isolation of the desired product upon extraction into organic solvent and, if necessary, purification by chromatography.

1.3.3.5 Functionalising the 4-pyridyl position

Chandrasekar and Chandrasekhar described a method for functionalising **btp** motifs in the 4-pyridyl position in their work on developing ditopic ligands **24**, Scheme 1.5.[117] This

strategy used citrazinic acid as a starting point,[118] which is brominated and converted into a methyl ester before introducing the alkyne functionality using the Sonogashira coupling discussed above and subsequently deprotecting the alkyne. The alkyne was used as a substrate for a CuAAC reaction, yielding **25**; saponification of the ester with LiOH gave **26**. Sequential conversion of the carboxylic acid into an acyl azide followed by thermal Curtius rearrangement and succeeding hydrolysis of the trifluoroacetamide provided the amino derivative **27** in good yield. Diazotisation of this compound, followed by reaction with KI produced the iodide derivative **28**. The resulting iodide was reacted with either bis(pinacolato)diboron to give directly-linked ditopic **btp** ligand **24a**, or aryl boronic acids to introduce mono- and diphenyl linkers, giving **24b–c**. Hecht and co-workers introduced an ester functionality in a different way: transforming citrizinic acid into a dichloro-derivative before introducing a 3,6,9-trioxadec-1-yl (Tg) ester functionality into the 4-pyridyl position of ligands **29** as shown in Scheme 1.6.[82]

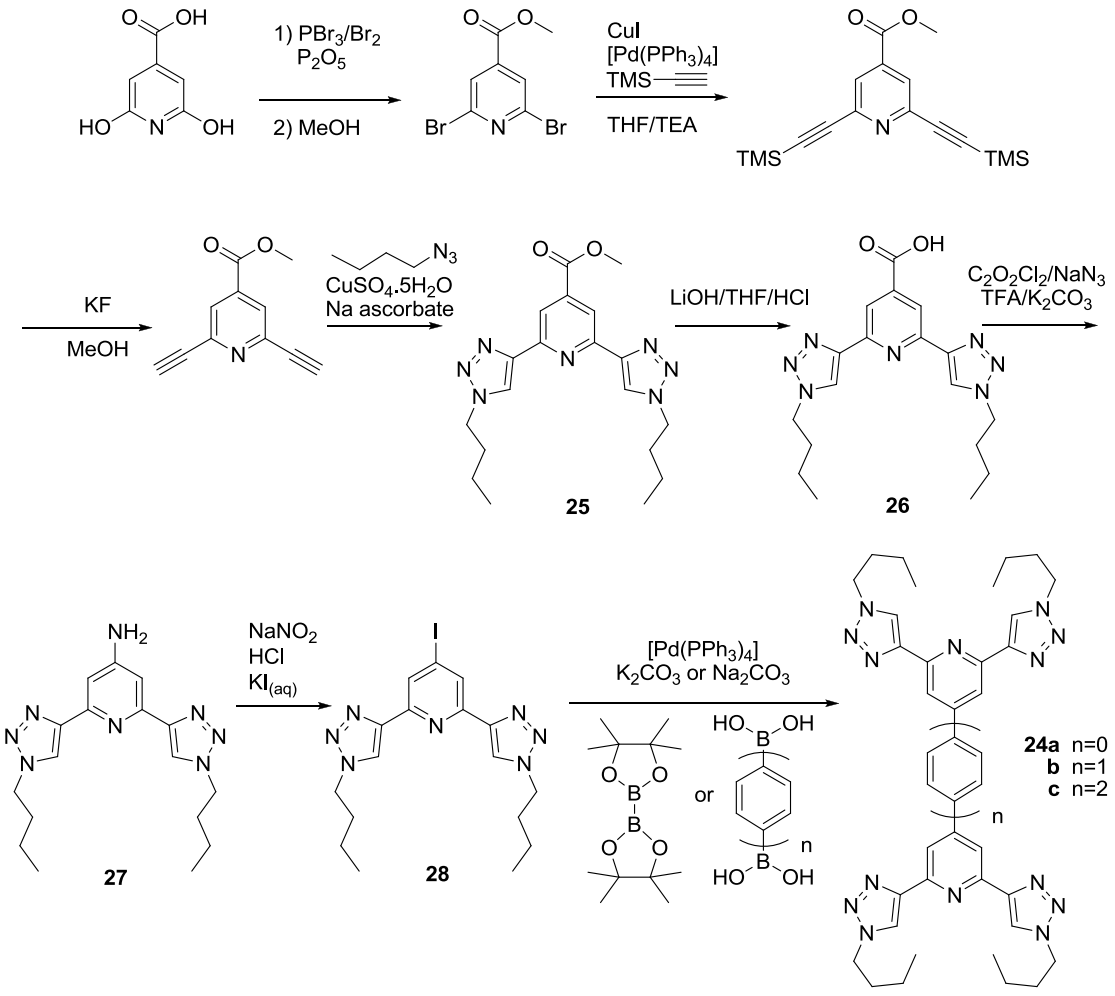

Scheme 1.5 Synthesis of ditopic 'back-to-back' ligands **24a–c**.[117]

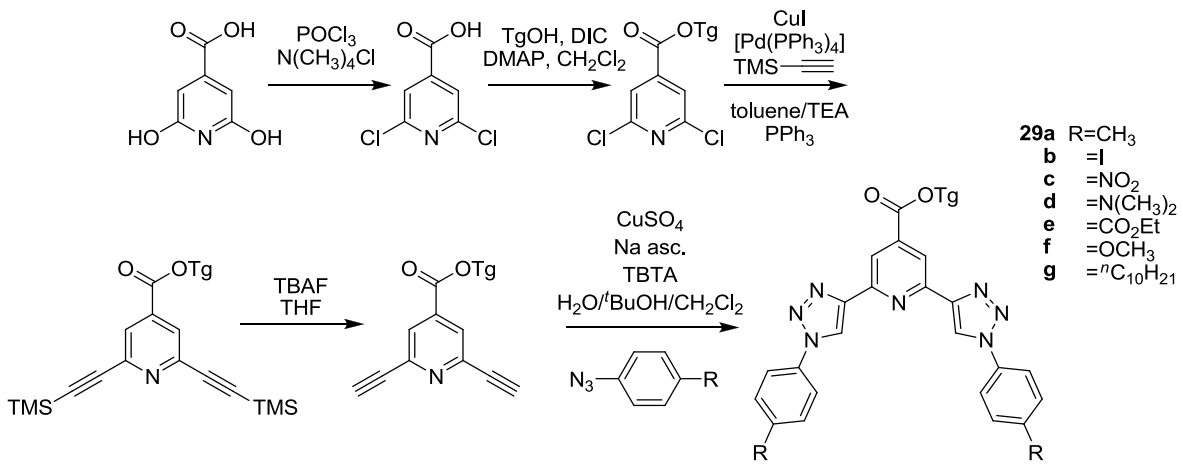

Scheme 1.6 Synthesis of ligands **29** from citrazinic acid.[82]

An alternative approach for introducing a substituent onto the pyridyl ring, Scheme 1.7, has exploited the ease of nitration of 2,6-dibromopyridine-*N*-oxide and allowed the introduction of ether chains to ligands such as **30**.[82,103,119] Finally, Schubert and co-workers have demonstrated a strategy, using a selective Sonogashira coupling to 2,4,6-tribromopyridine, a general scheme of which is shown in Scheme 1.8, to introduce alkyne-containing linkers into the 4-position of **31**, yielding ditopic ligands like **32**.[110,120,121]

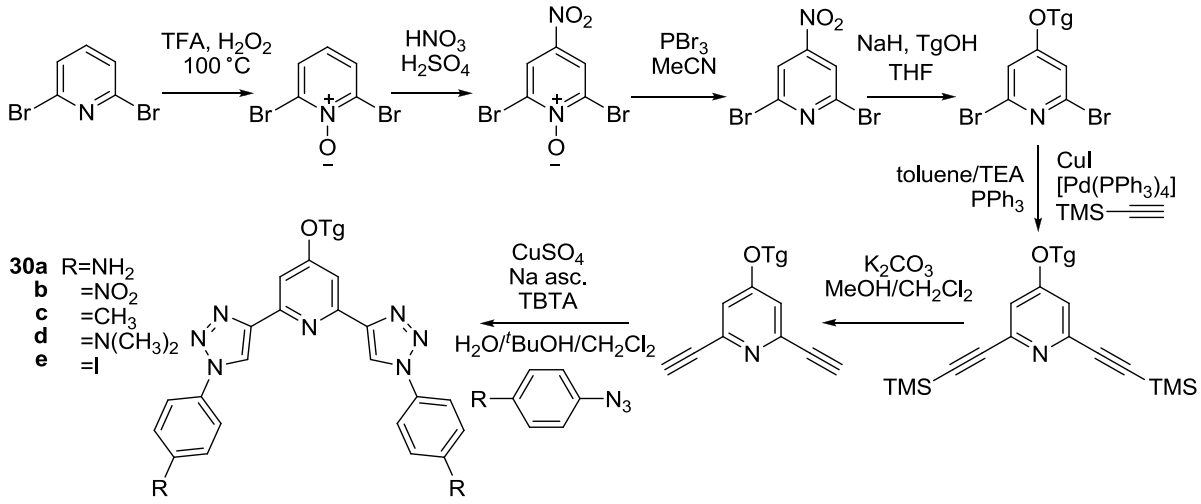

Scheme 1.7 Ether functionalisation yielding ligands **30**.[82]

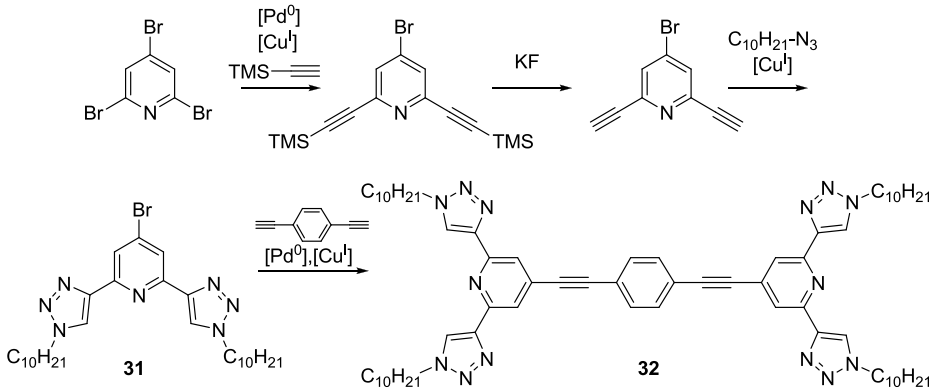

Scheme 1.8 Functionalisation at the 4-pyridyl position with alkyne-containing linker, yielding ligand **32**.

1.3.3.6 Stepwise 'click' reactions and asymmetric btp ligands

Several examples of **btp** ligands have been reported to date where it has been necessary to synthesise the **btp** core in a stepwise fashion, using several 'click' reactions. An example of such a ligand is that of Flood and co-workers, who prepared the 'triazolophane' macrocycles **33** for encapsulation of halide ions, Scheme 1.9.[102] This stepwise method avoids the possible polymerisation reactions that could occur in a one-pot synthesis. This approach required mono-deprotection of **21** by stirring for 30 minutes with KOH before purifying the desired compound by column chromatography. This type of stepwise preparation has also been employed by Hecht and co-workers to prepare asymmetric **btp** compounds, as shown in Scheme 1.10. Here, a 4-substituted 2,6-dibromopyridine initially underwent a Sonogashira coupling with triisopropylsilyl-ethyne (TIPS-ethyne), after which one TIPS group could be selectively removed upon reaction with TBAF, yielding **34** with one alkyne available to the 'click' reaction with a particular azide.

Subsequent removal of the other TIPS group allowed for substitution of a different azide, leading to **btp** ligand **35** with non-identical 'arms'.[82] A similar approach was reported to

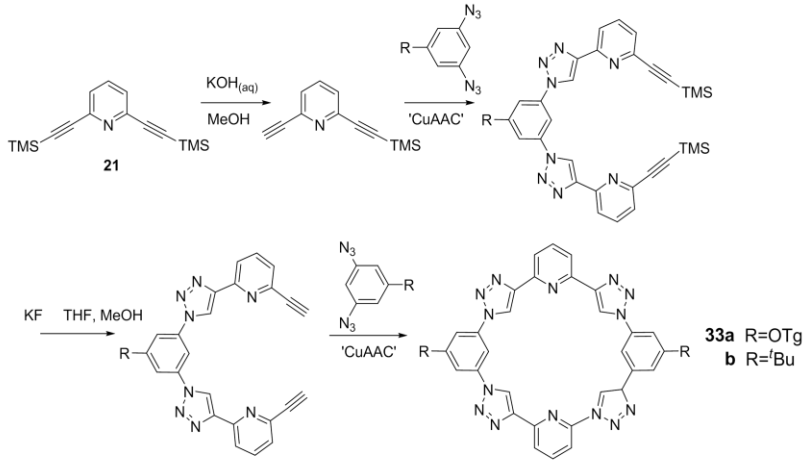

Scheme 1.9 Synthesis of triazolophanes **33** from **21** *via* stepwise 'click' reactions.[102]

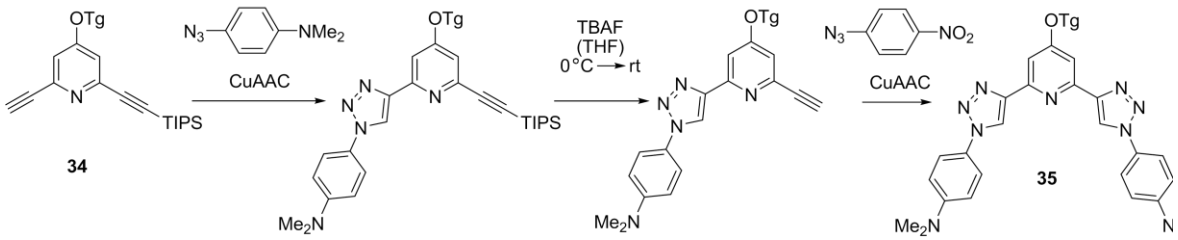

Scheme 1.10 Synthesis of asymmetric **btp** ligand **35**, from **34**.[82]

produce helically folding poly-**btp** compounds **36** by bidirectional growth with repetitive sequences of coupling monomers followed by deprotection of terminal alkynes.[103]

1.3.3.7 A non-'click' synthetic strategy

Only five molecules containing the **btp** motif have been reported which were not synthesised *via* the CuAAC reaction. Work published by Abarca and co-workers showed the unexpected synthesis of a symmetrical ligand **18** upon reaction of ketone **37** with tosylhydrazine in NaOH, due to triazolopyridine–pyridine ring rearrangement as shown in Scheme 1.11.[105,122,123] Other ligands containing varied fused ring systems were prepared in a similar manner from different ketones.[123]

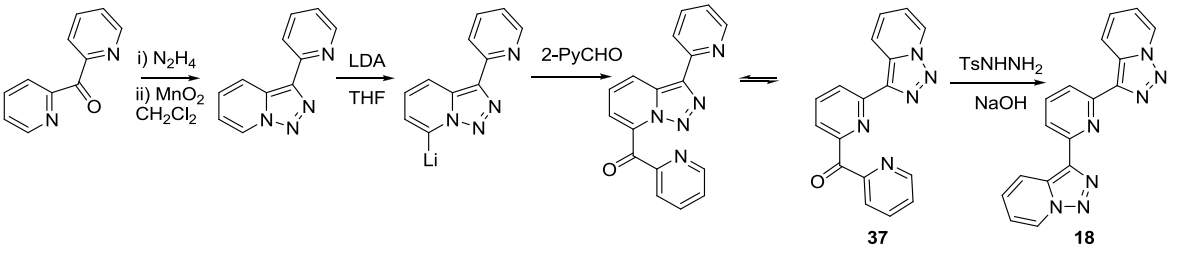

Scheme 1.11 Non-'click' synthetic approach to a **btp**-containing fused system **18**.[105]

1.3.3.8 Conformational switching of btp with cations and anions

The C–C bond connecting the pyridyl and triazolyl moieties of **btp** allows for free rotation, however, preference has been shown for different conformations under various conditions, as demonstrated in Figure 1.8. Coordination of this terdentate motif to metal ions results in a dramatic conformational switching in these ligands; the free ligands display the triazole moieties *anti-anti* (or '*kinked*') with respect to the pyridyl nitrogen atom. This is evidenced in the solid state by various X-ray crystal structures in the literature.[107,111,124-126] Due to favourable electrostatic interactions the *anti-anti* conformation of the **btp** core dominates in solution at neutral pH, while repulsion between nitrogen lone pairs destabilises the alternative. NOE NMR experiments have shown that interactions between pyridyl and

adjacent triazolyl protons are practically non-existent, but upon protonation, medium strength interactions are observed between these protons.[82] In the presence of a cation, such as metal ions or a proton, the *syn-syn* (or '*extended*') conformation is observed. This is again borne out in the solid state by a host of X-ray crystal structures of metal complexes.[70,72,82,107] This sensitivity to the presence of cations can be utilised to create nanoswitches sensitive to either metal ions[116] or pH changes.[111,127] In contrast to this, coordination compounds with anions all display **btp** in the *anti-anti* conformation;[102,103] the ability of the acidic triazole CH to hydrogen bond with anions being largely responsible for this conformation. Specific systems featuring this conformation will be discussed in Section 1.5.

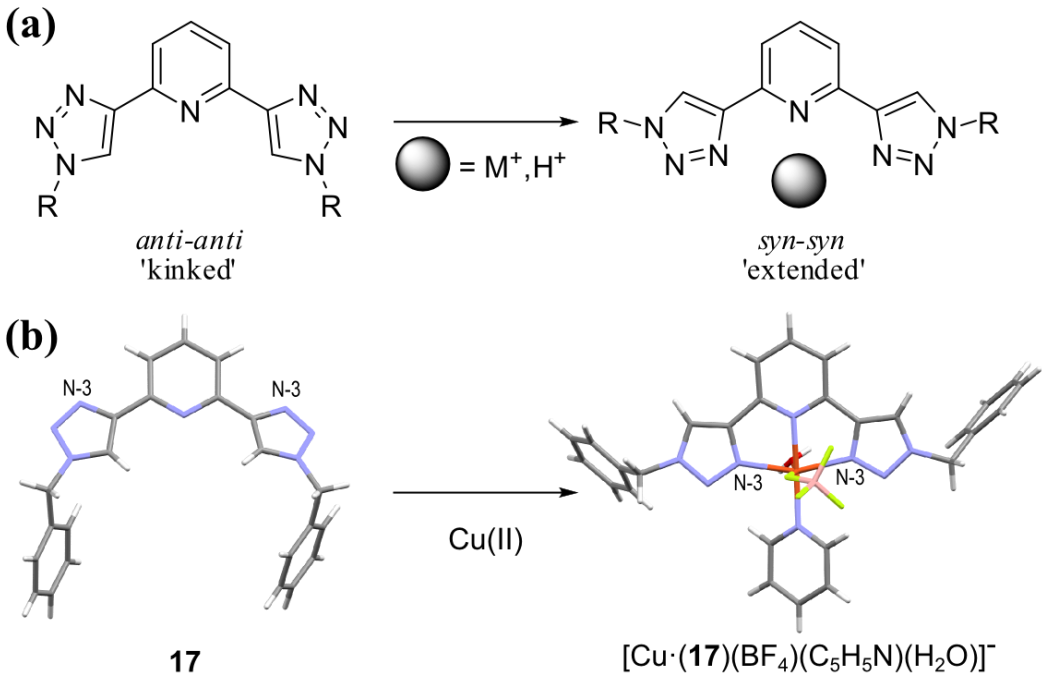

Figure 1.8 (a) Demonstration of conformational switching of the **btp** motif; **(b)** ligand **17** and its Cu(II) complex shown as examples of this switching.[111]

1.4 Metal coordination chemistry of btp

The coordination of **btp**-containing ligands has been reported with a range of transition metal and lanthanide ions. An overview of this metal coordination behaviour is given below, metal by metal. Interesting characteristics and properties of these systems, such as photophysical, magnetic, electrochemical, structural, sensing and materials applications, are also detailed.

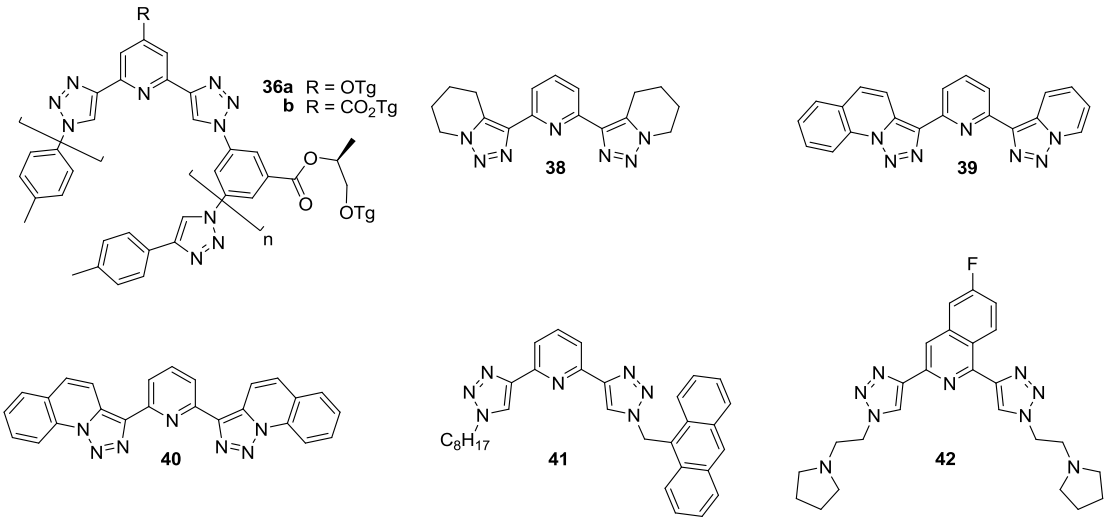

1.4.1 Copper

As discussed previously (Section 1.3.3), the first **btp** ligand synthesised, **17**, was employed as a stabilizing ligand for Cu(I) to increase the rate of the CuAAC reaction.[104] Sankararaman *et al.* obtained a crystal structure of this ligand and also its Cu(II) complex [Cu·(**17**)(BF_4)(C_5H_5N)(H_2O)](BF_4) (see Figure 1.8). This work demonstrated the two different conformations adopted by the ligand when isolated (*anti-anti*) and when coordinating a metal (*syn-syn*), as discussed in Section 1.3.3.8. The geometry about the Cu(II) ion was described as distorted octahedral with the pyridine and triazole moieties nearly in the same plane (with a dihedral angle of 7.5(2)° between the two triazole rings). It was also shown that ligand luminescence was quenched upon complexation.[111]

Crowley and co-workers reported [Cu·(**17**)Cl_2].[107] The complex adopted distorted square pyramidyl geometry and the authors noted with interest that the structure was very similar to that reported for an analogous **terpy** complex.[128]

Ligand **18**, its derivative **38** and related compounds **39** and **40**, prepared by Abarca and co-workers, were all fluorescent. Upon addition of Cu(II) to solutions of these compounds in a 98:2 ethanol–water mixture, the emission was dramatically quenched, allowing these compounds to be considered as 'switch-off' chemosensors for Cu(II).[123] The X-ray crystal structure of [Cu·(**18**)(H_2O)$_2$(BF_4)]BF_4·2H_2O was analysed in detail in order to understand the role that π-π stacking might play in magnetic exchange between paramagnetic Cu(II) centres, as well as contributions from ferromagnetic coupling along hydrogen bonds. Thermal variation of $\chi_m T$ (molar magnetic susceptibility per Cu(II) ion times temperature) yielded data which suggested the compound presented weak ferromagnetic coupling. It

was concluded that magnetic exchange through the hydrogen bonds was the most likely pathway.[129]

Both Zhu and Dash briefly mentioned Cu(II) quenching the florescence emission of ligands **22**, **41**[130] as well as compound **42**.[131] However, these systems will be discussed in more detail below in relation to their fluorescence emission enhancement upon interaction with Zn(II).

1.4.2 Zinc

The interactions of the fused-ring ligand **18** with Zn(II) have been studied.[122] Both $[Zn\cdot(\mathbf{18})]^{2+}$ and $[Zn\cdot(\mathbf{18})_2]^{2+}$ stoichiometries were observed by mass spectrometry and suitable crystals for X-ray diffraction studies were obtained of the bis-ligand complex, Figure 1.9(a). The addition of $Zn(ClO_4)_2$ to solutions of the fluorescent ligand in a 98:2 ethanol–water solvent mixture showed significant chelation enhancement of fluorescence. This was in contrast to the quenching effects observed upon addition of other divalent transition metal ions, such as Cu(II) as mentioned above. This Zn(II) complex was examined as a suitable fluorescence chemosensor for monovalent anions (*vide infra*, Section 1.5). Similar chelation enhancement of fluorescence was also observed for unsaturated ligand **38** and, to a lesser extent, for compounds **39** and **40**.[123] It is worth noting that the behaviour of these systems with anions has not been investigated to the best of our knowledge.

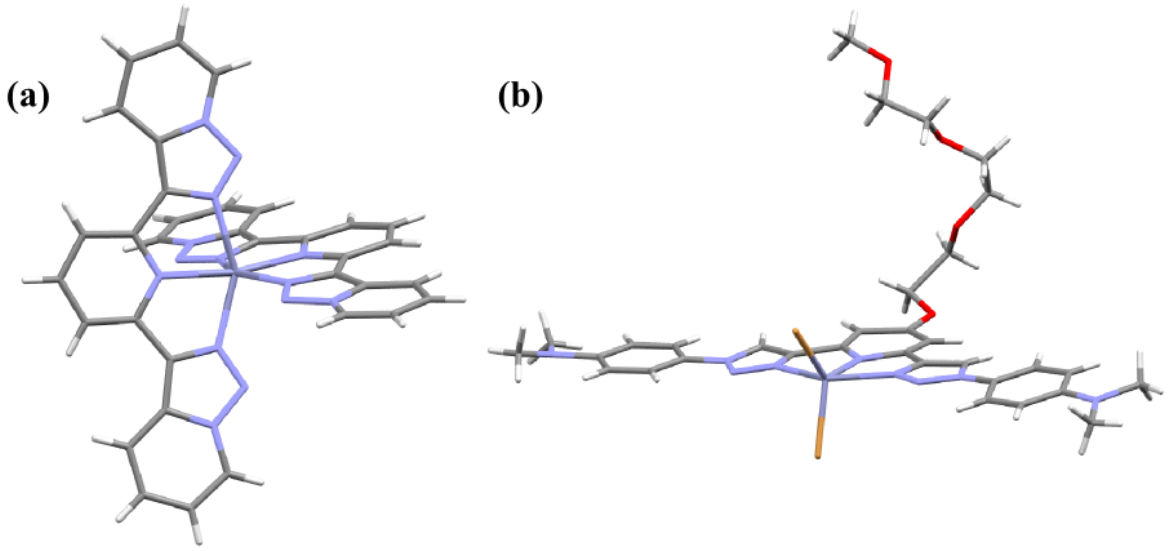

Figure 1.9 (a) Zn(II) complex with **18**. Solvent molecules and counterions have been omitted for clarity[122]. (b) Molecular structure of $[Zn\cdot(\mathbf{30a})Br_2]$. Co-crystallised $ZnBr_2$ molecules and solvent molecules have been omitted for clarity.

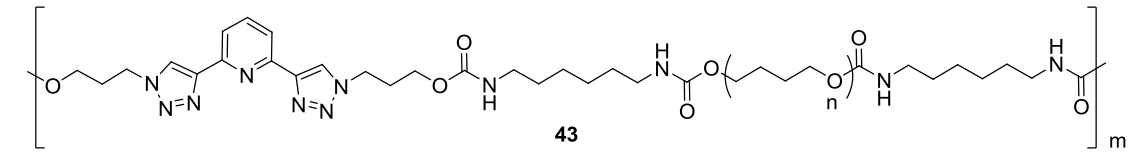

43

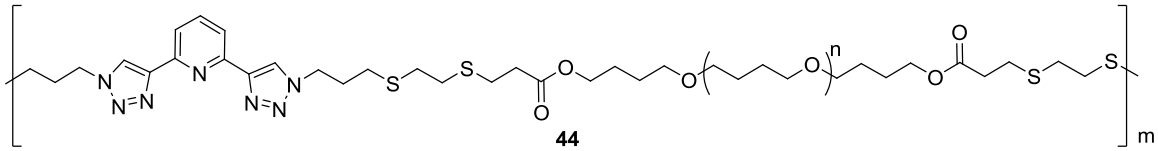

44

Hecht and co-workers published the molecular structure of the monoleptic Zn(II) complex [Zn·(**30a**)Br_2], see Figure 1.9(b), in which the Zn(II) coordination sphere was described as being a distorted square pyramidal geometry.[126] In separate work, Meudtner and Hecht briefly reported the formation of metallo-supramolecularly crosslinked gels from **btp**-containing polymers **36** upon addition of Zn(II).[116] However, this work has not, to the best of our knowledge, been followed up by the authors. However, Yuan *et al.* have produced gels upon addition of stoichiometric amounts of $Zn(CF_3SO_3)_2$ solutions to different **btp**-containing polymers **43** and **44** which demonstrated fluorescence under UV light irradiation and remarkable self-healing properties.[132-134] These gels showed little change in emission as a function of temperature, but displayed potential for chemosensing, since a number of chelating chemicals tested (*e.g.* **bipy**) caused deconstruction of the gel. These systems will be discussed in more detail in Section 1.7.6.

Zn(II) is well-established as an important biological analyte, with triazole-containing fluorescent sensors for this ion having been studied by Watkinson and co-workers.[135] Zhu and co-workers are interested in the development of fluorescent ligands for the determination of intracellular Zn(II) concentrations and as such investigated ligand **22**. In contrast to the monoleptic system formed under similar conditions for ligand **30a**, dileptic complex [Zn·(**22**)$_2$][$ZnCl_4$] was isolated from an equimolar mixture of ligand and $ZnCl_2$. The authors suggested that the lack of aryl 'arms' (and hence, π–π interactions) made the dileptic system favourable in the solid state for this octyl-substituted **btp** ligand. The ligand displayed the characteristic conformational change upon formation of the complex, which adopted a distorted octahedral geometry in the X-ray crystal structure. Isothermal titration calorimetry (ITC) and ^{1}H NMR studies suggested the formation of strong dileptic complexes of **22** in solution, with the monoleptic complex only being formed at higher Zn(II) concentrations.[130]

Coordination of Zn(II) to asymmetric anthryl ligand **41** caused a 10 nm red shift in the absorbance band assigned to the **btp** centre of the ligand indicating formation of the metal

complex.[130] Here, the anthryl emission was quenched upon addition of Zn(II) as a result of photoinduced electron transfer (PET) from the photoexcited anthryl group to the Zn(II)-bound **btp**; this conclusion was supported by frontier molecular orbital calculations and cyclic voltammetry (CV) measurements.

Dash and co-workers designed the water soluble pyrrolidinyl-appended **btp** ligand **42**, which could detect metal ions.[131] A wide range of metal ions were screened, but, as for the examples discussed above, addition of Zn(II) was shown to cause a significant 'turn-on' fluorescence response upon formation of a 1:1 complex; Zn(II) giving the greatest enhancement (20-fold) of all the ions tested. The sensor gave 3.2-fold selectivity for Zn(II) over Cd(II), an important result for biological sensing applications, as many Zn(II) sensors often show a high affinity for Cd(II). Moreover the sensor was found to be cell-membrane permeable and responsive to Zn(II) within living cells, such as the human melanoma cell line A375. These results, in conjunction with the quenching response of **42** to the presence of Fe(II) (*vide infra*), were combined to fabricate a molecular logic gate mimic, which will be discussed in more detail in Section 1.7.3.

1.4.3 Silver

Significant efforts have been made by both Crowley[81,107] and Schubert[112] to prepare Ag(I)-complexes of **btp**-containing ligands. The coordination connectivity of Ag(I) ions with **17** in the solid state has been elucidated by X-ray crystallography. The results were somewhat unexpected. Elemental analysis indicated that complexes with a 1:1 metal:ligand stoichiometry were formed, with the complex crystallising as a tetrameric tetrasilver cation containing Ag(I) ions which were bridged by various pyridyl and triazolyl nitrogen atoms in the ligand, as shown in Figure 1.10, with each Ag(I) ion adopting a distorted tetrahedral geometry.[107]

The complexation of Ag(I) with the related ligand **45** was also studied by elemental analysis and mass spectrometry. Elemental analysis suggested that this ligand adopts a 1:1 metal:ligand stoichiometry, however the ESI+ MS spectrum also contains a weak *m/z* peak corresponding to the $[Ag_3{\cdot}(\mathbf{45})_2](SbF_6)^{2+}$ ion, indicating that in solution a Ag(I) ion can bind within the central cavity between the various triazole units of the structure. Such behaviour has also been observed for the analogous 2,6-bis-(1,2,3-triazol-4-yl)benzene ligand, **btb**.[81]

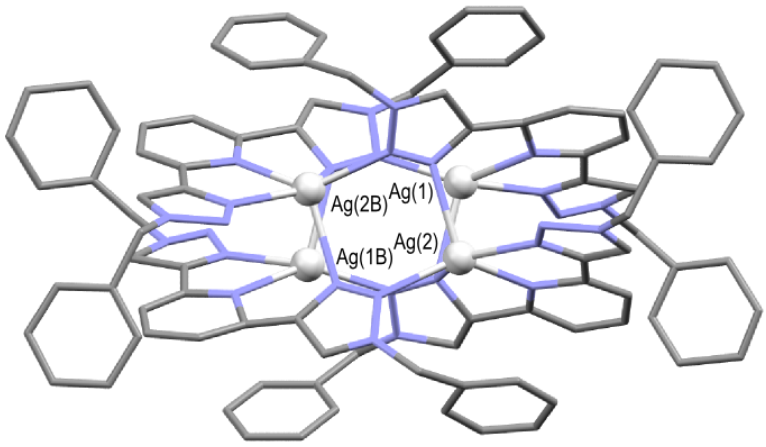

Figure 1.10 Molecular structure of tetrasilver cation formed with ligand **17**. Hydrogen atoms, solvent molecules and counterions have been omitted for clarity. Ag(I) atoms are labelled.[107]

1.4.4 Platinum

With the aim of developing optoelectronically applicable film-forming metallopolymers, Schubert and co-workers reported the ability of ditopic ligand **46** to form metallopolymers with the Pt(II) ion, as shown in Scheme 1.12. The racemic and branched alkyl chains in the ligand were selected to aid solubility of the planar Pt(II)-complexes and deter intermolecular π-stacking.[121] The optoelectronic properties of the metallopolymer were examined, with the complex showing a broad and intense MLCT transition in the visible range, which was red-shifted, and more intense than the individual ligand. No Pt(II)-centered emission was detectable. It was suggested that electronic communication might be possible between Pt(II) centres due to the organometallic Pt(II)-acetylene bond, which leads to ligand contribution to the HOMO.

Yam and co-workers reported the synthesis of a series of chloroplatinum(II) complexes [Pt·(**btp**)Cl]X (X=Cl^-, PF_6^-, $CF_3SO_3^-$) with ligands **17**, **19a**, **22**, **20** and **47a–c**, as well as a range of related luminescent alkynylplatinum(II) complexes. The chloroplatinum(II) complexes were found to be non-luminescent in solution at room temperature, however, the alkynylplatinum(II) complexes were observed to be luminescent, displaying large

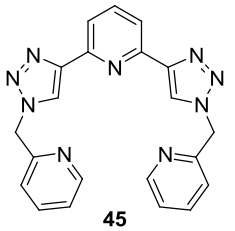

45

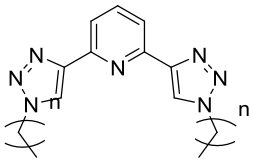

47a n=11
b n=13
c n=17

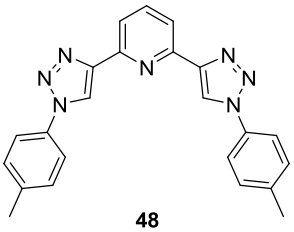

48

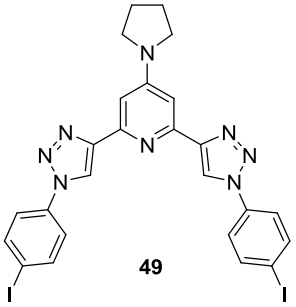

49

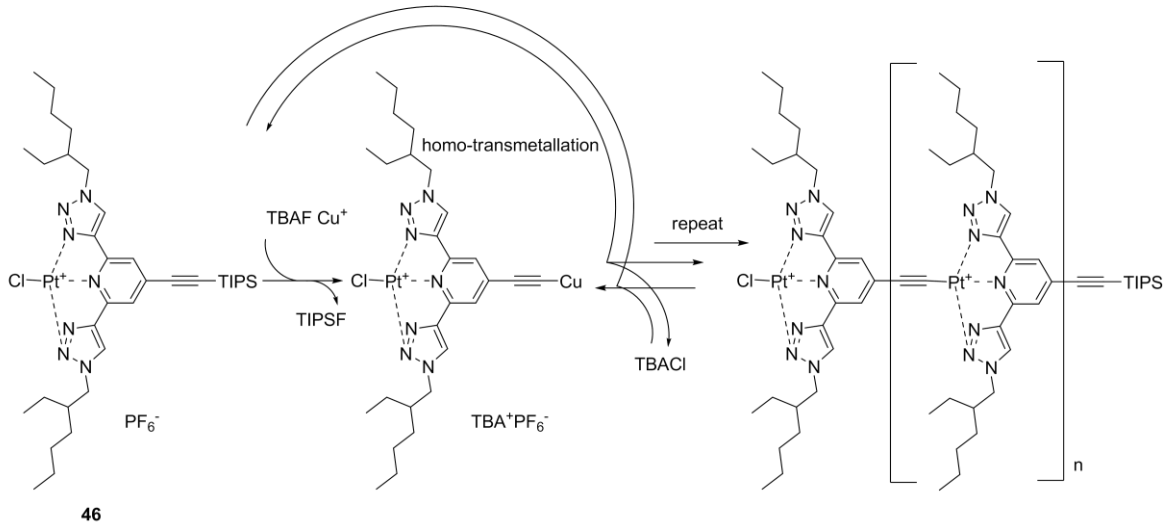

Scheme 1.12 Preparation of Pt(II) metallopolymer of **46**.[121]

Stokes shifts, microsecond lifetimes and an insensitivity to the various alkynyl substituents utilised, leading to the suggestion that emission originated from a [d_{z^2}(Pt)→π*(**btp**)] MLCT excited state. Electrochemical measurements of these complexes were also reported. Amphiphilic properties of complexes [Pt·(**47a**)Cl]Cl and [Pt·(**47a**)(C≡C–C_6H_5)]Cl were studied, showing the ability of these species to form stable and reproducible Langmuir-Blodgett films at the air-water interface.[136]

1.4.5 Palladium

Tolyl derivative **48** was developed as a model ligand for polymer synthesis of Pd(II)-containing polymers (discussed in more detail in Section 1.7.5 below). The crystal structure of this ligand displayed a crystallographic C_2 axis along the centre of the pyridine motif. Reaction with [Pd·(cod)Cl_2] yielded [Pd·(**48**)Cl][Pd(DMSO)Cl_3], the only Pd(II) complex of a discrete **btp** system in the literature, of which a crystal structure was also obtained.[137]

1.4.6 Lead

Zhu and co-workers investigated the coordination chemistry of two ligands **22** and **41** with Pb(II).[130] ^{1}H NMR titrations of **22** with the metal ion showed the likely formation of the 3:1 complex with chemical shifts suggesting a stronger binding of Pb(II) to the pyridyl nitrogen atoms than the triazolyl, perhaps in a bidentate manner. Up to 0.5 equivalents of Pb(II), the data suggests that a 2:1 complex was formed with a tridentate binding mode. The behaviour of anthryl ligand **41** with Pb(II) was similar to that discussed above for

Zn(II) (Section 1.4.2), with shifts in the absorbance band assigned to the **btp** centre and a quenching of anthryl emission, probably through an intramolecular PET pathway.

1.4.7 Iron

Iron complexes of **btp** ligands would be expected to attract significant interest for their magnetic properties, given that spin-crossover behaviour of other terdentate systems has been extensively investigated.[138-141] In fact, only one research group has investigated the magnetic behaviour of such systems, with others reporting coordination behaviour, effects of the metal ion on emission intensity and electrochemical properties. These systems will now be discussed.

Flood and co-workers have briefly demonstrated the capability of ligands **19a** and **19b** to coordinate Fe(II).[70] The UV-Vis spectrum of $[Fe\cdot(\mathbf{19b})_2](PF_6)_2$ displayed both MLCT and LC (ligand-centred) bands that were blue-shifted with respect to the **terpy** analogue; an effect which is attributed to the accessibility of higher energy excited states and the LUMO of the **btp** core being higher energy than that of **terpy**. The CV measurements confirmed this hypothesis; showing that the primary differences to the analogous **terpy** complexes were indeed associated with the ligand. CV measurements were also used to observe an increased quasi-reversible oxidation band in this complex upon addition of water. This behaviour was not observed with $[Fe\cdot(\mathbf{terpy})_2]^{2+}$ and was explained by the sterically unhindered 1,2,3-triazoles allowing for the formation of a heptadentate Fe(III) complex following oxidation, with a bound water molecule.

Upon addition of Fe(II) into aqueous solutions of sensor **42** (discussed above, Section 1.4.2), the fluorescence of the ligand was quenched, whereas addition of Fe(III) caused negligible changes in the ligand fluorescence.[131] Quenching was proposed to occur through a PET or EET (excitation energy transfer) mechanism. This 'switch-off' quenching response was also observed in live cells *in vitro*, allowing for imaging of intracellular Fe(II). The 'switch-off' response observed was coupled with the 'switch-on' response in the presence of Zn(II) for the fabrication of a molecular logic gate, which will be discussed further in Section 1.7.3.

Hecht, Limberg *et al.* produced the iron complex of **30a** in order to investigate the ligand field strength of this ligand and compare it with other terdentate ligands. The shorter than expected Fe–N bonds observed in the X-ray crystal structure at 116 K, which is shown in Figure 1.11, pointed to a low-spin state iron ion with an average length of 1.93 Å, compared to typical lengths between 2.1 and 2.2 Å for high-spin complexes.[82] This

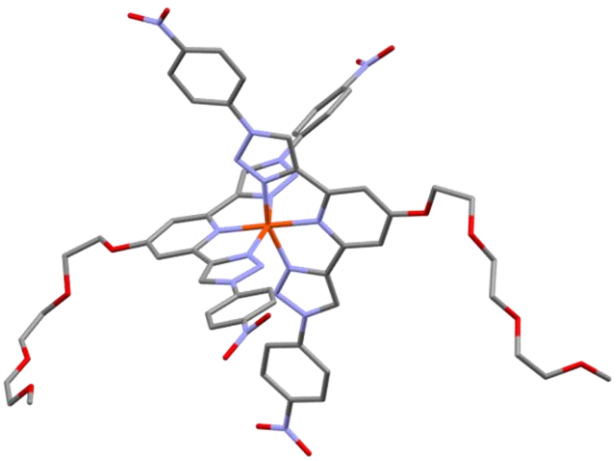

Figure 1.11 Molecular structure of [Fe(**30b**)$_2$](CF$_3$SO$_3$)$_2$. Only one cystallographically independent molecule is shown; hydrogens, counterions and solvent molecules have been omitted for clarity**.**

complex showed no thermochromic effects upon warming to room temperature. It was concluded that this ligand's field strength was higher than that of **bpp** and as such, more comparable to that of **terpy**.

Further investigations were undertaken into the magnetic properties of Fe(II)-complexes of **btp**-ligands **30b–c** and **49**.[126] When [Fe·(**30b**)$_2$](CF$_3$SO$_3$)$_2$ was heated to 200 °C, the red-brown powder changed its colour to yellow. The red-brown colour was not re-established upon cooling (even at very low temperatures over several days), but could be regenerated by dissolving the complex in CH$_3$CN. Measurement of χ_mT over the range of 5–400 K showed a partially reversible hysteresis in magnetic susceptibility between 325 and 400 K. Mössbauer spectra of the red-brown powdered sample were measured at a range of temperatures, and the data showed the predominance of the low-spin state from 7–295 K, while spectra of the yellow (heated) powder showed the predominance of the high-spin state. The conversion was claimed to be irreversible. Similar behaviour was noted for other **btp** ligands, but with variation in properties dependent upon substituents, with increasing donor character of the ligand decreasing the ligand-field strength.

Hecht and Meudtner also briefly reported the instantaneous formation of metallo-supramolecularly cross-linked gels of **36** upon addition of Fe(II) and other metal ions, but this will be discussed in Section 1.7.6.[116]

1.4.8 Ruthenium

Ru(II) is by far the most abundant transition metal which has been investigated with respect to its coordination chemistry with **btp**-containing ligands, with particular interest arising from the photophysical and electrochemical properties of these

complexes.[70,71,106,110,112,113,115,120,121,126,142,143] Flood and co-workers showed that Ru(II) forms stable coordination compounds with **19b**. X-ray crystal crystallography showed a 1:2 metal:ligand stoichiometry, with the ligands adopting a distorted octahedral geometry, as demonstrated in Figure 1.12(a) for complex [Ru·(**19b**)$_2$](PF$_6$)$_2$. The lack of steric interactions was thought to be responsible for these heightened distortions from octahedral symmetry. The effects of coordination on the electronic structure of this ligand also were investigated using UV-Vis absorption spectroscopy, where it was shown that the ligand-centred band was blue-shifted ~10 nm upon complexation to Ru(II). When compared to the UV-Vis spectrum of the **terpy** complex, both the MLCT and LC bands were blue-shifted but displayed similar band shapes. The optical properties of these complexes were concluded to be similar to their **terpy** analogues, and further studies utilising CV demonstrated that higher energy excited states were accessible as a result of the LUMO of the **btp** core being at a higher energy than that of **terpy**.[70]

A difficulty inherent to Ru(II) polypyridyl complexes is that tris-bidentate complexes generally show long excited-state lifetimes, but display isomerism, which may be inconvenient. In contrast, bis-terdentate complexes allow formation of linear assemblies without isomerism, but seldom have such advantageous long-lived excited states, due to radiationless deactivation of ^{3}MLCT state through the ^{3}MC state. Variation from the standard **terpy** ligands used in such research may overcome this challenge.[112,144,145] In a combined experimental and computational study of terdentate CuAAC-derived Ru(II) photosensitisers, the properties of a range of complexes including [Ru·(**50**)(**terpy**)](PF$_6$)$_2$ and [Ru·(**51**)(**terpy**)](PF$_6$) (where **51** is a cyclometallating **btb** ligand) were compared.[142] From X-ray crystal structure analysis, it was noted that Ru–N$_{pyr}$ bond lengths were shortened upon cyclometallation. Moreover, DFT calculations suggested that the HOMO of **50** was less destabilised, with almost pure Ru d_{xz} character. In contrast, cyclometallation by the phenyl moiety in ligand **51** destabilised the orbitals that are populated in the ^{3}MC states, which are relevant to the radiationless deactivation which is responsible for most [Ru·(**btp**)$_2$]$^{2+}$ complexes being non-luminescent. A photophysical model was presented claiming that while for the complex of **51,** ^{3}MC-ground state intersystem crossing occurs at high energies, for the **btp** ligand, this energy is at low levels and therefore readily accessible. Another approach for reducing radiationless deactivation of Ru(II)–**btp** complexes involves the use of cyclometallating triazolium derivatives, which will be discussed in Section 1.6.

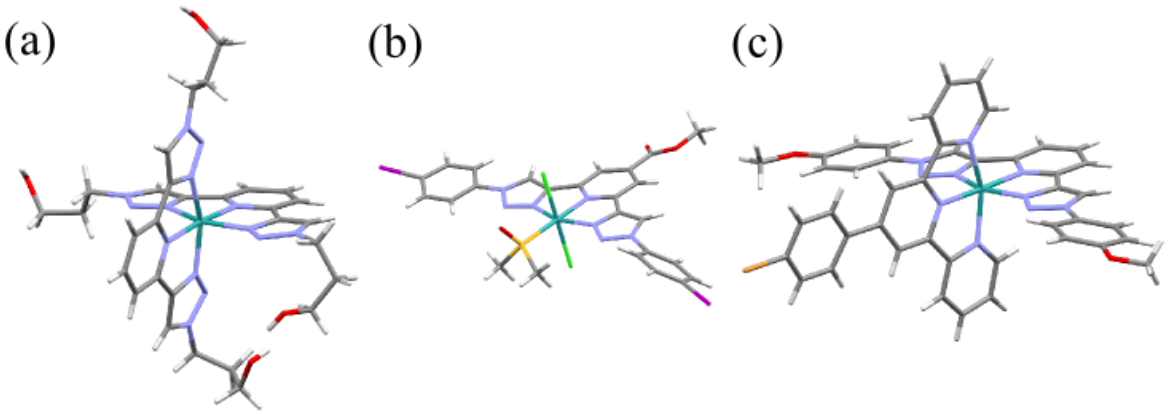

Figure 1.12 (a) Molecular structure of [Ru·(**19b**)$_2$](PF$_6$)$_2$ showing distorted octahedral geometry. Counterions have been omitted for clarity[70]; **(b)** Molecular structure of 1:1 Ru:**btp** complex [Ru·(**52**)Cl$_2$(DMSO)]. Co-crystallised molecule of unbound ligand **52** has been omitted for clarity.[126]; **(c)** Molecular structure of heteroleptic complex [Ru·(**55a**)(4-Br-ϕ-**terpy**)](PF$_6$)$_2$. Solvent molecules and counterions have been omitted for clarity.[113]

Hecht and co-workers synthesised a variety of **btp** ligands with different substituents and monitored the effects these variations in the ligand environment had on the properties of the complexes, including a number of Ru(II) complexes.[126] Substituents represented included electron-withdrawing and donating groups at both the terminal aryl moieties and central pyridine core. The potential applications of complexes with a labile ligand at one coordination site available to bind a substrate for activation during catalysis, for example, led Hecht and co-workers to synthesise a range of 1:1 Ru(II) complexes with **30c–d, 52** and **53**. Only a crystal structure of [Ru·(**52**)Cl$_2$(DMSO)] was obtained, and showed the ligand binding in a tridentate meridional mode, with two chloride ligands and a DMSO molecule (binding through the sulfur atom) occupying the remaining positions in the distorted octahedral geometry, as demonstrated in Figure 1.12(b).[126]

Hecht and co-workers have also described the synthesis of coordinatively saturated complexes of the form [Ru·(**btp**)$_2$](PF$_6$)$_2$ with ligands **30c, 49, 52** and **53,** as well as a heteroleptic system [Ru·(**30c**)(**30d**)](PF$_6$)$_2$, prepared by treatment of [Ru·(**30c**)Cl$_2$(DMSO)] with **30d** in the presence of NH_4PF_6. CV measurements of the four homoleptic complexes showed broadly similar behaviour. Qualitatively, however, the one-electron oxidation waves were strongly shifted depending on the attached ligand, particularly the electron-donating or -withdrawing properties of the substituent in the 4-pyridyl position of the **btp** ligand. The Ru(II) oxidation potential shifted over a range of more than 0.60 V with the range of ligands studied, from 0.58 V for **49**, with an electron-donating pyrrolidyl substituent to 1.19 V for **52** where the methyl ester substituent is electron-withdrawing. Variation of the 4-pyridyl substituents of these **btp** ligands was thus clearly shown to have

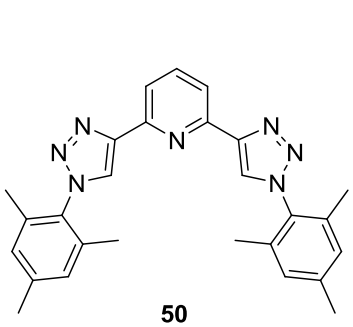

50

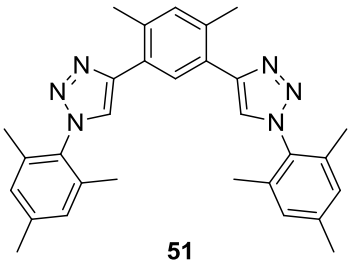

51

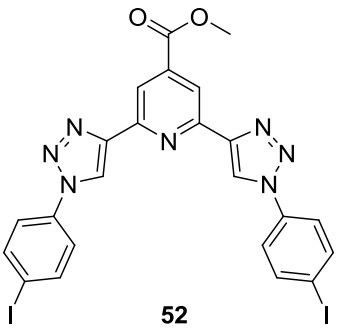

52

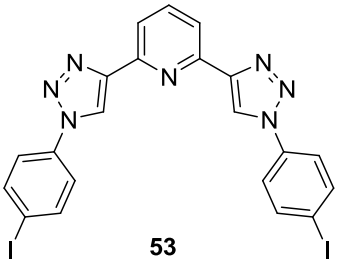

53

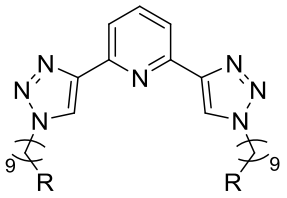

54a R=CH_3
b R=C_2H_4OH

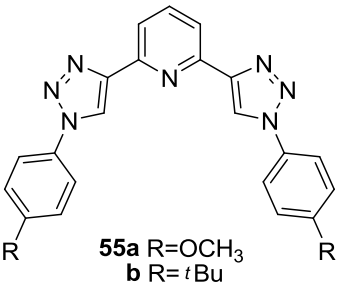

55a R=OCH_3
b R=*t*Bu

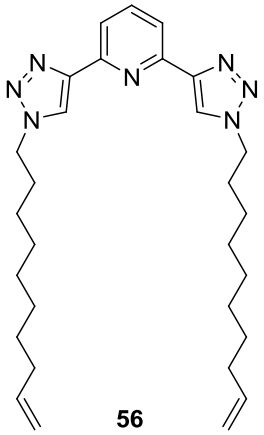

56

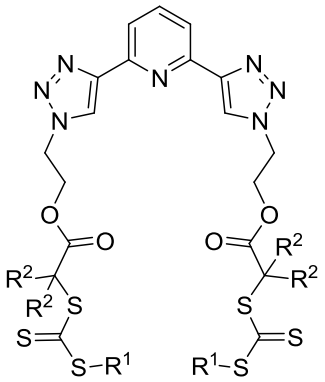

58a R^1=$C_{12}H_{25}$, R^2=CH_3
b R^1=CH_2Ph, R^2=H

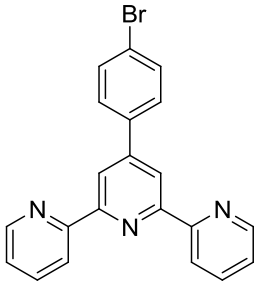

4-Br-ϕ-**terpy**

a direct effect on the redox properties of the derived complexes, which is potentially predictable and tuneable. Furthermore, plotting the half-wave potentials of these complexes against the Hammett σ_{para} values of the substituents[146] on the pyridyl moiety showed a clear linear relationship, further implying that predictable tuning of redox properties is possible by careful choice of ligand substituents. The effect of the 'arms' of the ligand (*i.e.* the *N*-triazolyl substituents) was observed to be minimal, with the complex of **30c** (which has a methyl terminal group in its 'arms') fitting the same linear relationship as all of the iodo-containing compounds. This property theoretically allows for robust functionalisation of a product in this position after a desirable oxidation potential has been achieved, *e.g.* for multifunctional systems.

In recent years, Schubert and various co-workers have published prolifically in the field of Ru(II) coordination by **btp**-containing ligands, mostly with regard to the preparation of heteroleptic Ru(II)-complexes of **terpy** and **btp** ligands,[112,113,115] and Ru(II) complexes containing π-conjugated ditopic **btp** ligands[110,120,121]. A range of heteroleptic systems, [Ru·(**54a–b**)(**terpy**)]$(PF_6)_2$, [Ru·(**54a–b**)(4-Br-ϕ-**terpy**)]$(PF_6)_2$ and [Ru·(**55a–b**)(4-Br-ϕ-**terpy**)]$(PF_6)_2$ were prepared and studied, with homoleptic complexes [Ru·(**54a**)$_2$]$(PF_6)_2$ and [Ru·(**terpy**)$_2$]$(PF_6)_2$ used as reference systems with which properties were compared.

Single crystals suitable for X-ray diffraction studies were obtained of [Ru·(**55a**)(4-Br-ϕ-**terpy**)]$(PF_6)_2$, with the structure shown in Figure 1.12(c). Compared to the homoleptic *bis*-**btp** complex, the interligand angle of the middle nitrogen atoms was shown to be closer to 180° (178.37° as opposed to 175°) and hence closer to the ideal undistorted octahedral geometry. The overall conclusion of this structural comparison was that the difference in coordination geometry when a **terpy** ligand is replaced with a **btp** ligand is only very small, hence from a coordination chemistry point of view, **btp** can be considered an analogue for **terpy** (*c.f.* discussion above).[113,115]

The photophysical properties of the heteroleptic complexes were found to be between those of the reference homoleptic complexes. Complex [Ru·(**54a**)(**terpy**)]$(PF_6)_2$ displayed an intense MLCT band at a wavelength (432 nm) exactly half way between the MLCT bands shown by the two homoleptic complexes, while the LC band was split in a distinctive fashion with two maxima corresponding to the peaks observed for the individual homoleptic complexes, indicating that the two ligands were electronically different in the Ru(II) coordination sphere. The blue-shift in the MLCT as **terpy** ligands were replaced with **btp** was attributed to more efficient back-bonding, raising the LUMO energy, as well as lowering of the HOMO with increasing π-acceptor character of the ligands.[113] It was also noted that whereas addition of the electron-withdrawing 4-

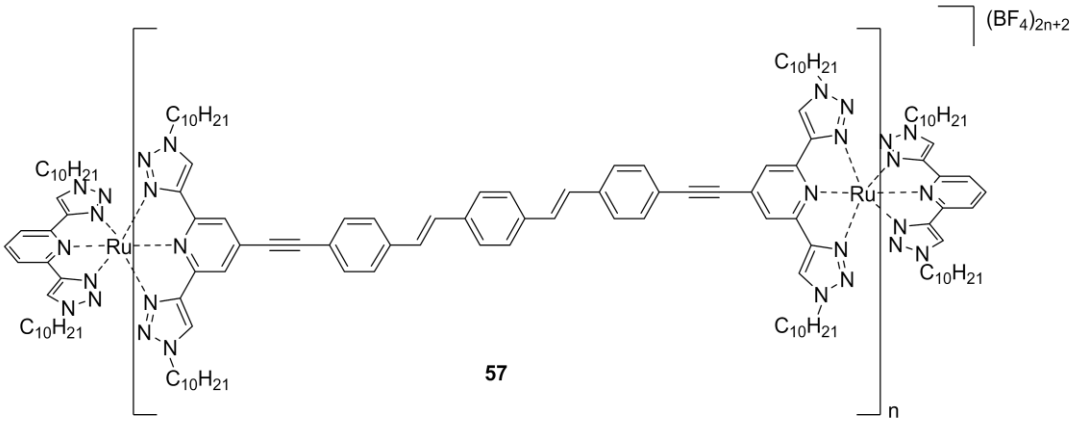

57

Figure 1.13 Metallopolymer of **57**, capped with **54a**.

bromophenyl group in the central 4-pyridyl position of **terpy** led to significant red-shift of the MLCT band, the variation of substituents between ligands **54, 55** and **56** seemed to have negligible influence on the complexes' photophysical properties. This is in agreement with the insensitivity of electrochemical properties to 'arm' substituents described above.

Ditopic ligands **32** and **57**, linked by π-conjugated spacers, were employed to form high-molar-mass Ru(II) coordination polymers.[110,120,121] With the aim of producing printable polymers with interesting optoelectronic properties, long alkyl chain 'arms' were introduced in order to increase solubility and overcome π-stacking, which is a common disadvantage of conjugated systems. The structure of the Ru(II)-metallopolymer of **57** is shown in Figure 1.13 as an example. The ligands were reported to have high extinction coefficients and medium to high quantum yields. With increased conjugation, the absorption became more intense and red shifted compared to 4-bromo substituted precursor ligand **31**, while the emission was slightly red shifted. Only the analogous polymer formed from **32** had any emission, albeit weak, assigned to the conjugated linker stabilising the **btp** ^{3}MLCT state. These metallopolymers were measured as being less viscous than analogous **terpy** polymers, which was suggested to arise from the greater steric freedom of the **btp** motif displays over **terpy**, which Flood and co-workers have commented upon.[70] Microscopy measurements performed upon the polymers using both AFM and TEM imaging techniques, showed relatively rigid rod-like structures, which exhibited some aggregation and coiling. Smooth films, however, could be formed on a quartz slide by drop-casting, indicating solution processability.

Compounds **58a–b** were designed as polymerisation precursors. Munuera and O'Reilly exploited the metal complexation ability of these **btp** motifs to introduce a coordination domain into the derived polymers so as to form higher order structures. In this case, utilising the ability of Ru(II) to afford bis-chelated systems, 4-armed 'star' metallo-polymers were obtained after polymerisation.[143] Ru(II) has been used to template the geometry of 'star-branched polymers' by Kakuchi and co-workers as well. These will be discussed further in Section 1.7.5.[71,147]

1.4.9 Lanthanides

The Ln(III) ions have attracted significant attention because of their unique magnetic and photophysical properties,[148-151] particularly their ability to provide long-lived characteristic and line-like emission upon sensitisation by coordinated ligands *via* the 'antenna' effect and consequently in their applications in supramolecular self-assembly chemistry, as our

group has demonstrated in series of publications.[4-6,9,64,68,152-155] Hence, they lend themselves to use in other applications such as in biological sensing, OLEDs, and as imaging agents, *etc*.[12,156]

Flood and co-workers proved that **btp**-ligand **19a** could form a stable coordination complex with Eu(III), which is to the best of our knowledge, the first example of such a system in the literature. X-ray diffraction studies demonstrated that three terdentate ligands were required to satisfy the high coordination numbers of Eu(III) (the molecular structure of $[Eu\cdot(\mathbf{19a})_3](ClO_4)_3$ is shown in Figure 1.14).[70] When compared with its **terpy** analogue, $[Eu\cdot(\mathbf{terpy})_3](ClO_4)_3$, subtle differences in the geometry were noted: whereas each pyridyl ring in the **terpy** ligand was seen to be tilted at angles to each other in order to avoid steric effects, the steric freedom afforded by the 1,2,3-triazole rings allowed the entire ligand to be almost planar and for each **19a** ligand to be mutually orthogonal. It was concluded, therefore, that the complex was more isotropic than its **terpy** analogue.[157] The complex exhibited characteristic line-like Eu(III) emission in solution, indicating coordination of **19a** to the metal centre and excitation of the ion by the 'antenna' effect.

Hecht and co-workers reported the synthesis of complexes $[Eu\cdot(\mathbf{30c})_3](CF_3SO_3)_3$ and $[Eu\cdot(\mathbf{30e})_3](CF_3SO_3)_3$. They also concluded from comparison of the X-ray crystal structure of $[Eu\cdot(\mathbf{30c})_3](CF_3SO_3)_3$ with **terpy** and also **bpp** analogues that the planar **btp** ligands are more favourable to the formation of Ln(III) complexes, providing better donor capabilities as well as increased steric freedom compared to the other terdentate azaaromatic ligands.[82]

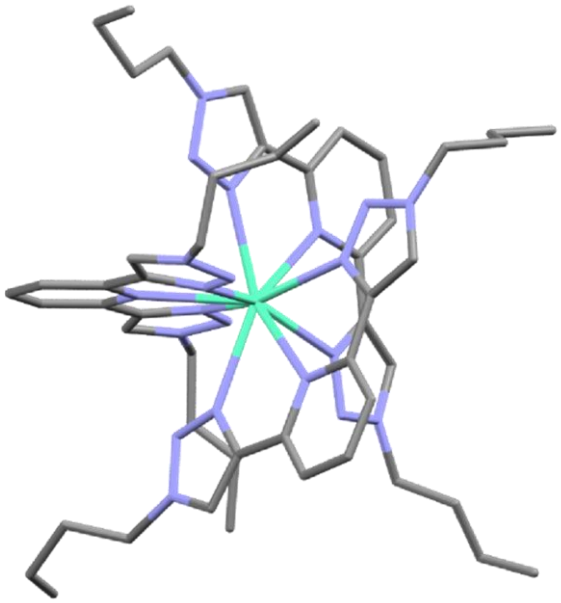

Figure 1.14 Molecular structure of $[Eu\cdot(\mathbf{19a})_3](ClO_4)_3$. Hydrogens and counterions have been omitted for clarity.[70]

These systems also display the characteristic red Eu(III) luminescence in both solid state and solution.

The synthesis of π-conjugated fluorescent back-to-back ditopic **btp** ligands was identified as a target by Chandrasekhar and Chandrasekar. These systems were ideal for coordination of Ln(III) ions because of the presence of the tridentate chelating motifs in both the front and back positions, allowing them to shield the ions completely from solvent molecules, thereby reducing solvent quenching of Ln(III) luminescence.[117] Three ditopic ligands **24a–c** were prepared with up to two phenyl linkers between the two **btp** units (see Scheme 1.5). Only the self-assembly of **24b** with Eu(III) was studied. The complex exhibited Eu(III)-centred luminescence bands, arising from the 'antenna' effect. The emission spectra are typical of complexes with low metal ion site symmetry, and are dominated by the hypersensitive $^5D_0 \rightarrow {}^7F_2$ transition.

More recently, complexes of ligand **17** with Sm(III), Eu(III), Tb(III) and Dy(III) have been evaluated as chemically stable bioimaging agents, suggesting significant potential future applications of such systems in a medical context.[158]

The **btp** motif has allowed exploitation of the Ln(III) coordination geometry and properties for applications with surfaces and materials. For instance, Brunet *et al.* described the covalent attachment of ligands **59** and **60** to a γ-zirconium phosphate surface, where they acted as sensitisers for Ln(III) emission and also circularly polarised luminescence (CPL) in the case of the chiral ligands.[109,159] In a further example, compounds **58a–b** acted as agents for RAFT (reversible addition fragmentation chain transfer) polymerisation, producing polymers which could be templated by Eu(III) to form 6-arm 'star-branched' polymers.[143] These applications will be discussed in more detail in Section 1.7.5 below.

Weng and co-workers reported the synthesis of multi-responsive self-healing metallo-supramolecular gels made from **btp**-containing polymers **43** and **44** which coordinated Eu(III) and Tb(III). The Eu(III) emission from these gels was quenched by heating (upon reversible conversion to sols), making such materials potentially valuable as luminescent temperature sensors. These systems will be discussed in Section 1.7.6.[132-134]

1.4.10 Other metal-containing systems

There are two other metal-containing **btp** systems that merit mentioning for completeness, although in both cases coordination of the metal ion was not through the terdentate motif itself, but rather through appended moieties. Crowley and co-workers have reported the

synthesis of ligand **23**, which had Fe(II)-containing organometallic ferrocenyl groups in its 'arms'. This compound crystallised in the triclinic space group P21/*n* and showed the characteristic *anti-anti* conformation of an uncoordinated ligand with the cyclopentadienyl rings of the ferrocene units in an eclipsed conformation.[107] Hecht and co-workers described the preparation of an interesting ligand **61**, which incorporated zinc porphyrin-appended 'arms'; further work on this system has not been forthcoming.[82]

1.5 Interactions of btp with anions

As well as interaction with metal ions, 1,2,3-triazoles have the ability to interact with anions *via* the triazolyl CH, and are capable of simultaneously binding metal ions and halide ions from salts,[160] or templating the formation of interlocked structures.[161,162] Considering this property of the triazoles, literature relating to the interactions between the **btp** motif and various anions is remarkably rare.[99]

Flood's group were the first to investigate the interactions between halide anions and **btp**-containing systems.[102] Following on from previous studies on tetraphenylene-based triazolophanes **62**, as shown in Figure 1.15,[163,164] it was deemed of interest to introduce pyridyl rings in place of two of the phenyl rings in these systems to alter the electronic character and size of the binding sites. The resulting triazolophanes **33a** and **33b** (see Scheme 1.9) were designed with a view to destabilising the 1:1 complexes formed with the tetraphenylene-based triazolophanes in favour of a 2:1 'sandwich' complex with the halide ions.

Halide binding of **33a** was studied using UV-Vis titrations, with addition of F^-, Cl^-, and Br^- leading to an absorbance minimum at 0.5 equivalents, owing to the 2:1 'sandwich' complex. Further addition of halide ions was shown to result in the formation of 1:1 complexes. The 2:1 complex with I^- was shown to be persistent in solution, in contrast to the other halides. A preliminary crystal structure (only partially solved as a result of weak diffraction) of [**33b**$_2$·I]TBA was presented which suggested the formation of a 2:1 'sandwich' complex with this ligand in the solid state. This **btp**-containing triazolophane framework was also investigated as a potential ionophore with selectivity towards halides in ion-selective electrodes.[165] Studies of the potentiometric responses of the **33a**-based electrode towards various anions showed selectivity towards I^-.

The complex [Zn·(**18**)]$^{2+}$, discussed above in Section 1.4.2, has a coordinatively unsaturated coordination sphere. The solvent molecules which occupy the three remaining positions could be readily displaced by anionic ligands and such behaviour should affect

the emission of the system. The interactions of the complex with various anions were studied, with a view to its application as an anion chemosensor.[122,123] Of a range of anions studied, including halides, thiocyanate, and nitrate, which were indeed shown to quench the complex's fluorescence upon addition in solution, the most remarkable results were observed for cyanide and nitrite ions.

Hecht and co-workers described oligomeric systems **63** (see Figure 1.15) which behaved as helically folding foldamers due to π–π stacking interactions.[103] As described in Section 1.3.3.8, oligomer **63b** was expected to undergo a structural change from *syn-syn* to *anti-anti* conformation upon protonation. Surprisingly, this effect was not observed upon addition of HCl as a source of protons, and in fact, the addition caused exact inversion of the circular dichroism (CD) signal of the helix, indicating an inversion of helicity; the inversion being proposed to arise from the presence of the Cl^- anion. Changes in the CD spectrum were also observed upon addition of F^- (increased intensity) and Br^- (inverted helicity and increased intensity). This is thought to be the first example of an achiral stimulus (halide ions) which promotes inversion of helicity in a foldamer.

1.6 Btp derivatives for photosensitiser and DSSC applications

In recent years, with photosensitiser applications in mind, a number of interesting systems, derived from **btp** have been reported. These will be briefly discussed.

The first such system reported by Schubert and co-workers was an *N*-heterocyclic carbene (NHC) **btp** triazolium derivative, **64**.[112] When compared to N^N^N **btp** ligands, this C^N^C carbene ligand was proposed to have superior σ-donating and only moderate π-accepting properties, which would destabilise the ^{3}MC state and maintain the energy of the ^{3}MLCT state, leading to the desired reduction in radiationless deactivation and hence an increase in excited-state lifetime compared to the (generally non-luminescent) Ru(II)–**btp** complexes.

Cyclometallated complex [Ru·(**64**)(**terpy**)]$(BF_4)_2$ was prepared, *via* a Ag(I)-carbene intermediate, Scheme 1.13, which prevented ligand **64** from undergoing a 5–3 methyl shift. The complex was shown by X-ray crystallography to display C^N^C-pincer coordination of the Ru(II) ion by the carbene ligand. The excited state lifetime measured (633 ns) is of similar magnitude to tris-bidentate [Ru·(**bipy**)$_3$]$(PF_6)_2$ and 2500 times longer than the analogous bis(**terpy**) complex. The photophysical and electrochemical properties of this system are promising for photosensitiser applications.

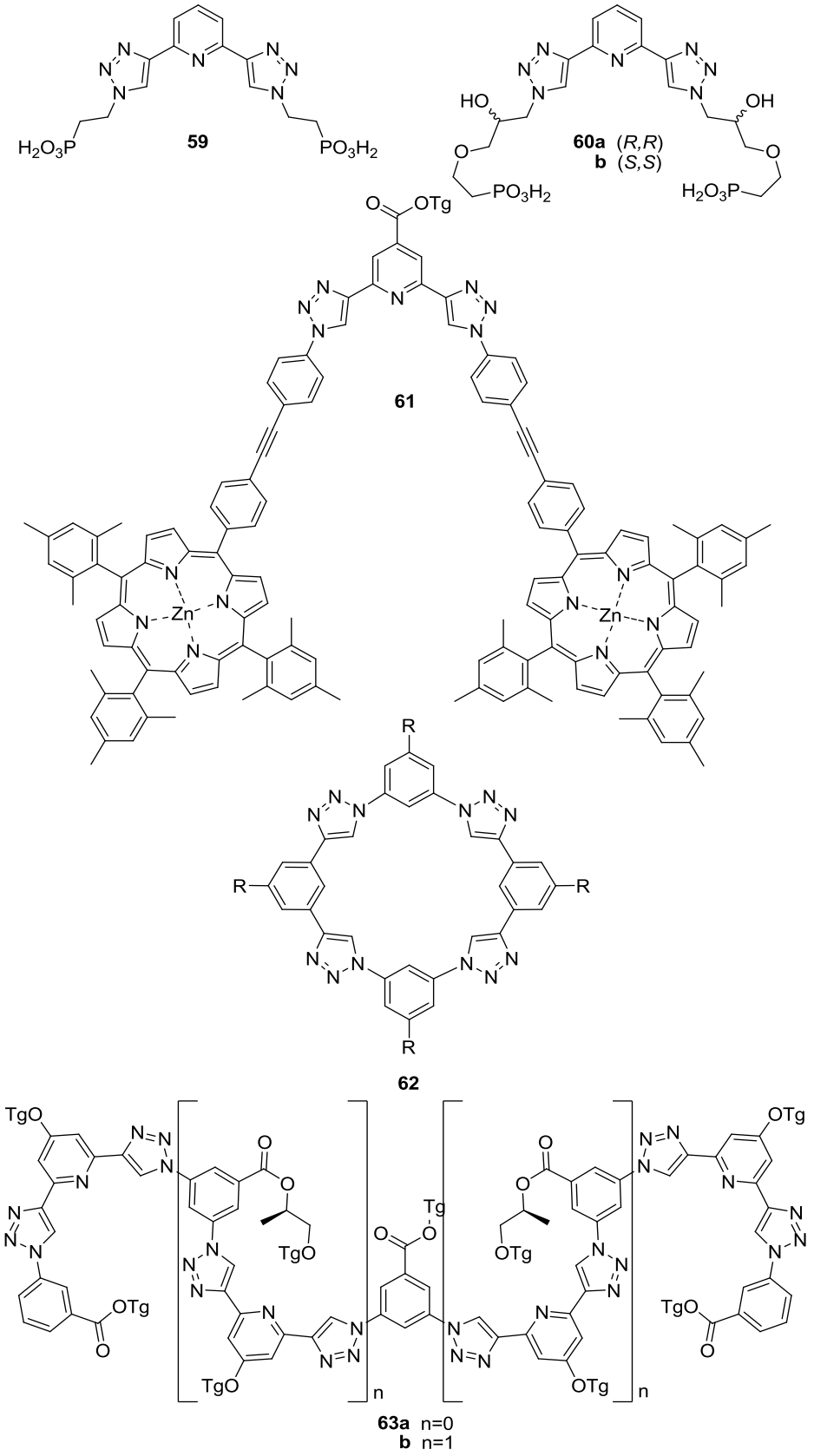

Figure 1.15 Ligands **59** and **60**, porphyrin-containing system **61**, general structure of triazolophanes **62** and foldamers **63**.

Berlinguette and co-workers also studied ligand **64**, along with **65** and the phosphonate derivative **66** for the purposes of stabilising Ru(II) sensitisers' anchoring to TiO_2 semiconductor surfaces, an important consideration in applying photosensitisers to dye-sensitised solar cell (DSSC) applications. This is usually achieved by introduction of a carboxylate 'anchoring group' into the sensitiser to provide electronic coupling to the semiconductor. However, these bonds are susceptible to hydrolysis if any water is present in the system. It was thought phosphonates would provide a more robust linkage, but lower charge-injection rates.

Four photosensitisers were prepared, $[Ru\cdot(\mathbf{64})(CO_2H–\mathbf{terpy})]^{2+}$, $[Ru\cdot(\mathbf{65})(CO_2H–\mathbf{terpy})]^{2+}$, $[Ru\cdot(\mathbf{66})(\mathbf{terpy})]^{2+}$ and $[Ru\cdot(\mathbf{66})(CO_2H–\mathbf{terpy})]^{2+}$, with carboxylate and/or phosphonate 'anchoring groups'. The study showed that the distinctive properties of different 'anchoring groups' could be exploited with the carboxylate on the ligand responsible for electronic communication with the semiconductor surface and using the stronger-binding phosphonates to provide a robust linkage between ligand and surface. This was concluded to be a broadly applicable strategy.[108]

More recently, ligand **67** has been prepared, with hydrophobic alkyl chains installed to increase solubility. Heteroleptic Ru(II) complexes with carboxylate-appended **terpy** of **67** only gave modest power conversions.[166]

Anionic 1,2,3-triazolate derivatives of **btp** have also been reported, such as **68**. These ligands have increased σ- and π-donor strengths, shifting the MLCT of Ru(II) complexes to longer wavelengths. These systems also possessed photophysical and electrochemical properties appropriate to use in DSSCs, showing promising performance with different types of electrolytes.[167]

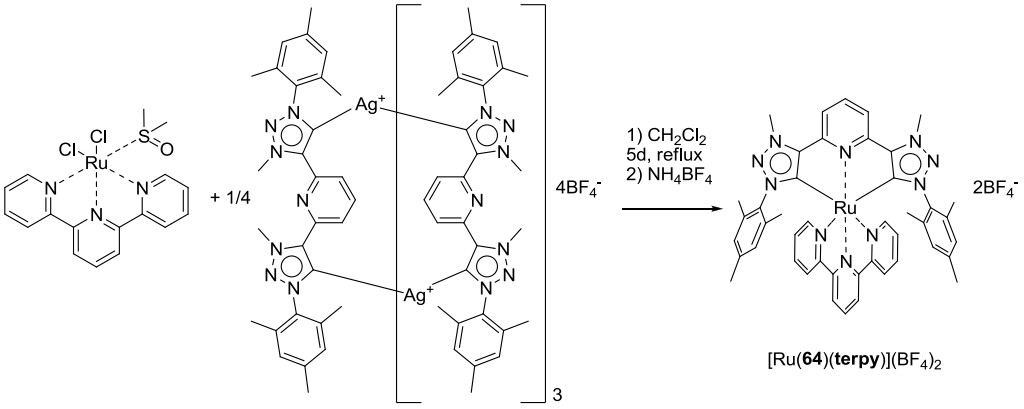

Scheme 1.13 Synthesis of $[Ru\cdot(\mathbf{64})(\mathbf{terpy})](BF_4)_2$.[112]

1.7 Further applications of btp

Btp ligands have been employed in several applications other than those discussed above. These will now be highlighted in several subsections, demonstrating that the **btp** motif has an important future as a supramolecular framework.

1.7.1 Catalysis

A symmetrical **btp** ligand with chiral pyrrolidin-2-ylmethyl arms **69** was synthesised as part of a study into new organo-catalysts for asymmetric Michael additions.[114] Compared with the other catalysts designed in the study (the **btb** analogue and a mono-(triazolyl)pyridyl analogue), **69** was the most diastereo- and enantioselective and, although slower than the other catalysts, the test reaction (Michael addition of cyclohexanone to nitrostyrene) proceeded to completion without any additives. It also showed activity for a range of substituted β-nitrostyrenes.

As briefly mentioned in Section 1.3.3 above, **17** was first synthesised as a ligand to stabilise Cu(I) catalyst in solution and increase the rate of the CuAAC reaction, although it was not the most effective ligand studied for this purpose.[104]

1.7.2 Enzyme inhibition

As part of a range of compounds designed as inhibitors of glycosyltransferase enzymes, asymmetric compounds **70**, containing both a nucleoside and a carbohydrate 'arm', were

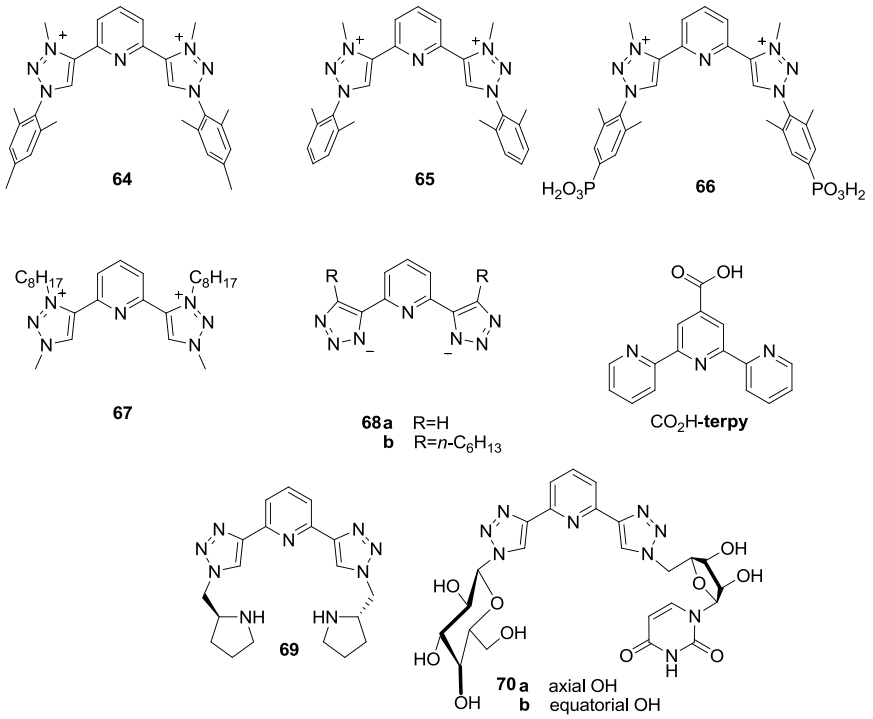

synthesised and evaluated. The particular enzymes studied were metal-dependent galactosyltransferases, and it was shown that the inhibitors chelated the Mn(II) ion. **70a** (axial) was a potent inhibitor of β-1,4-GalT and a weak inhibitor of the other enzymes, while **70b** was a weaker inhibitor.[168]

1.7.3 Molecular logic gates

The responses of molecular sensors to stimuli (temperature, pH or particular species such as metal ions) can be harnessed in the fabrication of molecular devices using Boolean logic with careful design, provided inputs and outputs can be clearly interpreted. The creation of logic gates from fluorophores that can mimic electronic counterparts has been reported and discussed, particularly by de Silva and co-workers.[169-171]

A number of research groups have reported differing responses of **btp** ligands to various metal ions, particularly with respect to enhancement or quenching of ligand emission. The groups of Abarca,[122,123] Zhu[130] and Dash[131] have all reported significant fluorescence enhancements of various ligands (**18**, **38**, **39**, **40**, **22**, **41** and **42**) upon addition of Zn(II) to solutions of the ligands as discussed above. They have also all reported quenching of fluorescence upon addition of other divalent metal ions, such as Fe(II), Cu(II) and Pb(II). Dash and co-workers were first, however, to bring these two responses together in the fabrication of a molecular logic gate, using heavy metal ions as inputs.

Table 1.1 Truth table for logic gate for detection of Zn(II) and Fe(II) by **42** at pH 7.0. [131]

Input 1 Zn(II)	**Input 2 Fe(II)**	**Output (25 μM 42) Intensity$_{(390\ nm)}$**
0 (0 μM)	0 (0 μM)	0
1 (25 μM)	0 (0 μM)	1
0 (0 μM)	1 (25 μM)	0
1 (25 μM)	1 (25 μM)	1

Sensor **42** was found to bind Zn(II) selectively and provide 20-fold emission enhancement (a 'switch-on' response), whereas Fe(II) led to a significant 'switch-off' response. Usefully, however, the sensor was much more selective (28-fold) for Zn(II) than Fe(II), and hence the emission was enhanced by Zn(II)-coordination, even in the presence of Fe(II), with quenching occurring only in the presence of Fe(II) alone.[131] The change in fluorescence intensity of the system around 390 nm was taken as the output. The truth table drawn up for these changes is given in Table 1.1.

Here, the emission of **42** alone [input(0,0)] at 390 nm was very weak and is was assumed as 0 for the logic operation. The addition of one equivalent of Zn(II) led to the 20-

fold increase in fluorescence intensity [input(1,0)] and is taken as a signal of 1 for the logic operation. In the presence of Fe(II) only [input(0,1)], the fluorescence intensity was quenched, giving a signal designated as 0, while the presence of 1 equivalent each of Zn(II) and Fe(II) [input(1,1)], the signal was enhanced, due to the high affinity of **42** for Zn(II) and this output was read as 1. The logic behaviour can be represented as a modified YES gate (with Fe(II) input left unconnected to the output). This is a remarkable and creative application of previously-observed properties of such **btp** systems.

1.7.4 Wave-guiding nanomaterials

Reversibly shape-shifting organic nanostructures which have waveguiding properties dependent on their dimensionality had never been reported before Chandrasekar and Chandrasekhar produced such materials from the ditopic planar **btp** ligand **24b** (see Scheme 1.5).

The mechanical deformation mechanisms were studied and included use of sonication, solvent changes and time-dependent self-assembly, allowing interconversion between nanosheets, nanotubes and nanorings (*i.e.* two-, one- and zero-dimensional materials). The nanostructures were determined by various microscopy methods (including SEM, FESEM and TEM).[125]

The optical waveguiding properties of these various nanostructures were studied by laser confocal microscopy. When an argon laser beam output (488 nm) was focussed orthogonally on the centre of a 2D nanosheet, light was found to propagate in all four directions, while focussing light on one edge preferentially directed light mostly to the opposite edge. Focussing the laser beam on the centre of the 1D nanotubes led to light propagation from both open ends of the tube, while focussing the beam on one end resulted

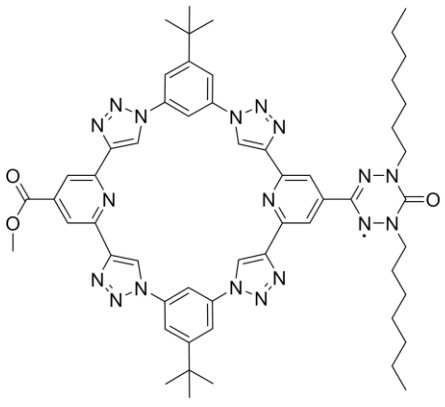

71

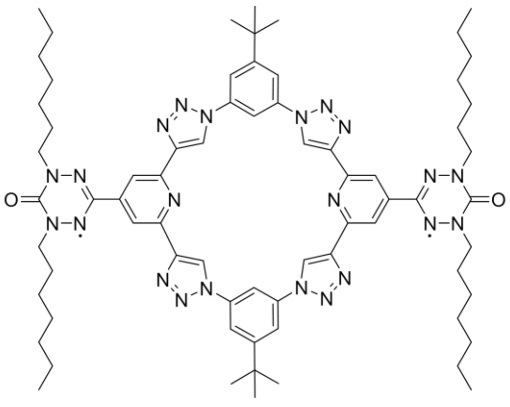

72

in light propagation out of the other end. This demonstrated that optical waveguiding behaviour in 1D or 2D was dependant on the nanostructures of **24b**, which could readily undergo shape-shifting between the 1D and 2D forms.[125]

The same group also reported paramagnetic hexagonal organic micro-tubes self-assembled from shape-persistent macrocycles **71** and **72**, which guided laser light from one end to the other.[172]

1.7.5 Incorporation into polymers, macromolecules and surfaces

The use of CuAAC reactions to construct various polymers and dendrimers has been reviewed by Turro *et al.*[94] Only a limited number of compounds containing the **btp** motif have been used for these purposes.

By installing chelating functionalities into polymers *via* the 'click-to-chelate' approach (such as architectures **73**), Kakuchi and co-workers assembled 3- and 4-arm 'star-branched' polymer structures about a Ru(II) centre, using the metal centre to determine the assembly geometry.[71,147] Study of an analogous complex $[Ru{\cdot}(\mathbf{17})_2](PF_6)_2$ confirmed the geometry of the polymer-appended complex. Polymers such as polystyrene, poly(*n*-butyl acrylate), poly(*n*-hexyl isocyanate), poly(caprolactone) and poly(styrene oxide) were used in various combinations. The polymer appended **btp** ligands **73** were prepared by the reaction of an azido-terminated polymer with 2,6-diethynylpyridine. Asymmetric ligands could also be prepared stepwise and complexes could be prepared as either homoleptic or heteroleptic star-branched polymers or copolymers. This proved a convenient methodology to introduce chelating sites into macromolecules, making them candidates for metal-templated synthesis.

Ligands **58a–b** were designed by Munuera and O'Reilly as RAFT polymerisation initiators containing the terdentate **btp** core, as previously mentioned. Polymerisation (*e.g.* with styrene or methyl methacrylate) followed by assembly around a Ru(II) or Eu(III) metal centre led to the formation of 4- or 6-arm 'star' polymers in the manner illustrated in Scheme 1.14.[143]

Hecht and co-workers described the formation of first and second generation **btp** dendrons **74** and **75**, which were studied upon self-assembly at the solid-liquid interface after physisorption onto highly oriented pyrolytic graphite (HOPG).[127,173] The three regioisomers of **74b** displayed ordered 2D self- assembly patterns in STM images, however, pronounced effects upon the self-assembly of the monolayers were noted as a result of differing substitution patterns of the phenyl rings. Protonation of **74** upon addition

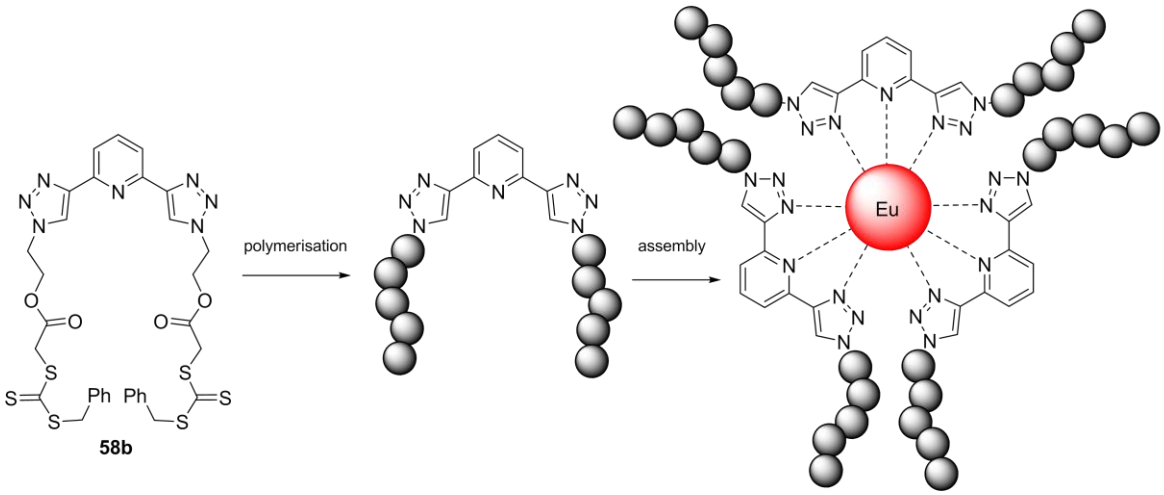

58b

Scheme 1.14 Illustration of the polymerisation–assembly strategy from **58b** employed by Munuera and O'Reilly leading to formation of 6-arm 'star-branched' polymer templated by Eu(III).

of trifluoroacetic acid caused structural reorganisation to occur at the solid-liquid interface; the authors concluded this was as a result of interconversion from *anti-anti* ('kinked') to *syn-syn* ('extended') geometry. This reorganisation (from 'rosette' to 'tetragon' motifs) of the *meta*-isomer of **74b** was possible to observe in real-time over about 20 minutes.[173]

Upon similar acidification of the *meta*-isomer of **75**, the conformation of the compound was also concluded to invert, with previous 'disordered' domains reorganizing into 'lamellar' assemblies.[127] Related shape-persistent flat dendrimers **76** and **77** behaved as disc-like amphiphiles, which stacked into cylindrical nanorods. The dendrimers with chiral tetra(ethyleneglycol) chains (*viz.* **76a** and **77a**) showed CD signals in aqueous solution, which was used to monitor the aggregation process. They also show thermo-sensitive transition from nanorods to a 2D hexagonal columnar lattice.[174]

Polymer **78** was prepared *via* a CuAAC reaction, yielding a soluble material which was employed as a suitable support for metal loading with Pd(II), where ^{1}H NMR spectroscopy

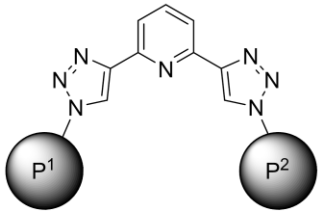

73

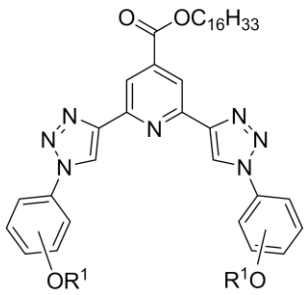

74a R=$C_{10}H_{21}$
b R=$C_{18}H_{37}$

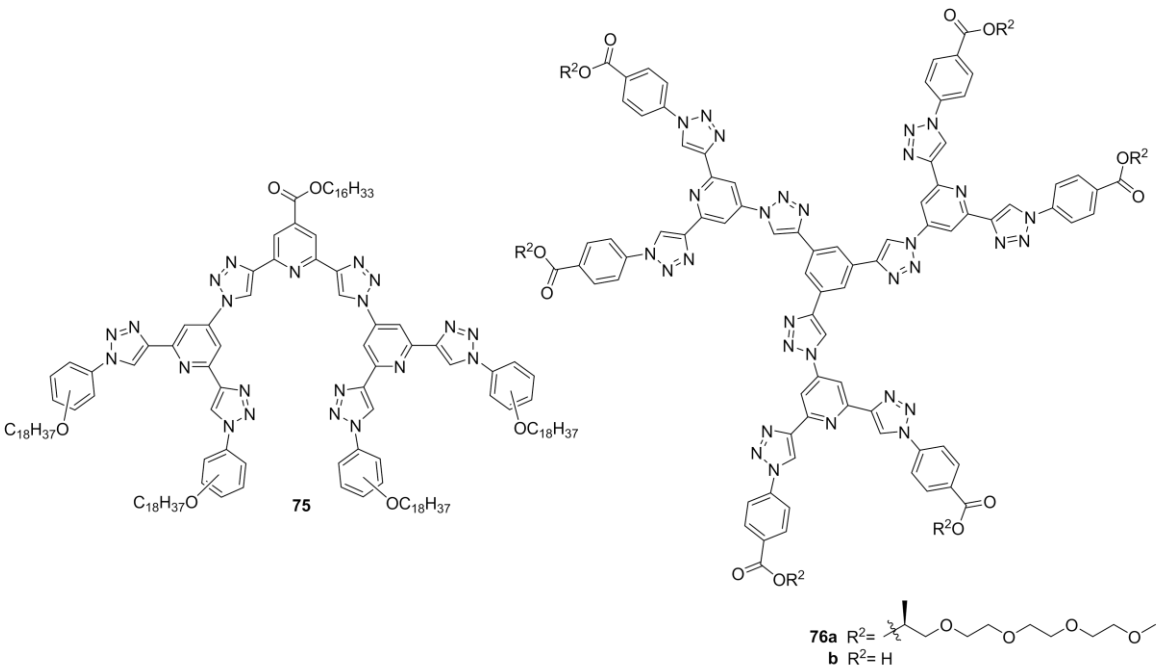

and elemental analysis were used as evidence of successful loading (the same research also yielded products with different spacers between the **btp** motifs, which were not further investigated).[137]

Organic phosphonates can be covalently attached to the surface of the inorganic species γ-zirconium phosphate by topotactic exchange, and as such, a **btp**-based phosphonate ligand **59** was prepared, with a view to producing a solid host which could efficiently sensitise the emission of Ln(III) ions (Eu(III) and Tb(III), specifically) *via* the 'antenna' effect.[109]

Compound **59** was also introduced into the inorganic framework by simply suspending the γ-zirconium phosphate colloidally in a water-acetone mixture at 80 °C for a few minutes with the ligand. Upon suspending this material with the chloride salts of Eu(III) and Tb(III), the expected line-like Ln(III) luminescence was measured from the material, consistent with sensitisation of the metal ion by the remarkable organic–inorganic material. γ-Zirconium phosphate is intrinsically dissymmetric, however in racemic mixtures no bulk optical activity was observed.

It had previously been shown that intercalating with an optically pure molecule gave rise to optical rotation.[175] With this in mind, chiral ligands **60** were introduced covalently into the framework to combine the ability to sensitise Tb(III) emission with optical activity to produce weak CPL signals in the solid state, a seldom-measured phenomenon.[159]

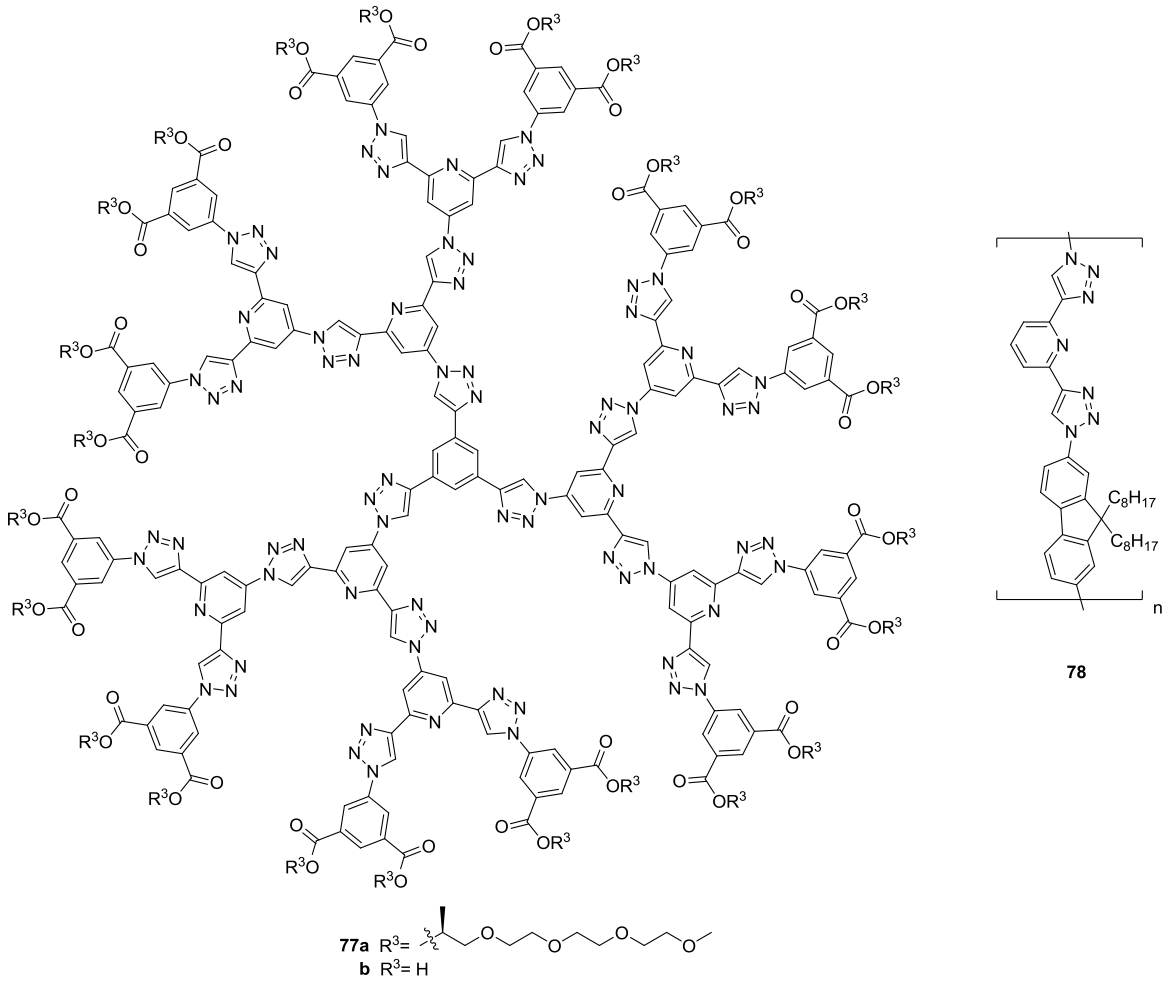

1.7.6 Metallo-supramolecular gels

Hecht and co-workers described two different systems of poly-**btp** polymers **63**[103] and **36**[116] in which the **btp** motif adopted the *anti-anti* conformation, giving rise to a helical conformation in the extended heteroaromatic strands. The interactions of **63** with anions is discussed in Section 1.5, above. **36**, on the other hand, showed the capacity to interact with metal ions, such as Zn(II), Fe(II) and Eu(III), to form metallo-supramolecular cross-linked gels upon characteristic inversion of conformation of the **btp** group (discussed above in Section 1.3.3.8).[116]

Weng and co-workers have also reported a number of **btp**-polymers **43**[132,134] and **44**[133] which form metallo-supramolecular gels upon coordination with Zn(II), Eu(III) and/or Tb(III) (*vide supra*) which were described as 'biomimetic' bulk materials. The rheological and optical properties of these gels were studied with various combinations of metal ions. Mechanical properties of the bulk gels can be tuned by changing the stoichiometric ratios of the metals and choosing the metal–ligand system. For instance Zn(II) forms stronger

less dynamic complexes with higher density of cross-linking due to its different coordination number.

These systems were shown to display remarkable self-healing properties when simply kept in a saturated toluene atmosphere. It proved possible to heal gels of different metal ion ratios together to form integrated gels that could be subjected to deformations such as bending and stretching without breaking at the joints. This is evidence of the dynamic nature of the self-healing of these metallo-supramolecular polymers.[132,134] These materials underwent reversible gel–sol transitions upon heating and cooling and, in the case of Eu(III)-containing gels, emission was quenched upon heating, allowing the system to be considered temperature sensors. They also showed sensitivity to chemical stimuli, for instance nerve gas agent mimic triethyl phosphate. Bidentate **bipy** was found to deconstruct Zn(II)-gels only and not Ln(III)-gels.[132] Both of these systems involved polymeric poly-btp components. More recently, Weng and co-workers have also reported self-healing **btp** systems with stress-sensing abilities,[176] and PEG-linked systems, which formed multiresponsive gels both in the presence and absence of Eu(III).[177]

1.8 Btp overview

The above account has clearly demonstrated that the **btp** motif shows a versatile range of coordination and supramolecular chemistry across *d*- and *f*-block metals as well as interacting with anions. Its applicability to wide-ranging fields, convenience of preparation and ease of derivatisation are all advantageous. From its first appearance in the literature in 2004 to date, the rate of **btp**-compounds being published has accelerated and looks set to continue as current researchers branch out in their use of these compounds and as the wider chemical research community becomes aware of the motif.

The **btp** motif is in many ways analogous to the ubiquitous **terpy** motif and other terdentate chelating architectures, allowing for its introduction into systems to vary the properties or characteristics of species previously purely based on **terpy** chemistry. Hecht and co-workers' application of **btp** ligands to Ru(II) poly-azaaromatic electrochemistry is an example of this kind of work. As has been shown in this article, the **btp** motif has predictable coordination chemistry, with the ligands and anion-complexes favouring an *anti-anti*, or 'kinked', geometry and metal complexes and protonated species favouring *syn-syn*, or 'extended', geometry, both with essentially planar **btp** units. The interconversion of these geometries has been exploited.

The coordination chemistry of **btp** ligands with Cu(II), Zn(II), Ag(I), Pt(II), Pd(II), Pb(II), Fe(II), Ru(II), Sm(III), Eu(III), Tb(III) and Dy(III) has been detailed, along with the properties and applications of these various complexes and coordination polymers. The interactions with anions have been described. The related triazolium derivatives have been discussed with respect to their potential as photosensitisers. Applications in catalysis, enzyme inhibition, molecular logic, wave-guiding nanomaterials, incorporation into polymers, surfaces and metallo-supramolecular gels have been discussed in more detail; and it is clear that more such supramolecular and nano-applications will appear in the near future. This class of chelating ligand is likely to become increasingly relevant in the coming years, particularly in supramolecular chemistry, solar cell research, magnetism, molecular logic and materials chemistry. We look forward to these exciting future developments; it is clear that the **btp** ligand has a major role to play across many areas of chemistry in the future. In this thesis, new **btp** ligands will be used to address the challenge of forming self-assemblies with *d*- and *f*-block metals; a detailed programme of this work is set out at the end of this Introduction, but prior to that, it is worth highlighting the development of the Ln(III)-directed route to new supramolecular systems which has been undertaken within the Gunnlaugsson laboratory over the last number of years. The next section summarises this work.

1.9 Advances in the Gunnlaugsson Group

The synthesis of elegant Ln(III)-directed self-assemblies such as bundles and helicates has been an important area of research in the Gunnlaugsson research group in recent years. As well as allowing exploration of the rich variety of possibilities of supramolecular assembly, these systems offer potential for functionalisation and use as luminescent probes and sensors.[178] Significant attention has also been given to cyclen-based systems, which utilise the properties of various Ln(III) ions for purposes such as ion sensing[10] and imaging, particularly as contrast agents for visualising microcracks in bones.[12,156] However, these systems are not closely related to those presented in this thesis, and so shall not be discussed here in detail. These systems have been studied in solution and also on solid surfaces, such as gold nanoparticles.[179] A review article has been published recently, discussing the latest work in the Gunnlaugsson laboratory at some length.[180]

There has also been a significant amount of acyclic structures prepared and studied within the group, particularly based upon amide derivatives of the terdentate **dpa** motif. These systems were capable of satisfying the high coordination number of the Ln(III) ions

through the formation of 1:3 metal:ligand self-assemblies. Dr Joseph Leonard and others developed novel self-assembled bundles, from chiral ligands **79**, which contain naphthalene chromophores as sensitising 'antennae'. Both enantiomers of this ligand formed highly symmetrical chiral bundles (the '*Trinity Sliotar*', $[Ln\cdot(\mathbf{79})_3](CF_3SO_3)_3$) self-assembled around Ln(III) centres, where Ln(III) = Tb(III), Sm(III), Eu(III), Nd(III) and Yb(III), featuring face-to-face π-π stacking in the solid state between the aromatic moieties, Figure 1.16. Chirality is transferred to the bundles from the ligands, yielding Δ and Λ complexes; hence, these systems give rise to CD spectra. The Ln(III) sits in a fully saturated environment, shielded from solvent molecules with a coordination number of 9. These complexes were luminescent and also displayed circularly polarised luminescence (CPL) as a result of their chiral nature.[4]

Dr Oxana Kotova has more recently investigated the effect of structural isomerism on the self-assembly of these chiral naphthalene containing **dpa** ligands by synthesising ligands **80**, Figure 1.16, finding that these formed less tightly packed structures in the solid state.[152] The isomers also had lower luminescent quantum yields than **79**. Solution spectroscopic studies of the self-assembly of **80** with Eu(III), using UV-Vis absorbance and emission titrations, were compared with solution studies for **79**, carried out by Dr Christophe Lincheneau. Both sets of isomers showed the presence of 1:1, 1:2 and 1:3 assemblies in solution; they were determined to have high global binding constants with

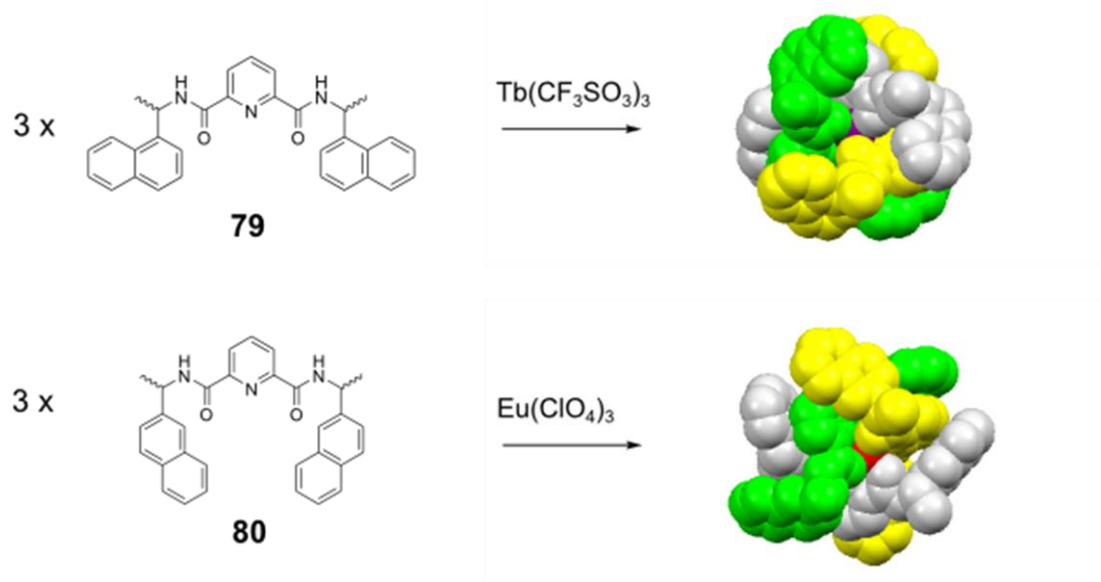

Figure 1.16 (a) Chiral ligand **79** forming the '*Trinity Sliotar*' bundle with Tb(III), (space-filling molecular structure of a Tb(III)-templated bundle is shown); and **(b)** structural isomer **80** and the molecular structure of the Eu(III)-templated bundle. (counterions, hydrogen atoms and solvent molecules omitted for clarity in both structures).

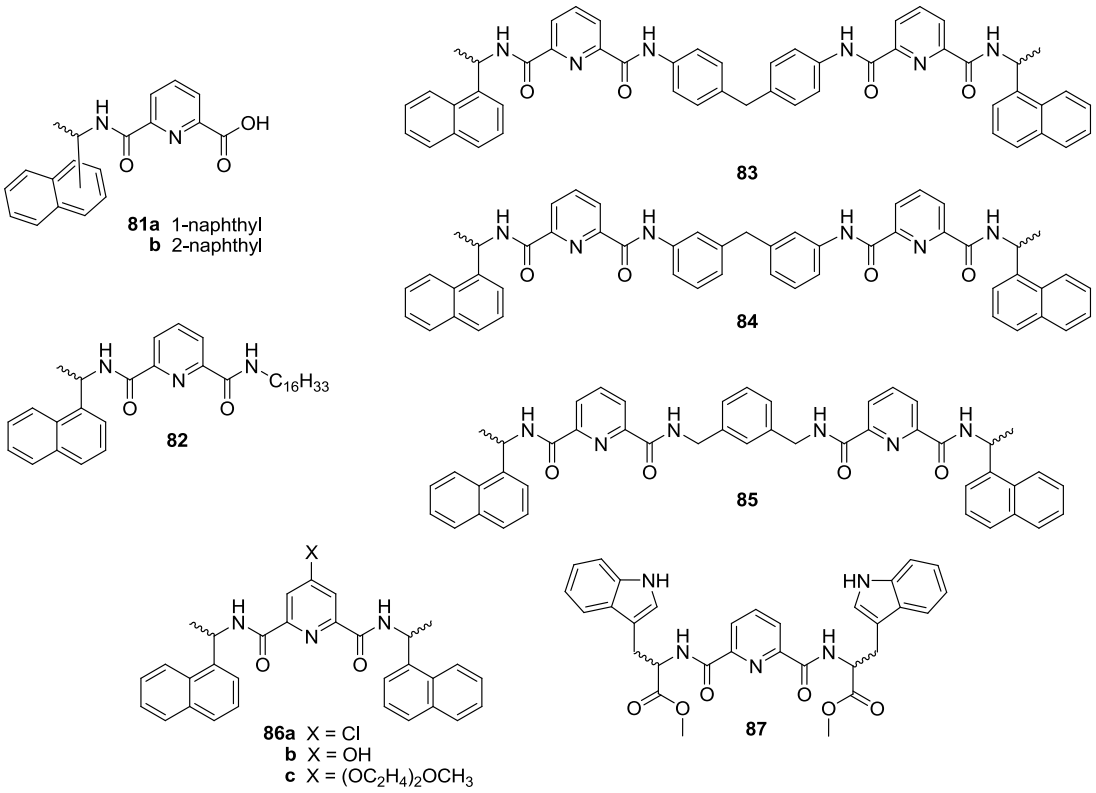

Eu(III) in both CH_3CN and CH_3OH solution, albeit with those of the 1-naphthyl isomer being slightly higher: $\log\beta_{1:3} \approx 19$ and ≈ 17 (in CH_3OH) for **79** and **80**, respectively.

By removing one of the naphthyl 'antennae' of **79**, asymmetrical ligands **81** were designed.[6,181] Ligands **81a** formed asymmetrical self-assembly bundles and were dubbed 'half-helicates'. Solution studies showed the formation of stable 1:1 and 1:3 self-assemblies, with $\log\beta_{1:3} \approx 20$.[6] The CD spectra of **81b** were seen to change dramatically upon addition of Eu(III).[181] Extension of the half-helicates to include a hydrophobic 'arm', allowed the formation of amphiphilic complexes of the form $[Ln\cdot(\mathbf{82})_3]^{3+}$, which developed self-assembled Langmuir monolayers on the water–air interface. These monolayers were transferred onto quartz slides, resulting in Langmuir–Blodgett films, which displayed characteristic Ln(III)-centred luminescence, where Ln(III) = Eu(III)[9] or Nd(III)[8], giving visible or NIR emission, respectively. The Eu(III) complexes also displayed CPL, the first example of CPL emission from a monolayer.

Further extending these systems by linking two **dpa** motifs together with a spacer, allowed the formation of dimetallic triple-stranded helicates, such as **83**[154], **84**[5] and **85**.[155] Their self-assembly behaviour with Ln(III) in solution was studied by Dr Floriana Stomeo, Dr Christophe Lincheneau and Dr Steve Comby. Various photophysical, and NMR titration studies suggested the formation of 2:3 helicate assemblies in solution. As

enantiomerically pure ligands were involved in forming these complexes, the helicates displayed CPL emission, as well as typical Ln(III)-centred emission.

These systems have been further derivatised in work carried out by Dr Niamh Murray and Dr David Caffrey, in which novel bundles incorporated functional groups at the 4-pyridyl position such as chloride, hydroxyl and polyethoxyethylene chains, yielding ligands **86** with a view to increasing water-solubility of these luminescent bundles and further functionalising them.[182,183] Dr Dawn Barry also undertook similar derivatisation of helicate ligands **83** with triethylene glycol chains attached to the 4-pyridyl position of both **dpa** motifs in search of increased water solubility, however precipitate still formed in aqueous CH_3OH solutions with greater than 50% water content.[184]

Dr Christophe Lincheneau reported synthesis of [2]- and [3]catenanes containing the **dpa** amide binding motif and closing terminal chains using Williamson ether synthesis and intramolecular olefin ring-closing metathesis with Grubbs' catalyst. Formation of these supramolecular structures was confirmed by MALDI HRMS and ^{1}H NMR analysis.[7,185]

Variation of the 'antenna' in these **dpa** compounds has also been investigated. Introducing tryptophan 'arms' in place of the naphthalene 'arms' led to the production of enantiomeric pair **87** which self-assembled with Eu(III) and Tb(III) in solution. Surprisingly, only the formation of 1:2 complexes were observed under thermodynamic conditions, while in solution, no evidence of the 1:3 assembly was seen, however the 1:1 assembly was observed to form at higher Ln(III) concentrations. These results demonstrate that the structural nature of the 'antenna' can have an impact on the self-assembly stoichiometry.[153]

1.10 Work described in this thesis

As shown above, derivatisation of the *'Trinity Sliotar'*-type ligands has led to interesting results. Variation of the 'antenna' and 4-pyridyl substituents have all been explored at length. Variation of the chelating motif, however, has not been investigated in the Gunnlaugsson laboratory; this is also expected to provide interesting compounds with complementary results.

The aims of the work reported in this thesis are the development of new **btp**-containing ligands with a range of functionalities and the study of their formation of supramolecular self-assembly structures, principally their self-assembly with various *d*- and *f*-metal ions.

Chapter 2 will report two new **btp** ligands and study their coordination chemistry with Ni(II), Ru(II), Ir(III) and Pt(II) by means of X-ray crystal structure analysis, NMR

spectroscopy, photophysical measurements and, in the case of the Ru(II) complexes, cyclic voltammetry. These were the first examples of Ni(II) and Ir(III) complexes with **btp** ligands. The ability of one of these complexes to form a metallo-supramolecular gel will also be presented.

Chapter 3 will focus on the self-assembly of **btp** ligands with Ln(III) ions in solution, including one of the ligands prepared in Chapter 2. A number of derivatives of this ligand will also be studied, including an allyl amide ligand, as well as a small library of amino-acid–appended derivatives. The serendipitous formation of a self-templated [2]catenane from the allyl amide derivative upon ring-closing metathesis will also be discussed. The self-assembly of the acyclic ligands will be studied, in particular by using spectroscopic titrations and exploring the emissive properties of the Ln(III)-directed self-assemblies.

Chapter 4 will present a number of chiral **btp** ligands including carbohydrate derivatives and ligands derived from chiral amines *via* a diazo-transfer–deprotection–'click' reaction. Full characterisation of these ligands will be discussed, in three cases including X-ray crystal structure analysis. Their self-assembly with Ln(III) will be explored by UV-Vis absorbance and luminescence spectroscopic titrations. Circular dichroism and circularly polarised luminescence will give further insight into these compounds, and CD titrations will also be used to determine stability constants for these Ln(III)-directed self-assemblies, a new application of this method.

Chapter 5 will provide detailed experimental methods, procedures and techniques used in the research described in the other chapters. References are listed in Chapter 6. Supplementary data, graphs, tables, results and spectra are included in various Appendices.

2. Transition metal coordination chemistry of novel btp ligands

2.1 Introduction

Transition metal ion complexes are widely studied, particularly with respect to their photophysical properties, electrochemical properties and potential biological applications. The d^6 metal ions Ru(II) and Ir(III) and d^8 metal ions Ni(II) and Pt(II) have all shown significant applications in biological systems, as cellular imaging agents,[186,187] DNA binders[61,62,68,188-190] and in anti-cancer treatment;[191] the complexes of these metals are usually kinetically inert and stable. As was discussed in detail in Chapter 1, pyridine-centred terdentate binding motifs are a particularly privileged coordinating environment for such metal ions. For example, 2,2′:6′,2″-terpyridine (**terpy**) and its derivatives are ubiquitous in the literature, featuring in dye-sensitised solar cells,[59] DNA and protein binding,[61,62] metallo-supramolecular coordination polymers,[63] and in ion sensing.[65-67] These ligands are, however, limited by the synthetic challenge involved in derivatising them, particularly with regard to introducing flanking 'arms' appended to the non-central heterocycles. An analogous binding motif which overcame this limitation would prove advantageous in developing new functional systems. Facile and modular synthesis of such ligands is of great interest and has, in recent years, led to increased interest in the 2,6-bis(1,2,3-triazol-4-yl)pyridine (**btp**) moiety, which has been reviewed extensively in the previous chapter, as well as in the article upon which that chapter is based.[69] **Btp**-based ligands can be obtained *via* the CuAAC 'click' reaction from a wide range of substrates.[70,82,100,101,107,111,124,125,143,174] The CuAAC reaction is a regioselective, high yielding and tolerant reaction that gives exclusively 1,4-disubstituted 1,2,3-triazole products.[77,80,81,86,104]

The **btp** binding motif is versatile. Flood *et al.* first demonstrated the ability of **btp** ligands (namely ligand **19**) to form stable coordination compounds[70] and in the more recent literature, all of which is discussed above in Chapter 1, other such compounds have been utilised in such diverse applications as tuning the optical properties of Ru(II)-polypyridyl complexes,[113] in the formation of metallo-supramolecular architectures[81] and polymers,[110] binding halides,[102] sensitisation of lanthanide luminescence in the solid state[109] and recently by Yuan *et al.*[132] in the formation of self-healing metallo-supramolecular gels from poly-**btp** polymers **43** and **44**. It can be seen that **btp** is a highly adaptable building block and hence it was decided to work with such ligands. In this chapter, the design, synthesis and characterisation of **btp** ligands **88** and **89** (Scheme 2.1) and their coordination chemistry with Ru(II), Ir(III), Ni(II) and Pt(II) is described, as well as various

structural, photophysical and electrochemical analyses of these complexes. This chapter is closely based on an article published in 2013.[72]

Ru(II) complexes with polypyridyl ligands have been studied in the past with particular interest being paid to their electrochemical and photophysical properties. Bis-terdentate complexes such as $[Ru(\mathbf{terpy})_2]^{2+}$ overcome isomerism and provide more linear structure than tris-bidentate complexes. Zhang *et al*. showed that the **btp** motif has very similar binding properties to **terpy**, with similar bond angles and lengths determined by X-ray diffraction therefore making study of such systems valuable as an analogue for **terpy**.[71] A number of Ru(II) complexes with **btp** have subsequently been recently reported, including **19**, **30** and **54**, which indeed showed such similar characteristics to the **terpy** analogues.[70,110,112,113,126,142] A survey of the literature suggests there are no previous published examples of Ir(III) complexes with **btp**-containing ligands. Given that Ir(III) is isoelectronic to Ru(II) and its complexes have long been of interest, due to their emission properties, their formation was chosen for investigation.[192]

The d^8 octahedral Ni(II) complexes are isostructural to the octahedral d^6 metal complexes, however, there have also been no previously reported complexes of **btp** ligands with Ni(II). At the time of publication of the article which this chapter is closely based on, only one example of the interaction between the **btp** motif and the square planar d^8 Pt(II) ion had been reported, where it was used in the formation of metallopolymers.[121] However, almost simultaneously to the publication of this work, the group of Professor Vivian Wing-Wah Yam reported a number of interesting luminescent **btp**–Pt(II) systems involving alkynyl ligands, which are described in Section 1.4.4.[136] The chemistry of Pt(II)-**terpy** derived systems is well-studied, often as a result of their ability to exhibit metal···metal interactions.[193,194]

There have only been three **btp**-based supramolecular gels previously reported in the literature. One responsive system, based on ligand **36**, exploited the conformational changes that **btp** undergoes upon binding a metal (*vide infra*) to interconvert between a helically folded polymer and a metallo-supramolecular cross-linked gel,[116] while the other work described self-healing polymeric materials based on **43** and **44**[132-134]. All of these systems involved polymeric poly-**btp** components; in this chapter, the first example of a metallo-supramolecular gel derived from discrete mono-**btp** components (*i.e.* ligand **89**) is described.

2.2 Design, synthesis and characterisation of novel ligands

For the purposes of the research presented in this thesis, new ligand frameworks based on the **btp** binding motif were designed. These frameworks needed to be functional and be readily derivatised in order to maximise their utility. Figure 2.1 shows the various features of the ligands which may be considered in this design: (a) the binding motif, which has been selected to be the versatile **btp** motif; (b) an available functional group, which can be conveniently derivatised, such as an ester or ether; (c) a chromophore or 'antenna' in the 'arms' of the ligand which absorbs light in order to give rise to emissive properties of the ligands and their complexes; (d) a position for a potential chiral centre; and (e) a position for potential further functionalization. Ligands **88** and **89** were designed to include an ester/carboxylate functional group in position (b), a phenyl chromophore in position (c), without a chiral centre and without functionalisation on the 4-pyridyl position of the **btp**. Derivatives based on extending these frameworks through derivatisation of functional group (b) will be presented in Chapter 3, while analogues which possess a chiral centre at position (d) and vary the chromophore will be considered in Chapter 4.

Both of these ligands were synthesised in a one-pot deprotection/'click' reaction from the relevant bromide and 2,6-bis((trimethylsilyl)ethynyl)-pyridine, **21**, as shown in Scheme 2.1. The azide intermediate was produced *in situ* by stirring the bromide with NaN_3 in DMF–H_2O at room temperature for an hour before adding $CuSO_4{\cdot}5H_2O$ and sodium

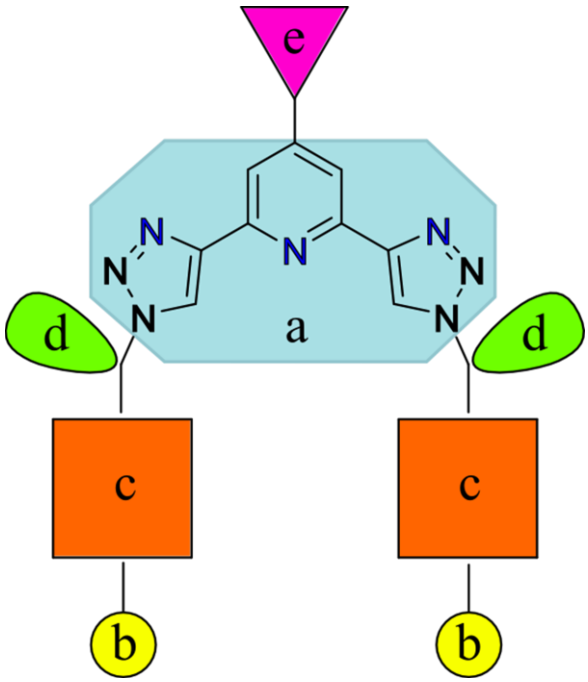

Figure 2.1 A schematic representation of the design considerations for desired functionality of **btp** ligand frameworks developed in this thesis, where (a)–(d) can all be synthetically modified.

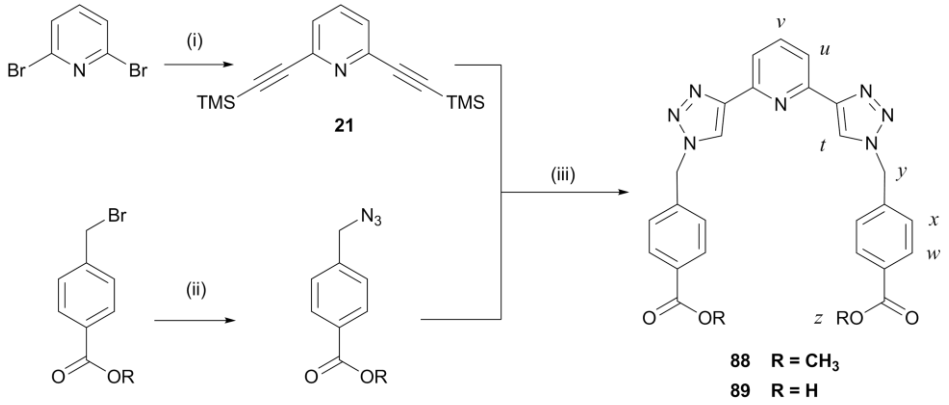

Scheme 2.1 Synthesis of ligands **88** and **89**. **(i)** CuI, $(PPh_3)_2PdCl_2$, THF/Et_3N (1:1), trimethylsilylacetylene, **0** °C→rt; **(ii)** NaN_3, rt, 1h, DMF–H_2O; **(iii)** $CuSO_4{\cdot}5H_2O$, sodium ascorbate, K_2CO_3, DMF–H_2O, rt, 18 h.

ascorbate, which produced Cu(I) in solution, the catalyst for the CuAAC reaction. Protected bis-alkyne **21** was deprotected *in situ* due to the presence of K_2CO_3, following a paradigm used by Fletcher *et al.*[106,195] This paradigm eliminates the need for purifying the free terminal alkynyl intermediate. The 'click' reaction was stirred at room temperature for 18 hours. Upon washing the reaction mixture with aqueous EDTA/NH_4OH solution, in order to scavenge Cu(I) ions, the ligands were obtained in high purity (confirmed by elemental analysis), which eliminated the need of any further purification, such as the use of chromatography, and moderate yields of 53% and 63%, respectively. Carboxylic acid ligand **89** could also be successfully prepared by ester hydrolysis of **88** in refluxing aqueous KOH solution in 50% yield. These ligands were fully characterised.

Due to the C_2-symmetry in both **88** and **89**, only a few resonances were observed in the ^{1}H-NMR spectra. The spectrum of **88** was recorded in both DMSO-d_6 and $CDCl_3$ solutions (both shown in Appendix A). The spectrum shown in Figure 2.2(a) (400 MHz, DMSO-d_6) displayed the expected number of resonances for **88**. The triazolyl peak appeared as a well resolved singlet at 8.72 ppm (marked *t* in Figure 2.2), a multiplet at 7.91–8.07 ppm was made up from the overlap of the pyridyl signals with one of the phenyl signals. The other resonance from the phenyl ring was observed at 7.45 ppm (marked *x*) and two singlets (*y* and *z*) at 5.81 and 3.84 ppm arose from the methylene and methyl ester moieties, respectively. Formation of the ligand was also confirmed by ESI+ MS analysis, where a signal at *m/z* = 532.1711 was observed, which corresponds to the $[M+Na]^+$ species, as well as IR spectroscopy, where a characteristic carbonyl stretch could be seen at 1729 cm^{-1}.

The carboxylic acid ligand **89** was found to have poor solubility in organic solvents. The ^{1}H-NMR spectrum (600 MHz, DMSO-d_6) was once again very simple as a result of the symmetry of the molecule (see Appendix A, Figure A.4). The resonance at 5.80 ppm arose

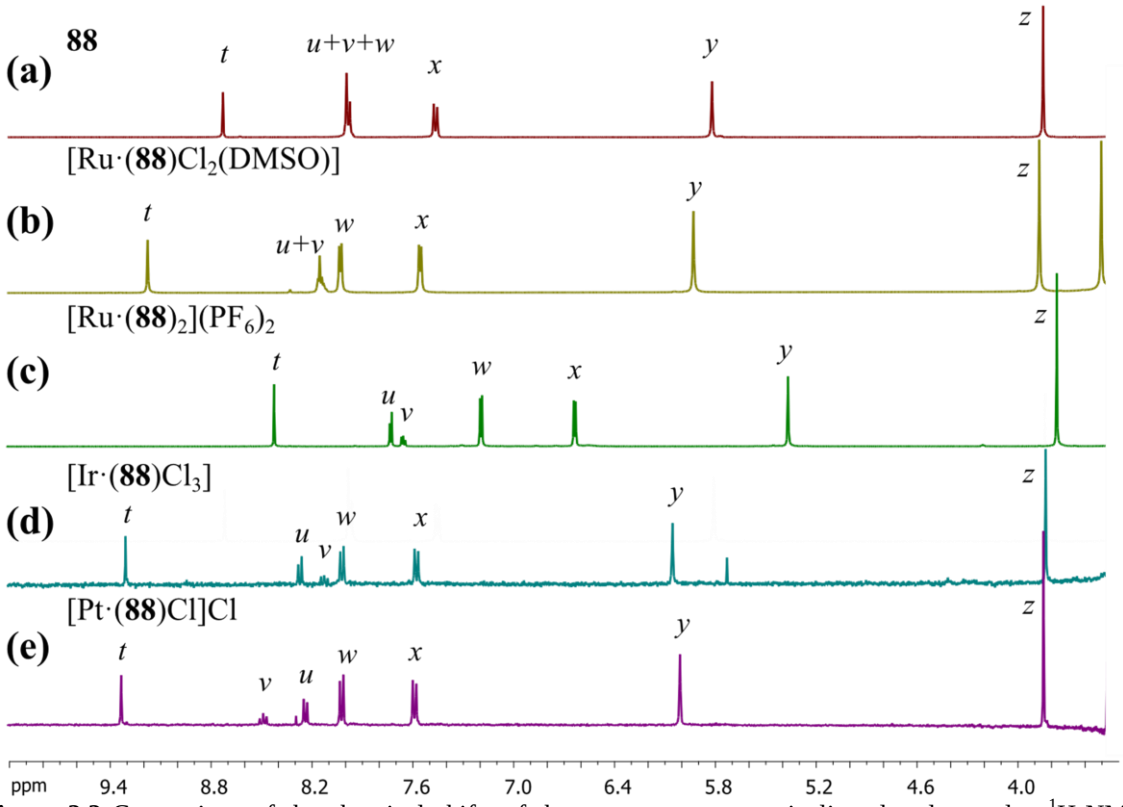

Figure 2.2 Comparison of the chemical shifts of the proton resonances in ligand and complex ^{1}H-NMR spectra of **(a)** Ligand **88** (400 MHz, DMSO-d_6); **(b)** [Ru·(**88**)Cl_2(DMSO)] (600 MHz, DMSO-d_6); **(c)** [Ru·(**88**)$_2$](PF_6)$_2$ (600 MHz, DMSO-d_6); **(d)** [Ir·(**88**)Cl_3] (400 MHz, DMSO-d_6); **(e)** [Pt·(**88**)Cl]Cl (400 MHz, DMSO-d_6). Peaks are labelled as follows: *t* (triazolyl CH), *u* (3- and 5-pyridyl CH), *v* (4-pyridyl CH), *w* and *x* (phenyl CH), *y* (CH_2), *z* (–OCH_3).

from the methylene linker, a doublet at 7.45 ppm related to four of the eight phenyl CH protons, the multiplet from 7.88–8.06 ppm resulted from the overlap of the remaining phenyl signal and the two pyridyl resonances, the singlet at 8.74 ppm was related to the triazolyl protons. A peak in the ESI− MS spectrum at *m/z* = 480.1423 corresponded to the deprotonated ligand species. Having successfully synthesised these ligands, the various *d*-metal ion complexes of **88** and **89** were next formed.

2.3 Formation and characterisation of *d*-metal complexes

The monoleptic Ru(II) complex of **88** was prepared upon treating ligand **88** with 1 molar equivalent of [$RuCl_2$(DMSO)$_4$] in $CHCl_3$ under reflux conditions for 10 hours in darkness and [Ru·(**88**)Cl_2(DMSO)] was collected upon filtration as a bright red solid in good yield (86%). Such monoleptic complexes have previously been used as intermediates when preparing heteroleptic Ru(II) complexes.[113] The ^{1}H-NMR spectrum (600 MHz, DMSO-d_6; Figure 2.2(b) and shown in full in Appendix A, Figure A.6) showed resonances shifted relative to the ligand, as well as a new resonance appearing at 3.49 ppm, arising from the bound DMSO molecule in the structure. ^{13}C-NMR (150 MHz, DMSO-d_6) resonances were also assigned, Figure A.7. MALDI+ HRMS analysis confirmed this, showing the presence

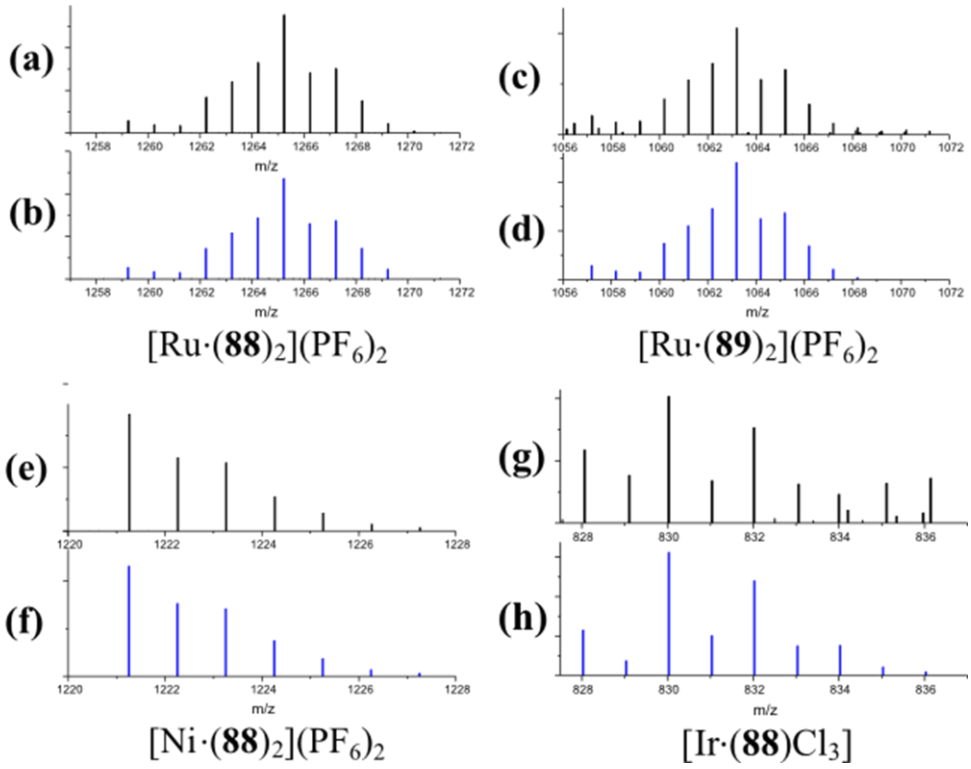

Figure 2.3 (a) Experimental and **(b)** calculated HRMS isotopic pattern distribution for $[Ru\cdot(\mathbf{88})_2]^{2+}$ HRMS (*m/z*) (MALDI+): Calculated for $C_{54}H_{46}N_{14}O_8F_6Pru^+$ *m/z* = 1265.2308 $[M-PF_6]^+$. Found *m/z* = 1265.2323; **(c)** Experimental and **(d)** calculated HRMS isotopic pattern distribution for $[Ru\cdot(\mathbf{89})_2]^{2+}$. HRMS (*m/z*) (MALDI+): Calculated for $C_{50}H_{37}N_{14}O_8Ru^+$ *m/z* = 1063.1962 $[M-2(PF_6)-H]^+$. Found *m/z* = 1063.1998; **(e)** Experimental and **(f)** calculated HRMS isotopic pattern distribution for $[Ni\cdot(\mathbf{88})_2]^{2+}$. HRMS (*m/z*) (MALDI+): Calculated for $C_{54}H_{46}N_{14}O_8NiF_6P^+$ *m/z* = 1221.2618 $[M-PF_6]^+$. Found *m/z* = 1221.2644; **(g)** Experimental and **(h)** calculated HRMS isotopic pattern distribution for $[Ir\cdot(\mathbf{88})Cl_3]$. HRMS (*m/z*) (ESI+): Calculated for $C_{27}H_{23}N_7O_4Cl_3IrNa^+$ *m/z* = 830.0404 $[M+Na]^+$. Found *m/z* = 830.0373.

of $[M-(DMSO)]^+$ species corresponding to *m/z* = 681.0213 with an isotopic distribution pattern matching the calculated one, Appendix A, Figure A.29. The IR spectrum, showed the carbonyl C=O stretch at 1715 cm^{-1}, shifted by 14 cm^{-1} relative to that of **88**.

The dileptic complex $[Ru\cdot(\mathbf{88})_2](PF_6)_2$ was prepared upon heating 2 equivalents of ligand **88** with 1 equivalent of $RuCl_3\cdot xH_2O$ under microwave irradiation to 120 °C for 40 minutes, and isolated by counterion exchange to the PF_6^- salt in modest yield (28%). The ^{1}H-NMR spectrum (600 MHz, DMSO-d_6) is shown in Figure 2.2(e). The doublet and triplet associated with pyridyl protons (*u* and *v*) are clearly resolved in this spectrum, at 7.71 and 7.64 ppm, respectively, not overlapping with any other resonances. Through use of HSQC and HMBC correlation spectroscopy, ^{13}C NMR resonances (150 MHz, DMSO-d_6) could also be assigned, including the quaternary carbonyl carbon at 165.9 ppm. The characteristic MALDI+ HRMS isotopic distribution pattern observed at *m/z* =1265.2323 matched that calculated for the $[M-PF_6]^+$ species, Figure 2.3(a–b). In order to ascertain that this complex was indeed a PF_6^- salt, ^{19}F and ^{31}P NMR spectra were obtained, showing a doublet at −70.6 ppm and an apparent quintet at −142.98 ppm, respectively, which are

characteristic of the PF_6^- moiety; a strong characteristic IR band at 828 cm^{-1} was also observed. Elemental analysis also helped further confirm the identity of the complex.

The $[Ru{\cdot}(\mathbf{89})_2](PF_6)_2$ complex was prepared in an identical manner in similarly modest yield (26%). ^{1}H-NMR spectroscopy (400 MHz, DMSO-d_6, Appendix A, Figure A.14) shows a resonance characteristic of the methylene linker protons at 5.67 ppm, two doublet signals at 7.19 and 7.86 ppm, pyridyl resonances at 8.36 and 8.45 ppm (a doublet and triplet, respectively) and a triazolyl resonance at 9.26 ppm. All of these signals were shifted relative to those in the parent ligand's spectrum, particularly those related to the triazolyl and pyridyl protons. MALDI+ HRMS analysis showed an isotopic distribution pattern at *m/z* = 1063.1998, which matched that calculated for the $[M-2(PF_6)-H]^+$ species, allowing confirmation that the dileptic complex was formed, Figure 2.3(c–d). ^{19}F and ^{31}P NMR and a strong IR band at 805 cm^{-1} also helped confirm the presence of PF_6^- counterions for this complex. Elemental analysis confirmed the identity of the product.

The dileptic Ni(II) complex $[Ni{\cdot}(\mathbf{88})_2](PF_6)_2$ was prepared like the Ru(II) complexes above, using $NiCl_2{\cdot}xH_2O$ as the metal source. The d^8 Ni(II) ion is paramagnetic, hence the signals in the ^{1}H-NMR (600 MHz, CD_3CN) spectrum were broadened and shifted. One signal was shifted as far downfield as 56.46 ppm (see Appendix A, Figure A.19); the proton resonances were not assigned. The isotopic distribution patterns measured in MALDI+ HRMS at *m/z* = 1221.2644 matched that calculated for the complex with one PF_6^- ion absent, Figure 2.3(e–f). As above, ^{19}F and ^{31}P NMR spectra and a strong IR band at 813 cm^{-1} supported the identification of the compound as a PF_6^- salt, and this was further confirmed by elemental analysis.

The formation of the monoleptic complex $[Ir{\cdot}(\mathbf{88})Cl_3]$ was also achieved by using conditions modified from those previously reported by Collin *et al.* for analogous **terpy** ligands (heating under microwave irradiation to 160 °C in $(CH_2OH)_2$ for 20 minutes).[196] This complex showed very poor solubility in a range of solvents. However, the ^{1}H-NMR spectrum (400 MHz, DMSO-d_6) was successfully recorded in a dilute solution, Figure 2.2(d). Compared to the spectrum of the parent ligand, the pyridyl resonances were much more resolved for this complex, appearing as a triplet and doublet at 8.15 and 8.30 ppm (*v* and *u*) and the triazolyl resonance (*t*) was significantly more deshielded at 9.33 ppm. The experimental and calculated ESI+ HRMS spectra are shown in Figure 2.3(g–h) and the isotopic distribution pattern centred at *m/z* = 830.0373 matched the theoretical pattern. This complex was found to be unstable and decomposed over a period of two weeks. It was also

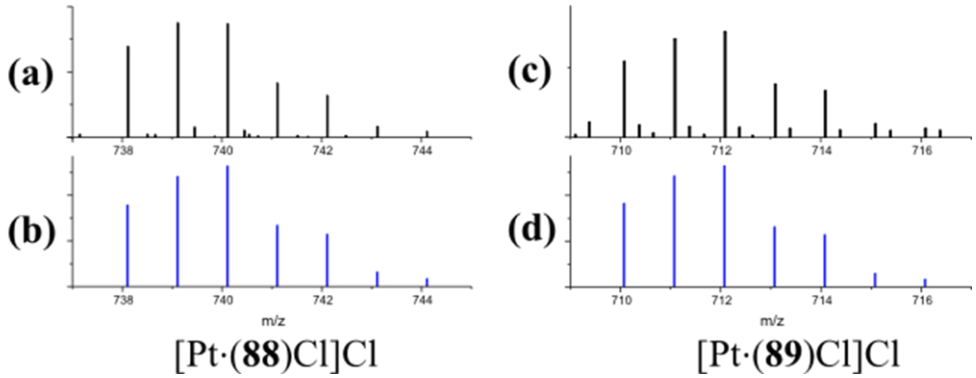

Figure 2.4 (a) Experimental and **(b)** calculated HRMS isotopic pattern distribution for [Pt·(**88**)Cl]Cl. HRMS (*m/z*) (ESI+): Calculated for $C_{27}H_{23}N_7O_4ClPt^+$ *m/z* = 739.1148 $[M]^+$. Found *m/z* = 739.1143; **(c)** Experimental and **(d)** calculated HRMS isotopic pattern distribution for [Pt·(**89**)Cl]Cl. HRMS (MALDI−): Calculated for $C_{25}H_{19}N_7O_4ClPt^-$ *m/z* = 711.0835 $[M-Cl]^-$. Found *m/z* = 711.0859.

shown to dissociate rapidly in DMSO solution over a period of six hours. Though not stable, it is the first example of an Ir(III)-**btp** complex to be reported to date.

Monoleptic Pt(II) complexes of both **88** and **89** were successfully obtained by reaction of the relevant ligand with *cis*-$[PtCl_2(DMSO)_2]$ in refluxing CH_3OH for 5 hours in darkness. [Pt·(**88**)Cl]Cl was recovered as a yellow solid in 20% yield. The ^{1}H-NMR spectrum of [Pt·(**88**)Cl]Cl (400 MHz, DMSO-d_6) is shown in Figure 2.2(e). Unlike the spectra of some of the other complexes, there were no overlapping resonances; the triplet arising from the 4-pyridyl proton (marked *v* in Figure 2.2) being shifted further downfield than the other pyridyl protons (*u* in Figure 2.2). The triazolyl resonances (*t*) was observed at 9.32 ppm was shifted relative to the ligand a similarly to the other monoleptic complexes. ESI+ HRMS analysis displayed an isotopic distribution pattern at *m/z* = 739.1143 which matched the calculated spectrum for the $[M]^+$ species, Figure 2.4(a–b). IR spectroscopy showed a carbonyl band at 1716 cm^{-1}. Elemental analysis confirmed the identity of the complex. The [Pt·(**88**)Cl]Cl complex was found to have limited solubility in most common solvents and it was shown to dissociate in DMSO solution over a few hours. The ^{1}H-NMR spectrum of [Pt·(**89**)Cl]Cl is shown in Appendix A Figure A.26 and HRMS spectra of both Pt(II) complexes are shown in Figure 2.4.

2.4 X-ray crystal structure analysis

In order to further characterise the compounds discussed above, a number of crystal structures were obtained; these provided insight into the solid-state structural properties of the compounds and their packing interactions, as well as giving information about the coordination geometry around the metal ion centre for the various complexes. The general crystallographic data and structure refinements are provided in Table 2.1. All X-ray diffraction data in this chapter were collected and refined by Dr Jonathan Kitchen, except

for the structure of [Ru·(**88**)Cl_2(DMSO)], for which by Dr Miguel Martínez-Calvo collected and refined the data; both were members of the Gunnlaugsson Group at the time. In the following section, these crystal structures are described and discussed, paying particular attention to the metal coordination sphere and hydrogen bonding interactions.

Single crystals of **88** were grown by slow evaporation of a solution in $CHCl_3$, yielding yellow plate-like crystals, from which the solid-state structure was determined at 108 K. The ligand crystallised in the low-symmetry triclinic space group $P\bar{1}$. The molecule, as displayed in Figure 2.5(a), adopted a 'horseshoe' configuration, which is in keeping with the *anti-anti* conformation shown previously for structurally similar **btp** ligands.[107,111,124-126] This is a result of electrostatic repulsion between the lone pairs of the pyridyl and 3-triazolyl nitrogen atoms; resulting in the triazolyl protons pointing into the cavity. Moreover, the plane of the **btp** motif was approximately orthogonal to the planes of the phenyl rings (88.29° and 88.38°). The molecules pack in an interdigitated manner, as shown inFigure 2.5(b), as a result of π–π interactions between the phenyl rings in the ligand's 'arms'. The planar **btp** motifs are also arranged parallel to each other. Moreover, hydrogen-bonding interactions between three of the four methylene CH protons with triazolyl nitrogen atoms as well as an interaction of the 5-pyridyl CH with the triazolyl nitrogen, are also observed. These interactions are all of the order of 2.6 Å in length and at angles between 158–165° (Details of these interactions are shown in Table 2.2).

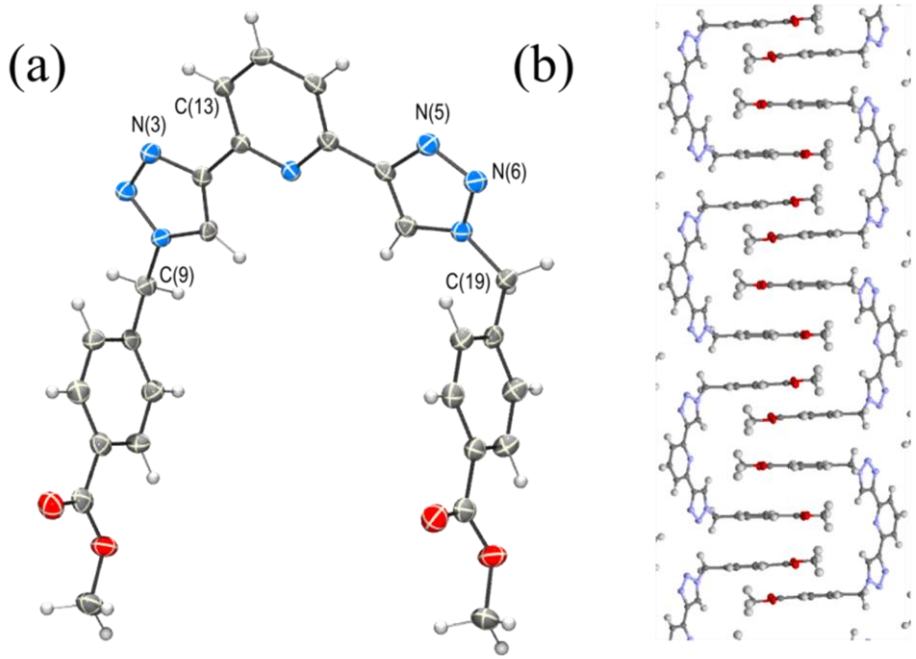

Figure 2.5 (a) Crystal structure of **88** shown with thermal ellipsoids at 50% probability. Hydrogen atom positions were calculated; **(b)** The 'interdigitated' packing structure of the ligand in the solid state.

Table 2.1 Selected crystallographic data and structure refinements for the structures in this chapter.

Compound	**88**	**[Ru·(89)$_2$](PF$_6$)Cl(CH$_3$CN)(H$_2$O)$_{0.5}$(EtOH)$_{1.25}$(Et$_2$O)$_{0.5}$**	**[Ru·(88)Cl$_2$(DMSO)](H$_2$O)(CH$_3$OH)**	**[Ni·(88)$_2$](PF$_6$)Cl(H$_2$O)(CH$_3$CN)**	**[Ir·(88)Cl$_3$](H$_2$O)$_{0.25}$(C$_2$H$_6$O$_2$)$_{0.25}$**
Formula	$C_{27}H_{23}N_7O_4$	$C_{56.50}H_{54.50}ClF_6N_{15}O_{10.25}PRu$	$C_{30}H_{29}Cl_2N_7O_6RuS$	$C_{56}H_{51}ClF_6N_{15}NiO_9P$	$C_{27.50}H_{25}Cl_3IrN_7O_{4.75}$
CCDC code	956219	956220	Not submitted	956222	956221
m.w. (g·mol^{-1})	509.52	1398.14	787.63	1317.25	808.07
T (K)	108(2)	108(2)	100(2)	108(2)	100(2)
Crystal system	Triclinic	Triclinic	Monoclinic	Triclinic	Monoclinic
Space group	$P\bar{1}$	$P\bar{1}$	$P2_1/c$	$P\bar{1}$	$P2_1/c$
a (Å)	6.3501(13)	12.235(2)	14.7556(14)	14.4083(10)	15.4149(18)
b (Å)	12.965(3)	17.491(4)	13.5998(13)	14.8238(11)	14.1809(19)
c (Å)	14.859(3)	17.627(4)	17.8903(17)	16.2001(12)	15.627(2)
α (°)	92.45(3)	105.76(3)	90	108.541(3)	90
β (°)	101.17(3)	105.52(3)	113.576(2)	91.506(3)	105.781(9)
γ (°)	100.30(3)	93.49(3)	90	115.862(3)	90
V (Å^3)	1176.9(4)	3461.4(12)	3290.4(5)	2896.2(4)	3287.2(7)
Z	2	2	4	2	4
F(000)	532	1421	1600	1356	1620
D_c (Mg·m$_{-3}$)	1.438	1.333	1.590	1.51	1.673
μ (mm^{-1})	0.101	0.367	0.757	1.952	10.497
GOF on F^2	1.214	1.103	1.026	1.039	1.072
R_1 [I>2σ(I)]	0.0639	0.0705	0.0261	0.0497	0.047
wR_2 [I>2σ(I)]	0.1262	0.2099	0.0681	0.1257	0.1226

Table 2.2 Hydrogen bond distances and angles in the packing structure of **88** [Å and °]

D-H···A	d(D-H)	d(H···A)	d(D···A)	∠(DHA)
C(19)-H(19B)···N(5)	0.990	2.583	3.545(3)	164.1
C(9)-H(9A)···N(3)	0.990	2.606	3.572(3)	165.3
C(9)-H(9B)···N(6)	0.990	2.541	3.497(3)	162.2
C(13)-H(13)···N(3)	0.949	2.633	3.532(3)	158.1

A crystal structure of [Ru·(**88**)$_2$](PF$_6$)$_2$ in the triclinic space group $P\bar{1}$ was also obtained. Clear connectivity could be ascertained, but the data were not of sufficient quality to be fully refined; a picture of this structure is shown in Appendix A (Figure A.42). The flanking 'arms' of the structure were uninfluenced by any intermolecular interactions, with two distinct conformations of the complex being present in the unit cell. The coordination sphere about the Ru(II) ion clearly had a pseudo-octahedral geometry, but further analysis of the structure will not be given. The geometry of the coordination sphere was similar to that seen for the analagous dileptic complex with ligand **89**, and the structural data associated with this complex will now be discussed in detail.

Yellow crystals of complex [Ru·(**89**)$_2$](PF$_6$)Cl were grown by diffusion of diethyl ether into CH$_3$CN. The [Ru·(**89**)$_2$](PF$_6$)Cl crystallised in the triclinic space group $P\bar{1}$. When compared with the structure of ligand **88**, the triazole rings are rotated, with the N(3), N(5), N(43) and N(45) atoms coordinating the Ru(II) ion (see Figure 2.6). The Ru(II) adopts an N$_6$ coordination sphere and is distorted from an octahedral geometry. The angle formed between the pyridyl nitrogen atoms and the Ru(II) centre is only slightly distorted at 176.5°, while the intraligand triazolyl N–Ru–N angles are all approximately 157°; deviating from the ideal of 180°. The distances between the pyridyl nitrogen atoms and the Ru(II) centre are slightly shorter than those between the triazolyl nitrogen atoms and the metal.

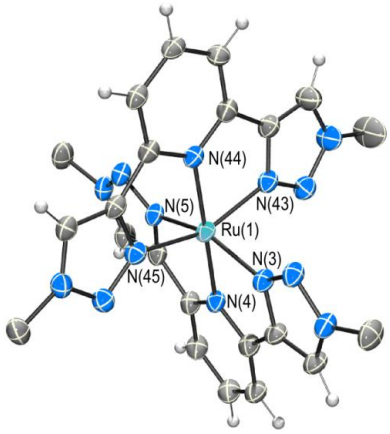

Figure 2.6 Thermal ellipsoid representation of the coordination sphere of [Ru·(**89**)$_2$](PF$_6$)Cl with thermal ellipsoids at 50% probability. Ligand 'arms', solvents and counterions have been omitted to more clearly show the atoms of interest. The **btp** motifs are arranged in a pseudo-octahedral geometry about the Ru(II) centre. Angles and bond lengths are given in Table 2.3. Full structure is shown in Figure 2.7.

Table 2.3 Selected bond lengths [Å], angles [°] and distortion parameters [°] for dileptic Ru(II) and Ni(II) complexes and their **terpy** analogues

	[Ru·(89)$_2$](PF$_6$)Cl	**[Ru·(terpy)$_2$](PF$_6$)$_2$**[a]	**[Ni·(88)$_2$](PF$_6$)Cl**	**[Ni·(terpy)$_2$](ClO$_4$)$_2$·H$_2$O**[b]
M(1)-N(4)	2.021(4)	1.974(7)	2.046(2)	2.024(8)
M(1)-N(44)	2.023(4)	1.981(7)	2.036(2)	1.984(9)
M(1)-N(3)	2.051(4)	2.065(7)	2.088(2)	2.146(11)
M(1)-N(43)	2.051(4)	2.076(6)	2.122(2)	2.116(10)
M(1)-N(5)	2.057(4)	2.065(6)	2.078(2)	2.113(11)
M(1)-N(45)	2.078(4)	2.067(6)	2.132(2)	2.108(10)
N(4)-M(1)-N(44)	176.50(14)	178.8(3)	175.43(8)	177.4(6)
N(3)-M(1)-N(5)	156.79(15)	158.4(3)	154.31(8)	156.1(4)
N(43)-M(1)-N(45)	156.60(15)	159.1(2)	154.24(8)	155.3(4)
Σ[c]	102.5	93.3	121.4	107.0

[a] Data from Lashgari *et al.*[74] [b] Data from Rae *et al.*[197] [c] Distortion parameter $\Sigma=\Sigma|(90°-\theta)|$ for *cis*-N–M–N angles.

Selected bond lengths and angles between the coordinating nitrogen atoms and the Ru(II) centre are shown in Table 2.3. The mean planes of the two coordinating ligands' **btp** motifs were nearly orthogonal, at an angle of 87.99°. This geometry is broadly in agreement with bond angles and lengths reported for similar **btp** structures previously reported, such as [Ru·(**19b**)$_2$](PF$_6$)$_2$, for which the angle between the pyridyl nitrogen atoms and the Ru(II) centre was reported as 175° and the intraligand N–Ru–N angles were 157°;[70] and [Ru·(**53**)$_2$](PF$_6$)$_2$, where these angles were reported as 178° and 157°, respectively.[126] Both of these compounds were discussed in Chapter 1. The complex's geometry was also much like that of the well-studied [Ru·(**terpy**)$_2$](PF$_6$)$_2$, the bond lengths and angles of which are shown in Table 2.3 for convenient comparison.[74] Similarly to the **terpy** analogue, the pyridyl N–Ru bond lengths are shorter than the triazolyl N–Ru distances. However, the difference between these two measurements is less significant than for **terpy** with variations of less than 0.06 Å, as opposed to nearly 0.10 Å. The angles are also more distorted from octahedral than the **terpy** analogue by approximately 2° in each case and the distortion parameter, Σ,[198] for this structure (equal to the sum of the deviations of each *cis*-N–Ru–N angle from the ideal of 90°) is 102.5°, which is more distorted from the ideal than the **terpy** structure, for which Σ is 93.3°, *cf.* Table 2.3. This structural analogy between **btp** and **terpy** complexes has been noted by other researchers in the past,[70,71,126] and has been further confirmed for these new structures.

Having described the arrangement of the coordination sphere about the Ru(II) ion, the remainder of the ligand structure will now be discussed. The 'arms' of each ligand were arranged differently as shown in Figure 2.7, with all of the terminal carboxylic acid groups being involved in hydrogen bonding in the solid state. One carboxylic group CO(1)O(2)H

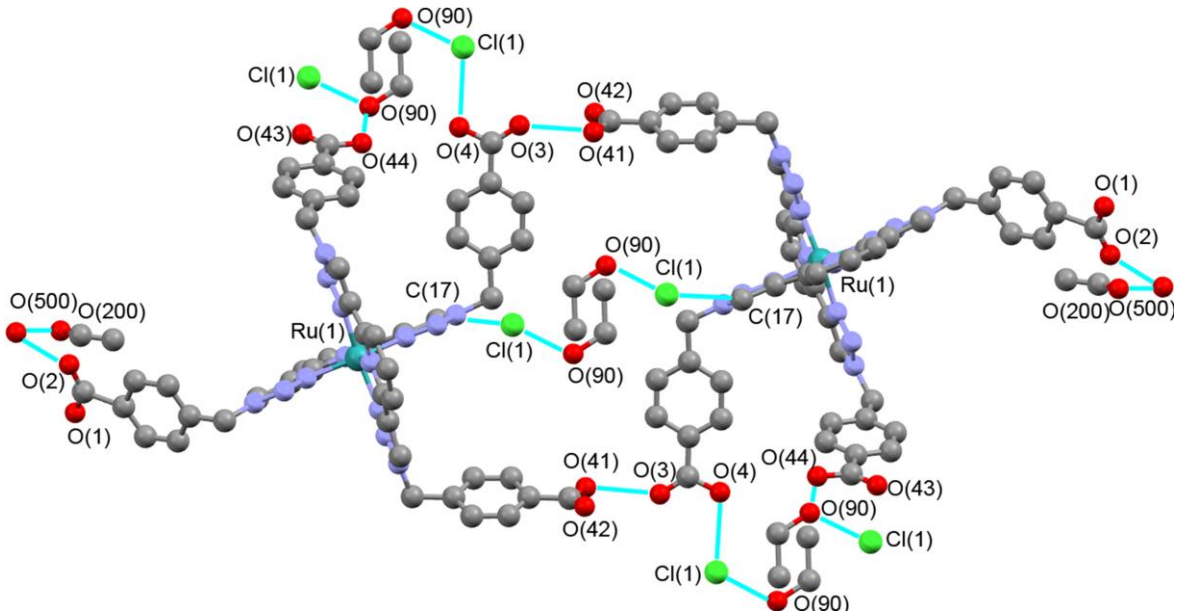

Figure 2.7 A ball and stick model of the X-ray crystal structure of [Ru·(**89**)$_2$](PF$_6$)Cl, showing hydrogen-bonding interactions. Molecules of CH_3CN and Et_2O not involged in hydrogen bonding interactions, and PF_6^- counterion, as well as hydrogen atoms are omitted for clarity.

hydrogen bonds to a water molecule HO(500)H, which in turn hydrogen bonds to an ethanol molecule (O(200)). The two ligands show intermolecular hydrogen bonding between CO(4)O(3)H and CO(42)O(41)H with a donor–acceptor distance O(41)···O(3) measuring 2.766(6) Å. O(4) also interacts with the Cl^- counterion (O(4)-H(4X)···Cl(1) = 2.980(4) Å, 176.8°. CO(43)O(44)H hydrogen bonds to the hydroxyl group (O(90)) of one disordered ethanol molecule, which also shows interactions with the Cl^- ion, leading to a repeatable coordination network. Triazolyl C(17)H displays an interaction with Cl(1) which will be discussed in more detail below. Selected hydrogen bonding distances and angles are shown in Table 2.4.

Table 2.4 Hydrogen bond lengths [Å] and angles [°] for [Ru·(**89**)$_2$](PF$_6$)Cl.

D–H···A	d(D–H)	d(H···A)	d(D···A)	∠(DHA)
O(2)-H(2X)···O(200)	0.85	2.40	3.26(4)	179.0
O(111)-H(11X)···O(100)	0.92	2.62	3.390(19)	141.3
O(41)-H(41)···O(3)	0.84	1.93	2.766(6)	172.9
O(4)-H(4X)···Cl(1)	0.90	2.08	2.980(4)	176.8
O(44)-H(44X)···O(90)	0.91	1.68	2.573(6)	165.2
O(44)-H(44X)···O(90)	0.91	1.68	2.573(6)	165.2
O(200)-H(200)···O(2)	0.85	2.57	3.26(4)	137.4
O(90)-H(90X)···Cl(1)	0.86	2.18	3.048(6)	178.6
C(17)-H(17) ···Cl(1)	0.95	2.857	3.589(5)	134.7

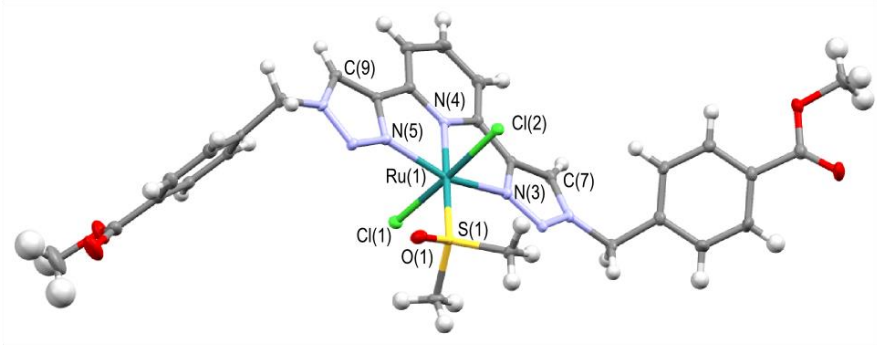

Figure 2.8 Molecular structure of [Ru·(**88**)Cl_2(DMSO)] with thermal ellipsoids at 50% probability. Solvent molecules are omitted for clarity.

Monoleptic Ru(II) complex [Ru·(**88**)Cl_2(DMSO)] crystallised in the monoclinic space group $P2_1/c$ with one molecule in the asymmetric unit as shown in Figure 2.8, as well as one CH_3OH molecule with the oxygen atom disorder over two sites. The crystallised form showed the two chlorides in the apical positions of the distorted octahedron around the Ru(II) ion, and one molecule of DMSO coordinating the metallic centre through the sulfur atom. This is analogous to a structure of [Ru·(**terpy**)Cl_2(DMSO)] reported by Zeissel *et al.*,[199] and similar to [Ru·(**52**)Cl_2(DMSO)] described in Chapter 1.[126]

The bond lengths and angles in the complex are comparable to those in an analogous **terpy** structure also as shown in Table 2.5, however, the **btp** structure is more distorted from octahedral symmetry than the **terpy** complex, as shown by distortion parameters of Σ = 55.8° and 48.9°, respectively. The structure shows non-classical hydrogen bonding between the triazolyl C(7)–H and the oxygen atom of the DMSO molecule, with a donor–acceptor distance of 2.979(3) Å with an angle of 159.7°. There is also non-classical hydrogen bonding with the chloride ion, which will be discussed below.

Table 2.5 Selected bond lengths [Å], angles [°] and distortion parameters [°] for monoleptic Ru(II) and Ir(III) complexes and their **terpy** analogues

	[Ru·(88)Cl_2 (DMSO)]	**[Ru·(terpy)Cl_2 (DMSO)]**[a]	**[Ir·(88)Cl_3]**	**[Ir·(terpy)Cl_3]**[b]
M(1)-N(4)	2.0201(18)	1.980(6)	1.996(5)	1.927(3)
M(1)-N(3)	2.0604(18)	2.081(6)	2.057(5)	2.044(3)
M(1)-N(5)	2.0738(18)	2.081(6)	2.022(5)	2.049(3)
M(1)-Cl(3)	2.4048(6)	2.404(2)	2.3543(18)	2.370(1)
M(1)-Cl(1)	2.4023(6)	2.404(2)	2.3559(17)	2.3556(7)
M(1)-S(1)/Cl(2)	2.2554(6)	2.268(3)	2.3585(17)	2.3466(8)
N(4)-M(1)-S(1)/Cl(2)	179.93(6)	180.00	175.83(16)	177.34(8)
N(3)-M(1)-N(5)	157.00(7)	157.6(3)	159.3(2)	161.3(1)
Cl(3)-M(1)-Cl(1)	175.95(2)	178.7(1)	179.27(6)	179.51(3)
Σ[c]	55.8	48.9	52.1	44.4

[a] Data from Ziessel *et al.*[199] [b] Data from Sheldrick and co-workers.[200] [c] Distortion parameter $\Sigma=\Sigma|(90°-\theta)|$ for *cis*-N–M–N angles.

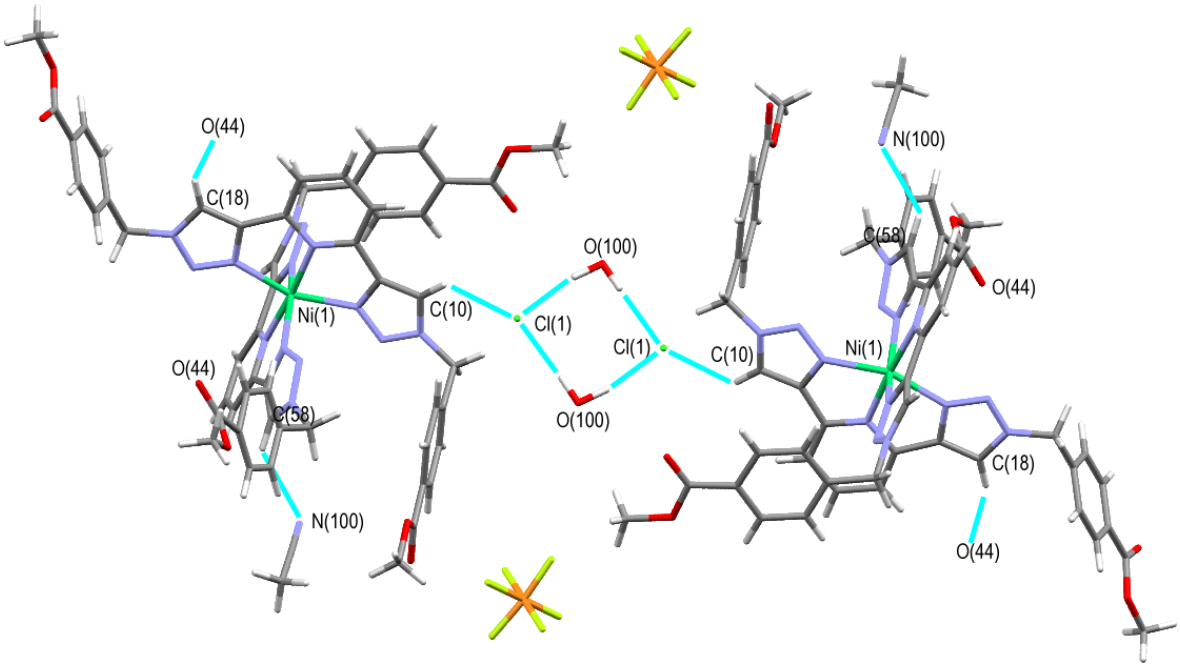

Figure 2.9 Capped stick model of the packing structure of [Ni·(**88**)$_2$](PF$_6$)Cl, highlighting hydrogen bonding interactions.

Lilac crystals of the Ni(II) complex of ligand **88** were obtained upon diethyl ether diffusion into a CH_3CN solution of the complex. [Ni·(**88**)$_2$](PF$_6$)Cl crystallised in the triclinic space group $P\bar{1}$, like the dileptic Ru(II) complexes above, with one molecule in the asymmetric unit. The structure has a distorted octahedral geometry around the metal centre, with *cis*-N–Ni–N bond angles ranging from 77.15(8)°–106.93(8)° and *trans*-N–Ni–N angles ranging from 154.24(8)°–175.43(8)°. This structure is more distorted from octahedral geometry than the [Ru·(**89**)$_2$](PF$_6$)Cl structure, with a distortion parameter of 121.4°. The comparison of this structure to a **terpy** analogue (Table 2.3), showed that the geometry is significantly more distorted from octahedral, the average pyridyl N–Ni bond lengths are slightly longer and the average triazolyl N–Ni bonds are slightly shorter (2.105 Å compared to 2.121 Å for **terpy**).[197] The distortion parameter of the **terpy** structure is also lower, with a value of 107.0°. The packing of the [Ni·(**88**)$_2$](PF$_6$)Cl complex is shown in Figure 2.9. In contrast to the carboxylic acid 'arms' in the structure of [Ru·(**89**)$_2$](PF$_6$)Cl

Table 2.6 Hydrogen bond lengths and angles for [Ni·(**88**)$_2$](PF$_6$)Cl [Å and °].

D-H···A	d(D-H)	d(H···A)	d(D···A)	∠(DHA)
O(100)-H(10X)···Cl(1)	0.978	2.2273	3.193(2)	169.3
O(100)-H(10Y)···Cl(1)	0.921	2.3105	3.221(3)	169.6
C(10)-H(10A) ··Cl(1)	0.950	2.7042	3.434(3)	134.1
C(9)-H(9B) ··N(100)	0.990	2.721	3.687(4)	165.0
C(58)-H(58A) ··N(100)	0.950	2.626	3.357(6)	134.2
C(18)-H(18A) ··O(44)	0.950	2.129	2.993(6)	150.7
C(50)-H(50A) ··F(1)	0.950	2.509	3.295(3)	140.2
C(50)-H(50A) ··F(2)	`0.950	2.346	3.277(3)	166.3

above, the methyl ester ligand 'arms' of ligand **88** do not have any hydrogen bonding interactions with each other. Both hydrogen atoms of the interstitial water molecule display hydrogen bonding interactions to the chloride ions in the structure (O(100)–H···Cl(1) = 3.193(2) and 3.221(3) Å, ∠(O(100)–H···Cl(1)) = 169.3 and 169.6°), while the chloride also interacts with one of the triazolyl protons C(10)H (*vide infra*). There is also a solvent···π interaction between the water molecule and N(7) of one of the triazole rings. The lone pair on O(100) of the water molecule points towards the ring. This interaction has an O···centroid distance of 3.297 Å. Selected bond lengths and angles are provided in Table 2.6.

Small single crystals of the [Ir·(**88**)Cl_3] complex were grown by vapour diffusion of diethyl ether solution into a DMF solution. Like the other monoleptic complex above, [Ir·(**88**)Cl_3] crystallised in the monoclinic space group $P2_1/c$ with one molecule in the asymmetric unit as shown in Figure 2.10. The structure contains one quarter occupancy ethylene glycol and one quarter occupancy water molecule. One of the ester groups was disordered over two sites with relative occupancies of 50% for each site disorder, only one position is shown in Figure 2.10 and full refinement details are provided in Appendix A. The Ir(III) adopts a distorted octahedral geometry, with an N_3Cl_3 coordination sphere. The intraligand triazolyl *trans*-N–Ir–N angle, much like the structures already discussed, is distorted from a purely octahedral geometry by 159.3(2)°. The pyridyl N–Ir distance (1.996(5) Å) was shorter than the triazolyl N–Ir distances (2.057(5) and 2.022(5) Å). The bond lengths and angles in the complexes are comparable to those in an analogous **terpy** structure as shown in Table 2.5.[200] Comparison of the distortion parameters for both structures shows that [Ir·(**88**)Cl_3] is more distorted (Σ = 52.1°) from pure octahedral than the **terpy** analogue (Σ = 44.4°). No crystals of the Pt(II) complexes suitable for X-ray

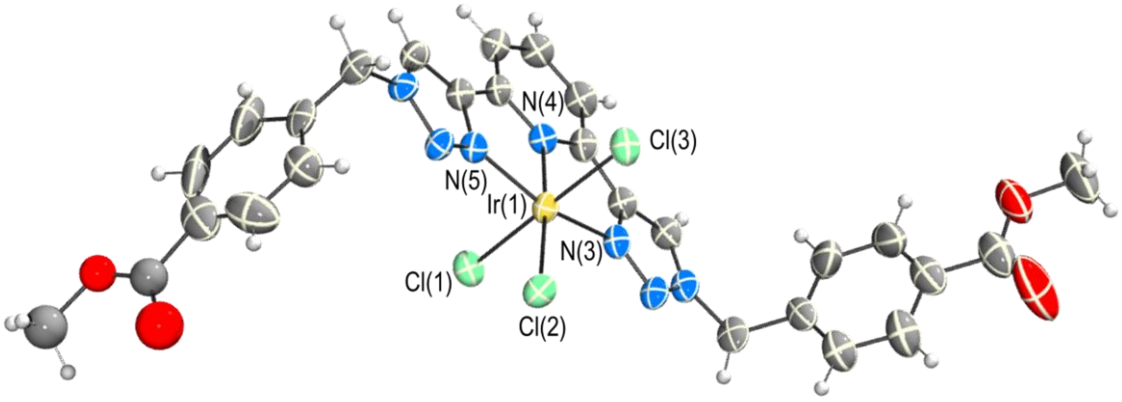

Figure 2.10 X-ray crystal structure of [Ir·(**88**)Cl_3]. Thermal ellipsoids at 50% probability. Only one position of the disordered ester group is shown. Selected bond lengths and angles are shown in Table 2.5.

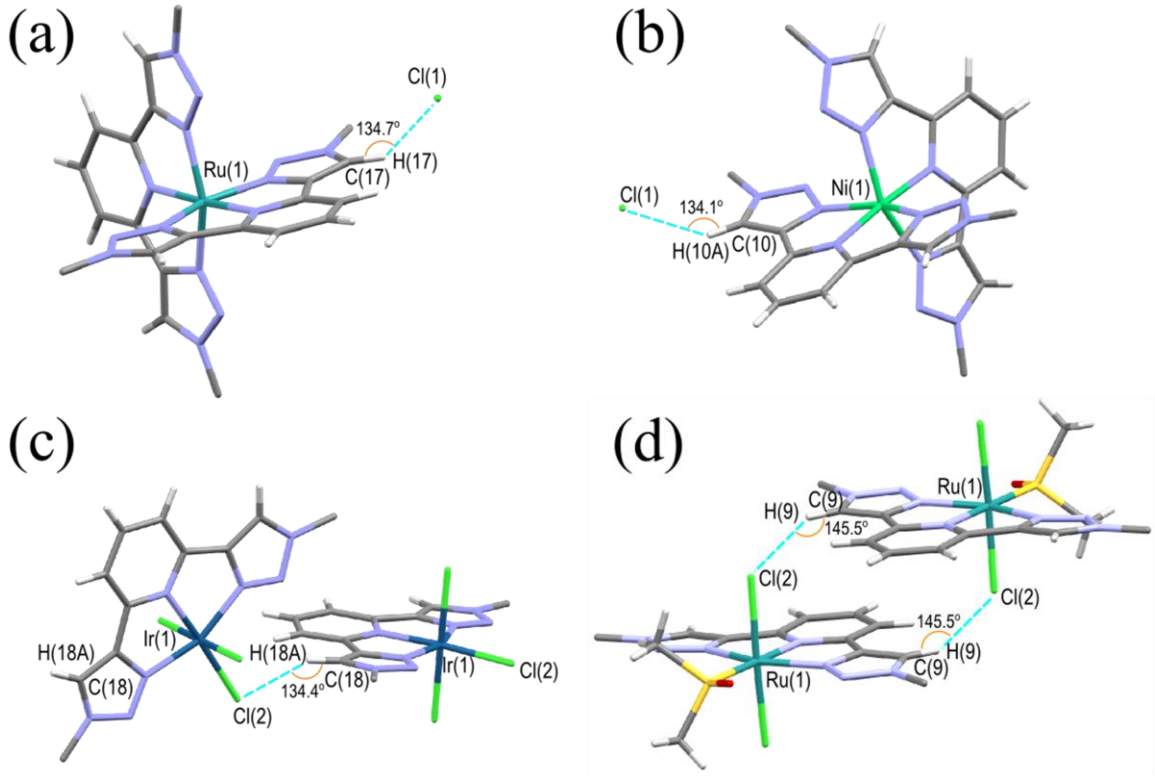

Figure 2.11 Non-classical triazolyl C–H···Cl^- hydrogen bonding in the structure of **(a)** [Ru·(**89**)$_2$](PF$_6$)Cl; **(b)** [Ni·(**88**)$_2$](PF$_6$)Cl; **(c)** [Ir·(**88**)Cl$_3$]; and **(d)** [Ru·(**88**)Cl$_2$(DMSO)]. For clarity, solvents, counterions (other than chloride) and ligand 'arms' have been omitted. Hydrogen bond lengths are shown in Table 2.7.

crystallography were obtained; this was due mostly to the poor solubility of these complexes in most common solvents.

The structures of the four complexes [Ru·(89)$_2$](PF$_6$)Cl, [Ni·(88)$_2$](PF$_6$)Cl, [Ir·(88)Cl$_3$] and [Ru·(88)Cl$_2$(DMSO)] all displayed non-classical hydrogen bonding interactions between the acidic triazole CH and chloride ions present in the structures (examples shown in Figure 2.11). As well as binding cations, such as *d*-block metals, it has been shown that 1,2,3-triazole ligands are capable of recognising anions. Anion receptors have been reported which take advantage of these interactions, for instance to simultaneously bind both metal ions and halide from salts such as KCl,[160] or template the formation of interlocked structures.[161] The research group of Professor Amar Flood have synthesised a range of 'triazolophane' macrocycles, some based on the btp motif, which can encapsulate

Table 2.7 Non-classical hydrogen bond lengths [Å] and angles [°] for all four complexes. (D=donor, A=acceptor)

Complex	D-H···A	d(D-H)	d(H···A)	d(D···A)	∠(DHA)
[Ru·(**89**)$_2$](PF$_6$)Cl	C(17)-H(17)···Cl(1)	0.950	2.857	3.589(5)	134.7
[Ni·(**88**)$_2$](PF$_6$)Cl	C(10)-H(10A) ··Cl(1)	0.950	2.7042	3.434(3)	134.1
[Ir·(**88**)Cl$_3$]	C(18)-H(18A) ··Cl(2)	0.950	2.623	3.358(8)	134.4
[Ru·(**88**)Cl$_2$(DMSO)]	C(9)-H(9)···Cl(2)	0.930	2.854	3.659(2)	145.5

halide ions in their cavities,[102,163-165] however, despite their potential for interesting interactions triazole C–H···Cl^- bonds have not been widely investigated, but studies published with structural data consistently report donor–acceptor distances of the order of 3.5 Å.[99,102,201] The bond lengths and angles for the C–H···Cl^- bonds in the first three structures shown in Figure 2.11(a–c) and Table 2.7 are very similar to each other, with H···Cl^- distances of 2.6–2.8 Å and with donor–acceptor distances being between 3.3–3.6 Å. The Cl^- being located about 134° out of the plane of the C–H bond in all cases. The monoleptic Ru(II) complex forms a dimer, Figure 2.11(d), and has a weaker interactions between the triazolyl C–H and Cl^-, with a long H···Cl^- distance of 2.85 Å at a large angle of 145.5° out of the plane. Having structurally characterised the aforementioned complexes, we next investigated the emergent supramolecular properties of $[Ru\cdot(89)_2]^{2+}$, which was serendipitously discovered to form a gel under certain conditions.

2.5 Formation of supramolecular metallogels

The structural analysis of $[Ru\cdot(\mathbf{89})_2](PF_6)Cl$ discussed above, Figure 2.7, suggests the potential of this compound for the formation of supramolecular metallogels due to the presence of polymer chains within its crystal structure through hydrogen bond interactions between the carboxylic groups and chloride anions. There currently exists a great interest within the field of supramolecular and materials chemistry in the search for such new materials with various functional properties that are different from their monomeric components.[202-204] Previous work in the Gunnlaugsson laboratory has shown the use of lanthanide ions for the formation of luminescent organic metallogels (or supramolecular gels) from tripodal **terpy**-based ligands and self-assembly Langmuir–Blodget films from compounds such as **82** as mentioned in Section 1.9.[8,9,64] The former, it was recently shown can be used as a matrix for the growth of inorganic salt nanowires (*e.g.* NaCl, KCl and KI)[205] while others have used this idea to create optically healable supramolecular polymers[206] or potential luminescent reporters for micro-environmental changes.[207,208]

Here the supramolecular metallogel of $[Ru\cdot(\mathbf{89})_2](PF_6)Cl$ was formed in several steps by preparing an ethanol solution of the dichloride complex followed by addition of a saturated aqueous solution of NH_4PF_6 with subsequent formation of a precipitate (the bis-(PF_6) complex). The supranatant was then decanted off and left to stand overnight resulting in the formation of viscous yellow soft material, which was identified as gel by simple "inversion test" as seen in the inset in Figure 2.12.[204] The gel exhibited luminescence

similar to that of the ligand (*vide infra*). ^{1}H-NMR (400MHz, DMSO-d_6) and HRMS, shown in Figure 2.13, confirmed that the gel contained the $[Ru\cdot(\mathbf{89})_2]^{2+}$ species.

The fibrous nature of the gels was revealed by helium ion microscopy (HIM) and scanning electron microscopy (SEM), Figure 2.12. Both analyses showed similar structure of the material but HIM allowed higher quality data to be obtained compared to SEM. It is hypothesised that the fibres consist of Ru(II) complexes connected together through hydrogen bonding forming in a similar manner to the network found by solid state structural analysis, Figure 2.7, involving carboxylic groups, chloride anions and solvent molecules. The average width of the fibres was found to be in a range of 100±25 nm (by HIM); while the secondary order arrangement of the fibres can be found under higher magnification with a width of 20±5 nm, Figure 2.12(b). These images were measured by Dr Oxana Kotova and Dr Alan Bell in Professor John Boland's laboratory in the Centre for Adaptive Nanostructure and Nanodevices at Trinity College, Dublin.

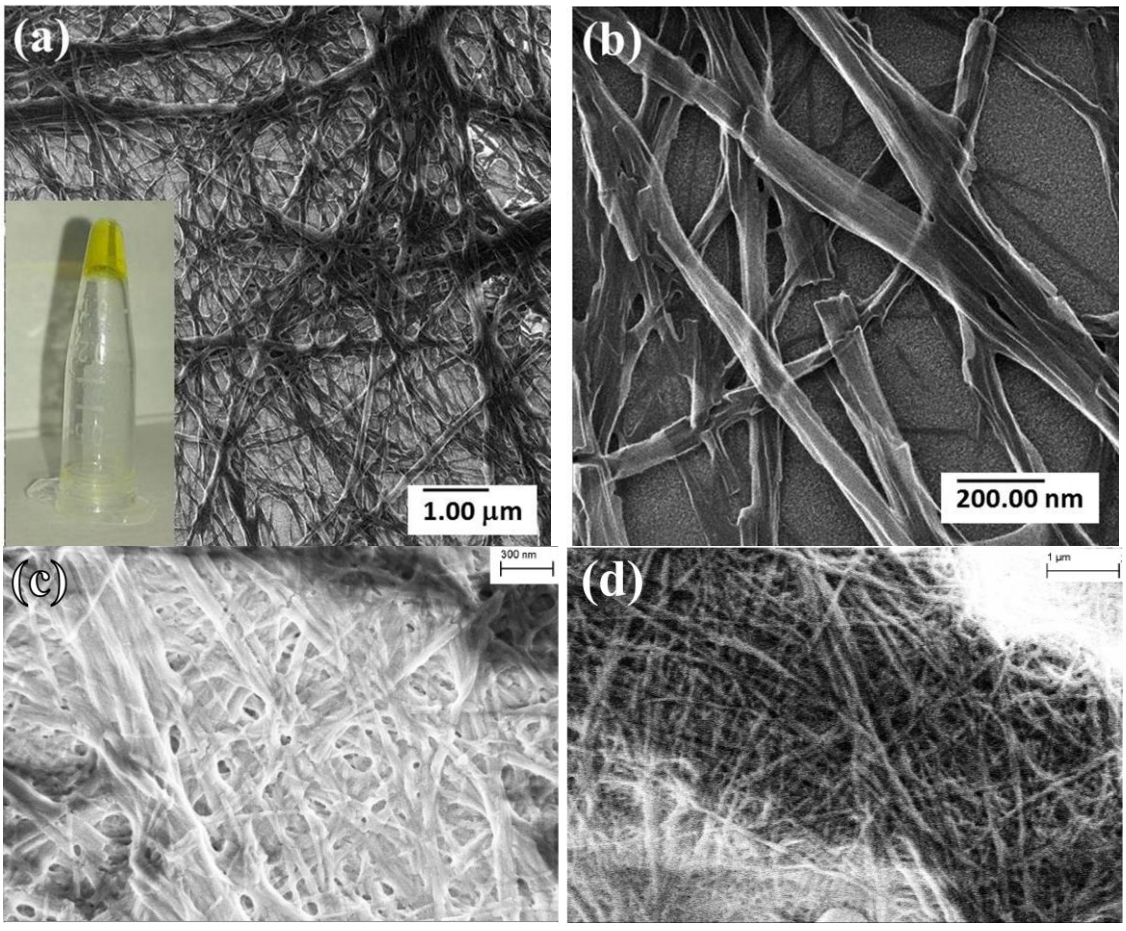

Figure 2.12 Images of Ru(II) gel showing its fibrous microstructure: **(a, b)** HIM images; **(c, d)** SEM images. The inset in **(a)** shows the formation of the metallogel in ethanol.

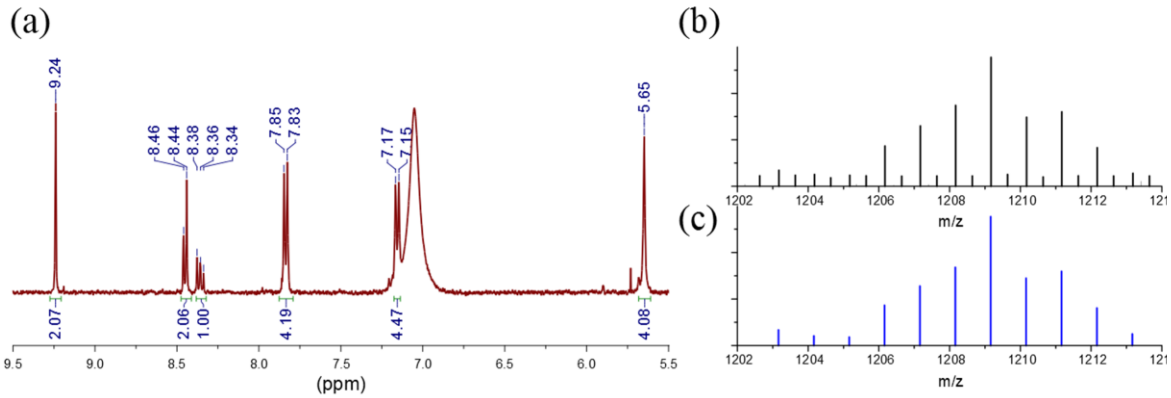

Figure 2.13 Characterisation of dried out sample of metallosupramolecular gel, proving the presence of $[Ru\cdot(\mathbf{89})_2]^{2+}$ **(a)** ^{1}H-NMR (400 MHz, DMSO-d_6) spectrum; **(b)** experimental and **(c)** calculated HRMS isotopic distribution pattern. Calculated for $C_{50}H_{38}N_{14}O_8RuPF_6^+$ $[M-Cl]^+$ *m/z* = 1209.1682. Found *m/z* = 1209.1732.

Structural analysis of the other *d*-metal complexes investigated in this work did not suggest the formation of supramolecular metallogels was as likely, since they lack the terminal carboxylic groups, which gave rise to extended hydrogen bonding networks. Attempts to obtain similar materials for these complexes in a range of solvents (CH_3OH, C_2H_5OH, CH_3CN, *inter alia*.) were, on all occasions, not successful. Interestingly, solutions of the isolated $[Ru\cdot(\mathbf{89})_2](PF_6)_2$ did not form gels, suggesting that the Cl^- ions were essential to gel formation. However, simple structural modification of these ligands by, for instance, incorporating functional groups, such as large polymer chains, either at the central pyridyl unit or on the arms themselves, could open up an avenue for the creation of new functional materials. By simply employing coordination with other metal ions, such as the *f*-metal ions, or the use of mixed transition and lanthanide metal ions, their interesting luminescent and magnetic properties could be exploited in these materials. Such further developments are foreseen for analogues of **88** and **89** in the future. Indeed, such analogues with a carboxylate substituent in the 4-pyridyl position are under development by a new Ph.D. student in the Gunnlaugsson laboratory, Mr Eoin McCarney, whose work follows on from that presented in this thesis and these systems are showing promising preliminary results with respect to their ability to form gels and supramolecular metallogels with *f*-metal ions. These systems will be discussed again towards the end of this thesis.

2.6 Photophysical investigations

The ligands and their complexes have been fully characterised and in most cases structurally characterised, with insight given into the coordination behaviour of these

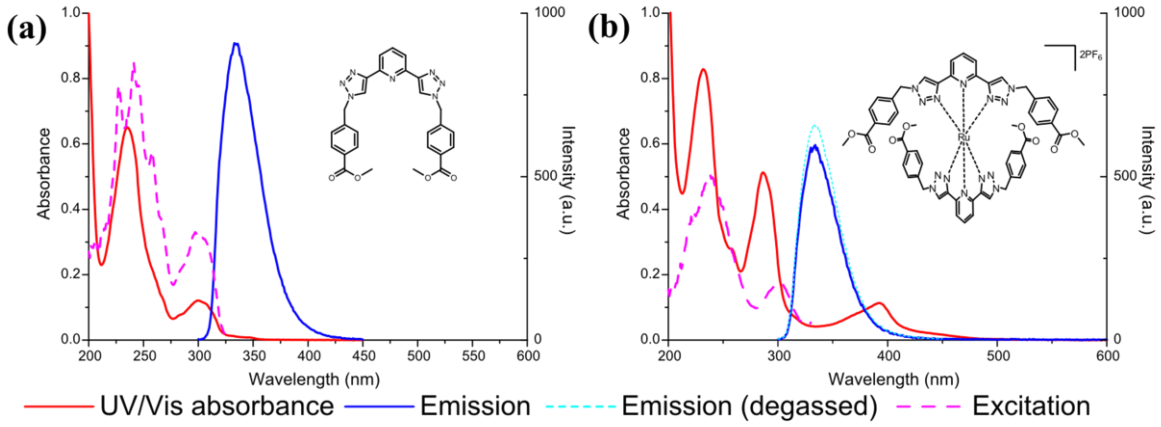

Figure 2.14 Photophysical spectra in CH_3CN for **(a)** ligand **88** in CH_3CN; and **(b)** dileptic complex $[Ru\cdot(\mathbf{88})_2](PF_6)_2$.

ligands with a range of metal ions. Ru(II) and Ir(III) complexes, in particular, but also Pt(II) complexes are often found to possess desireable luminescence properties. As such, the photophysical properties of all of the compounds discussed above were assessed and the results are discussed below. All the photophysical properties were investigated in spectroscopic grade CH_3CN solution, a polar aprotic solvent with low viscosity in which all the compounds were sufficiently soluble to perform UV-Vis absorbance, excitation and emission spectroscopy at a concentration of *ca.* 10^{-5} M; all measurements were performed in this concentration range, unless otherwise stated. The degree of UV transparency and relatively high dielectric constant of CH_3CN make it an appropriate solvent for both photophysical and electrochemical measurements (*vide infra*).

The UV-Vis absorbance spectrum of ligand **88** at room temperature displayed two bands with absorption maxima at 235 nm (ε 45000 M^{-1} cm^{-1}) and 300 nm (ε 8700 M^{-1} cm^{-1}) upon excitation of this ligand, a broad emission band centred at 335 nm was observed, Figure 2.14(a). This emission exhibited a lifetime of ~2.5 ns. Ligand **89** had almost identical spectroscopic behaviour, see Appendix A Figure A.46.

The absorbance spectrum of $[Ru\cdot(\mathbf{88})_2](PF_6)_2$ in CH_3CN, shown in Figure 2.14(b), showed bands similar to those of the ligand, but blue-shifted, only slightly in the case of the band centred at 232 nm, but by *ca.* 15 nm for the band at 286 nm, the band tentatively assigned to the **btp** n→π* transitions. The spectrum also exhibits a new MLCT band at 395 nm.

Bis-terdentate Ru(II) complexes (including $[Ru(\mathbf{terpy})_2]^{2+}$) are often practically non-luminescent, due to thermal population from their ^{3}MLCT excited states to a close-lying non-emitting metal centred (^{3}MC) excited states, Figure 2.15 (redrawn from Dinda *et al.*[209]). It has been reported that modifying the ligand structures can, however, raise the

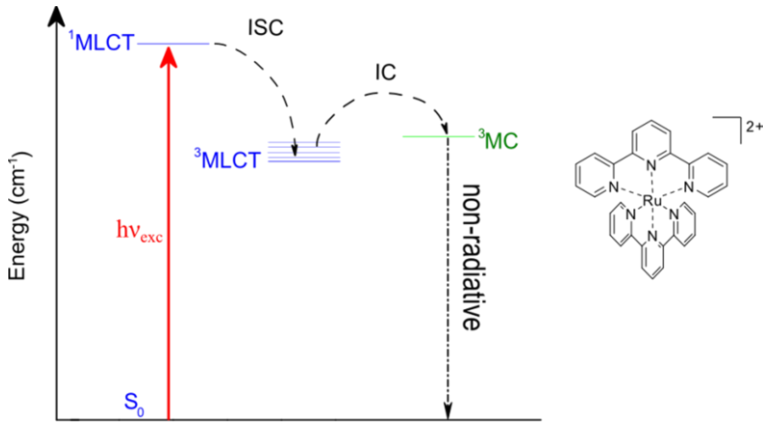

Figure 2.15 Schematic Jablonski diagram for [Ru·(**terpy**)$_2$]$^{2+}$, showing thermal population of the ^{3}MC from the ^{3}MLCT state.

energy of the ^{3}MC state and hence, increase the luminescence arising from such structurally modified complexes. Perfect octahedral geometry about the metal ion is thought to increase the ^{3}MC energy by leading to a strong ligand field.[209] However, since it has been shown in the structural studies above that the coordination environment in these complexes is distorted significantly from pure octahedral geometry (Σ = 102.5°), we did not necessarily expect [Ru·(**88**)$_2$](PF$_6$)$_2$ to be highly luminescent in solution. Indeed, as has been the case with most **btp**-based ligands discussed in Section 1.4.8 above, as well as simple **terpy**-based ligands, [Ru·(**88**)$_2$](PF$_6$)$_2$ showed no long-lived luminescence at room temperature, as only a ligand-centred fluorescence band at 335 nm ($\tau \approx$ 2.5 ns) similar to that of the ligand was observed. Moreover, degassing the solution led to only a slight enhancement in the luminescence intensity; confirming that there were no emissive bands which were quenched by the presence of triplet O$_2$. The excitation spectrum observed broadly matched the profile of that of the ligand.

In light of this, luminescence emission spectra of [Ru·(**88**)$_2$](PF$_6$)$_2$ were also recorded at 77 K, but unfortunately, no emission was observed. Similarly, the spectroscopic properties of [Ru·(**89**)$_2$](PF$_6$)$_2$ were found to follow an almost identical path to [Ru·(**88**)$_2$](PF$_6$)$_2$, only giving rise to very weak luminescence, Figure A.47. A sample of the metallogel derived from this species was immobilised on a quartz slide and the solid state luminescence measured at room temperature, and as had been seen for both the [Ru·(**88**)$_2$](PF$_6$)$_2$ and [Ru·(**89**)$_2$](PF$_6$)$_2$, complexes, only ligand-centred emission (centred at 310 nm) was observed for the metallogel and is shown in Figure 2.16.

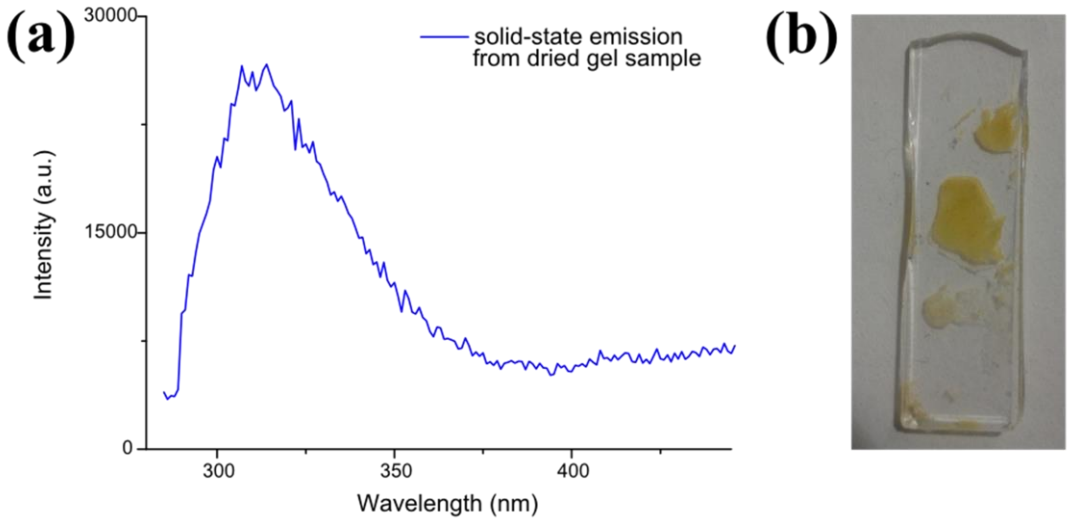

Figure 2.16 (a) Emission spectrum from metallosupramolecular gel of $[Ru\cdot(\mathbf{89})_2]^{2+}$ immobilised on a quartz slide at room temperature. **(b)** Photograph of dried gel sample on a quartz slide.

Monoleptic complex $[Ru\cdot(\mathbf{88})Cl_2(DMSO)]$ had quite different properties to those seen above. The absorbance bands recorded for $[Ru\cdot(\mathbf{88})Cl_2(DMSO)]$, Figure 2.17(a), were centred at 230, 302, 354 and 450 nm. In the analogous **terpy** complex, a similar spectrum was observed, with the low energy band assigned to an MLCT transition.[199] The complex displayed an emission centred at 335 nm as well as a very broad but significantly less intense luminescence band with its maximum at 475 nm, upon excitation at room temperature. The excitation spectrum of the higher energy band gave a spectrum matching the profile of the ligand absorbance spectrum. At 77 K, the emission was, however, found to be centred at 285 nm with a broad band of comparable intensity being also observed at longer wavelengths; being centred at 475 nm, as shown in Figure 2.17(a).

The absorbance profile of $[Ir\cdot(\mathbf{88})Cl_3]$ displayed a band at 232 nm with a shoulder at 260 nm. A band centred at 293 nm tailed off until 480 nm. For the analogous **terpy** complex, these weak low energy bands were ascribed to formally forbidden $S_0 \rightarrow T$ transitions as a result of the heavy atom effect of Ir(III).[210] At room temperature, there was a ligand centred luminescence band observed at 330 nm, while at 77 K, a broad luminescence centred at 450 nm became much more apparent; the fluorescence band at 335 nm being seen as a shoulder in the spectrum, Figure 2.17(b).

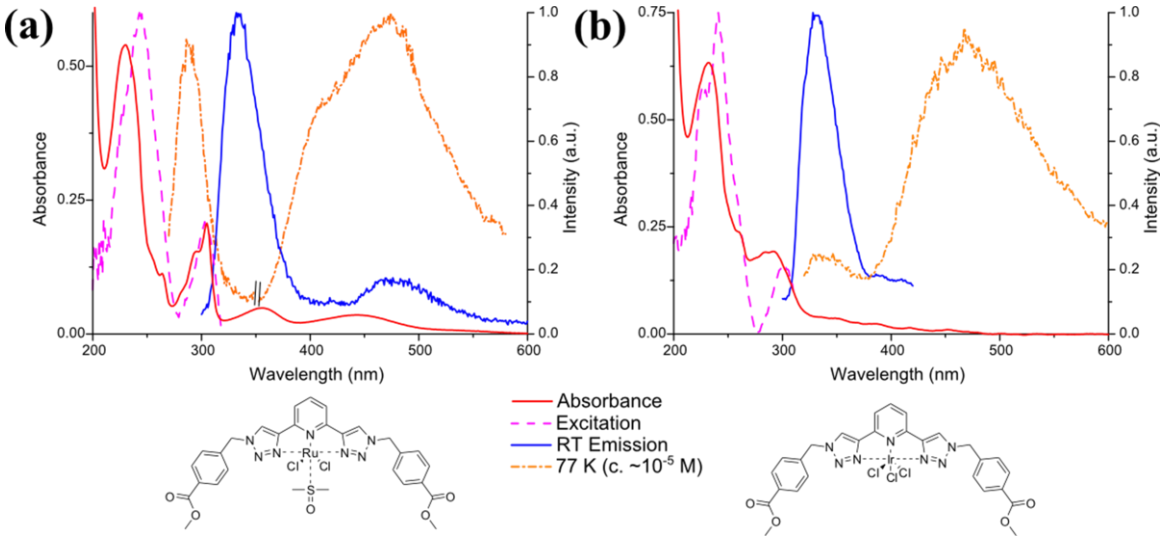

Figure 2.17 Photophysical spectra in CH_3CN of **(a)** [Ru·(**88**)Cl_2(DMSO)]; and **(b)** [Ir·(**88**)Cl_3]. UV-Vis absorbance (red), excitation (magenta), room temperature emission (blue), emission at 77 K for glass with concentration of *ca.* 10^{-5} M (orange). In **(a)**, the low temperature emission spectrum is cut where a different filter had to be applied.

For [Pt·(**88**)Cl]Cl a broad absorbance profile was observed in CH_3CN, with a maximum at 222 nm and tailing to 400 nm, Figure 2.18(a). The band centred at 353 nm was tentatively assigned to the MLCT transition by analogy to similar compounds in the literature, such as [Pt·(**19a**)Cl]Cl.[136] Planar Pt(II) complexes have been reported to have complicated emission behaviour, particularly at low temperature, as a result of the potential for stacking in solution, leading to Pt(II)–Pt(II) interactions, as well as interactions between the aromatic ligands;[194] the emission spectra for complexes such as [Pt(**terpy**)Cl]$^+$ are known to vary with concentration as well. At room temperature, only the ligand centred emission was observed for [Pt·(**88**)Cl]Cl, being centred at 333 nm. Lack of ^{3}MLCT emission has for chloroplatinum(II) complexes has been previously commented on by Bailey *et al.* and Yam and co-workers for **terpy**-based and **btp**-based systems, respectively; it was postulated that the ^{3}MLCT state could be quenched by the thermally accessible low-lying ^{3}(d–d) excited state by non-radiative decay.[136,194] However, when recorded in CH_3CN glasses (concentration of *ca.* 10^{-5} M) at 77 K, two broad emission bands were observed at 442 nm and 578 nm, for [Pt·(**88**)Cl]Cl, Figure 2.18(a). Bands of similar energies have been assigned to $^3(\pi^*\rightarrow\pi)$ emission and interligand π–π interactions respectively for the analogous **terpy** complex.[194] A longer wavelength emission band observed for the **terpy** systems arising from Pt(II)–Pt(II) interactions was not observed for [Pt·(**88**)Cl]Cl. More dilute glasses (concentration of *ca.* 10^{-6} M) show a ligand centred emission band at 335 nm as well as a weakly structured emission around 450 nm. This

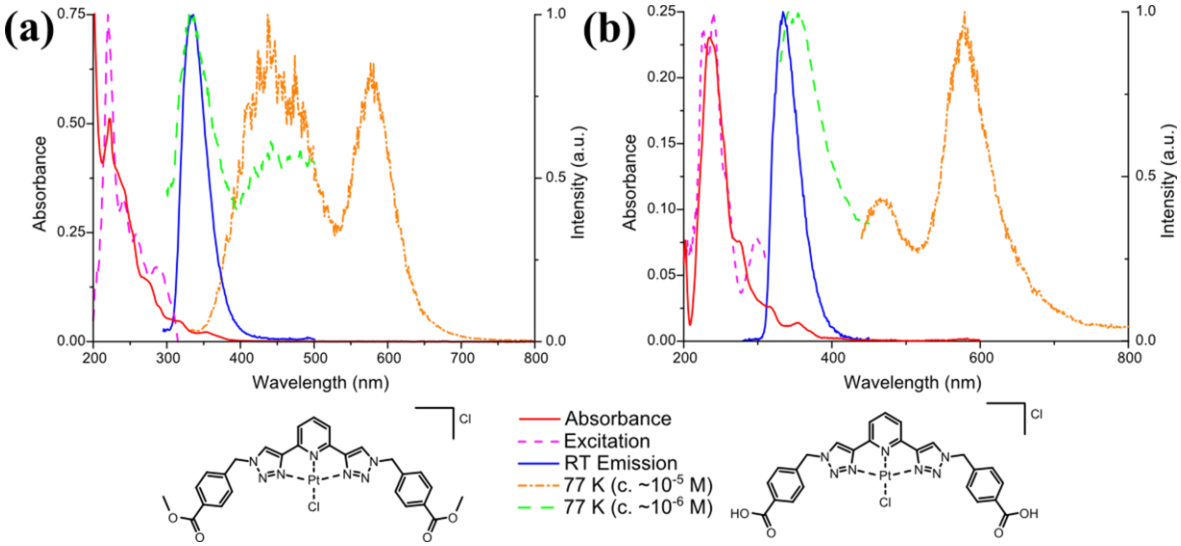

Figure 2.18 Photophysical spectra in CH_3CN of **(a)** [Pt·(**88**)Cl]Cl; and **(b)** [Pt·(**89**)Cl]Cl. UV-Vis absorbance (red), excitation (magenta), room temperature emission (blue), emission at 77 K for glass with concentration of *ca.* 10^{-5} M (orange) and emission at 77K for dilute glass with concentration of *ca.* 10^{-6} M (green).

emission spectrum closely resembles the spectra for the other monoleptic complexes discussed above. Complex [Pt·(**89**)Cl]Cl displayed very similar photophysical behaviour with concentrated glasses displaying emission at 460 and 572 nm, while at lower concentrations, two overlapping bands at 340 and 355 nm were observed, Figure 2.18(b).

In summary, all the complexes synthesised above show only ligand centred emission at room temperature in CH_3CN, with the exception of [Ru·(**88**)Cl_2(DMSO)], which displayed a weak emission at 475 nm. At low temperature (77 K), all of the monoleptic complexes did, however, display more detailed emission spectra. In addition to photophysical properties, the electrochemical properties of transition metal complexes such as those above, are regularly studied;[126,211] the electrochemical properties of the Ru(II) and Ir(III) complexes will, as such, be discussed in the following section.

2.7 Electrochemistry

As was discussed above in Section 1.4.8, the electrochemical properties of Ru(II)–**btp** complexes have often been investigated, particularly by Hecht and co-workers, who showed that variation of the ligand structure may lead to notable changes in the Ru(II)/Ru(III) oxidation potential, ranging from 0.58 V for [Ru·(**49**)$_2$](PF_6)$_2$, with an electron-donating pyrrolidyl substituent to 1.19 V for [Ru·(**52**)$_2$](PF_6)$_2$, where the methyl ester substituent is electron-withdrawing.[126] The electrochemistry of the Ru(II) complexes of ligands **88** and **89** was investigated by cyclic voltammetry (CV) in CH_3CN solution (see

Figure 2.19, Figure A.48). These measurements were performed in collaboration with Professor Martin Albrecht and Dr Vivienne Leigh with assistance from Mr Bryan Hogan at University College Dublin.

Both the [Ru·(**88**)$_2$](PF$_6$)$_2$ and [Ru·(**89**)$_2$](PF$_6$)$_2$ showed fully reversible metal-centred oxidation of Ru(II) to Ru(III) at a potential of 1.42 V v. SCE (saturated calomel electrode), Table 2.8. Variation of the ligand 'arms' from 4-(methylcarboxy)benzyl to 4-(carboxy)benzyl had almost no impact on the donor properties of the chelating ligand, which is in agreement with the remote location of these functional groups and their similar electronic impact. The oxidation potentials are higher than those reported for **terpy**-type complexes, *e.g.* +1.30 V (v. SCE) for [Ru·(**terpy**)$_2$](PF$_6$)$_2$,[211] which may be a direct consequence of the five- v. six-membered peripheral heterocycles and the ensuing better mutual alignment of metal coordination axes and the lone pairs in the **terpy** system. While a related **btp** complex [Ru·(**19b**)$_2$]$^{2+}$ with alkyl substituents at the triazole units featured a redox behaviour similar to [Ru·(**terpy**)]$^{2+}$,[70] Hecht and co-workers reported very similar oxidation potentials to those observed here for a **btp** complex with 4-iodophenyl 'arms'

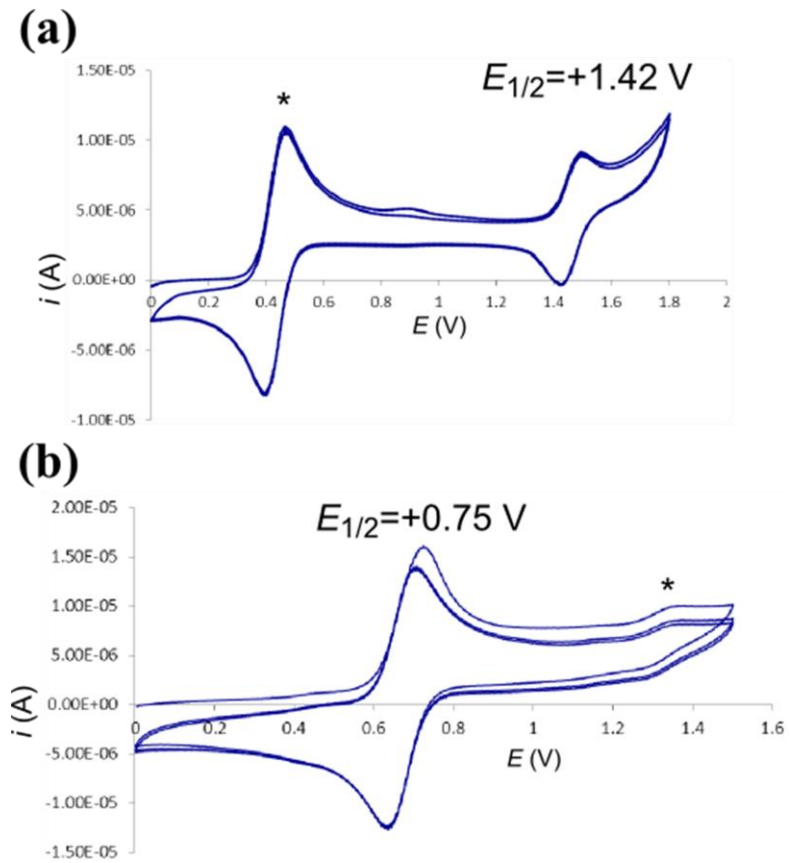

Figure 2.19 Cyclic voltammagrams of **(a)** [Ru·(**88**)$_2$](PF$_6$)$_2$ using Fc$^+$/Fc as internal standard ($E_{1/2}$ = +0.40 V (ΔE_p = 72 mV), marked with an asterisk); **(b)** [Ru·(**88**)Cl(DMSO)], using [Ru·(**bpy**)$_3$]$^{2+}$/[Ru·(**bpy**)$_3$]$^{3+}$ as internal standard ($E_{1/2}$ = +1.39V (ΔE_p = 55 mV), marked with an asterisk). TBA(PF$_6$) (0.1 mM) was used as supporting electrolyte.

Table 2.8 Half-wave potentials and anodic–cathodic peak separations of redox curves for Ru(II) complexes.

Complex	$E_{1/2}$ [V]	ΔE_p [mV]
[Ru·(**88**)$_2$](PF$_6$)$_2$	+1.42[a]	70
[Ru·(**89**)$_2$](PF$_6$)$_2$	+1.42[a]	60
[Ru·(**88**)Cl$_2$(DMSO)]	+0.75[b]	58

[a] sweep rate 100 mV s^{-1}, [NBu$_4$]PF$_6$ as supporting electrolyte (1 mM), potentials v. SCE using Fc$^+$/Fc as internal standard ($E_{1/2}$ = +0.40 V (ΔE_p = 72 mV); [b] [Ru·(**bpy**)$_3$]$^{2+}$/[Ru·(**bpy**)$_3$]$^{3+}$ as internal standard ($E_{1/2}$ = +1.39 V (ΔE_p = 55 mV). TBA(PF$_6$) (0.1 mM) was used as supporting electrolyte.

($E_{1/2}$ = +1.06 v. Fc/Fc$^+$, that is, +1.46 V v. SCE).[126] This similarity suggests a minor influence of the triazole substituent on the metal oxidation potential, which is in agreement with the weaker orbital alignment between **btp** and the octahedral ruthenium centre as compared to **terpy**-type systems.

As expected, neutral [Ru·(**88**)Cl$_2$(DMSO)] was much easier oxidised ($E_{1/2}$ = +0.75 V) than the cationic complexes, Table 2.8. The CH$_3$CN oxidation potential is slightly higher than that reported for the analogous **terpy** complex [Ru·(**terpy**)Cl$_2$(DMSO)] at +0.68 V (recorded in DMSO).[199] CV spectra of [Ru·(**88**)Cl$_2$(DMSO)] in both CH$_3$CN and CH$_3$NO$_2$ were identical, (see Appendix A, Figure A.49) suggesting that potential solvent exchange reactions due to the coordinating nature of CH$_3$CN are irrelevant. [Ir·(**88**)Cl$_3$] showed no oxidation up to solvent discharge potential.

2.8 Conclusions

In this chapter, the design and synthesis of novel terdentate **btp** ligands **88** and **89** in one pot by using 'click' chemistry was presented. These were fully characterised using various spectroscopic techniques, and their coordination behaviour with various *d*-block metal ions explored (*viz.* Ru(II), Ni(II), Ir(III) and Pt(II)). The X-ray crystal structures of ligand **88** as well as [Ru·(**89**)$_2$](PF$_6$)Cl, [Ru·(**88**)Cl$_2$(DMSO)], [Ni·(**88**)$_2$](PF$_6$)Cl and [Ir·(**88**)Cl$_3$] were obtained and structural analysis allowed for investigation into the coordination geometry of these ligands with Ru(II), Ni(II) and Ir(III). The coordination sphere of these structures closely resembled the distorted octahedral geometry of analogous **terpy** structures, although in all cases the distortion parameter, Σ, was higher for the **btp** structure. The triazole rings played an important role in these structures, with the nitrogen atoms acting as hydrogen bond acceptors and the C–H acting as a hydrogen bond donor.

The four complexes showed non-classical triazolyl C–H···Cl$^-$ hydrogen bonding interactions with three showing very similar C–H···Cl$^-$ distances and bond angles, while

the monoleptic Ru(II) complex showed longer distances and the molecules assembled as a dimer in the solid state. The photophysical behaviour of these complexes in solution was also studied, with only ligand-centred fluorescence observed at room temperature for all complexes except [Ru·(**88**)Cl_2(DMSO)]. Low temperature studies showed no emission for the dileptic complex, and a broad band centred at *ca.* 450 nm for each of the monoleptic complexes [Ru·(**88**)Cl_2(DMSO), [Ir·(**88**)Cl_3] and [Pt·(**88**)Cl]Cl. Concentrated glasses of [Pt·(**88**)Cl]Cl and [Pt·(**89**)Cl]Cl showed new emission bands consistent with stacking behaviour. Future development of the Pt(II) systems to include alkynyl ligands in place of the ancilliary chloro ligand, such as was done in work by Yam and co-workers, would be expected to result in complexes which are emissive at room temperature.[136,193,208] Electrochemical measurements of Ru(II) complexes showed that these compounds had higher oxidation potentials than similar **btp** systems in the literature, and were also higher than analogous **terpy** compounds.

The X-ray crystal structure of complex $[Ru\cdot(\mathbf{89})_2]^{2+}$ showed an extensive hydrogen-bonding network involving the carboxylic acid 'arms' of the ligand, chloride anions and solvent molecules. This complex was shown to form gels in EtOH solution and microscopy images of these gels (using both helium ion microscopy and scanning electron microscopy) showed a fibrous structure with fibre widths in the range of 100±25 nm. When immobilised on a quartz slide, this gel exhibited ligand-centred emission much like that seen for the complex in solution. In future, systems based on these could potentially be further developed for application as materials with functions including surface healing or oxidation–reduction response, but such work will not be explored in this thesis.

Having investigated the interactions of these **btp** ligands with a range of *d*-block metals, it is now of interest to explore the interactions of these ligands, and their derivatives, with *f*-block metals. This shall be discussed in the following chapters.

3. Lanthanide-directed self-assembly of btp ligands

3.1 Introduction

The coordination chemistry of the **btp** [2,6-bis(1,2,3-triazol-4-yl)pyridine] motif with many transition metal ions, *viz.* Cu(I),[104] Cu(II),[107,111] Zn(II),[126] Ag(I),[107] Pt(II),[121,136] Pd(II),[137] Pb(II),[130] Fe(II)[70,82,126] and Ru(II)[70,71,106,110,112,113,115,120,121,126,142,143] has been reviewed in detail in Chapter 1 and new work in this area was presented in the previous chapter. The most studied *d*-block metal ion, by far, in such studies is Ru(II). Hecht and co-workers have prepared a range of mono- and dileptic Ru(II)–**btp** complexes with ligands including **49** and **52** and tuned their electrochemical properties upon variation of the ligand.[126] Schubert *et al.* compared such systems' photophysical behaviour with analogous **terpy**-based systems and also reported mixed heteroleptic **terpy**–**btp** complexes (using ligands **54** and **55** with intermediate properties).[112,113,115] The coordination chemistry of novel **btp** ligands **88** and **89** with Ru(II), Ir(III), Ni(II) and Pt(II) was discussed in Chapter 2, where their photophysical and electrochemical properties were compared with **terpy** analogues.[72] It was also shown that **89** could give rise to metallogels with Ru(II).

While the **btp** motif has been explored extensively with respect to its *d*-metal coordination chemistry, there is a surprising paucity in the literature of examples of **btp** systems coordinating the *f*-block ions. The trivalent lanthanide ions, Ln(III), possess unique photophysical and magnetic properties, which make their study highly desirable for optoelectronic and bioimaging applications;[212] this will be discussed in the following sections. The need to explore the **btp** motif within lanthanide chemistry prompted the development of the work presented in this chapter, focusing on the use of Ln(III) ions to direct, through their high coordination requirements, the formation of novel functional and luminescent supramolecular self-assembled structures.

Previous work from the Gunnlaugsson laboratory, discussed in Section 1.9, has shown how Ln(III) are capable of forming self-assemblies, such as bundles,[4] helicates[5] half-helicates[6] and interlocked systems such as a [3]catenane[7] with **dpa** derivatives, as well as luminescent Langmuir–Blodgett films[8,9] and supramolecular gels based on the **terpy** motif[64]. As discussed in Section 1.4.9 above, Flood *et al.* displayed that **btp** compound **19a** can form stable coordination compounds with Eu(III), sensitising characteristic line-like emission from the metal centre *via* the 'antenna' effect (*vide infra*),[70] while Hecht and co-workers also reported Eu(III) complexes with ligands **30a** and **30e**.[82] 'Back-to-back' ditopic **btp** ligands, **24**, have also been used to sensitise Ln(III) luminescence.[117] Brunet and co-workers described covalently attaching **btp**-containing organic phosphonates, such

as **59** and **60**, to the surface of the γ-zirconium phosphate by topotactic exchange to produce a solid host which could efficiently sensitise the emission of Ln(III) ions.[109,159] O'Reilly and co-workers used Eu(III) coordinated by **btp** ligands **58** containing RAFT polymerisation agents to template 'star-branched' polymeric structures.[143] For more detailed discussion of these prior examples of Ln(III)–**btp** systems, see Section 1.4.9 above.

Some of the key features of lanthanide metal ions and their complexes, particularly their photophysical properties will now be introduced. Thereafter an investigation of the self-assembly behaviour of **btp** ligand **88** with Eu(III) and Tb(III) ions will be presented (Section 3.3), followed by similar preparation of an allyl amide appended derivative, **90**, which was capable of undergoing olefin ring-closing metathesis, yielding a self-templated [2]catenane as a result of a range of supramolecular interactions (Section 3.6). This is the first example of such an interlocked molecule based on the **btp** framework. The Eu(III)-directed self-assembly of ligand **90** in solution will then be detailed (Section 3.8). The majority of the chapter will then focus on the synthesis, characterisation and Ln(III)-directed self-assembly studies of a range of amino-acid **btp** derivatives, **91**. The studies detailed in this chapter are the first examples of Ln(III)-directed self-assembly of **btp** ligands being monitored by spectroscopic titrations and global stability constants being determined for these processes.

3.2 Lanthanide metal ions and their complexes

The lanthanides are the elements of the first period of the *f*-block, extending from La (atomic number 57) to Lu (atomic number 71). Although when considered together with Sc and Y, they are often termed *rare earths*, this historical term is misleading since such elements are actually more abundant in the earth's crust than, for example, silver, platinum and gold.[148,213] The lanthanide metal ions (Ln) display a large and varied range of coordination numbers of anywhere between 6 and 12, with the most extensively studied ions, Eu(III) and Tb(III), commonly displaying coordination numbers of 9.[2] The most stable lanthanide oxidation state is tripositive, Ln(III); these ions are 'hard' Lewis acids, and thus show preferable binding to 'hard' bases, such as oxygen, nitrogen and fluoride. The lanthanides are unique among the elements of the periodic table in their markedly similar chemical properties across the series, particularly in their oxidation states.[149,214]

The lanthanide metals possess unique magnetic and photophysical properties, which has led to increasing interest in recent years, arising from their potential applications in

medical diagnostics,[214-216] optical imaging,[11] and technological applications such as in light emitting diodes (LEDs) and telecommunications[217]. The importance of lanthanides for optical and magnetic materials has for a long time led to extensive study of their physical properties and solid state chemistry.[148] More recently, the development of contrast agents for magnetic resonance imaging (MRI) and luminescent chemosensors for optical imaging of cells[12,149] has shifted the focus towards their coordination chemistry in solution. These properties have also attracted increasing interest in the field of supramolecular chemistry.[218]

The small, regular decrease in ionic radii across the period, known as the 'lanthanide contraction', is a result of poor shielding of nuclear charge by the 4*f* orbitals, which derives from the high angular nodality of these orbitals. As nuclear charge increases across the lanthanide series, electrons experience a greater nuclear effect. This results in similar reactivity across the lanthanide series.[149]

3.2.1 Photophysical properties of the lanthanides

Lanthanide luminescence arises from the decay of electronically excited states with concomitant emission of a photon. Advantageous properties of lanthanide luminescence include long-lived excited states, long wavelength emission, sharp characteristic line-like emission bands and large *pseudo*-Stokes shifts.

The unique photophysical properties of the lanthanides are largely a result of the shielding of the 4*f* orbitals by the filled 5*s* and 5*p* orbitals. They are governed by their electronic configuration, which shows a general trend of filling the 4*f* orbitals; electrons successively occupy the 4*f* orbitals following Hund's rule, whereby each orbital is occupied singly before any orbital is doubly occupied. This leads to the paramagnetism of Ln(III) ions. Their electronic configurations are given by [Xe]$4f^n$ where n = 0–14.[219] Due to the core nature of the 4*f* electrons, which are shielded from the coordination environment by the $5s^2 5p^6$ electrons, little vibrational coupling with the environment is seen, and hence the energies of the electronic levels are well-defined and vary little with chemical environment; the emission bands are narrow and ion-specific, leading to pure colours and, potentially, high emission efficiencies.[212,217]

With the exception of La(III) and Lu(III), the Ln(III) ions are luminescent, either displaying fluorescence (*e.g.* Pr(III), Nd(III), Ho(III), Er(III), and Yb(III)), or phosphorescence (*e.g.* orange Sm(III), red Eu(III), Gd(III) which emits in the UV, green Tb(III), yellow Dy(III), and blue Tm(III)).[148] Luminescence arising from the radiative

decay, through photon emission, from an electronically excited state is described as fluorescent if there is no change in spin multiplicity upon decay from the lowest occupied Ln(III) excited state to the highest vibronic level of the ground state. The energies and term symbols of these orbitals are given in Figure 3.1.[148]

Eu(III) and Tb(III) have large energy gaps between their lowest excited states and highest levels of their ground states, making them appropriate for efficient luminescence behaviour, with emission in visible wavelengths: ΔE = 12,300 cm^{-1} ($^5D_0 \rightarrow {}^7F_6$; red emission) and ΔE = 14,800 cm^{-1} ($^5D_4 \rightarrow {}^7F_0$; green emission), respectively. Gd(III), on the other hand, has a very large energy gap, ΔE = 32,100 cm^{-1} ($^6P_{7/2} \rightarrow {}^8S_{7/2}$; UV emission) and hence organic chromophores generally do not sensitise this emission.

The *f–f* transitions required to excite Ln(III) are Laporte-forbidden, and hence Ln(III) have very low extinction coefficients, making direct excitation of the metal centre inefficient.[11] The lanthanide excited state, however, can be populated using a sensitising chromophore, *via* a process called the 'antenna' effect, which will be discussed presently. Since these electronic transitions are formally forbidden, the decay process is also forbidden and is hence slow, leading to long lifetimes of Ln(III)-centred emission from

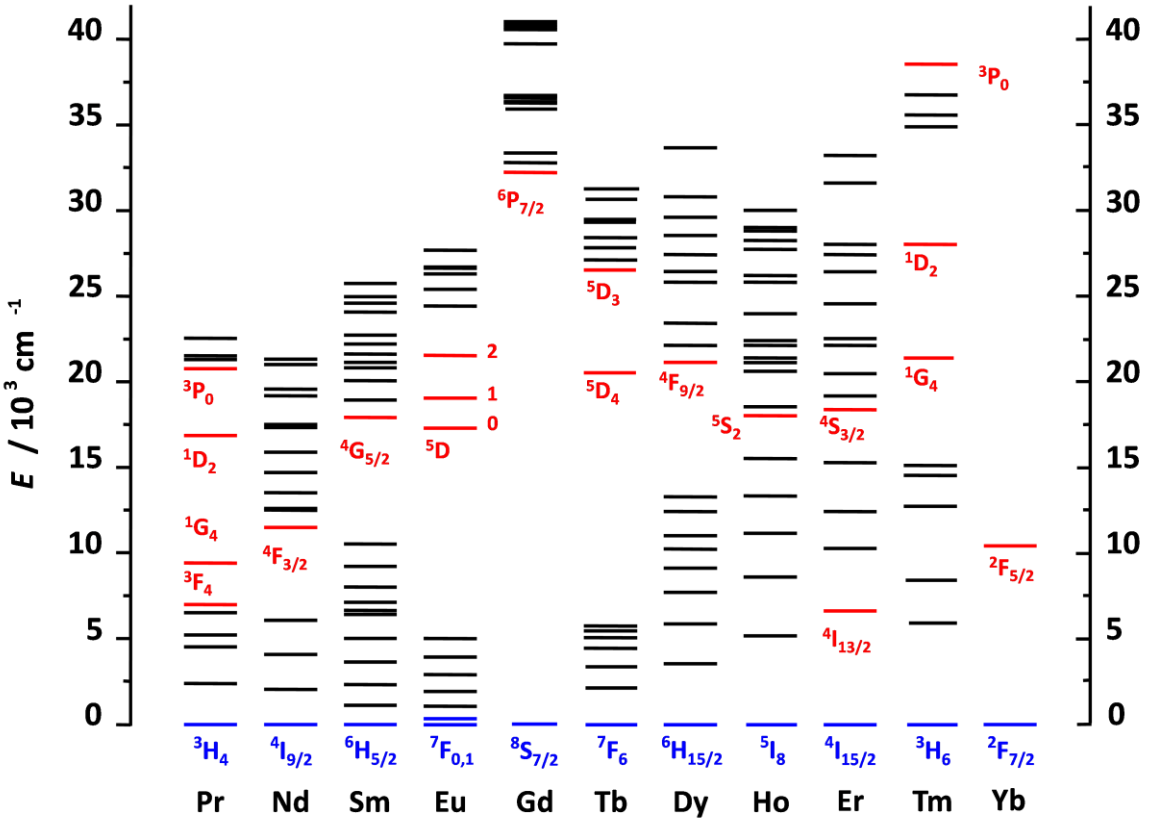

Figure 3.1 Partial energy level diagrams for lanthanide aquo ions. Important states for emission are shown in red (excited states) and blue (ground states) and labelled.

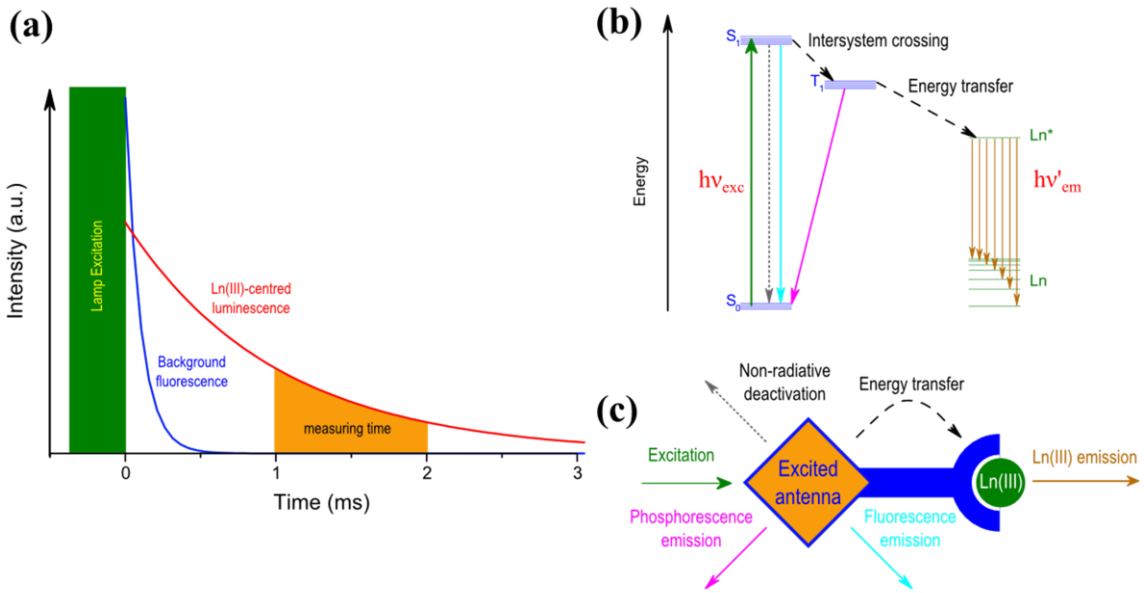

Figure 3.2 (a) Long-lived Ln(III)-centred emission compared with background fluorescence; **(b)**: a Jablonski energy level diagram illustrating indirect excitation of Ln(III) *via* the 'antenna effect', where the S_0, S_1 and T_1 states represent those of the 'antenna' or chromophore; **(c)** a schematic diagram of the process, showing various routes of electronic deactivation available for an excited Ln(III) complex.

excited state, which falls in the range of microseconds (*e.g.* Yb, Nd) to milliseconds (*e.g.* Eu, Tb).[220] Such long-lived excited states are advantageous for overcoming the challenge of biological autofluorescence and, indeed, background fluorescence in general. As shown in Figure 3.2(a), Ln(III) containing species may act as useful probes in biological media, with luminescence lifetimes several orders of magnitude longer than the autofluorescence of endogenous chromophores, such as those in proteins or nucleic acids.[221]

The 'antenna' effect is illustrated in Figure 3.2. To efficiently populate the Ln(III) excited state and overcome the obstacle of forbidden transitions, a sensitising chromophore (or 'antenna') may be incorporated into the complex system, allowing *indirect* excitation.[220] As shown by the Jablonski diagram,[149] Figure 3.2(b), the sensitising 'antenna' absorbs electromagnetic radiation, exciting it from the singlet ground state (S_0) to singlet excited state (S_1). A change in spin multiplicity, termed intersystem crossing (ISC), causes a change in state to a longer lived triplet excited state (T_1). The excited 'antenna' then transfers energy to the excited state of the lanthanide ion, generating an excited ion (Ln^*).[212] Energy may be dispersed either by emission of light (luminescence) or *via* a range of non-radiative deactivation mechanisms (*vide infra*). This indirect excitation of Ln(III) allows for the desirable photophysical properties of the lanthanides to be exploited.

An efficient 'antenna' for a Ln(III) complex should ideally be a chromophore with a high extinction coefficient allowing for effective energy absorption. The energy difference between triplet excited state of the ligand and the accepting level of Ln(III) must be sufficient (>1,700 cm^{-1}) such that thermally activated energy back-transfer is minimised.[220] The 'antenna' and the lanthanide ion should not be far apart in space, since the proposed mechanisms for energy transfer are distance dependent.[150] Förster's resonance energy transfer mechanism falls off as a function of distance at a rate of r^{-6},[222] while Dexter's mechanism is a through-bond interaction and acts on a shorter distance scale, with a dependence of e^{-r}.[223]

Quenching of the excited states of Ln(III) complexes occurs principally through non-radiative deactivation *via* collisions with various oscillators within the lanthanide coordination sphere. This process must be minimised, as will be discussed in Section 3.2.2 below.

3.2.2 Lanthanide luminescence quenching

Non-radiative deactivation of Ln(III) excited state (Ln^*) occurs primarily by means of a process known as quenching.[149] Quenching involves energy transfer from Ln^* to solvent molecules through vibrational collisions with solvent molecules or with O–H, N–H, and C–H oscillators within the Ln(III) coordination sphere. It is advantageous to minimise this energy transfer process by appropriately encapsulating the Ln(III) and preventing vibrating oscillators from solvents, such as water, from entering into the coordination sphere and binding to Ln(III). The number of metal-bound water molecules (the hydration state, *q*) is proportional to the rate of quenching. Horrocks and co-workers developed an equation to determine the hydration state of a Eu(III) or Tb(III) complex based on the observation that O–D isotopic oscillators reduce the excited state lifetimes of Eu^* and Tb^* to a far lesser extent than O–H oscillators.[224,225] This equation was further modified by Parker *et al.*[226] to include the effects of N–H and C–H oscillators (*x*) on this deactivation process, where relevant. The general Horrocks Equation is given as Equation 3.1 below:

$$q^{Ln(III)} = A\left\{\left(\frac{1}{\tau_{H_2O}} - \frac{1}{\tau_{D_2O}}\right) - B - Cx\right\} \qquad \text{Equation 3.1}$$

The two Ln(III) ions chiefly studied in this thesis will be Eu(III) and Tb(III). For these metal ions, the coefficients have been determined as A = 1.2, B = 0.25 and C = 0.075; and A = 5, B = 0.06 and C = 0, respectively.[212,226] A similar method, measuring lifetimes in CH_3OH and CD_3OD can also be used, with different values for the coefficients.

The quenching process highlights the need for multidentate ligands, capable of obstructing solvent coordination when attempting to construct highly efficient luminescent lanthanide complexes. This consideration, as well as the presence of sensitising chromophores in the ligands to indirectly excite the metal ion *via* intramolecular energy transfer, is essential to the selection of ligand.[224] These prerequisites are discussed in the following section.

3.2.3 Ligand choices for Ln(III) complexes

Ligands chosen to form complexes with Ln(III) ions must fulfil certain criteria to be highly luminescent. To effectively bind the ions, ligands must contain appropriately located Lewis basic donor atoms, which must form kinetically inert and thermodynamically stable complexes while satisfying the high coordination numbers of the Ln(III) ions, as described in Section 3.2. These requirements will now be discussed in detail.

Ln(III) possess relatively high charge densities and there is strong electrostatic character to their bonding, as the ions are polarising and hard Lewis acids. This hard Lewis acidity results in a preference for ligands incorporating atoms which can act as hard Lewis bases or which are readily polarisable. Hence, ligands used in Ln(III) complexation often contain combinations of amines, carboxylic acids, hydroxyl groups and nitrogen-containing heterocycles, such as pyridines.[11]

As discussed above, Ln(III) have high coordination requirements. In order to satisfy such requirements, a number of different approaches to ligand choice have been made,[148] some examples of which are shown in Figure 3.3. Macrocyclic ligands, such as **92**[227], have long been of interest due to the inherent kinetic stability of their complexes and because they provide a large number of donor atoms to satisfy the high coordination requirements of the Ln(III). Crown ethers and calixarene derivatives include some of the motifs which have been exploited to encapsulate Ln(III) ions efficiently, while cyclen-based macrocycles have recently been used as luminescent sensors and imaging agents.[12,228-230] The podand approach, involving multidentate ligands such as **93**[231], can also be used to satisfy the Ln(III) coordination requirements.

In self-assembly systems, a number of Lewis base containing ligands coordinate around Ln(III) centres in defined geometries, thus satisfying the coordination requirements. An elaborate example of such coordination is that displayed by ligand **94**[232], shown in Figure 3.3, which is a '*helicate*' system; the ligands, possessing two distinct terdentate binding sites, interweave in a helical fashion about the metal centres in order to fulfil the metal

ions' coordination requirements. Much of the prior research in the Gunnlaugsson group discussed in Section 1.9 above concerned such Ln(III)-directed self-assemblies including bundles,[4] half-helicates[6] and [3]catenanes.[7]

Owing to the high coordination numbers of the Ln(III) ions, multidentate ligands will be required in order to construct self-assemblies which satisfy these requirements. These ligands should also contain 'antennae' of appropriate energy to sensitise Ln(III)-centred emission, as well as in appropriate positions. Terdentate ligands, such as **btp** ligands, fulfilling these conditions may be designed.

Formation of supramolecular systems may be monitored using a variety of techniques including NMR, crystallography and mass spectrometry. NMR techniques are not always as useful when self-assembly is directed by paramagnetic Ln(III) ions, since proton resonances can become very broad. Fortunately, in the case of emissive Ln(III) self-assemblies, the characteristic photophysical features of the ions allow for monitoring of self-assembly processes in solution *via* relatively simple spectroscopic techniques such as UV-Vis absorbance, fluorescence and phosphorescence spectroscopy, as well as more specialised chiroptical spectroscopy, when optically pure compounds are used (see Chapter 4). Upon complexation, the Ln(III) ions' unique emission spectra may be sufficiently perturbed such that complex formation as a function of metal addition to ligand (or *vice versa*) may be precisely monitored.

In the previous chapter, the design, synthesis and characterisation of btp ligands **88** and **89** was presented. Carboxylic acid ligand **89** proved to have poor solubility in many organic solvents. Ligand 88, however, was readily soluble in a range of solvents. Ligand 88 was shown to be a competent metal-chelator with *d*-metals, with the photophysical properties of these complexes having been assessed in Section 2.6 above. These *d*-metal ion complexes were found to only give rise to ligand centred emission (with the exception of [Ru·(**88**)Cl_2(DMSO)]). The design of this ligand, as described in Figure 2.1 incorporated a chromophore (namely a phenyl ring) which could act as a sensitising 'antenna' which will allow for the formation of Ln(III) complexes with interesting photophysical properties. Hence, bearing in mind both the confirmed metal ion coordination capabilities of **88** and the advantageous properties of the *f*-metals outlined above, its coordination chemistry and self-assembly with Eu(III) and Tb(III) will be explored in the following sections. All solution studies were, unless otherwise stated, carried out in the polar aprotic solvent CH_3CN for consistency with the results reported in Chapter 2, and were undertaken at 23 °C.

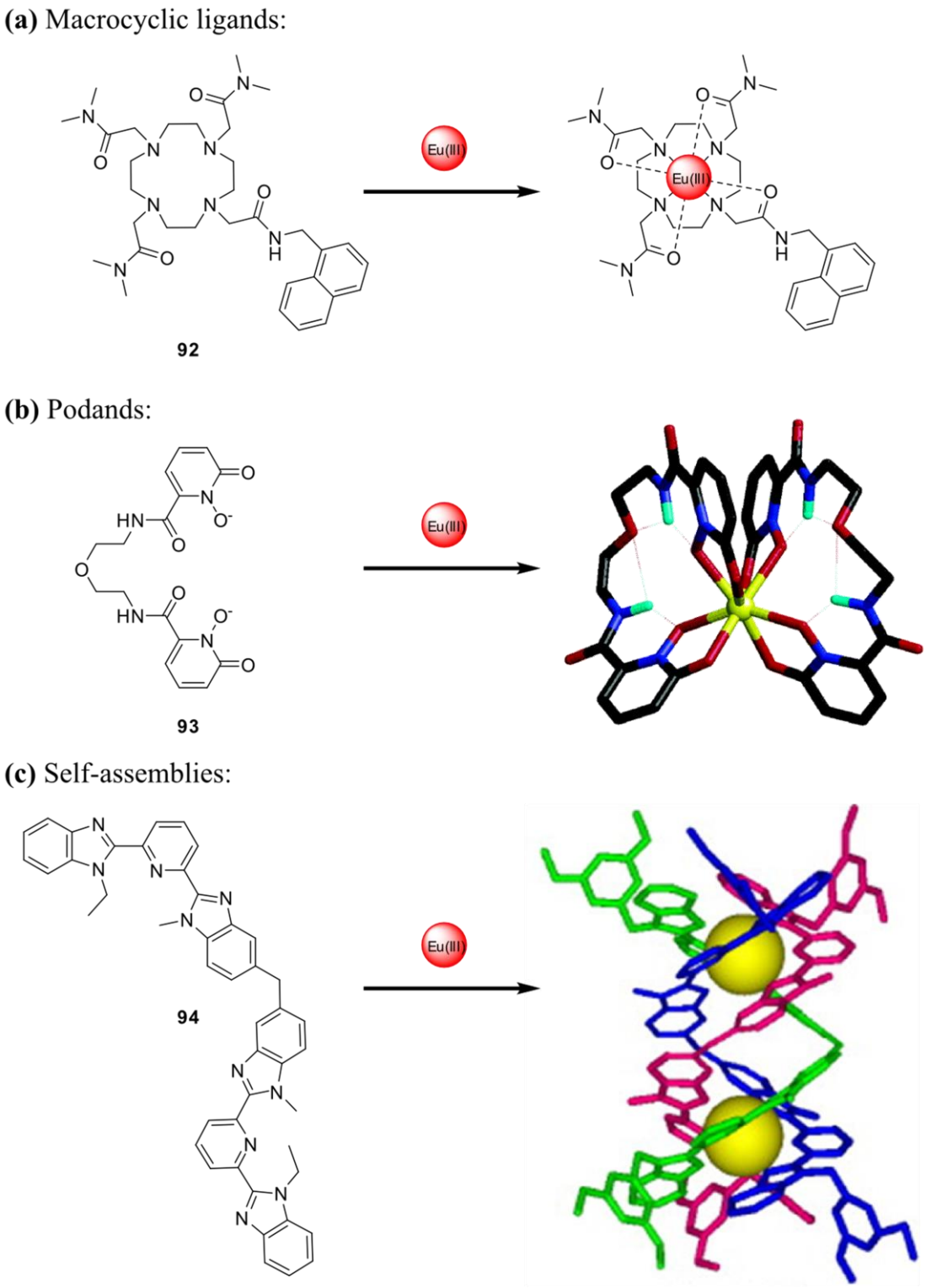

Figure 3.3 Synthetic strategies for coordination of Ln(III) by supramolecular systems in order to satisfy the high coordination requirements. **(a)** a derivatised cyclen macrocycle, **92**; **(b)** Podand approach, with ligand **93**; **(c)** self-assembly methods for forming complex supramolecular architectures such as helicate **94**.

3.3 Preparation and photophysical studies of Ln(III) complexes of ligand 88

By adapting a procedure developed in the Gunnlaugsson group for the formation of Ln(III) complexes of acyclic ligands based on the **dpa** motif, the 1:3 complexes of **88** were prepared under thermodynamic control by a microwave irradiation reaction of **88** with 0.33 equivalents of Eu(III) or Tb(III) triflate salt in CH_3OH solution at 70 °C for 20 minutes. The reaction mixture was filtered and the complexes recovered as off-white solids upon diffusion of diethyl ether into a CH_3OH solution in *ca.* 30% yield. Successful complexation was confirmed by MALDI+ mass spectrometry, where the characteristic isotopic distribution patterns of the measured peaks matched the calculated spectra (see Figure 3.4 and Figure 3.5). Infrared spectroscopy of the complex also shows changes with respect to the ligand, including the shift of the carbonyl band by 10 cm^{-1} from 1729 cm^{-1} to 1719 cm^{-1}, as well as general changes in the fingerprint region, including the presence of a broad band centred at 1275 cm^{-1} associated with the triflate ($CF_3SO_3^-$) anions, Appendix B.

Photophysical measurements in CH_3CN solution were made of the thermodynamically prepared metal ion complexes mentioned above. Compared to the UV-Vis absorbance spectrum of the ligands, Chapter 2, upon complexation with Eu(III) or Tb(III), the ligand band centred at 300 nm was red shifted to 315 nm, tentatively assigned to the n→π* transitions in the **btp** centre, while the band assigned to π→π* transitions was slightly blue shifted to 230 nm. Ligand **88** was shown to sensitize Ln(III) emission, *via* the 'antenna' effect (*vide supra*) upon excitation into either of these bands in CH_3CN solution, with characteristic red and green emission clearly visible to the naked eye under irradiation with

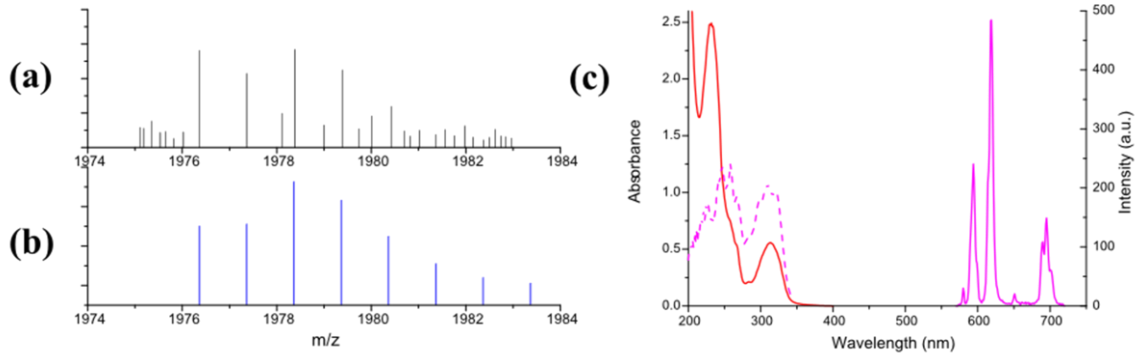

Figure 3.4 (a) Experimental and **(b)** calculated HRMS isotopic pattern distribution for [Eu·(**88**)$_3$](CF$_3$SO$_3$)$_3$. Calculated for $C_{83}H_{69}N_{21}O_{18}S_2F_6Eu^+$ *m/z* = 1978.3688 $[EuL_3(CF_3SO_3)_2]^+$. Found *m/z* = 1978.3783; **(c)** UV-Vis absorbance (red), excitation (dashed magenta) and Eu(III) phosphorescence (magenta) spectra of a [Eu·(**88**)$_3$](CF$_3$SO$_3$)$_3$ solution in CH_3CN.

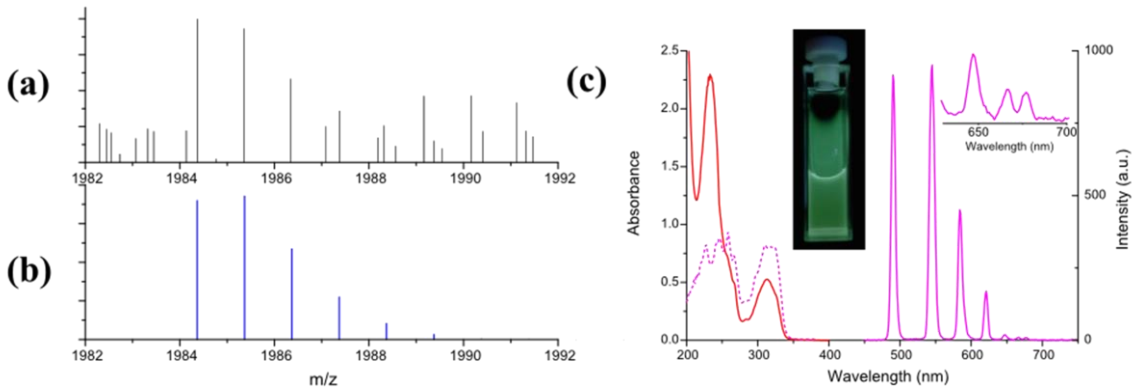

Figure 3.5 **(a)** Experimental and **(b)** calculated HRMS isotopic pattern distribution for [Tb·(**88**)$_3$](CF$_3$SO$_3$)$_3$. Calculated for $C_{83}H_{69}N_{21}O_{18}S_2F_6Tb^+$ *m/z* = 1984.3729 [EuL$_3$(CF$_3$SO$_3$)$_2$]$^+$. Found *m/z* = 1984.3695; **(c)** UV-Vis absorbance (red), excitation (dashed magenta) and Tb(III) phosphorescence (magenta) spectra of [Tb·(**88**)$_3$](CF$_3$SO$_3$)$_3$ in CH$_3$CN solution; (*insets L–R*) photograph of a CH$_3$CN solution of the complex under irradiation with UV light, displaying bright naked-eye emission; and magnified detail of thephosphorescence spectrum between 630 and 700 nm, showing weak Tb(III) *f–f* transitions.

a hand-held UV lamp for Eu(III) and Tb(III) complexes, respectively. For [Eu·(**88**)$_3$](CF$_3$SO$_3$)$_3$, Figure 3.4(c), characteristic line-like emission bands were observed at λ = 579, 593, 617, 650 and 694 nm, assigned to the $^5D_0 \rightarrow {}^7F_J$ transitions (J = 0–4), whereas for the Tb(III) complex, Figure 3.5, emission bands were observed at λ = 490, 545, 585, 621 nm, assigned to the $^5D_4 \rightarrow {}^7F_J$ transitions (J = 6–3). The inset in Figure 3.5(c) shows a magnification of three emission bands observed at λ = 645, 666 and 676 nm and assigned to the $^5D_4 \rightarrow {}^7F_{2-0}$ Tb(III) transitions, which are typically weak.[233] The excitation spectra of both Ln(III) complexes have profiles broadly matching the two bands of the absorbance spectra. To the naked eye, the Tb(III) complex was significantly brighter than the Eu(III) complex; this will be discussed quantitatively in terms of total quantum yields below.

In order to further understand the energy transfer process of the Ln(III) complexes, the approximate energy levels of the relevant excited states of ligand **88** (singlet and triplet states) were determined. The energy of S_1 (singlet state) was estimated by considering the ligand fluorescence emission with an emission band ranging from 300–420 nm with a maximum at 335 nm (*vide supra*), indicating an energy of ~32,800 cm^{-1}. Since the energy level of T_1 (triplet state) is insensitive to the identity of Ln(III), a complex with Gd(III) was prepared, as described above for the other complexes. The lowest lying excited level of Gd(III) is located at much higher energy than Eu(III) or Tb(III), Figure 3.1, and hence organic ligands like **88** tend not to sensitise Gd(III)-centred emission, allowing evaluation of T_1.[29,233] The phosphorescence spectrum of [Gd·(**88**)$_3$](CF$_3$SO$_3$)$_3$ in CH$_3$CN, measured at 77 K displayed a broad structured emission with maxima at 408, 434, 454, and 464 nm

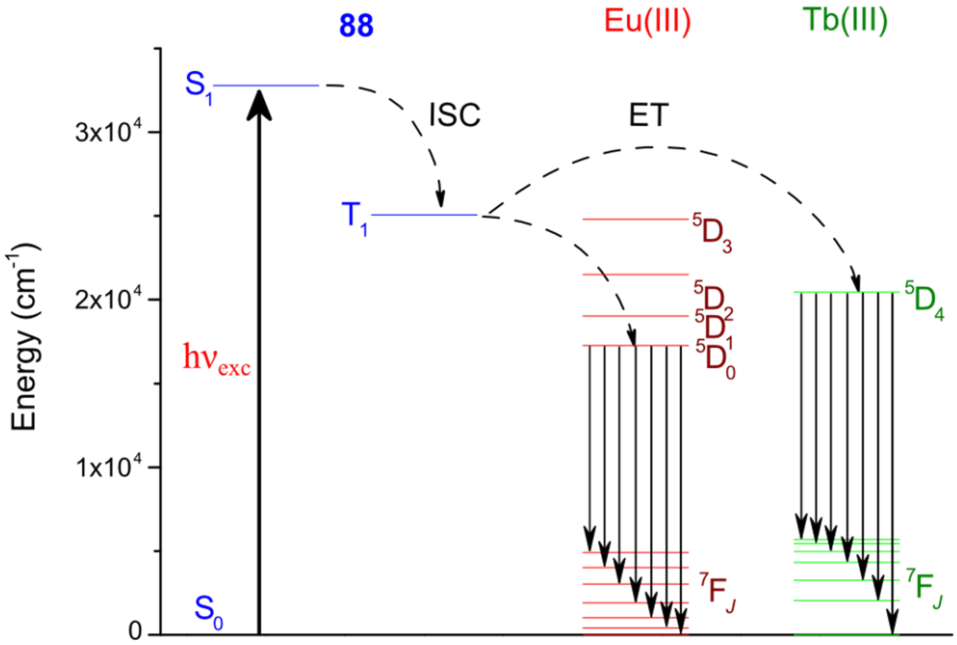

Figure 3.6 Schematic energy level diagram of the simplified energy transfer processes involved in ligand **88** sensitising Eu(III) and Tb(III)-centred luminescence.

(shown in Appendix B). The energy of T_1 was determined as ~24,500 cm^{-1}. These results are shown schematically in the energy level diagram in Figure 3.6 (Ln(III) energy levels taken from reference[234]), which shows the simplified energy transfer process leading to sensitisation of Ln(III) emission, occurring *via* the initial excitation of the S_1 followed by intersystem crossing to T_1. The energy of T_1 closely matches that of the Eu(III) $^5D_0$ and Tb(III) $^5D_4$ states, allowing for energy transfer and population of the Ln(III) excited states.

The energy differences between the triplet energy level of **88** and the relevant Ln(III)-centred levels were approximately 7000 and 4000 cm^{-1} for Eu(III) and Tb(III) respectively; such gaps are too high to allow effective back energy transfer to either of these systems, which would repopulate T_1 prior to eventual quenching by triplet O_2.[220] This was further demonstrated by recording the Tb(III) emission in aerated and degassed solution, both of which gave rise to identical spectra, indicating that no quenching by O_2 was observed.[235] The ligand is ideally positioned to sensitise Tb(III) in particular, and, as such, the Tb(III) complex was expected to possess a higher quantum efficiency.

Table 3.1 Photophysical properties of Ln(III) complexes of **88**: luminescence lifetimes, hydration states and total quantum yields in CH_3CN.

Complex	τ_{H2O} **(ms)**	τ_{D2O} **(ms)**	q **(±0.5)**[a]	**Φ (%)**[b]
[Eu·(**88**)$_3$]$(CF_3SO_3)_3$	1.06±0.05	1.98±0.01	0.2	2.4±0.4
[Tb·(**88**)$_3$]$(CF_3SO_3)_3$	0.81±0.14	0.85±0.28	−0.5	70±12

[a]Hydration states were calculated using the equation $q = A(\left(\frac{1}{\tau_{H2O}} - \frac{1}{\tau_{D2O}}\right) - B)$, where for Eu(III), A = 1.2, B = 0.25 and for Tb(III), A = 5.0, B = 0.06.[212,226]; [b]Quantum yields in CH_3CN were estimated by a relative method,[236] compared with Cs_3[Ln·(**dpa**−2H)$_3$][21,22] according to the equations shown in the Experimental Chapter

Luminescence lifetimes in H_2O and D_2O were determined for the $[Ln\cdot(\mathbf{88})_3](CF_3SO_3)_3$ complexes, by fitting the Ln(III) excited state decay profiles of the most intense Ln(III) transitions (the $^5D_0 \rightarrow {}^7F_2$ band centred at 616 nm for Eu(III), and the $^5D_4 \rightarrow {}^7F_6$ band centred at 490 nm for Tb(III), respectively) to mono-exponential decays. The complexes were not fully soluble in aqueous media, but sufficiently so to give reliable emission lifetimes. The lifetimes in deuterated solvent (D_2O) were longer than those in H_2O as a result of decreased luminescence quenching, as was discussed in Section 3.2.2. These data were next used to determine hydration states of the complexes, *q*, by utilising the Parker-modified Horrocks equation, Equation 3.1 above.[224,226] These data are shown in Table 3.1. The complexes seem to be coordinatively saturated; indicating the successful formation of 1:3 (metal:ligand) complexes as the dominant (or the only) stoichiometry, where the hydration state is ~ 0. Each of the ligands can act as terdentate ligands, giving a total coordination number of nine around the Ln(III) ions with no metal bound water molecules. Quantum yields, Φ, in CH_3CN were also determined by a relative method, using $Cs_3[(Ln\cdot(\mathbf{dpa}-2H)_3]$ as secondary standards, as suggested by Chauvin and co-workers.[60, 61] The efficiency of sensitisation of the Tb(III) excited state by this ligands was indeed high, *ca.* 70%, while the quantum yield of the Eu(III) complex was significantly more modest (2.4±0.4%).

The ^{1}H-NMR spectra of Ln(III) complexes are often very complicated and difficult to interpret as a result of the paramagnetic nature of many of the Ln(III) ions, including Eu(III) and Tb(III), with six unpaired electrons each, which can broaden and shift proton resonances, sometimes beyond recognition. For some highly symmetrical **dpa**-based systems previously studied in the Gunnlaugsson group, however, the spectra with Eu(III) have been found to be reasonably well resolved,[6,7] and as such the NMR spectroscopy of Ln(III) complexes of **88** was also explored. The ^{1}H NMR spectrum (400 MHz, CD_3CN) of $[Eu\cdot(\mathbf{88})_3](CF_3SO_3)_3$, Figure 3.7, was reasonably simple, although quite different to that of the ligand (*vide supra*, Chapter 2) with many resonances undergoing paramagnetic shifts. The most notable upfield shifts related to the triazolyl and pyridyl CH resonances. The spectral changes shall be discussed in detail in the following section. The Tb(III) complex gave a much more complicated and broader spectrum, which was not readily assigned. It is shown in Appendix B.

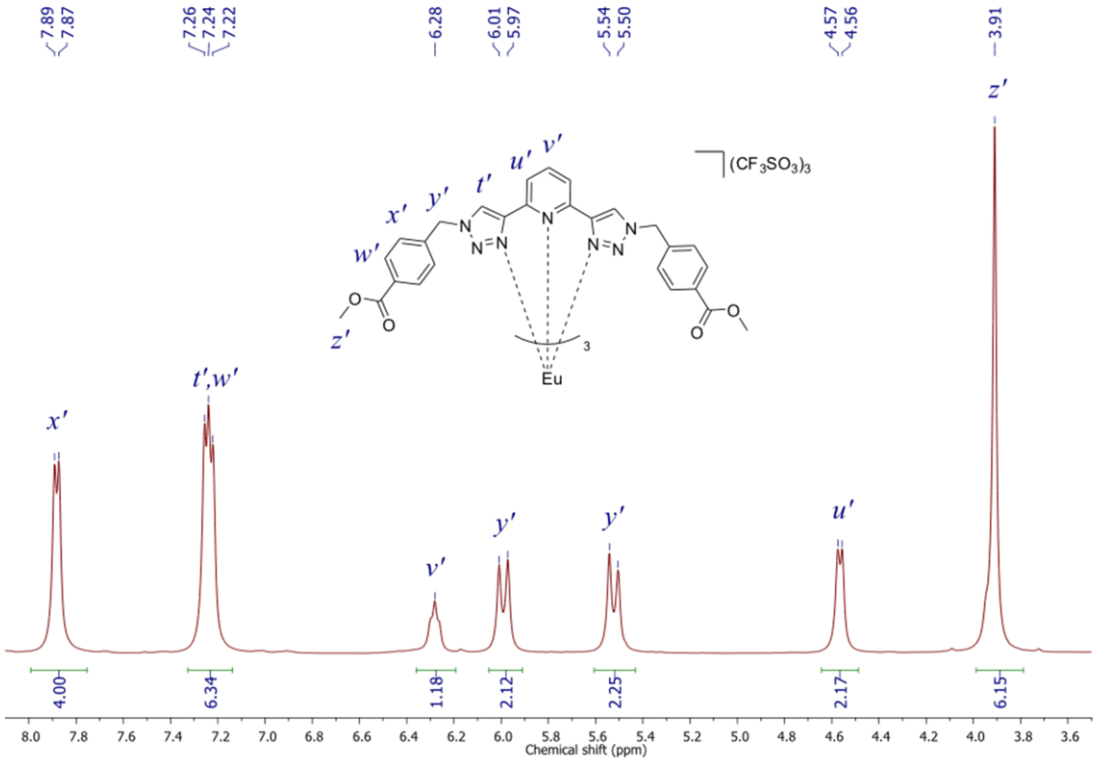

Figure 3.7 Labelled ^{1}H NMR (400 MHz, CD_3CN) spectrum of [Eu·(**88**)$_3$](CF$_3$SO$_3$)$_3$.

3.4 ^{1}H NMR titration of ligand 88 with Eu(III)

In light of the fact that the Eu(III) complex ^{1}H-NMR spectrum differed significantly from the ligand spectrum, but still yielded a clear and conveniently assigned spectrum, titrations were undertaken to observe the changes in the spectrum of ligand **88** and the different self-assembly species formed in a solution of CD_3CN as a function of equivalents of Eu(III) with a view to understanding the geometry of the free ligand, as compared with the coordinating ligand and monitoring the binding process. Titrations were not undertaken with Tb(III), since as stated above, the resultant ^{1}H-NMR spectra upon complexation with Tb(III) were not as clearly assigned.

The most significant spectral changes to **88** occurred up to the addition of 0.5 equivalents of Eu(III), as shown in Figure 3.8, followed thereafter by increased broadening and complexity of resonances. The resonance arising from the methyl ester moiety in ligand **88** underwent a slight downfield shift upon self-assembly, with the free ligand signal (3.86 ppm, labelled *z*) disappearing completely by 0.5 equivalents and being replaced by a signal at 3.89 ppm (labelled *z′*). Simultaneously, shifts were observed in the aromatic region. Most significant among these was the disappearance of the triazolyl resonance at 8.40 ppm (*t*) upon addition of 0.5 equivalents of Eu(III); this resonance was determined by 2D NMR spectroscopy (see Appendix B) to overlap with one of the phenyl CH signals at 7.23 ppm

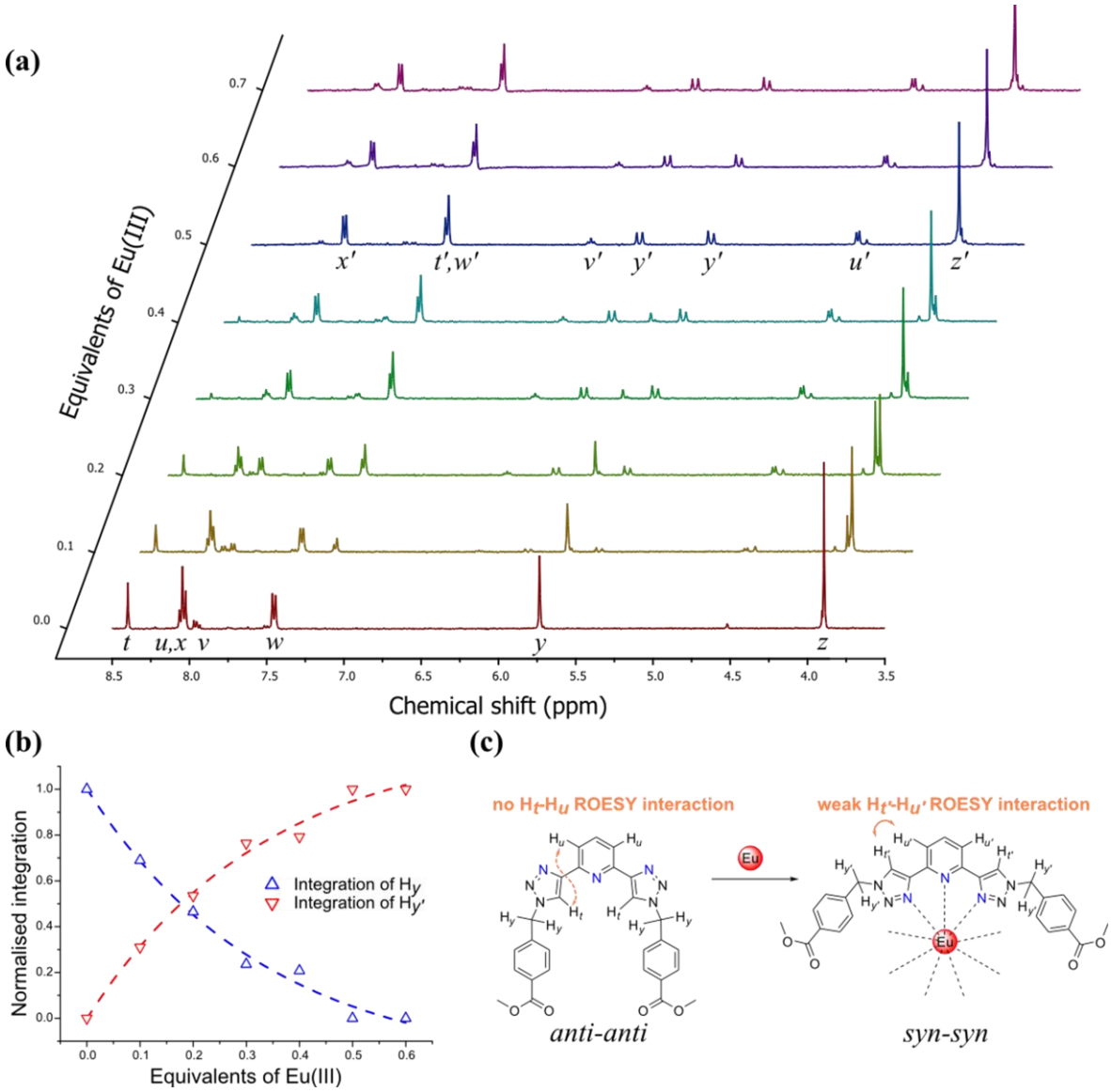

Figure 3.8 (a) ^{1}H NMR (400 MHz, CD_3CN) titration of ligand **88** upon addition of Eu(CF_3SO_3) solution; **(b)** a graph showing ratios of the integrations of the methylene resonanaces (labelled *y*) of each species as a function of equivalents of Eu(III) added; **(c)** schematic representation of the interconversion between *anti-anti* and *syn-syn* conformation of **88** upon complexation. [**88**] = 1.1×10^{-3} M.

in the complex (*t′*). The triplet pertaining to the 4-pyridyl proton showed a significant paramagnetic upfield shift from 7.91 ppm (*v*) to 6.27 ppm (*v′*), an exchange which was also complete by 0.5 equivalents; the 3- and 5-pyridyl proton signal (*u*) shifted dramatically upfield as well, but this is less clearly monitored as a result of the ligand peak overlapping with one of the phenyl proton signals, only becoming clearly resolved as a doublet (labelled *u′*) at 4.54 ppm upon complexation (confirmed by selective ROESY and HSQC, see Appendix B). These magnitudes of upfield pyridyl shifts were similar to those reported for **dpa** as a result of the protons near the Eu(III) ion becoming increaseingly shielded.[17] The phenyl protons (*w* and *x*) experienced less dramatic upfield changes. Interestingly, the CH_2 signal at 5.7 ppm (*y*) split into two doublets upon complexation; this would suggest a locking of the ligand 'arms' into a conformation where free rotation of this bond is no longer possible on the NMR timescale. Figure 3.8(b) shows the interconversion of these two signals by representing the relative integrations of the resonances marked *y* and *y′* as a function of equivalents of equivalents of Eu(III) added.

Through the use of selective ROESY experiments (shown in Appendix B), information about the spatial conformation of the free ligand and the ligand as part of the complex was obtained. Consistent with the *anti-anti* structure seen in the crystal structure of **88**, shown above, Figure 2.5,[72] the triazolyl proton did not show any through-space interactions with the 3-pyridyl protons. This 'horseshoe' conformation was similar to that seen by other similar compounds in the literature and was discussed in Section 1.3.3.8.[107,111,124-126] Upon addition of 0.5 equivalents of Eu(III), however, the new species showed weak interactions between the 3-pyridyl protons and the triazolyl resonance, consistent with the inversion of triazolyl conformation in the **btp** motif to *syn-syn* geometry (as schematically represented in Figure 3.8(c)), as has been previously reported for similar systems, resulting from the nitrogen lone-pairs binding the metal ion.[82] These solution state results also correspond with the *syn-syn* geometry seen in the X-ray crystal structures of *d*-metal ion complexes in Chapter 2. The study of changes in the ^{1}H-NMR spectra clearly shows the formation of Ln(III)-directed self-assemblies under kinetic control. As described in Section 3.2.3 above, such processes can also be studied by spectrophotometric means; this is desirable, particularly in light of advantageous photophysical properties of these assemblies. These spectroscopic titration studies will now be discussed.

3.5 Spectroscopic titrations of 88 with Ln(III)

Having shown the competency of **btp** ligands for binding Ln(III) ions through formation of emissive thermal complexes and monitoring the self-assembly of **88** with Eu(III) in CD_3CN by ^1H NMR spectroscopy, more detailed investigations of this self-assembly were carried out in CH_3CN, monitored by measuring UV-Vis absorbance, fluorescence, and Ln(III)-centred luminescence spectra upon addition of Eu(III) or Tb(III) triflate salt solutions to ligand solutions at lower concentrations of *ca.* 10^{-5} M (accurate concentrations were determined using the Beer–Lambert Law). Monitoring spectral changes as a function of Ln(III) concentration will allow the determination of global stability constants for these self-assembly processes.

3.5.1 Titrations with Eu(III)

The overall changes in the UV-Vis absorption spectrum of a CH_3CN solution of **88** were monitored as a function of Eu(III) concentration, Figure 3.9(a). A slight blue shift and concomitant decrease in absorbance was observed for the band centred at 235 nm, stabilising at 232 nm, while the other band, associated with the n→π* transitions of the **btp** (centred at 300 nm for the ligand) underwent a more significant red shift of 15 nm with an increase in absorbance. The spectral changes displayed an isosbestic point at 303 nm. The spectra after these changes under kinetic control matched the spectra recorded above for the metal complex $[Eu\cdot(\mathbf{88})_3](CF_3SO_3)_3$, prepared under thermodynamic control. Experimental binding isotherms at various wavelengths showed that changes to the

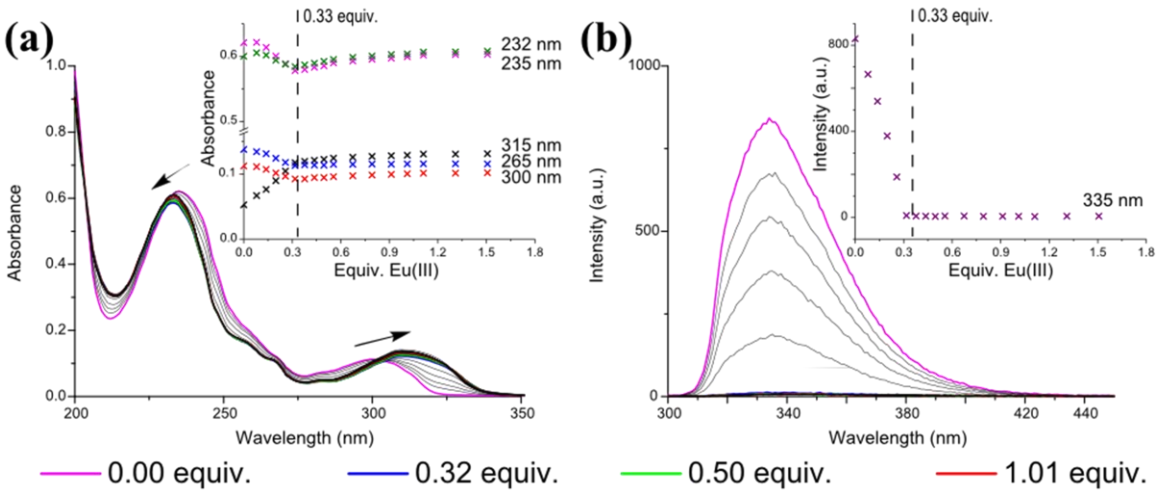

Figure 3.9 Titration plots of **88 v.** Eu(III) in CH_3CN. **(a)** UV-Vis spectral changes; *inset*: experimental binding isotherms (×) at various wavelengths; **(b)** changes in fluorescence; *inset*: experimental binding isotherm at 335 nm (×). [**88**] = 1.3×10^{-5} M.

absorbance spectra were largely finished upon addition of approximately 0.33 equivalents of $Eu(CF_3SO_3)_3$. These changes were indicative of equilibrium displacement and evolution of different stoichiometric species in solution as the Eu(III) concentration was increased. Fluorescence was observed upon excitation into the $\pi \rightarrow \pi^*$ band. The changes in these fluorescence emission spectra were also recorded, Figure 3.9(b), with the ligand fluorescence centred at 335 nm being gradually quenched up until the addition of 0.33 equivalents, after which this ligand fluorescence band was no longer observed. This behaviour was reproducible and suggested an energy transfer process away from the excited S_1 state of the ligand, namely excitation of the Eu(III) excited state *via* the 'antenna' effect (*vide supra*).

The consequent emergence of long-lived Eu(III) luminescence emission as a result of this sensitisation process was monitored by recording the phosphorescence spectra upon excitation of the ligand into either absorption band. Over the course of titrations with $Eu(CF_3SO_3)_3$, Figure 3.10, gradual enhancement of the characteristic Eu(III) luminescence spectrum was observed upon addition of 0→0.33 equivalents of metal ion solution, indicating energy transfer from the 'antenna' to the Eu(III) centre and, as such, successful formation of the 1:3 Ln(III)-directed self-assembly in solution. In particular, the $^5D_0 \rightarrow {}^7F_{1-4}$ transitions were observed, with emission bands centred at 595, 617, 645 (very weak) and 696 nm respectively. After 0.33 equivalents, there was a sharp decrease in the emission intensity at these wavelengths, Figure 3.10(b), which suggests that the 1:3 species was the

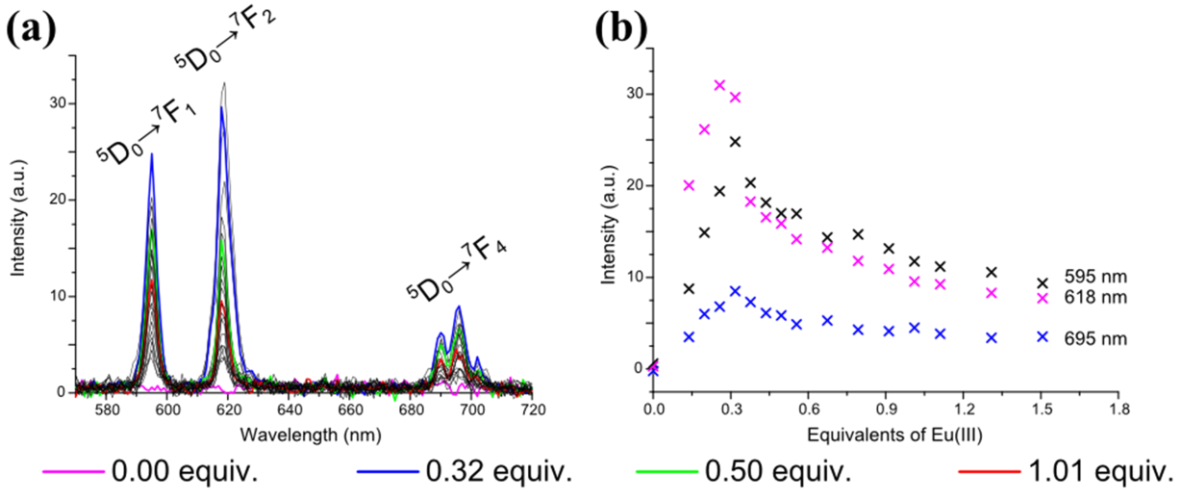

Figure 3.10 (a) Changes in phosphorescence upon addition of $Eu(CF_3SO_3)_3$ solution in CH_3CN, showing characteristic Eu(III) transition bands; **(b)** experimental binding isotherms at characteristic wavelengths for each of these transitions (×).[**88**] = 1.3×10^{-5} M.

most emissive stoichiometry. As the Eu(III) concentration increased, an equilibrium shift caused less emissive species (*viz.* 1:2 and 1:1 stoichiometries) to become more prevalent species in solution, leading to the observed intensity changes. These clear changes in both the ground state and excited electronic state spectra provide clear insight into the formation of self-assemblies in CH_3CN solution upon addition of Eu(III), with the formation of a 1:3 stoichiometry clearly suggested by the binding isotherms for all these titrations, which show 0.33 equivalents as a key point of change in the binding behaviour. The self-assembly behaviour with Tb(III) was also monitored by the same methods. This is discussed in the following section.

3.5.2 Titrations with Tb(III)

The spectroscopic changes observed upon addition of a solution of $Tb(CF_3SO_3)_3$ to **88** were comparable to those discussed above for Eu(III). The UV-Vis spectrum of **88** changed in an identical way, with the 15 nm red shift of the band centred at 300 nm being the most significant of the changes, which were complete upon addition of 0.33 equivalents, Appendix B. The broad fluorescence of the ligand centred at 335 nm, *vide supra*, was quenched by this point in the titration also, and the most emissive Tb(III)-containing species was formed at 0.33 equivalents, with phosphorescence spectra displaying characteristic Tb(III) luminescence bands, centred at 490, 545, 585, 621, 645, 666 and 677 nm (the $^5D_4 \rightarrow {}^7F_J$ transitions, where J = 6–0). The $^5D_4 \rightarrow {}^7F_{2-0}$ bands are typically weak and not always seen in titrations. Following 0.33 equivalents of Tb(III), the

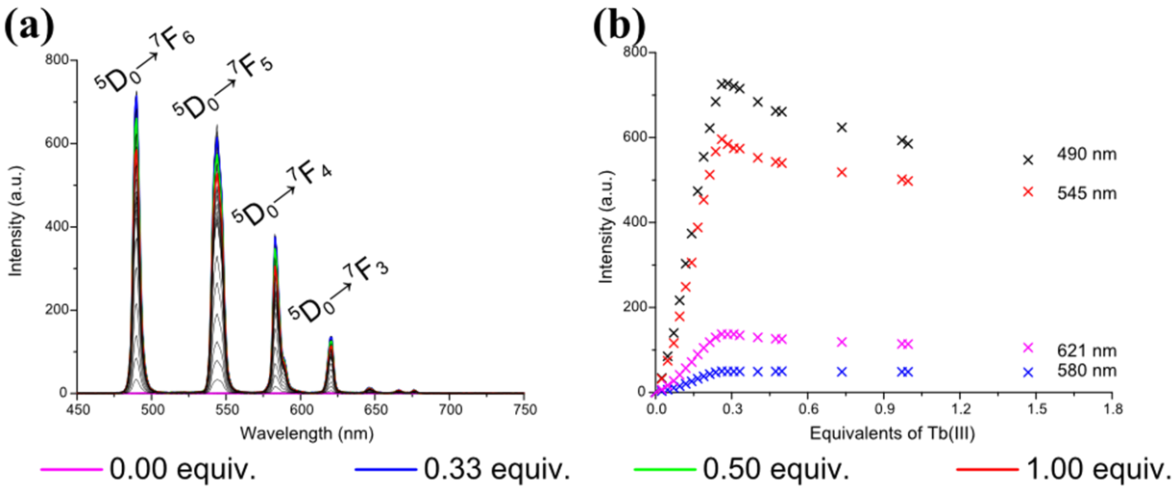

Figure 3.11 (a) Changes in phosphorescence of **88** upon addition of $Tb(CF_3SO_3)_3$ solution in CH_3CN, showing characteristic Tb(III) transition bands; **(b)** experimental binding isotherms at characteristic wavelengths for each of these transitions (×).[**88**] = 1.4×10^{-5} M.

emission bands assigned to the Tb(III) phosphorescent transitions began to decrease in intensity as the equilibrium shifted away from the most luminescent 1:3 species towards less emissive 1:2 and 1:1 stoichiometries, Figure 3.11. The Ln(III)-centred emission, however, was not quenched as dramatically for Tb(III) as it was for Eu(III) above, suggesting that these other stoichiometric species are still reasonably luminescent. The data collected in the course of these titrations should be able to provide insight into the various species present in these systems and their stability of formation. The next section will focus on such analysis of these titrations.

3.5.3 Fitting of titration data

In order to gain a better understanding of this solution self-assembly behaviour and obtain a more detailed view on the formation of different stoichiometric species in solution, spectroscopic changes were analysed by fitting the global changes to various **btp**:Ln(III) complexation equilibria by non-linear regression analysis using the ReactLab Equilibria[237] software; global stability constants, β, for each equilibrium were estimated.

$$\mathrm{Ln(III)} + (\mathbf{btp}) \overset{\beta_{1:1}}{\rightleftharpoons} [\mathrm{Ln}\cdot(\mathbf{btp})]^{3+} \qquad \text{Equation 3.2}$$

$$\mathrm{Ln(III)} + 2(\mathbf{btp}) \overset{\beta_{1:2}}{\rightleftharpoons} [\mathrm{Ln}\cdot(\mathbf{btp})_2]^{3+} \qquad \text{Equation 3.3}$$

$$\mathrm{Ln(III)} + 3(\mathbf{btp}) \overset{\beta_{1:3}}{\rightleftharpoons} [\mathrm{Ln}\cdot(\mathbf{btp})_3]^{3+} \qquad \text{Equation 3.4}$$

The global stability constants, β, are an expression of the product of the formation constants, K, of the various stepwise equilibria which make up the binding processes, Equations 3.5–3.7. For example, $\beta_{1:3} = K_{1:1} \times K_{1:2} \times K_{1:3}$. In this thesis, the global binding constants will be presented in logarithmic form, as logβ, throughout.

$$\mathrm{Ln(III)} + (\mathbf{btp}) \overset{K_{1:1}}{\rightleftharpoons} [\mathrm{Ln}\cdot(\mathbf{btp})]^{3+} \qquad \text{Equation 3.5}$$

$$[\mathrm{Ln}\cdot(\mathbf{btp})]^{3+} + (\mathbf{btp}) \overset{K_{1:2}}{\rightleftharpoons} [\mathrm{Ln}\cdot(\mathbf{btp})_2]^{3+} \qquad \text{Equation 3.6}$$

$$[\mathrm{Ln}\cdot(\mathbf{btp})_2]^{3+} + (\mathbf{btp}) \overset{K_{1:3}}{\rightleftharpoons} [\mathrm{Ln}\cdot(\mathbf{btp})_3]^{3+} \qquad \text{Equation 3.7}$$

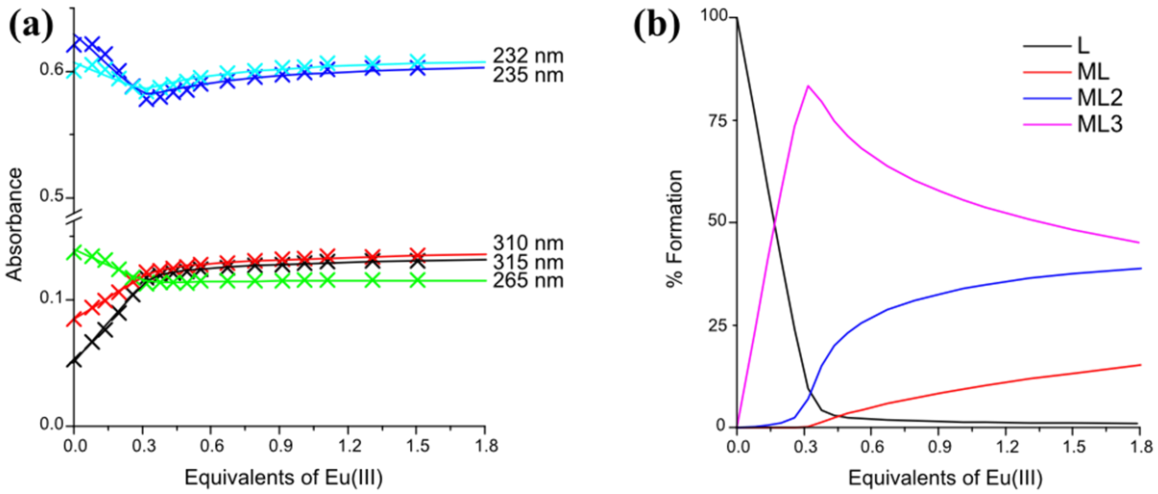

Figure 3.12 (a) Experimental (×) and calculated (–) UV-Vis absorbance binding isotherms for the titration of **88** with Eu(III); **(b)** Calculated speciation distribution diagram, showing the percentage formation of various stoichiometries as a function of equivalents of Eu(III).

Stability constants were estimated for the assemblies of ligand **88** with Eu(III) from the UV-Vis absorbance, fluorescence and Eu(III) luminescence titration data.

UV-Vis titration data were fit to the various equilibria listed above until a model converged. Binding constants of $\log\beta_{1:1}$ = 6.0 ± 0.1, $\log\beta_{1:2}$ = 13.0 and $\log\beta_{1:3}$ = 19.8 were determined for this system. Figure 3.12(a) shows the experimental binding isotherms overlaid with the isotherms calculated from these stability constants, which match each other very closely. Figure 3.12(b) shows the speciation distribution diagram calculated using these parameters, showing the dominance, *ca.* 85%, of the 1:3 stoichiometry (ML3) at 0.33 equivalents, according to this model and the gradual increase in formation of the 1:2 and 1:1 stoichiometries (ML2 and ML, respectively) thereafter, although they never dominate the speciation distribution.

Similarly, Figure 3.13(a) shows the measured Eu(III)-centred luminescence spectral data overlaid with the model calculated with stability constant values of $\log\beta_{1:1}$ = 7.2 ± 0.1, $\log\beta_{1:2}$ = 14.8 and $\log\beta_{1:3}$ = 20.7 for the three stepwise equilibria. These stability constants are roughly additive, suggesting that the binding processes of each new ligand to the assembly had a similar formation constant *K*. The accompanying speciation distribution diagram differs from that calculated from the UV-Vis data in terms of the relative concentrations of the 1:3 and 1:2 species, however, it models the formation of the 1:1 stoichiometry very similarly. In this model, the ML3 species reached a formation maximum of 63% at 0.33 equivalents of Eu(III) The more dramatic changes in the luminescence spectrum after 0.33 equivalents allow further insight into the binding process than the minor changes in the ground state described above.

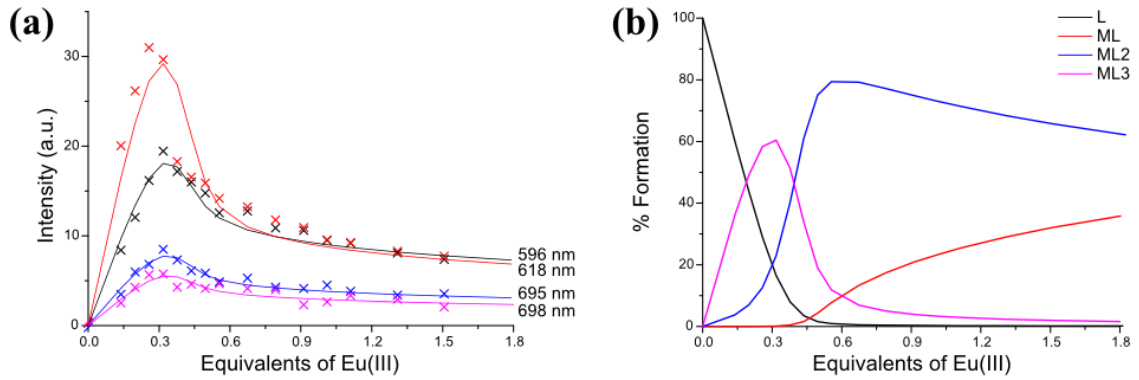

Figure 3.13 (a) Experimental (×) and calculated (–) Eu(III)-centred emission binding isotherms for the titration of **88** with Eu(III); **(b)** Calculated speciation distribution diagram, showing the percentage formation of various stoichiometries as a function of equivalents of Eu(III) .

The binding behaviour of both Eu(III) and Tb(III) follow broadly similar trends, as was seen in the titrations above and, as such, fitting of the UV-Vis data, Figure 3.14, and phosphorescence data, Figure 3.15, for the Tb(III) titrations gave comparable global stability constants to those determined for the Eu(III)-directed self-assembly. The calculated binding isotherms for the UV-Vis titration very closely matched the experimental data and are shown at a number of different wavelengths in Figure 3.14(a), while the associated speciation distribution diagram showed the maximum of formation of the 1:3 species, in *ca.* 60% yield, at 0.33 equivalents of Tb(III), followed by subsequent formation of the ML2 and ML species. The speciation diagram for the Tb(III)-centred emission titration gave a consistent picture of the formation of the 1:3 stoichiometry at 0.33 equivalents as well. These models were also very similar to that determined for the Eu(III)-centred emission above.

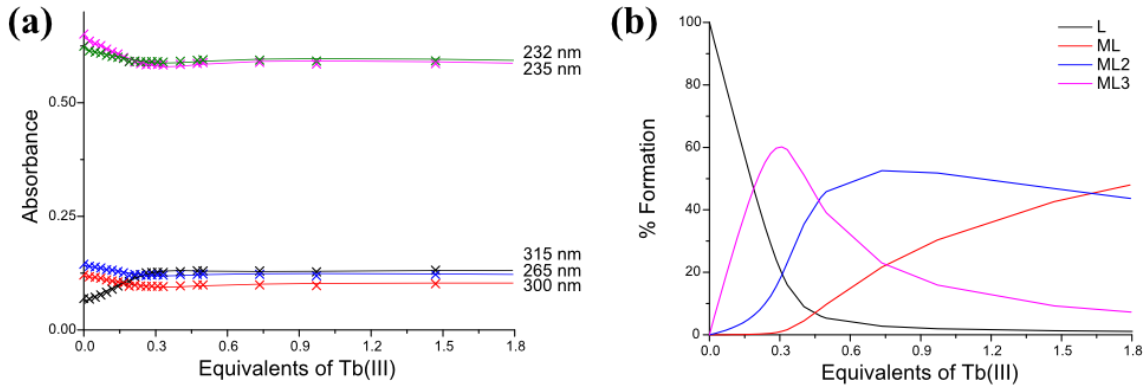

Figure 3.14 (a) Experimental (×) and calculated (–) UV-Vis absorbance binding isotherms for the titration of **88** with Tb(III); **(b)** Calculated speciation distribution diagram, showing the percentage formation of various stoichiometries as a function of equivalents of Tb(III).

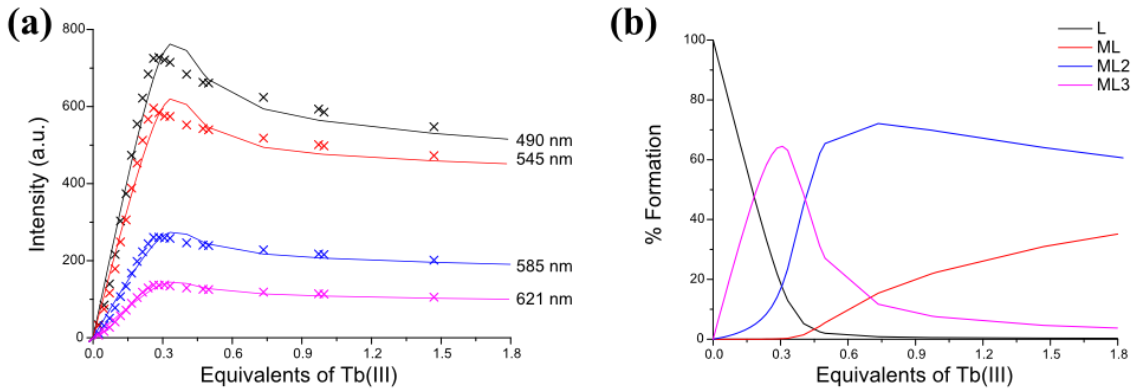

Figure 3.15 (a) Experimental (×) and calculated (–) Tb(III)-centred emission binding isotherms for the titration of **88** with Tb(III); **(b)** Calculated speciation distribution diagram, showing the percentage formation of various stoichiometries as a function of equivalents of Tb(III)

The binding constants for the self-assembly of ligand **88** with Ln(III), summarised in Table 3.2, were quite high, and in good agreement with the range of values reported for similar compounds in the literature, such as **79** ($\log\beta_{1:3}$ = 20.3 ± 0.5) and **80** ($\log\beta_{1:3}$ = 21.6 ± 0.4).[29,152,238,239] This suggests that these ligands are capable of forming very stable coordination compounds with Ln(III) in CH_3CN solution. The Eu(III) and Tb(III) assembly stabilities were determined to be similar in the course of these investigations. It is reasonable to hypothesise that derivatives of this ligand framework, prepared by extending the carbonyl functionality of ligand **88** would form similarly stable self-assemblies, along with the introduction of further functionality, as described in Figure 2.1(b) above. The remainder of this chapter will focus on the synthesis of such derivatives and the study of their self-assembly with Ln(III) ions in the same way as described in the preceding sections.

Table 3.2 Binding constants determined from titrations of **btp** ligand **88** v. Ln(III) in CH_3CN. [**88**] ≈ 10^{-5} M.

		Eu(III)			**Tb(III)**		
Ligand		**$\log\beta_{1:1}$**	**$\log\beta_{1:2}$**	**$\log\beta_{1:3}$**	**$\log\beta_{1:1}$**	**$\log\beta_{1:2}$**	**$\log\beta_{1:3}$**
88	UV	6.0±0.1	13.0 [a]	19.8 [a]	6.5 [a]	13.0 [a]	18.9±0.1
	Fluor.	6.9 [a]	—	22.2±0.1	—	—	—
	Phos.	7.2±0.1	14.8 [a]	20.7 [a]	6.9 [a]	14.2±0.1	20.2±0.1

[a] Value fixed.

3.6 Allyl amide derivative of 89 and catenane formation

An early goal of the research undertaken as part of these Ph.D. studies was the preparation of mechanically interlocked structures, templated by Ln(III) ions, such as [n]catenanes. Only one example of such a Ln(III)-templated catenane system, based on the **dpa** motif, has been published to date.[7] This system, developed in the Gunnlaugsson group, appended allyl-terminated triethylene glycol ‘chains’ onto the **dpa** binding motif, which were

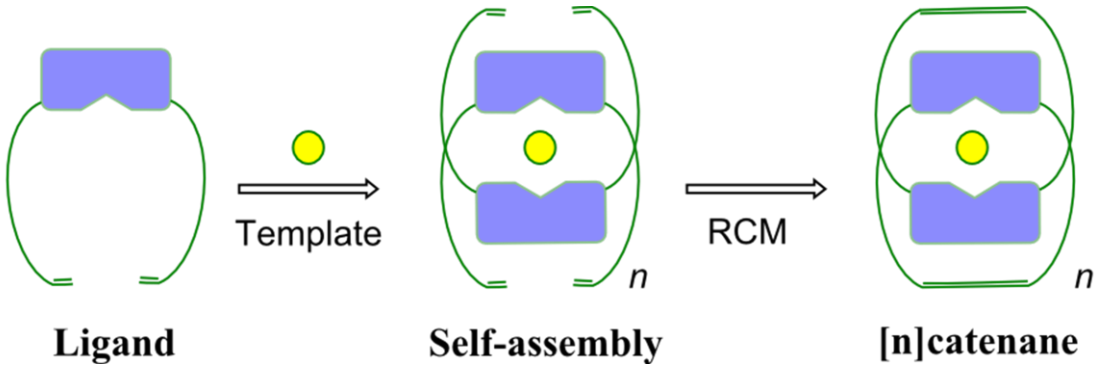

Figure 3.16 Strategy for templated formation of [n]catenanes, *via* ring-closing methathesis.

macrocyclised using Grubbs-catalysed olefin ring-closing metathesis (RCM). Leigh and co-workers have reported a Ln(III)-templated molecular trefoil knot, which also employed olefin RCM to 'clip' together three ligands pre-organised around the metal ion.[240] Such strategies towards the formation of interlocked molecules by RCM have been reported for *d*-metal ion-templated systems by Leigh *et al.*[241,242] as well as by White and Beer for anion-templated systems.[161] This strategy is summarised in Figure 3.16, where two or more of an olefin-appended ligand are templated by supramolecular interactions, such as metal coordination, anion binding or other weaker forces; finally the ligand 'threads' are closed by RCM, resulting in an interlocked system, such as [n]catenanes.

In pursuit of such systems, derivatisation of carboxylic acid ligand **89** *via* amide bond formation presented itself as a facile and modular route to extended functionality, Scheme 3.1, and introduce terminal olefin groups. Conversion of **89** to its acid chloride derivative upon reflux in $SOCl_2$, followed by reaction with an excess of allyl amine in freshly distilled CH_2Cl_2 under a $CaCl_2$ guard tube at room temperature for 18 hours yielded the desired product, **90**, as a white solid in good yield (61%) and purity (confirmed by elemental analysis). This ligand, possessing terminal olefin 'arms' was expected to be a

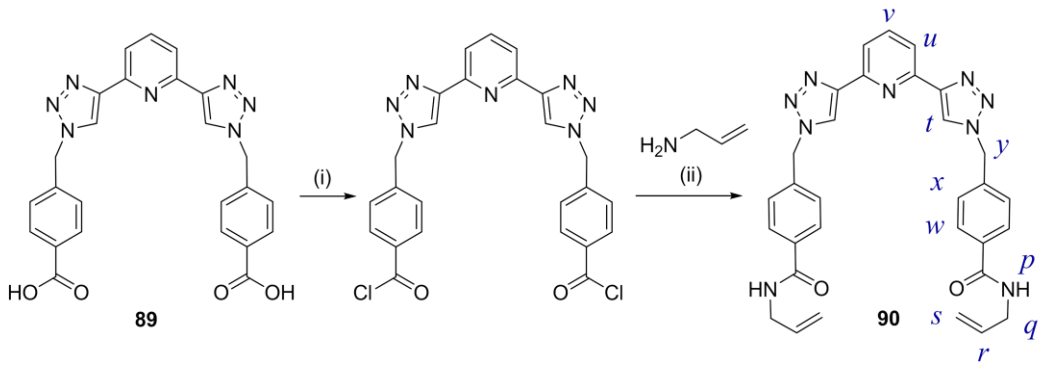

Scheme 3.1 Synthesis of ligand **90**. (i) $SOCl_2$, Δ, 18 h; (ii) CH_2Cl_2, rt, 18 h.

promising precursor for the formation of macrocycles through RCM, with a view to forming interlocked systems, as described in Figure 3.16 above.

This compound showed characteristic ^{1}H-NMR (600 MHz, DMSO) shifts, Figure 3.17. The allyl moieties gave rise to an apparent triplet at 3.90 ppm (labelled *q*), due to the CH_2 adjacent to NH, 5.08 and 5.15 ppm, two doublets of doublets arising from terminal olefin protons (labelled *s*), and 5.89 ppm, a multiplet arising from the non-terminal olefin CH (labelled *r*). A singlet at 5.77 ppm was due to the methylene linkers between triazolyl and phenyl rings (labelled *y*), while the phenyl rings displayed two doublets at 7.43 and 7.88 ppm (*w* and *x*) and the triazolyl protons gave rise to a singlet at 8.71 ppm (labelled *t*). The signals for the three pyridyl protons overlap at 7.98 ppm. NH COSY allowed the assignment of the broad triplet proton signal at 8.66 ppm as arising from the NH protons. ^{13}C-NMR resonances (150 Mz, DMSO-d_6) were also assigned with the assistance of 2D NMR correlation spectroscopy (spectra given in Appendix B). A characteristic signal in HRMS analysis (ESI+) at *m/z* = 560.2547 corresponded to the species $[M+H]^+$. The carbonyl band in the IR spectrum of the ligand was shifted with respect to the starting material, appearing at 1641 cm^{-1}, a characteristic band for an amide.

Next, as a preliminary study before introducing a Ln(III) ion into the system to template interlocked structures, the ligand was subjected to RCM, in order to investigate if it is a

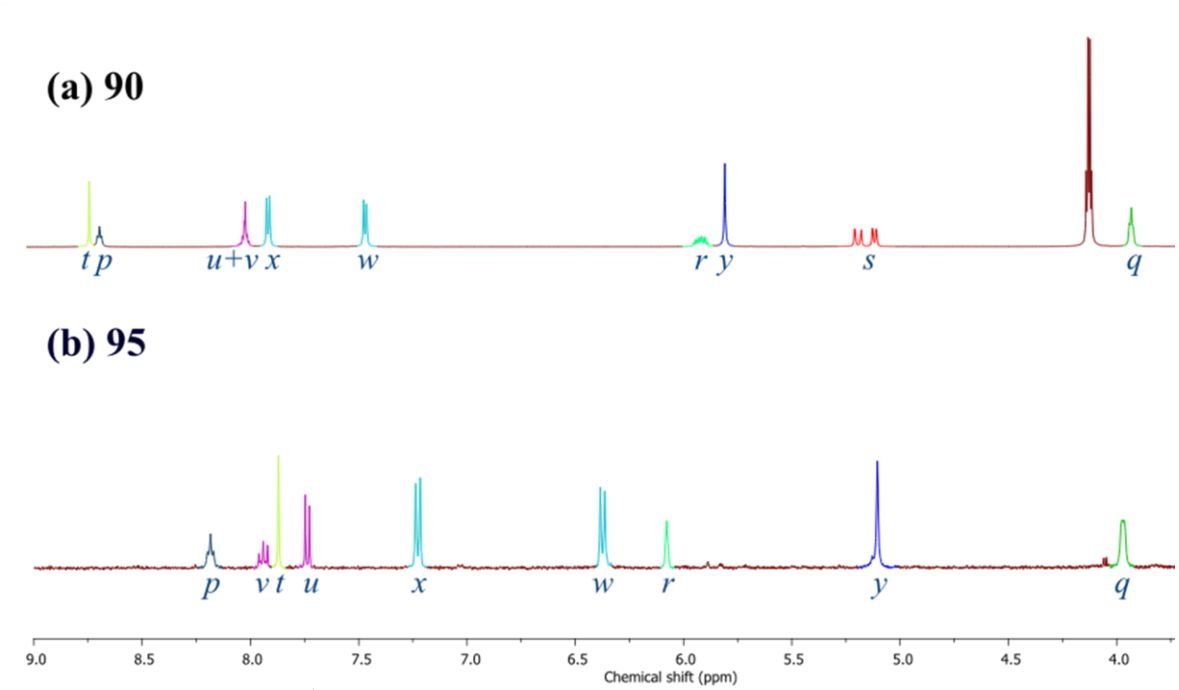

Figure 3.17 Comparison of ^{1}H NMR (DMSO-d_6) spectra of **(a)** olefin ligand **90** and **(b)** RCM product **95**. Proton resonances are labelled.

suitable ligand for the formation of macrocycles. Olefin RCM allows the macrocyclisation of an acyclic molecule with two terminal alkenes to produce a ring with one less carbon. Grubbs' carbene catalytic agents are well known for lowering the activation energy of this process.[243]

In order to prepare this compound, a degassed solution of **90** in distilled CH_2Cl_2 at room temperature was stirred under argon with the Grubbs–Hoveyda second generation catalyst for 24 hours. The reaction mixture was filtered to remove unreacted starting material, concentrated under reduced pressure and triturated with CH_3OH to yield the product, **95**, as a white solid in 26% yield. ^{1}H-NMR analysis (400 MHz, DMSO-d_6) showed that the resonances related to the terminal olefin in **90** (labelled *s* in Figure 3.17) disappeared in the spectrum of the RCM product and an apparent singlet resonance appeared at 6.08 ppm due to the remaining olefin protons (labelled *r*); these signals were indicative of successful RCM. Other proton shifts, however, were unexpected: the triazolyl CH resonance (labelled *t*) was dramatically shielded in the spectrum of **95**, suggesting it occupied quite a different chemical environment to the triazolyl proton in the starting material. The amide NH proton resonance (labelled *p*, assigned by NH COSY) was also shifted upfield. Most unexpectedly, however, the proton resonances assigned to the phenyl rings were heavily shielded, the two signals moving from 7.43 and 7.88 ppm to 6.42 and 7.27 ppm (labelled *x* and *w*) and the methylene linker CH_2 resonances (labelled *y*) were shifted upfield to 5.15 ppm. These NMR changes suggested a more dramatic change in the chemical environment for many of the protons than would be expected from macrocyclisation alone. The ^{13}C-NMR (150 MHz, DMSO-d_6) resonances were also assigned with the aid of HSQC and HMBC experiments, Appendix B.

Serendipitously, long thin colourless prismatic crystals were found to grow from slow evaporation of a CH_3CN solution of **95**. These crystals were suitable for X-ray diffraction analysis and allowed determination of the structure of **95**. The compound crystallised in the monoclinic $P2_1/c$ space group and, surprisingly, instead of the structure of the expected macrocyclic compound, in fact **95** was found to have formed self-templated [2]catenanes. The asymmetric unit contained two crystallographically distinct molecules of this [2]catenane structure, along with two water molecules. The diffraction data were collected and refined by Dr Salvador Blasco, a member of the Gunnlaugsson group, Table 3.3.

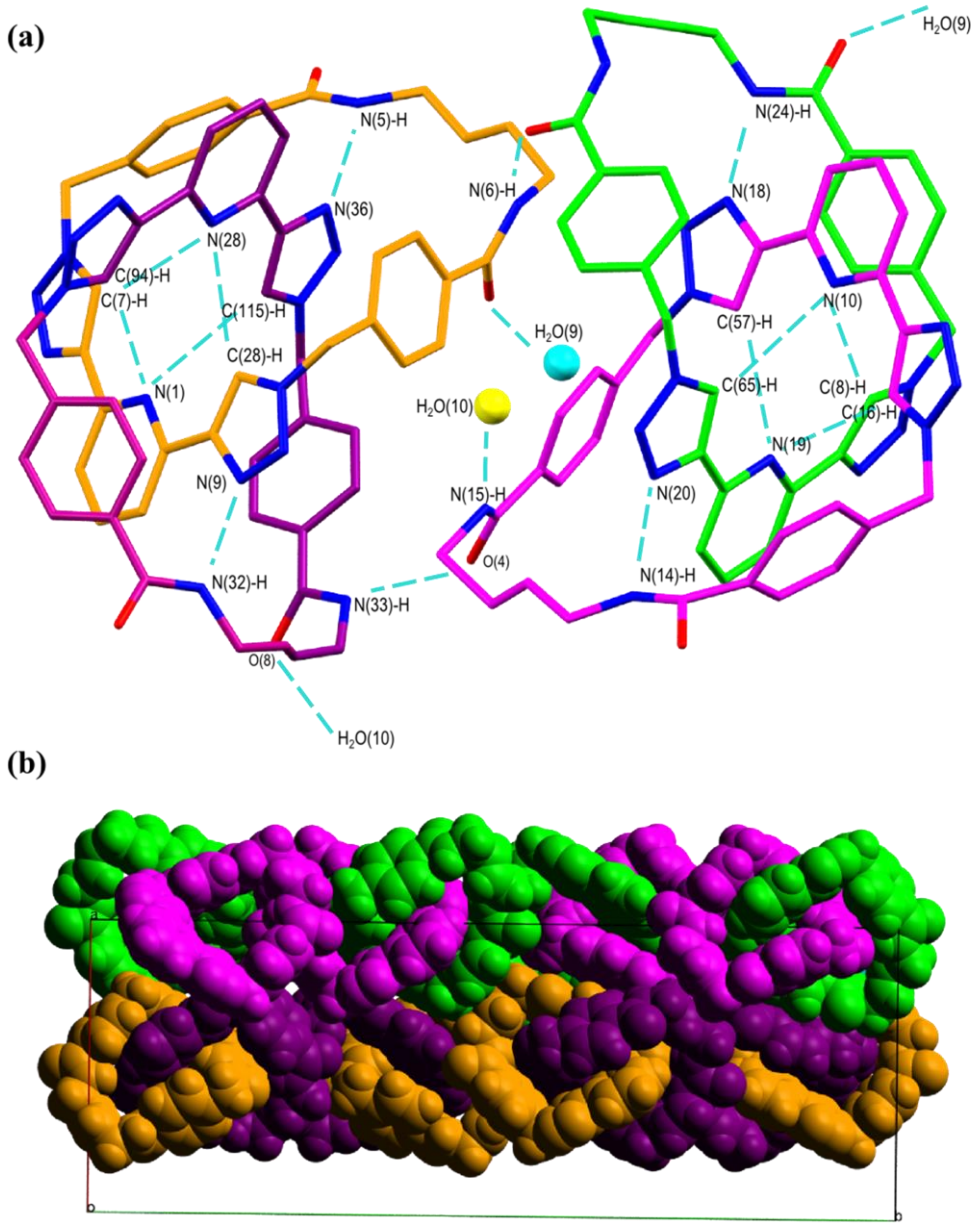

Figure 3.18 (a) Capped stick model of the asymmetric unit of the X-ray crystal structure of [2]catenane, **95**, showing the various hydrogen bonding and non-classical hydrogen bonding interactions present in the solid state, in particular those associated with the **btp–btp** dimer formation, as well as amide hydrogen bonds. The asymmetric unit contains two [2]catenanes and two H_2O molecules. Hydrogen atoms are omitted for clarity. **(b)** Packing structure of **95**, showing the unit cell, viewed along the c-axis. Solvent molecules are omitted for clarity.

This elegant supramolecular architecture shown in Figure 3.18 exhibits a range of non-covalent interactions pre-organising the constituent molecules together in the observed conformation. The ability of the triazolyl C–H to act as a non-classical hydrogen bond donor, as was seen in the various *d*-metal complex solid state structures determined in Chapter 2, resulted in the unexpected formation of a **btp–btp** dimeric hydrogen bond arrangement, with each pair of triazoles binding the pyridine of the other catenane 'thread'.

These hydrogen bonds all have donor–acceptor lengths ranging from 3.415(10)–3.700(12) Å. This pattern has not been observed before for **btp** systems.

There were also a significant number of amide hydrogen bonding interactions in the structure, as indicated in Figure 3.18(a), such as those between protons attached to N(5), N(14), N(24) and N(32) forming hydrogen bonds with one of the nitrogen atoms of various triazole rings. The donor-acceptor bond length for N(5)–H(5)···N(36), for example, was 2.980(10) Å. Amides were also shown to form hydrogen bonds with the H_2O molecules in the structure. All hydrogen bond lengths and angles are summarised in a table in Appendix B. The [2]catenane also showed significant π–π stacking between the phenyl rings of one catenane 'thread' and either the triazole or pyridine aromatic rings of the **btp** motif of the other 'thread'. All of these stacking interaction had centroid–centroid distances of *ca.* 4.1 Å. This range of interactions results in a well ordered and tightly packed solid state structure, as shown in the depiction of the unit cell in Figure 3.18(b), which contains 16 [2]catenane molecules.

Table 3.3 Selected crystallographic data and structural refinements for [2]catenane **95**.

Compound	**95**
Formula	$4(C_{29}H_{25}N_9O_2)\cdot 2(H_2O)$
Formula weight (g mol^{-1})	2162.35
T (K)	100(2)
Crystal system	Monoclinic
Space group	$P2_1/c$
a (Å)	18.9402(7)
b (Å)	52.2019(10)
c (Å)	10.7223(4)
α (°)	90
β (°)	92.705(2)
γ (°)	90
V (Å^3)	10589.5(7)
Z	4
F(000)	4528
D_c (Mg m^{-3})	1.356
μ (mm^{-1})	0.75
GOF on F^2	1.03
R1 [$I > 2\sigma(I)$]	0.099
wR2 [$I > 2\sigma(I)$]	0.237

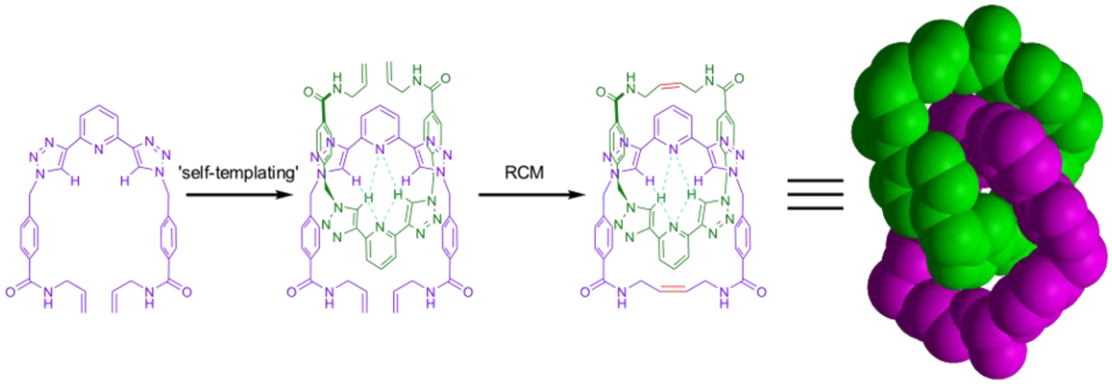

Scheme 3.2 Schematic representation of the formation of 'self-templated' [2]catenane, **95**, showing the tight packing of the structure by means of a space-filling model of the X-ray crystal structure, with hydrogen atoms omitted.

The formation of this remarkable interlocked structure from the ligand alone upon RCM, suggests that ability of the acidic triazolyl C–H to act as a hydrogen bond donor is exploited in order for molecules of **90** to self-template the formation of [2]catenanes *via* these supramolecular interactions; RCM is a favourable reaction for this pre-organised system, resulting in the tightly-packed and stable [2]catenane shown. This proposed scheme is outlined in Scheme 3.2. The formation of the interlocked species was further confirmed by the appearance of characteristic peaks upon HRMS analysis in both ESI+ and MALDI+. The MALDI+ spectra showed peaks at *m/z* = 1063.4346 and 1085.4147 which were assigned to the $[M+H]^+$ and $[M+Na]^+$ species, A selective ROESY experiment, Appendix B, also supported the formation of interlocked systems, showing weak through-space interactions between the phenyl rings and the **btp** motif, which is consistent with the stacking behaviour seen in the solid state structure.

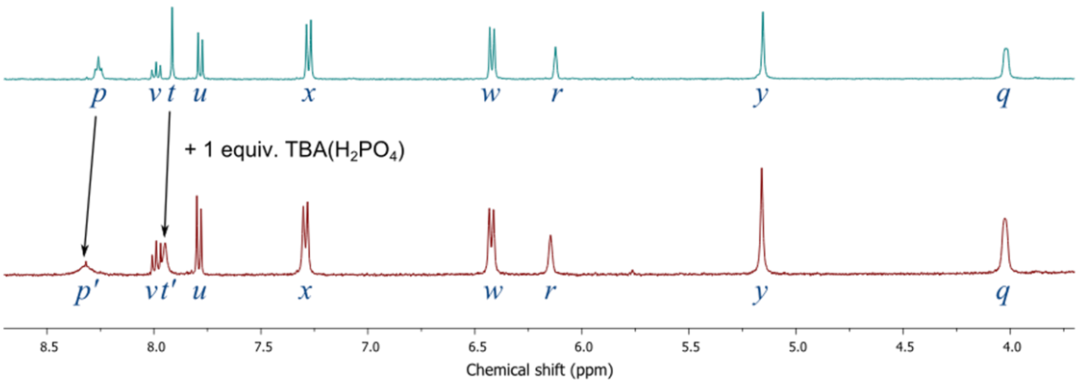

Figure 3.19 Changes in ^{1}H-NMR spectra (400 MHz, DMSO-d_6) of [2]catenane **95** upon addition of 1 equivalent of TBA(H_2PO_4). Resonances which underwent shifts upon anion binding are indicated as *p′* (amide NH) and *t′* (triazolyl CH).

The central cavity of the [2]catenane structure is rich in hydrogen bond donors and, accordingly, appears an attractive site for anion binding. Some preliminary anion binding tests were carried out upon addition of 1 equivalent of the tetrabutylammonium salts of a range of anions to a sample of **95** in DMSO-d_6 solution and comparing the ^{1}H-NMR spectra (400 MHz). This work was carried out in collaboration with Ms Anna Aletti and Mr Dermot Gillen, both members of the Gunnlaugsson group. For the range of anions tested so far, namely Cl^-, NO_3^-, $H_2PO_4^-$ and HSO_4^-; no changes were observed, except for $H_2PO_4^-$. Modest shifts in the amide NH and triazolyl CH proton resonances were observed, Figure 3.19, suggesting the formation of hydrogen bonds between these moieties and the bound anion. These preliminary results suggest the [2]catenane has potential to act as a phosphate-specific anion binding molecule. Investigations into these properties are on-going.

Having formed this serendipitous supramolecular self-assembled interlocked structure, **95**, it was next undertaken to study the self-assembly processes of the allyl amide **90** with Eu(III), in order to explore its ability to bind this metal ion and then the potential of using Eu(III) to template the formation of Ln(III)-directed interlocked systems. The preparation of the Eu(III) complex of **90** will first be discussed.

3.7 Preparation and photophysical studies of Eu(III) complex of allyl amide ligand 90

The Eu(III) complex was prepared upon microwave irradiation of **90** with 0.33 equivalents of Eu(III) or triflate salt in CH_3OH solution at 70 °C for 20 minutes and it was recovered as an off-white solid upon diffusion of diethyl ether into a CH_3OH solution. Successful formation of the 1:3 complex was confirmed by ESI+ mass spectrometry, Figure 3.20(a), where a peak at *m/z* = 990.3048 possessed a characteristic isotopic distribution matching that of the calculated spectrum for $[Eu\cdot(\mathbf{90})_3](CF_3SO_3)^{2+}$, Appendix B. Evidence was also seen in the MALDI+ HRMS spectrum of the 1:2 species, with a peak observed at *m/z* = 1420.3672.

The ^{1}H NMR spectrum (400 MHz, CD_3CN) of the complex, Figure 3.20(c), showed shifts of proton resonances relative to the ligand similar to those seen for **88** above, with the pyridyl signals appearing more deshielded as a triplet at 6.32 ppm and a doublet at 4.61 ppm (labelled *v′* and *u′*, respectively). The triazolyl CH resonance (labelled *t′*) also shifted upfield to 7.26 ppm, where it overlapped with one of the phenyl proton signals.

The photophysical properties of the complex formed under thermodynamic control were measured, Figure 3.20(b). The UV-Vis absorbance spectrum closely resembled that of [Eu·(**88**)$_3$](CF$_3$SO$_3$)$_3$ above, with a broad absorbance band centred at 313 nm and a higher energy band at 232 nm, featuring a shoulder at 267 nm. Exciting into either of these bands gave rise to a Eu(III)-centred emission spectrum, exhibiting bands at 580, 594, 618, 650 and 695 nm, related to the $^5D_0 \rightarrow {}^7F_J$ transitions (J = 0–4, respectively). The excitation spectrum of the ΔJ =2 transition, gave a spectrum with a strong band at 308 nm and a weaker band centred at 256 nm. The sensitisation of the Eu(III) emission was not exceptionally efficient, with a quantum yield of 5.4 ± 1.0% determined. A hydration state of $q \approx 0$ (−0.3 ± 0.5) was determined from luminescence lifetime measurements (τ_{H2O} = 1.62 ± 0.01 ms, τ_{D2O} = 1.65 ± 0.01 ms); this supports the formation of a 1:3 complex stoichiometry with no metal bound solvent molecules.

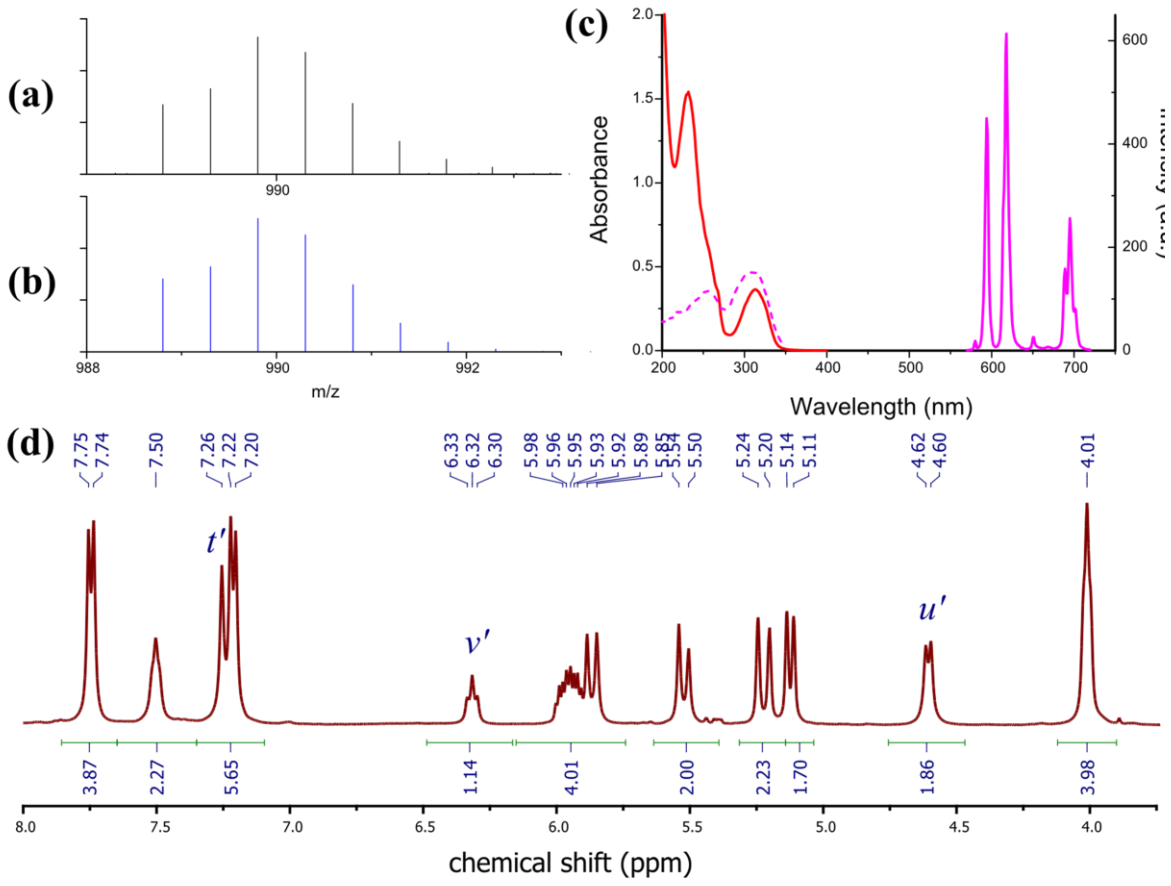

Figure 3.20 **(a)** Experimental and **(b)** calculated HRMS isotopic pattern distribution for [Eu·(**90**)$_3$](CF$_3$SO$_3$)$_3$. Calculated for $C_{94}H_{87}N_{27}O_9SF_3Eu^{2+}$ *m/z* = 990.3050 [EuL$_3$(CF$_3$SO$_3$)]$^{2+}$. Found *m/z* = 990.3048; **(c)** UV-Vis absorbance (red), excitation (dashed magenta) and Eu(III) phosphorescence (magenta) spectra of [Eu·(**90**)$_3$](CF$_3$SO$_3$)$_3$; **(d)** ^{1}H NMR (400 MHz, CD$_3$CN) spectrum of [Eu·(**90**)$_3$](CF$_3$SO$_3$)$_3$.

3.8 Spectroscopic titrations of 90 with Eu(III)

3.8.1 Titration with Eu(III)

The UV-Vis absorbance spectrum of ligand **90** resembled that of **88** above, with a band centred at 300 nm (ε 10,100 M^{-1} cm^{-1}) and another at 236 nm (ε 53,900 M^{-1} cm^{-1}). Upon addition of $Eu(CF_3SO_3)_3$ solution in CH_3CN (at a ligand concentration of 1.1×10^{-5} M), the band at 300 nm underwent a significant red shift to 314 nm, while the higher energy band experienced a slight blue shift to 231 nm along with a hypochromic effect, Figure 3.21(a). A clear isosbestic point was observed at 304 nm for these changes. The majority of spectral changes were complete upon addition of 0.33 equivalents of metal ion, as can be clearly seen in the binding isotherms at various wavelengths, Figure 3.21(b), suggesting the kinetic formation of the 1:3 complex in solution at this point in the titration. As hypothesised above, these changes were analogous to those observed for **88**.

Ligand fluorescence, a broad band centred at 335 nm, Figure 3.22(a), was shown to quench rapidly upon addition of Eu(III), being completely switched off by 0.33 equivalents. Excitation spectra of this emission showed two bands which matched the ligand absorbance spectrum, indicating that the emission originated from the ligand excited state. Simultaneously, Eu(III)-centred emission sensitised *via* the 'antenna' effect, Figure 3.22(b), was switched on with addition of $Eu(CF_3SO_3)_3$, forming the most luminescent species (the 1:3 assembly) at 0.33 equivalents and gradually decreasing in luminescence thereafter as the equilibrium shifted towards less emissive stoichiometric species, such as the 1:2 and 1:1 complexes. Fitting these spectroscopic data, as was done above in Section

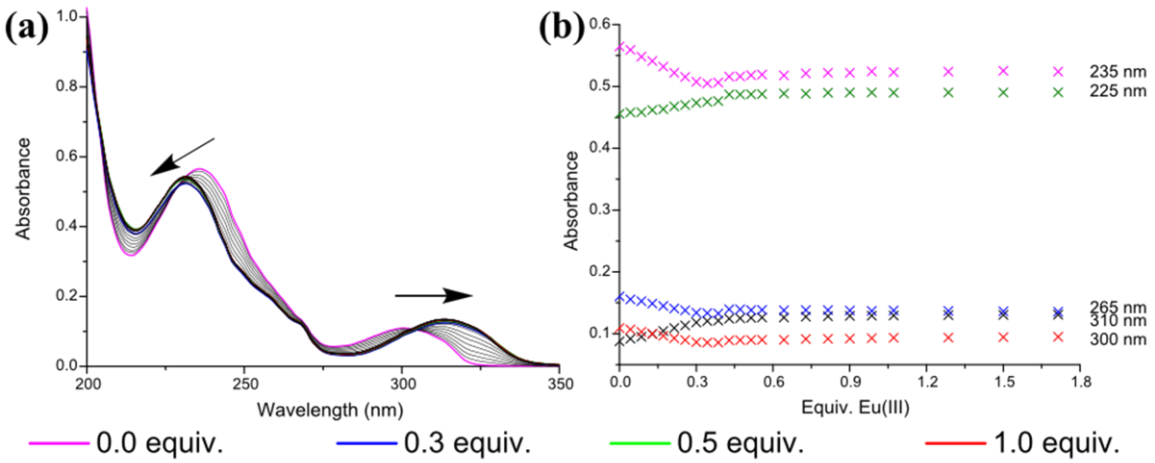

Figure 3.21 Titration plots of **90** v. Eu(III) in CH_3CN. **(a)** UV-Vis spectral changes; **(b)** Experimental UV-Vis binding isotherms (×) at various wavelengths. [**90**] = 1.1×10^{-5} M.

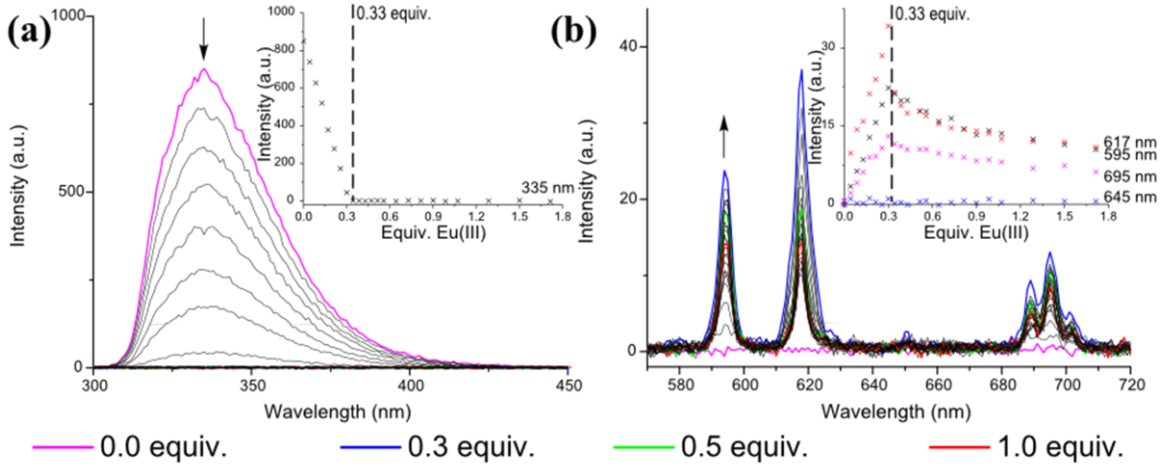

Figure 3.22 Titration plots of **90** v. Eu(III) in CH_3CN. **(a)** Changes in fluorescence; *inset*: experimental binding isotherm at 335 nm (×); **(b)** Changes in phosphorescence upon addition of $Eu(CF_3SO_3)_3$ solution in CH_3CN, showing characteristic Eu(III) transition bands; *inset:* experimental binding isotherms at various wavelengths (×).[**90**] = 1.1×10^{-5} M.

3.5.3 will provide further insight into the speciation over the course of the titrations and the stability of these self-assemblies.

3.8.2 Fitting of titration data

These titration data, for UV-Vis and phosphorescent Eu(III)-centred emission, were fit to theoretical models by non-linear regression analysis using ReactLab Equilibria software, as discussed in Section 3.5.3 above. For the UV-Vis absorbance data, where no dramatic ground state spectral changes occurred after 0.33 equivalents, models containing the 1:2 stoichiometric species did not converge, so global stability constants could only be obtained for the 1:1 and 1:3 species; these were determined to be 6.7 ± 0.1 and 20.9 ± 0.2, respectively. Fitting the data for the Eu(III)-centred emission from the excited state using these values of $\log\beta_{1:1}$ and $\log\beta_{1:3}$, allowed $\log\beta_{1:2}$ to be determined as 14.8 ± 0.1. The fitting curves and calculated speciation distribution diagrams are shown in Appendix B. As expected, the speciation distribution diagrams resemble those calculated above for **88**, with, for example, the 1:3 species formed in 65% yield at 0.33 equivalents of Eu(III) according to the diagram derived from fitting the Eu(III)-centred emission. Since the olefin-appended ligand can form stable 1:3 complexes in CH_3CN solution, the next step was to form a macrocycle using ring-closing metathesis.

3.9 Towards Ln(III)-templated [n]catenanes of 90

Ligand **90** was shown above to be capable of self-templating the formation of [2]catenanes. Analogous interlocked systems, possessing the desirable optical properties of the Ln(III)

ions have long been a goal in the Gunnlaugsson group, but only one example of such a system has been reported for **dpa**-based 'threads'.[7] The strategy outlined in Figure 3.16 foresaw the formation of such systems by initial complexation of the ligand 'threads' (i.e. **90**) with the Eu(III) 'template' followed by olefin RCM to close the ligands into macrocycles, as was seen for **95** above.

Using the same conditions described above for the synthesis of **95**, attempts were made to subject $[Eu\cdot(\mathbf{90})_3](CF_3SO_3)_3$ to RCM *in situ*, in order to form a [3]catenane. Unfortunately, all of these attempts proved unsuccessful, with no evidence of this reaction proceeding observed by HRMS analysis, ^{1}H-NMR or TLC. Various different catalysts were employed, namely Grubbs' first and second generation catalysts and the Grubbs–Hoveyda second generation catalyst and the reaction was attempted at elevated temperatures. It is likely that, when templated by the metal ion, with the **btp** motif in the *syn-syn* conformation that formation of the small macrocycle is unfavourable. In the formation of **95**, the pre-organisation of the ligand dimer is proposed to make the ring-formation more likely, since many supramolecular forces are at play in templating the two 'threads' together; much of this pre-organisation would be absent in $[Eu\cdot(\mathbf{90})_3](CF_3SO_3)_3$. It is also worth noting that even cursory analysis of the packing structure of [2]catenane **95**, Figure 3.18(b), shows how tightly interlocked the structures are, leaving little room available for a Eu(III) ion in the cavity left available for macrocycles of this size. Indeed, the attempted synthesis of $[Eu\cdot(\mathbf{95})](CF_3SO_3)_3$, introducing Eu(III) directly into the [2]catenane, was unsuccessful and only **95** itself was recovered from the reaction mixture, confirming that **95** is incapable of including Eu(III) ions. It should be noted that similar attempts to form Ru(II)-directed [2]catenanes of this ligand were also unsuccessful. Formation of the complexes would be expected to result in the ligand taking up a *syn-syn* geometry, by analogy to the results of the ^{1}H-NMR titrations of **88** above, resulting in the allyl 'arms' being orientated further away from each other and, hence, making RCM less favourable.

In the course of the studies carried out in the preceding sections, allyl appended ligands **90** were prepared which could undergo olefin RCM to form self-assembled [2]catenane **95**, the structure of which was confirmed by single crystal X-ray diffraction analysis. The Eu(III)-directed self-assembly of these ligands was also explored, with a view to formation of Eu(III)-templated interlocked structures by similar methods, however, $[Eu\cdot(\mathbf{90})_3](CF_3SO_3)_3$ did not undergo RCM and did not form [3]catenanes as hoped. It is

anticipated that modification of the ligand framework to introduce longer 'chains' into the structures, such as polyethylene glycol groups to provide better flexibility to these systems might allow favourable substrate for Ln(III)-templated RCM-mediated catenane formation, but, to date no such modified systems have successfully resulted in the desired interlocked system and, as such, they will not be discussed further in this thesis.

The facility of the coupling reaction, which produced ligand **90** suggested the possibility of incorporating a range of amines into the **btp** ligand frameworks designed above through amide bond formation. The amino acids are a readily-available range of amines of biological interest, which might give the luminescent Ln(III) complexes formed from amino acid containing analogues of **88** favourable properties for medicinal or imaging applications. The introduction of these amino acid residues will be discussed in the remainder of the chapter.

3.10 Introduction of amino acids

Recently, a number of Ln(III) complexes of bis(benzyl)-**btp**, **17**, have been evaluated as chemically stable bioimaging agents, suggesting the potential utility of such compounds for biological applications, although it is worth noting that these complexes were delivered to cells as suspensions in ethanol and showed little solubility in aqueous media.[158] With a view to introducing ligands, such as ligand **88**, into the biological arena, derivatives analogous to **88** with appended amino acid methyl ester moieties were prepared. Amino acids are small, convenient, and mostly chiral residues, which are ubiquitous in nature, acting as the building blocks for peptides and proteins. Incorporation of peptides into Ln(III) probes has been shown to facilitate their selective uptake into specific cells, such as the selective internalisation of a Ln(III)–cyclen complex appended with tetrapeptide tuftsin into macrophages.[244]

Incorporation of amino acids into **btp** scaffolds such as **89** provides a facile route towards a range of derivatives **91**, Scheme 3.3, which were all chiral, apart from **91-Gly**, which contains the optically inactive Gly residue. The Ln(III) complexes prepared from these ligands have the potential to display activity in biological systems, and could act as building blocks for peptide-appended **btp** systems. The ligands were prepared through straightforward amide coupling reactions. The synthesis and characterisation of seven such ligands will now be presented, along with investigations of their self-assembly behaviour with Eu(III) and Tb(III) ions. The outcome of this self-assembly can be considered as

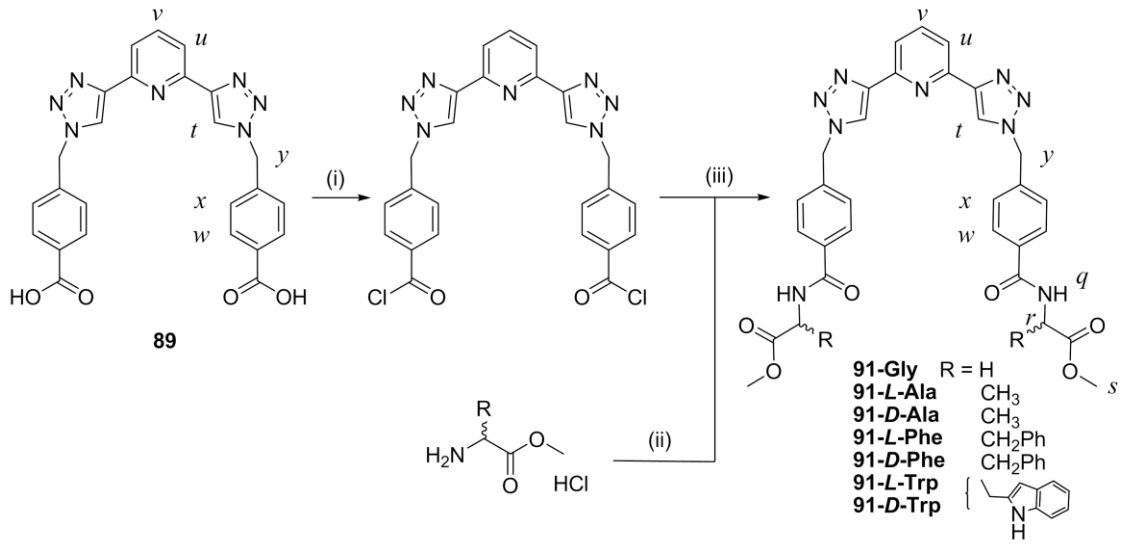

Scheme 3.3 Synthesis of ligands **91**. (i) $SOCl_2$, Δ, 18 h; (ii) Et_3N, rt, 1 h; (iii) CH_2Cl_2, rt, 18 h.

Ln(III)-directed synthesis of 'peptide bundles'; spectroscopic studies in CH_3CN solution allowed the determination of global stability constants for various stoichiometric species.

3.11 Amino-acid derivative synthesis, characterisation and photophysical properties

Having shown that **88** and **90** were excellent candidates for use in Ln(III)-directed self-assembly, it was next chosen to explore **89**, the hydrolysed form of **88**, as a platform for further derivatisation with a view to developing more functional ligands, which also have potential for forming higher-order self-assembly structures, such as gels. To exploit this possibility of **btp** ligands, methyl ester-protected amino acids were coupled with both carboxylic acid groups of ligand **89** in order to produce a small library of bis-substituted **btp** ligands, **91**. This was simply achieved as shown in Scheme 3.3 by first converting **89** into its acid chloride derivative upon treatment with $SOCl_2$. The methyl ester-protected amino acids (as HCl salts), Gly, Ala, Phe and Trp (the latter of which has been employed in the literature as a naturally-occurring 'antenna' for Tb(III) emission[245,246]), were stirred with triethylamine in CH_2Cl_2 for an hour, before adding to the acid chloride and stirring at room temperature. Both *L*- and *D*-enantiomers of the chiral amino acids Ala, Phe and Trp were used. Solvent was removed under reduced pressure and the product triturated with cold CH_3OH, furnishing the amide products, for each of the amino acids, as off-white solids in moderate yields of 47–61% and high purity upon filtration (as confirmed by elemental analysis, Experimental Chapter). These analogues of **88** were fully characterised.

Like the parent ligand, the successfully functionalised new ligands were symmetircal, as was evident from ^{1}H-NMR analysis. The simplicity of the ^{1}H-NMR spectra (600 MHz, DMSO-d_6) of **91** confirmed the formation of ligands possessing C_2 symmetry, only differing from the previously reported spectra of **88** and **89**[72] in the presence of resonances arising from the amino acid moieties, with the spectra of enantiomeric pairs being identical, hence only the ligands containing two *L*-amino acid residues as 'arms' will be discussed in this section with the spectra of the *D*-amino acid derivatives being shown in Appendix B.

The ^{1}H-NMR (600 MHz, DMSO-d_6) of **91-Gly**, shown in Figure 3.23(a), displayed a resonance relating to the methyl ester protecting group at 3.65 ppm (labelled *s*), a doublet arising from the Gly CH_2 at 4.02 ppm (*r*) and a signal at 5.79 ppm from the methylene linker between the triazole and phenyl rings (*y*). The aromatic region consisted of a pair of phenyl doublets at 7.46 and 7.89 ppm, two pyridyl resonances, overlapping as a multiplet from 7.93–8.05 ppm (*u* and *v*), a triazolyl resonance at 8.72 ppm (*t*) and a triplet resonating at 8.97 ppm assigned to the amide NH protons (*q*). All NH proton resonances were

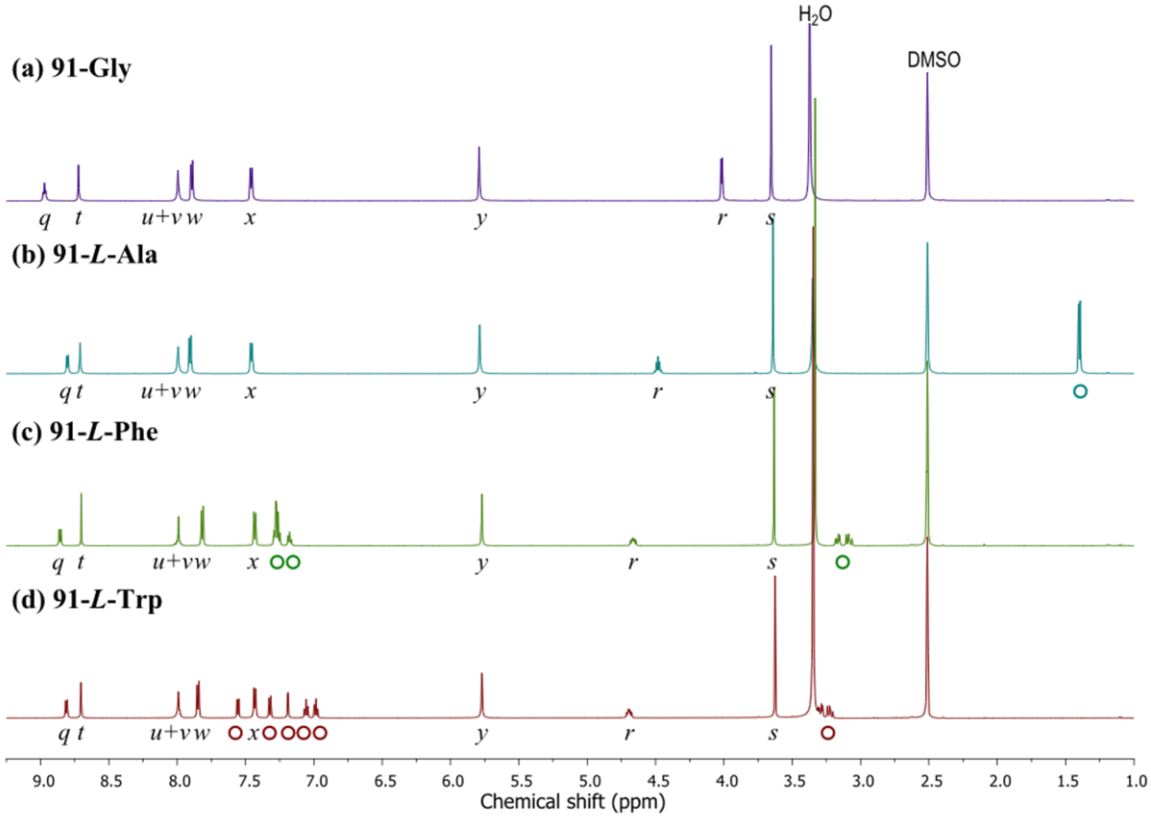

Figure 3.23 ^{1}H-NMR spectra (600 MHz, DMSO-d_6) of ligands **(a) 91-Gly**, **(b) 91-*L*-Ala**, **(c) 91-*L*-Phe** and **(d) 91-*L*-Trp** (resonance at 10.5 ppm from indolyl NH not shown). Resonances are labelled as follows: *q* (amide NH), *r* (α-protons in amino acid residue), *s* (–OCH_3), *t* (triazolyl CH), *u* (3- and 5-pyridyl CH), *v* (4-pyridyl CH), *w* and *x* (phenyl CH), *y* (CH_2), ○ (peaks particular to amino acid side-chain). Spectra of **91-*D*-Ala**, **91-*D*-Phe** and **91-*D*-Trp** were identical to their enantiomers and are shown in Appendix B.

assigned by NH COSY, see Appendix B.

As expected, the ^{1}H-NMR spectrum (600 MHz, DMSO-d_6) of **91-*L*-Ala** was very similar to that of the Gly derivative above, differing only in the presence of the chiral methyl side-chain, resonating at 1.40 ppm as a doublet (marked in Figure 3.23(b) with a ○) and a resonance centred at 4.48 ppm arising from the adjacent chiral CH (*r*) of the Ala residue. The NH resonance was also shifted upfield, appearing as a doublet at 8.80 ppm. Similarly, the **91-*L*-Phe** ^{1}H-NMR spectrum (600 MHz, DMSO-d_6, Figure 3.23(c)) closely resembled the Ala derivative described above, the benzyl CH_2 protons appearing as multiplets between 3.05–3.19 ppm and the α-protons at 4.66 ppm with further resonances occurring at 7.15–7.20 and 7.25–7.30 ppm, for the aryl protons. Again, the amide NH resonance (*q*) appeared at a different chemical shift of 8.86 ppm.

The ^{1}H-NMR spectrum (600 MHz, DMSO-d_6) of **91-*L*-Trp** was the most complicated of the ligands described herein, as is evident from Figure 3.23(d), with aliphatic resonances similar to those seen for **91-*L*-Phe**; the indole peaks appeared as a pair of triplets at 6.98 and 7.06 ppm and three doublets at 7.19, 7.32 and 7.55 ppm. These resonances were well resolved from the two phenyl CH doublets at 7.43 and 7.84 ppm (labelled *x* and *w*, respectively), the pyridyl multiplet at 7.96–8.03 ppm and the triazolyl resonance at 8.70 ppm (*t*). **91-*L*-Trp** showed two NH resonances. The amide signal appeared as a doublet at 8.81 ppm, while the indole NH resonated downfield at 10.80 ppm (see Appendix B).

^{13}C-NMR (150 MHz, DMSO-d_6) spectra of these ligands were also fully assigned (see Experimental Chapter) with the aid of 2D NMR techniques such as HSQC and HMBC, Appendix B. ESI MS analysis confirmed the identity of all the aforementioned ligands (*e.g.* the signal at *m/z* = 652.2632 for **91-*D*-Ala** was assigned to the $[M+H]^+$ species). Moreover, the successful synthesis of these amide derivatives **91** was evident in the IR spectra, all of which displayed characteristic amide carbonyl band (*e.g.* at 1642 cm^{-1} for **91-*D*-Ala**), in addition to the ester carbonyl band (*e.g.* at 1741 cm^{-1} for **91-*D*-Ala**). All IR spectra are shown in Appendix B.

Having prepared and fully characterised seven new **btp** ligands, their photophysical properties were next probed in CH_3CN solution in a similar manner to that described for **88** above.

3.12 General photophysical properties of ligands 91

Ligands **91-Gly**, **91-Ala** and **91–Phe** showed broadly similar UV-Vis absorbance profiles in CH_3CN solution, Figure 3.24, with distinct bands centred at 300 nm, assigned to n→π*

transitions from the **btp** core, and 235 nm, assigned to π→π* transitions from the various aromatic rings in the structures. These spectra were qualitatively almost identical to that of **88**, which is shown for comparison.

For **91-Phe**, the lower wavelength band was broader and shifted by a few nanometres relative to the parent ligand **88** and had a larger extinction coefficient (λ_{max} = 237 nm, ε 50,900 M^{-1} cm^{-1}). These changes are likely a result of the two extra phenyl rings in the structure. **91-Trp** show a broader absorbance profile with a maximum centred at 223 nm, a shoulder around 235 nm and a sharp peak at λ_{max} = 290 nm overlapping with a broader band resembling the 300 nm-band in all of the other ligands. This is consistent with the absorbance profile of Trp-containing ligands reported in the Gunnlaugsson group previously.[153] Upon excitation into any of the bands, all ligands **91** displayed a broad fluorescence band centred at 335 nm, like **88** above. Excitation spectra of this emission across the range of ligands were practically identical and matched the general structure of the absorbance profiles, the exception being **91-Trp**, where the excitation spectrum resembled just those bands associated with the **btp** 'core', not those which are associated

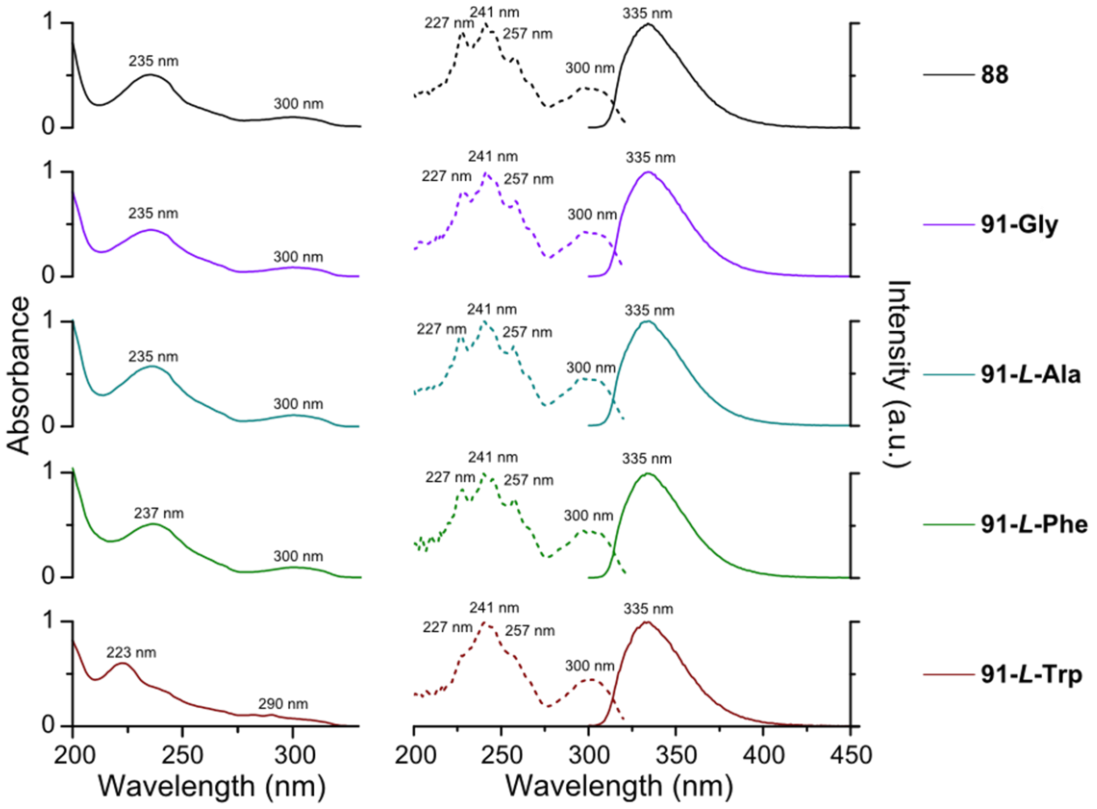

Figure 3.24 UV-Vis absorption, excitation and fluorescence spectra of ligands **88**, **91-Gly**, **91-*L*-Ala**, **91-*L*-Phe** and **91-*L*-Trp** (the spectra of **91-*D*-Ala**, **91-*D*-Phe** and **91-*D*-Trp** are shown in Appendix B).

with the Trp moieties (*viz.* the bands at 223 and 290 nm). This suggested that fluorescence arises chiefly from the excited state of the **btp** moiety of these ligands rather than the amino acid side-chains. CD spectra of ligands **91** were weak and poorly resolved, but did show subtle difference between the enantiomers.

3.13 Preparation and photophysical studies of Ln(III) complexes

Having synthesised, characterised and analysed the basic photophysical properties of **91**, 1:3 Ln(III) complexes of **91** were prepared as described in Section 3.3 above upon microwave irradiation of suspensions of the ligand and $Ln(CF_3SO_3)_3$ (Ln = Eu or Tb) in CH_3OH at 70 °C for 20 minutes. After filtration of the reaction mixture, the complexes, $[Ln\cdot(\mathbf{91})_3](CF_3SO_3)_3$, were recovered as off-white solids upon diffusion of diethyl ether into the CH_3OH solution, with successful complexation being confirmed by MALDI+ mass spectrometry analysis,

Table **3.4**, where the characteristic isotopic distribution patterns of the measured peaks matched the calculated spectra. The observed and calculated isotopic distribution patterns for both enantiomers of $[Tb\cdot(\mathbf{91\text{-}Trp})_3](CF_3SO_3)_3$ are shown in Figure 3.25; all other HRMS spectra are shown in Appendix B. Evidence was also seen in the MALDI+ spectra of fragmentation into the 1:2 and, in some cases, 1:1 stoichiometries. These peaks are listed in the Experimental section. Unfortunately, crystals of these systems of sufficient quality for crystal structural analysis were not obtained, despite numerous attempts

Table 3.4 Calculated and experimental HRMS (MALDI+) signals for the various Ln(III) complexes of **91**.

Complex	calculated *m/z*	experimental *m/z*, MALDI+
[Eu·(91-Gly)$_3$](CF$_3$SO$_3$)$_2$$^+$	2320.4975	2320.4885
[Eu·(91-*L*-Ala)$_3$](CF$_3$SO$_3$)$_2$$^+$	2404.5914	2404.5989
[Eu·(91-*D*-Ala)$_3$](CF$_3$SO$_3$)$_2$$^+$	2404.5914	2404.5710
[Eu·(91-*L*-Phe)$_3$](CF$_3$SO$_3$)$_2$$^+$	2860.7792	2860.7832
[Eu·(91-*D*-Phe)$_3$](CF$_3$SO$_3$)$_2$$^+$	2860.7792	2860.7866
[Eu·(91- *L*-Trp)$_3$](CF$_3$SO$_3$)$_2$$^+$	3094.8446	3094.8521
[Eu·(91-*D*-Phe)$_3$](CF$_3$SO$_3$)$_2$$^+$	3094.8446	3094.8599
[Tb·(91-Gly)$_3$](CF$_3$SO$_3$)$_2$$^+$	2326.5016	2326.5088
[Tb·(91-*L*-Ala)$_3$](CF$_3$SO$_3$)$_2$$^+$	2410.5955	2410.6018
[Tb·(91-*D*-Ala)$_3$](CF$_3$SO$_3$)$_2$$^+$	2410.5955	2410.6016
[Tb·(91-*L*-Phe)$_3$](CF$_3$SO$_3$)$_2$$^+$	2866.7833	2866.7837
[Tb·(91-*D*-Phe)$_3$](CF$_3$SO$_3$)$_2$$^+$	2866.7833	2866.7734
[Tb·(91- *L*-Trp)$_3$](CF$_3$SO$_3$)$_2$$^+$	3100.8487	3100.8418
[Tb·(91-*D*-Trp)$_3$](CF$_3$SO$_3$)$_2$$^+$	3100.8487	3100.8623

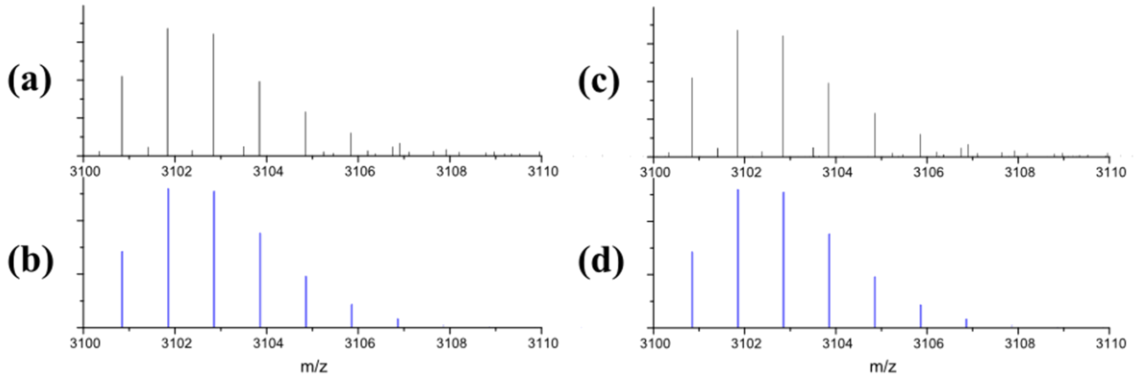

Figure 3.25 (a) Experimental and **(b)** calculated HRMS isotopic pattern distribution for [Tb·(**91-*L*-Trp**)$_3$](CF$_3$SO$_3$)$_3$. Calculated for $C_{149}H_{129}N_{33}O_{24}F_6S_2Tb^+$ *m/z* = 3100.8487 [TbL$_3$(CF$_3$SO$_3$)$_2$]$^+$. Found *m/z* = 3100.8418; **(c)** Experimental and **(d)** calculated HRMS isotopic pattern distribution for [Tb·(**91-*D*-Trp**)$_3$](CF$_3$SO$_3$)$_3$. Calculated for $C_{149}H_{129}N_{33}O_{24}F_6S_2Tb^+$ *m/z* = 3100.8487 [TbL$_3$(CF$_3$SO$_3$)$_2$]$^+$. Found *m/z* = 3100.8623.

including diethyl ether diffusion into both CH_3OH and CH_3CN solutions, slow evaporations from both of these solutions and diffusion of $(CH_3)_2CHOH$ into CH_3CN solution. Hence, the properties of these complexes were probed by using solution state analysis only, such as UV-Vis absorption spectroscopy, emission and excitation spectroscopy and NMR analysis.

Compared to the UV-Vis absorbance spectra of the relevant ligands, upon complexation with either Eu(III) or Tb(III), the ligand band centred at 300 nm (assigned to the **btp** motif) was red shifted by *ca.* 15 nm, indicating the successful formation of the complexes, similar to the changes observed in Section 3.3 above. Two examples of these absorbance spectra can be seen in Figure 3.26 for [Eu·(**91-*L*-Phe**)$_3$](CF$_3$SO$_3$)$_3$ and [Tb·(**91-*L*-Phe**)$_3$](CF$_3$SO$_3$)$_3$. For the complexes of ligands **91-Trp**, this red shift resulted in the **btp** absorbance band, which overlapped with Trp absorbance bands in the ligand spectrum to emerge as a clearly resolved band, centred at 315 nm, Appendix B.

IR spectra of the complexes differed very little from those of the ligands, but all featured a broad band associated with the $CF_3SO_3^-$, which was centred at 1248 cm^{-1} for [Eu·(**91–Gly**)$_3$](CF$_3$SO$_3$)$_3$, for example. The carbonyl bands in the spectra were shifted only slightly (1–2 cm^{-1}) with respect to the ligand spectra, indicating that they played no significant role in the coordination interactions between the ligands and Ln(III) ions. Spectra of enantiomeric ligands were identical. All IR spectra are shown in Appendix B.

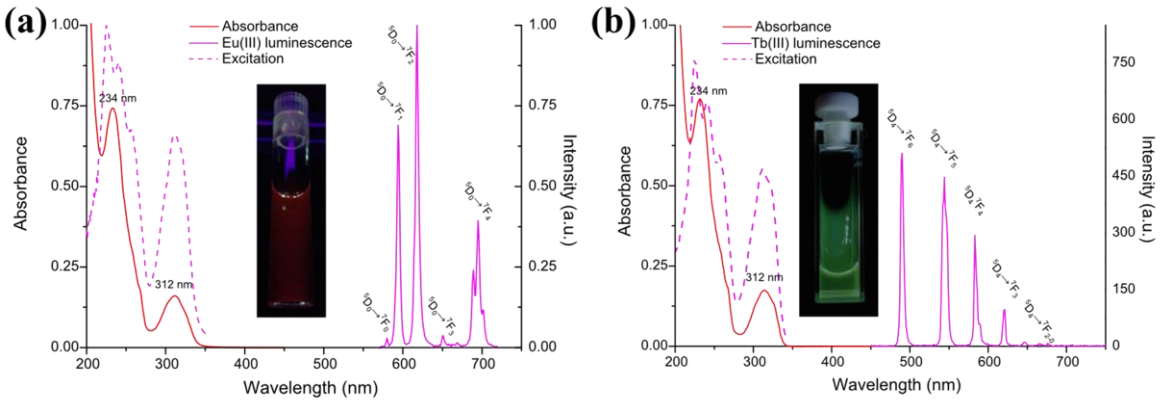

Figure 3.26 UV-Vis absorption (red), sensitised Eu(III) luminescence (magenta) and excitation spectra (dashed magenta) of **(a)** [Eu·(**91-*L*-Phe**)$_3$](CF$_3$SO$_3$)$_3$ in CH$_3$CN; **(b)** [Tb·(**91-*L*-Phe**)$_3$](CF$_3$SO$_3$)$_3$ in CH$_3$CN; *insets:* photographs of the characteristic red Eu(III) and green Tb(III) emission of solutions of [Ln·(**91-*L*-Phe**)$_3$](CF$_3$SO$_3$)$_3$ visible to the naked eye under UV irradiation.

The complexes all showed characteristic Ln(III)-centred emission spectra in CH$_3$CN solution upon excitation of the higher energy absorbance band, confirming the ability of the **btp** ligands to sensitize the Ln(III) excited states in these complexes successfully, while, in contrast, ligand fluorescence was quenched. For Eu(III) complexes, characteristic line-like emission bands were observed at λ = 579, 593, 617, 650 and 694 nm, assigned to the $^5D_0 \rightarrow {}^7F_J$ transitions (J = 0–4). As an example, the Eu(III)-centred emission spectrum of the **91-*L*-Phe** complex is shown in Figure 3.26(a). For the Tb(III) complexes, emission bands were observed at λ = 490, 545, 585, 621 nm, assigned to the $^5D_4 \rightarrow {}^7F_J$ transitions (J = 6–3), as well as weaker bands arising from the transitions to the J = 2–0 states, which are typically very weak, Figure 3.26(b). The sensitisation process was further confirmed by recording the excitation spectra of the various Ln(III) emission bands, which were seen to structurally match the absorbance spectra; examples are shown as dashed magenta traces in Figure 3.26. The nearly idenitcal photophysical spectra for all of these complexes are shown in Appendix B. Moreover, the complexes were clearly luminescent to the naked eye, even at low concentrations, upon irradiation with a hand-held UV lamp, as is demonstrated by the photographs of CH$_3$CN solutions of Ln(III) complexes shown as insets in Figure 3.26. In these photographs, the green Tb(III) emission is clearly brighter than red Eu(III) emission; these different emission properties will be quantified presently (*vide infra*).

In previous work in the Gunnlaugsson laboratory,[4-6,9,86,152,154,181] it has been shown that acyclic ligands based on the **dpa** motif, such as **79**, **80** and **81b** which have been derivatised with chiral chromophores as 'antennae' can give rise to sensitised Ln(III) chiral emission, upon complexation with visibly emitting Ln(III) ions and subsequent excitation of the 'antennae'. This was demonstrated by using circularly polarised luminescence (CPL) spectroscopy, by observing the chiroptical emission of Sm(III), Tb(III) and Eu(III), where such enantiomerically pure complexes gave rise to spectra that are mirror images with opposite signs for the various transitions. Similarly, other researchers including Muller and Parker have demonstrated the same for either cyclic or acyclic ligands, such as **2**.[29,32,247-251] As all of the ligands presented here (except **91-Gly**) possess chiral amino acids adjacent to phenyl 'antennae', CPL spectra of these complexes were recorded by Dr Robert Peacock at University of Glasgow. However, these complexes only gave negligible CPL spectra for the Ln(III)-centred emission, the best results being observed for [Tb·(**91-*L*-Trp**)$_3$](CF$_3$SO$_3$)$_3$ and [Tb·(**91-*D*-Trp**)$_3$](CF$_3$SO$_3$)$_3$, showing very weak signals, Figure 3.27, sufficient only to confirm that these complexes were formed as a pair of enantiomers. Unlike the aforementioned **dpa** complexes, where the chiral 'antennae' were close to the Ln(III) ion, giving rise to strong CPL emission, in the case of the complexes reported here, the chirality of the amino acid side chain seems to be too remote from the binding site to

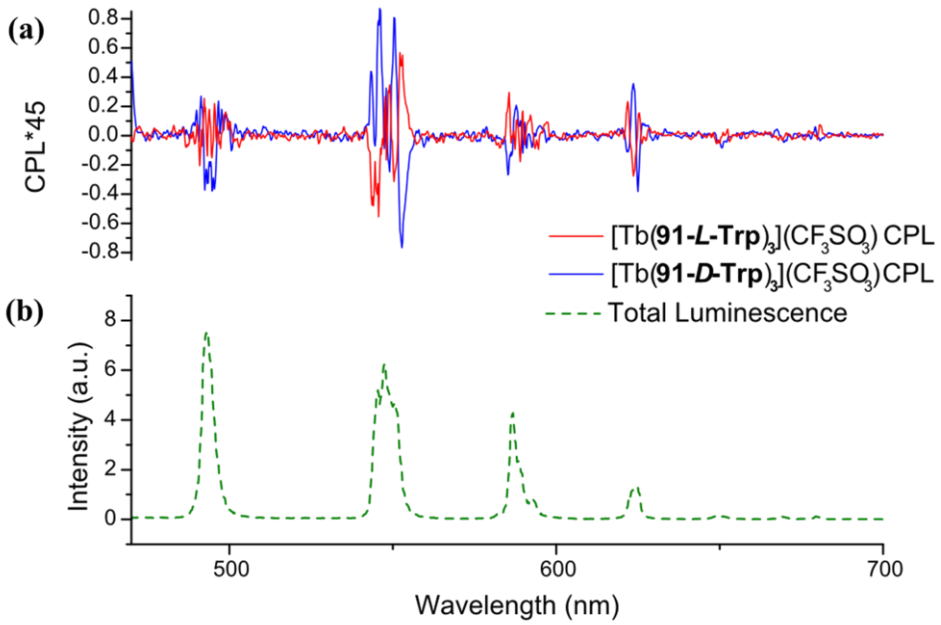

Figure 3.27 (a) CPL spectra of [Tb·(**91-*L*-Trp**)$_3$](CF$_3$SO$_3$)$_3$ and [Tb·(**91-*D*-Trp**)$_3$](CF$_3$SO$_3$)$_3$ in CH$_3$CN; and **(b)** the total luminescence spectrum.

have any significant impact on the nature of the complex formed and hence the CPL signal observed. CPL and related techniques will be discussed in more detail in Chapter 4, where **btp** ligands with chirality adjacent to the binding site are described.

Luminescence lifetimes (τ) of these complexes were determined in H_2O and D_2O by fitting decay profiles of emission from the most intense Ln(III) luminescence band to mono-exponential decay curves, namely the $^5D_0 \rightarrow {}^7F_2$ band centred at 616 nm for Eu(III), and the $^5D_4 \rightarrow {}^7F_6$ band centred at 490 nm for Tb(III). Although the complexes were not fully soluble in aqueous media, emission spectra could be measured and reliable lifetime values determined. For both ranges of complexes, the **91-Ala** complexes possessed the longest lifetimes in aqueous environment, with $\tau = 2.71 \pm 0.01$ ms and 2.83 ± 0.02 ms in H_2O and D_2O, respectively, for [Eu·(**91-*L*-Ala**)$_3$](CF$_3$SO$_3$)$_3$, while for the Tb(III) complexes, the lifetimes were generally shorter, with, for instance, [Tb·(**91-*D*-Ala**)$_3$](CF$_3$SO$_3$)$_3$ displaying lifetimes of 1.68 ± 0.08 ms and 1.65 ± 0.03 ms in H_2O and D_2O, respectively. These values, Table 3.5, are similar to those commonly seen for **dpa** based ligands. With the exception of the Trp derivatives, all lifetimes were longer than those reported for the analogous **88** complexes above.

These lifetime values were substituted into the Horrocks Equation, Equation 3.1, to determine hydration states, *q*, of the complexes. A hydration state of $q \sim 0$ was calculated for each complex, as described in Section 3.3 above, indicating the presence of a single fully coordinated species, i.e. a 1:3 metal-ligand stoichiometry, where the solvation sphere contains no bound water molecules. Lifetimes and hydration states of these complexes are detailed in Table 3.5, along with total luminescence quantum yields, Φ. As for ligands **88** above, total quantum yields were determined relative to Cs$_3$[Ln·(**dpa**−2H)$_3$][21,22] and the Tb(III) complexes were significantly more emissive in CH_3CN solution than the Eu(III) complexes. The values of Φ for the Eu(III) complexes were modest, ranging from 2.1–3.0% for the Gly, Ala and Phe derivatives. Ligands **91-Trp** were significantly lower (<0.5%), most likely because the Trp 'antenna' is a poor sensitiser for Eu(III). These results demonstrate that these 1:3 complexes possess comparable photophysical properties to those seen for 1:3 complexes formed from **dpa** systems such as **2**, **79** and **80**.[29,152,239] Remarkably, however, the quantum yields of the Tb(III) complexes were much higher, ranging between 6.3–61% (with the Trp derivatives, once again, being much less bright than the rest of the systems).

Table 3.5 Photophysical properties of Ln(III) complexes of ligands **91**: luminescence lifetimes, hydration states and total quantum yields in CH_3CN.

	[Eu·(**L**)$_3$](CF$_3$SO$_3$)$_3$				[Tb·(**L**)$_3$](CF$_3$SO$_3$)$_3$			
Ligand	τ_{H2O} **(ms)**	τ_{D2O} **(ms)**	q^a **(±0.5)**	Φ^b **(%)**	τ_{H2O} **(ms)**	τ_{D2O} **(ms)**	q^a **(±0.5)**	Φ^b **(%)**
91-Gly	1.17±0.39	1.81±0.04	0.1	3.0±0.9	1.26±0.27	1.48±0.12	0.3	53±9.4
91-*L*-Ala	2.71±0.01	2.83±0.02	−0.3	2.2±0.4	1.66±0.04	1.64±0.01	−0.3	54±10
91-*D*-Ala	2.80±0.05	2.78±0.10	−0.3	2.1±0.4	1.68±0.08	1.65±0.03	−0.4	57±10
91-*L*-Phe	2.31±0.04	2.28±0.01	−0.3	2.2±0.4	1.23±0.01	1.25±0.01	−0.2	61±11
91-*D*-Phe	2.65±0.05	2.72±0.01	−0.3	2.5±0.4	1.24±0.03	1.23±0.03	−0.3	46±8.1
91-*L*-Trp	1.07±0.04	1.38±0.05	−0.1	0.3±0.1	0.76±0.02	0.85±0.01	0.4	11±1.9
91-*D*-Trp	0.68±0.03	1.25±0.10	0.5	0.4±0.1	0.83±0.01	0.84±0.01	−0.3	6.3±1.1

[a]Hydration states were calculated using the equation $q = A(\left(\frac{1}{\tau_{H2O}} - \frac{1}{\tau_{D2O}}\right) - B)$, where for Eu(III), A = 1.2, B = 0.25 and for Tb(III), A = 5.0, B = 0.06.[212,226]; [b]Quantum yields in CH_3CN were estimated by a relative method,[21,22] compared with Cs$_3$[Ln·(**dpa**−2H)$_3$][236] according to the equations shown in the Experimental Chapter.

Similar differences between Eu(III) and Tb(III) quantum yields in CH_3CN solution were seen for **88** in Section 3.3 above. It was noted that the energy of the triplet excited state of that ligand was closely matched to the energy of the $^5D_4$ Tb(III) excited state and therefore likely to act as a good sensitising 'antenna' for Tb(III) emission. These ligands are analogous and therefore would be expected to have similar energy values for T_1. While such ligands are quite well matched to the $^5D_0$ Eu(III) excited state, there is potential for non-radiative deactivation processes within the lower-lying ^5D energy state manifold, which would result in less efficient energy transfer and hence lower quantum yields. The quantum yields for [Eu·(**91**)$_3$](CF$_3$SO$_3$)$_3$ were of the same order as for [Eu·(**88**)$_3$](CF$_3$SO$_3$)$_3$ above, but all of the Tb(III) complexes here showed lower values of Φ than for [Tb·(**88**)$_3$](CF$_3$SO$_3$)$_3$ (Φ = 70 ± 12%). Nonetheless, the Tb(III) complexes of the Gly, Ala and Phe derivatives are very luminescent 'peptide bundles', self-assembly structures which have the potential to prove useful as biologically-compatible imaging agents.[252]

Although ^{1}H-NMR spectra of paramagnetic Ln(III) complexes are often difficult to interpret due to broadening and dramatic shifting of proton resonances, in the case of some of the Eu(III) complexes with ligands **91**, the ^{1}H-NMR spectra were relatively well resolved, albeit quite shifted (particularly those resonances close to the **btp** binding motif). The spectrum (400 MHz, CD_3OD) of [Eu·(**91-Gly**)$_3$](CF$_3$SO$_3$)$_3$ is shown in Figure 3.28 as an example, with the various peaks labelled and assigned. As above, for ligand **88**, the most notable upfield shifts were seen for pyridyl (labelled *u′* and *v′*) and triazolyl (labelled *t′*) proton resonances, with the 3- and 5-pyridyl signal appearing at a chemical shift where

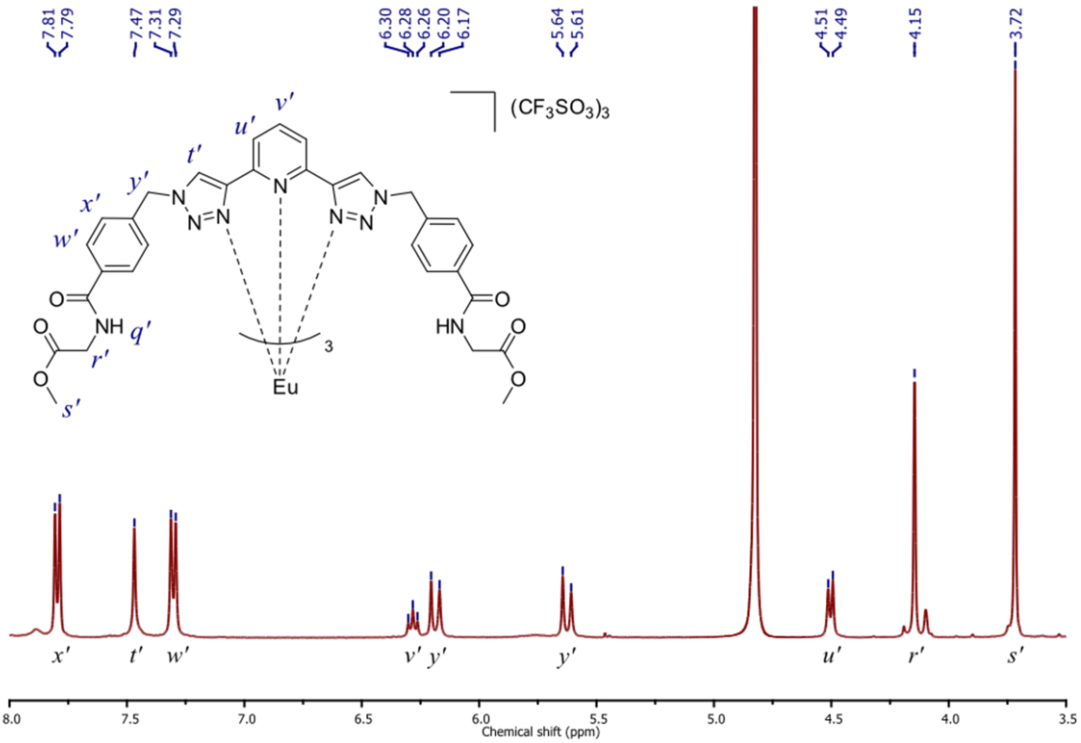

Figure 3.28 ^{1}H-NMR spectrum (400 MHz, CD_3OD) of [Eu·(**91-Gly**)$_3$]$(CF_3SO_3)_3$, showing dramatically shifted peaks, compared to the ligand spectrum.

aliphatic protons are usually observed. The Tb(III) complexes all displayed very broadened ^{1}H-NMR spectra (400 MHz, CD_3CN) with resonances shifted upfield and downfield. These spectra were not assigned, as was possible for that of [Eu·(**91-Gly**)$_3$]$(CF_3SO_3)_3$.

3.14 Spectroscopic titrations of ligands 91 with Ln(III)

Having shown the ability of **btp** ligands **91** to form emissive complexes under thermodynamic control with Ln(III) ions, more detailed investigations of the kinetic self-assembly process were carried out in CH_3CN and monitored by measuring UV-Vis absorbance, fluorescence, and Ln(III) luminescence spectra upon addition of Eu(III) or Tb(III) triflate salt solution to ligand solutions at concentrations of *ca.* 10^{-5} M (accurate concentrations were determined using the Beer–Lambert Law). Like those titrations shown above for **88** and **90**, all measurements were carried out at 23 °C.

3.14.1 Titrations with Eu(III)

The spectroscopic changes of ligand **91-Gly** in CH_3CN solution upon addition of $Eu(CF_3SO_3)_3$, Figure 3.29(a), yielded very similar results to those seen above for **88** upon self-assembly with Eu(III), displaying the same shifts in absorbance bands over the first 0.33 equivalents of Eu(III) solution, namely a red shift of *ca.* 15 nm in the band centred at

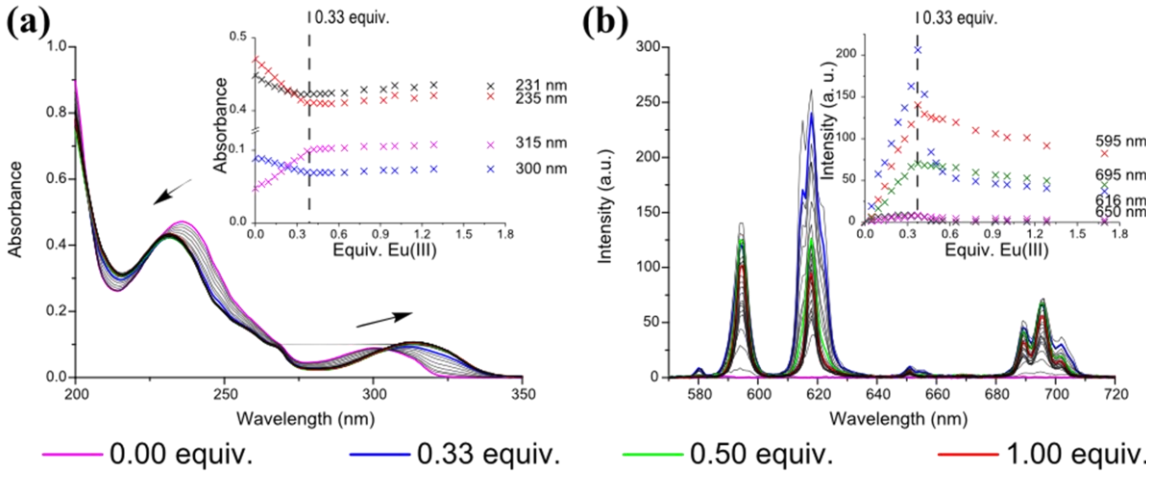

Figure 3.29 Titration plots of **91-Gly** v. Eu(III) in CH_3CN. **(a)** UV-Vis spectral changes; *inset*: experimental binding isotherms (×) at various wavelengths; **(b)** changes in Eu(III)-centred phosphorescence spectra; *inset*: experimental binding isotherm each $^5D_0 \rightarrow {}^7F_J$ transition (×). [**91-Gly**] = 1.2×10^{-5} M.

300 nm and concomitant blue shift from 236 to 232 nm of the band assigned to the π→π* transitions. Concomitantly, quenching of ligand fluorescence (centred at 335 nm) was observed, along with the evolution of characteristic, long-lived Eu(III) emission, which reached a maximum at 0.35 equivalents, an indication that the 1:3 species is the most luminescent species formed. Subsequently decreases in intensity were observed as metal ion concentration increased, an indication of the formation of other self-assemblies in solution, and that this shift in equilibrium causes the formation of less emissive species (such as the 1:2 and 1:1 species) to become the most dominant species in solution.

As well as resembling the results seen for **88** and **90**, this binding behaviour shows similar trends, particularly in the Eu(III)-centred emission titration profiles to **dpa**-based systems previously studied in the Gunnlaugsson group, such as **81**,[9,181] **82**,[9] and **79**[152,185] and **80**[152]. This suggests that **btp** ligands have analogous behaviour to their **dpa** counterparts and are indeed good candidates for such self-assembly formation.

The behaviour of both enantiomers of **91-Ala** are broadly similar to each other and to the simpler ligand above, which is unsurprising since the small methyl side-chain in Ala is far-removed from the binding site, impacting little on the binding stoichiometry of the system. The titration plots and binding isotherms for **91-*L*-Ala** v. Eu(III) are shown in Figure 3.30(a) as an example of the changes in UV-Vis absorbance and in Figure 3.30(b) as an example of changes in Eu(III)-centred emisssion. Upon addition of metal ion, a slight blue shift from 236 to 232 nm was observed in the higher energy band of the UV-Vis absorbance spectrum, while the band centred at 300 nm was red shifted by *ca.* 15 nm with

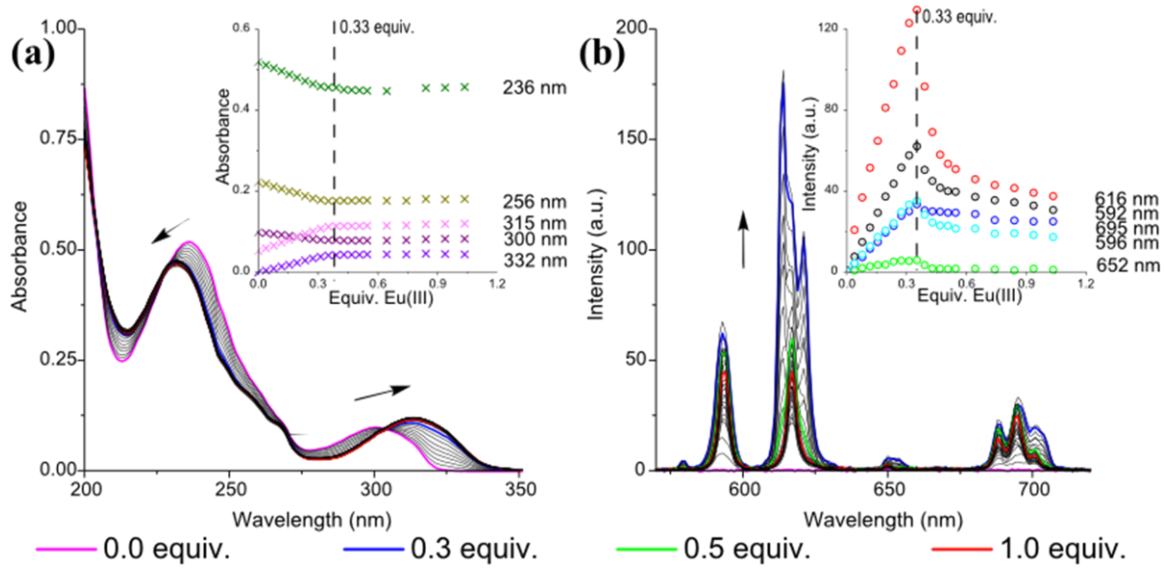

Figure 3.30 Titration plots of **91-*L*-Ala** v. Eu(III) in CH_3CN. **(a)** UV-Vis spectral changes; *inset*: experimental binding isotherms (×) at various wavelengths; **(b)** Changes in Eu(III) luminescence; *inset*: experimental binding isotherms (○) at various wavelengths. Fluorescence spectral changes are shown in Appendix B. [**91-*L*-Ala**] = 1.3×10^{-5} M.

an increase in absorbance. These changes were accompanied by the appearance of an isosbestic point at 304 nm. The changes in the excited state of this ligand was simultaneously monitored; the fluorescence was found to be completely quenched after addition of 0.35 equivalents of Eu(III). This would support the sensitisation of the Eu(III) excited state, which, indeed was confirmed by observing the evolution of Eu(III)-centred emission; the luminescence intensity increased to a maximum intensity at the addition of 0.33 equivalents of Eu(III) before being gradually quenched, Figure 3.30(b), in the same manner as seen for the Gly derivative above. The hypersensitive $^5D_0 \rightarrow {}^7F_2$ transition, which is sensitive to the coordination geometry was split into two bands between 0→0.33 equivalents as the 1:3 species formed, thereafter the shape became less defined, but finally resolved as a single peak from 0.5 equivalents onwards. This shows that significant changes in the symmetry of the Eu(III) coordination environment occur upon formation of the 1:2 and 1:1 stoichiometric species at higher metal ion concentration.

The **91-Phe** ligands displayed slightly different behaviour to the aforementioned Gly- and Ala-derivatives in solution. The UV-Vis spectra underwent similar changes to those above, however, here the changes continued until 0.5 equivalents of $Eu(CF_3SO_3)_3$ were added. The band at 300 nm red shifted to 315 nm, while the higher energy absorbance band underwent a slight blue shift with concomitant hypochromic effect. These changes are

shown for both enantiomers in Figure 3.31, along with binding isotherms showing the changes in absorbance at particular wavelengths over the course of the titration.

Although ground state spectral changes continued until 0.5 equivalents, changes to the fluorescence were complete by 0.33 equivalents, by which point, the broad emission band at 335 nm was completely quenched. The sensitised Eu(III)-centred luminescence was enhanced between 0→0.33 equivalents of $Eu(CF_3SO_3)_3$, reaching a maximum at 0.33 equivalents of Eu(III), suggesting that the 1:3 complex was the most emissive species. After this point in the titration, the emission intensity of the hypersensitive $^5D_0 \rightarrow {}^7F_2$ dropped off markedly from 0.33→0.5 equivalents and was then more gradually quenched

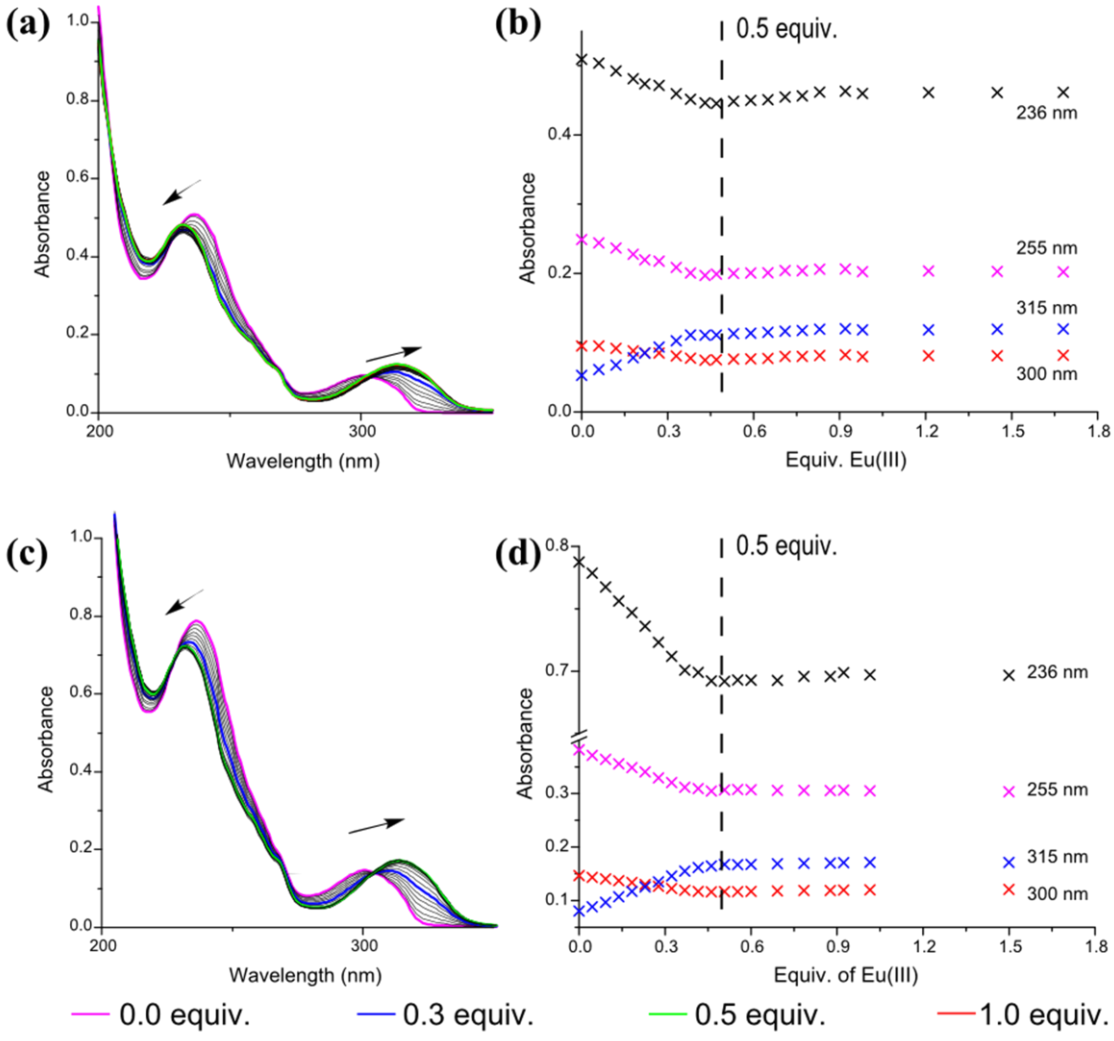

Figure 3.31 Titration plots of enantiomers **91-*L/D*-Phe** v. Eu(III) in CH_3CN. **(a)** UV-Vis spectral changes for **91-*L*-Phe** at a concentration of 1.0×10^{-5} M; **(b)** experimental binding isotherms (×) at various wavelengths; **(c)** UV-Vis spectral changes for **91-*D*-Phe** at a concentration of 1.5×10^{-5} M; **(d)** experimental binding isotherms (×) at various wavelengths.

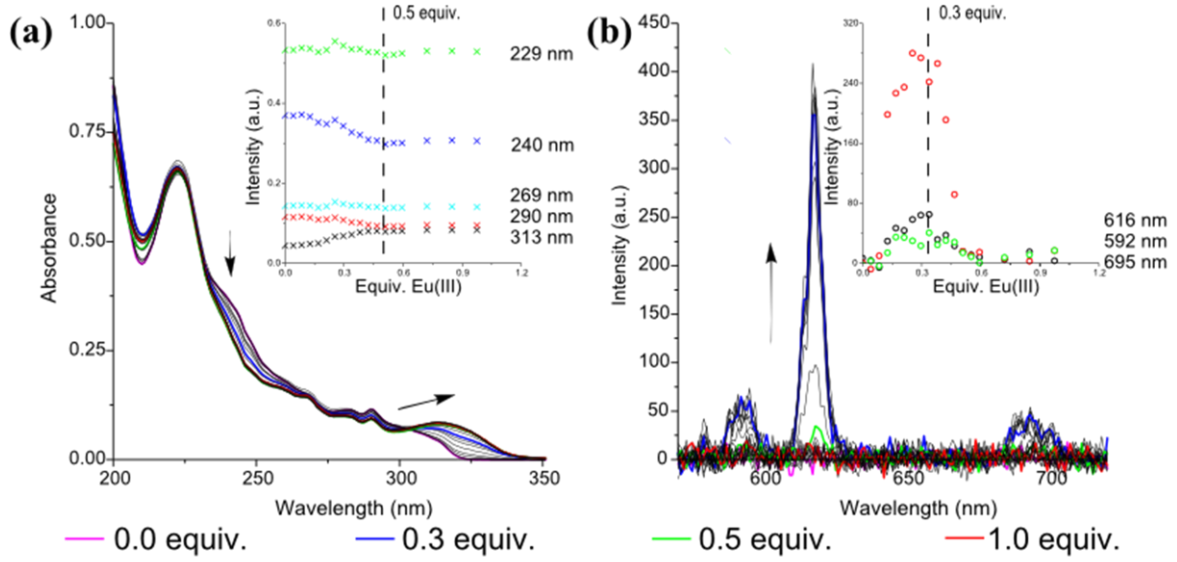

Figure 3.32 Titration plots of **91-*L*-Trp** v. Eu(III) in CH_3CN. **(a)** UV-Vis spectral changes; *inset*: UV-Vis experimental binding isotherms (×) at various wavelengths; **(b)** Changes in Eu(III) luminescence; *inset*: luminescence experimental binding isotherms (○) at various wavelengths. Fluorescence spectral changes are shown in Appendix B. [**91-*L*-Trp**] = 0.8×10^{-5} M.

along with the other emission bands as excess Eu(III) was added to the solutions and the less emissive 1:2 and 1:1 stoichiometries were formed.

The changes observed for ligands **91-Trp** are worth commenting on, as these possessed more complicated absorbance spectra to those seen above, as the Trp residues gave rise to some distinctive absorption bands not seen in the aforementioned Gly-, Ala- and Phe-derived ligands, *cf.* Figure 3.24. The Trp-based band centred at 290 nm decreased in intensity upon addition of metal ion until 0.5 equivalents, while the shoulder centred at 236 nm disappeared altogether.

Simultaneously, the band centred at 232 nm decreased in intensity as a function of Eu(III) concentration; a band centred at 315 nm also evolved as a result of the metal-binding behaviour, Figure 3.32(a). The fluorescence emission was also quenched upon addition Eu(III), these changes continuing up to the addition of 0.5 equivalents, after which the S_1 state of the ligand was no longer seen to radiatively decay. As a result of the 'antenna' effect, emission from Eu(III) excited states evolved as the metal ion was added to the solution of binding ligand. These ligands were not very efficient, however, at sensitising Eu(III) luminescence, as can be seen from the noisiness of the phosphorescence spectra in Figure 3.32(b); this is in accordance with the low total quantum yields determined in Section 3.13 above. Similarly to the other ligands above, the Eu(III)-centred

luminescence in these self-assembly systems peaked at 0.33 equivalents of Eu(III) and was subsequently quenched. After the addition of 1.0 equivalent of Eu(III), no more emission was seen. These observations indicated that the 1:3 stoichiometry was the most emissive species, as was the case for all ligands discussed thus far and that the 1:2 and 1:1 assemblies were not luminesncent. All spectra discussed but not shown in this section are given in Appendix B.

All of these ligands, **91**, showed reasonably consistent self-assembly in CH_3CN solution with $Eu(CF_2SO_3)_3$ salt, which could be repeated with consistent results, across the series. In particular, all systems showed a Eu(III)-centred emission maximum at 0.33 equivalents of Eu(III), clearly showing that a 1:3 self-assembly was formed in solution and that it was the most emissive species formed. Subsequent decreases in luminescence upon adding more $Ln(CF_3SO_3)_3$ indicate that the other potential stoichiometric systems are less emissive, which is consistent with results seen for **dpa** systems discussed in Section 1.9. The 1:2 and 1:1 stoichiometric assemblies would have unsaturated coordination sphere, and hence the metal ion would be accessible to solvent molecules, leading to the quenching in Eu(III) luminescence observed. The changes in the ground state were also reasonably consistent, with the disappearance of the band centred at 300 nm in the UV-Vis absorbance spectra characteristic of the loss of free ligand from the solution and the concomitant emergence of the new band at 315 nm characteristic of the formation of Eu(III) complexes. This diagnostic **btp** binding band gives these systems an advantage over the **dpa** systems, for which changes in the UV-Vis absorbance spectra may often be subtle and have less unambiguous interpretations. While the absorbance changes for **91-Gly** and **91-Ala** were complete by 0.33 equivalents, those for **91-Phe** and **91-Trp** continued until 0.5 equivalents. Such behaviour was seen previously for Trp-derived ligand **87**, which formed 1:2 self-assemblies.[153] This suggests that, at least for these latter ligands, 1:2 stoichiometric assemblies are formed to some extent; these will be considered when choosing models to fit these data in Section 3.14.3 below.

Both the Eu(III) and Tb(III) complexes formed under thermodynamic control were discussed above, and the emissive properties of the Tb(III) complexes were shown to be better. Hence, the analogous self-assembly processes of ligands **91** with $Tb(CF_3SO_3)_3$ in CH_3CN solution will now also be explored and compared to the Eu(III) results.

3.14.2 Titrations with Tb(III)

In a similar way to that described for Eu(III), the changes in the various spectroscopic properties of these ligands upon titrating with $Tb(CF_3SO_3)_3$ were evaluated. The results yielded very similar trends to those seen from the above titrations. The spectroscopic changes in the UV-Vis absorbance and Tb(III) luminescence spectra over the course of the titration of a solution of **91-Gly** in CH_3CN are shown in Figure 3.33. In the UV-Vis absorbance spectrum, the 235 nm absorption was shifted to 232 nm, with concomitant reduction in absorbance as well as the familiar significant red shift from 300 nm to 315 nm of another band, as observed upon complexation for all **btp** systems discussed so far, with an associated isosbestic point being observed at 305 nm. These changes were all complete upon addition of 0.33 equivalents of Tb(III).

Fluorescence emission spectral changes were measured simultaneously, showing a broad ligand fluorescence band centred at 335 nm. This fluorescence was gradually quenched

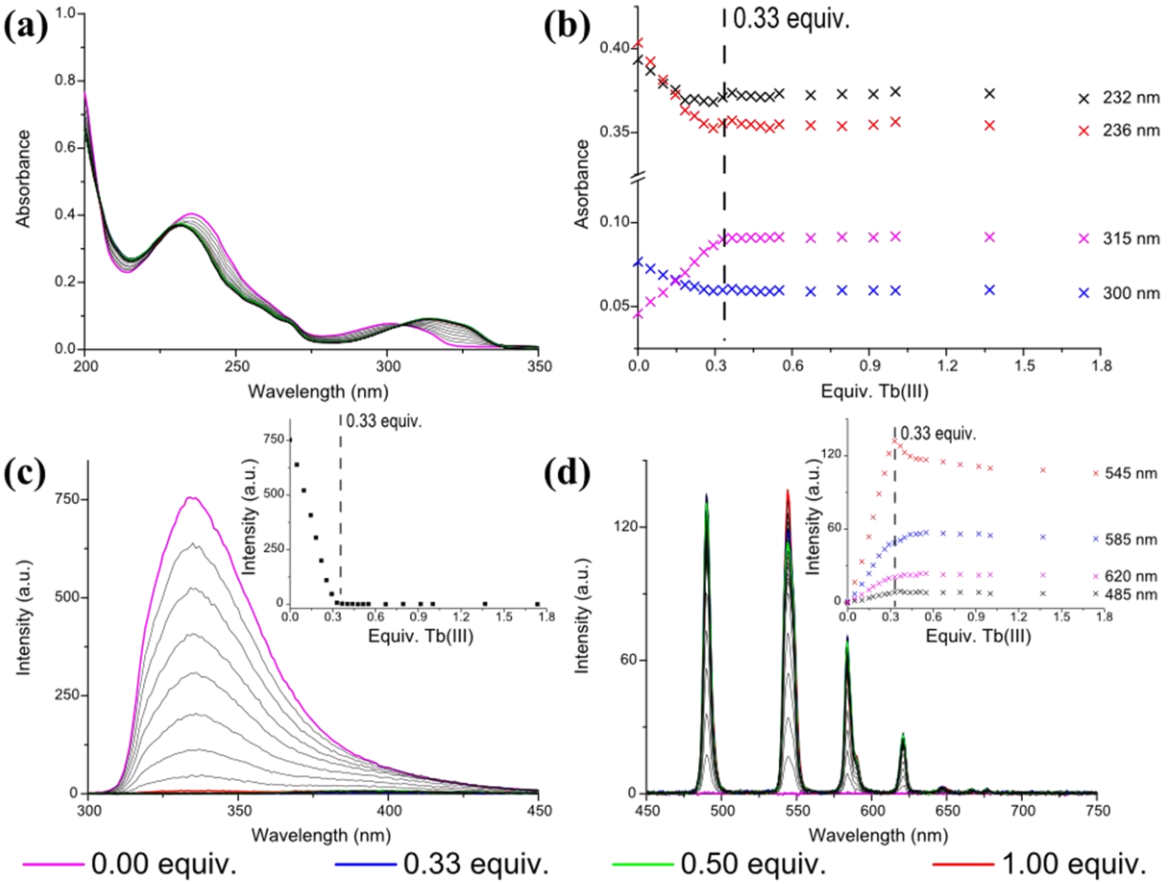

Figure 3.33 Titration plots of **91-Gly** v. Tb(III) in CH_3CN. **(a)** UV-Vis spectral changes; **(b)** experimental binding isotherms (×) at various wavelengths; **(c)** Changes in fluorescence emission spectra; *inset:* experimental binding isotherms (×) at λ_{max}; **(d)** Changes in Tb(III) luminescence; *inset*: experimental binding isotherms (×) at various wavelengths. [**91-Gly**] = 1.0×10^{-5} M.

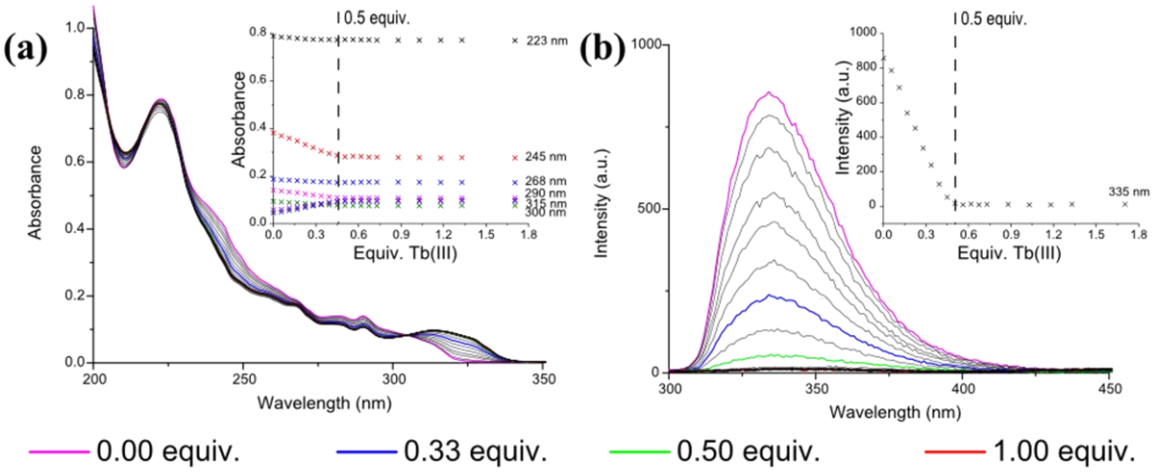

Figure 3.34 Titration plots of **91-*D*-Trp** v. Tb(III) in CH_3CN. **(a)** UV-Vis spectral changes; *inset:* experimental binding isotherms (×) at various wavelengths; **(b)** Changes in fluorescence emission spectra; *inset:* experimental binding isotherms (×) at λ_{max}. [**91-*D*-Trp**] = 1.0×10^{-5} M.

upon addition of 0→0.33 equivalents of the metal ion, Figure 3.33(c). The luminescence band related to the $^5D_4 \rightarrow {}^7F_5$ transition (centred at 545 nm) reached a maximum at 0.33 equivalents while all other bands, namely the bands at 490, 585 and 621 nm assigned to the $^5D_4 \rightarrow {}^7F_J$ transitions (J = 6, 4 and 3), steadily increased until 0.5 equivalents before reaching a plateau. For **91-Ala** and **91-Phe**, very similar changes to those discussed previously were also seen in the UV-Vis absorbance, fluorescence and Tb(III)-centred emission.

Changes in the UV-Vis absorbance spectrum of **91-Trp** were almost identical to those seen above upon interaction with Eu(III). Upon addition of Tb(III), the absorbance band at 290 nm underwent a hypochromic shift, while the distinctive shoulder centred at 236 nm disappeared and a new band, characteristic of **btp** complex formation, centred at 315 nm emerged, Figure 3.34(a). All of these changes continued up until the addition of approximately 0.5 equivalents of Tb(III). A concomitant quenching of fluorescence emission intensity was observed from 0→0.5 equivalents, Figure 3.34(b), while Tb(III)-centred emission increased up to the addition of 0.33 equivalents of metal ions before intensity reached a plateau (the band relating to the $^5D_4 \rightarrow {}^7F_6$ transition experienced a slight fall-off in intensity before reaching a plateau at 0.5 equivalents).

The main differences between the titration studies for the Eu(III) and Tb(III) additions were the increased Ln(III)-centred luminescence intensity of these systems, which was expected, given that the 1:3 complexes gave significantly higher quantum yields with Tb(III) compared to Eu(III), as seen in Section 3.13. It was also worth noting that, in

contrast to the trends observed in the preceding section, Tb(III)-centred emission was not dramatically quenched after 0.33 equivalents, as for Eu(III), but rather reached a plateau after *ca.* 0.5 equivalents. This suggests that the 1:2 and 1:1 self-assembly structures formed at higher concentrations of Tb(III) were also quite luminescent. The absorbance and fluorescence trends, however, follow those seen for the above systems and for **dpa** systems with Eu(III). The data collected in this and the preceding section allowed the Ln(III)-directed self-assembly processes of ligands **91** in CH_3CN to be assessed. Next these data will be used to determine global stability constants of self-assembly formation, as well as provide information on the different stoichiometric assemblies present in solution.

3.14.3 Fitting of spectroscopic data to quantify binding affinity of 91

In order to gain further insight into the solution self-assembly behaviour of these amino acid derivatives at room temperature and the formation of different stoichiometric species in CH_3CN, the UV-Vis absorbance and Ln(III) emission titration data above for ligands **91** were analysed by fitting the global spectral changes to models of the stepwise equilibria in Equation 3.2–3.4 by non-linear regression least-squares fitting using ReactLab Equilibria,[237] as discussed in Section 3.5.3 above. This allowed global stability constants, logβ, to be determined for these systems, as shown in Table 3.6. In a few cases the fluorescence data were also fit, but generally calculated models did not fit well to the fluorescence data, either not converging or not displaying a good match between the experimental data and calculated curves. This was probably due to the fact that after quenching of the ligand fluorescence, these titrations provide no more information on the makeup of the system, only accurately reporting on the elimination of free ligand from the solution.

Models including various combinations of the equilibria describing the formation of 1:1, 1:2 and 1:3 complexes were compiled by the program and fits were attempted until the model converged, predicting spectra matching the experimental data quite closely. In most cases, all three equilibria were included, but in a few cases, including the Tb(III)-directed self-assembly of **91-Gly**, models containing the 1:2 species did not converge and binding constants could only be determined by excluding this species from the analysis. This kind of data fitting has been carried out previously on **dpa** systems, such as **81**,[9,181] **82**,[9] and **79**,[152,185] although in all these cases an older program called SPECFIT[253,254] was used. In most cases, when fitting these data, it was necessary to fix the value of logβ for at least one of the stoichiometries. Analogy to similar systems, *e.g.* **88** and **90** and the aforementioned

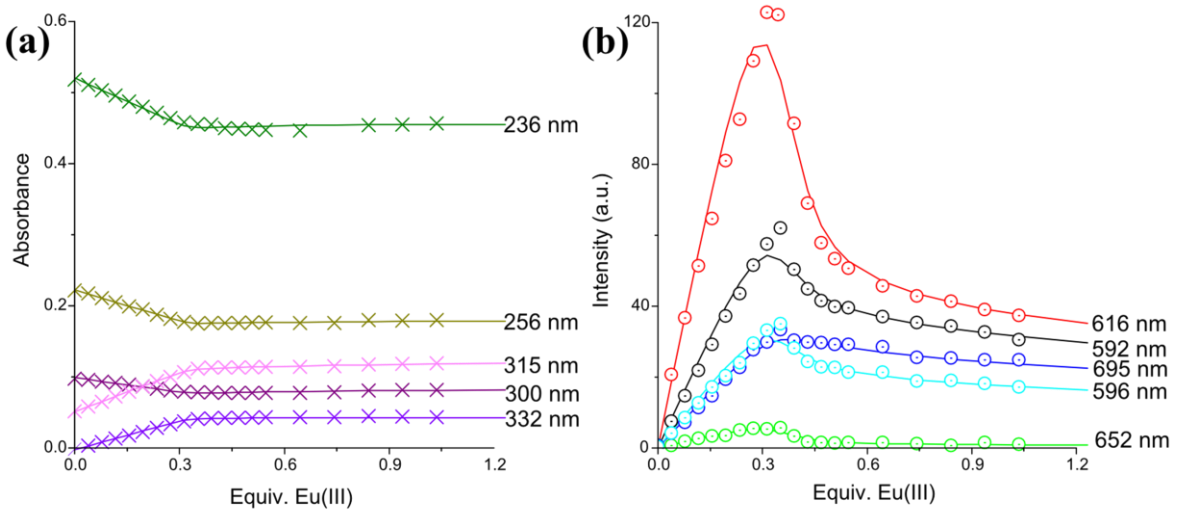

Figure 3.35 Fitting curves for titrations of **91–*L*-Ala** v. Eu(III) **(a)** Experimental UV-Vis absorbance binding isotherms at various wavelengths (×) and calculated fitting curves; **(b)** Experimental Eu(III)-centred emission binding isotherms at various transitions (○) and calculated fitting curves.

dpa systems allowed appropriate initial values to be selected to start the fitting calculations.

As examples of how closely the models fit the experimental data, the fitting curves for the UV-Vis absorbance and Ln(III)-centred emission data are shown for the titration of **91-*L*-Ala** with Eu(III), Figure 3.35; these curves were calculated with global stability constants of $\log\beta_{1:1}$ = 8.0 ± 0.1, $\log\beta_{1:2}$ = 14.8 ± 0.1 and $\log\beta_{1:3}$ = 21.8 ± 0.2 for the UV-Vis absorbance data and $\log\beta_{1:1}$ = 7.3 ± 0.1, $\log\beta_{1:2}$ = 15.2 and $\log\beta_{1:3}$ = 21.5 ± 0.1 for the phosphorescence data. It is worth noting that the model in Figure 3.35(b) does not perfectly model the sharp change in Eu(III)-centred emission at 0.33 equivalents for the most intense $^5D_0 \rightarrow {}^7F_2$ transition, however at all other points in the titration, the model adheres very closely to the experimental data. The binding constants determined from the various different titrations for both enantiomers were broadly similar, Table 3.6.

The fitting curves of **91-*L*-Phe** with Tb(III) are shown in Figure 3.36, as an example of the fitting of a Tb(III) system. As seen above, the fitting curves for the UV-Vis absorbance data matched the experimental data very closely, did the Tb(III)-centred emission data, with the exception of the sharp change in emission at 0.33 equivalents in the $^5D_4 \rightarrow {}^7F_5$ band, which none of the calculated models could perfectly predict. These fitting curves were calculated with global binding constants of $\log\beta_{1:1}$ = 7.3, $\log\beta_{1:2}$ = 14.6 and $\log\beta_{1:3}$ = 20.9 ± 0.1; and $\log\beta_{1:1}$ = 7.3, $\log\beta_{1:2}$ = 15.2 and $\log\beta_{1:3}$ = 21.6 ± 0.1, respectively. Fitting curves for all of the other systems not shown here are given in Appendix B and model the experimental data similarly well.

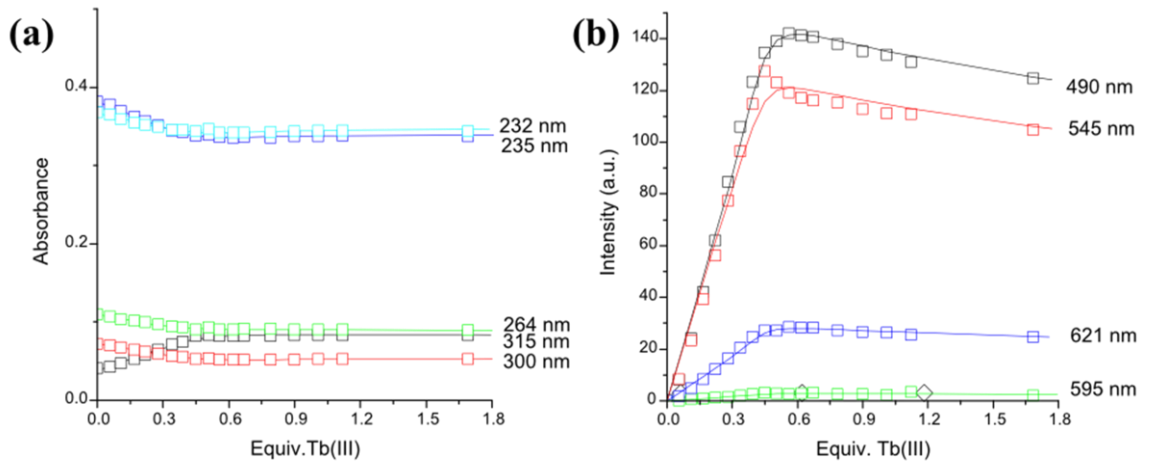

Figure 3.36 Fitting curves for titrations of **91–*L*-Phe** v. Tb(III) **(a)** Experimental UV-Vis absorbance binding isotherms at various wavelengths (□) and calculated fitting curves; **(b)** Experimental Eu(III)-centred emission binding isotherms at various transitions (□) and calculated fitting curves.

All global stability constants, logβ, determined for the various titrations of ligands **91** are given in Table 3.6. Remarkably, these values were of similar magnitude across the whole series of ligands, with log$\beta_{1:1}$ ranging from 6.6–8.5, log$\beta_{1:2}$ of 14.2–17.3 and log$\beta_{1:3}$ of 19.8–23.0. In all but one case, the constants estimated from phosphorescence measurements were higher than absorbance data. It is interesting that although the quantum

Table 3.6 Binding constants determined from titrations of **btp** ligands with Ln(III) in CH_3CN. [L] ≈ 10^{-5} M.

		Eu(III)			Tb(III)		
Ligand		**log$\beta_{1:1}$**	**log$\beta_{1:2}$**	**log$\beta_{1:3}$**	**log$\beta_{1:1}$**	**log$\beta_{1:2}$**	**log$\beta_{1:3}$**
91-Gly	UV	6.5 [a]	14.3±0.1	21.2 [a]	6.9 [a]	—	22.7±0.7
	Phos.	7.3±0.1	15.2 [a]	21.4±0.1	6.9±0.1	—	20.5±0.1
91-*L*-Ala	UV	8.0±0.1	14.8±0.1	21.8±0.2	7.2±0.1	14.4	21.6±0.1
	Fluor.	7.4 [a]	14.3 [a]	21.4±0.1	7.2 [a]	—	22.1±0.1
	Phos.	7.3±0.1	15.2 [a]	21.5±0.1	6.9±0.1	14.6 [a]	22.0±0.1
91-*D*-Ala	UV	7.7±0.1	14.7 [a]	20.1±0.1	6.9 [a]	14.4±0.1	20.0±0.1
	Phos.	8.5±0.1	15.6 [a]	21.7±0.1	7.2 [a]	14.6±0.1	20.7±0.1
91-*L*-Phe	UV	7.1±0.1	14.9 [a]	21.2±0.1	7.3 [a]	14.6 [a]	20.9±0.1
	Phos.	7.9±0.01	16.3 [a]	21.0 [a]	7.3 [a]	15.2 [a]	21.6±0.1
91-*D*-Phe	UV	7.1 [a]	14.6 [a]	21.5±0.1	6.9 [a]	13.9 [a]	21.7±0.1
	Phos.	8.5±0.2	17.3±0.3	23.0±0.4	—	—	—
91-*L*-Trp	UV	6.6 [a]	14.2 [a]	20.2±0.1	6.8 [a]	14.7 [a]	21.4±0.1
	Fluor.	—	—	—	6.8 [a]	14.9±0.1	20.4 [a]
	Phos.	7.7 [a]	14.9±0.1	19.7 [a]	6.8 [a]	15.0 [a]	21.7±0.1
91-*D*-Trp	UV	6.6±0.1	14.2±0.2	20.7±0.3	6.8±0.2	14.9±0.3	21.3±0.4
	Fluor.	7.7 [a]	16.8±0.1	23.7 [a]	—	—	—
	Phos.	7.7±0.1	14.6±0.1	19.8±0.1	6.8 [a]	16.2±0.2	21.3 [a]

[a] Value fixed

yields of the Ln(III) complexes (*vide supra*) vary significantly between the Eu(III) and Tb(III) complexes, the binding behaviour is clearly similar for both with the same ligands. This suggests the binding processes for both these similarly sized trivalent ions are analogous, and the emission properties are only dependent on energy transfer from the ligand to Ln(III) ($T_1 \rightarrow {}^5D_J$) and not on the binding strength. It is also worth commenting on how global stability constants were comparable for all of the ligands **91**, regardless of which amino acid was appended. They also vary little from the parent ligand **88** above, or the allyl amide derivative **90**, suggesting that the increased steric bulk of the ligands does not have a significant deleterious effect on the binding capacity of these **btp** ligands. These binding constants also compared well with **dpa** based ligands previously reported in the Gunnlaugsson group such as such as **79** and **80**, for which $\log\beta_{1:3} = 20.3 \pm 0.5$ and 21.6 ± 0.4, respectively in CH_3CN solution.[152] It is remarkable that changing the binding motif from **dpa** to **btp** results in similar binding behaviour, although **btp** ligands consistently have stability constants at the higher end of the range reported for **dpa** ligands.

Speciation distribution diagrams were calculated from all these fits. Some examples are shown in Figure 3.37, and it can be seen that they generally follow the same trends. These diagrams show the percentage formation of a given species (i.e. ligand, or Ln(III) complex) as a function of concentration of the metal ion, expressed here in equivalents of Ln(III) added. The examples shown were chosen to match the examples of fitting curves shown above, namely the Eu(III) titrations with **91-*L*-Ala,** Figure 3.37(a–b), and the Tb(III) titration with **91-*L*-Phe**, Figure 3.37(c–d); for each the speciation distribution diagram calculated for the UV-Vis absorbance titration and the Ln(III)-centred emission titration are shown. The calculated speciation distribution diagrams for all of the remaining titrations are shown in Appendix B.

These demonstrated that for all the titrations, the 1:3 stoichiometry was initially formed in high yield up to a maximum at 0.33 equivalents of Ln(III). For instance, in the case of **91-*L*-Ala** with Eu(III), the 1:3 self-assembly was calculated to form in 87% or 73% according to the absorbance and Eu(III)-centred emission, respectively, Figure 3.37(a–b). The percentage formation of the 1:3 self-assembly of **91-*L*-Phe** with Tb(III) was calculated to form in 67% by both techniques, Figure 3.37(c–d). After 0.33 equivalents, the formation of the 1:2 species became apparent, eventually followed by the formation of the 1:1 complex at higher Eu(III) concentrations. Fitting absorbance data tended to calculate higher maximum percentage formation of the 1:3 complexes than fitting the phosphorescence data, which tended to suggest higher percentage formation of the 1:2 self-

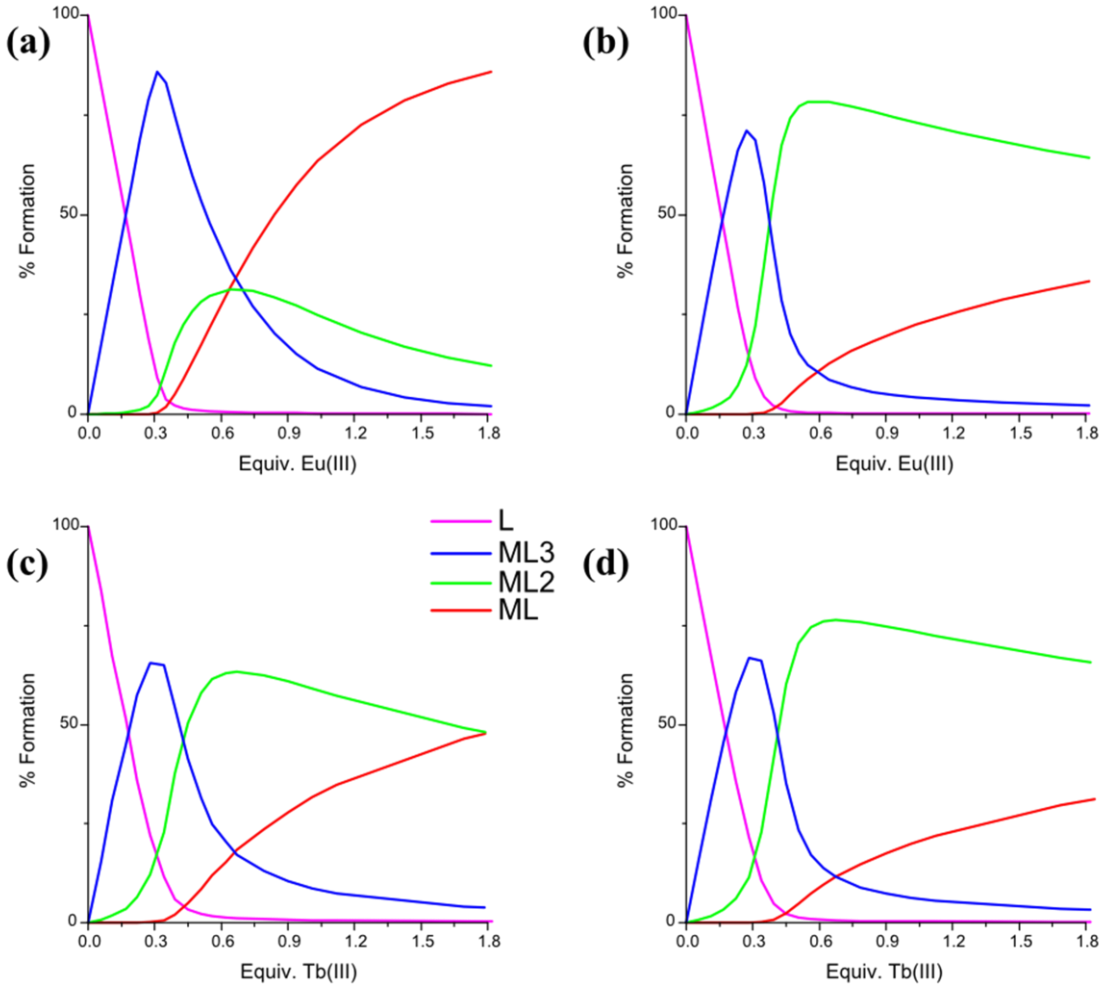

Figure 3.37 Some examples of calculated speciation distribution diagrams, showing the percentage formation of the ligand (L), the 1:3 complex (ML3), 1:2 metal complex (ML2) and 1:1 metal complex (ML) as a function of equivalents of Ln(III). Calculated from **(a)** UV-Vis absorbance titration of **91-*L*-Ala** v. Eu(III); **(b)** Eu(III)-centred emission titration of **91-*L*-Ala** v. Eu(III); **(c)** UV-Vis absorbance titration of **91-*L*-Phe** v. Tb(III); **(b)** Tb(III)-centred emission titration of **91-*L*-Phe** v. Tb(III).

assemblies. This kind of behaviour is similar to that seen for **88** above and also to that seen in previous work using **dpa** derivatives, such as **2**, **79**, **80** and **82**, where the 1:3 complexes were calculated to form in high yields in solution, further demonstrating the similar coordination properties of the two binding motifs.

All of these results demonstrate that amino acid conjugated **btp** ligands can be used to form novel self-assembly structures where the final assembly contains 6, 4 or 2 mono-peptide conjugates. Conjugation of short oligopeptides in place of simple amino acids would further enhance the biomimetic aspects of these structures. Since all of the ligands **91** are based on methyl ester protected amino acid residues, they could be further modified, with a view to achieving better solubility in aqueous solution, or with the objective of forming higher order self-assemblies and novel materials (such as gels) for instance by

simple hydrolysis and interactions with metal ions with a view to forming novel functional MOFs and soft materials. These goals have not been achieved yet, but form the basis of intended future work on these systems. A feature of the design of these ligands, **91**, was the intention that they would have increased biological relevance by virtue of the appended biomolecules incorporated into their structure. In order to investigate the potential of the luminescent complexes discussed above in this context, it was undertaken to attempt introduction of these complexes into cells and investigate their effects, if any. These complexes were very soluble in CH_3CN, however, this is not an appropriate solvent for biological studies, so, given the poor solubility of the complexes in water, solutions of the complexes needed to be dissolved in an alcohol, such as ethanol for testing. These studies are discussed in the next section.

3.15 Investigations of $[Ln\cdot(\mathbf{91})_3](CF_3SO_3)_3$ in aqueous media

In order to introduce these complexes into biological systems, solutions of Ln(III) complexes $[Ln\cdot(\mathbf{91})_3](CF_3SO_3)_3$ were prepared in ethanol at a concentration of 0.5 mg/mL (the complexes were not very soluble in ethanol, either). The purpose of this was to study their behaviour in cells, as had previously been described for Ln(III) complexes of bis-benzyl **btp** ligand **17**.[158] Cell viability assays of all of these were carried out by Dr Salvador Blasco, a member of the Gunnlaugsson group, by incubating HeLa cells in these solutions for 24 hours followed by Alamar Blue assay, showing quantitative survival of cells in all cases, within experimental error. However, neither epifluorescence nor confocal microscopy of cells incubated with solutions of $[Ln\cdot(\mathbf{91})_3](CF_3SO_3)_3$ showed any emission. This was unexpected, considering, in particular how high the quantum yields of the Tb(III) complexes in CH_3CN were. Indeed, these results suggested that these complexes were either completely quenched in biological media or that they were dissociating under these conditions.

To test these hypotheses, the photophysical spectra of $[Tb\cdot(\mathbf{91\text{-}Gly})_3](CF_3SO_3)_3$ dissolved in an ethanol–H_2O mix were measured. Surprisingly the UV-Vis absorbance spectrum resembled that of the free ligand and only extremely weak Tb(III)-centred emission was observed. Further tests were carried out upon a solution in CH_3CN of $[Tb\cdot(\mathbf{91\text{-}Gly})_3](CF_3SO_3)_3$ to study its behaviour upon addition of protic solvents, observing how quickly this conversion of complex to ligand occurred, Figure 3.38. Addition of approximately 10% (v/v) of either ethanol or H_2O to the solution resulted in complete

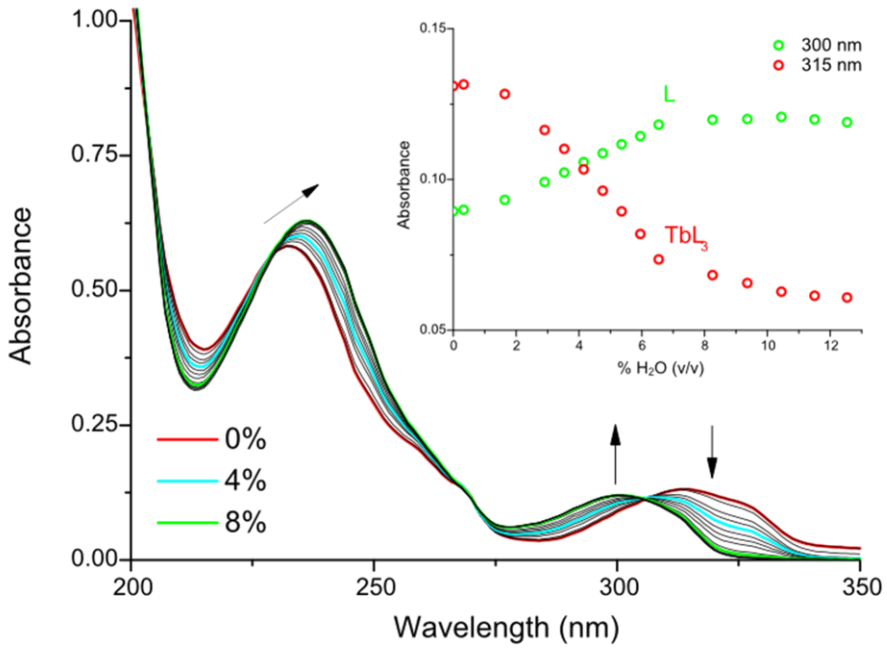

Figure 3.38 UV-Vis spectra of a CH_3CN solution of [Tb·(**91-Gly**)$_3$]$(CF_3SO_3)_3$ upon addition of H_2O, showing the dissociation of the complex by the addition of *ca.* 10% (v/v) H_2O upon monitoring of characteristic absorbance bands (inset).

quenching of Tb(III) luminescence and the characteristic shift of the absorbance band at 315 nm to 300 nm suggested the release of free ligand.

These observations, unfortunately suggest that these complexes are not stable in solution in competitive aqueous media, and, as a result, will be unsuitable for use as biological probes *in vivo* or *in vitro* in their current form. It is worth noting, that the [Ln·(**17**)$_3$]$(CF_3SO_3)_3$ studied by Indapurkar and co-workers were not very water soluble either and were in fact delivered to cells as suspensions resulting in a small amount phosphorescence observed from particles coating the cells; this behaviour was not seen for the complexes of **91**. As such, other strategies will need to be explored to introduce **btp** systems such as those discussed in this chapter to aqueous or indeed biological media and the water-soluble analytes, for which phosphorescence quenching or enahancement could act as a probe. One such strategy is discussed in the next section.

3.16 Towards overcoming the obstacle of incompatability with aqueous media

The dissociation process described in the previous section is not yet fully understood, but it may relate to the hydrogen bonding capability of the triazolyl C–H, which could interact with polar solvents and anions in solution favouring the *anti–anti* conformation. In Chapter 2, it was indeed shown by X-ray crystallography that these triazolyl protons could take part in hydrogen bonding. A potential step which would help overcome this is the introduction

of sterically hindering aryl groups into the 4-triazolyl position, eliminating this hydrogen bond donor. There is precedent in the literature for high-yielding Pd(II)-catalysed arylation of 1,2,3-triazoles, which would be followed.[255]

Without further chemical functionalisation, however, incorporation of such systems into solid matrices would allow for exploitation of their emissive properties in aqueous media by preventing dissociation by means of restricting the freedom of the molecules.

Hydrogels, polymeric materials which swell in water without dissolving, have been investigated for a range of applications, including drug delivery[256] and antigen sensing[257]. Ln(III)-containing hybrid hydrogels have been reported[258], as well as non-covalent incorporation of Ln(III) complexes into hydrogels[259]. Previous work in the Gunnlaugsson group has shown how cyclen-based Ln(III) complexes encapsulated in hydrogel matrices may act as sensors for pH.[260,261]

Preliminary investigations into such systems, incorporating ligands **88** and **89** have begun and show promising results. The ligands were encapsulated in a cross-linked poly(HEMA) matrix (HEMA = (hydroxyethyl)methacrylate) by suspending the relevant **btp** ligand (*ca.* 0.05% w/w of the polymerising mixture) in a solution of HEMA along with cross-linker ethylene glycol dimethacrylate and radical initiator AIBN, followed by curing in an oven at 90 °C for 5 hours. The resultant materials were rigid transparent gels, which became soft upon swelling in water. When these gels were instead swelled in aqueous $Ln(CF_3SO_3)_3$ solution, they gave rise to characteristic Ln(III)-centred emission when submerged in aqueous media or when dried, as seen above for the complexes, namely red emission for Eu(III) and green emission for Tb(III), Figure 3.40(a–b), indicating that self-assembly processes with the Ln(III) ions can occur within the matrix of the polymer. This strategy, yielding, as it did, luminescent materials, which are accessible to the solution, provided an avenue for these Ln(III)–**btp** systems to be used to interrogate aqueous analytes, despite their instability in aqueous solution. This is a greatly advantageous scenario. If the luminescence of such materials was affected by an analyte, it could be used as a one-use probe by dipping into a solution containing the analyte, or indeed as a coating for a flow system, sensing changes in the flowing solution.

One obvious class of analytes suggested by the C–H···Cl^- interactions observed in the X-ray crystal structures of the various complexes shown in Chapter 2, are the halides; the triazolyl C–H has shown a capacity to hydrogen bond with halides, and this would be expected to affect the luminescence of a Ln(III)–**btp** system. Titrations of $[Tb{\cdot}(\mathbf{88})_3](CF_3SO_3)_3$ in CH_3CN upon addition of F^- show that the anion causes dissociation

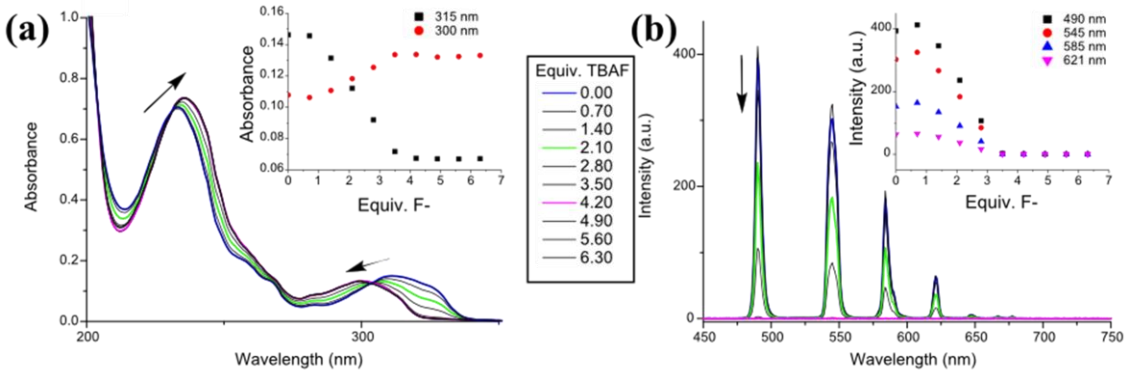

Figure 3.39 Titrations of $[Tb{\cdot}(\mathbf{88})_3](CF_3SO_3)_3$ with TBAF in CH_3CN. **(a)** UV-Vis absorbance spectral changes; *inset:* binding isotherms at 300 and 315 nm as a function of equivalents of F^-; **(b)** Tb(III)-centred luminescence spectral changes; *inset:* binding isotherms at the bands associated with each $^5D_4 \rightarrow {}^7F_{6-3}$ transition. Changes in fluorescence are shown in Appendix B.

of the complex, Figure 3.39, implying that such systems cannot act as stable anion sensors in solution, however, the Tb(III)-swelled gel containing **89** shows potential as an anion sensor, with selective quenching of Tb(III) emission in solutions containing KF, but no quenching for other potassium halides.

Gel luminescence can be recovered by soaking the gel in $Na(CF_3SO_3)$ solution, suggesting that the Tb(III) ions do not leave the gel as a result of the sensing process, and hence the sensing behaviour can be reversible. Figure 3.40(c–d) shows the remarkable

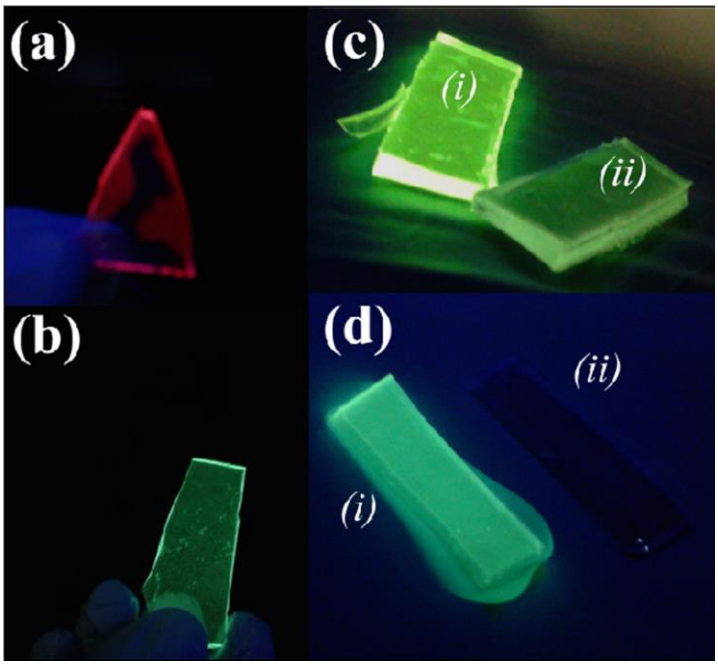

Figure 3.40 Images of **btp** containing crosslinked poly(HEMA) hydrogels: **(a)** Gel containing ligand **89** swelled in aqueous Eu(III) solution; **(b)** Gel containing ligand **89** swelled in aqueous Tb(III) solution; **(c)** Tb(III)-gel interactions with aqueous KF solution at *(i)* 0 hours and *(ii)* 3 hours; **(d)** Tb(III)-gel interactions with aqueous KF solution at *(i)* 0 hours and *(ii)* 24 hours.

naked-eye decreases in luminescence when the Tb(III) gel was treated with a F^- solution, quenching fully over the course of 24 hours. These studies are on-going in collaboration with Mr Samuel Bradberry.[262]

3.17 Conclusions

In this chapter, the Ln(III)-directed self-assembly behaviour of nine ligands **88**, **90** and **91** in CH_3CN was investigated. This is the first example of Ln(III)-directed self-assembly of **btp** systems being studied upon titration under kinetic control, and one of only a few examples of Ln(III)–**btp** systems which have been reported. Amide ligands **90** and **91** were synthesised upon facile reaction of the relevant amine with the acid chloride derivative of **89** in good yields. Seven new **btp** ligands, **91**, all contained methyl ester protected amino acid residues, which were incorporated at the aryl 'arms' of the ligands, enabling further functionalisation of these systems in the future *via* the carboxylate terminus. **88**, **90** and **91** were all fully characterised by various techniques including ^{1}H- and ^{13}C-NMR spectrscopy, HRMS analysis and IR spectroscopy.

Analysis of the Gd(III) complex of **88** allowed the determination of the triplet excited state of the ligand, and showed that such **btp** ligands were well matched to sensitise Eu(III) and Tb(III) emission *via* the 'antenna' effect. Indeed, ligands **88**, **90** and **91** all formed stable, luminescent complexes with Ln(III) triflate salts, displaying characteristic sensitised Eu(III) or Tb(III) line-like emission profiles, demonstrating modest and very high quantum yields for Eu(III) and Tb(III) complexes, respectively. For example, in the case of $[Ln\cdot(\mathbf{88})_3](CF_3SO_3)_3$, $\Phi_{Eu(III)} = 2.4 \pm 0.4$ % and $\Phi_{Tb(III)} = 70 \pm 12$ %. A hydration state of $q \approx 0$ was determined for each complex, indicating the absence of water molecules bound in the first coordination sphere of the metal ion and the ability of these ligands to satisfy the high coordination requirements of Ln(III) by formation of 1:3 complexes. The interactions of ligand **88** with Eu(III) ions in CD_3CN was studied through ^{1}H NMR studies, showing that the **btp** motif can bind this metal ion.

Olefin-containing ligand **90** underwent RCM in the presence of the Hoveyda–Grubbs second generation catalyst, yielding a remarkable self-templated [2]catenane, **95**, the tightly-packed structure of which was confirmed by single crystal X-ray diffraction analysis. The [2]catenane was shown by preliminary ^{1}H NMR studies to bind $H_2PO_4^-$. More in-depth exploration of this system is on-going. The aim of the design of ligand **90** was to form Ln(III)-templated [3]catenanes by subjecting $[Eu\cdot(\mathbf{90})_3](CF_3SO_3)_3$ to similar RCM conditions; this strategy was not successful, probably due to the size and rigidity of

the macrocycle ring. In future, the introduction of more flexible chains, such as hydrophilic polyethylyene glycol chains, or long hydrophobic alkyl chains would be expected to yield more suitable candidates for Ln(III)-templated catenane formation, whereas the ligand discussed was an ideal candidate for self-templated [2]catenane formation.

Photophysical spectroscopic titrations of **88**, **90** and **91** with Ln(III) were carried out in CH_3CN at 23 °C in order to monitor the kinetic self-assembly behaviour of these ligands in solution. The global stability constants determined for the various self-assembled species by non-linear regression analysis, with the ReactLab Equilibria software,[237] were high. For example, $\log\beta_{1:3}$ for the various Ln(III)–**btp** self-assembly processes was determiined to range from 18.9–23.0. These values of $\log\beta$ were comparable to the range of global stability constants previously reported for other terdentate systems, which can have $\log\beta_{1:3}$ values anywhere from 17.2 ± 0.3 for a deprotonated **pytz** ligand[263] to 23.8 ± 0.2 for **dpa** ligand **2**[29]. The values of global stability constants varied very little throughout the series of ligands investigated, pointing to similar binding behaviour for all these **btp** ligands, minimally affected by the nature of the flanking 'arms'.

Unfortunately, these complexes were found to dissociate when fully dissolved in aqueous media, which precludes the possibility of effectively using such systems as biological probes in solution in their current form, since the dissociation of the complexes results in a loss of luminescence. The dissociated complexes, i.e. the ligands, were however found to be non-toxic to HeLa cells in concentrations up to 0.5 mg/mL in ethanol. Encapsulating such systems in a hydrogel polymer matrix (*e.g.* crosslinked poly(HEMA)) is being explored as a strategy to overcome this limitation and has shown some promise of allowing the luminescent properties of such systems to be exploited in an aqueous environment for anion sensing, being selective for F^- over the other halides. Further investigations into these hydrogel materials are on-going.

This chapter has focussed on the introduction of further functionality into the **btp** ligand framework designed in Chapter 2, of which **88** was the simplest example, by coupling amines to the carbonyl site in this ligand scaffold; this resulted in functionalities quite far from the binding motif, as evidenced by the poor chiroptical properties of ligands **91**, despite the chirality of the amino acid residues. These functionalisations were not found to have a deleterious effect on the binding stabilities of the ligands; however they did not result in systems which exhibited good CD or CPL properties. In order to achieve this, the next chapter will discuss the introduction of new optically active functionalities adjacent to the **btp** motif, in the hope of imparting good chiroptical properties to the Ln(III)-directed

self-assembly systems formed. Having explored the incorporation of amino acid residues into a **btp** framework in this chapter, the other readily-accessible biological chiral pool, the carbohydrates will be investigated in Chapter 4 by preparation of a number of carbohydrate-derivatised ligands. Subsequently, optically active **btp** ligands synthesised by coupling chiral amines directly to the **btp** site by use of a new diazo-transfer–'click' paradigm will be presented, which yield complexes for which CD titrations could be carried out and which sensitise Ln(III)-centred CPL emission.

4. Introducing chirality: Synthesis and lanthanide-directed self-assembly of optically active btp ligands

4.1 Introduction

In the preceding chapters, the coordination chemistry of optically inactive ligands containing the **btp** motif with transition metals and lanthanides was described, as well as the self-assembly of a number of chiral ligands, **91**, with Ln(III). These compounds, however, did not display significant chiroptical properties, as was demonstrated by the very weak CD spectra and negligible CPL signals of their complexes discussed briefly in Chapter 3. It was postulated that the chiral centres of the amino acid reidues were too remote from the **btp** binding moiety to significantly impact on the coordination environment of the metal ions. The chirality is also remote from any chromophores. In Figure 2.1, discussing ligand design, it was pointed out that position (d) was an appropriate site to introduce chirality. This chapter will present a number of ligands with chiral centres closer to the binding site, exhibiting more significant optical activity which is transferred to the Ln(III)-directed assemblies. This optical activity can be monitored by chiroptical techniques. The design of the various new ligands described in this chapter will be outlined in Section 4.3.

4.2 Chirality and chiroptical spectroscopy

Chiral Ln(III) complexes exhibit interesting chiroptical properties,[29,32,247-251] namely circular dichroism (CD) and circularly polarised luminescence (CPL); these techniques shall be briefly introduced in this section. This chapter will then focus on the design, synthesis, self-assembly behaviour with Ln(III) and chiroptical properties of a number of new **btp** ligands synthesised from carbohydrate substrates and chiral amines *via* a one-pot diazo-transfer–deprotection–'click' methodology. While CD spectroscopy has been regularly used to monitor supramolecular interactions, such as folding and formation of larger self-assembly systems,[264] carrying out CD titrations to investigate the self-assembly of metal ion complexes is relatively unexplored, in particular with the Ln(III) ions.[265] The changes in CD spectra for many of the systems in this chapter were significant upon addition of Ln(III), and, as such, these changes were fit to determine global stability constants. Determination of stability constants of Ln(III) self-assembly formation from CD titrations has not previously been reported, except in work involving **dpa**-based ligands **81b** by Dr Oxana Kotova *et al.*, conducted in the Gunnlaugsson laboratory simultaneously to the studies presented in this chapter.[181]

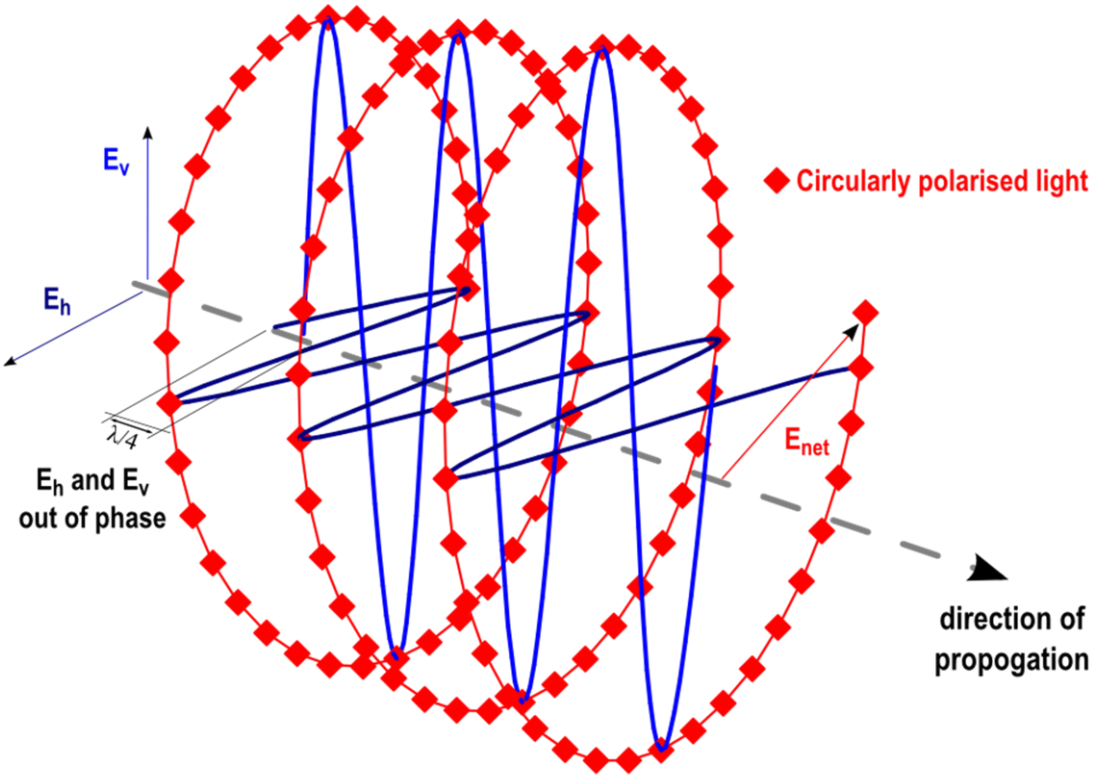

Figure 4.1 Schematic diagram of circularly polarised light, E_{net}, made up from the sum of horizontally, E_h, and vertically, E_v, polarised light offset by one quarter of a wavelength, and seen by an observed as the electric field vector, E_{net}, rotating in a circular fashion over time.

A molecule lacking an axis of improper rotation is chiral and hence exists as two non-superimposable enantiomeric forms which are mirror images of each other.[266] Such compounds are referred to as 'optically active', since the enantiomers interact with electromagnetic radiation in equal but opposite ways to each other, rotating polarised light as it passes through the sample. As a result of the inversion of geometry between enantiomers, they may show a preferential binding to particular chiral substrates. Such systems have been used as probes for chiral biological substrates such as DNA[267], proteins[268] *etc*. Chirality can be expressed at a supramolecular level as well as a molecular level, and as such chiral complexes and self-assemblies can be formed upon the use of chiral components such as enantio-resolved non-racemic coordinating ligands, thereby transferring chirality to the coordination environment of the metal centre in the assembly.[266]

Unlike linearly polarised light, in which oscillations are limited to a single plane, circularly polarised light consists of horizontally and vertically polarised light, the polarisation states of which are out of phase with each other by a quarter of a wave. The

net electric field vector is thus, when observed from a fixed point, seen to change in direction in a circular manner without altering in strength, as illustrated in Figure 4.1. Optically active enantiomeric pairs interact with light in different ways to each other, rotating electromagnetic radiation as it passes through the sample in solution. The difference in magnitude of either absorption or emission of a sample of left- and right-handed circularly polarised light can allow study of the chirality of the system. As a result of these differing interactions with light, there exist 'chiroptical' spectroscopic techniques which allow further characterisation of such chiral systems and self-assemblies; these chiroptical spectroscopic techniques are not available to the achiral molecules. CD can be considered a chiral analogue to UV-Vis absorbance, while CPL is a chiral analogue to emission spectroscopy. These techniques will be introduced now.

4.2.1 Circular dichroism

Circular dichroism (CD) refers to the differential absorption of left- (*L*) and right-handed (*R*) polarised light by optically active compounds, resulting in radiation with elliptical polarisation.[269] A CD spectropolarimeter measures this difference in absorption, ΔA, Equation 4.1. Enantiomers will give CD signals of equal magnitude and opposite signs.

$$\Delta A = A_L - A_R \qquad \text{Equation 4.1}$$

The CD signal is, however, for historical reasons, usually reported in millidegrees of ellipticity (θ). The relationship between ΔA and θ is shown in Equation 4.2

$$\theta = \frac{\Delta A}{32982} \qquad \text{Equation 4.2}$$

CD provides reflects structural properties of the system's electronic ground state.

4.2.2 Circularly polarised luminescence

Circularly polarised luminescence (CPL) acts as a technique to further probe the chiral nature of luminescence, which is presented in this thesis particularly to understand the chiral nature of the coordination sphere of the Ln(III) metal ion within a number of complexes. It may be considered an emission equivalent to CD.[247] It should be noted that all the CPL measurements reported herein were carried out by our collaborator Dr Robert Peacock in the University of Glasgow. Similarly to CD above, the intensity of the CPL signal, ΔI, is defined as the difference in emission of left- and right-handed circularly polarised light, Equation 4.3.

$$\Delta I = I_L - I_R \qquad \text{Equation 4.3}$$

The luminescence dissymmetry factor, g_{lum}, can be used to describe the degree of CPL at a given wavelength, or for a given Ln(III) electronic transition. As shown in Equation 4.4, this factor is the ratio between the CPL signal and the total luminescence intensity, I_{TL}, at this wavelength.

$$g_{lum} = \frac{I_L - I_R}{I_L + I_R} = \frac{\Delta I}{I_{TL}} \qquad \text{Equation 4.4}$$

Optically active Ln(III) complexes are ideal candidates for chiral CPL probes, by virtue of their long lifetimes, line-like emission bands and large pseudo-Stokes shifts,[266] as well as often possessing significantly higher g_{lum} values than chiral organic molecules.[247] Such probes have been used to report on the environments, (*e.g.* pH, anion concentration, protein signatures) particularly in a biological context.[247]

Hence, bearing in mind the advantageous properties that optically active Ln(III)-directed self-assemblies can possess, in this chapter, a number of chiral **btp** ligands, derived from either carbohydrates or chiral amines, and their Ln(III) complexes, will be presented. These compounds will be characterised and their self-assembly properties studied by various spectroscopic techniques with particular attention paid to their chiroptical properties.

4.3 Design of chiral btp ligands

As was discussed in previous chapters, when designing **btp** ligands, various aspects of the molecule framework can be altered to change the functionality of the ligands, Figure 4.2. Of particular concern in the design of new ligands in this chapter are variation of the position marked (c) and introduction of chirality in position (d). The **btp** ligands developed in this chapter would be expected to possess some of the same advantageous properties seen for **88**–**91** in the preceding chapters, such as their ability to coordinate metal ions and sensitise Ln(III)-centred luminescence.

Ligands **96**–**98**, described in Section 4.4, below vary the functionality of the aforementioned ligand, by introducing optically active carbohydrate moieties into the flanking ‘arms’ of the **btp** ligand, Figure 4.2(c). **96** was designed to include allyl chains, in a way analogous to allyl amide ligand **90** described above; the chirality of this molecule was still quite remote from the binding motif. Ligands **97** and **98** were designed, coupling the optically active sugars directly to the **btp** motif *via* the anomeric position, thus introducing chirality adjacent to the binding site, Figure 4.2(d).

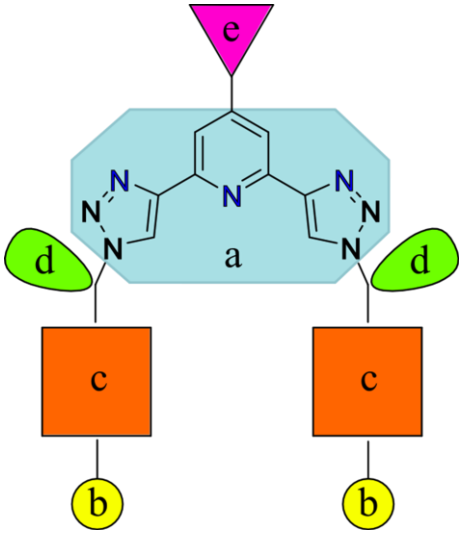

Figure 4.2 A schematic representation of the design considerations for desired functionality of **btp** ligand frameworks developed in this thesis.

Ligands **99**–**101**, described in Section 4.5 and onwards were also designed to include chirality adjacent to the binding site, Figure 4.2(d). These ligands, derived from chiral amines, included aromatic 'antennae' in the position labelled (c) in Figure 4.2 in order to better sensitise the Ln(III) excited state and give rise to favourable emission properties. Phenyl and naphthyl chromophores were employed in the design of these ligands.

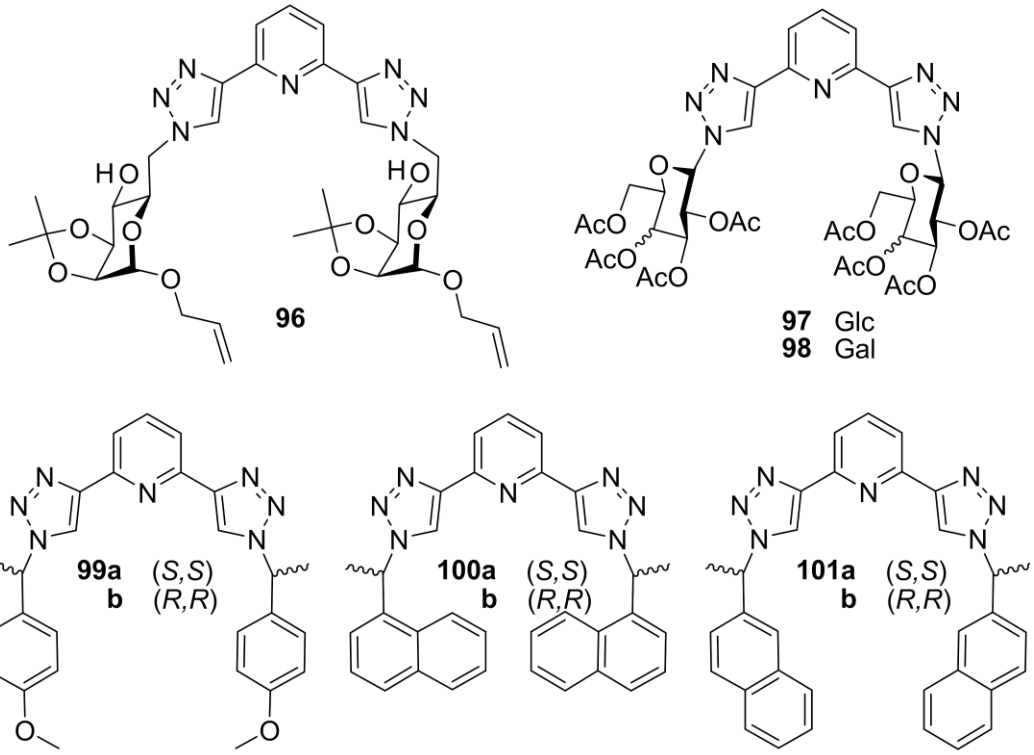

4.4 Carbohydrate-derived btp ligands

A survey of the literature suggests that only two **btp** compounds, **70**, containing carbohydrate moieties exist, published by Wang *et al.* as part of a library of glycosyltransferase inhibitors, as described above in Section 1.7.2.[168] These ligands were asymmetrical, featuring a carbohydrate 'arm' and a nucleoside 'arm'.[168] Carbohydrates are optically active motifs, which will impart chiroptical properties onto the **btp** ligands which contain these moieties, as well as potentially furnishing them with biological relevance, although they do lack strongly absorbing chromophores. Having conjugated **btp** systems with amino acids in Chapter 3, showing the ability to introduce another class of biomolecule into such structures was desireable. As such, the synthesis and characterisation of carbohydrate-containing ligands **96**–**98**, along with the Eu(III)-directed self-assembly behaviour of **96** will be presented in the following sections. This research project is on-going, and as such, the self-assembly behaviour of ligands **97** and **98** with Ln(III) was not investigated to date.

4.4.1 Synthesis of ligand 96

A symmetrical carbohydrate-containing **btp** ligand, **96** was designed as a carbohydrate-based analogue to all amide ligand **90**. The allyl-appended carbohydrate azide precursor was prepared from D-mannose, in 4 steps, Scheme 4.1, by Dr Ciaran O'Reilly, a researcher at Trinity College, Dublin based on literature procedures.[270,271] This azide was reacted with **21** *via* the CuAAC 'click' reaction, as described in Chapter 2 above[72] to yield the desired ligand **96**. The ligand was isolated as a white solid upon flash column chromatography

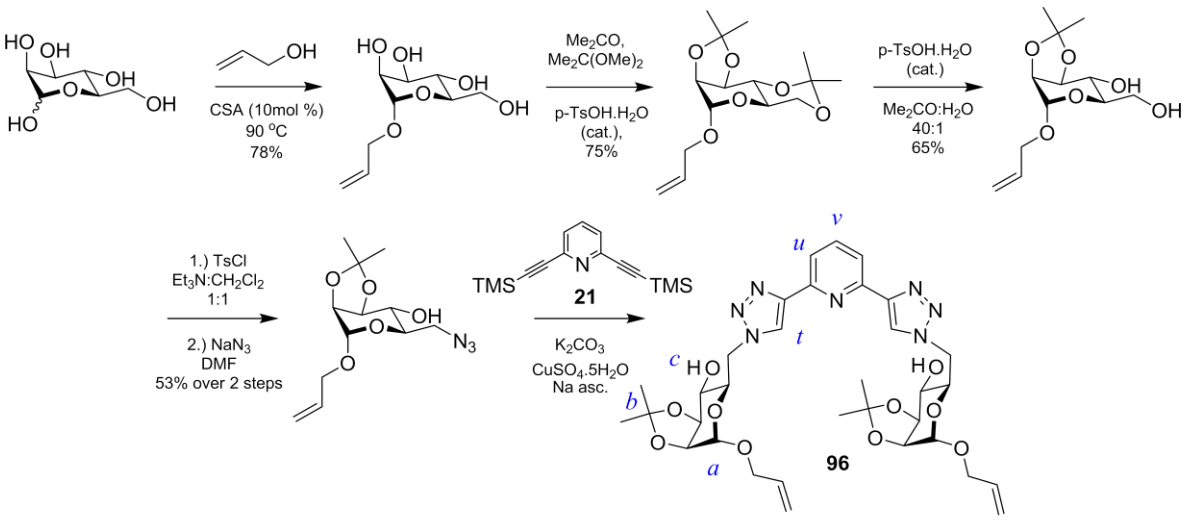

Scheme 4.1 Preparation of ligand **96** from D-mannose

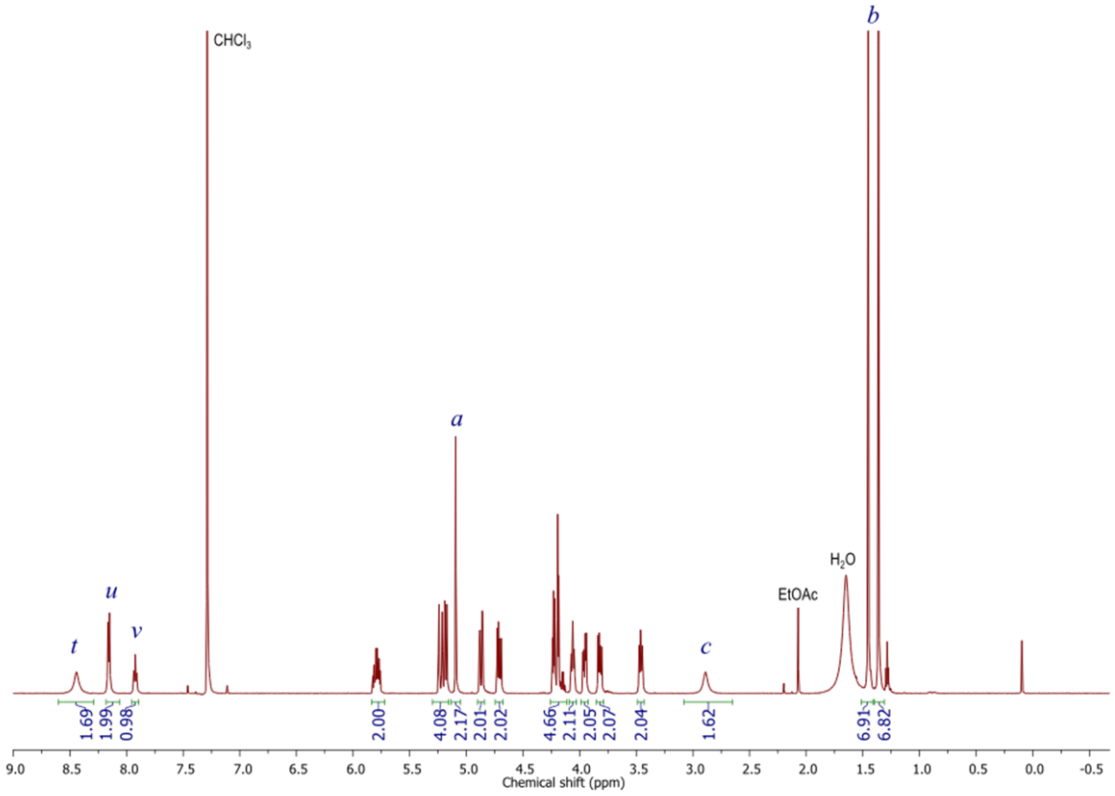

Figure 4.3 ^{1}H NMR (600 MHz,$CDCl_3$) of ligand **96**. Labelled resonances correspond to labels in Scheme 4.1.

(EtOAc–hexanes gradient on silica) in 33% yield. The ^{1}H-NMR spectrum (600 MHz, $CDCl_3$), Figure 4.3, showed characteristic resonances from the isopropylidene protecting groups at 1.36 and 1.45 ppm (labelled *b* in Figure 4.3), and a broad singlet at 2.89 ppm from the OH groups (labelled *c*). The remaining CH peaks from the sugar moiety were observed at 3.42–3.49, 4.02–4.09 and 4.14–4.25 ppm as multiplets with the anomeric CH giving rise to an apparent singlet at 5.09 ppm (labelled *a*). The olefin moieties gave rise to resonances at 3.78–3.99, 5.15–5.25 and 5.75–5.84 ppm, all multiplets. The aromatic region of the spectrum was quite simple, with pyridyl resonances at 7.92 and 8.16 ppm (labelled *v* and *u*, respectively) and a triazolyl resonance (labelled *t*) centred at 8.44 ppm. The ^{13}C-NMR spectrum (150 MHz, $CDCl_3$) was also assigned with the aid of 2D NMR experiments, Appendix C. MALDI+ HRMS analysis showed a peak at *m/z* = 698.3171, corresponding to the protonated species.

The UV-Vis absorbance spectrum of the ligand in CH_3CN displayed bands centred at 237 nm (ε 32,200 M^{-1} cm^{-1}) and 300 nm (ε 10,700 M^{-1} cm^{-1}), Figure 4.4(a). Excitation into either absorbance band of the ligand resulted in a broad fluorescence band centred at 335 nm, similarly to those seen for **88** and **91** in Chapters 2 and 3, respectively. The

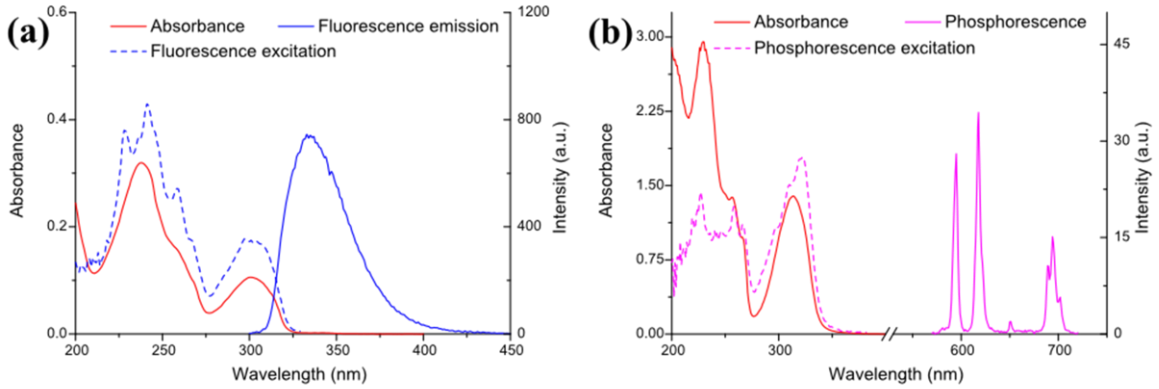

Figure 4.4 Photophysical spectra in CH_3CN solution of **(a)** ligand **96**, showing UV-Vis absorbance, fluorescence and fluorescence excitation spectra, [**96**] = 1.0×10^{-5} M; **(b)** complex [Eu·(**96**)$_3$]$(CF_3SO_3)_3$, showing UV-Vis absorbance, Eu(III)-centred phosphorescence emission and phosphorescence excitation spectra (at concentration of 4.4×10^{-5} M).

excitation spectrum of this emission corresponded to the absorbance bands measured for the ligand.

4.4.2 Formation of Eu(III) complex of 96

The Eu(III) complex was formed upon heating with $Eu(CF_3SO_3)_3$ in CH_3OH for 20 minutes to 70 °C under microwave irradiation and was collected as an off-white solid by diethyl ether diffusion into CH_3OH solution. The hydration states, *q*, of the resulting complex were determined by measuring the luminescence lifetimes in both H_2O and D_2O and substituting these values into the Horrocks Equation, Equation 3.1. The system was found to have a hydration state of ~0, indicating the formation of the 1:3 stoichiometric species, Table 4.1, with zero metal-bound water molecules.

Formation of this stoichiometry was further confirmed by ESI+ HRMS analysis, where a signal at *m/z* = 1197.4003 matched the isotopic distribution pattern predicted for [Eu·(**96**)$_3$]$(CF_3SO_3)^{2+}$, Appendix C. The complex showed the characteristic 15 nm red shift of the ligand absorbance band centred at 300 nm, as seen for all **btp** ligands in Chapter 3 upon complexation, Figure 4.4(b), as well as sensitising Eu(III)-centred luminescence, with bands arising from the $^5D_0 \rightarrow {}^7F_{1-4}$ transitions observed; excitation spectra confirmed that this luminescence was sensitised by the ligand. The total quantum yield, Φ, was, however, quite low at only 1.9 ± 0.3%, indicating that the sensitisation of Eu(III) emission is not very efficient for these systems. The absence of a strongly absorbing chromophore in the ligand structure is perhaps responsible for this poor sensitisation.

Table 4.1 Photophysical properties of Eu(III) complex of ligand **96**: luminescence lifetimes, hydration states and total luminescence quantum yield in CH_3CN.

Complex	τ_{H2O} **(ms)**	τ_{D2O} **(ms)**	q **(±0.5)**[a]	**Φ (%)**[b]
$[Eu\cdot(\mathbf{96})_3](CF_3SO_3)_3$	2.6 ± 0.2	2.9 ± 0.2	−0.3	1.9±0.3

[a]Hydration states were calculated using the equation $q = A(\left(\frac{1}{\tau_{H2O}} - \frac{1}{\tau_{D2O}}\right) - B)$, where for Eu(III), A = 1.2, B = 0.25.[212,226] [b]Quantum yields in CH_3CN were estimated by a relative method,[236] compared with $Cs_3[Eu\cdot(\mathbf{dpa}-2H)_3]$[21,22] according to the equations shown in the Experimental Chapter.

The IR spectra, Appendix C, of ligand and complex differed little in general profile, however the band associated with the free hydroxyl groups at 3386 cm^{-1} was seen to shift to 3410 cm^{-1-} upon complexation, and a clear broad band centred at 1243 cm^{-1} in the complex spectrum confirmed the presence of the $CF_3SO_3^-$ counterions. The ^{1}H-NMR spectrum (400 MHz, CD_3CN, Appendix C) of the complex was broadened and shifted as a result of the paramagnetism of the Eu(III) ion and, consequentially, the resonances were not assigned.

This Eu(III)-centred self-assembly structure can be described as a luminescent Ln(III)-templated 'glyco-cluster', containing, as it does, six tightly packed carbohydrate motifs, held together by a Ln(III) ion; such structures templated by *d*-metal ions have been reported before.[272] As stated previously, this project is on-going, and as such the formation of Tb(III) complexes with **96** has not yet been achieved, although this complex would be expected to have higher quantum yields, consistent with the measurements reported in Chapter 3 for the Ln(III) complexes of **88** and **91**, where the quantum yields for Tb(III) complexes (Φ = 6.3–70%) were significantly higher than those of the Eu(III) complexes (Φ = 0.3–3.0%). Having successfully formed the 1:3 Eu(III)-directed self-assembly complex under thermodynamic control, it was next undertaken to explore the kinetic formation of these assemblies in CH_3CN solution by means of various spectroscopic titrations.

4.4.3 Spectroscopic titrations of 96 with Eu(III)

The changes in the various photophysical spectra of **96** in CH_3CN solution, namely UV-Vis absorbance, fluorescence, sensitised Eu(III)-centred emission and, notably, CD, were monitored upon addition of a solution of $Eu(CF_3SO_3)_3$, in the same manner as described for ligands **88**–**91** in Chapter 3. The concentration of **96** was 1 × 10^{-5} M for all measurements except the CD titrations, where a higher concentration (2.8 × 10^{-5} M) was used as a result of the relatively weak CD signals of this ligand. Monitoring Ln(III)-directed self-assembly by CD has not been much exploited previously, as discussed above, and as such, these chiroptical titrations of the optically active system are of particular

interest. CH_3CN was chosen as the solvent for these titrations for reasons of consistency, allowing direct comparison of this system's behaviour to that of the other **btp** self-assembly systems described in Chapter 3. This ligand is also very soluble in CH_3OH and titrations in this solvent will be carried out in future, to compare its behaviour in more competitive protic media.

The UV-Vis absorbance spectra upon addition of $Eu(CF_3SO_3)_3$ solution showed changes in both of the main absorbance bands, Figure 4.5(a), with the higher energy band undergoing a blue shift of 7 nm to 230 nm with concomitant hypochromicity, while the lower energy band, tentatively assigned to n→π* transitions in **btp**, was seen to undergo a red shift of 15 nm to 315 nm. All significant spectral changes had occurred upon addition of 0.33 equivalents of Eu(III), as can be seen from the inset in Figure 4.5(a).

Simultaneous monitoring of the ligand excited state was carried out by monitoring the ligand fluorescence band centred at 335 nm upon excitation at 237 nm. The intensity of this emission dropped off dramatically with addition of Eu(III) to the ligand solution and showed almost complete quenching by 0.33 equivalents, after which no more fluorescence emission was observed (see Appendix C). This behaviour is identical to that seen for other **btp** ligands, such as **88** in Chapter 3. This suggested that the ligand, upon formation of Eu(III)-directed self-assemblies sensititised the Eu(III) excited states *via* the 'antenna' effect by transferring energy from the ligand S_1 excited state to Eu(III) instead of undergoing fast radiative emission

The characteristic Eu(III) phosphorescence spectrum was, indeed, observed upon

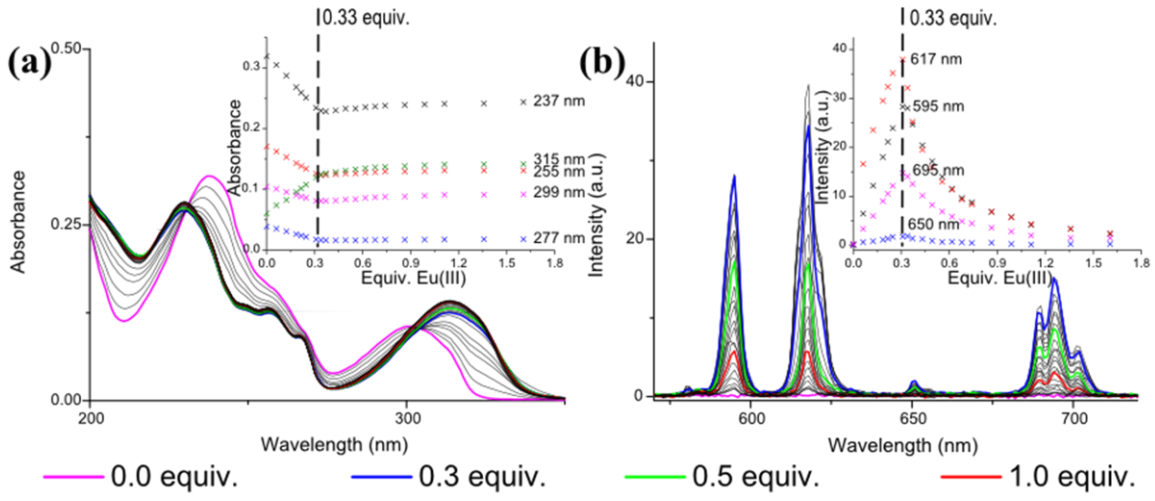

Figure 4.5 (a) UV-Vis absorbance spectral changes upon addition of $Eu(CF_3SO_3)_3$ to a solution of **96** in CH_3CN; **(b)** Phosphorescence spectral changes upon addition of Eu(III); (*insets*) experimental binding isotherms (×) at various wavelengths for each titration. [**96**] = 1×10^{-5} M.

addition of $Eu(CF_3SO_3)_3$ to the ligand solution, Figure 4.5(b). The emission bands assigned to the $^5D_0 \rightarrow {}^7F_{0-4}$ bands increased in intensity upon addition of the metal ion up until 0.33 equivalents, suggesting the formation of an emissive 1:3 stoichiometric assembly. Upon addition of further aliquots of Eu(III), the intensity of the spectra decreased steadily as the equilibrium in solution shifted away from the ML3 species towards less emissive stoichiometries. The emission was nearly completely quenched by 1.4 equivalents of $Eu(CF_3SO_3)_3$, as seen in the inset in Figure 4.5(b).

The chiral carbohydrate moiety was not directly adjacent to the binding **btp** motif in this ligand, and so similar poor chiroptical properties might be expected as were seen above for **91**. Ligand **96**, however, gave a weak but distinctive CD spectrum with a negative band at 300 nm, matching the UV-Vis absorbance band at the same wavelength, as well as a higher energy band around 230 nm. As such, titrations upon addition of Eu(III) were undertaken to observe any spectral changes which occurred. The spectra were found to be quite noisy, and not very well resolved, but clear changes could indeed be seen, particularly the decrease of the band at 300 nm, to be replaced by a negative band centred at 315 nm, Figure 4.6, which again corresponded to the band at similar energy observed in the UV-Vis absorbance measurements. The shape of the spectra recorded for the self-assemblies did not suggest the presence of exciton coupling for this system. It would be expected that optically active systems with the chiral centre adjacent to the sensitising 'antenna' and the binding **btp** motif would give more intense chiroptical signals; such compounds will be presented in the latter part of this chapter.

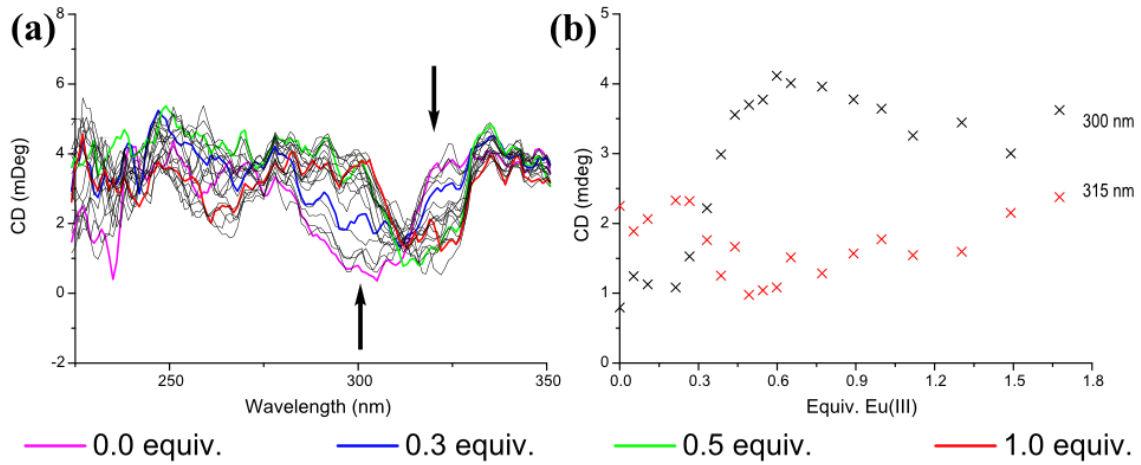

Figure 4.6 (a) CD titration showing spectral changes for a solution of **96** in CH_3CN upon addition of $Eu(CF_3SO_3)_3$; **(b)** Experimental binding isotherms (×) at both 300 nm and 315 nm for the two wavelengths with most significant changes. **[96]** = 2.8×10^{-5} M.

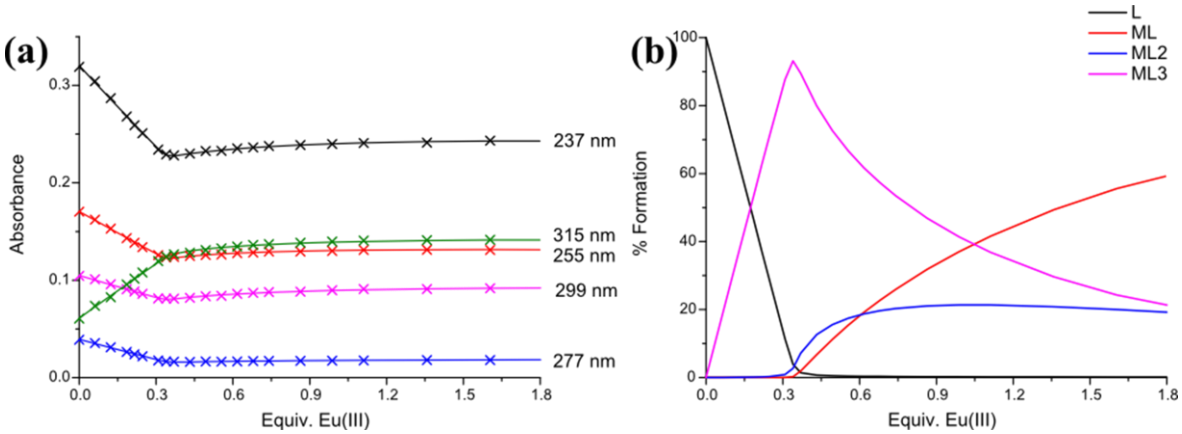

Figure 4.7 (a) Experimental (×) and calculated (–) binding isotherms for UV-Vis titration of **96** with Eu(III) at various wavelengths; **(b)** Calculated speciation distribution diagram of the titration for various metal:ligand (M:L) stoichiometric species.

4.4.4 Fitting of titration data and estimation of global stability constants

Fitting these various spectral changes to theoretical models was carried out using non-linear regression analysis program ReactLab Equilibria[237] by modelling the changes to stepwise equilibria between the ligand and the metal as described in Section 3.5.3 above. Unfortunately, the Eu(III)-centred emission could not be fit; no models containing combinations of the various Ln(III)–**btp** equilibria converged. However, for the UV-Vis data, values of the global stability constant for the three binding processes were found to be $\log\beta_{1:1}$ = 7.7±0.1, $\log\beta_{1:2}$ = 14.8 and $\log\beta_{1:3}$ = 22.6±0.1. These values were analogous to those seen in Chapter 3 for ligands **88**, **90** and **91**, suggesting a similar binding process. Fits of experimental binding isotherms to theoretical isotherms along with the calculated speciation distribution diagram are shown in Figure 4.7. This model suggested that the formation of the 1:3 species in CH_3CN occurs with high yield (>95% at 0.33 equivalents of Eu(III)) and results in a very stable species which persisted as the most dominant species in solution until *ca.* 1.2 equivalents of Eu(III) were added, after which the 1:1 assembly was calculated to dominate. The 1:2 self-assembly structure was not the most prevalent at any point in the titration.

For the CD data, the values of $\log\beta_{1:1}$ and $\log\beta_{1:2}$ were found to be higher than for the absorbance data (8.9±0.1 and 16.3), while $\log\beta_{1:3}$ was similar, 22.2±0.2. As mentioned above, fitting of CD titration data for such metal ion-directed systems is a largely unexploited technique, only being exploited very recently by other researchers in the Gunnlaugsson group,[181] hence, the comparability of the values derived from fitting CD

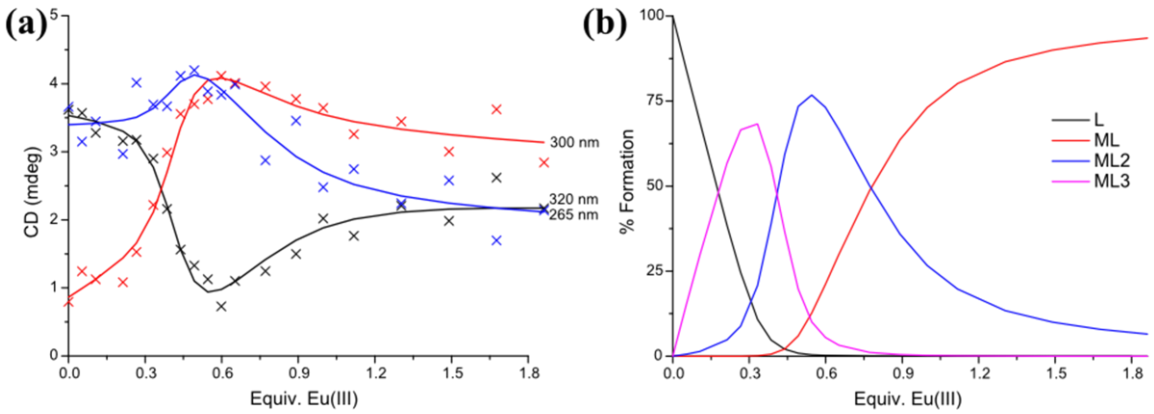

Figure 4.8 Fitting of CD titration data of **96** v. Eu(III); **(a)** Experimental (×) and calculated (–) binding isotherms at a number of wavelengths; **(b)** Calculated speciation distribution diagram.

titrations to those determined by the commonplace practice of fitting UV-Vis titration data, even when the CD signals were very weak, suggests that there is great potential for CD titrations to be employed as a further means of determining Ln(III) binding constants for chiral self-assembly systems along with determination of species stoichiometry in solution. This result is remarkable, as it allows direct monitoring of the chiral nature of the system as well as the binding interactions between the ligand and Ln(III) simultaneously. The fitting curves and calculated speciation distribution diagram from this fit are shown in Figure 4.8 The speciation profile calculated from this model differs from that derived from fitting the UV-Vis absorbance data, suggesting a much more dominant 1:2 stoichiometry, reaching a maximum at 0.5 equivalents of Eu(III).

Given the weak nature of the CD signals obtained, some caution should be taken with the global stability constants determined by this method. That being said, since such remarkable results can be obtained from fitting these noisy CD titration data, which are comparable with results obtained by more established methods, it was concluded that even better results could be obtained by applying the same techniques to other systems which displayed more dramatic and well resolved CD spectra. As such, it was deemed worthwhile to synthesise **btp** ligands, such as **99** and **100**, with the chiral centre adjacent to the binding site to enhance the chiroptical properties of such systems. These will be discussed from Section 4.5 onwards. Firstly, however, the synthesis and characterisation of carbohydrate-based **btp** systems **97** and **98** will be detailed and the future studies which are foreseen for these compounds will also be briefly discussed.

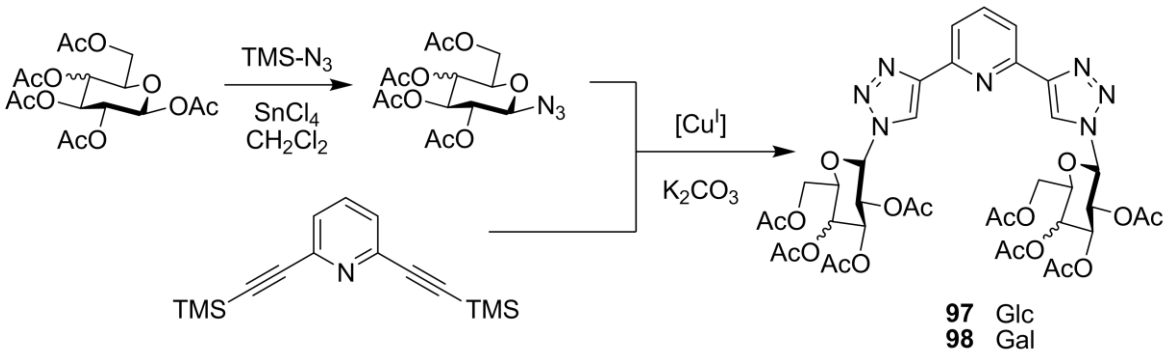

Scheme 4.2 Synthesis of carbohydrate-appended **btp** ligands.

4.4.5 Further carbohydrate derivatives and future work

Recently, two further carbohydrate-appended **btp** ligands have also been prepared, featuring a chiral centre in close proximity to the binding motif. In depth studies of the self-assembly of these recently-synthesised ligands with Ln(III) ions have not been completed to date and shall not be reported in this thesis. Their synthesis and characterisation, however, will be detailed before moving on to a series of chiral ligands developed from chiral amines in Section 4.5 below.

Dr Ciaran O'Reilly synthesised the carbohydrate azide precursors, introducing the azide functionality into peracetylated glucose (a sugar with all the acetyl groups in the equatorial position) and galactose (where the acetyl group in the C-4 position is axial) according to established procedures upon treatment with TMS–N_3 and $SnCl_4$.[273] These carbohydrates were then selected to act as azide substrates for the CuAAC reaction with **21** as described previously, yielding **97** and **98**, respectively in good yields (77–82%), Scheme 4.2.

The successful formation of both ligands was confirmed by HRMS analysis (MALDI+), with both structural isomers displaying a peak closely matching that calculated for the $[M+Na]^+$ species (*m/z* = 896.2562). The ^{1}H-NMR spectrum (600 MHz, DMSO-d_6) of **97** displayed four resonances between 1.84 and 2.06 ppm relating to the acetate protecting groups. Six well resolved signals arose from the protons of the carbohydrate ring, including a multiplet at 4.08–4.23 ppm arising from the CH_2 group and a doublet at 6.48 ppm arising from the anomeric CH protons. The pyridyl protons appeared as a multiplet at 7.99–8.08 ppm, while the triazolyl protons resulted in a signal at 9.03 ppm. Ligand **98** gave a ^{1}H-NMR (600 MHz, DMSO-d_6) spectrum, which, although as well resolved as that for **97**, was distinct and showed resonances at different chemical shifts. The acetate signals around 2.0 ppm were spread wider, with one resonance at 2.25 ppm. Among the

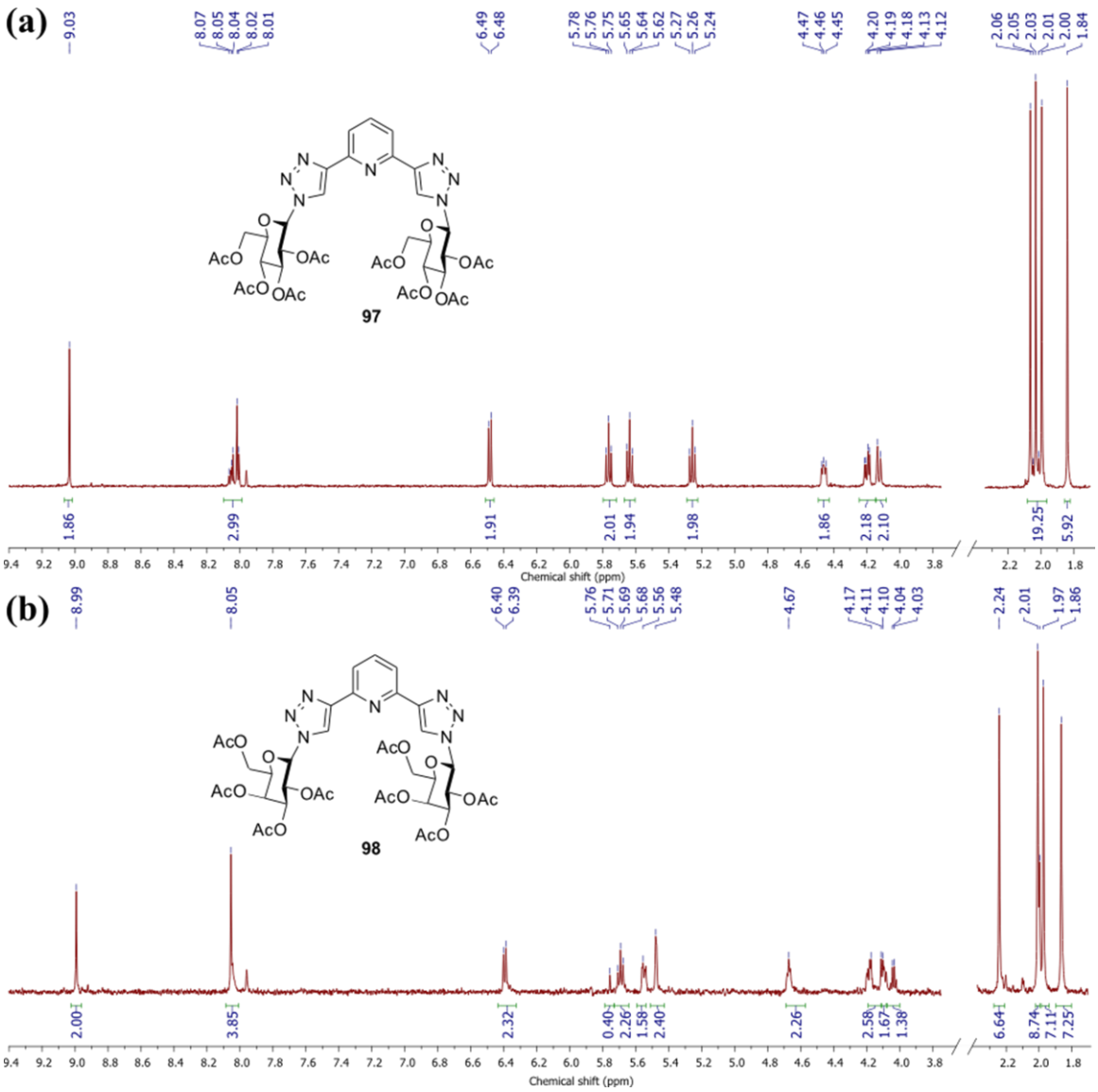

Figure 4.9 ^{1}H NMR spectra (600 MHz, DMSO-d_6) of ligands **(a) 97**; and **(b) 98**.

differences in the carbohydrate region of the spectrum was the shift of the anomeric proton resonance to 6.40 ppm. The pyridyl protons gave rise to an apparent singlet at 8.06 ppm, whereas the triazolyl CH once again displayed a singlet at 9.00 ppm. The ^{13}C-NMR (150 MHz, DMSO-d_6) resonances were also assigned for both ligands by use of 2D NMR experiments such as HSQC and HMBC, Appendix C. IR spectra for both ligands featured carbonyl bands at 1742 and 1744 cm^{-1} for **97** and **98**, respectively, arising from the acetyl protecting groups.

Single crystals of **98** were grown by slow diffusion of $(CH_3)_2CHOH$ into a DMSO-d_6 solution as colourless hexagonal plates. X-ray diffraction data were collected and refined by Dr Salvador Blasco, a member of the Gunnlaugsson group, Table 3.3. The ligand

Table 4.2 Selected crystallographic data and structural refinements for ligand **98**.

Compound	**98**
Formula	$C_{37}H_{43}N_7O_{18}$
Formula weight	873.78
T (K)	100(2)
Crystal system	Trigonal
Space group	$P3_221$
a (Å)	13.033(15)
b (Å)	13.033(15)
c (Å)	44.95(5)
α (°)	90
β (°)	90
γ (°)	120
V (Å^3)	6613(17)
Z	6
F(000)	2748
D_c (Mg m^{-3})	1.316
μ (mm^{-1})	0.91
GOF on F^2	1.12
R1 [$I > 2\sigma(I)$]	0.070
wR2 [$I > 2\sigma(I)$]	0.175

crystallised in the trigonal space group $P3_221$. The asymmetric unit contains two distinct residues, each being half a molecule of **98**, the other half of each molecule being generated by symmetry. These two complete molecules are shown in Figure 4.10(a); weak supramolecular interactions between the carbohydrate moieties of the adjacent molecules cause them to stack in the manner seen, all C–H···O distances were of the order of 3.5 Å and are shown in a table in Appendix C.

The **btp** motifs of the two crystallographically distinct molecules were also shown to intertwine by non-classical hydrogen bonding interactions between the triazolyl C–H and the pyridyl nitrogen atoms of the other **btp** motif, with hydrogen bond lengths of C–H···N = 3.511(10) and 3.482(9) Å, Figure 4.10(b). This dimeric interaction resembled that seen in the structure of the [2]catenane **95** in Chapter 3. The triazole rings of **btp** were found to be slightly twisted out of the plane of the pyridyl rings by *ca.* 13° in this elegant structure. The unit cell of this crystal structure contained 6 molecules (Z = 6, Table 3.3); the two molecules shown in Figure 4.10(a) repeat in a left-handed 3_2 screw axis, Figure 4.10(c).

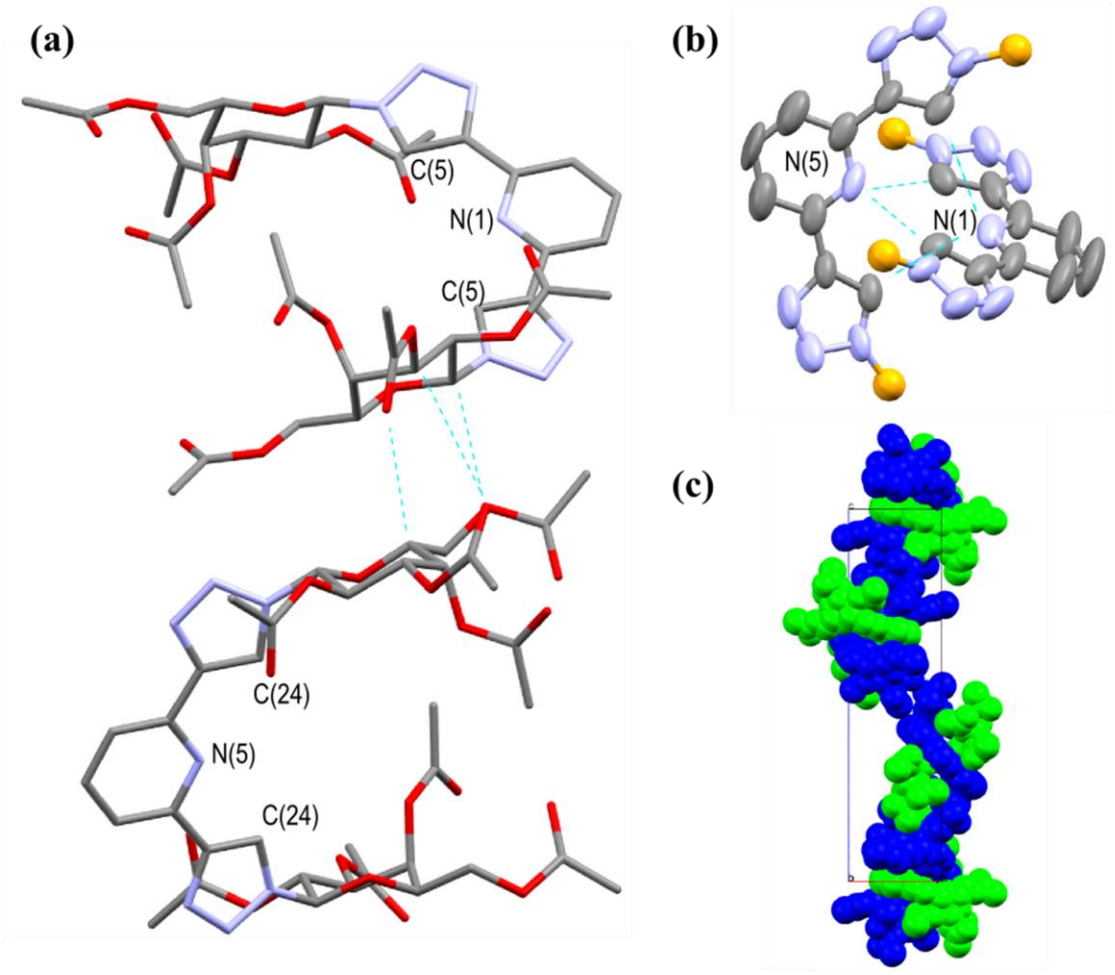

Figure 4.10 Projections of the X-ray crystal structure of **98**, showing various features of the structure (omitting hydrogen atoms for clarity): **(a)** A capped stick model showing the two distinct molecules in the structure packing due to weak supramolecular interactions between the adjacent sugar moieties; **(b)** A thermal ellipsoid model showing the non-classical hydrogen bonding interactions between the two **btp** motifs; the carbohydrate arms are omitted for clarity (represented as orange spheres); **(c)** A space-filling model, showing the packing of the molecules with a $C3_2$ screw-axis.

It can be clearly seen from this crystal structure that introducing carbohydrates moieties into these ligand structures increases the range of supramolecular interactions at play for the systems. Ln(III)-directed self-assemblies based on these ligands are expected to show equally interesting supramolecular behaviour, perhaps being able to interact with other carbohydrates or carbohydrate-binding proteins, such as lectins.

The Ln(III)-directed self-assembly and photophysical properties of **97** and **98**, as well as a range of analogues prepared from other simple peracetylated sugars will be investigated like **96** in the near future, with both Eu(III) and Tb(III), with a view to preparing luminescent Ln(III)-templated 'glycoclusters'. Such novel supramolecular assemblies would be good candidates for reporting on biological analytes by means of changes in luminescence. Other future work envisaged for these carbohydrate systems will involve

subjecting **96** to Grubbs-catalysed ring-closing metathesis, like **90** in Chapter 3 in an attempt to make carbohydrate-containing interlocked systems, such as [3]catenanes; mechanically encapsulating the metal ion inside the structure would increase the stability of these architectures in solution.

Having detailed the synthesis and characterisation of carbohydrate-based **btp** ligands **96**–**98**, studied the Eu(III)-directed self-assembly of **96** in CH_3CN solution and provided an overview of the future direction of this research, a range of different optically active ligands **99**–**101** derived from chiral amines will now be introduced. A convenient methodology for synthesising chiral **btp** ligands from amine starting materials will be described in the next section, followed by characterisation of the resultant ligands and investigations of the Ln(III)-directed self-assembly of two of these, with particular attention paid to their chiroptical properties, namely CD and CPL. These self-assembly systems give rise to much stronger CD signals than **96** above, and so will allow in-depth studies of the Ln(III)-binding processes by means of this technique.

4.5 A new one-pot synthesis of chiral btp ligands (99–101) from amines

In Figure 4.2, it was pointed out, when designing new **btp** ligands, that, as well as introducing chirality to position (d), it was possible to change the chromophore in position (c) also. The ligands discussed in the remainder of this chapter feature different chromophore 'antennae': a phenyl ring, as already seen above, for ligand **99**; and naphthyl rings for regioisomeric ligands **100** and **101**. As described in Chapter 1, much research has been carried out in the Gunnlaugsson laboratory[4,6,152-154,180] and by other research groups,[29] into **dpa** ligands synthesized from chiral amines and their Ln(III) complexes. Of particular relevance here are the '*Trinity Sliotar*' ligands **79** and **80**, with naphthyl chromophores, and ligand **102**, containing methoxyphenyl chromophores, which was synthesised in good yield (80%) in contribution to a separate project with Dr Jennifer Jones, the results of which are unpublished.[274] Analogues of such compounds containing the 1,2,3-triazole in place of an amide bond were not previously reported but are desirable, given the triazole's often-cited qualities as an isostere for the amide bond.[95,98,275]

As a result of the enantiomeric nature of the **btp** ligands synthesised in the following sections and their formation of chiral Ln(III) complexes, their chiroptical properties will be studied using CD and CPL techniques. The changes in the CD spectra of these ligands were much more dramatic than those seen for **96** above and more significant than changes seen by Albrecht and co-workers for a Ln(III) host–guest complex[265]. The changes in CD

spectra were so dramatic upon interactions with Ln(III) that, like for the **dpa** system recently reported in the Gunnlaugsson group[181], it was possible to probe the self-assembly process in depth and determine global stability constants for Ln(III) self-assemblies from fitting CD titrations, which were comparable to those found by more conventional UV-Vis absorbance and luminescence titrations.

For the synthesis of the proposed ligands, a new one-pot synthesis from amine starting materials was developed, inspired by previous strategies in the literature, such as an amine–alkyne CuAAC methodology which was previously reported,[276] relying on the relatively unstable trifluoromethanesulfonyl azide as a diazo transfer reagent. Imidazole-1-sulfonyl azide ($ImSO_2N_3$) hydrochloride salt was reported as a more robust shelf-stable diazo-transfer agent,[277] and consequently Stonehouse *et al.* employed this agent in a three-component 'click' reaction,[278] while Xie presented a route to form triazoles from aldehydes and amines also using $ImSO_2N_3$ in its neutral form.[279] More recently, however, it has been reported that the hydrochloride salt is more sensitive than originally thought,[280] leading the authors to suggest the sulfuric acid salt as a more stable alternative. Hence, the new modular and mild synthesis of symmetrical **btp** ligands from chiral amines and protected alkynes, which is presented in this chapter, makes use of the more robust $ImSO_2N_3 \cdot H_2SO_4$ as a diazo-transfer agent. A series of chiral **btp** ligands **99**–**101** were synthesised by the same general method.

This one-pot *diazo-transfer–deprotection–'click'* reaction has two steps catalysed by Cu(II) and Cu(I), respectively, Scheme 4.3, proceeds at room temperature, from a chiral amine starting material, yielding the chiral **btp** ligands in good purity (confirmed by elemental analysis) and with retention of stereochemistry (confirmed by CD and consistent with mechanistic studies of the diazo-transfer reaction[281]). As the synthetic procedure was the same for all the designed ligands (**99**–**101**), only the synthesis of ligands **99a** (*S,S*-enantiomer) and **99b** (*R,R*-enantiomer) will now be discussed in detail, particularly with regard to the various colour changes observed. The characterisation of the ligands **99**–**101**

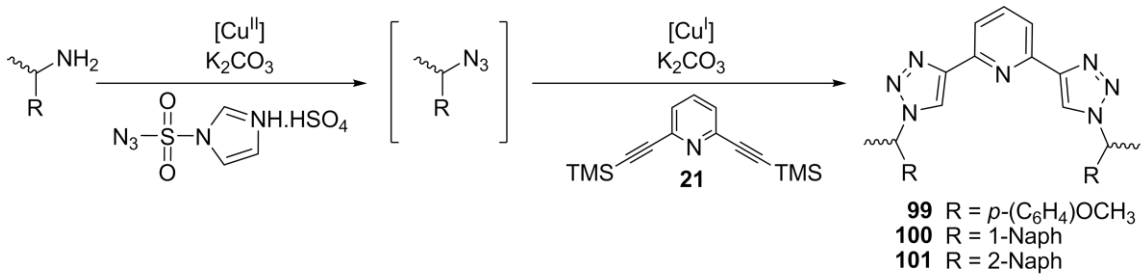

Scheme 4.3 General scheme for the one-pot diazo-transfer–deprotection–'click' reaction for synthesis of chiral **btp** ligands **99**–**101**.

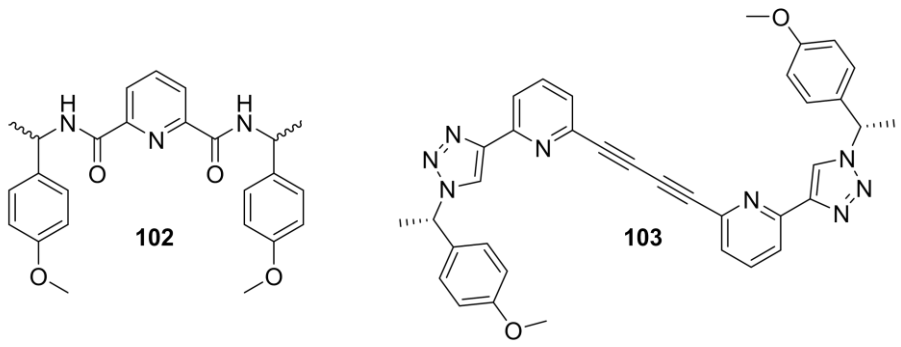

will then be presented. Later in this chapter, the photophysical properties of ligands **99** and **100** and their Ln(III) complexes, including CD and CPL spectra will be discussed. Ln(III)-directed self-assembly of chiral **btp** ligands **99** and **100** in CH_3CN solution was also studied and global stability constants of the various self-assemblies were estimated from UV-Vis absorbance, Ln(III)-centred emission and CD titration data.

The reaction could be monitored by dramatic colour changes in the reaction mixture over the course of the multi-step reaction. These changes for the synthesis ligand **99** are shown in Figure 4.11, along with a reaction scheme; these changes allowed the progress of the reaction to be monitored easily by eye. The initial mixture of Cu(II), chiral amine and $ImSO_2N_3{\cdot}H_2SO_4$ was a bright cyan colour. Upon stirring for 5 hours in the presence of K_2CO_3, a lilac suspension, Figure 4.11(b), had been formed. This colour change corresponded with the conversion of amine to azide, as monitored by TLC and was not observed if insufficient base was added. Upon addition of sodium ascorbate (to reduce Cu(II)→Cu(I)), dilution with aqueous *tert*-butanol solution and subsequent degassing of the reaction mixture, a dull pale yellow colour was observed, Figure 4.11(c), before

Figure 4.11 Schematic representation of the synthesis of ligands **99** demonstrating colour changes during the course of the reaction: **(a)** Cyan mixture of amine, $CuSO_4{\cdot}5H_2O$, $ImSO_2N_3{\cdot}H_2SO_4$ and K_2CO_3 in CH_3OH (t = 0 hours); **(b)** Lilac suspension upon formation of the azide (t = 5 hours); **(c)** Dull yellow suspension after addition of sodium ascorbate and degassing mixture (t = 5.5 hours); **(d)** Orange reaction mixture upon completion of CuAAC reaction (t = 18 hours).

addition of the protected dialkyne **21** in DMF. When the reaction proceeded under ambient atmosphere, a small amount of the Glaser coupling product was observed in the reaction mixture (*e.g.* **103**, which was isolated and characterised, see Appendix C); inert atmosphere produced only the desired **btp** product. When the reaction was complete, the orange colour shown in Figure 4.11(d) was observed after 18 hours. After aqueous workup, **99** was isolated with retention of stereochemistry (confirmed by X-ray crystallography and CD, *vide infra*) by precipitation from CH_3OH or flash chromatography in moderate yield (48–50%). This same colour-changing behaviour has also been seen in our hands with other amines (*e.g.* 1-(naphthyl)ethylamines for **100** and **101**).

4.5.1 Characterisation of ligands 99–101

The ^{1}H-NMR spectrum (600 MHz, DMSO-d_6) of ligand **99a**, Figure 4.12, displayed characteristic proton resonances, which were assigned with the aid of ^{13}C NMR, HSQC and HMBC spectra, Appendix C. The spectrum was quite simple, as a result of the symmetry of the molecule. The two methyl groups were seen at quite different chemical shifts, with a doublet at 1.95 ppm (labelled *s*) arising from the chiral CH_3 groups and the singlet at 3.74 ppm relating to the methoxy groups (labelled *z*). A quartet centred at 6.00

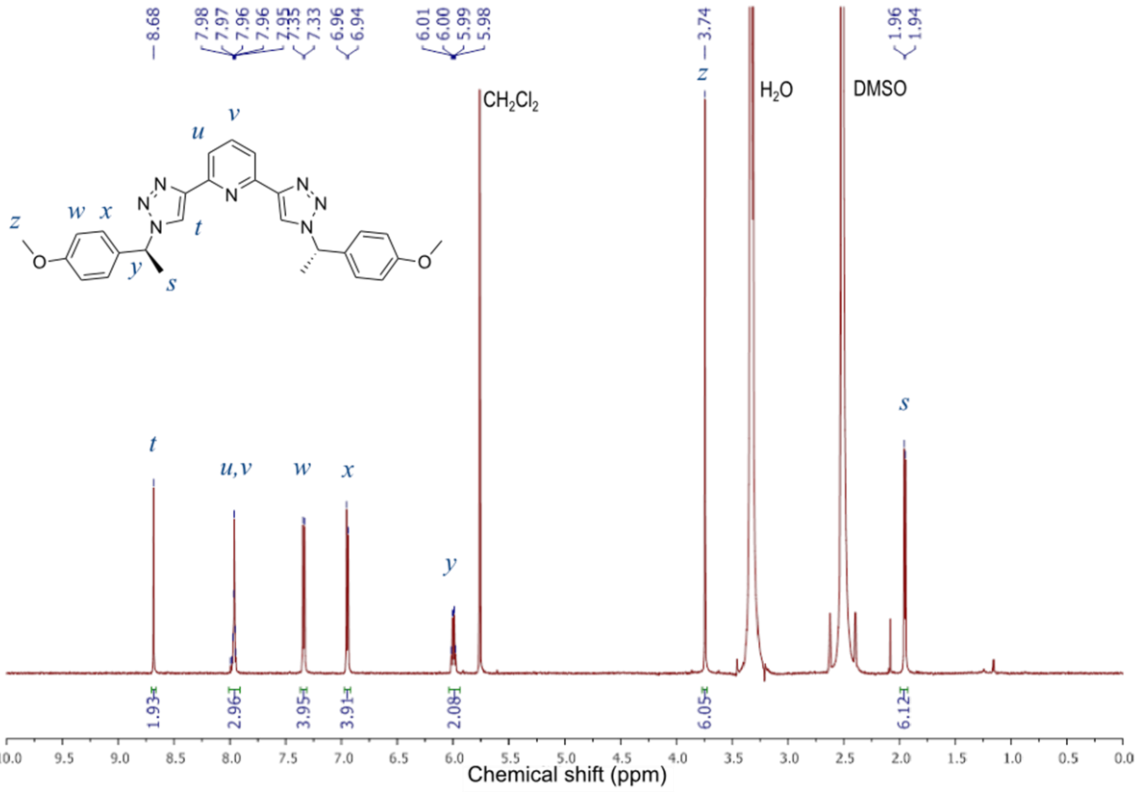

Figure 4.12 ^{1}H NMR spectrum (600 MHz, DMSO-d_6) of ligand **99a**, with resonances labelled.

ppm indicated the presence of the CH group at the chiral centre of the molecule (labelled *y*), adjacent to the methyl group. In the aromatic region of the spectrum, four signals were observed: two doublets at 6.95 and 7.34 ppm were related to the phenyl CH atoms (*w* and *x*), the multiplet around 7.95 ppm resulted from the overlap between two pyridyl resonances (labelled *u* and *v*), and the final peak, a singlet at 8.68 ppm, was the characteristic triazolyl CH resonance (labelled *t*). ESI+ HRMS analysis gave a peak at *m/z* = 482.2307, corresponding to the $[M+H]^+$ species. The identical ^{1}H-NMR spectrum of **99b** is shown in Appendix C. ESI+ HRMS analysis of this enantiomer gave a peak at *m/z* = 504.2125, corresponding to $[M+Na]^+$.

100, a **btp** analogue of the '*Trinity Sliotar*', **79**, mentioned in Section 1.9, was prepared in good yield (72–75%) by the same one-pot method described in Scheme 4.3. Formation of the desired ligand was confirmed by HRMS analysis, with both enantiomers showing a peak assigned to the $[M+Na]^+$ species at *m/z* = 544.2219 and 544.2206 for **100a** and **100b**, respectively. The ^{1}H-NMR spectrum (600 MHz, DMSO-d_6) of **100b** displayed characteristic proton resonances. A doublet at 2.07 ppm arose from the chiral methyl group, while a quartet at 6.89 ppm related to the CH at the chiral centre. All of the other resonances were in the aromatic region: a doublet at 7.43 ppm and a multiplet between 7.50–7.63 ppm arose from the naphthyl protons, the complex multiplet between 7.91–8.01 ppm related to both naphthyl protons and the 4-pyridyl proton, while the 3- and 5-pyridyl protons gave rise to a doublet resonance centred at 8.23 ppm. The triazolyl CH resonance was found at 8.65 ppm. The NMR spectra of both enantiomers of **100** are shown in Appendix C. The IR spectra of both ligands showed bands characteristic of naphthyl-containing compounds at 776, 1570, 1604 and 3067 cm^{-1}. Such bands have been previously observed for ligands such as **79**.[4]

Ligand **101**, an isomer of **100** was also synthesised to demonstrate that the one-pot methodology is applicable to a range of chiral amines. Both ligands displayed HRMS signals in MALDI+ for the $[M+Na]^+$ species, calculated for *m/z* = 544.226. The ^{1}H-NMR spectrum (600 MHz, DMSO-d_6) of **101a** demonstrated a doublet at 2.07 ppm arising from the chiral CH_3 protons and coupled with the resonance at 6.22 ppm, a quartet assigned to the proton on the chiral centre. A number of multiplets in the aromatic region were characteristic of the naphthyl moieties, while the pyridyl CH resonances overlapped at 7.99 ppm and the triazolyl signal appeared at 8.78 ppm. In-depth studies into the Ln(III) self-assembly behaviour of **101** have not been undertaken to date, and, as such, will not be discussed in this thesis.

4.5.2 X-ray crystallography of 99 and its dpa analogue 102

Single crystals suitable for X-ray diffraction analysis of both enantiomers of ligand **99** were obtained upon slow evaporation of a DMF–H_2O solution. Both crystallised in the orthorhombic $C222_1$ space group. X-ray diffraction data for these ligands were collected and refined by Dr Miguel Martínez-Calvo, Table 4.3. The X-ray crystal structures were identical, but mirror images of each other. There were two molecules in the asymmetric unit of the structure and, as a result of non-classical triazolyl hydrogen bonding to the pyridyl nitrogen of the adjacent molecule, a 'double helix' structure occurred in the solid state, as shown in Figure 4.13. These hydrogen bonds had C–H···N distances ranging from 2.458(2)–2.608(3) Å (see Table in Appendix C). The **btp** motifs of the two molecules were nearly orthogonal to each other (85°). A similar 'interweaving' pattern was seen in the structure of **96** above, Figure 4.10(b).

As mentioned in Section 4.5 above, **102** is a **dpa** analogue of **btp** ligand **99a**. This was

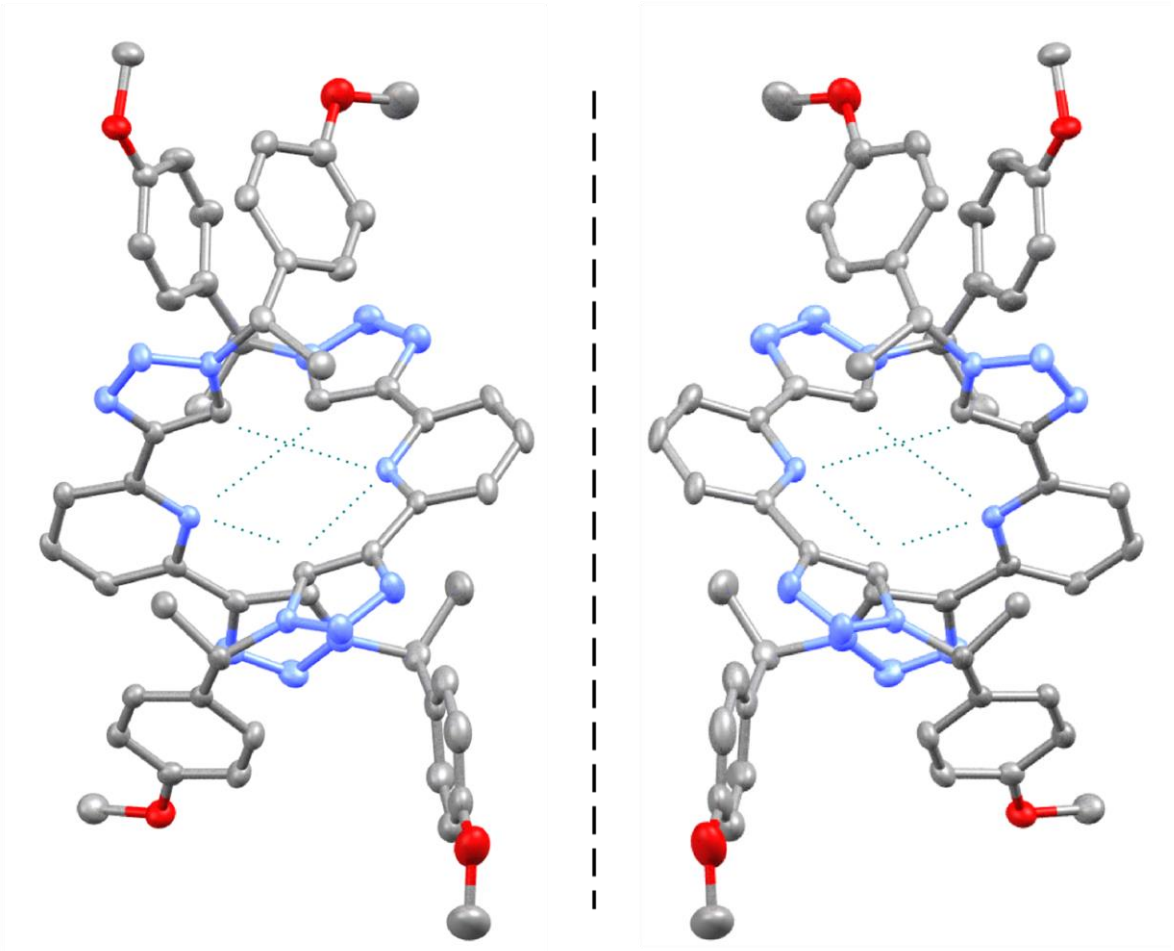

Figure 4.13. X-ray crystal structures of the *S*,*S*- and *R*,*R*-enantiomers of ligand **99**, shown with thermal ellipsoids at 50%. Hydrogen bonding between triazoles and adjacent pyridines is shown by a dashed line. Hydrogen atoms have been omitted for clarity.

synthesised and characterised by a number of methods (see Appendix C), including X-ray crystallography.[274] White needle-like crystals were obtained on recrystallisation of the compound from CH_3OH. The data were collected and resolved by Dr Jonathan Kitchen, Table 4.3. This crystal structure allows for direct comparison between the structural features of **btp** and **dpa** ligands with identical flanking 'arms', particularly the hydrogen-bonding interactions.

The structure of **102** also featured hydrogen-bonding. In this case, the amide protons hydrogen bonded to an amide carbonyl oxygen atom from another molecule. The structure did not form a 'double helix'-type structure as was seen for the **btp** analogues above. The N–H···O distances were 2.9199(16) and 2.9784(16) Å. In contrast to the **btp** structure, there is also some π–π stacking evident in the **dpa** ligand between the pyridine ring and one phenyl ring of an adjacent molecule (3.713 Å). In the **btp** structures, both phenyl 'arms' protruded at an angle of *ca.* 109° from the plane of the triazole rings in all cases, while in the structure of **102**, the two 'arms' protruded at different angles of 112° and 109°. These differences can be seen in a comparison of the two structures in Figure 4.14.

Table 4.3 Selected crystallographic data and structure refinements

Compound	**99a**	**99b**	**102**
Formula	$C_{27}H_{27}N_7O_2$	$C_{27}H_{27}N_7O_2$	$C_{25}H_{27}N_3O_4$
CCDC code	1019214	1019215	—
Formula weight	481.56	481.56	433.50
T (K)	111(2)	293(2)	100(2)
Crystal system	Orthorhombic	Orthorhombic	Tetragonal
Space group	$C222_1$	$C222_1$	$P4_3$
a (Å)	10.0935(15)	10.0910(15)	12.8728(12)
b (Å)	27.370(4)	27.262(4)	12.8728(12)
c (Å)	36.577(6)	36.585(6)	13.7227(15)
α (°)	90	90	90
β (°)	90	90	90
γ (°)	90	90	90
V (Å^3)	10105(3)	10065(3)	2274.0(4)
Z	16	16	4
F(000)	4064	4064	920
D_c (Mg m^{-3})	1.266	1.271	1.266
μ (mm^{-1})	0.084	0.084	0.704
GOF on F^2	1.045	1.043	1.065
R1 [$I > 2\sigma(I)$]	0.0392	0.0479	0.0283
wR2 [$I > 2\sigma(I)$]	0.1013	0.1242	0.0742

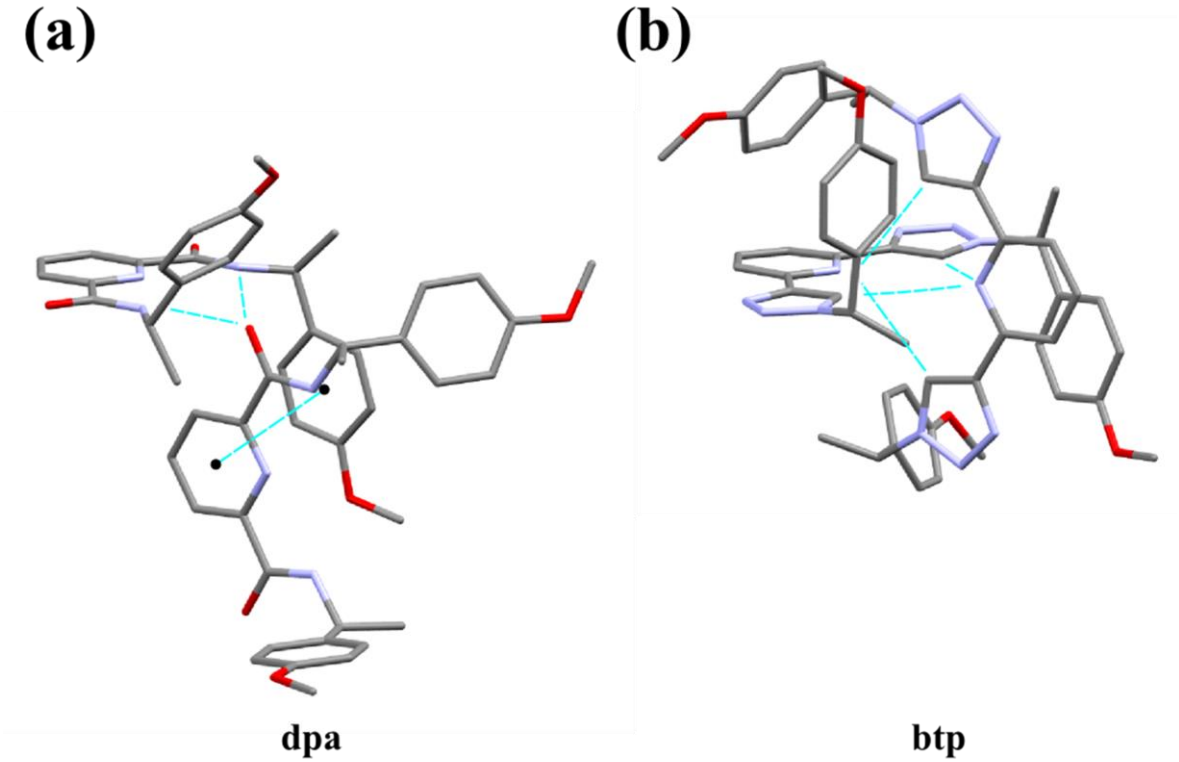

Figure 4.14 Comparison of the hydrogen-bonding and π-π stacking behaviour in the X-ray crystal structures of **dpa** ligand **102** and **btp** ligand **99**.

These structural analyses confirmed the chiral nature of these new ligands **99** and showed elegant supramolecular interactions between ligand molecules in the solid state. These studies also allowed comparison with the **dpa** analogue of these **btp** systems, showing that, despite their structural similarity, these molecules do not exhibit identical behaviour in the solid state and, in fact, form quite different hydrogen-bonding patterns.

Having synthesised these chiral **btp** ligands in a one-pot synthesis and fully characterised them, the following sections will focus on Ln(III)-directed self-assembly formation under both thermodynamic and kinetic control in CH_3CN solution.

4.6 Formation of lanthanide complexes of 99

With a view to investigating the ability of ligands **99** to sensitise Ln(III)-centred emission, complexes Eu(III) and Tb(III) were obtained by adding 0.33 equivalents of the relevant $CF_3SO_3^-$ salt to a CH_3OH suspension of the ligand. The reaction mixture was heated under microwave irradiation for 20 minutes at 70 °C and the complexes were isolated as off-white solids upon diffusion of diethyl ether into the filtered reaction mixture. Formation of the desired complexes was confirmed by HRMS MALDI+ isotopic distribution pattern matching. The experimental and calculated mass spectra for [Eu·(**99a**)$_3$](CF$_3$SO$_3$)$_3$ and

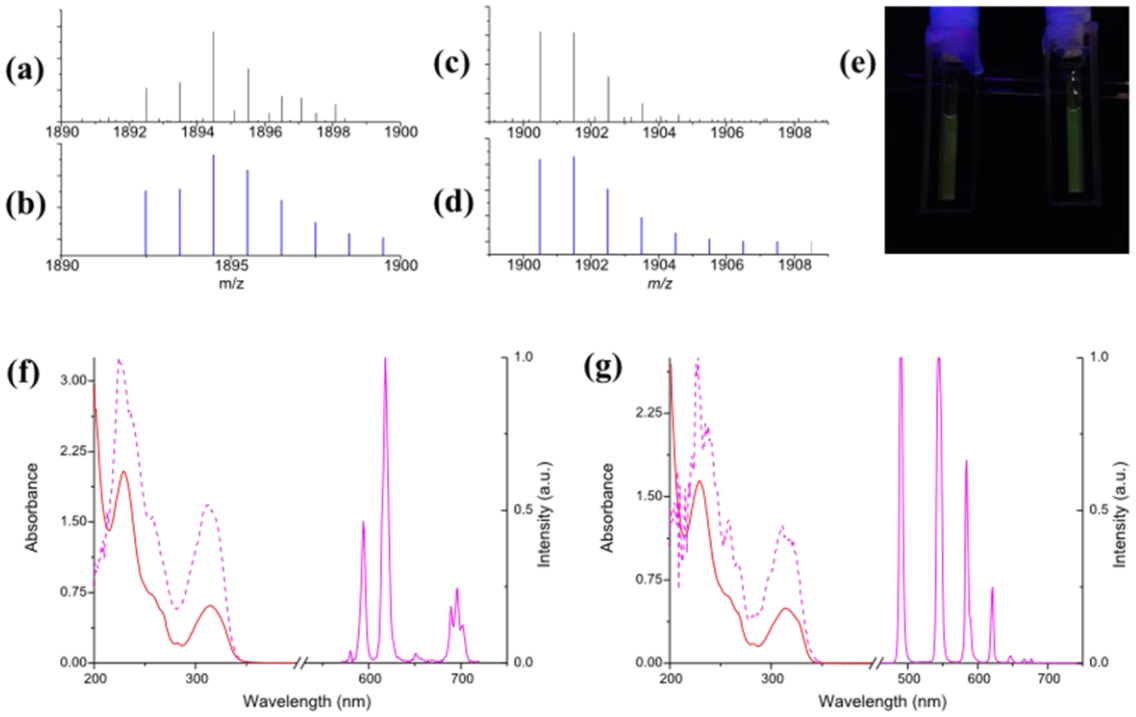

Figure 4.15 (a) Experimental and **(b)** calculated HRMS (MALDI+) spectra of [Eu·(**99a**)$_3$](CF$_3$SO$_3$)$_3$. Calculated for $C_{83}H_{81}N_{21}O_{12}F_6S_2Eu^+$ *m/z* = 1894.4932 $[EuL_3(CF_3SO_3)_2]^+$. Found *m/z* = 1894.4982; **(c)** Experimental and **(d)** calculated HRMS (MALDI+) spectra of [Tb·(**99a**)$_3$](CF$_3$SO$_3$)$_3$. Calculated for $C_{83}H_{81}N_{21}O_{12}F_6S_2Tb^+$ *m/z* = 1900.4973 $[TbL_3(CF_3SO_3)_2]^+$. Found *m/z* = 1900.5034. Spectra for the other enantiomers are shown in Appendix C; **(e)** Photographs of CH$_3$CN solutions of [Tb·(**99**)$_3$](CF$_3$SO$_3$)$_3$ under irradiation with UV light; **(f–g)** Photophysical spectra of [Eu·(**99b**)$_3$](CF$_3$SO$_3$)$_3$ and [Tb·(**99b**)$_3$](CF$_3$SO$_3$)$_3$ in CH$_3$CN solution: UV-Vis absorbance (red), phosphorescence excitation (dashed magenta) and Ln(III)-centred emission (magenta).

[Tb·(**99a**)$_3$](CF$_3$SO$_3$)$_3$ are shown in Figure 4.15, where it can be clearly seen that the experimentally measured spectra (peaks at *m/z* = 1894.4982 and 1900.5034, respectively) closely match those calculated for [Ln·(**99a**)$_3$](CF$_3$SO$_3$)$_2^+$ in each case. The identical spectra for ligand **99b** are shown in Appendix C. The ^{1}H-NMR spectra (400 MHz, CD$_3$CN) of these complexes with paramagnetic Ln(III) ions were broadened, shifted and split, and as such resonances were not assigned. The spectra were identical for both enantiomeric pairs of each complex [Ln·(**99**)$_3$](CF$_3$SO$_3$)$_3$ and are shown in Appendix C.

These complexes were observed to luminesce under irradiation with UV light, as can be seen from photographs of the Tb(III) complexes in solution in Figure 4.15(e). The sensitisation of the ligand by these ligands was confirmed by measuring photophysical spectra of [Ln·(**99**)$_3$](CF$_3$SO$_3$)$_3$ in CH$_3$CN solution, Figure 4.15(f–g), where the characteristic Ln(III)-centred emission bands were observed for both complexes, and were assigned to the $^5D_0 \rightarrow {}^7F_{0-4}$ transitions for the Eu(III) complexes and the $^5D_4 \rightarrow {}^7F_{6-0}$ transitions for the Tb(III) complexes. Excitation spectra of these emission bands matched the profile of the complex UV-Vis absorbance spectra.

Having shown that these complexes have Ln(III)-centred luminescence profiles, hydration states of the complexes were determined by measuring their luminescence lifetimes in H_2O and D_2O, using the Parker-modified Horrocks equation, Equation 3.1. The Eu(III) complexes showed long aqueous lifetimes (~2.4 ms, see Table 4.4) and a hydration state of ~0 was determined, indicating that the metal ion is fully bound by these ligands and not exposed to solvent molecule oscillators which would quench the emission. A hydration state of ~0 was also determined for the Tb(III) complexes. This exclusion of solvent molecules from the inner coordination sphere is consistent with 1:3 complex formation, where three terdentate molecules satisfy the high coordination requirements of the Ln(III) ions.

Table 4.4 Photophysical properties of complexes $[Ln\cdot(\mathbf{99})_3](CF_3SO_3)_3$: luminescence lifetimes, calculated hydration states, *q*, and total luminescence quantum yields in CH_3CN.

Complex	τ_{H2O} **(ms)**	τ_{D2O} **(ms)**	**q (±0.5)**[a]	**Φ**[b] **(%)**
$[Eu\cdot(\mathbf{99a})_3](CF_3SO_3)_3$	2.47±0.19	2.71±0.10	−0.3	0.8±0.1
$[Eu\cdot(\mathbf{99b})_3](CF_3SO_3)_3$	2.38±0.17	2.99±0.12	−0.2	0.5±0.1
$[Tb\cdot(\mathbf{99a})_3](CF_3SO_3)_3$	1.23±0.20	1.26±0.17	−0.2	56±10
$[Tb\cdot(\mathbf{99b})_3](CF_3SO_3)_3$	1.40±0.01	1.35±0.05	−0.4	67±12

[a]Calculated from Horrocks equation (Equation 3.1): for Eu(III), A = 1.2, B = 0.25 and C = 0.075; and for Tb(III) A = 5, B = 0.06 and C = 0;[212,226] [b]Quantum yields in CH_3CN were estimated by a relative method,[236] compared with $Cs_3[Ln\cdot(\mathbf{dpa}-2H)_3]$[21,22] according to the equations shown in the Experimental Chapter.

The total luminescence quantum yields, Φ, of these complexes in CH_3CN solution were poor for the Eu(III) complexes (<1%) but very high for the Tb(III) complexes (56–67%), Table 4.4, suggesting that these chiral ligands are more suited to sensitisation of the latter ion. These values were comparable to, but lower than, quantum yields observed for a very efficient Ln(III) sensitising system based on deprotonated **pytz** ligands[263], and they are similar to the quantum yields obtained for non-chiral ligand **88** in Chapter 3. This difference between the quantum yield of both Ln(III) complexes was clear to the naked eye upon viewing solutions of these complexes under irradiation with a UV lamp; a photograph of solutions of $[Tb\cdot(\mathbf{99})_3](CF_3SO_3)_3$ under such conditions is shown in Figure 4.15(e), however a photograph of the Eu(III) complex could not be easily taken since the emission was dull.

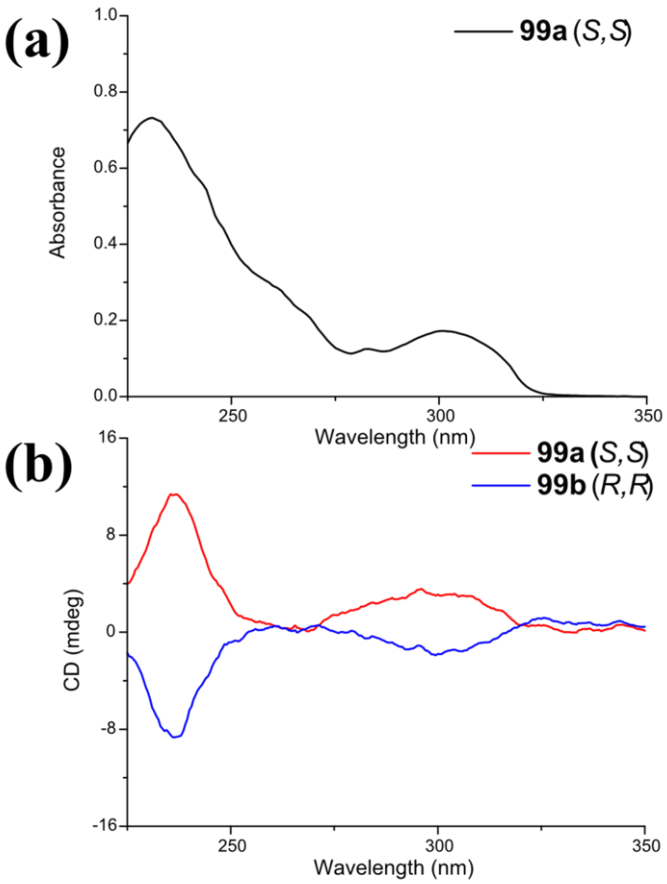

Figure 4.16 Photophysical spectra of ligands **99** measured in CH_3CN at room temperature: **(a)** UV-Vis absorbance spectrum of **99a**; **(b)** CD spectra of ligands **99a** and **99b**. [**99**] = 1.4×10^{-5} M.

4.7 Photophysical spectroscopy of 99 and Ln(III) complexes

4.7.1 Absorbance and circular dichroism

UV-Vis absorbance spectra of ligands **99a** and **99b** were measured in CH_3CN, showing a band centred at 300 nm (assigned to **btp** n→π* transitions), with a slight shoulder at 283 nm, as well as a broader band with a maximum at 230 nm (assigned to the π→π* transitions in the aromatic rings), Figure 4.16(a). The UV-Vis absorbance spectra for both ligands were identical. The enantiomers, however, will have differing chiroptical properties. Indeed, they gave CD spectra of opposite signs, with **99a** displaying positive peaks centred at 300 and 236 nm, while **99b** had negative signals at the same wavelengths, Figure 4.16(b). These bands correspond closely to the main absorbance bands.

The UV-Vis spectra of the Ln(III) complexes of **99** resembled those of the ligands, but the band centred at 300 nm underwent a red shift to 315 nm (the spectrum of [Eu·(**99a**)$_3$](CF$_3$SO$_3$)$_3$ is shown in Figure 4.17(a) as an example). The CD spectra of the complexes [Ln·(**99**)$_3$](CF$_3$SO$_3$)$_3$, Figure 4.17(b), however, were quite different to those of

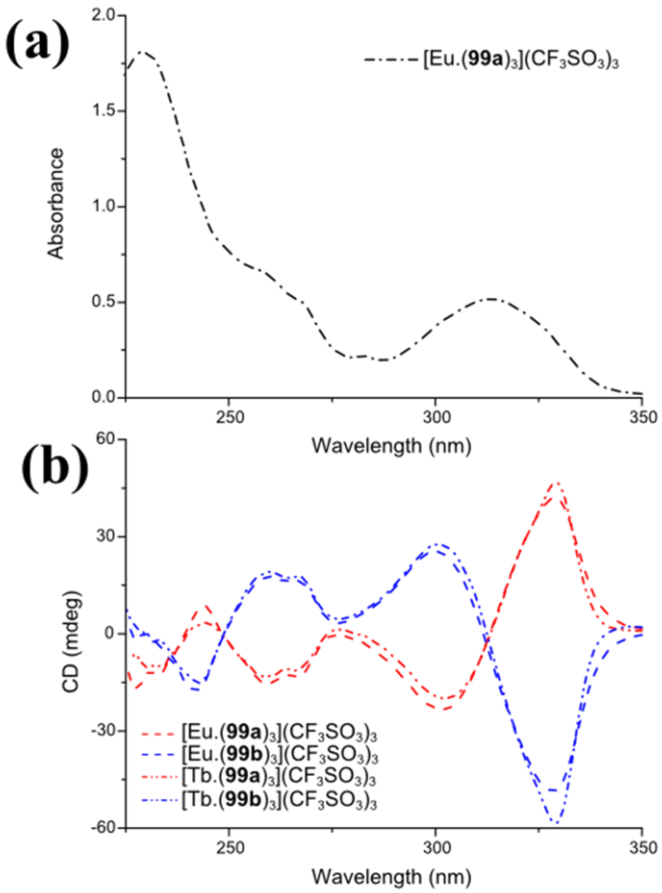

Figure 4.17 Photophysical spectra of the Ln(III) complexes of ligands **99** measured in CH_3CN at room temperature: **(a)** UV-Vis absorbance spectrum of [Eu·(**99a**)$_3$]$(CF_3SO_3)_3$; **(b)** CD spectra of the Eu(III) and Tb(III) complexes ([Ln·(**99**)$_3$]$(CF_3SO_3)_3$).

the ligands but were nearly identical for both Eu(III) and Tb(III) complexes. The spectra all display the Cotton effect in at least one of the bands, that is the bands are split in such a way that they cross zero at the absorption maximum and exhibit signals of opposite signs either side of zero; the dramatic changes were proposed to arise as a result of exciton coupling between the chromophores in adjacent ligands, brought together by the metal-directed self-assembly.[282] The spectra of the complexes of **99a** showed a large positive exciton couplet with a Davydov splitting of *ca.* 27 nm, arising from splitting of the 315 nm-centred absorbance band. Davydov splitting is the distance between the two apparent peaks in a band exhibiting the Cotton effect. A broad negative band centred at 260 nm, with a shoulder at 267 nm as well as a positive band centred at 242 nm were also observed. These high energy bands may also be assigned to a positive exciton couplet, but are less clearly resolved. The complexes of **99b** gave equal and opposite spectra.

These studies confirmed that the ligands formed retained the chirality of the amine starting materials, and also were capable of transferring this chirality into the Ln(III)-

directed self-assembly structures, which were also enatiomerically pure. The notable shifts in the UV-Vis absorbance spectra upon complexation are similar to those seen before for **btp** ligands, such as **88**, **90**, **91** and **96**, however the dramatic changes in CD spectra were remarkable and much more significant than those seen for **96** above. Consequentially, these systems are perfect candidates for CD titrations, as will be described in Section 0 below. Before describing titration studies of the self-assembly processes, however, the emission and CPL properties of these systems will be detailed.

4.7.2 Luminescence and circularly polarised luminescence

Upon excitation of ligand solution in CH_3CN, a fluorescence band centred at 335 nm was observed, as was previously seen for similar ligands, such as **88** in Chapter 3;[72] this corresponds to the ligand S_1 excited state. The ligands were capable of sensitising the characteristic Ln(III) luminescence, upon formation of the complexes as described above. Excitation into of the n→π* absorbance band resulted in the observation of characteristic Ln(III)-centred emission bands. For Eu(III) complexes, emission bands were observed at λ = 593, 617, 650 and 694 nm, arising from the $^5D_0 \rightarrow {}^7F_J$ transitions (J = 1–4), whereas for Tb(III) complexes emission bands were observed at λ = 487, 541, 580, 619 nm, which were assigned to the $^5D_4 \rightarrow {}^7F_J$ transitions (J = 6–3), Figure 4.18 (green traces). Emission related to the $^5D_0 \rightarrow {}^7F_0$ transition in the complexes [Eu·(**99**)$_3$](CF$_3$SO$_3$)$_3$ was not observed, and the $^5D_0 \rightarrow {}^7F_2$ transition was quite weak compared to the $^5D_0 \rightarrow {}^7F_1$ transition. These observations suggest the tris-**btp** complex adopts D_3 symmetry in solution.

As a result of their chiral nature, the complexes with both Eu(III) and Tb(III) were shown to exhibit CPL spectra, with each enantiomer displaying signals of equal magnitude and opposite sign for each band characteristic of a specific f–f electronic transition, Figure 4.18 (red and blue traces). For [Eu·(**99a**)$_3$](CF$_3$SO$_3$)$_3$, the $^5D_0 \rightarrow {}^7F_{1,3}$ bands were negative, while the $^5D_0 \rightarrow {}^7F_2$ band was positive; the $^5D_0 \rightarrow {}^7F_4$ transition band was split into three peaks in the total luminescence and the CPL signal for the central band was positive, while the flanking bands crossed the axis and were negative. The inverse was true for the complex of **99b**. For [Tb·(**99**)$_3$](CF$_3$SO$_3$)$_3$, all four bands observed were split such that they crossed the axis, but the central peak of the $^5D_4 \rightarrow {}^7F_5$ transition was positive, with a negative central band for the complex of **99b**. All CPL measurements were performed by Dr Robert Peacock at University of Glasgow, Scotland.

These measurements confirm the enantiomeric and chiral nature of these compounds, and also that the chirality of the ligands influences the coordination sphere of the Ln(III) ion. However, the complexes possess quite low luminescence dissymmetry factors, g_{lum} (see Equation 4.4, above), when compared to previous work by Muller[29] and by our group,[4,152,154] suggesting that the twist away from symmetrical arrangement is small. For instance, g_{lum} for the most intense transitions in the Eu(III) complex, $^5D_0 \rightarrow {}^7F_1$ and $^5D_0 \rightarrow {}^7F_2$, are −0.016 and +0.023 for **99a**, Table 4.5. The dissymmetry factor for the $^5D_4 \rightarrow {}^7F_3$ transition of the Tb(III) complexes was the largest observed, with a value of +0.085 for **99a** and −0.081 for **99b**. These values are comparable with chiral organic fluorophores.[283] The Eu(III) complexes of the *S*-enantiomers of **79** and **80**, for example, possessed g_{lum} values for the $^5D_0 \rightarrow {}^7F_2$ transition of −0.26 and −0.16, respectively.[152] Since g_{lum} values for these systems were an order of magnitude lower than those observed for analogous **dpa** systems previously studied within the group, it was concluded that the

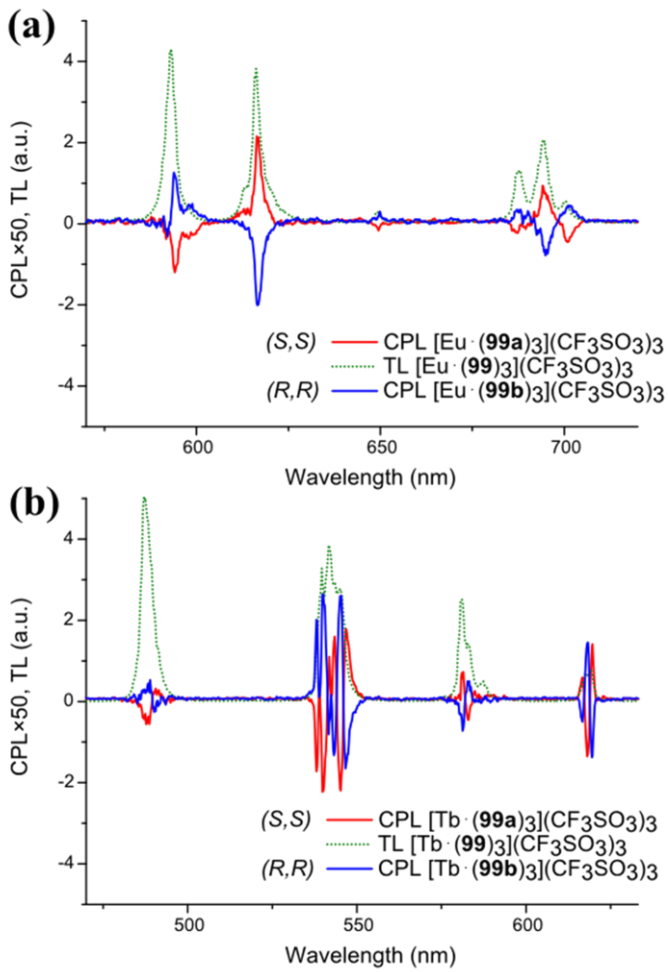

Figure 4.18 Total luminescence spectra Circularly polarized luminescence spectra in CH_3CN of both enantiomers and of **(a)** complexes [Eu·(**99**)$_3$](CF$_3$SO$_3$)$_3$; and **(b)** [Tb·(**99**)$_3$](CF$_3$SO$_3$)$_3$.

Table 4.5 Luminescence dissymmetry factors, g_{lum}, of the various transtitions of the Eu(III) and Tb(III) complexes of ligands **99**.

Electronic Transition	**Wavelength (nm)**	g_{lum}	
		[Eu·(**99a**)$_3$](CF$_3$SO$_3$)$_3$	[Eu·(**99b**)$_3$](CF$_3$SO$_3$)$_3$
$^5D_0 \rightarrow {}^7F_1$	594.0	−0.016	+0.014
$^5D_0 \rightarrow {}^7F_2$	616.4	+0.023	−0.024
$^5D_0 \rightarrow {}^7F_3$	649.0	−0.025	+0.029
$^5D_0 \rightarrow {}^7F_4$	694.5	+0.016	−0.014
		[Tb·(**99a**)$_3$](CF$_3$SO$_3$)$_3$	[Tb·(**99b**)$_3$](CF$_3$SO$_3$)$_3$
$^5D_4 \rightarrow {}^7F_6$	487.0	−0.003	+0.002
$^5D_4 \rightarrow {}^7F_5$	541.6	+0.008	−0.009
$^5D_4 \rightarrow {}^7F_4$	579.9	+0.003	−0.003
$^5D_4 \rightarrow {}^7F_3$	619.7	+0.085	−0.081

decrease in influence of ligand chirality on the coordination sphere of the Ln(III) was due to the **btp** motif, which is more rigidly planar than the former system and therefore perhaps less geometrically influenced by the chirality of its substituents.

The preceding sections, analysing the chiroptical spectroscopic properties of these Ln(III) complexes fulfil the initial aim of this chapter, which was to synthesise ligands which could impart these properties to Ln(III)-directed self-assemblies. The following section will explore the self-assembly processes in CH_3CN under kinetic control by means of various spectroscopic titrations, including the chiroptical CD technique.

4.8 Spectroscopic titrations of 99 with Ln(III) ions

Having noted the changes in UV-Vis absorbance, CD and luminescence spectra between the ligands and the thermodynamically prepared complexes in the preceding sections, it was next undertaken to exploit these spectral changes to monitor the kinetic formation of Ln(III)-directed self-assemblies in CH_3CN solution. Once again, this aprotic polar solvent was chosen to allow direct comparison between the results obtained here and the results in previous chapters. All spectra were measured at 23° C unless otherwise specified, and the results were reproducible.

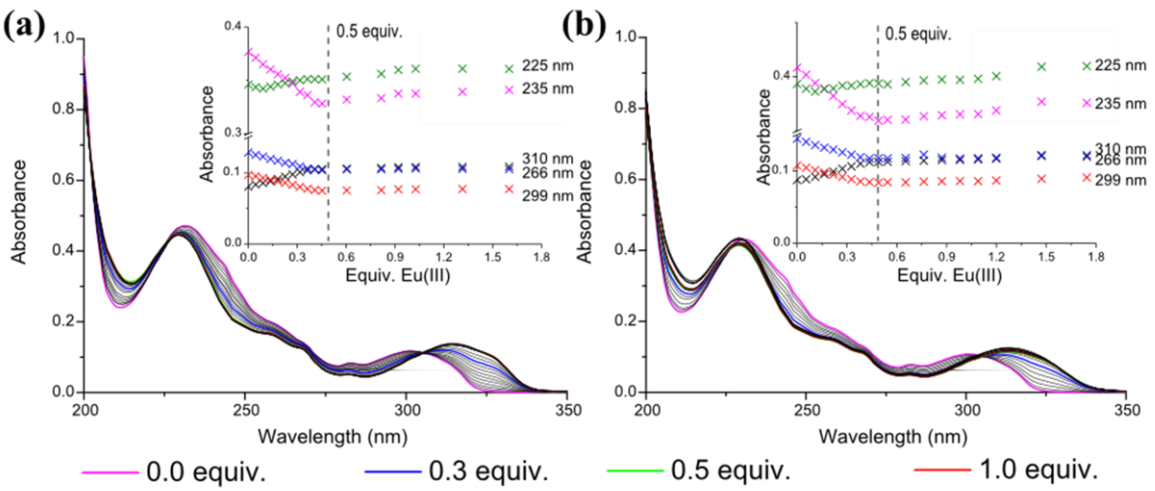

Figure 4.19 UV-Vis absorbance titrations of **(a)** ligand **99a**; and **(b)** ligand **99b** with $Eu(CF_3SO_3)_3$ in CH_3CN. [**99a**] = 0.8×10^{-5} M, [**99b**] = 0.9×10^{-5} M. Insets show experimental binding isotherms at a number of wavelengths.

4.8.1 UV-Vis absorbance titrations

The changes in the UV-Vis absorbance spectrum of a solutions of ligands **99** were monitored as a function of equivalents of Ln(III) added in CH_3CN solution. Upon addition of $Ln(CF_3SO_3)_3$ solution (Ln = Eu, Tb), the UV-Vis absorbance band centred at 300 nm, tentatively assigned to n→π* transitions, underwent a 15 nm red shift, while the more absorbing band at 231 nm shifted slightly to 229 nm with a concomitant hypochromic effect. These changes for the Eu(III) titrations with both enantiomers are shown in Figure 4.19. The majority of spectroscopic changes were complete upon addition of 0.5 equivalents, with only subtle changes seen therafter, as can be seen from the experimental binding isotherms shown as insets in Figure 4.19. The titration data possessed an isosbestic point at *ca.* 308 nm. The changes in UV-Vis absorbance spectra for the titrations with Tb(III) were identical, and are shown in Appendix C. These changes were remarkably similar to those seen for the other **btp** ligands detailed in Chapter 3.

Having probed the changes in the ground state upon binding of Ln(III) ions with UV-Vis absorbance titrations, it was next undertaken to investigate the changes in the excited states by means of emission titrations. These results will be discussed in the following section.

4.8.2 Fluorescence and Ln(III)-centred emission titrations

Simultaneously to the above monitoring in changes to the ground state of the ligand, the changes in the excited states of these systems upon addition of $Ln(CF_3SO_3)_3$ were also measured. Both the fluorescence and the Ln(III)-centred phosphorescence emission spectral changes were monitored as a function of equivalents of Ln(III) added to a CH_3CN

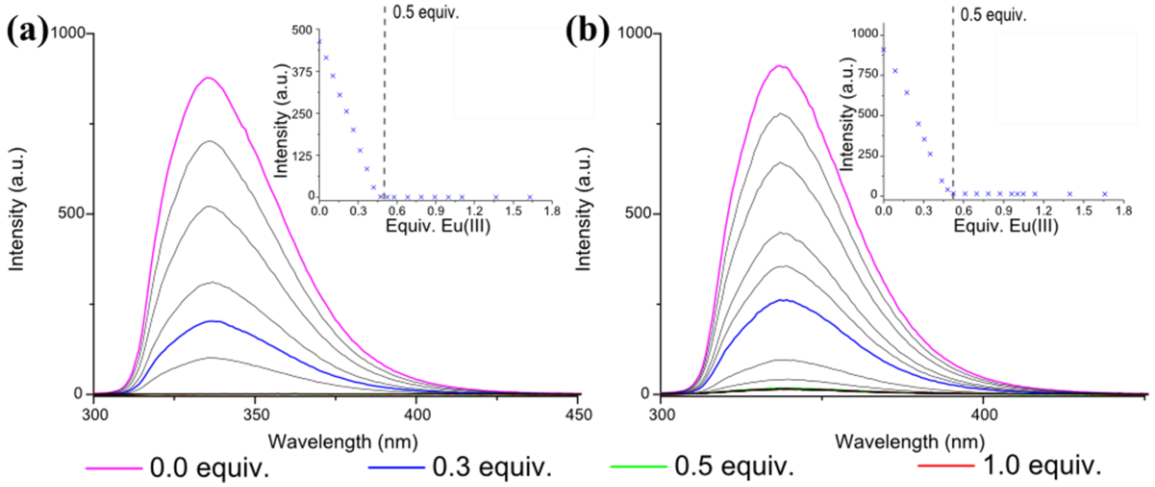

Figure 4.20 Fluorescence emission titrations of **(a)** ligand **99a**; and **(b)** ligand **99b** with $Eu(CF_3SO_3)_3$ in CH_3CN. [**99**] = 1×10^{-5} M. Insets show experimental binding isotherms at λ_{max}.

solution of **99**. Upon excitation of the ligand at 230 nm, i.e. the π→π* absorbance band, a broad fluorescence band centred at 335 nm was observed, corresponding to the ligand excited state. Excitation spectra of this emission matched the profile of the ligand UV-Vis absorbance spectrum. This emission was gradually quenched upon addition of 0→0.5 equivalents of Ln(III), as the self-assemblies form and energy is transferred to the Ln(III) excited states *via* the 'antenna' effect. These changes for the Eu(III) titrations of both enantiomers of **99** are shown in Figure 4.20. The Tb(III) titrations, which also show quenching of fluorescence from 0→0.5 equivalents of metal ion addition, are shown in Appendix C.

As fluorescence was quenched, the characteristic Ln(III)-centred emission spectra, as discussed for the isolated complexes in Section 4.7.2 above, were sensitised by ligands **99**, reaching a maximum intensity at 0.5 equivalents of Ln(III) ions. The Eu(III)-centred luminescence spectra, Figure 4.21(a), featuring the $^5D_0\rightarrow{}^7F_J$ transitions (J = 0–4) were quenched significantly after 0.5 equivalents, although the emission was never fully switched off up to 3.5 equivalents. Tb(III)-centred luminescence, featuring the $^5D_4\rightarrow{}^7F_J$ transitions (J = 6–0) is shown in Figure 4.21(b). This luminescence levelled off after 0.5 equivalents and only decreased in intensity gradually on addition of excess of Tb(III). The Tb(III) emission was much more intense than that of Eu(III), as a result of the differences in quantum yields discussed above. The titrations for **99a** are shown in Figure 4.21, while the identical plots for **99b** are given in Appendix C. These results suggest that, unlike the ligands described in Chapter 3, the 1:2 complexes of these ligands are still luminescent,

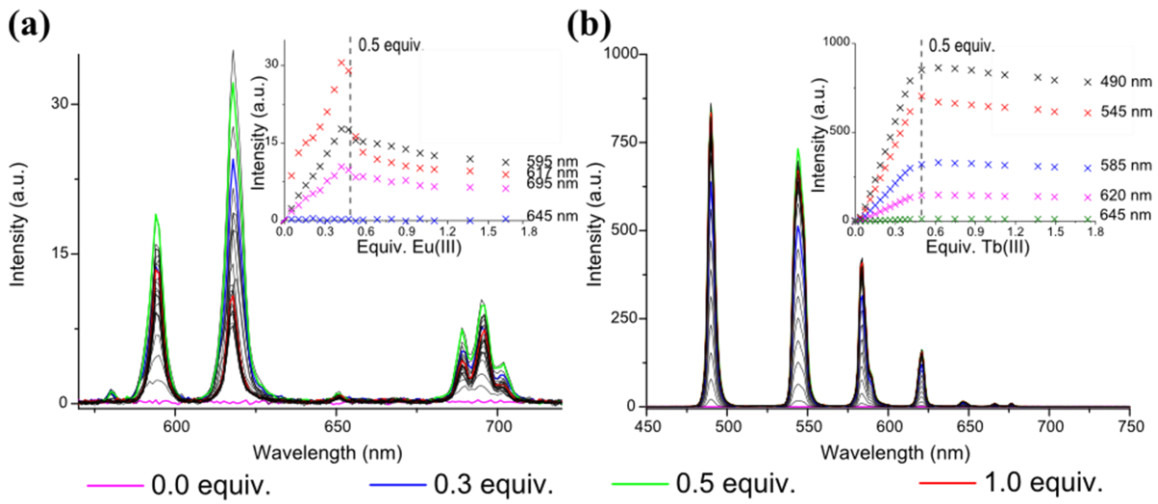

Figure 4.21 (a) Eu(III)-centred phosphorescence emission titrations of ligand **99a** with $Eu(CF_3SO_3)_3$ in CH_3CN, showing characteristic emission bands relating to Eu(III) transitions $^5D_0 \rightarrow {}^7F_J$ (J=0–4), [**99a**]=0.9×10^{-5} M; **(b)** Tb(III)-centred phosphorescence emission titrations of ligand **99a** with $Tb(CF_3SO_3)_3$ in CH_3CN, showing characteristic emission bands relating to Tb(III) transitions $^5D_4 \rightarrow {}^7F_J$ (J=6–0), [**99a**] = 1.0×10^{-5} M.

since emission does not begin to be quenched until the addition of 0.5 equivalents of Ln(III) in all cases.

In the preceding sections, investigation of the binding processes was carried out in the same way as described for ligands without chirality **88** and **90** and for ligands with negligible chiroptical properties **91** by use of UV-Vis absorbtion and emission spectroscopy. In the next section, the noteworthy chiroptical properties of these systems, outlined in Section 4.7.1 above, will be exploited to monitor the self-assembly process through CD titration studies. Such studies have not been frequently reported for Ln(III)-directed self-assembly, but such a titration was described in Section 4.4.3 above for weakly CD-active ligand **96**. This ligand is expected to yield much more insightful results.

4.8.3 CD titrations of 99

In light of the marked differences between the CD spectra of ligands **99** and their Ln(III) complexes in Section 4.7.1 above, these measurements were also used to monitor the progress of the Ln(III)-directed self-assembly of these ligands under kinetic control in CH_3CN solution. Hence, CD titrations upon addition of $Ln(CF_3SO_3)_3$ solutions to **99** and were carried out and the characteristic spectroscopic changes plotted. The results were practically identical for either Eu(III) or Tb(III). The plots of titrations for both enantiomers with Eu(III) are shown in Figure 4.22; they are mirror images of each other. The very similar titration plots with Tb(III) are shown in Appendix C.

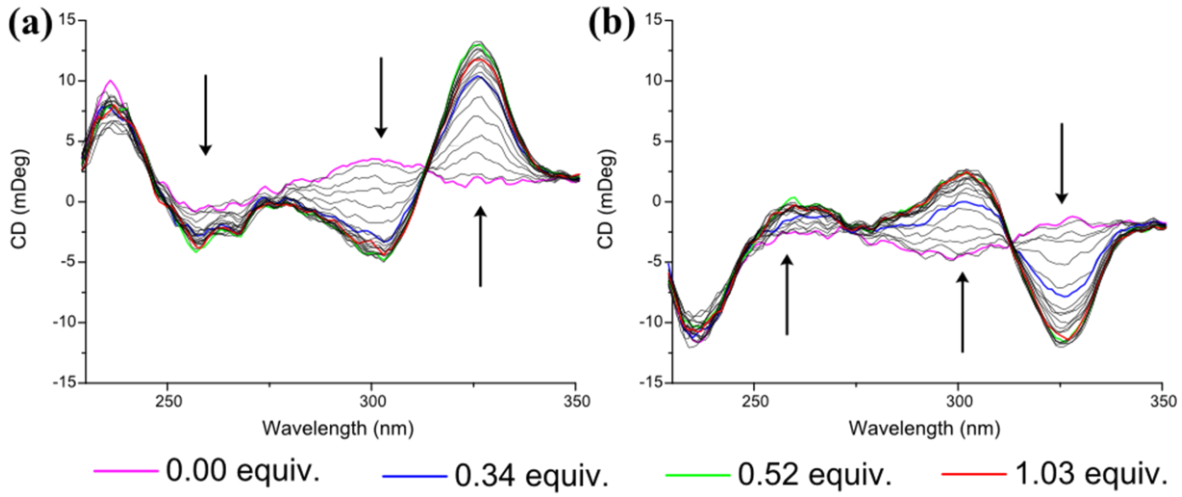

Figure 4.22 CD titration data upon addition of a solution of $Eu(CF_3SO_3)_3$ to CH_3CN solutions of **(a)** ligand **99a**; and **(b)** ligand **99b**. ([**99**] = 1.4×10^{-5} M). Spectra at 0.00, 0.34, 0.52 and 1.03 equivalents of Eu(III) are highlighted.

The ligand spectrum, as discussed above, featured bands centred at 300 and 235 nm of equal signs, for instance, for **99a**, both bands were positive, Figure 4.22(a) (magenta trace). Throughout the course of the titration, minimal changes were observed in the band centred at 235 nm, however at higher wavelengths, the band related to the n→π* transitions underwent a red shift and exhibited a Cotton effect as a result of exciton coupling upon self-assembly around the Ln(III) ion, which brought identical chromophores into close spatial proximity. For **99a**, this band appeared as a positive exciton couplet centred at 315 nm (which matches the energy of the corresponding UV-Vis absorbance band), featuring Davydov splitting of *ca.* 27 nm between the apparent maximum and minimum points in the split band's CD profile, while for the enantiomer **99b**, this band appeared as a negative exciton couplet, Figure 4.22(b). All major spectral changes were complete upon addition of 0→0.5 equivalents, after which point the spectra all maintained the general profile of the Ln(III) complex spectra discussed above. This titration show an isoelliptic point at *ca.* 313 nm.

These dramatic changes allow for clear observation of the interconversion from free ligand to Ln(III) complex, with unmistakable shifts in the CD profile reporting on the behaviour of the chiral ligands as a function of equivalents of Ln(III) added. Fitting of these data to theoretical models, discussed in the next section, represents a new departure for Ln(III)-directed self-assembly stability constant determination, having only been previously reported recently by others in the Gunnlauggson group[181], and in Section 4.4.4 above.

4.8.4 Fitting of titration data and estimation of global stability constants

As described for all the other **btp** ligands above, such as **88**, **90**, **91** and **96**, and as exploited for chiral **dpa** systems in the past, such as **2**, **79** and **81**, further insight into the binding stoichiometries and the stability of these Ln(III) self-assemblies may be obtained upon fitting the spectroscopic changes from these titrations to theoretical models. Each of the UV-Vis absorbance, luminescence and CD titration data were fit using the non-linear regression analysis program ReactLab Equilibria and global stability constants were thus determined.[237] For each set of titration data, the self-assembly processes were fit to the same stepwise equilibria detailed in Section 3.5.3 above, Equations 3.2–3.4. All attempts to fit the ligand fluorescence titrations were, unfortunately, unsuccessful.

For the UV-Vis absorbance titration data of **99a**, upon addition of $Eu(CF_3SO_3)_3$ in CH_3CN, values of logβ for the various equilibria were found to be 6.7 ± 0.1, 13.4 and 20.9 ± 0.1 for the 1:1, 1:2 and 1:3 metal:ligand self-assemblies, respectively, with very similar results for ligand **99b**. Values of binding constants for ligand **99a** with Tb(III) were of similar magnitudes, with logβ = 6.8, 13.9 ± 0.1 and 20.4, for each of the ligand coordination processes and were closely matched by the *R,R*-enantiomer. All estimated global stability constants are summarised in Table 4.6.

The experimental binding isotherms at various wavelengths and the matching theoretical binding isotherms calculated with these stability constants for **99a** are shown in Figure 4.23(a) and it can be seen that the calculated curves fit the experimental data closely. Figure 4.23(b) shows the calculated speciation distribution diagram calculated from these data, showing the calculated percentage abundance of each species as a function of

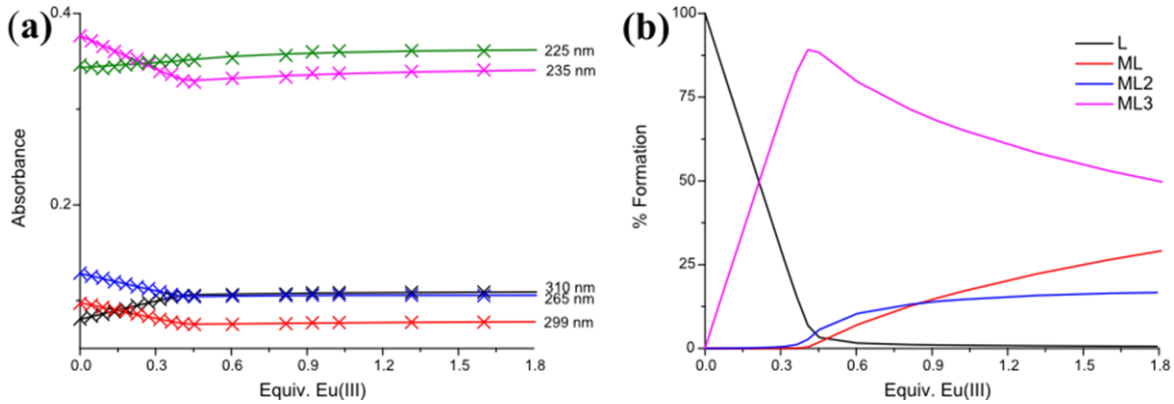

Figure 4.23 Fitting of UV-Vis absorbance titration data for ligand **99a** with $Eu(CF_3SO_3)_3$ in CH_3CN: **(a)** Experimental binding isotherms (×) and fitting curves (solid lines) calculated using ReactLab Equilibria at a range of wavelengths; and **(b)** calculated speciation distribution diagram, showing the percentage abundance of the ligand and the various metal:ligand stoichiometries as a function of equivalents of Eu(III).

Table 4.6 Global stability constants determined from UV-Vis absorbance, Ln(III)-centred phosphorescence and CD titrations of ligands **99** with Ln(III) in CH_3CN.

		Eu(III)			Tb(III)		
Ligand		**log$\beta_{1:1}$**	**log$\beta_{1:2}$**	**log$\beta_{1:3}$**	**log$\beta_{1:1}$**	**log$\beta_{1:2}$**	**log$\beta_{1:3}$**
99a	UV	6.7±0.1	13.4 [a]	20.9±0.1	6.8 [a]	13.9±0.1	20.4 [a]
99b	UV	6.7 [a]	13.8±0.1	20.9 [a]	6.8±0.1	14.5 [a]	20.4±0.1
99a	Phos.	7.0±0.1	13.8 [a]	19.0±0.1	6.8±0.1	13.7 [a]	20.8±0.1
99b	Phos.	7.0 [a]	13.2±0.1	18.9 [a]	6.6±0.1	13.7 [a]	20.3±0.1
99a	CD	7.7 [a]	14.9±0.1	21.0 [a]	7.6±0.1	14.1±0.1	20.4 [a]
99b	CD	7.7±0.1	14.9 [a]	21.0±0.1	7.1±0.1	14.2 [a]	20.4 [a]

[a] Value fixed.

equivalents of Eu(III). The 1:3 self-assembly was predicted to form in *ca.* 90% yield in solution at 0.33 equivalents of Eu(III). According to this model, which fit to the UV-Vis absorbance data, the 1:2 and 1:1 stoichiometries only existed in lower concentrations at any point, while the free ligand was not fully converted into complex until *ca.* 0.5 equivalents; this is why UV-Vis absorbance changes persist to this point, only stopping when there is no more free ligand present. This model was similar to that seen for the titration of **88** with Eu(III) in Chapter 3. Similar plots for the other sets of UV-Vis data are given in Appendix C, all predicting high concentrations of the 1:3 species at 0.33 equivalents, and also that this structure was very stable over the course of the titration, however the Tb(III) titrations support a model which suggests the formation of a more stable 1:2 stoichiometry, which dominates the solution after the addition of 0.5 equivalents of Tb(III); this is, again, consistent with the models fit for the titrations of **88** with Tb(III).

For the Eu(III)-centred luminescence titrations, the global stability constants for each of the stepwise equilibria describing the self-assembly of both enantiomers of **99** with Eu(III) were determined as log$\beta_{1:1}$ = 7.0 ± 0.1, log$\beta_{1:2}$ =13.8 and log$\beta_{1:3}$ = 19.0±0.1, Table 4.6. Experimental binding isotherms and calculated fitting curves, as well as calculated speciation distribution curves are shown in Appendix C.

Titrations monitoring the Tb(III)-centred emission upon addition of $Tb(CF_3SO_3)_3$ to **99** were also fit to theoretical models. The experimental binding isotherms and the fitting curves, which match the data very well, for the titration of **99a** with Tb(III) are shown in Figure 4.25(a). These curves were calculated with global stability constants of log$\beta_{1:1}$ = 6.8 ± 0.1, log$\beta_{1:2}$ =13.7 and log$\beta_{1:3}$ = 20.8±0.1. The constants for the enantiomeric system were comparable, Table 4.6. The speciation distribution diagrams for these models, *e.g.* Figure 4.25(b), show the stepwise formation of first the 1:3 stoichiometry, up to a maximum of

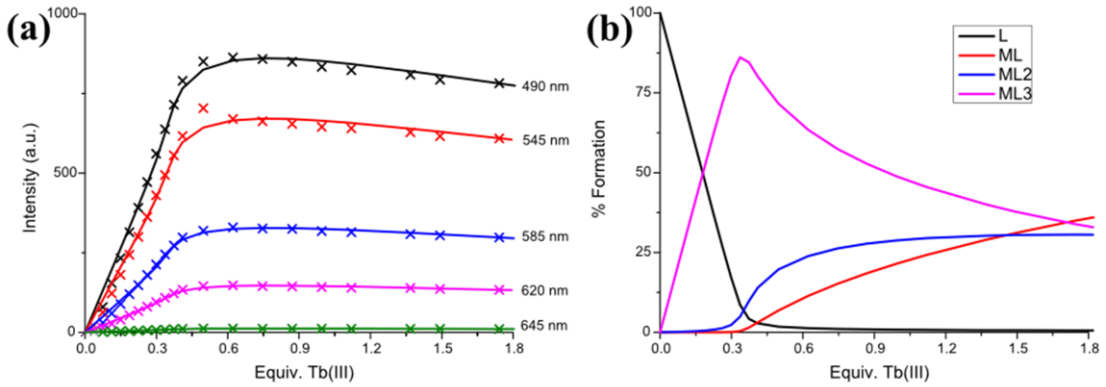

Figure 4.25 (a) Experimental binding isotherms (×) and calculated fitting curves (solid lines) for Tb(III)-centred phosphorescence titration with **99a**; and **(b)** calculated speciation distribution diagram, showing the percentage abundance of the ligand and the various metal: ligand stoichiometries as a function of equivalents of Tb(III)

75–90% at 0.33 equivalents of Tb(III), followed by the formation of the 1:2 stoichiometry , and finally the emergence of the 1:1 stoichiometry at higher concentrations of metal ion.

CD titration data were fit to theoretical models too, as above, giving binding constants of $\log\beta_{1:1}$ = 7.7, $\log\beta_{1:2}$ = 14.9 ± 0.1 and $\log\beta_{1:3}$ = 21.0 for Eu(III) with **99a** and identical results for **99b**. The experimental binding isotherms and fitting curves for the titration of Tb(III) with both enantiomers of **99** are shown in Figure 4.24; these were calculated with global stability constant values of $\log\beta_{1:1}$ = 7.6 ± 0.1, $\log\beta_{1:2}$ = 14.1 ± 0.1 and $\log\beta_{1:3}$ = 20.4 for the *S,S*-enantiomer and $\log\beta_{1:1}$ = 7.1 ± 0.1, $\log\beta_{1:2}$ = 14.2 and $\log\beta_{1:3}$ = 20.4 for the *R,R*-enantiomer, Table 4.6. Fitting curves for the other titrations and calculated speciation distribution diagrams are shown in Appendix C. The speciation distribution diagrams calculated for the Eu(III) titrations are shown in Figure 4.27. These models indicate the formation of the 1:3 assembly in high concentration (*ca.* 65%) at 0.33 equivalents of Eu(III), with subsequent formation of the 1:2 and the 1:1 self-assemblies. The free ligands

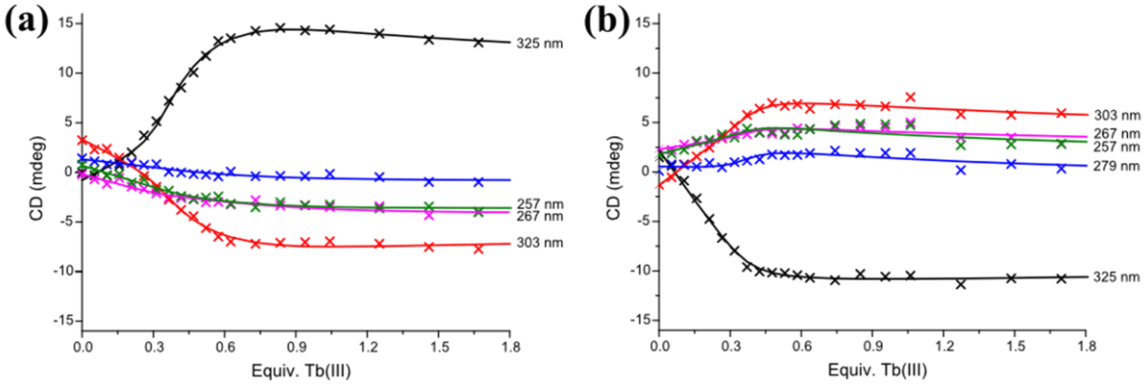

Figure 4.24 Experimental binding isotherms (×) and calculated fitting curves (solid lines) for CD titrations with $Tb(CF_3SO_3)_3$ of **(a) 99a**; and **(b) 99b**.

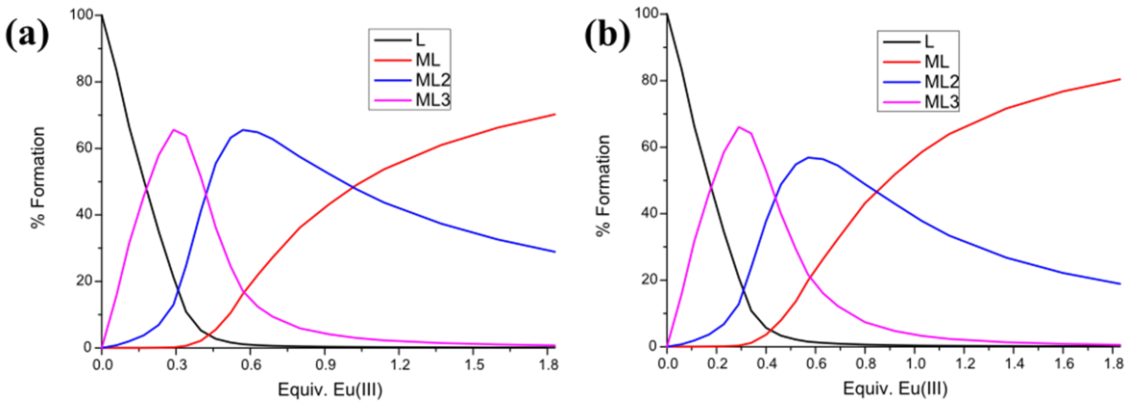

Figure 4.27 Calculated speciation distribution diagrams for CD titrations of $Eu(CF_3SO_3)_3$ with ligands **(a) 99a**; and **(b) 99b**.

persisted in solution, according to these models, until *ca.* 0.5 equivalents, after which the changes in the CD spectra were practically unchanged upon further addition of Ln(III). Consequentially, although the speciation distribution diagrams derived from the Tb(III) CD titrations, Appendix C, model the formation of the 1:3 self-assembly and disappearance of free ligand very similarly, they differ in the calculated relative abundances of the 1:2 and 1:1 stoichiometries at higher Tb(III) concentrations, since there were minimal spectroscopic difference between these species.

Since significant changes occur in the CD spectra upon complexation, recalculated spectra for each stoichiometry can be considered a 'fingerprint' for each species in solution, Figure 4.26, however, as indicated above, this is most applicable to definitively distinguishing the ligand from the metal complexes; this demonstrates the potential for CD

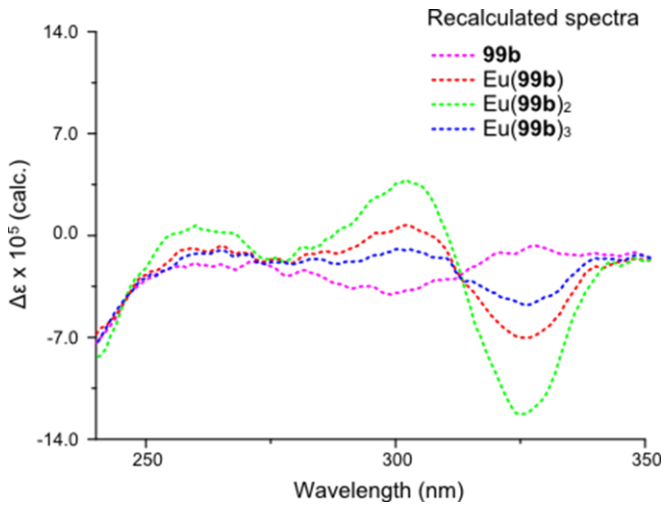

Figure 4.26 Recalculated CD spectra of each stoichiometric species upon self-assembly of **99b** with Eu(III) in CH_3CN.

titrations to probe the metal-directed self-assembly of supramolecular systems, as an alternative to, or in complement to the other well-established spectroscopic techniques described above. Satisfyingly, the values of global stability constants determined by all of the techniques discussed above, including CD titrations, are very similar to each other. This allows a reasonable degree of confidence in the results determined by this new method, thereby validating the technique, which is expected to be applied systematically to chiral self-assembly formation studies with Ln(III) ions in future.

As well as having comparable values of logβ across the different techniques, these values for **99** are also comparable to both those reported in the previous chapter for optically inactive ligands. They compare well with similar compounds in the literature, also. The log$\beta_{1:3}$ values were higher than some, such as the deprotonated **pytz** ligands reported by Mazzanti and co-workers[263], a bis(diisopropylamide)-derivative of **dpa** reported by Le Borgne *et al.*[239] and half-helicate **81b** (17.2, 17.6 and 17.4 respectively); and lower than others, including chiral **dpa** ligands **2**[29] and a bis(diethylamide)-derviative reported by Bünzli and co-workers[15] (23.8 and 22.3, respectively). However, most **dpa** ligands previously studied within the Gunnlaugsson group, discussed in Section 1.9 above, had global binding constants of a similar order of magnitude to those reported here, *e.g.* **79** and **80** (20.3 and 21.6, respectively).[152] Before moving on and presenting similar self-assembly studies with ligand **100**, some preliminary work will briefly be discussed, where ligands **99** were encapsulated in polymeric hydrogel matrices and swollen in aqueous Ln(III) solutions to produce luminescent materials.

4.9 Preliminary hydrogel studies

As discussed in Section 3.16 above, hydrogels can form functional materials with applications such as drug delivery[256] and antigen sensing[257]. Encapsulation of Ln(III)-sensitising systems into hydrogels may, for instance, act as sensors for pH.[260,261] It was expected that incorporating the ligands described above into hydrogel matrices would result in materials possessing chiral luminescent properties.

Suspending a single enantiomer of ligand **99** (0.05% w/w), along with cross-linker ethylene eglycol dimethacrylate (1% w/w) and radical initiator AIBN (1% w/w) in liquid monomer HEMA, followed by incubation in an oven at 90 °C for 4 hours, encapsulated the **btp** binding pocket into brittle transparent plastic materials, namely cross-linked poly(HEMA). These materials, however, when swelled in aqueous $Ln(CF_3SO_3)_3$ solutions, gave rise to flexible transparent soft hydrogels, which were clearly luminescent and gave

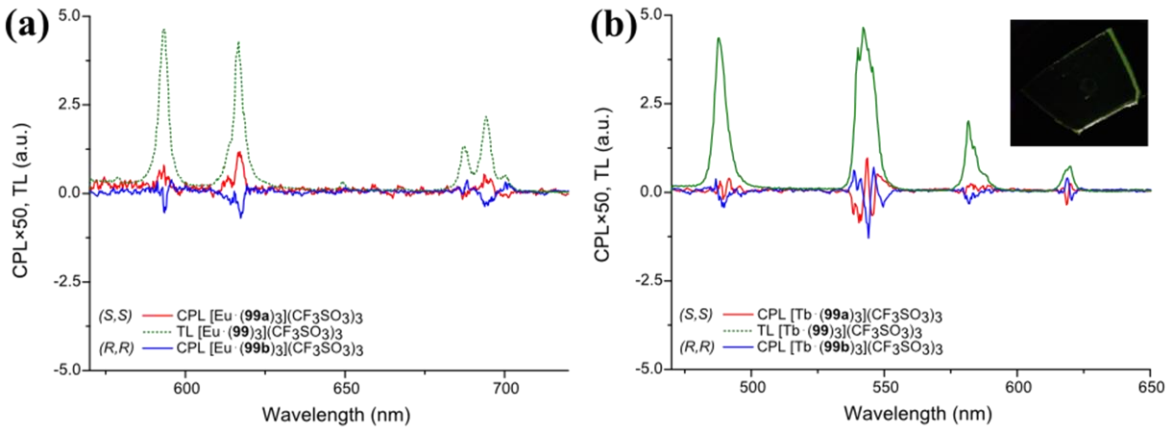

Figure 4.28 Total luminescence and CPL spectra of HEMA hydrogels containing both enantiomers of **99** swelled in aqueous solutions of **(a)** $Eu(CF_3SO_3)_3$; **(b)** $Tb(CF_3SO_3)_3$; *inset*: photograph of a gel containing **99a** swelled with $Tb(CF_3SO_3)_3$ under irradiation with UV light.

rise to characteristic Ln(III)-centred emission under UV light irradiation; these emission profiles are shown as dashed green traces in Figure 4.28, and the coloured phosphorescence was clearly visible to the naked eye under a UV lamp (*cf.* inset in Figure 4.28(b)). This sensitisation of Ln(III)-centred luminescence is indicative of a self-assembly process occurring within the polymer matrix. The CPL spectra of dried samples of these hydrogels, with the Ln(III) ion incorporated, were measured, Figure 4.28, and the material was indeed shown to impart the ligands' ability to sensitise CPL emission to the new material. This work was undertaken in contribution to an on-going project in collaboration with Mr Samuel Bradberry, a member of the Gunnlaugsson group, and Dr Robert Peacock in University of Glasgow.[262]

UV-Vis absorbance spectra of this gels showed a broad band centred around 310 nm, characteristic of the **btp** motif, although below 260 nm the matrix absorbed dramatically and no other peaks could be seen. Ln(III)-centred emission spectra from the poly(HEMA) materials resemble those measured for the complexes in solution, with excitation spectra for all hydrogels, Appendix C, showing peaks centred at 320 nm and 260 nm, which broadly match the excitation spectra of the complexes in solution. The hydrogel CPL spectra, however, differ significantly from those of the complexes in CH_3CN solution in Section 4.7.2 above. For the Eu(III)-containing materials, all of the bands have the same sign (all are positive for the hydrogel encapsulating ligand **99a**), in contrast to the complex solution CPL spectrum, where the $^5D_0 \rightarrow {}^7F_1$ transition gave a band of the opposite sign. It is worth noting that the Eu(III) total luminescence shows the $^5D_0 \rightarrow {}^7F_0$ transition, which was not seen for the solution CPL of $[Eu\cdot(\mathbf{99})_3](CF_3SO_3)_3$ above, suggesting a decrease in

Table 4.7 Luminescence dissymmetry factors, g_{lum}, of the various transtitions of the Eu(III) and Tb(III) – swelled hydrogels with ligands **99** encapsulated.

Electronic Transition	**Wavelength (nm)**	g_{lum}	
		[Eu·(**99a**)$_3$](CF$_3$SO$_3$)$_3$	[Eu·(**99b**)$_3$](CF$_3$SO$_3$)$_3$
$^5D_0\rightarrow{}^7F_1$	594.0	+0.005	−0.005
$^5D_0\rightarrow{}^7F_2$	616.7	+0.010	−0.008
$^5D_0\rightarrow{}^7F_4$	694.5	+0.011	−0.007
		[Tb·(**99a**)$_3$](CF$_3$SO$_3$)$_3$	[Tb·(**99b**)$_3$](CF$_3$SO$_3$)$_3$
$^5D_4\rightarrow{}^7F_6$	488.0	+0.003	−0.002
$^5D_4\rightarrow{}^7F_5$	544.0	+0.011	−0.013
$^5D_4\rightarrow{}^7F_4$	582.5	+0.006	−0.007
$^5D_4\rightarrow{}^7F_3$	618.5	−0.022	+0.026

complex symmetry within the material, perhaps with the presence of a bound water molecule. The CPL spectra of the Tb(III)-containing hydrogels differed less significantly from the complex solutions, with the $^5D_4\rightarrow{}^7F_{5,3}$ transitions showing similar shapes and signs. The $^5D_4\rightarrow{}^7F_{6,4}$ transitions, however, were not split and did not cross the x-axis for these hydrogels (both bands are positive for the Tb(III)-swelled hydrogel encapsulating ligand **99a**). The luminescence dissymmetry factors, g_{lum}, Table 4.7, for these systems also differed from the complex solutions and were generally lower for the Eu(III) systems (*e.g.* +0.010 v. +0.023 for the $^5D_0\rightarrow{}^7F_2$ transition), and of similar magnitude for the Tb(III) systems (*e.g.* +0.008 v. +0.011 for the $^5D_4\rightarrow{}^7F_5$ transition). The stoichiometry of the species within the material is, as yet, uncertain. Further studies on these systems will be undertaken in the future to ascertain this information.

Having studied the self-assembly behaviour of **99** with Ln(III) ions in depth and showing these ligands to be suitable for the formation of chiral emissive Ln(III) complexes with chiroptical properties, it was next undertaken to investigate the same self-assembly processes with ligands **100**, the **btp** analogue of the '*Trinity Sliotar*' ligands **79** studied at length in the Gunnlaugsson group previously.[4,152] Here Eu(III) was chosen as the Ln(III) ion for these studies, since this was used in previous studies of the **dpa** analogies, in order to allow for direct comparison. The naphthyl chromophores have been shown to act as 'antennae' for Eu(III)-centred emission previously. The self-assembly process will then be monitored by UV-Vis absorbance, fluorescence, Eu(III)-centred luminescence and CD titrations in Section 4.12.

4.10 Formation of Eu(III) complexes of 100

Eu(III) complexes of naphthyl ligand **100** were formed similarly to the other Ln(III) complexes discussed thus far by microwave irradiation with 0.33 equivalents of $Eu(CF_3SO_3)_3$ in CH_3OH at 70 °C for 20 minutes. These ligands were shown to sensitise the characteristic Eu(III) emission spectrum, Figure 4.29(a), with excitation spectra which match the general structure of the absorbance spectrum. Hence the luminescence lifetimes of the most intense emission at 617 nm were recorded. These complexes were particularly insoluble in aqueous media and did not give reliable lifetimes, hence luminescence lifetimes were measured in CH_3OH and CD_3OD solutions. Hydration states of the complexes, *q*, were determined according to Horrocks Equation, modified for this solvent system. The *q* values determined are lower than expected (−0.7 ± 0.5), however they seem to suggest the absence of bound water molecules and formation of fully coordinatively saturated 1:3 self-assemblies, but also that some other quenching processes beyond inner sphere solvent quenching is at play in these systems.

The successful formation of $[Eu\cdot(\mathbf{100})_3](CF_3SO_3)_3$ was, however, confirmed by ESI+ HRMS analysis, with the complexes of both enantiomers giving an isotopic distribution pattern matching the calculated signal for $[Eu\cdot(\mathbf{100})_3](CF_3SO_3)^{2+}$ at *m/z* = 933.2875, Figure 4.29. Although these ligands did sensitise the characteristic Eu(III)-centred emission, their total quantum yields, Φ, were low at 1.3 and 1.4 ± 0.2 % for the *S,S*- and *R,R*-enantiomers, respectively. This is, however, a better sensitising 'antenna' for Eu(III) than **99** above, albeit significantly less efficient that the **dpa** analogue **79**, the *S,S*-enantiomer of which

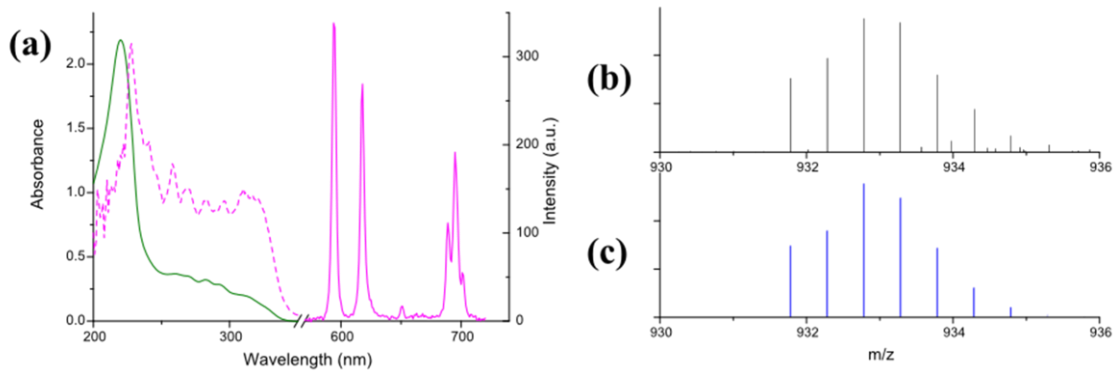

Figure 4.29 (a) Photophysical spectra of a CH_3CN solution of $[Eu\cdot(\mathbf{100a})_3](CF_3SO_3)_3$: UV-Vis absorbance (green), Eu(III)-centred emission (magenta) and excitation spectrum (dashed magenta); **(b)** Experimental and **(c)** calculated HRMS (ESI+) spectra of $[Eu\cdot(\mathbf{100a})_3](CF_3SO_3)_3$. Calculated for $C_{100}H_{81}N_{21}O_3F_3SEu^{2+}$ *m/z* = 933.2800 $[EuL_3(CF_3SO_3)]^{2+}$. Found *m/z* = 933.2887.

formed luminescent Eu(III) complexes with quantum yields of 7.6 ± 0.5 %. The Tb(III) complexes might be expected to be more emissive based on observations for the **btp** ligands described above. Studies with Tb(III) have not yet been undertaken, but will be carried out in the future. The IR spectra of these complexes were quite simple and dominated by bands at 778, 1028, 1155 and 1250 cm^{-1}, the latter associated with the $CF_3SO_3^-$ counterions and the others resembling ligand bands. The ^{1}H-NMR spectra (400 MHz, CD_3CN) of these complexes, shown in Appendix C, were broadened and shifted dramatically by the paramagnetic Eu(III) ions, and so were not assigned; the spectra were identical for both of the enantiomeric complexes.

Having shown that ligands **100** can form emissive Eu(III), it was next undertaken to investigate the basic photophysical spectroscopic properties of these ligands and complexes in CH_3CN solution. All measurements were carried out at 23 °C.

Table 4.8 Photophysical properties of complexes [Eu·(**100**)$_3$](CF$_3$SO$_3$)$_3$: luminescence lifetimes, calculated hydration states, *q*, and total luminescence quantum yields in CH_3CN.

Complex	τ_{CH3OH} **(ms)**	τ_{CD3OD} **(ms)**	***q*** **(±0.5)**[a]	**Φ**[b] **(%)**
[Eu·(**100a**)$_3$](CF$_3$SO$_3$)$_3$	2.24±0.05	2.09±0.15	−0.7	1.3±0.2
[Eu·(**100b**)$_3$](CF$_3$SO$_3$)$_3$	2.00±0.09	1.81±0.06	−0.7	1.4±0.2

[a]Calculated from the Horrocks equation (Equation 3.1): for Eu(III), A = 2.4, B = 0.25 and C = 0.075;[212,226] [b]Quantum yields in CH_3CN were estimated by a relative method,[236] compared with $Cs_3[Eu\cdot(\mathbf{dpa}-2H)_3]$[21,22] according to the equations shown in the Experimental Chapter.

4.11 Photophysical spectroscopy of 100 and Eu(III) complexes

4.11.1 Absorbance and circular dichroism

The UV-Vis absorbance spectra of **100** displayed a broad absorbance profile, Figure 4.30(a). A shoulder centred at 300 nm was related to the **btp** motif, resembling similar shoulder seen for **91-Trp** in Chapter 2, while the fine structure peaks at 292, 280 and 270 nm related to the naphthalene π→π* transitions. There was also a higher-energy, very absorbing band centred at 223 nm, with a shoulder at 245 nm. The identical spectrum of **100a** is shown in Appendix C.

The two enantiomers of **100** gave CD signals of equal magnitude and opposite sign with two distinctive bands centred at 300 and 230 nm. Both bands appeared to show a weak Cotton effect of the same sign (positive couplets for **100a** and negative for **100b**). The 230 nm transition was much more intense and had a shoulder at 245 nm, Figure 4.30(b). These spectra differ from both those of **99** above, and those of **79**[152] which did not show the Cotton effect for the ligands CD bands.

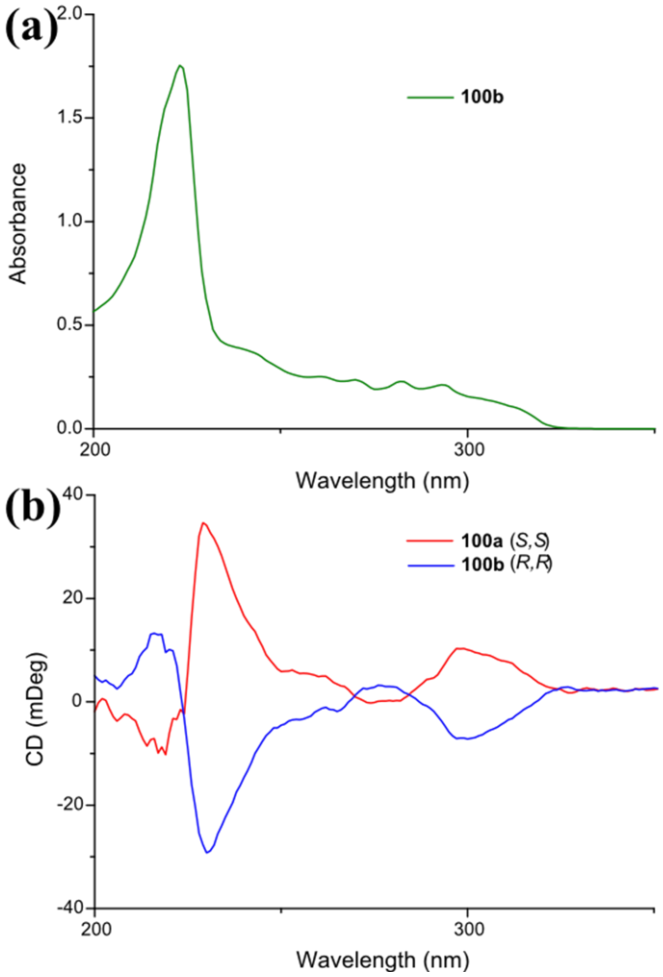

Figure 4.30 Photophysical spectra of ligands **100** measured in CH_3CN at room temperature: **(a)** UV-Vis absorbance spectrum of **100b**; **(b)** CD spectra of ligands **100a** and **100b**. [**100**] = 1.2×10^{-5} M.

The most significant changes seen in the UV-Vis absorbance spectra of **100** upon complexation of the ligand were in the lowest energy absorbance band, which was seen to shift to 315 nm; this shift was analogous to those changes in the n→π* absorbance band seen in all the **btp** ligands discussed above. The same order of red shift was observed in the CD spectra. The Cotton effect was also seen in the CD spectra of these complexes; this red shifted band exhibited exciton coupling, appearing as a positive couplet in the spectrum of [Eu·(**100a**)$_3$](CF$_3$SO$_3$)$_3$ centred at 315 nm with Davydov splitting of *ca.* 27 nm, Figure 4.31(b). This behaviour resembled that seen for **99** above. The complex of **100b** featured a negative exciton couplet. The remainder of the spectra, as measured by either technique, changed only slightly in response to complexation.

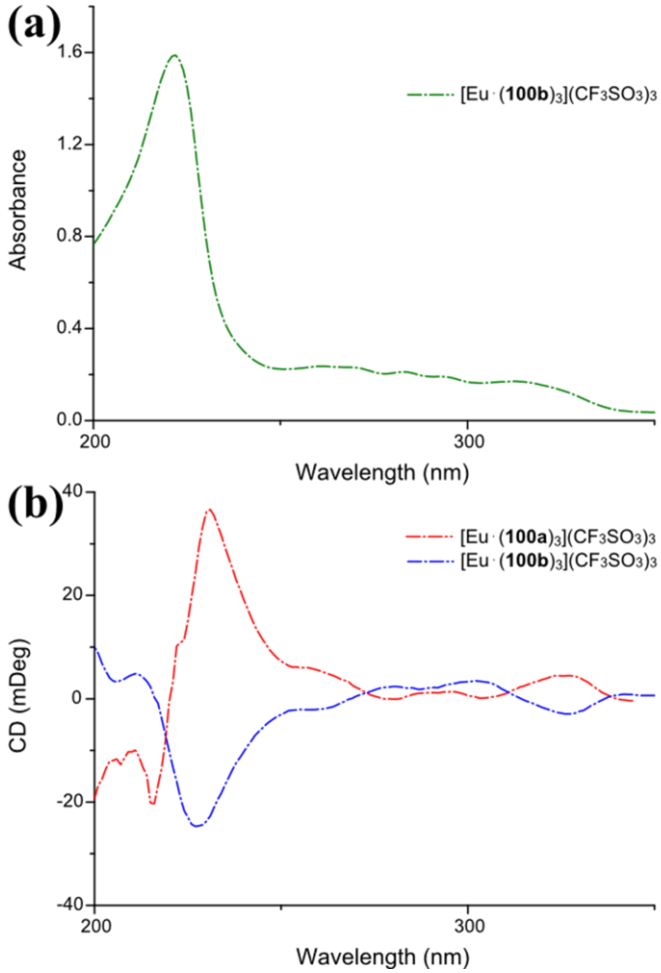

Figure 4.31 Photophysical spectra of complexes of [Eu·(**100**)$_3$](CF$_3$SO$_3$)$_3$ measured in CH$_3$CN at room temperature: **(a)** UV-Vis absorbance spectrum of [Eu·(**100b**)$_3$](CF$_3$SO$_3$)$_3$; **(b)** CD spectra of the Eu(III) complexes of both enantiomers of **100**.

These studies confirmed that the ligands formed retained the amine chirality, and were capable of transferring this chirality into the structure of the Ln(III)-directed self-assemblies formed, which were also enatiomerically pure. The dramatic changes in CD spectra were remarkable and similar to those seen above for **99**. Consequentially, these systems are perfect candidates for CD titrations, which will be described in Section 4.12.3. Before embarking on description of titration studies of the self-assembly processes, the emission and CPL properties of these systems will be detailed.

4.11.2 Luminescence and circularly polarised luminescence

These ligands **100** exhibited the same kind of fluorescence from the ligand excited state at 335 nm as was seen for all of the other **btp** ligands described in this thesis. As was mentioned above, these ligands are capable of sensitising the excited states of the Eu(III) ion *via* the 'antenna' effect and giving rise to characteristic emission. The profile of the

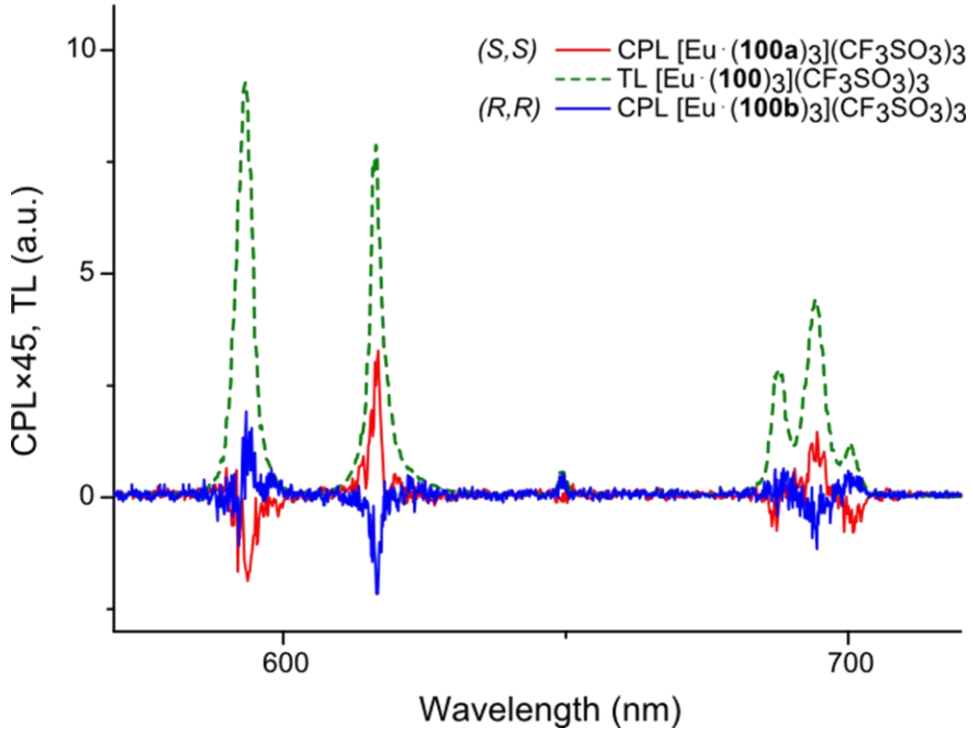

Figure 4.32 Eu(III)-centred emission total luminescence spectrum and CPL spectra (×45) of [Eu·(**100a**)$_3$](CF$_3$SO$_3$)$_3$ and [Eu·(**100b**)$_3$](CF$_3$SO$_3$)$_3$ measured in CH$_3$CN at room temperature.

Eu(III)-centred emission spectra of complexes [Eu·(**100**)$_3$](CF$_3$SO$_3$)$_3$ in CH$_3$CN, Figure 4.32, differ significantly from those of the complexes of **99** above. Most notably, the band, associated with the $^5D_0 \rightarrow {}^7F_1$ transition is larger than the hypersensitive $^5D_0 \rightarrow {}^7F_2$ emission band, suggesting a species with a centre of inversion. The absence of the $\Delta J = 0$ band is also supportive of this hypothesis.

The weak CPL spectra of [Eu·(**100**)$_3$](CF$_3$SO$_3$)$_3$ in CH$_3$CN are shown in Figure 4.32. The luminescence dissymmetry factors, g_{lum}, for the strongest transitions were small: −0.008, 0.014 and 0.008 for the $^5D_0 \rightarrow {}^7F_J$ transitions, where J = 1, 2 and 4, respectively. These are an order of magnitude lower than the g_{lum} values measured for the analogous complexes with **79**, *e.g.* for the $^5D_0 \rightarrow {}^7F_2$ transition of [Eu·(**79**)$_2$](CF$_3$SO$_3$)$_3$ had a dissymmetry factor of −0.16.[152] As discussed above, the rigidity of the **btp** moiety may be responsible for decreasing the effect the chiral centre has on the coordination sphere of the

Table 4.9 Luminescence dissymmetry factors, g_{lum}, of the various transtitions of the Eu(III) complexes of ligands **100**.

Electronic Transition	**Wavelength (nm)**	g_{lum}	
		[Eu·(**99a**)$_3$](CF$_3$SO$_3$)$_3$	[Eu·(**99b**)$_3$](CF$_3$SO$_3$)$_3$
$^5D_0 \rightarrow {}^7F_1$	593.0	-0.008	+0.010
$^5D_0 \rightarrow {}^7F_2$	616.4	+0.014	−0.017
$^5D_0 \rightarrow {}^7F_4$	694.5	+0.008	−0.006

Eu(III) ion, as compared to the **dpa** ligands, however this is still one of the first examples of a **btp** ligand sensitising Ln(III)-centred CPL emission. The spectra were also of the opposite sign to the '*Trinity Sliotar*' complexes, meaning that absolute configuration (Δ/Λ) of the complexes could not be confidently assigned by analogy as was done for complexes **81b** in the absence of a crystal structure.[181]

As has been done for the other systems described in this thesis, the self-assembly titrations of **100** with Eu(III) in CH_3CN solution was investigated by means of spectroscopic titrations . This will be discussed in the following sections.

4.12 Spectroscopic titrations of 100 with Eu(III)

4.12.1 UV-Vis absorbance titrations

The changes in the UV-Vis absorbance spectrum of solutions of ligands **100** were monitored as a function of equivalents of $Eu(CF_3SO_3)_3$ added in CH_3CN solution. Upon addition of Ln(III) solution, the UV-Vis absorbance bands centred at 292, 282 and 270 nm decreased in absorbance as the shoulder centred at 300 nm red shifted by 15 nm becoming more resolved upon self-assembly. A shoulder seen in the ligand spectra at 245 nm disappeared upon complexation while the strongly absorbing band at 224 nm underwent a concomitant hypochromic shift. All of these changes were identical for both enantiomers, as is shown in Figure 4.33. The majority of changes were complete upon addition of 0.33 equivalents of metal ion for both enantiomers of the ligand, as shown in the insets in Figure 4.33, however the broad band centred at 223 nm continued to display slight

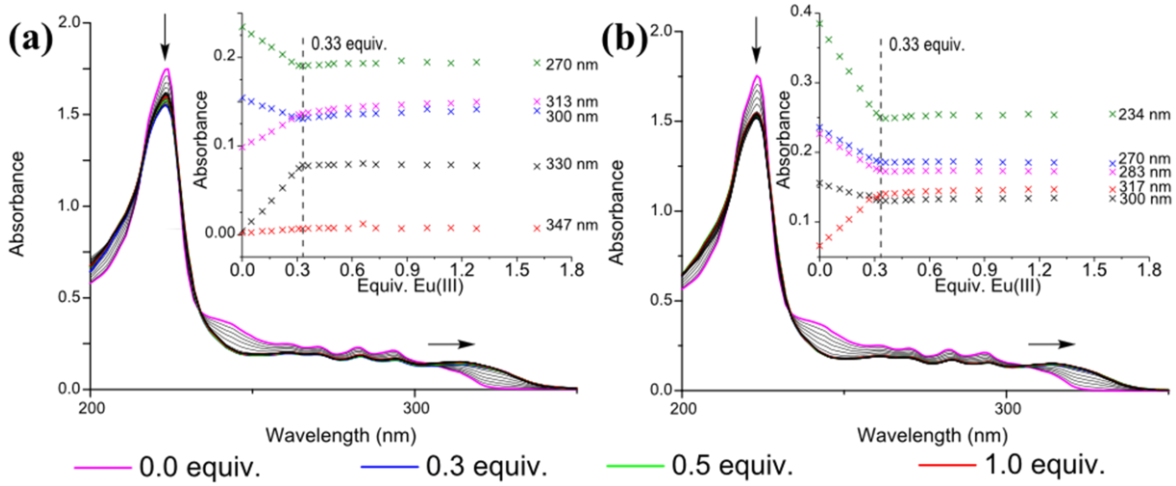

Figure 4.33 UV-Vis absorbance spectral changes upon addition of Eu(III) in CH_3CN for **(a) 100a** and **(b) 100b**. [**100**] ≈ 1.1×10^{-5} M in each case. Insets show experimental binding isotherms at various wavelengths.

hyperchromicity as addition of Eu(III) continued beyond 0.33 equivalents. The titration data displayed isosbestic points at 215, 227, 234 and 305 nm.

These observations suggest that the 1:3 assembly is formed initially, after which there are only minor spectral changes upon further addition of metal ion. Having monitored the ground state changes of this system, the changes in the excited states were next investigated, by means of fluorescence and phosphorescence titration studies.

4.12.2 Fluorescence and Eu(III)-centred emission titrations of 100

The changes in the fluorescence and Ln(III)-centred phosphorescence emission were monitored as a function of equivalents of $Eu(CF_3SO_3)_3$ added to a CH_3CN solution of the ligand as well. Ligand fluorescence from **100**, a broad band centred at 335 nm, was gradually quenched upon addition of 0→0.33 equivalents of Eu(III), as the self-assemblies form, after which it never recovered, Figure 4.34(a). This behaviour is identical to that seen for all **btp** ligands described in this thesis. Upon complexation with the Eu(III) ion, the ligands sensitise the metal ion excited states *via* the 'antenna' effect, thereby quenching radiative emission from the ligand excited state.

The characteristic Eu(III)-centred emission spectra, which evolved as a result of this sensitisation process, and which were discussed previously for the complexes prepared under thermodynamic control, were observed to develop, upon delayed measurement of luminescence, after addition of the Eu(III) salt solution to the ligand, which was itself non-phosphorescent. The $^5D_0 \rightarrow {}^7F_J$ (J = 1–4) were observed clearly in the complex spectra,

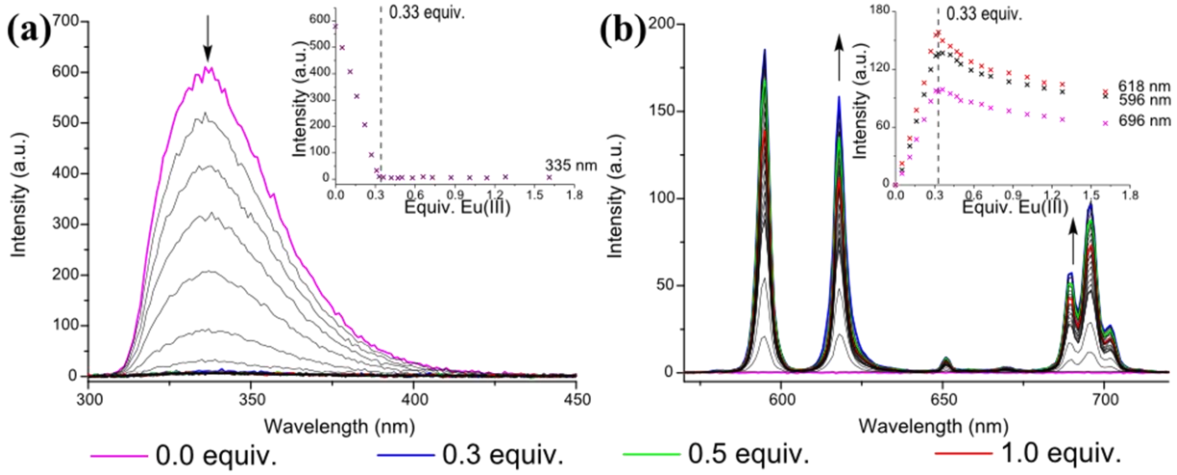

Figure 4.34 (a) Fluorescence emission titrations of ligand **100a** with $Eu(CF_3SO_3)_3$ in CH_3CN. [**100a**] = 1×10^{-5} M; **(b)** Eu(III)-centred phosphorescence emission titrations of ligand **100a** with $Eu(CF_3SO_3)_3$ in CH_3CN, showing characteristic emission bands relating to Eu(III) transitions $^5D_0 \rightarrow {}^7F_J$ (J=1–4). [**100a**]=1.1×10^{-5} M. Insets show experimental binding isotherms at various wavelengths. Plots of the titrations with **100b** are shown in Appendix C.

Figure 4.34(b). The most emissive species was formed upon addition of 0.33 equivalents of Eu(III), thereafter intensity was observed to decrease gradually, however, the signal intensity was still strong for all bands dropping to only *ca.* 40% of peak intensity at 3.6 equivalents of metal ion. This observed behaviour suggests that these self-assemblies were stable and persistent in solution.

These ligands were optically active, as demonstrated in Section 4.11, and displayed noteworthy spectroscopic differences in the CD profiles of the ligand and complex. CD titrations will hence also be used to monitor the self-assembly processes in CH_3CN solution and in the Section 4.12.4, the new practice of fitting these CD titrations will be used to determine global stability constants.

4.12.3 CD titrations of 100

The ligand CD spectra of **100**, as described above, possessed two major bands at 230 nm and 300 nm. In the case of **100a**, these bands were both postitive. Upon addition of $Eu(CF_3SO_3)_3$ to the ligand solution, the higher energy band gradually blue-shifted a few nanometres and increased slightly in ellipticity. The band at 300 nm, on the other hand, underwent a red-shift of approximately 15 nm as well as experiencing exciton coupling and appearing as a positive couplet with Davydov splitting of *ca.* 27 nm. These changes were largely complete upon addition of 0.5 equivalents of Eu(III), after which no further dramatic changes were seen in the CD spectra of the systems.

This Cotton effect in the n→π* band is diagnostic of the complexation of ligand **100** and allows its formation to be monitored clearly by CD spectroscopy. Fitting these changes to

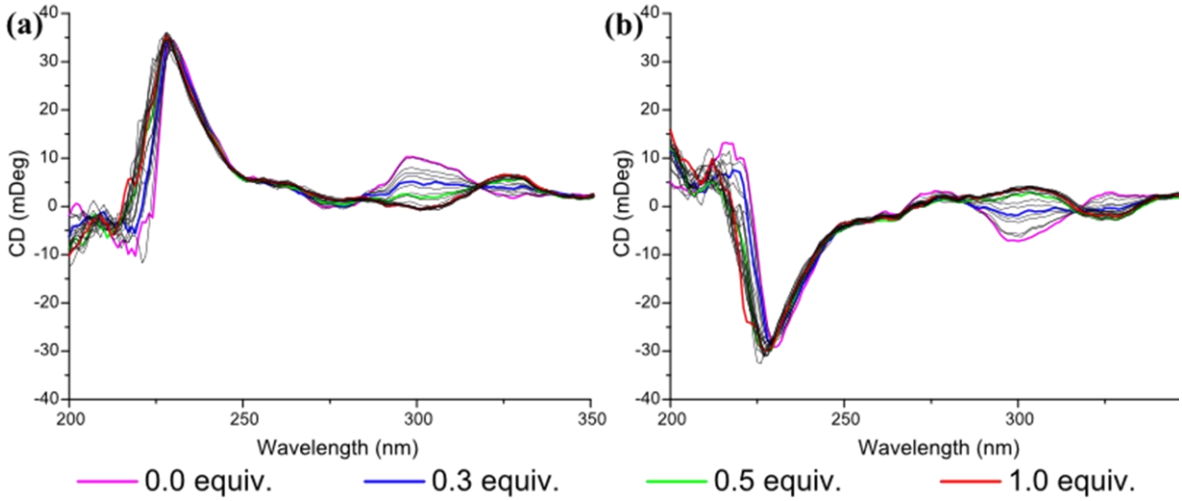

Figure 4.35 CD titration data upon addition of a solution of $Eu(CF_3SO_3)_3$ to a CH_3CN solution of **(a)** ligand **100a**; and **(b) 100b**. ([**100**] ≈ 1.25×10^{-5} M). Spectra at 0.0, 0.3, 0.5 and 1.0 equivalents are highlighted.

theoretical models, as well as those seen for the absorbance, and phosphorescence changes above will be detailed in the next section, providing further insight into the self-assembly processes.

4.12.4 Fitting of titrations

The above titrations all demonstrated that the Eu(III) ion was able to direct self-assembly of ligands **100**; significant changes were seen in both the ground state and excited states of the systems upon addition of $Eu(CF_3SO_3)_3$ and, as such, these data could be used to determine the stability of the self-assemblies formed. Global stability constants of each species were estimated by fitting the UV-Vis absorbance, luminescence and CD titration data using the non-linear regression analysis program ReactLab Equilibria.[237] No attempts to fit the fluorescence titration data were successful. For each set of titration data, the self-assembly process was fitted to a model compiled by considering combination of the stepwise equilibria detailed in Section 3.5.3 above.

For the UV-Vis absorbance data of **100a**, however, upon addition of $Eu(CF_3SO_3)_3$ in CH_3CN, although there were practically no spectral changes after the addition of 0.33 equivalents of Eu(III), the data were able to be fit to models containing the 1:1, 1:2 and 1:3 stoichiometric species. Stability constants $\log\beta$ were found to be $\log\beta_{1:1}$ = 7.4, $\log\beta_{1:2}$ = 14.8 ± 0.1 and $\log\beta_{1:3}$ = 21.4 respectively, with very similar results for ligand **100b**. The calculated binding isotherms fit well to these data, as is shown in Figure 4.36(a). The calculated speciation distribution diagram, Figure 4.36(b), suggests the formation of the 1:3 complex in high yield (>75%) at 0.33 equivalents, followed by subsequent formation

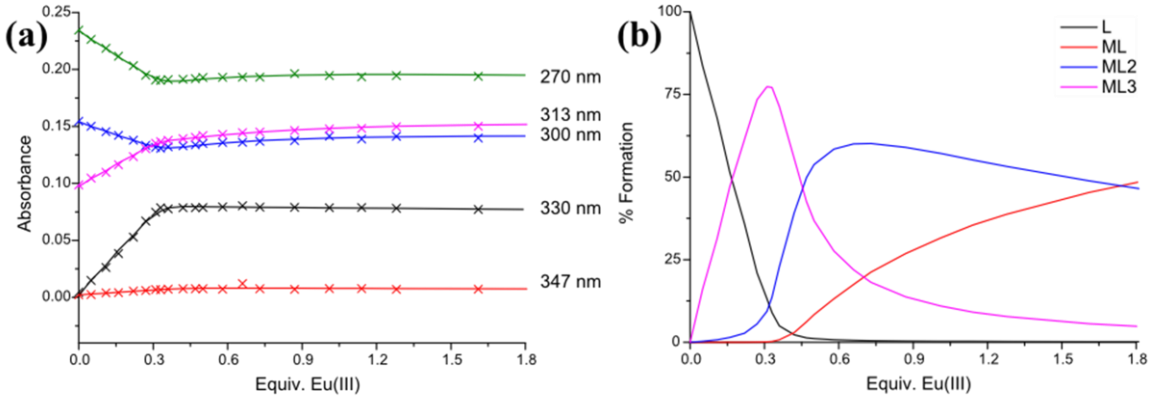

Figure 4.36 Fitting of UV-Vis absorbance titration data for ligand **100a** with $Eu(CF_3SO_3)_3$ in CH_3CN: **(a)** Experimental binding isotherms (×) and fitting curves (solid lines) calculated using ReactLab Equilibira at a range of wavelengths; and **(b)** calculated speciation distribution diagram, showing the percentage abundance of ligand and the various metal:ligand stoichiometries as a function of equivalents of Eu(III).

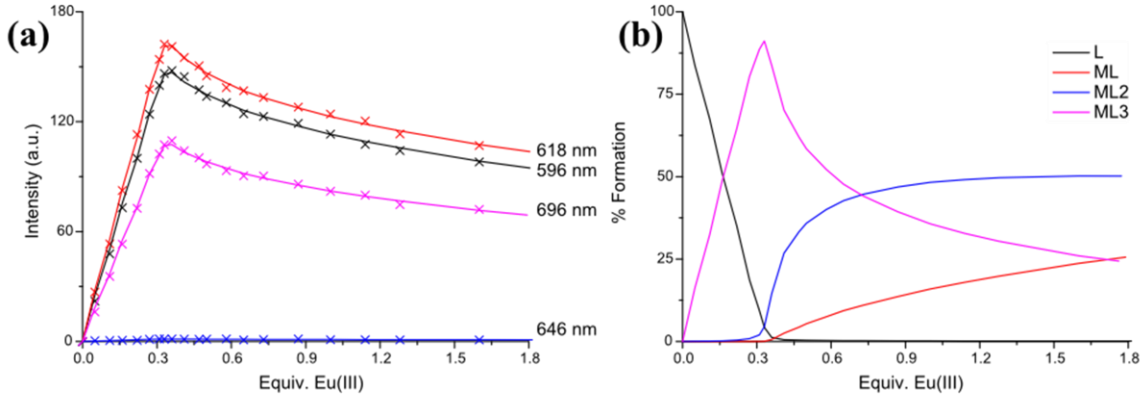

Figure 4.37 Fitting of Eu(III)-centred phosphorescence titration data for ligand **100b** with $Eu(CF_3SO_3)_3$ in CH_3CN: **(a)** Experimental binding isotherms (×) and fitting curves (solid lines) calculated using ReactLab Equilibira at a range of wavelengths; and **(b)** calculated speciation distribution diagram, showing the percentage abundance of the ligand and the various metal: ligand stoichiometries as a function of equivalents of Eu(III).

of the 1:2 self-assembly and finally a 1:1 complex as Eu(III) concentration increases. The global stability constants reported here are comparable to those determined for **91** and **99** above. They were higher than the binding constants determined for the direct **dpa** structural analogue **79**, for which $\log\beta_{1:1} = 6.4 \pm 0.3$ and $\log\beta_{1:3} = 20.3 \pm 0.5$; the '*Trinity Sliotar*' UV-Vis absorbance titration data did not fit to models containing the 1:2 self-assembly species.

Eu(III)-centred luminescence titration data were shown to fit well to a similar model, containing all of the potential self-assembly formation processes, converging with global stability constants for **100b** with Eu(III) of $\log\beta_{1:1} = 7.3 \pm 0.1$, $\log\beta_{1:2} = 15.2$ and $\log\beta_{1:3} = 22.7 \pm 0.1$. The results for the enantiomer, ligand **100a** were similar, Table 4.10. The fitting curves for these data matched the experimental data very well, Figure 4.37(a). The calculated speciation distribution diagram for this model, Figure 4.37(b), indicated the

Table 4.10 Global stability constants determined from UV-Vis absorbance, luminescence and CD titrations of ligands **100** with Ln(III) in CH_3CN.

Ligand	**Ln(III)**		**$\log\beta_{1:1}$**	**$\log\beta_{1:2}$**	**$\log\beta_{1:3}$**
100a	Eu(III)	UV	7.4 [a]	14.8±0.1	21.4 [a]
100b	Eu(III)	UV	7.4 [a]	14.6±0.1	21.4 [a]
100a	Eu(III)	Phos.	7.4±0.1	15.4±0.1	23.3 [a]
100b	Eu(III)	Phos.	7.3±0.1	15.2 [a]	22.7±0.1
100a	Eu(III)	CD	8.9±0.1	16.0 [a]	23.3±0.2
100b	Eu(III)	CD	8.6±0.1	16.0 [a]	22.7±0.1

[a] Value fixed.

formation of the 1:3 self-assembly in near quantitative yields at 0.33 equivalents followed by the less stable formation of the 1:2 complex, which never exceeded 50% formation. The 1:1 species was predicted by this model to gradually increase in abundance as excess of Eu(III) was added, but never dominated in solution.

The CD titration data were fit to similar models. For the self-assembly of **100b** with Eu(III), binding constants of $\log\beta_{1:1}$ = 8.6 ± 0.1, $\log\beta_{1:2}$ = 16.0 and $\log\beta_{1:3}$ = 22.7 ± 0.1 were determined. Similar constants were determined for **100a**, Table 4.10. The calculated binding isotherms can be seen in Figure 4.38(a) to match the experimental CD titration data well. The speciation distribution diagram calculated from this model also indicated the formation of the 1:3 self-assembly in high yield (>75%) in solution at 0.33 equivalents of Eu(III), however it differed from the speciation diagrams determined by the other methods in the profile of the formation of the 1:2 species, which reached a mamimum formation of *ca.* 50% at 0.6 equivalents before decreasing in concentration and being replaced by 1:1 species formation. This difference in calculated behaviour after the formation of the 1:3 complex is analogous to the differences seen between the models calculated from UV-Vis absorbance and CD titration data for **99** above. Ln(III)-directed self-assembly CD titration fitting, which is, as has been stated a number of times already, a new application of this spectroscopic technique, also tend to give higher global stability constants than the other techniques implemented. This systematic difference between the methods should be borne in mind when interpreting the results from this insightful technique.

The results presented here suggest that, although this **btp** ligand forms less luminescent complexes with Eu(III), it forms more stable self-assemblies in CH_3CN solution, when

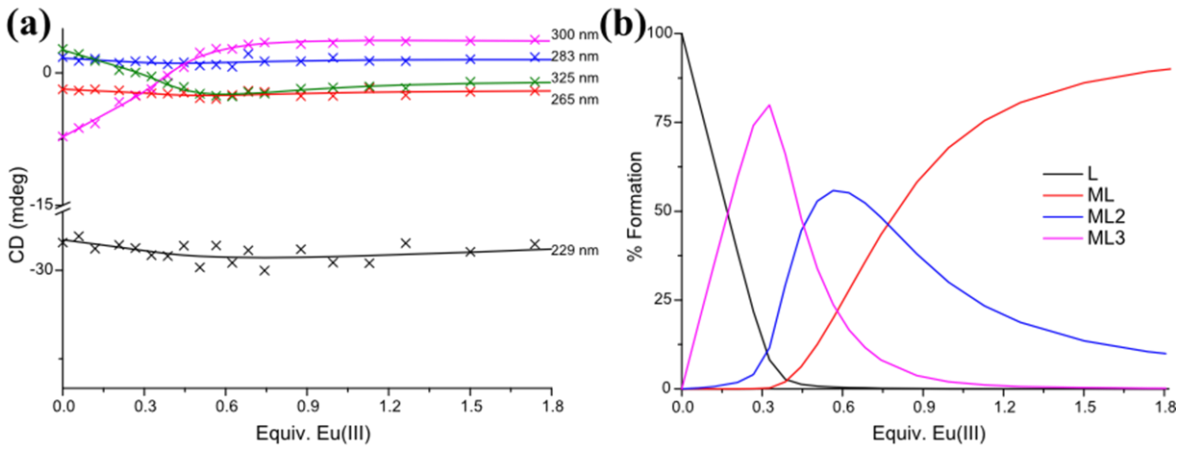

Figure 4.38 CD titration of ligand **100b** with $Eu(CF_3SO_3)_3$ in CH_3CN: **(a)** Experimental CD binding isotherms (×) and fits (solid lines) calculated using ReactLab Equilibria, at a range of wavelengths and **(b)** calculated speciation diagram, showing the percentage abundance of the ligand and the various metal:ligand stoichiometries as a function of [Eu(III)].

compared with its **dpa** analogue **79**.[152] This indicates that **btp** ligands are, indeed, good candidates to act as analogues of the well-studied **dpa** systems. The above sections have shown the ability of chiral **btp** ligands to form stable, luminescent complexes, featuring the desired chiroptical properties for which they were designed and fitting of various different titrations allowed this stability to be quantified by a variety of complementary methods, including the new paradigm of fitting CD titrations for Ln(III)-directed self-assembly.

4.13 Conclusions

This chapter focussed on developing a number of optically active **btp** ligands and exploiting their chirality to monitor their self-assembly behaviour with Ln(III) ions in solution by spectroscopic means including CD titrations. A series of sugar-containing **btp** ligands, **96**, **97** and **98** were synthesised and fully characterised, including by X-ray crystallography, in the case of **98**. Allyl-appended D-mannose-derivative **96** formed luminescent Eu(III)-directed self-assembly complexes, with Φ = 1.9%; these were described as Ln(III)-templated 'glyco-clusters'. The self-assembly behaviour of this ligand in CH_3CN was studied by UV-Vis absorbance, emission and CD spectroscopy; fitting the UV-Vis and CD results allowed the determination of global stability constants for this system.

Three enantiomeric pairs of chiral **btp** ligands, **99**–**101** were conveniently synthesised, using a new one-pot two-stage diazo-transfer–deprotection–'click' reaction from chiral amines and a protected bis-alkyne, **21**, and characterised; each stage of this reaction was catalysed by copper. X-ray crystal structures of both ligands **99a–b** were obtained. Ln(III) complexes were prepared, which exhibited characteristic lanthanide-centred luminescence; the quantum yields of $[Tb\cdot(\mathbf{99})_3](CF_3SO_3)_3$ were rather high (Φ = 56–67%), while the Eu(III) complexes had much more modest quantum yields. The chiral nature of the ligands was exploited to obtain CPL emission, including when immobilised in a solid cross-linked poly(HEMA) matrix. CD spectra were also studied, with each enantiomeric spectrum being a mirror image of the other. UV-Vis absorbance and luminescence titrations were carried out in CH_3CN and the data fit to theoretical models, giving reasonably high global stability constants for the 1:1, 1:2 and 1:3 ligand:metal stoichiometric self-assemblies (*e.g.* from the emission data for **99a** with Eu(III) logβ for each species were determined as 7.0 ± 0.1, 13.8 and 19.0 ± 0.1). CD titrations were also undertaken of these enantiomeric self-assembly systems, a process uniquely available for chiral compounds, allowing further confirmation of the high binding constants with comparable values of logβ. The binding

behaviour of '*Trinity Sliotar*' analogue, **100**, with Eu(III) was also studied in CH_3CN by UV-Vis absorbance, emission and CD spectroscopy and these data were used to determine global stability constants. These systems were found to form self-assemblies that were less luminescent than their **dpa** analogues, but with higher stability constants.

4.14 Future perspectives

Throughout this thesis a number of distinct research strands have been presented, which will be summarised presently. Many of these investigations have opened avenues of research which may be followed further in the future. Some of these avenues will now be briefly described.

In Chapter 2, the formation of a metallo-supramolecular gel was discussed. It was alluded to that modification of these ligands by derivatisation of the 4-pyridyl position of **btp** was expected to produce ligands which could more easily form such gels. Indeed, a ligand **104**, designed as the basis of a final year undergraduate research project, was prepared by Mr Eoin McCarney and the promising gelator properties of this ligand with Ln(III) ions is currently under investigation as part of his Ph.D. studies. In fact, such 4-pyrdiyl derivatisation of any of the ligands described above would endow them with increased functionality. Hydrolysed versions of ligands **91**, such as **105** and **106** would also show promise for these applications.

In Chapter 3, [2]catenane **95** was shown to have the potential to bind anions with some selectivity. This project is in its early stages and more work must be done on ascertaining the global stability constants of this binding process, as well as tuning the cavity size by synthesising olefin ligands such as **107** and examining the effect this has on anion selectivity. Overcoming the inability of ligand **90** to form Ln(III)-templated [n]catenanes was proposed to be possible by preparing derivatives such as **108**, **109** and **110**. Some of these ligands were prepared in poor yields but merit further study.

Two strategies were proposed in Chapter 3 for overcoming the tendency of the Ln(III)–**btp** systems described to dissociate in aqueous solution. The first was arylation of the 1,2,3-triazole rings, yielding ligands such as **111**. The second strategy involved encapsulation of ligands into hydrogel matrices. Promising results from this strategy have been reported already and this on-going project in conjunction with Mr Samuel Bradberry is expected to allow the preparation of a number of further functional materials.

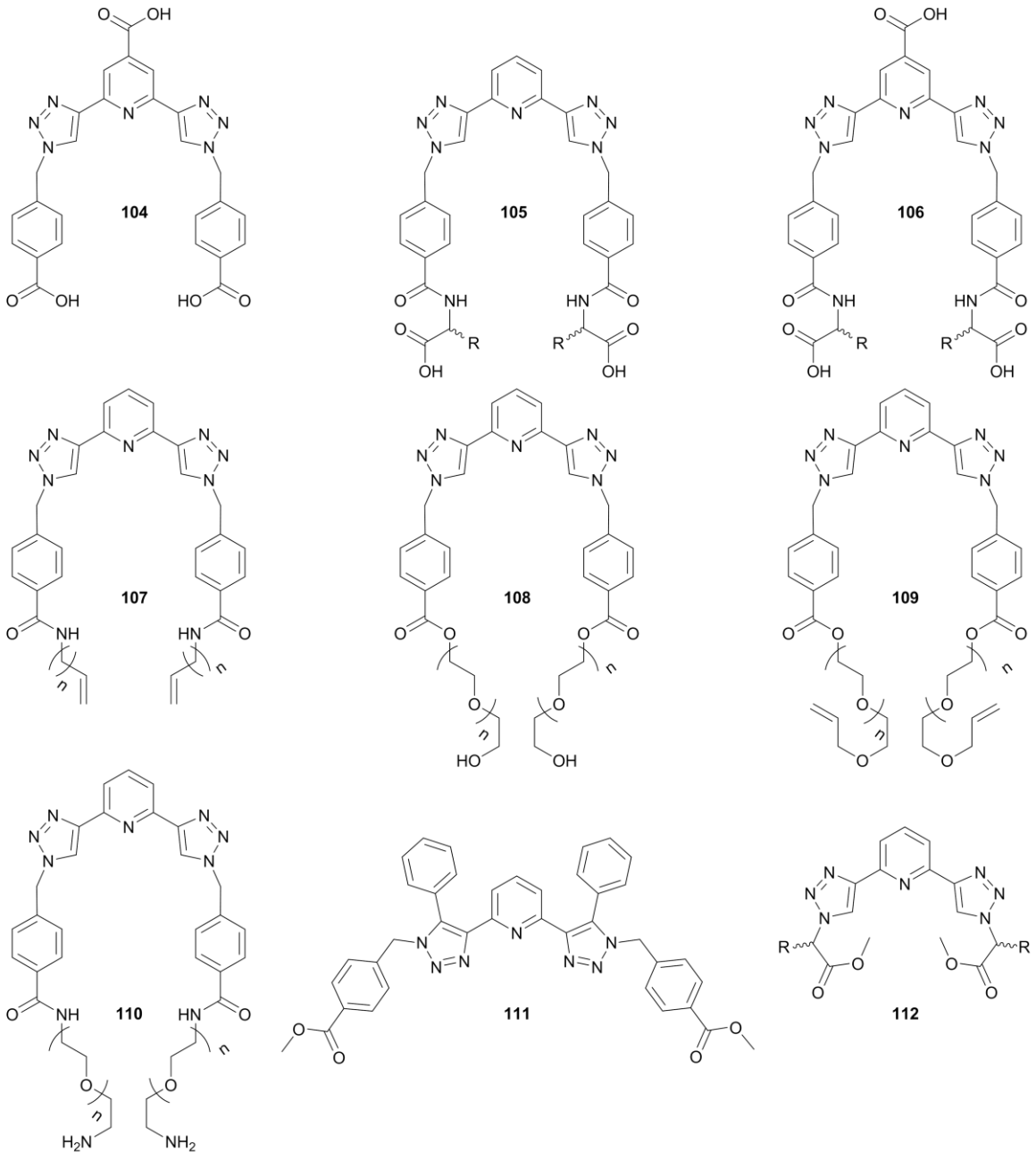

Much of the work described in Chapter 4 represents recent results. Studies into the self-assembly behaviour with Ln(III) of carbohydrate ligands **97** and **98**, along with a number of other mono- and disaccharide derivatives, will be undertaken in the future and compared to the results discussed earlier in this chapter. These luminescent systems will be explored for potential biological sensing applications, perhaps upon encapsulation into hydrogel matrices. Ligand **101**, a structural isomer of **100**, while synthesised and characterised has not yet been studied in depth to explore the effects of ligand isomerism on the luminescence and self-assembly properties of the **btp** ligands with Ln(III). Moreover, given that the one-pot diazo-transfer–deprotection–'click' reaction developed in this

chapter is applicable to a large range of amine substrates, yielding **btp** ligands, a number of further series of compounds may be developed and their self-assembly behaviour assessed. An obvious future avenue of research, combining themes from Chapter 3 and 4, will involve exploring the properties of **btp** ligands **112** synthesised from α-amino acids, *via* an α-azido acid intermediate using this reaction in order to exploit their natural optical activity in close proximity to the binding site, allowing for chiroptical studies.

Studies of any of the Ln(III)–**btp** described in this thesis could be carried out with different Ln(III) ions than those described to form self-assemblies with differing properties, such as visibly emitting Sm(III) complexes, near IR emitting Nd(III) complexes or highly paramagnetic Gd(III) complexes. Carrying out self-assembly studies in different solvents, such as CH_3OH, also merits exploration in the future in order to investigate the solvent effect on the self-assembly processes described above by comparison of the global stability constants determined in different media.

4.15 Final summary

This thesis has described a variety of research displaying the versatility of the **btp** motif and some of its applications in forming supramolecular self-assembly structures, particularly with metal ions. Chapter 1 introduced the **btp** motif and described its facility of synthesis through the Cu(I)-catalysed alkene–azide 'click' reaction. The prior research published on the coordination chemistry and anion binding behaviour of ligands containing this motif was discussed, as well as some specific applications and the formation of higher order structures, such as metallo-supramolecular gels. This chapter also summarised preceding research in the Gunnlaugsson laboratory on the Ln(III)-directed self-assembly of **dpa**-based molecules.

Chapter 2 described the design and synthesis of two **btp** ligands **88** and **89** by a one-pot CuAAC 'click' reaction as well as the preparation of Ru(II), Ni(II), Ir(III) and Pt(II) complexes, which were all characterised. The X-ray crystal structures of a number of these compounds were determined and the photophysical properties of all ligands and complexes were explored at both room temperature and 77 K. At room temperature, only [Ru·(**88**)Cl_2(DMSO)] was found to exhibit emission other than ligand-centred fluorescence. The complexes displayed more interesting emission properties at low temperature. Ethanol solutions containing $[Ru\cdot(\mathbf{89})_2]^{2+}$ formed metallo-supramolecular gels, which were imaged using SEM and HIM.

Chapter 3 primarily described Ln(III)-directed self-assembly formation (under both thermodynamic and kinetic control) of luminescent complexes with ligands **88**, **90** and the range of amino-acid derivatised ligands **91**. The total luminescence quantum yields of these complexes in CH_3CN were found to be modest for Eu(III) complexes (Φ = 0.4–3.0 %) and moderate to very high for Tb(III) complexes (Φ = 6.3–70 %). Monitoring these self-assembly processes in CH_3CN upon addition of $Ln(CF_3SO_3)_3$ by UV-Vis absorbance, fluorescence and Ln(III)-centred emission titrations and fitting of these data to theoretical models, by using non-linear regression analysis software ReactLab Equilibria, indicated the formation of 1:3, 1:2 and 1:1 metal:ligand stoichiometric species, respectively, upon increased concentration of Ln(III) ion. Relatively high global stability constants for the 1:3 complexes were determined ($\log\beta_{1:3}$ = 18.9–23.0). This chapter also described the RCM formation of a self-templated [2]catenane, **95**, which was pre-organised by a range of supramolecular interactions, as seen in the X-ray crystal structure. This interlocked structure showed promise for anion-binding applications, selectively hydrogen bonding with $H_2PO_4^-$ (and not with Cl^-, NO_3^- or HSO_4^-).

Chapter 4 described the design and synthesis of optically active **btp** ligands from both carbohydrate azide and chiral amine precursors. The latter class of molecule was prepared using a new diazo-transfer–deprotection–'click' protocol in moderate to excellent yields. Three of these new **btp** ligands were characterised by X-ray crystallography, showing the same **btp–btp** hydrogen bonding dimer formation which templated the formation of [2]catenane **95** in Chapter 3. These ligands formed emissive Ln(III) complexes, which gave rise to CPL emission in the case of **99** and **100**. The self-assembly of a number of these chiral ligands with Ln(III) in CH_3CN solution was monitored by UV-Vis absorbance, fluorescence and Ln(III)-centred emission spectroscopy and the data fit to theoretical models as in Chapter 3. Remarkably, data from CD titrations were also fit by similar methods and allowed determination of global stability constants with comparable values to those determined by other methods. These results recommend this technique as a complementary method to the aforementioned spectroscopic techniques for monitoring Ln(III)-directed self-assembly in solution.

All of these results demonstrate the ability of **btp** systems to form both optically active and optically inactive supramolecular assemblies with *d*-metals, *f*-metals and, indeed, themselves by altering the functionality of the **btp** substituents through facile derivatisation reactions.

5. Experimental

5.1 General methods and materials

All chemicals were purchased from commercial sources and unless specified used without further purification. Melting points were determined using an Electrothermal IA9000 digital melting point apparatus. Elemental analysis was carried out at the Microanalytical Laboratory, School of Chemistry and Chemical Biology, University College Dublin. Infrared spectra were recorded on a Perkin Elmer Spectrum One FT-IR Spectrometer fitted with a universal ATR sampling accessory. NMR spectra were recorded using a Bruker DPX-400 Avance spectrometer or Agilent DD2/LH spectrometer, operating at 400.13 MHz for ^{1}H-NMR, 100.6 MHz for ^{13}C-NMR, or a Bruker AV-600 spectrometer, operating at 600.1 MHz for ^{1}H-NMR and 150.2 MHz for ^{13}C-NMR. All spectra were recorded using commercially available deuterated solvents, and were referenced to solvent residual proton signals. All ^{1}H–^{1}H coupling constants, *J*, are quoted with an accuracy of ±0.3 Hz. Electrospray mass spectra were measured on a Micromass LCT spectrometer calibrated using a leucine enkephaline standard. MALDI Q-Tof mass spectra were carried out on a MALDI Q-Tof Premier (Waters Corporation, Micromass MS technologies, Manchester, UK) and high-resolution mass spectrometry was performed using Glu-Fib as an internal reference (peak at *m/z* = 1570.677). All microwave reactions were carried out in 2–5 mL or 10–20 mL Biotage Microwave Vials in a Biotage Initiator Eight EXP microwave reactor.

5.1.1 X-ray Crystallography

X-ray data were collected on either a Rigaku Saturn 724 CCD Diffractometer (for **88**[(a)] and [Ru·(**89**)$_2$](PF$_6$)Cl[(a)]) using graphite-monochromated Mo-Kα radiation (λ = 0.71073 Å) or a Bruker Apex2 Duo (for [Ru·(**88**)Cl$_2$(DMSO)] [(b)], [Ni·(**88**)$_2$](PF$_6$)Cl[(a)], [Ir·(**88**)Cl$_3$] [(a)], **95**[(c)], **99a**[(b)], **99b**[(b)], **98**[(c)] and **102**[(a)]) using a high intensity Cu-Kα radiation source (λ = 1.54178 Å). The data sets from the Rigaku Saturn-724 diffractometer were collected using Crystalclear-SM 1.4.0 software. Data integration, reduction and correction for absorption and polarisation effects were all performed using the Crystalclear-SM 1.4.0 software. Space group determination, was obtained using Crystalstructure ver.3.8 software. The datasets collected on the Bruker Apex2 Duo were processed using Bruker APEXv2011.8-0 software. All structures were solved by direct methods (SHELXS-97/14) and refined against all F^2 data (SHELXL-97/14) using shelXle.[284,285] All H-atoms, except for O–H protons, were positioned geometrically and refined using a riding model with d(CH$_{aro}$) = 0.95 Å, *U*iso = 1.2*U*eq (C) for aromatic, d(CH) = 0.99 Å, *U*iso = 1.2*U*eq (C) for CH$_2$ and

0.98 Å, *U*iso = 1.2*U*eq (C) for CH_3. O–H protons were found from the difference map and fixed to the attached atoms with $U_H = 1.2U_O$.

Data were collected and refined by (a) Dr Jonathan Kitchen, (b) Dr Miguel Martínez-Calvo or (c) Dr Salvador Blasco. Crystallographic data for most of these structures has been deposited with the Cambridge Crystallographic Data Centre, (CCDC, 12 Union Road, Cambridge CB21EZ, UK; http://www.ccdc.cam.ac.uk). Copies can be obtained free of charge on quoting the deposition numbers 956219–956222, 1019214–1019215.

5.1.2 Microscopy studies of the gels

To image the gel samples by scanning electron microscopy (SEM), they were deposited manually onto clean silicon samples with a thick silicon dioxide layer. The spatula and glass pipettes used for dosing and silicon pieces used as substrates were all cleaned thoroughly by sonication in HPLC grade acetone followed by HPLC grade propan-2-ol. The gels were manually drop cast on to the silicon at room temperature and dried during 5 days at ambient conditions. Low kV SEM was carried out using the Zeiss ULTRA Plus using either an SE2 or in-lens detector and the Zeiss Orion Plus Helium Ion Microscope using an SE2 detector, both in the Advanced Microscopy Laboratory, CRANN, Trinity College Dublin. The samples prepared for the imaging did not have any additional conductive layer cover. Beam energies for the helium ion were 30-35 kV with probe currents ranging from 0.1–1.5 pA. A 10 μm beam limiting aperture was employed for all the images. Images were formed by collecting the secondary electrons generated during the helium ion interacting with the specimen atoms. Charge control was achieved using an electron flood gun. After each line scan charge neutralisation was applied. The image was acquired using either 32 or 64 line averaging. These measurements were undertaken by Dr Oxana Kotova, Dr Alan Bell and Prof. John Boland in the Centre for Adaptive Nanostructures and Nanodevices in Trinity College, Dublin.

5.1.3 Cyclic voltammetry

Electrochemical studies were carried out using a Metrohm Autolab Potentiostat Model PGSTAT101 employing a gastight three electrode cell under an argon atmosphere. A platinum disk with 7.0 mm^2 surface area was used as the working electrode and polished before each measurement. The reference electrode was Ag/AgCl, the counter electrode was a Pt foil. In all experiments Bu_4NPF_6 (0.1 M in dry CH_3CN) was used as supporting electrolyte with analyte concentrations of approximately 1 mM. The ferrocenium/ferrocene

redox couple was used as an internal reference ($E_{1/2}$ = 0.40 V vs. SCE).[286] These measurements were carried out by Prof. Martin Albrecht, Dr Vivienne Leigh and Bryan Hogan in the Albrecht laboratory in University College Dublin.

5.1.4 Photophysical measurements

Unless otherwise stated, all photophysical measurements were carried out at 23° C in HPLC CH_3CN solution at a concentration of *ca.* 10^{-5} M.

UV-Visible absorbance spectra were measured in 1 cm quartz cuvettes on a Varian Cary 50 spectrophotometer. Baseline correction was applied for all spectra. Emission spectra and luminescence lifetimes were measured on a Varian Cary Eclipse luminescence spectrometer. All the stock solutions were prepared in CH_3CN. Measurements were taken at room temperature. Some emission spectra were also recorded on a Fluorolog FL-3−22 spectrometer from Horiba-Jobin-Yvon Ltd. This instrument was equipped with a dewer of liquid nitrogen, allowing for measurements at 77 K. A Jobin Yvon FluoroHub single photon counting controller fitted with an appropriate wavelength Jobin Yvon NanoLED was used to measure lifetimes, which were determined from the observed decays using DataStation v2.4.

CD spectra were measured in 1 cm quartz cuvettes on a Jassco J-810-150S spectrometer, which was under a constant flow of nitrogen. Baseline correction was applied for all spectra. CPL spectra were measured by Dr Robert Peacock at University of Glasgow. A tuneable dye laser was used to excited Ln(III) emission with argon ion laser as a pump source. The emission monochromator was calibrated by passing scattered light from a low powered HeNe laser through the detection system. The optical detection system consisted of a photoelastic modulator operating at 50 kHz and a linear polariser, which together acted as a circular analyser, a long pass filter, focussing lens and a 0.22 m double monochromator. Emitted light was detected by a cooled photomultiplier tube (operating in photon counting mode). The 50 kHz photoelastic modulator reference signal was used to direct incoming pulses into two separate counters: an up counter, which counts every photon pulse (measuring total luminescence, $I = I_L + I_R$) and an up/down counter, which adds pulses when the analyser transmits left circularly polarised light and subtracts when right circularly polarised light (providing a measure of the differential emission intensity, $\Delta I = I_L - I_R$).

5.1.5 Quantum yield determination

Quantum yields of the Ln(III) complexes were estimated by a relative method[236], using a solution of $Cs_3[Ln\cdot(\mathbf{dpa}-2H)_3]$ in 0.1 M Tris buffer (pH = 7.45) with an optical density at 279 nm, A_{ref}, of *ca.* 1.0 as a standard, as recommended by Chauvin and co-workers.[21,22] The reference quantum yields have been determined as Φ_{ref} = 24±2.5 % for the Eu(III) complex and Φ_{ref} = 22±2.5 % for the Tb(III) complex.

An emission spectrum was measured of a solution of $Cs_3[Ln\cdot(\mathbf{dpa}-2H)_3]$, with an absorbance at 279 nm, A_{ref}, of 0.975 for $Cs_3[Eu\cdot(\mathbf{dpa}-2H)_3]$ and 1.001 for $Cs_3[Tb\cdot(\mathbf{dpa}-2H)_3]$, and the integrated intensity under the curve of the emission spectra, I_{ref}, was calculated. The refractive index of the standard solution, n_{ref}, was 1.35). Spectra of each complex in CH_3CN (n = 1.3341) were measured at similar optical densities and the same instrumental settings, and the integrated luminescence intensities, I, were calculated. Estimated quantum yields, Φ, were calculated according to the following equation:

$$\Phi = \frac{n^2}{n_{ref}^2} \times \frac{A_{ref}}{A} \times \frac{I}{I_{ref}} \times \Phi_{ref}$$

5.1.6 ^{1}H NMR titration

A ligand stock solution in CD_3CN with known concentration was prepared ([**88**] = 1.1 mM). 600 μL of this solution was added to a standard NMR tube. 3–6 μL aliquots of a $Eu(CF_3SO_3)_3$ stock solution in CD_3CN ([Eu(III)] = 21.8 mM) were added between measurements of ^{1}H-NMR spectra on a Bruker DPX-400 Avance spectrometer operating at 400.13 MHz.

5.1.7 General procedure for hydrogel formation

Ligand-encapsulating HEMA hydrogels were prepared according to a procedure reported previously by researchers in the Gunnlaugsson group.[261] For the formation of all of the gels described in this thesis, HEMA was stirred with ethylene glycol dimethacrylate (1% w/w), which acted as a cross-linker, AIBN radical initiator (1% w/w) and the relevant **btp** ligand (0.05% w/w). The mixture was injected into a mould using a spacer of 1 mm between glass plates. Polymerisation occurred in an oven at 90 °C over 5 hours. To swell these materials, they were soaked in either water, or aqueous $Ln(CF_3SO_3)_3$ solutions, in order to form self-assembled Ln(III) assemblies within the material and give rise to Ln(III)-centred luminescent materials.

5.2 Syntheses of ligands and complexes discussed in Chapter 2

2,6-Bis((trimethylsilyl)ethynyl)pyridine (21)

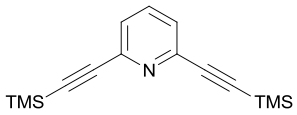

Protected bis-alkyne **21** was prepared from 2,6-dibromopyridine by Sonogashira coupling using a modified literature procedure.[287,288] The reaction mixture was stirred at room temperature under argon atmosphere for 24 hours, using a dry 1:1 triethylamine:THF solvent system. The solution was diluted with ethyl acetate and stirred vigorously with a solution of EDTA/NH_4OH for 1 hour. The reaction mixture was then extracted with ethyl acetate and washed with saturated $NaHCO_3$ solution and brine before drying over $MgSO_4$ and concentrating under reduced pressure, yielding a brown solid. Crude product was filtered through a silica plug, washing in hexane/CH_2Cl_2 (1:1) and the eluent concentrated under reduced pressure, yielding **21** as a tan coloured solid (3.100 g, 11.41 mmol, 68%). m.p. 90.3–98.7 °C (Lit. m.p. 97–99 °C).[289] HRMS (*m/z*) (ESI+): Calculated for $C_{15}H_{22}NSi_2^+$ *m/z* = 272.1291 $[M+H]^+$. Found *m/z* = 272.1299; δ_H (400 MHz, $CDCl_3$): 0.28 (s, 18H, TMS), 7.41 (d, 2H, 3- and 5-pyr CH, *J* = 7.8 Hz), 7.62 (t, 1H, 4-pyr CH, *J* = 7.8 Hz); FT-IR (ATR, cm^{-1}): 3052 (strong), 2962, 2900, 2154 (C≡C), 1558, 1440, 1249, 1206, 1163, 1082, 985, 953, 836, 811 (strong), 759, 734, 702, 656.

General Procedure A: Synthesis of btp ligands 88 and 89

To a solution of the relevant bromide (4.65 mmol) in 15 mL DMF/water (4:1) was added sodium azide (0.332 g, 4.65 mmol) and the reaction mixture stirred for 1 hour, yielding the azide derivative, which was not isolated, and therefore used without further purification. To this solution was added **21** (0.631 g, 2.33 mmol). $CuSO_4 \cdot 5H_2O$ (0.232 g, 0.930 mmol) and sodium ascorbate (0.368 g, 1.86 mmol) were added to the reaction mixture, followed by anhydrous K_2CO_3 (0.650 g, 4.70 mmol) and stirred at room temperature for 18 hours in a further 15 mL 4:1 DMF/water. EDTA/NH_4OH solution was added to the reaction mixture and stirred for 1 hour before isolating the product.

2,6-Bis(1-(4-(methylcarboxy)benzyl)-1,2,3-triazol-4-yl)pyridine (88)

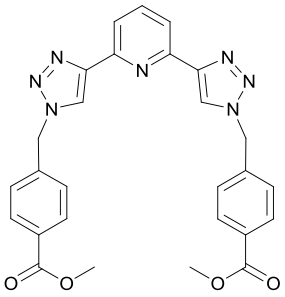

Ligand **1** was prepared according to *General Procedure A* from methyl 4-(bromomethyl)benzoate and was isolated upon extraction with $CHCl_3$, washing the organic layer with brine. Concentration under reduced pressure and trituration with cold CH_3OH followed by recrystallisation from boiling CH_3OH yielded ligand **88** as an off-white solid (1.27 g, 2.49 mmol, 53%). m.p. 221.1–223.5 °C. HRMS (*m/z*) (ESI+): Calculated for $C_{27}H_{23}N_7O_4Na^+$ *m/z* = 532.1709 $[M+Na]^+$. Found *m/z* = 532.1711; Calculated for $C_{27}H_{23}N_7O_4$, C = 63.65, H = 4.55, N = 19.24. Found C = 63.38 H = 4.52 N = 19.29. δ_H (400 MHz, DMSO): 3.84 (s, 6H, $–OCH_3$), 5.81 (s, 4H, CH_2), 7.45 (d, 4H, Ph CH, *J* = 8.2 Hz), 7.91–8.07 (m, 7H, Ph CH and pyr CH), 8.72 (s, 2H, triazolyl CH); δ_C (150 MHz, $CDCl_3$): 52.4 ($–OCH_3$), 53.8 (CH_2), 119.4 (3- and 5-pyridyl CH), 122.1 (triazolyl CH), 127.8 (phenyl CH), 130.3 (Ph CH), 130.6 (qt, Ph), 137.8 (4-pyr CH), 139.3 (qt, Ph), 148.8 (qt, triazolyl), 149.7 (qt, 2- and 6-pyr), 166.3 (C=O). FT-IR (ATR, cm^{-1}): 3154, 3078 (ar C–H st), 3010, 2956 (C–H st), 2845 ($O–CH_3$ st), 2101, 1729 (C=O st), 1608 and 1572 (C–C γ), 1511, 1436, 1426, 1314, 1278, 1236, 1214, 1196, 1155, 1109, 1085, 1044, 1022, 991, 973, 843, 820, 797, 782, 756, 732, 687, 667.

2,6-Bis(1-(4-(carboxy)benzyl)-1,2,3-triazol-4-yl)pyridine (89)

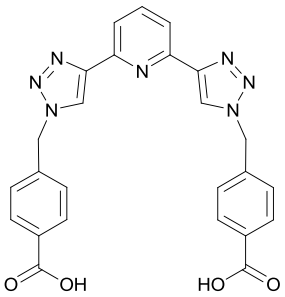

Carboxylic acid ligand **89** was synthesised according to *General Procedure A* from 4-(bromomethyl) benzoic acid. It was isolated upon acidification of the EDTA/NH_4OH solution by dropwise addition of concentrated HCl solution until pH 7 was reached. **89** was collected as a beige solid upon suction filtration (0.705 g, 1.46 mmol, 63%). Product decomposed over 284 °C. HRMS (*m/z*) (ESI−): Calculated for $C_{25}H_{18}N_7O_4^-$ *m/z* = 480.1426 $[M−H]^−$. Found *m/z* = 480.1423; Calculated for $C_{25}H_{19}N_7O_4·0.5H_2O$, C = 57.46, H = 3.86, N = 18.76. Found C = 57.39, H = 3.75, N = 18.92. δ_H (600 MHz, DMSO): 5.80 (s, 4H, CH_2), 7.45 (d, 4H, Ph CH, *J* = 8.7 Hz), 7.91–8.03 (m, 7H, Ph CH and pyr CH), 8.74 (s, 2H, triazolyl CH); δ_C (150 MHz, DMSO-d_6): 52.8 (CH_2), 118.7 (3- and 5-pyr CH), 124.1 (triazolyl CH), 128.2 (Ph CH), 129.9 (Ph CH), 130.6 (Ph qt), 138.1 (4-pyr CH), 140.8 (Ph qt), 147.5 (triazolyl qt), 149.8 (2- and 4-pyr qt), 167.03 (C=O); FT-IR (ATR, cm^{-1}): 3083 (ar C–H st), 2938 (C–H st),

1719, 1692 (C=O st), 1642, 1614, 1531, 1467, 1420, 1400, 1285, 1242, 1198, 1176, 1106, 1047, 942, 822, 800, 725.

Monoleptic Ru(II) complex ([Ru·(88)Cl_2(DMSO)])

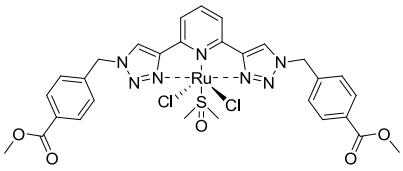

Precursor *cis*-[$RuCl_2(DMSO)_4$] was prepared in a microwave reaction according to a literature procedure from $RuCl_3 \cdot 3H_2O$.[290] To this complex (0.029 g, 0.059 mmol) was added the ligand **88** (0.030 g, 0.059 mmol) and 5 mL $CHCl_3$ and the resulting mixture refluxed in darkness for 10 hours before isolating the product upon filtration and washing with ether, yielding a bright red solid (0.039 g, 0.051 mmol, 86%). Product decomposed over 216 °C. HRMS (*m/z*) (MALDI+): Calculated for $C_{27}H_{23}N_7O_4Cl_2Ru^+$ *m/z* = 681.0232 $[M-(DMSO)]^+$. Found *m/z* = 681.0213; Calculated for $C_{29}H_{29}N_7O_5SRuCl_2 \cdot 0.5CHCl_3$, C = 43.25, H = 3.63, N = 11.97. Found C = 43.60, H = 3.39, N = 11.83; δ_H (600 MHz, DMSO-d_6): 3.49 (s, 6H, coordinated DMSO), 3.86 (s, 6H, $–OCH_3$), 5.92 (s, 4H, CH_2), 7.54 (d, 4H, Ph CHs, *J* = 8.0 Hz), 8.01 (d, 4H, Ph CHs, *J* = 8.0 Hz), 8.07–8.18 (m, 3H, pyr CH), 9.16 (s, 2H, triazolyl CH); δ_C (150 MHz, DMSO-d_6): 46.8 (coordinated DMSO), 52.6 ($–OCH_3$), 54.3 (CH_2), 119.0 (pyr CH), 125.7 (triazolyl CH), 128.9 (Ph CH), 130.1 (Ph CH), 137.8 (pyr CH), 140.2 (qt), 149.9 (qt), 150.9 (qt), 166.1 (qt); FT-IR (ATR, cm^{-1}): 3443 (br), 3011, 2925, 1715 (strong), 1614, 1580, 1418, 1283 (strong), 1185, 1108 (strong), 1085, 1018, 993, 961, 931, 809, 749, 718, 677.

***General Procedure B*: Synthesis of dileptic Ru(II) and Ni(II) complexes**

To the relevant ligand (2 equiv.) was added 5 mL aqueous ethanol solution (70% v/v). The solution was degassed, by bubbling argon through the system, and $RuCl_3 \cdot 3H_2O$ or $NiCl_2$ (1 equiv.) added. This was stirred for 40 minutes at 120 °C under microwave irradiation. The reaction mixture was filtered through celite and concentrated under reduced pressure. Ethanol was added to solubilise the complex before centrifuging. The supernatant was decanted off and a few drops of saturated aqueous NH_4PF_6 solution were added before centrifuging again. The solution was decanted off and the solid which had formed was dissolved in CH_3CN and concentrated under reduced pressure, yielding a solid.

Dileptic Ru(II) complex of 88 ([Ru·(88)$_2$](PF$_6$)$_2$)

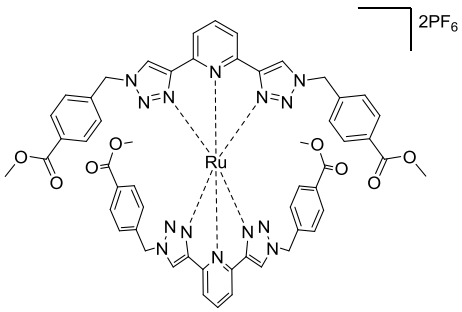

Complex [Ru·(**88**)$_2$](PF$_6$)$_2$ was prepared according to *General Procedure B* from ligand **88** (0.056 g, 0.11 mmol) and $RuCl_3 \cdot 3H_2O$ (0.012 g, 0.05 mmol), yielding a bright yellow solid (0.015 g, 0.01 mmol, 28%). This was dissolved in CH_3CN and crystallised *via* diethyl ether diffusion. m.p. 236.1–238.0 °C. HRMS (*m/z*) (MALDI+): Calculated for $C_{54}H_{46}N_{14}O_8F_6PRu^+$ *m/z* = 1265.2308 $[M-PF_6]^+$. Found *m/z* = 1265.2323; Calculated for $C_{54}H_{46}N_{14}O_8F_{12}P_2RuNa^+$ *m/z* = 1433.1848. Found *m/z* = 1433.1832. $[M+Na]^+$; Calculated for $C_{54}H_{46}N_{14}O_8RuP_2F_{12} \cdot 3H_2O$, C = 44.30, H = 3.58, N = 13.39. Found C = 44.22, H = 3.17, N = 13.39; δ_H (600 MHz, DMSO-d_6): 3.75 (s, 6H, –OCH_3), 5.35 (s, 4H, CH_2), 6.62 (d, 4H, Ph CH, *J* = 7.0 Hz), 7.18 (d, 4H, Ph CH, *J* = 7.0 Hz), 7.64 (t, 1H, 4-pyr CH, *J* = 6.9 Hz), 7.71 (d, 2H, 3- and 5-pyr CH, *J* =6.8 Hz), 8.41 (s, 2H, triazolyl CH); δ_C (150 MHz, DMSO-d_6): 52.6 (–OCH_3), 54.5 (CH_2), 120.8 (4-pyr CH), 127.2 (triazolyl CH), 128.4 (Ph CH), 130.0 (Ph CH), 138.4 (3-, 5-pyr CH), 139.4 (Ph qt), 150.3 (triazolyl qt), 165.9 (carbonyl qt); δ_F (376 MHz, DMSO-d_6): −70.6 (d, PF_6, *J* = 706.1 Hz); δ_P (162 MHz, DMSO-d_6): −142.98 (apparent quin, PF_6, *J* = 711.4 Hz); FT-IR (ATR, cm^{-1}): 3322, 1711, 1640, 1618, 1572, 1646, 1428, 1281, 1191, 1111, 828 (strong), 730.

Dileptic Ru(II) complex of 89 ([Ru·(89)$_2$](PF$_6$)$_2$)

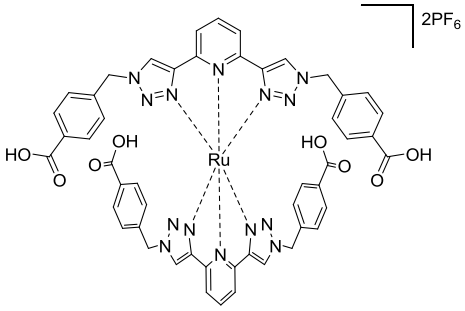

Complex [Ru·(**89**)$_2$](PF$_6$)$_2$ was prepared according to *General Procedure B*, using dicarboxylate **89** (0.100 g, 0.21 mmol) and $RuCl_3 \cdot 3H_2O$ (0.023 g, 0.11 mmol), yielding a bright yellow solid (0.069 g, 0.06 mmol, 26%). This was re-dissolved in a 1:1 mixture of CH_3CN and ethanol and crystallised *via* diethyl ether diffusion. A large yellow crystal was formed and structure determined by X-ray diffractometry. m.p. 206.5–209.6 °C. HRMS (*m/z*) (MALDI+): Calculated for $C_{50}H_{37}N_{14}O_8Ru^+$ *m/z* = 1063.1962 $[M-2(PF_6)-H]+$. Found *m/z* = 1063.1998; Calculated for $C_{50}H_{38}N_{14}O_8RuP_2F_{12} \cdot 3H_2O$, C = 42.65 H = 3.15 N = 13.93. Found C = 42.05 H = 2.58 N = 13.70; δ_H (400 MHz, DMSO-d_6): 5.67 (s, 8H, CH_2), 7.19 (d, 8H, Ph CH, *J* = 8.2 Hz**),** 7.86 (d, 8H, Ph CH, *J* = 8.2 Hz), 8.36 (t, 2H, 4-pyr CH, *J* = 7.7 Hz), 8.45 (d, 4H, 3- and 5-pyr CH, *J* = 7.7 Hz), 9.26 (s, 4H, triazolyl CH); δ_C (150 MHz, DMSO-d_6): 53.8 (CH_2),

120.0 (3-, 5-pyr CH), 126.3 (triazolyl CH), 127.7 (Ph CH), 129.7 (Ph CH), 131.0 (Ph qt), 137.5 (4-pyr CH), 137.8 (Ph qt), 149.0 (pyr qt), 149.5 (triazolyl qt), 166.3 (C=O qt); δ_F (376 MHz, DMSO-d_6): −70.6 (d, PF_6, J = 711.4 Hz); δ_P (162 MHz, DMSO-d_6): −142.99 (apparent quin, PF_6, J = 711.2 Hz); FT-IR (ATR, cm^{-1}): 3321, 2921, 2850, 1695, 1615, 1576, 1421, 1261, 1111, 1056, 1020, 805 (strong).

Ni(II) complex of 88 ([Ni·(88)$_2$](PF$_6$)$_2$)

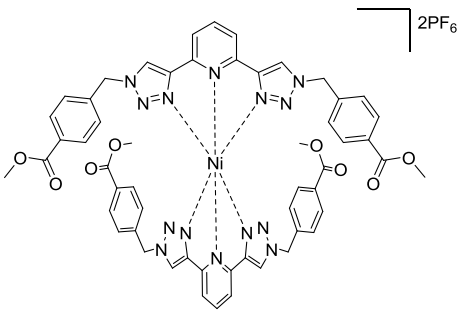

Complex [Ni·(**88**)$_2$](PF$_6$)$_2$ was prepared according to *General Procedure B* using **88** (0.100 g, 0.20 mmol) and anhydrous $NiCl_2$ (0.013 g, 0.10 mmol). Ether diffusion into a CH_3CN solution yielded lilac needle-like crystalline solid (0.020 g, 0.014 mmol, 20%). m.p. 189.9–193.8 °C; HRMS (*m/z*) (MALDI+): Calculated for $C_{54}H_{46}N_{14}O_8NiF_6P^+$ *m/z* = 1221.2618. Found *m/z* = 1221.2644; Calculated for $C_{54}H_{46}N_{14}O_8NiP_2F_{12}\cdot H_2O$, C = 46.81, H = 3.49, N = 14.15. Found C = 46.83, H = 2.98, N = 13.78; δ_H (600 MHz, CD_3CN): 3.84 (br), 5.49 (br), 6.41 (br), 7.86 (br), 17.48 (br), 29.94 (br), 56.46 (br); δ_C (150 Hz, CD_3CN, assigned by CH COSY): 50.2, 126.2; δ_F (376 MHz, CD_3CN): −73.4 (d, PF_6, J = 706.6 Hz); δ_P (162 MHz, CD_3CN): −144.6 (apparent quin, PF_6, J = 706.4 Hz); FT-IR (ATR, cm^{-1}): 3077, 2615, 2301, 1714 (strong), 1615, 1592, 1579, 1512, 1474, 1435, 1419, 1316, 1279 (strong), 1217, 1183, 1110 (strong), 1065, 1053, 1020, 967, 813 (strong), 770, 726 (strong), 619, 604, 589, 576, 555 (strong).

Ir(III) Complex of 88 ([Ir·(88)Cl$_3$])

Complex [Ir·(**88**)Cl_3] was synthesised using a modified literature procedure.[196,291] Ligand **88** (0.210 g, 0.41 mmol) and $IrCl_3\cdot xH_2O$ (0.130 g, 0.41 mmol) were suspended in ethylene glycol (5 mL). The reaction mixture was degassed before heating at 160 °C in darkness for 20 minutes under microwave irradiation. The reaction mixture was allowed to cool to room temperature before filtering to collect precipitate. The precipitate was washed with ethanol, H_2O and Et_2O, yielding complex [Ir·(**88**)Cl_3] as a yellow solid (0.166 g, 0.210 mmol, 50%). Product decomposed over 330 °C. HRMS (*m/z*) (ESI+): Calculated for $C_{27}H_{23}N_7O_4Cl_3IrNa^+$ *m/z* = 830.0404 $[M+Na]^+$. Found *m/z* = 830.0373; Calculated for $C_{27}H_{23}N_7O_4IrCl_3\cdot C_2H_6O_2$, C = 40.03, H = 3.36, N = 11.27. Found C = 39.37, H = 3.05, N = 10.99; δ_H (400 MHz, DMSO-

d_6): 3.86 (s, 6H, –OCH_3), 6.08 (s, 4H, CH_2), 7.61 (d, 4H, Ph CH, *J* = 8.3 Hz), 8.05 (d, 4H, Ph CH, *J* = 8.3 Hz), 8.15 (t, 1H, 4-pyr CH, *J* = 7.8 Hz), 8.30 (d, 2H, 3- and 5-pyr CH, *J* = 7.8 Hz), 9.33 (s, 2H, triazolyl CH); δ_C (150 MHz, DMSO-*d_6*, assigned from CH COSY): 52.7 (–OCH_3), 55.2 (CH_2), 120.4 (3-, 5-pyr CH), 127.5 (triazolyl CH), 129.2 (Ph CH), 130.2 (Ph CH), 141.1 (4-pyr CH); FT-IR (ATR, cm^{-1}): 3498, 3124, 2955, 1723 (strong), 1615, 1594, 1478, 1431 (strong), 1349, 1277 (strong), 1219, 1187, 1110 (strong), 1085, 1074, 1052, 1022, 953, 869, 807, 770, 753, 726 (strong), 713, 687, 658, 634, 622.

General Procedure C: Preparation of Pt(II) complexes

Precursor *cis*-[$PtCl_2(DMSO)_2$] was prepared from $K_2[PtCl_4]$ according to a literature procedure and used without further purification.[292] To this complex (1 equiv.) was added ligand **88** or **89** (1 equiv.) and the suspension refluxed in CH_3OH in darkness for 5 hours. The reaction mixture was cooled over ice before isolation of the product.

Pt(II) complex of 88 ([Pt·(88)Cl]Cl)

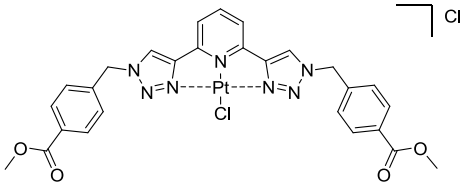

According to *General Procedure C*, ligand **88** (0.081 g, 0.16 mmol) was treated with *cis*-[$PtCl_2(DMSO)_2$] (0.069 g, 0.16 mmol). Product was purified by filtering the reaction mixture, concentrating the filtrate, re-dissolving this in $CHCl_3$ and centrifuging. The supernatant was decanted off and the process repeated until the supernatant was colourless. The resultant yellow solid was the pure complex [Pt·(**88**)Cl]Cl (0.024 g, 0.032 mmol, 20%). Product decomposed over 250 °C. HRMS (*m/z*) (ESI+): Calculated for $C_{27}H_{23}N_7O_4ClPt^+$ *m/z* = 739.1148 $[M-Cl]^+$. Found *m/z* = 739.1143; Calculated for $C_{27}H_{23}N_7O_4PtCl_2 \cdot 0.5H_2O$, C = 39.55 H, = 2.84, N = 11.74. Found C = 40.07, H = 2.42, N = 11.70; δ_H (400 MHz, DMSO-*d_6*): 3.83 (s, 6H, –OCH_3), 6.00 (s, 4H, CH_2), 7.57 (d, 4H, Ph CH, *J* = 8.3 Hz), 8.01 (d, 4H, Ph CH, *J* = 8.3 Hz), 8.22 (d, 2H, 3, 5-pyr CH, *J* = 8.0 Hz), 8.47 (t, 1H, 4-pyr CH, *J* = 8.0 Hz), 9.32 (s, 2H, triazolyl CH); FT-IR (ATR, cm^{-1}): 3423, 3076, 2953, 1716 (strong), 1614, 1595, 1579, 1512, 1479, 1434, 1418, 1313, 1280 (strong), 1223, 1184, 1110 (strong), 1074, 1047, 1019, 965, 840, 812, 747, 725 (strong), 687, 659.

Pt(II) complex of 89 ([Pt·(89)Cl]Cl)

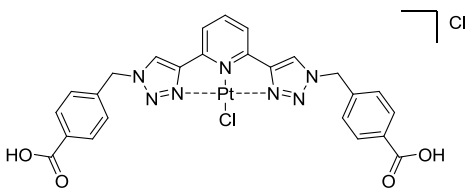

According to *General Procedure C*, **89** (0.183 g, 0.38 mmol) was treated with *cis*-[$PtCl_2(DMSO)_2$] (0.161 g, 0.38 mmol). Product was isolated upon filtration and washed with CH_3OH, $CHCl_3$ and Et_2O, yielding [Pt·(**89**)Cl]Cl as a yellow solid (0.212 g, 0.298 mmol, 78%). Product decomposed over 350 °C HRMS (MALDI+): Calculated for $C_{25}H_{19}N_7O_4ClPt^+$ *m/z* = 711.0835 $[M-Cl]^+$. Found *m/z* = 711.0859; Calculated for $C_{25}H_{19}N_7O_4PtCl_2 \cdot 1.5CHCl_3$, C = 34.35, H = 2.23, N = 10.58. Found C = 34.02, H = 2.01, N = 10.33; δ_H (600 MHz, CD_3OD): 5.96 (s, 4H, CH_2), 7.65 (d, 4H, *J* = 8.3 Hz, Ph CH), 8.06–8.18 (m, 6H, Ph CH and 3-, 5-pyr CH), 8.39 (t, 1H, *J* = 8.2 Hz, 4-pyr CH), 9.13 (s, 2H, triazolyl CH); δ_C (150 MHz, CD_3OD): 55.7 (CH_2), 120.5 (3- and 5-pyr CH), 127.1 (triazolyl CH), 128.4 (Ph CH), 130.1 (Ph CH), 131.5 (qt), 142.3 (4-pyr) CH, 148.1 (qt), 151.3 (qt), 151.7 (qt), 167.3 (C=O qt); FT-IR (ATR, cm^{-1}): 3424, 3077, 2635, 1698 (strong), 1614, 1580, 1480, 1419, 1388, 1279 (strong), 1182, 1116 (strong), 1073, 1049, 1017, 818 (strong), 752 (strong), 729 (strong).

5.3 Synthesis of ligands and complexes discussed in Chapter 3

2,6-bis(1-(4'-(-*N*-allyl-phenylcarboxamide)methylene)-1,2,3-triazol-4-yl)pyridine (90)

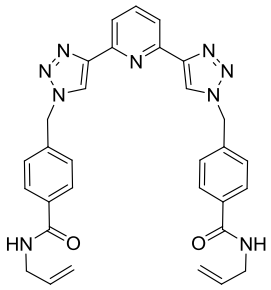

Ligand **89** (0.20 g, 0.42 mmol) was suspended in 4 mL of $SOCl_2$ and heated to 80 °C for 18 hours under a $CaCl_2$ guard tube. $SOCl_2$ was removed by vacuum distillation and the acid chloride suspended in distilled CH_2Cl_2 and used without further purification. δ_H (400 MHz, $CDCl_3$): 5.79 (s, 4H, CH_2), 7.43 (d, 4H, Ph CH, *J* = 8.1 Hz), 7.93 (d, 4H, Ph CH, *J* = 8.1 Hz), 7.99 (app s, 3H, pyr CH), 8.75 (s, 2H, triazolyl CH); FT-IR (ATR, cm^{-1}): 3081, 2981, 2883, 2511, 1778, 1738 (C=O), 1703, 1642, 1608, 1466, 1415, 1397, 1273, 1241, 1207, 1174, 1087, 1047, 966, 884, 814, 780, 775, 746, 732, 706, 658.

To this acid chloride was added distilled CH_2Cl_2 (10 mL). An excess of allyl amine (1 mL) was added and the reaction stirred at room temperature for 18 hours under a $CaCl_2$ guard tube. The reaction mixture was concentrated under reduced pressure and the product triturated a number of times with CH_3OH and separated by centrifugation. The product was collected as a white solid (0.143 g, 0.26 mmol, 61%) by filtering a suspension of the product in CH_3OH. m.p. 225.3–226.8 °C. HRMS (*m/z*) (ESI+): Calculated for

$C_{31}H_{30}N_9O_2^+$ *m/z* = 560.2522 $[M+H]^+$. Found *m/z* = 560.2547; Calculated for $C_{62}H_{58}N_{18}O_4Na^+$ *m/z* = 1141.4785 $[2M+Na]^+$. Found *m/z* = 1141.4424. Calculated for $C_{31}H_{29}N_9O_2 \cdot 0.5H_2O$, C = 61.98, H = 5.03, N = 20.99. Found C = 61.84, H = 4.70, N = 20.58; δ_H (600 MHz, DMSO-*d*$_6$): 3.90 (app t, 4H, allyl CH_2), 5.08 (dd, 2H, ^1J = 1.5 Hz, ^3J = 10.3 Hz, terminal olefin CH), 5.15 (dd, 2H, ^1J = 1.5 Hz, ^3J = 17.2 Hz, terminal olefin CH), 5.77 (s, 4H, CH_2), 5.89 (m, 2H, olefin CH), 7.43 (d, 4H, *J* = 8.2 Hz, Ph CH), 7.88 (d, 4H, *J* = 8.2 Hz, Ph CH), 7.98 (m, 3H, pyr CH), 8.66 (br t, 2H, *J* = 5.5 Hz, NH), 8.71 (s, 2H, triazolyl CH); δ_C (150 MHz, DMSO-*d*$_6$): 41.8 ($NHCH_2$), 53.0 (CH_2), 115.4 (terminal olefin CH_2), 118.9 (pyridyl CH), 124.1 (triazolyl CH), 128.1 (Ph CH), 134.6 (qt), 135.7 (olefin CH), 139.2 (pyr CH), 147.7 (qt), 150.1 (qt), 165.9 (C=O); FT-IR (ATR, cm^{-1}): 3314 (N–H st), 3116, 3078, 2913, 1642 (C=O), 1575, 1545, 1505, 1454, 1448, 1418, 1340, 1324, 1307, 1235, 1198, 1139, 1055, 1013, 999, 933, 842, 843, 806, 768, 725, 692, 671.

[2]Catenane 95.

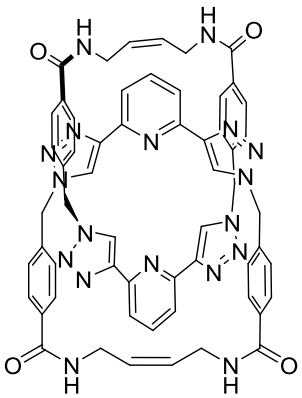

Ligand **90** (0.020 g, 0.035 mmol) was suspended in distilled CH_2Cl_2 (20 mL). The suspension was degassed with argon before adding the Hoveyda–Grubbs II catalyst (10 mol%) and stirring under argon at room temperature for 24 hours. The reaction mixture was filtered through celite and the filtrate collected and concentrated under reduced pressure. Trituration with CH_3OH yielded **95** as a white solid (0.005 g, 0.009 mmol, 26%). HRMS (*m/z*) (MALDI+): Calculated for $C_{58}H_{51}N_{18}O_4$ *m/z* = 1063.4341 $[M+H]^+$. Found *m/z* = 1063.4346; Calculated for $C_{58}H_{50}N_{18}O_4Na$ *m/z* = 1085.4159 $[M+Na]^+$. Found *m/z* = 1085.4147; δ_H (600 MHz, DMSO-*d*$_6$): 4.02 (br s, 8H, NHC$\underline{H}_2$), 5.15 (s, 8H, CH_2), 6.12 (br s, 4H, olefin CH), 6.42 (d, 8H, Ph CH, *J* = 8.2 Hz), 7.27 (d, 8H, Ph CH, *J* = 8.2 Hz), 7.78 (d, 4H, 3- and 5-pyr CH, *J* = 8.0 Hz), 7.92 (s, 4H, triazolyl CH), 7.99 (t, 2H, 4-pyr CH, *J* = 8.0 Hz), 8.22 (br s, 4H, NH); δ_C (150 MHz, DMSO-*d*$_6$): 40.1 (NH$\underline{C}H_2$, overlaps with solvent peak, assigned by HSQC), 52.5 (CH_2), 118.7 (3- and 5-pyr CH), 121.2 (triazolyl CH), 126.2 (Ph CH), 127.2 (Ph CH), 128.2 (olefin CH), 134.0 (Ph qt), 136.9 (Ph qt), 137.9 (4-pyr CH), 147.3 (triazolyl qt), 148.7 (pyr qt), 165.4 (c+O qt); FT-IR (ATR, cm^{-1}): 3748, 3262 (br), 3106, 2962, 1638 (s), 1611, 1572, 1534, 1503, 1460, 1428, 1350, 1296, 1261, 1232, 1200, 1153, ,1084, 1045, 1021, 993, 969, 861, 817 (s), 797, 761, 731, 705, 670, 663.

***General Procedure D*: Synthesis of amino-acid derivatives, 91**

As for **90**, above, ligand **89** (0.20 g, 0.42 mmol) was suspended in 4 mL of $SOCl_2$ and heated to 80 °C for 18 hours and $SOCl_2$ was removed by vacuum distillation to yield the acid chloride, which was suspended in distilled CH_2Cl_2 and used without further purification.

In a separate reaction vessel, the hydrochloride salt of the relevant amino acid methyl ester (3.3 equivalents) was suspended in distilled CH_2Cl_2 and stirred for 1 hour with an excess of triethylamine (0.2 mL) at room temperature. The two suspensions were added together and stirred at room temperature for 18 hours under a $CaCl_2$ guard tube. The reaction mixture was concentrated under reduced pressure. The product was isolated upon trituration with CH_3OH and collected by filtration, washing with CH_3OH and diethyl ether, yielding the amide as a white or off-white solid.

91-Gly

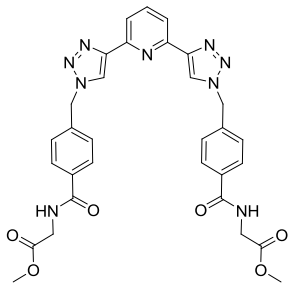

Yield: 51%. Mp: 136–141 °C. HRMS (*m/z*) (ESI+): Calculated for $C_{31}H_{30}N_9O_6^+$ *m/z* = 624.2319 $[M+H]^+$. Found *m/z* = 624.2308; calculated for $C_{31}H_{29}N_9O_6 \cdot 0.75NaCl \cdot 0.75H_2O$, C = 54.68, H = 4.51, N = 18.51. Found C = 55.02, H = 4.11, N = 18.45; δ_H (600 MHz, DMSO-d_6): 3.65 (s, 6H, $COOCH_3$), 4.02 (d, 4H, CH_2, *J* = 5.8 Hz), 5.79 (s, 4H, CH_2), 7.46 (d, 4H, Ph CH, *J* = 8.0 Hz), 7.89 (d, 4H, Ph CH, *J* = 8.0 Hz), 7.93–8.05 (m, 3H, pyr CH), 8.72 (s, 2H, triazolyl CH), 8.97 (t, 2H, NH, *J* = 5.8 Hz); δ_C (150 MHz, DMSO-d_6): 41.5 (Gly CH), 52.1 (CH_3), 53.0 (CH_2), 118.9 (pyr CH), 124.1 (triazolyl CH), 128.1 (Ph CH), 128.2 (Ph CH), 133.8 (Ph qt), 138.6 (pyr CH), 139.6 (Ph qt), 147.7 (triazolyl qt), 150.1 (pyr qt), 166.5 (amide C=O), 170.6 (ester C=O); FT-IR (ATR, cm^{-1}): 3339, 3079, 2956, 2285, 2167, 2080, 1981, 1740, 1645, 1615, 1575, 1544, 1505, 1436, 1402, 1371, 1321, 1303, 1263, 1212, 1160, 1115, 1095, 1052, 1020, 993, 979, 803, 765, 732, 694, 663.

91-*L*-Ala

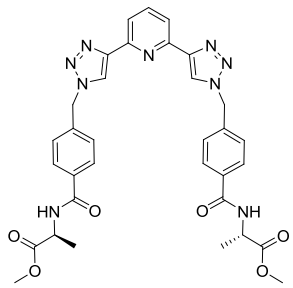

Yield: 57%. Mp: 253–254 °C. HRMS (*m/z*) (ESI+): Calculated for $C_{33}H_{34}N_9O_6^+$ *m/z* = 652.2632 $[M+H]^+$. Found *m/z* = 652.2653; calculated for $C_{33}H_{33}N_9O_6 \cdot H_2O$, C = 59.19, H = 5.27 N = 18.82. Found C = 58.86, H = 4.86 N = 18.88; δ_H (600 MHz, DMSO-d_6): 1.40 (d, 6H, Ala CH_3, *J* = 7.2 Hz), 3.64 (s, 6H, $COOCH_3$), 4.48 (quin, 2H, Ala CH, *J* = 7.2 Hz), 5.79 (s, 4H, CH_2), 7.46 (d, 4H, Ph CH, *J* = 8.1 Hz), 7.91 (d, 4H, Ph CH, *J* = 8.1 Hz), 7.99 (app s, 3H, pyr CH), 8.71 (s, 2H, triazolyl CH), 8.81 (d, 2H, NH, *J* = 7.0 Hz); δ_C (150 MHz, DMSO-d_6): 17.0, 48.6 (Ala CH), 52.2 ($COO\underline{C}H_3$), 53.0 (CH_2), 118.9 (pyr CH), 124.0 (triazolyl CH), 128.1 (Ph CH), 128.3 (Ph CH), 133.9 (qt), 138.6 (pyr CH), 139.5 (qt), 147.7 (qt), 150.1 (qt), 166.1 (qt), 173.4 (qt); FT-IR (ATR, cm^{-1}): 3353, 3169, 2957, 2162, 2050, 1741, 1642, 1609, 1577, 1532, 1505, 1459, 1438, 1426, 1380, 1359, 1320, 1271, 1238, 1212, 1198, 1167, 1096, 1080, 1045, 1021, 993, 980, 939, 876, 849, 801, 790, 776, 759, 742, 660.

91-*D*-Ala

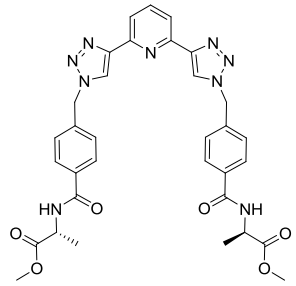

Yield: 48%. Mp: 254–255 °C. HRMS (*m/z*) (ESI+): Calculated for $C_{33}H_{34}N_9O_6^+$ *m/z* = 652.2632 $[M+H]^+$. Found *m/z* = 652.2635; calculated for $C_{33}H_{33}N_9O_6 \cdot NaCl \cdot 0.5H_2O$, C = 55.63, H= 4.38, N = 17.64. Found C = 55.46, H = 4.73, N = 17.64; δ_H (600 MHz, DMSO-d_6): 1.40 (d, 6H, Ala CH_3, *J* = 7.2 Hz), 3.64 (s, 6H, $COOCH_3$), 4.48 (quin, 2H, Ala CH, *J* = 7.2 Hz), 5.79 (s, 4H, CH_2), 7.46 (d, 4H, Ph CH, *J* = 8.2 Hz), 7.91 (d, 4H, Ph CH, *J* = 8.3 Hz), 7.94–8.06 (m, 3H, pyr CH), 8.71 (s, 2H, triazolyl CH), 8.81 (d, 2H, NH, *J* = 7.0 Hz); δ_C (150 MHz, DMSO-d_6): 16.8, 48.2 (Ala CH), 51.8 ($COO\underline{C}H_3$), 52.6 (CH_2), 118.5 (pyr CH), 123.7 (triazolyl CH), 127.7 (Ph CH), 127.9 (Ph CH), 133.5 (qt), 138.3 (pyr CH), 139.1 (qt), 147.4 (qt), 149.7 (qt), 165.7 (qt), 173.0 (qt); FT-IR (ATR, cm^{-1}): 3351, 3168, 2957, 2162, 2046, 1741, 1642, 1609, 1577, 1532, 1505, 1460, 1438, 1426, 1380, 1359, 1346, 1315, 1271, 1238, 1212, 1198, 1167, 1135, 1096, 1080, 1045, 1021, 993, 980, 938, 876, 849, 801, 790, 759, 742, 660.

91-*L*-Phe

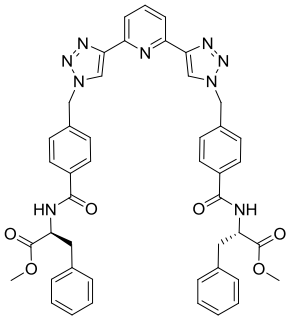

Yield: 61%. Mp: 139–148 °C. HRMS (*m/z*) (ESI+): Calculated for $C_{45}H_{41}N_9O_6Na^+$ *m/z* = 826.3078 $[M+Na]^+$. Found *m/z* = 826.3071; calculated for $C_{45}H_{41}N_9O_6 \cdot 0.5NaCl \cdot H_2O$, C = 63.50, H = 5.09, N = 14.81. Found C = 64.04, H = 4.84, N = 14.74; δ_H (600 MHz, DMSO-d_6): 3.05–3.19 (m, 4H, Phe side-chain CH_2), 3.63 (s, 6H, $COOCH_3$), 4.63–4.70 (m, 2H, stereogenic Phe CH), 5.77 (s, 4H, CH_2), 7.15–7.20 (m, 2H, Phe *p*-Ph CH), 7.25–7.30 (m, 8H, Phe *m*- and *o*-Ph CH), 7.43 (d, 4H, Ph CH adjacent to CH_2, *J* = 8.3 Hz), 7.82 (d, 4H, Ph CH adjacent amide bond, *J* = 8.3 Hz), 7.96–8.01 (m, 3H, pyr CH), 8.70 (s, 2H, triazolyl CH), 8.86 (d, 2H, NH, *J* = 7.9 Hz); δ_C (150 MHz, DMSO-d_6): 36.5 (Phe CH_2), 52.3 ($COO\underline{C}H_3$), 53.0 (CH_2), 54.6 (Phe CH), 118.9 (pyr CH), 124.1 (triazolyl CH), 126.8 (Phe *o*-Ph CH), 128.1 (Ph CH), 128.2 (Ph CH), 128.5 (Phe Ph CH), 129.4 (Phe Ph CH), 133.8, 137.9, 138.7 (pyr CH) 139.6, 147.7, 150.1, 166.3, 172.4. FT-IR (ATR, cm^{-1}): 3442, 3375, 3156, 3055, 3031, 2949, 1736, 1639, 1604, 1574, 1524, 1495, 1458, 1436, 1352, 1279, 1217 (s), 1198, 1175, 1152, 1088, 1045, 1021, 992, 977, 921, 864, 803, 736.

91-*D*-Phe

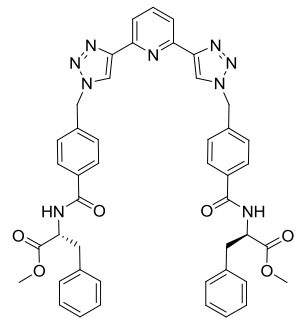

Yield: 47%. Mp: 141–149 °C. HRMS (*m/z*) (ESI−): HRMS (*m/z*) (ESI−): Calculated for $C_{45}H_{40}N_9O_6^-$ *m/z* = 802.3107 $[M-H]^-$. Found *m/z* = 802.3115; calculated for $C_{45}H_{41}N_9O_6 \cdot 1.5H_2O$, C = 65.05, H = 5.34, N = 15.17. Found C = 64.88, H = 5.08, N = 14.69; δ_H (600 MHz, DMSO-d_6): 3.05–3.19 (m, 4H, Phe side-chain CH_2), 3.63 (s, 6H, $COOCH_3$), 4.63–4.70 (m, 2H, stereogenic Phe CH), 5.77 (s, 4H, CH_2), 7.15–7.20 (m, 2H, Phe *p*-Ph CH), 7.25–7.30 (m, 8H, Phe *m*- and *o*-Ph CH), 7.43 (d, 4H, Ph CH adjacent to CH_2, *J* = 8.3 Hz), 7.81 (d, 4H, Ph CH adjacent amide bond, *J* = 8.3 Hz), 7.96–8.01 (m, 3H, pyr CH), 8.70 (s, 2H, triazolyl CH), 8.86 (d, 2H, NH, *J* = 7.9 Hz); δ_C (150 MHz, DMSO-d_6): 36.2 (Phe CH_2), 52.0 ($COO\underline{C}H_3$), 52.7 (CH_2), 54.3 (Phe CH), 118.6 (pyr CH), 123.8 (triazolyl CH), 126.5 (Phe *o*-Ph CH), 127.8 (Ph CH), 127.9 (Ph CH), 128.2 (Phe Ph CH), 129.0 (Phe Ph CH), 133.5, 137.6, 138.3 (pyr CH) 139.2, 147.4, 149.8, 166.0, 172.1; FT-IR (ATR, cm^{-1}): 3320, 3132, 3055, 3031, 2949, 1736, 1643, 1611, 1575, 1530, 1497, 1456, 1433, 1352, 1279, 1215 (s), 1198, 1175, 1152, 1083, 1043, 1019, 992, 977, 914, 864, 806, 741.

91-*L*-Trp

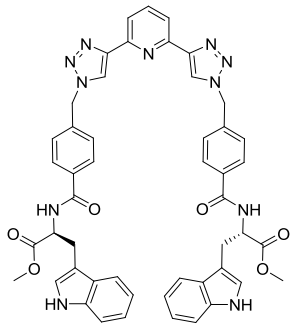

Yield: 47%. Mp: 170–173 °C. HRMS (*m/z*) (ESI+): Calculated for $C_{49}H_{43}N_{11}O_6Na^+$ *m/z* = 904.3295 $[M+Na]^+$. Found *m/z* = 904.3250; calculated for $C_{49}H_{43}N_{11}O_6 \cdot 1.25H_2O$, C = 65.07, H = 5.07, N = 17.03. Found C = 64.86, H = 4.57, N = 17.09; δ_H (600 MHz, DMSO-d_6): 3.19–3.29 (m, 4H, Trp side-chain CH_2), 3.62 (s, 6H, $COOCH_3$), 4.69 (ddd, 2H, sterogenic Trp CH, *J*=7.4 Hz, 9.0 Hz, 5.2 Hz), 5.77 (s, 4H, CH_2), 6.98 (t, 2H, indolyl CH, *J*=7.4 Hz), 7.06 (t, 2H, indolyl CH, *J*=7.4 Hz), 7.19 (d, 2H, indolyl CH, *J* = 2.2 Hz), 7.32 (d, 2H, indolyl CH, *J* = 8.0 Hz), 7.43 (d, 4H, Ph CH, *J* = 8.3 Hz), 7.55 (d, 2H, indolyl CH, *J* = 8.0 Hz), 7.84 (d, 4H, Ph CH, *J* = 8.3 Hz), 7.96–8.03 (m, 3H, pyr CH), 8.70 (s, 2H, triazolyl CH), 8.81 (d, 2H, amide NH, *J* = 7.4 Hz), 10.80 (s, 2H, indolyl NH); δ_C (150 MHz, DMSO-d_6): 26.6 (Trp CH_2), 51.9 (CH_3), 52.6 (CH_2), 53.8 (stereogenic CH), 109.9 (Trp qt), 111.4 (Trp CH), 118.0 (Trp CH), 118.4 (Trp CH), 118.6 (pyr CH), 121.0 (Trp CH), 123.6 (Trp CH), 123.7 (triazolyl CH), 127.0 (Trp qt), 127.7 (Ph CH), 127.9 (Ph CH), 133.5 (Ph qt), 136.1 (Trp qt), 139.2 (Ph qt), 147.4 (triazolyl qt), 149.8 (pyr qt), 166.0 (amide C=O), 172.4 (ester C=O); FT-IR(ATR, cm^{-1}): 3441, 3387, 3155, 3055, 2953, 1737, 1640, 1611, 1575, 1525, 1497, 1458, 1437, 1346, 1279, 1217, 1196, 1176, 1153, 1089, 1045, 1021, 1012, 992, 977, 930, 865, 803, 766, 735, 673.

91-*D*-Trp

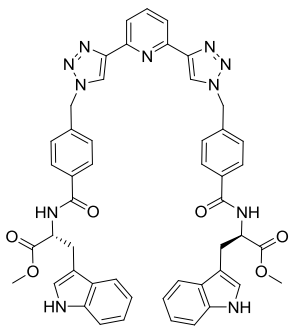

Yield: 60%. Mp: 168–171 °C. HRMS (*m/z*) (ESI+): Calculated for $C_{49}H_{44}N_{11}O_6^+$ *m/z* = 882.3476 $[M+H]^+$. Found *m/z* = 882.3440; calculated for $C_{49}H_{43}N_{11}O_6 \cdot 0.5NaCl \cdot 2H_2O$, C = 62.13, H = 5.00, N = 16.27. Found C = 62.40, H = 4.58, N = 16.73; δ_H (600 MHz, DMSO-d_6): 3.19–3.29 (m, 4H, Trp side-chain CH_2), 3.62 (s, 6H, $COOCH_3$), 4.69 (ddd, 2H, stereogenic Trp CH, *J*=7.4 Hz, 9.0 Hz, 5.2 Hz), 5.77 (s, 4H, CH_2), 6.98 (t, 2H, indolyl CH, *J*=7.4 Hz), 7.06 (t, 2H, indolyl CH, *J*=7.4 Hz), 7.19 (d, 2H, indolyl CH, *J* = 2.2 Hz), 7.32 (d, 2H, indolyl CH, *J* = 8.0 Hz), 7.43 (d, 4H, Ph CH, *J* = 8.3 Hz), 7.55 (d, 2H, indolyl CH, *J* = 8.0 Hz), 7.84 (d, 4H, Ph CH, *J* = 8.3 Hz), 7.96–8.03 (m, 3H, pyr CH), 8.70 (s, 2H, triazolyl CH), 8.81 (d, 2H, amide NH, *J* = 7.4 Hz), 10.81 (s, 2H, indolyl NH); δ_C (150 MHz, DMSO): 26.9 (Trp CH_2), 52.2 (CH_3), 53.0 (CH_2), 54.1 (stereogenic CH), 110.2 (Trp qt), 111.8 (Trp CH), 118.3 (Trp CH), 118.7 (Trp CH), 118.9 (pyr CH), 121.3 (Trp CH), 124.0

(Trp CH), 124.1 (triazolyl CH), 127.3 (Trp qt), 128.1 (Ph CH), 128.3 (Ph CH), 133.8 (Ph qt), 136.4 (Trp qt), 139.5 (Ph qt), 147.7 (triazolyl qt), 150.1 (pyr qt), 166.3 (amide C=O), 172.8 (ester C=O); FT-IR (ATR, cm^{-1}): 3441, 3388, 3158, 3057, 2954, 1738, 1639, 1611, 1576, 1525, 1496, 1459, 1437, 1347, 1280, 1217, 1197, 1176, 1152, 1089, 1046, 1021, 1012, 993, 977, 927, 864, 804, 766, 735, 674.

General Procedure E: Synthesis of Ln(III) complexes of btp ligands

Btp ligand (1 equivalent) and $Ln(CF_3SO_3)_3{\cdot}6(H_2O)$ (0.35 equivalents) were suspended in CH_3OH (6 mL) and heated to 70 °C under microwave irradiation for 20 minutes. The complexes were isolated as amber solids upon diffusion of Et_2O into a CH_3OH solution.

$[Eu{\cdot}(88)_3](CF_3SO_3)_3$

HRMS (*m/z*) (MALDI+): Calculated for $C_{83}H_{69}N_{21}O_{18}S_2F_6Eu^+$ *m/z* = 1978.369 $[EuL_3(CF_3SO_3)_2]^+$. Found *m/z* = 1978.378; calculated for $C_{56}H_{46}EuF_6N_{14}O_{14}S_2^+$ *m/z* = 1469.187 $[EuL_2(CF_3SO_3)_2]^+$. Found *m/z* = 1469.175; calculated for $C_{29}H_{23}EuF_6N_7O_{10}S_2^+$ *m/z* = 960.006 $[EuL(CF_3SO_3)_2]^+$. Found *m/z* = 960.003; calculated for $C_{84}H_{69}N_{21}O_{21}S_3F_9Eu{\cdot}6CH_2Cl_2{\cdot}1.5(CH_3)_2NCOH$, C = 50.57, H = 4.10, N = 14.04. Found C = 50.89, H = 3.60, N = 14.49; δ_H (400 MHz, CD_3CN): 3.91 (s, $–OCH_3$), 4.57 (d, 3- and 5-pyr CH), 5.52 (d, CH_2), 6.00 (d, CH_2), 6.28 (m, 4-pyr CH), 7.24 (m, Ph CH and triazolyl CH), 7.89 (d, Ph CH); FT-IR (ATR, cm^{-1}): 3112, 2955, 1719, 1615, 1589, 1468, 1435, 1275, 1254, 1223, 1156, 1109, 1067, 1029, 963, 875, 808, 727.

$[Eu{\cdot}(90)_3](CF_3SO_3)_3$

HRMS (*m/z*) (ESI+): Calculated for $C_{94}H_{87}N_{27}O_9SF_3Eu^{2+}$ *m/z* = 990.3050 $[EuL_3(CF_3SO_3)]^{2+}$. Found *m/z* = 990.3048; Calculated for $C_{63}H_{58}N_{18}O_7F_3SEu^+$ *m/z* = 1420.3621 $[EuL_2(CF_3SO_3)]^+$. Found *m/z* = 1420.3672; δ_H (400 MHz, CD_3CN): 4.01 (br s, 4H, allyl CH_2), 4.61 (d, 2H, pyr CH, *J* = 7.5 Hz), 5.10–5.25 (m, 4H, terminal olefin CH), 5.52 (d, 2H, CH_2, *J* = 14.5 Hz), 5.87 (d, 2H, CH_2, *J* = 14.5 Hz), 5.87–6.02 (m, 2H, olefin CH), 6.32 (t, 1H, 4-pyr, *J* = 7.5 Hz), 7.19–7.29 (m, 6H, Ph CH and triazolyl CH), 7.50 (app s, 2H, NH), 7.06 (d, 4H, Ph CH, *J* = 7.5 Hz); FT-IR (ATR, cm^{-1}): 3340, 3095, 1638, 1617, 1588, 1571, 1542, 1506, 1468, 1431, 1348, 1245, 1224, 1158, 1123, 1067, 1028, 993, 922, 844, 806, 758, 727, 694, 670, 660.

[Eu·(91-Gly)$_3$](CF$_3$SO$_3$)$_3$

HRMS (*m/z*) (MALDI+): Calculated for $C_{95}H_{87}N_{27}O_{24}S_2F_6Eu^+$ *m/z* = 2320.498 $[EuL_3(CF_3SO_3)_2]^+$. Found *m/z* = 2320.489; calculated for $C_{64}H_{58}N_{18}O_{18}S_2F_6Eu^+$ *m/z* = 1697.273 $[EuL_2(CF_3SO_3)_2]^+$. Found *m/z* = 1697.282; calculated for $C_{96}H_{87}N_{27}O_{27}S_3F_9Eu·1.25NaCl$, C = 45.32, H = 3.45, N = 14.87. Found C = 45.67, H = 2.92, N = 14.74; δ_H (400 MHz, CD_3OD): 3.72 (s, 6H, OCH_3), 4.15 (m, 4H, Gly CH_2), 4.50 (d, 2H, 3- and 5-pyr CH, *J* = 7.8 Hz), 5.63 (d, 2H, CH_2, *J* = 14.3 Hz), 6.19 (d, 2H, CH_2, *J* = 14.3 Hz), 6.28 (t, 1H, 4-pyr CH, *J* = 7.8 Hz), 7.30 (d, 4H, Ph CH, *J* = 8.0 Hz), 7.47 (br s, 2H, triazolyl CH), 7.79 (d, 4H, Ph CH, *J* = 8.0 Hz); FT-IR (ATR, cm^{-1}): 3345, 3101, 2956, 1737, 1643, 1617, 1572, 1541, 1504, 1467, 1454, 1438, 1248, 1222, 1160, 1122, 1067, 1029, 1011, 993, 951, 867, 847, 806, 773, 728, 659.

[Eu·(91-*L*-Ala)$_3$](CF$_3$SO$_3$)$_3$

Mp: 154–160 °C. HRMS (*m/z*) (MALDI+): Calculated for $C_{101}H_{99}N_{27}O_{24}S_2F_6Eu^+$ *m/z* = 2404.591 $[EuL_3(CF_3SO_3)_2]^+$. Found *m/z* = 2404.599; Calculated for $C_{68}H_{66}N_{18}O_{18}S_2F_6Eu^+$ *m/z* = 1753.336 $[EuL_2(CF_3SO_3)_2]^+$. Found *m/z* = 1753.330; δ_H (400 MHz, CD_3OD): 1.45–1.58 (m), 3.71 (d), 3.72 (s), 4.54 (d), 4.58–4.68 (m), 5.58–5.67 (m), 6.15 (d), 6.30 (q), 7.26–7.35 (m), 7.47 (s), 7.80 (t), 8.05 (d); FT-IR (ATR, cm^{-1}): 3340, 3107, 1737, 1645, 1617, 1574, 1538, 1504, 1454, 1250, 1223, 1160, 1122, 1067, 1029, 994, 807, 774, 728, 661.

[Eu·(91-*D*-Ala)$_3$](CF$_3$SO$_3$)$_3$

Mp: 151–157 °C. HRMS (*m/z*) (MALDI+): Calculated for $C_{101}H_{99}N_{27}O_{24}F_6S_2Eu^+$ *m/z* = 2404.591 $[EuL_3(CF_3SO_3)_2]^+$. Found *m/z* = 2404.571; Calculated for $C_{68}H_{66}N_{18}O_{18}F_6S_2Eu^+$ *m/z* = 1753.336 $[EuL_2(CF_3SO_3)_2]^+$. Found *m/z* = 1753.337; δ_H (400 MHz, CD_3OD): 1.45–1.58 (m), 3.71 (d), 3.72 (s), 4.54 (d), 4.58–4.68 (m), 5.58–5.67 (m), 6.15 (d), 6.30 (q), 7.26–7.35 (m), 7.47 (s), 7.80 (t), 8.05 (m); FT-IR (ATR, cm^{-1}): 3340, 3107, 1737, 1644, 1617, 1574, 1538, 1505, 1456, 1250, 1223, 1161, 1124, 1067, 1029, 994, 951, 807, 773, 728, 659.

[Eu·(91-*L*-Phe)$_3$](CF$_3$SO$_3$)$_3$

HRMS (*m/z*) MALDI+: Calculated for $C_{137}H_{123}N_{27}O_{24}S_2F_6Eu^+$ *m/z* = 2860.7792 $[EuL_3(CF_3SO_3)_2]^+$. Found *m/z* = 2860.7832; calculated for $C_{92}H_{82}N_{18}O_{18}S_2F_6Eu^+$ *m/z* = 2057.461 $[EuL_2(CF_3SO_3)_2]^+$. Found *m/z* = 2057.453; calculated for $C_{138}H_{123}N_{27}O_{27}F_9S_3Eu·NaCl·3H_2O$, C = 53.05, H = 4.16, N = 12.10. Found C = 52.62, H =

3.63, N = 11.91; δ_H (400 MHz, CD_3OD): 1.99 (m), 2.76 (br s), 3.06–3.19 (m), 3.45–3.47 (m), 3.69 (d), 3.73 (s), 4.45 (d), 4.86–4.97 (m), 5.51–5.60 (m), 5.96–6.13 (m), 7.01 (t), 7.10–7.18 (m), 7.19–7.31 (m), 7.42 (d), 7.63–7.72 (m), 7.77 (br s), 7.93 (d); FT-IR (ATR, cm^{-1}): 3330, 3107, 1737, 1649, 1617, 1575, 1536, 1498, 1468, 1455, 1437, 1250, 1223, 1153, 1120, 1067, 1029, 994, 857, 806, 726, 700, 661.

[Eu·(91-*D*-Phe)$_3$](CF$_3$SO$_3$)$_3$

HRMS (*m/z*) MALDI+: Calculated for $C_{137}H_{123}N_{27}O_{24}S_2F_6Eu^+$ *m/z* = 2860.779 $[EuL_3(CF_3SO_3)_2]^+$. Found *m/z* = 2860.787; calculated for $C_{92}H_{82}N_{18}O_{18}S_2F_6Eu^+$ *m/z* = 2057.461 $[EuL_2(CF_3SO_3)_2]^+$. Found *m/z* = 2057.458; calculated for $C_{138}H_{123}N_{27}O_{27}F_9S_3Eu·1.25NaCl·3H_2O$, C = 52.81, H = 4.14, N = 12.05. Found C = 53.22, H = 3.65, N = 11.92; δ_H (400 MHz, CD_3OD): 1.99 (m), 2.76 (br s), 3.06–3.19 (m), 3.45–3.47 (m), 3.69 (d), 3.73 (s), 4.45 (d), 4.86–4.97 (m), 5.51–5.60 (m), 5.96–6.13 (m), 7.01 (m), 7.10–7.18 (m), 7.19–7.31 (m), 7.42 (d), 7.63–7.72 (m), 7.77 (br s), 7.93 (d); FT-IR (ATR, cm^{-1}): 3330, 3107, 1735, 1648, 1617, 1575, 1536, 1498, 1468, 1455, 1437, 1251, 1223, 1153, 1120, 1067, 1029, 993, 857, 806, 726, 701, 661.

[Eu·(91-*L*-Trp)$_3$](CF$_3$SO$_3$)$_3$

Mp: 164–171 °C. HRMS (*m/z*) (MALDI+): Calculated for $C_{149}H_{129}N_{33}O_{24}F_6S_2Eu^+$ *m/z* = 3094.845 $[EuL_3(CF_3SO_3)_2]^+$. Found *m/z* = 3094.852; Calculated for $C_{100}H_{86}N_{22}O_{18}F_6S_2Eu^+$ *m/z* = 2212.497 $[EuL_2(CF_3SO_3)_2]^+$. Found *m/z* =2212.507; δ_H (400 MHz, CD_3OD): 0.88 (m), 1.15 (t), 1.27 (m), 2.13 (s), 2.76 (br s), 3.11 (s), 3.28 (m), 3.46 (s), 3.66 (m), 4.31 (d), 4.55 (s), 4.82 (br s), 5.47 (d), 5.70 (s), 5.94 (d), 6.37 (s), 6.93 (t), 7.03 (m), 7.11 (m), 7.18 (m), 7.26 (d), 7.38 (d), 7.50 (d), 7.59 (m), 7.71 (d), 7.93 (br s), 8.54 (br s); FT-IR (ATR, cm^{-1}): 3313, 3101, 2953, 1736, 1648, 1618, 1573, 1535, 1500, 1458, 1435, 1341, 1249, 1223, 1156, 1121, 1097, 1067, 1029, 1010, 994, 806, 742, 660.

[Eu·(91-*D*-Trp)$_3$](CF$_3$SO$_3$)$_3$

Mp: 168–173 °C. HRMS (*m/z*) (MALDI+): Calculated for $C_{149}H_{129}N_{33}O_{24}F_6S_2Eu^+$ *m/z* = 3094.845 $[EuL_3(CF_3SO_3)_2]^+$. Found *m/z* = 3094.860; Calculated for $C_{100}H_{86}N_{22}O_{18}F_6S_2Eu^+$ *m/z* = 2212.497 $[EuL_2(CF_3SO_3)_2]^+$. Found *m/z* =2212.502; δ_H (400 MHz, CD_3OD): 0.90 (m), 1.16 (t), 1.27 (m), 2.13 (s), 2.78 (br s), 3.11 (s), 3.29 (m), 3.46 (s), 3.67 (m), 4.31 (d), 4.55 (s), 4.83 (br s), 5.47 (d), 5.71 (s), 5.94 (d), 6.37 (s), 6.95 (t), 7.03 (m), 7.12 (m), 7.20 (m), 7.27 (d), 7.40 (d), 7.52 (d), 7.61 (m), 7.72 (d), 7.94 (br s), 8.55 (br s); FT-IR (ATR,

cm^{-1}): 3312, 3110, 2953, 1735, 1642, 1618, 1573, 1534, 1500, 1458, 1437, 1341, 1249, 1222, 1156, 1123, 1097, 1066, 1029, 1010, 993, 806, 741, 660.

$[Tb\cdot(\mathbf{88})_3](CF_3SO_3)_3$

HRMS (*m/z*) MALDI+: Calculated for $C_{83}H_{69}N_{21}O_{18}S_2F_6Tb^+$ *m/z* = 1984.373 $[TbL_3(CF_3SO_3)_2]^+$. Found *m/z* = 1984.370; Calculated for $C_{56}H_{46}N_{14}O_{14}S_2F_6Tb^+$ *m/z* = 1475.192 $[TbL_2(CF_3SO_3)_2]^+$. Found *m/z*= 1475.191; calculated for $C_{84}H_{69}N_{21}O_{21}S_3F_9Tb\cdot 2.5NaCl\cdot 4CH_3OH$, C = 43.88, H = 3.56, N = 12.21. Found C = 44.10, H = 3.26, N = 11.67; δ_H (400 MHz, CD_3CN): −0.41 (br s), 1.77 (s), 2.68 (br s), 2.78 (s), 2.90 (s), 3.25 (br s), 3.89 (s), 5.02 (br s), 5.71 (s), 6.16 (br s), 6.63 (br s), 7.28 (s), 7.43 (d), 7.59 (s), 8.01 (d), 8.37 (s), 9.61 (br s); FT-IR (ATR, cm^{-1}): 3119, 2956, 1716, 1616, 1589, 1435, 1253, 1223, 1154, 1108, 1068, 1028, 807, 727, 661.

$[Tb\cdot(\mathbf{91\text{-}Gly})_3](CF_3SO_3)_3$

HRMS (*m/z*) MALDI+: Calculated for $C_{95}H_{87}N_{27}O_{24}S_2F_6Tb^+$ *m/z* = 2326.502 $[TbL_3(CF_3SO_3)_2]^+$. Found *m/z* = 2326.509; calculated for $C_{64}H_{58}N_{18}O_{18}S_2F_6Tb^+$ *m/z* = 1703.278 $[TbL_2(CF_3SO_3)_2]^+$. Found *m/z* = 1703.273; calculated for $C_{96}H_{87}N_{27}O_{27}S_3F_9Tb\cdot NaCl$, C = 45.48, H = 3.46, N = 14.92. Found C = 45.67, H = 2.92, N = 14.74; δ_H (400 MHz, CD_3CN): 1.39 (br s), 1.77 (m), 2.57 (br s), 3.70 (br s), 3.88 (br s), 4.22 (br m), 4.90 (br s), 5.45 (s), 5.69 (s), 6.49 (br s), 7.12 (br s), 7.91 (br m), 10.77 (br s); FT-IR (ATR, cm^{-1}): 3345, 3106, 2953, 1741, 1649, 1618, 1589, 1574, 1541, 1505, 1469, 1455, 1438, 1408, 1370, 1247, 1213, 1183, 1158, 1123, 1068, 1060, 1029, 1011, 995, 976, 867, 849, 807, 773, 757, 729, 709, 691, 660.

$[Tb\cdot(\mathbf{91\text{-}}\boldsymbol{L}\mathbf{\text{-}Ala})_3](CF_3SO_3)_3$

HRMS (*m/z*) MALDI+: Calculated for $C_{101}H_{99}N_{27}O_{24}S_2F_6Tb^+$ *m/z* = 2410.596 $[TbL_3(CF_3SO_3)_2]^+$. Found *m/z* = 2410.602; calculated for $C_{102}H_{99}N_{27}O_{27}S_3F_9Tb\cdot 3.1(CH_3)_2NCOH$, C = 47.95, H = 4.36, N = 15.12. Found C = 48.50, H = 3.83, N = 14.90; δ_H (400 MHz, CD_3CN): −2.48, 1.77, 2.65 (br s), 3.70 (s), 3.79 (s), 4.32–4.52 (m), 5.45 (s), 5.69 (s), 6.65–6.75 (br m), 7.18 (br s), 7.29 (br s), 7.42 (d), 7.59 (s), 7.83 (d), 8.02 (d), 8.36 (s), 10.30 (br s); FT-IR (ATR, cm^{-1}): 3348, 3170, 2957, 1741, 1642, 1617, 1577, 1531, 1504, 1458, 1438, 1425, 1379, 1358, 1346, 1271, 1238, 1213, 1163, 1095, 1080, 1068, 1045, 1029, 1021, 993, 980, 938, 876, 849, 841, 801, 790, 775, 759, 742, 730, 660.

[Tb·(91-*D*-Ala)$_3$](CF$_3$SO$_3$)$_3$

HRMS (*m/z*) MALDI+: Calculated for $C_{101}H_{99}N_{27}O_{24}S_2F_6Tb^+$ *m/z* = 2410.596 $[TbL_3(CF_3SO_3)_2]^+$. Found *m/z* = 2410.602; δ_H (400 MHz, CD_3CN): −2.48 1.77, 2.65 (br s), 3.67 (m), 3.77 (s), 4.10–4.50 (m), 5.45 (s), 5.69 (s), 6.06 (br s), 6.58 (br s), 7.05 (br s), 7.18 (br s), 7.29 (br s), 7.42 (d), 7.59 (s), 7.83 (d), 8.02 (d), 8.36 (s), 10.15 (br s); FT-IR (ATR, cm^{-1}): 3350, 3167, 2957, 1741, 1642, 1617, 1577, 1534, 1504, 1457, 1438, 1426, 1379, 1358, 1346, 1271, 1239, 1214, 1163, 1095, 1080, 1068, 1045, 1029, 1021, 993, 980, 938, 876, 849, 841, 802, 790, 775, 759, 742, 730, 660.

[Tb·(91-*L*-Phe)$_3$](CF$_3$SO$_3$)$_3$

HRMS (*m/z*) MALDI+: Calculated for $C_{137}H_{123}N_{27}O_{24}S_2F_6Tb^+$ *m/z* = 2866.783 $[TbL_3(CF_3SO_3)_2]^+$. Found *m/z* = 2866.784; calculated for $C_{138}H_{123}N_{27}O_{27}F_9S_3Tb·1.25NaCl·0.5H_2O$, C = 53.47, H = 4.03, N = 12.20. Found C = 53.25, H = 3.50, N = 12.01; δ_H (400 MHz, CD_3CN): 1.00 (s), 1.25 (m), 1.77 (s), 2.58 (br m), 2.82 (m), 3.00–3.22 (m), 3.52 (s), 3.68 (s), 3.72 (s), 4.59 (br s), 4.71 (br s), 5.68 (s), 6.11 (br s), 6.57 (br s), 6.75 (br s), 7.08–7.25 (m), 7.73 (m), 8.35 (s), 9.60 (br s); FT-IR (ATR, cm^{-1}): 3312, 2955, 1737, 1645, 1617, 1573, 1536, 1498, 1469, 1455, 1436, 1250, 1222, 1154, 1121, 1097, 1067, 1029, 994, 875, 806, 727, 700, 660.

[Tb·(91-*D*-Phe)$_3$](CF$_3$SO$_3$)$_3$

HRMS (*m/z*) MALDI+: Calculated for $C_{137}H_{123}N_{27}O_{24}S_2F_6Tb^+$ *m/z* = 2866.783 $[TbL_3(CF_3SO_3)_2]^+$. Found *m/z* = 2866.773; calculated for $C_{92}H_{82}N_{18}O_{18}F_6S_2Tb^+$ *m/z* = 2063.465 $[EuL_2(CF_3SO_3)_2]^+$. Found *m/z* = 2063.465; calculated for $C_{138}H_{123}N_{27}O_{27}F_9S_3Tb·NaCl·2.5H_2O$, C = 53.01, H = 4.13, N = 12.12. Found C = 52.62, H = 3.63, N = 11.91; δ_H (400 MHz, CD_3CN): 1.00 (s), 1.25 (m), 1.77 (quin), 2.25 (br m), 2.70 (br m), 2.85 (m), 3.00–3.28 (m), 3.51 (s), 3.68 (s), 3.73 (s), 4.58 (br s), 4.71 (br s), 5.68 (s), 6.10 (br s), 6.59 (br s), 6.72 (br s), 7.08–7.25 (m), 7.72 (m), 8.35 (s), 9.70 (s); FT-IR (ATR, cm^{-1}): 3313, 2981, 1736, 1643, 1617, 1573, 1535, 1498, 1469, 1456, 1437, 1249, 1222, 1153, 1121, 1096, 1067, 1029, 994, 859, 806, 727, 700, 660.

[Tb·(91-*L*-Trp)$_3$](CF$_3$SO$_3$)$_3$

HRMS (*m/z*) MALDI+: Calculated for $C_{149}H_{129}N_{33}O_{24}F_6S_2Tb^+$ *m/z* = 3100.849 $[TbL_3(CF_3SO_3)_2]^+$. Found *m/z* = 3100.842; calculated for $C_{150}H_{129}N_{33}O_{27}F_9S_3Tb·NaCl·6H_2O$, C = 52.70, H = 4.16, N = 13.52. Found C = 52.91, H = 3.61, N = 13.44; δ_H (400 MHz, CD_3CN): 9.48 (br d), 8.33 (br s), 8.01 (m), 7.73 (d), 7.57

(m), 7.47 (m), 7.37 (d), 7.21 (m), 7.14 (m), 7.02 (m), 6.80 (s), 6.48 (br s), 5.67 (br s), 5.45 (s), 4.89 (m), 4.07 (q), 3.76 (br s), 3.66 (br s), 3.61 (br s), 3.28 (m), 1.77 (q), 1.19 (t), 1.00 (s), −2.48 (s); FT-IR (ATR, cm^{-1}): 3311, 2981, 1736, 1648, 1618, 1573, 1534, 1500, 1458, 1437, 1342, 1250, 1223, 1157, 1124, 1097, 1067, 1029, 994, 807, 743, 659.

[Tb·(91-*D*-Trp)$_3$](CF$_3$SO$_3$)$_3$

HRMS (*m/z*) MALDI+: Calculated for $C_{149}H_{129}N_{33}O_{24}F_6S_2Tb^+$ *m/z* = 3100.849 $[TbL_3(CF_3SO_3)_2]^+$. Found *m/z* = 3100.862; calculated for $C_{150}H_{129}N_{33}O_{27}S_3F_9Tb·0.75H_2O$, C = 55.17, H = 4.03, N = 14.15. Found C = 54.68, H = 3.83, N = 13.98; δ_H (400 MHz, CD_3CN): 9.66 (br s), 9.19 (s), 8.33 (br s), 8.01 (m), 7.73 (d) 7.56 (m), 7.37 (d), 7.26 (m), 7.19 (m), 7.12 (m), 7.02 (m), 6.79 (s), 6.66 (br s), 5.67 (br s), 5.45 (s), 4.90 (m), 4.07 (q), 3.82 (br s), 3.67 (d), 3.56 (m), 3.28 (d), 1.77 (q), 1.21 (t), 1.00 (s), −2.48 (s); FT-IR (ATR, cm^{-1}): 3327, 2981, 1734, 1645, 1618, 1574, 1532, 1501, 1458, 1436, 1343, 1250, 1223, 1157, 1124, 1097, 1067, 1029, 994, 806, 742, 660.

5.4 Synthesis of ligands and complexes discussed in Chapter 4

***General Procedure F*: Synthesis of carbohydrate-appended btp ligands**

The relevant precursor carbohydrate azide (0.54 mmol) was stirred in 60% aqueous ^{t}BuOH solution (40 mL). To this was added $CuSO_4·5H_2O$ (0.054 g, 0.22 mmol), sodium ascorbate (0.086 g, 0.43 mmol) and K_2CO_3 (0.105 g, 0.78 mmol). The reaction mixture was degassed and a DMF solution (5 mL) of bis-alkyne **21** (0.076 g, 0.28 mmol) was added by syringe. The reaction was stirred for 4 days. The reaction mixture was concentrated under reduced pressure and pure product isolated as described for each individual compound. In each case, the precursor carbohydrate azides were prepared by Dr Ciaran O'Reilly.

Ally-appended D-mannose derivative (96)

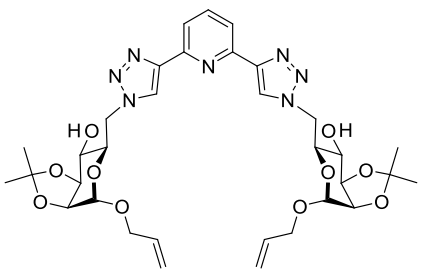

Treatment of D-mannose with allyl alcohol and catalytic camphorsulfonic acid, as described by Lin *et al.* introduced an allyl group in the anomeric position.[270] Subsequent isopropylidene protection and selective deprotection were carried out according to established protocols.[271] Treatment of this compound with TsCl in a 1:1 triethylamine–CH_2Cl_2 solution and subsequent reaction with NaN_3 in DMF yielded the carbohydrate azide precursor, which was used to prepared ligand **96** according to *General*

Procedure F. The reaction mixture was diluted with aqueous EDTA/NH_4OH solution and stirred for 1 hour before extracting into EtOAc. The organic layers were washed with brine and dried over $MgSO_4$ before concentrating under reduced pressure. The brown oil obtained was purified upon flash column chromatography (EtOAc–hexane gradient) yielding the pure compound as a white solid. Yield: 33%. m.p. 117–122 °C; HRMS (*m/z*) (MALDI+): Calculated for $C_{33}H_{44}N_7O_{10}^+$ *m/z* = 698.3150 $[M+H]^+$. Found *m/z* = 698.3171; δ_H (600 MHz, $CDCl_3$): 1.36 (s, 6H, isopropylidene CH_3), 1.45 (s, 6H, isopropylidene CH_3), 2.89 (br s, 2H, OH), 3.42–3.49 (m, 2H, saccharide CH), 3.78–3.99 (m, 4H, olefin CH_2), 4.02–4.09 (m, 2H, saccharide CH), 4.14–4.25 (m, 4H, saccharide CH), 4.67–4.91 (m, 4H, CH_2), 5.09 (app s, 2H, anomeric CH), 5.15–5.25 (m, 4H, allyl CH_2), 5.75–5.84 (m, 2H, olefin CH), 7.92 (t, 1H, 4-pyr CH, *J* = 7.7 Hz), 8.16 (d, 2H, 3- and 5-pyr CH, *J* = 7.7 Hz), 8.44 (br s, 2H, triazolyl CH); δ_C (100 MHz, $CDCl_3$): 26.0 (isopropylidene CH_3), 27.8 (isopropylidene CH_3), 51.1 (CH_2), 68.1 (olefin CH_2), 68.6 (5-hexose CH), 70.1, 75.5, 77.8, 96.2, 109.7 (isopropylidene qt), 118.4 (allyl CH_2), 119.4 (3- and 5-pyr CH), 124.4 (triazolyl CH), 132.8 (olefin CH), 138.2 (4-pyr CH), 149.4 (pyr qt); FT-IR (ATR, cm^{-1}): 3386, 2984, 2932, 1608, 1576, 1431, 1373, 1219, 1167, 1137, 1072, 978, 857, 808, 787, 729.

Glucose derivative (97)

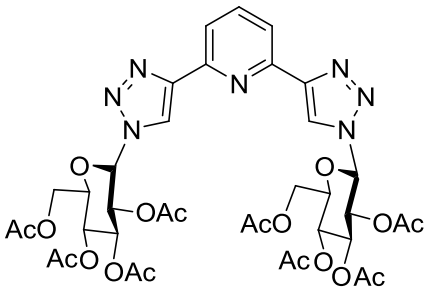

Peracetylated glucose was treated with TMS–N_3 and $SnCl_4$ according to an established protocol to introduce azide functionality into the anomeric position.[273] Ligand **97** was prepared according to *General Procedure F* from this peracetylated glucose azide. The reaction mixture was concentrated under reduced pressure, diluted with distilled water and extracted four times into EtOAc. The combined organic layers were concentrated under reduced pressure, yielding **97** as a beige solid. Yield: 77%. HRMS (*m/z*) (MALDI+): Calculated for $C_{37}H_{43}N_7O_{18}Na^+$ *m/z* = 896.256 $[M+Na]^+$. Found *m/z* = 896.2549; δ_H (600 MHz, DMSO-d_6): 1.84 (s, 6H, Ac CH_3), 2.00 (s, 6H, Ac CH_3), 2.03 (s, 6H, Ac CH_3), 2.06 (s, 6H, Ac CH_3), 4.08–4.23 (m, 4H, CH_2), 4.43–4.49 (m, 2H, 5-hexose CH), 5.28 (t, 2H, 4-hexose CH, *J* = 9.5 Hz), 5.64 (t, 2H, 3-hexose CH, *J* = 9.5 Hz), 5.76 (t, 2H, 2-hexose CH, *J* = 9.3 Hz), 6.48 (d, 2H, anomeric CH, *J* = 9.3 Hz), 7.99–8.08 (m, 3H, pyr CH), 9.03 (s, 2H, triazolyl CH); δ_C (100 MHz, DMSO-d_6): 19.9 (Ac CH_3), 20.2 (Ac CH_3), 20.4 (Ac CH_3), 20.5 (Ac CH_3), 62.0 (CH_2), 67.6, 70.4, 72.0,

73.3, 84.1, 119.0, 122.5, 138.6, 147.7 (triazolyl qt), 149.2 (pyr qt), 168.68 (Ac C=O), 169.7 (Ac C=O), 169.5 (Ac C=O), 170.0 (Ac C=O); FT-IR (ATR, cm^{-1}): 2960, 2219, 2162, 2050, 1742, 1610, 1575, 1434, 1368, 1219, 1149, 1098, 1034, 919, 814, 762.

Galactose derivative (98)

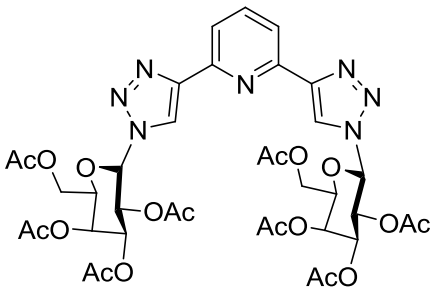

Peracetylated galactose was treated with TMS–N_3 and $SnCl_4$ according to an established protocol to introduce azide functionality into the anomeric position.[273] Ligand **98** was prepared according to *General Procedure F* from this peracetylated galactose azide. The reaction mixture was concentrated under reduced pressure, diluted with distilled water and extracted four times into EtOAc. The combined organic layers were concentrated under reduced pressure, yielding **98** as a brown solid. Yield: 82%. Decomposed above 200 °C; HRMS (*m/z*) (MALDI+): Calculated for $C_{37}H_{43}N_7O_{18}Na^+$ *m/z* = 896.256 $[M+Na]^+$. Found *m/z* = 896.2564; δ_H (600 MHz, DMSO-*d*$_6$): 1.87 (s, 6H, Ac CH_3), 1.98 (s, 6H, Ac CH_3), 2.01 (s, 6H, Ac CH_3), 2.25 (s, 6H, Ac CH_3), 4.06–4.23 (m, 4H, CH_2), 4.68 (t, 2H, 5-hexose CH, *J* = 6.09 Hz), 5.48 (d, 2H, 4-hexose CH, *J* = 3.2 Hz), 5.56 (dd, 2H, 3-hexose CH, J_1 = 3.2 Hz, J_2 = 10.1 Hz), 5.60–5.70 (m, 2H, 2-hexose CH), 6.40 (d, 2H, anomeric CH, *J* = 9.2 Hz), 8.04–8.09 (m, 3H, pyr CH), 9.00 (s, 2H, triazolyl CH); δ_C (150 MHz, DMSO-*d*$_6$): 20.0 (Ac CH_3), 20.3 (Ac CH_3), 20.4 (Ac CH_3), 20.5 (Ac CH_3), 61.6 (CH_2), 67.3 (CH), 67.9 (CH), 70.3 (CH), 73.1 (CH), 84.6 (anomeric CH), 119.1 (pyr CH), 122.8 (triazolyl CH), 138.5 (pyr CH), 147.5 (triazolyl qt), 149.3 (pyr qt), 168.7 (Ac C=O), 169.5 (Ac C=O), 169.9 (Ac C=O), 170.0 (Ac C=O); FT-IR (ATR, cm^{-1}): 3404, 2983, 1744, 1663, 1578, 1437, 1369, 1214, 1159, 1092, 1049, 956, 922, 814.

***General Procedure G*: Synthesis of chiral btp ligands 99–101**

Chiral amine (0.20 mmol) was added to a suspension of $ImSO_2N_3 \cdot H_2SO_4$ (0.24 mmol, 65 mg), K_2CO_3 (0.40 mmol, 55 mg) and $CuSO_4 \cdot 5H_2O$ (0.04 mmol, 10 mg) in CH_3OH (1.7 mL). Significant colour change was observed after 5h, then 0.5 mL of an aqueous solution of sodium ascorbate (0.09 mmol, 18 mg) and K_2SO_3 (0.20 mmol, 28 mg) was added along with 0.75 mL ^{t}BuOH and the reaction mixture degassed with argon. Bis-alkyne **21** (0.11 mmol, 30 mg) in DMF (0.3 mL) was added by syringe and the reaction stirred at room temperature for 18h. Reaction mixture was concentrated, aqueous EDTA/NH_4OH solution

added and product extracted into CH_2Cl_2. The product was isolated wither upon trituration with CH_3OH or flash chromatography.

2,6-bis(1-((*S*)-1-(4-methoxyphenyl)ethyl)-1*H*-1,2,3-triazol-4-yl)pyridine (99a)

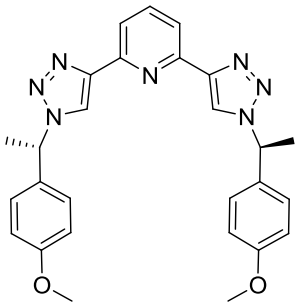

Ligand **99a** was synthesized according to the general procedure from (*S*)-(−)-1-(4-methoxyphenyl)ethylamine. Yield: 50%. m.p. 130–132 °C; HRMS (*m/z*) (ESI+): Calculated for $C_{27}H_{28}N_7O_2^+$ *m/z* = 482.2304 $[M+H]^+$. Found *m/z* = 482.2307; calculated for $C_{27}H_{27}N_7O_2$, C = 67.34, H = 5.65, N = 20.36. Found C = 67.26, H = 5.58, N = 20.30; δ_H (600 MHz, DMSO-d_6): 1.95 (d, 6H, chiral CH_3, *J* = 7.0 Hz), 3.74 (s, 6H, OCH_3), 6.00 (q, 2H, chiral CH, *J* = 7.0 Hz), 6.95 (d, 4H, Ph CH, *J* = 8.7 Hz), 7.34 (d, 4H, Ph CH, *J* = 8.7 Hz), 7.91–8.01 (m, 3H, pyr CH), 8.68 (s, 2H, triazolyl CH); δ_C (150 MHz, DMSO-d_6):δ = 21.3 (chiral CH_3), 55.5 (OCH_3), 59.4 (chiral CH), 114.4 (Ph CH), 118.8 (3- and 5-pyr CH), 122.3 (triazolyl CH), 128.1 (Ph CH), 133.2 (Ph qt), 138.6 (4-pyr CH), 147.4 (triazolyl qt), 150.2 (pyr qt), 159.3 (Ph qt); FT-IR (ATR, cm^{-1}): 3108, 2978, 2934, 2840, 1610, 1586, 1571, 1513, 1461, 1431, 1380, 1351, 1308, 1292, 1249, 1219, 1200, 1180, 1124, 1088, 1029, 1010, 993, 984, 828, 817, 778, 747, 710, 694, 684, 673.

2,6-bis(1-((*R*)-1-(4-methoxyphenyl)ethyl)-1*H*-1,2,3-triazol-4-yl)pyridine (99b)

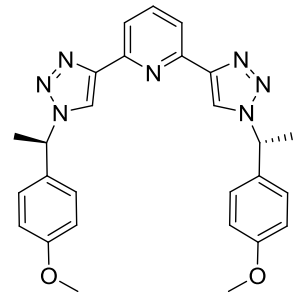

Ligand **99b** was synthesized according to the general procedure from (*R*)-(+)-1-(4-methoxyphenyl)ethylamine. Yield: 48%. m.p. 125–127 °C; HRMS (*m/z*) (ESI+): Calculated for $C_{27}H_{27}N_7O_2Na^+$ *m/z* = 504.2124 $[M+Na]^+$. Found *m/z* = 504.2125; calculated for $C_{27}H_{27}N_7O_2$, C = 67.34, H = 5.65, N = 20.36. Found C = 66.71, H = 5.28, N = 20.03; δ_H (600 MHz, DMSO-d_6): 1.95 (d, 6H, chiral CH_3, *J* = 7.0 Hz), 3.74 (s, 6H, OCH_3), 6.00 (q, 2H, chiral CH, *J* = 7.0 Hz), 6.95 (d, 4H, Ph CH, *J* = 8.6 Hz), 7.34 (d, 4H, Ph CH, *J* = 8.6 Hz), 7.95–7.98 (m, 3H, pyr CH), 8.69 (s, 2H, triazolyl CH); δ_C (150 MHz, DMSO-d_6):δ = 21.3 (chiral CH_3), 55.5 (OCH_3), 59.4 (chiral CH), 114.4 (Ph CH), 118.8 (3- and 5-pyr CH), 122.3 (triazolyl CH), 128.1 (Ph CH), 133.2 (Ph qt), 138.5 (4-pyr CH), 147.4 (triazolyl qt), 150.2 (pyr qt), 159.3 (Ph qt); FT-IR (ATR, cm^{-1}): 3108, 2978, 2935, 2838, 1610, 1586, 1571, 1513, 1462, 1431, 1380, 1351, 1307,

1291, 1249, 1219, 1201, 1180, 1125, 1087, 1028, 1010, 993, 984, 829, 815, 778, 747, 709, 694, 683, 673.

2,6-bis(1-((*S*)-1-(naphthalen-1-yl)ethyl)-1*H*-1,2,3-triazol-4-yl)pyridine (100a)

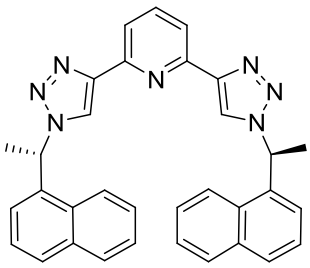

Ligand **100a** was synthesized according to the general procedure from (*S*)-(−)-1-(1-naphthyl)ethylamine. Yield: 75%. m.p. 180–183 °C; HRMS (*m/z*) (MALDI+): Calculated for $C_{33}H_{27}N_7Na^+$ $[M+Na]^+$ *m/z* = 544.2226. Found *m/z* = 544.2219; δ_H (600 MHz, DMSO-d_6): 2.07 (d, 6H, CH_3, *J* = 7.0 Hz), 6.89 (q, 2H, chiral CH, *J* = 7.0 Hz), 7.43 (d, 2H, Naph CH, *J* = 7.2 Hz), 7.50–7.65 (m, 6H, Naph CH), 7.91–8.02 (m, 7H, Naph CH and 4-pyr CH), 8.24 (d, 2H, 3- and 5-pyr CH, *J* = 8.3 Hz), 8.67 (s, 2H, triazolyl CH); δ_C (150 MHz, DMSO-d_6): 21.2 (CH_3), 55.9 (chiral CH), 118.6 (Naph CH), 122.6 (triazolyl CH), 122.7 (pyr CH), 123.7 (Naph CH), 125.6 (Naph CH), 126.1 (Naph CH), 126.9 (Naph CH), 128.8 (Naph CH), 128.9 (Naph CH), 130.0 (Naph qt), 133.4 (Naph qt), 136.1 (Naph qt), 138.3 (4-pyr CH), 147.1 (triazolyl qt), 149.8 (pyr qt); FT-IR (ATR, cm^{-1}): 3067, 2983, 1604, 1570, 1512, 1427, 1378, 1332, 1256, 1213, 1169, 1105, 1079, 1035, 1018, 991, 860, 817, 801, 776, 671.

2,6-bis(1-((*R*)-1-(naphthalen-1-yl)ethyl)-1*H*-1,2,3-triazol-4-yl)pyridine (100b)

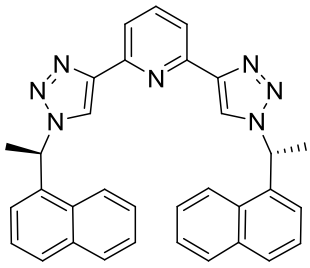

Ligand **100b** was synthesized according to the general procedure from (*R*)-(+)-1-(1-naphthyl)ethylamine. Yield: 72%. m.p. 182–185 °C; HRMS (*m/z*) (ESI+): Calculated for $C_{33}H_{27}N_7Na^+$ $[M+Na]^+$ *m/z* = 544.2226. Found *m/z* = 544.2206; δ_H (600 MHz, DMSO-d_6): 2.08 (d, 6H, CH_3, *J* = 7.0 Hz), 6.90 (q, 2H, chiral CH, *J* = 7.0 Hz), 7.43 (d, 2H, Naph CH, *J* = 7.2 Hz), 7.50–7.65 (m, 6H, Naph CH), 7.91–8.02 (m, 7H, Naph CH and 4-pyr CH), 8.24 (d, 2H, 3- and 5-pyr CH, *J* = 8.4 Hz), 8.66 (s, 2H, triazolyl CH); FT-IR (ATR, cm^{-1}): 3067, 2988, 1605, 1570, 1512, 1427, 1379, 1332, 1256, 1213, 1170, 1097, 1079, 1036, 1019, 991, 859, 817, 801, 775, 672.

2,6-bis(1-((*S*)-1-(naphthalen-2-yl)ethyl)-1*H*-1,2,3-triazol-4-yl)pyridine (101a)

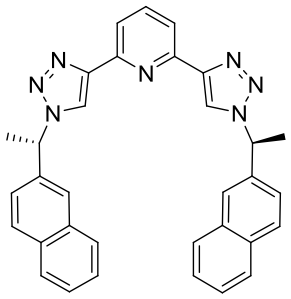

Ligand **101a** was synthesized according to the general procedure from (*S*)-(−)-1-(2-naphthyl)ethylamine. Yield: 84%. m.p. 132–139 °C; HRMS (*m/z*) (MALDI+): Calculated for $C_{33}H_{27}N_7Na^+$ $[M+Na]^+$ *m/z* = 544.2226. Found *m/z* = 544.2227; δ_H (600 MHz, DMSO-d_6): 2.07 (d, 6H, CH_3, *J* = 7.0 Hz), 6.22 (q, 2H, chiral CH, *J* = 7.0 Hz), 7.50 (dd, 2H, Naph CH, J_1 = 8.6 Hz, J_2 = 9.4 Hz), 7.51–7.57 (m, 4H, Naph CH), 7.90–7.96 (m, 8H, Naph CH), 7.99 (app s, 3H, pyr CH), 8.78 (s, 2H, triazolyl CH); δ_C (150 MHz, DMSO-d_6): 21.2 (CH_3), 60.0 (chiral CH), 118.9 (pyr CH), 122.7 (triazolyl CH), 124.7 (Naph CH), 125.5 (Naph CH), 126.8 (Naph), 126.9 (Naph CH), 127.9 (Naph CH), 128.3 (Naph CH), 128.9 (Naph CH), 132.8 (Naph qt), 133.0 (Naph qt), 138.6 (Naph qt), 138.6 (pyr CH), 147.5 (triazolyl qt), 150.2 (pyr qt); FT-IR (ATR, cm^{-1}): 3118, 3057, 2984, 2964, 1603, 1572, 1508, 1428, 1382, 1335, 1257, 1218, 1161, 1127, 1093, 1036, 993, 949, 903, 860, 808, 778, 750, 725, 658.

2,6-bis(1-((*R*)-1-(naphthalen-2-yl)ethyl)-1*H*-1,2,3-triazol-4-yl)pyridine (101b)

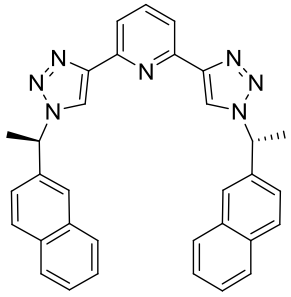

Ligand **101b** was synthesized according to the general procedure from (*R*)-(+)-1-(2-naphthyl)ethylamine. Yield: 53%. m.p. 128–132 °C; HRMS (*m/z*) (MALDI+): Calculated for $C_{33}H_{27}N_7Na^+$ $[M+Na]^+$ *m/z* = 544.2226. Found *m/z* = 544.2210; δ_H (600 MHz, DMSO-d_6): 2.07 (d, 6H, CH_3, *J* = 7.0 Hz), 6.22 (q, 2H, chiral CH, *J* = 7.0 Hz), 7.50 (app d, 2H, Naph CH, *J* = 8.6 Hz), 7.51–7.57 (m, 4H, Naph CH), 7.90–7.96 (m, 8H, Naph CH), 7.99 (app s, 3H, pyr CH), 8.78 (s, 2H, triazolyl CH); δ_C (150 MHz, DMSO-d_6): 21.2 (CH_3), 60.0 (chiral CH), 118.8 (pyr CH), 122.7 (triazolyl CH), 124.7 (Naph CH), 125.5 (Naph CH), 126.8 (Naph), 126.9 (Naph CH), 127.9 (Naph CH), 128.3 (Naph CH), 128.9 (Naph CH), 132.8 (Naph qt), 133.0 (Naph qt), 138.6 (Naph qt), 138.6 (pyr CH), 147.5 (triazolyl qt), 150.2 (pyr qt); FT-IR (ATR, cm^{-1}): 3118, 3057, 2985, 2964, 1604, 1574, 1509, 1430, 1383, 1336, 1258, 1216, 1164, 1128, 1094, 1037, 993, 951, 900, 860, 808, 779, 750, 664.

N^2,N^6-bis((*S*)-1-(4-methoxyphenyl)ethyl)pyridine-2,6-dicarboxamide (102)

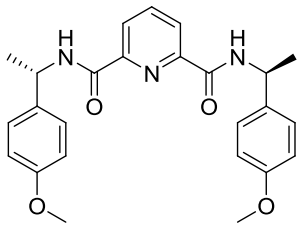

(*S*)-(−)-1-(4-methoxyphenyl)ethylamine (0.18 mL, 1.20 mmol), **dpa** (0.100 g, 0.60 mmol), hydroxybenzotriazole (0.355 g, 2.32 mmol) and triethylamine (0.355 mL, 2.40 mmol) were added together in freshly distilled CH_2Cl_2 (30 mL) and cooled to 0 °C over an ice bath. After 30 minutes, EDCI (1-ethyl-3-(3-dimethylaminopropyl)carbodiimide) (0.459 g, 2.40 mmol) was added to this. The reaction mixture was stirred at 0 °C for a further 1 hour under inert atmosphere and then heated to room temperature and stirred overnight. The reaction mixture was washed three times with saturated aqueous $NaHCO_3$ solution and the organic layers concentrated under reduced pressure. The crude product was recrystallized from hot CH_3OH, yielding **102** as white needle-like crystals (0.194 g, 0.44 mmol, 75%). m.p. 159–164 °C. HRMS (*m/z*) (MALDI+): Calculated for $C_{25}H_{27}N_3O_4Na^+$ *m/z* = 456.1899 $[M+Na]^+$. Found *m/z* = 456.1891; δ_H (400 MHz, $CDCl_3$): 1.56 (d, 6H, OC<u>H</u>$_3$, *J* = 6.8 Hz), 4.45 (br s, 2H, NH), 5.08–5.35 (m, 2H, chiral CH), 6.88 (d, 4H, Ph CH, *J* = 8.7 Hz), 7.28 (d, 4H, Ph CH, *J* = 8.7 Hz), 7.80 (br, 2H, triazolyl CH), 7.99 (t, 1H, 4-pyr CH, *J* = 7.8 Hz), 8.31 (d, 2H, 3- and 5-pyr CH, *J* = 7.8 Hz); FT-IR (ATR, cm^{-1}): 3275, 2974, 2929, 2832, 1671, 1638, 1614, 1586, 1509, 1442, 1376, 1335, 1326, 1308, 1287, 1247, 1215, 1204, 1177, 1167, 1124, 1103, 1078, 1033, 1009, 999, 934, 870, 829, 810, 733, 694, 674, 644.

1,4-bis(6-(1-((*S*)-1-(4-methoxyphenyl)ethyl)-1*H*-1,2,3-triazol-4-yl)pyridin-2-yl)buta-1,3-diyne (103)

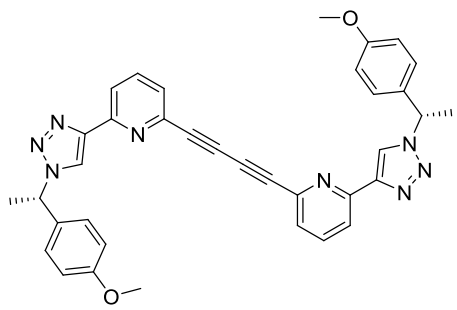

Compound **103** was isolated when **99a** was synthesised without degassing the reaction mixture by means of flash column chromatography. HRMS (*m/z*) (ESI+): Calculated for $C_{36}H_{32}N_8O_2Na^+$ *m/z* = 631.2546 $[M+Na]^+$. Found *m/z* = 631.2548; δ_H (400 MHz, $CDCl_3$): 1.98 (d, 6H, CH_3, *J* = 7.0 Hz), 5.84 (q, 2H, chiral CH, *J* = 7.0 Hz), 6.89 (d, 4H, Ph CH, *J* = 8.9 Hz), 7.24–7.29 (app m, 4H, Ph CH [overlaps with C<u>H</u>Cl_3]), 7.39 (d, 4H, pyr CH, *J* = 7.8 Hz), 7.74 (app t, 2H, 4-pyr CH, *J* = 7.8 Hz), 8.18 (d, 2H, pyr CH, *J* = 7.8 Hz).

Preparation of Ln(III) complexes of chiral btp ligands

The following complexations were carried out as described in *General Procedure E* above.

$[Eu·(96)_3](CF_3SO_3)_3$

HRMS (*m/z*) (ESI+): Calculated for $C_{100}H_{129}N_{21}O_{33}F_3SEu^{2+}$ *m/z* = 1197.3990 $[EuL_3(CF_3SO_3)]^{2+}$. Found *m/z* = 1197.4003; δ_H (400 MHz, CD_3CN): 0.84–0.92 (m), 1,27–1.45 (m), 1.52 (s), 1.62 (s), 2.64 (br s), 3.25–3.35 (m), 3.38–3.54 (m), 3.69 (d), 3.78 (d), 3.85–3.95 (m), 3.95–4.02 (m), 4.05–4.22 (m), 4.45–4.53 (m), 4.61–4.71 (m), 4.85 (s), 4.87–4.95 (m), 5.98–5.24 (m), 5.33 (s), 5.40 (s), 5.48 (s), 5.65–5.82 (m), 5.83 (m), 6.09 (m), 6.38 (t), 7.20 (s), 7.35 (s); FT-IR (ATR, cm^{-1}): 3410, 3125, 2988, 2932, 1619, 1590, 1469, 1430, 1376, 1244, 1222, 1164, 1139, 1067, 1028, 978, 856, 814, 786, 760, 723, 662.

$[Eu·(99a)_3](CF_3SO_3)_3$

HRMS (*m/z*) (MALDI+): Calculated for $C_{83}H_{81}N_{21}O_{12}F_6S_2Eu^+$ *m/z* = 1894.4932 $[EuL_3(CF_3SO_3)_2]^+$. Found *m/z* = 1894.4982; Calculated for $C_{56}H_{54}N_{14}O_{10}F_6S_2Eu^+$ *m/z* = 1413.2705 $[EuL_2(CF_3SO_3)_2]^+$. Found *m/z* = 1413.2678; δ_H (400 MHz, CD_3CN): 1.61 (d, *J* = 9.7 Hz), 1.76 (d, *J* = 7.1 Hz), 3.73–3.87 (m), 4.64 (d, *J* = 7.8 Hz), 4.94 (d, *J* = 7.9 Hz), 5.37 (q, *J* = 6.9 Hz), 5.80 (q, *J* = 7.8 Hz), 6.35 (t, *J* = 7.9 Hz), 6.63 (t, *J* = 7.9 Hz), 6.79 (d, *J* = 8.5 Hz), 6.86 (d, *J*= 8.5 Hz), 7.04 (d, *J* = 8.5 Hz), 7.15 (t, *J* = 9.7 Hz), 7.26 (s); FT-IR (ATR, cm^{-1}): 3503, 3102, 2983, 2840, 1612, 1586, 1515, 1467, 1248, 1179, 1155, 1122, 1052, 1028, 835, 815, 791, 752, 663.

$[Eu·(99b)_3](CF_3SO_3)_3$

HRMS (*m/z*) (MALDI+): Calculated for $C_{83}H_{81}N_{21}O_{12}F_6S_2Eu^+$ *m/z* = 1894.4932 $[EuL_3(CF_3SO_3)_2]^+$. Found *m/z* = 1894.5000; Calculated for $C_{56}H_{54}N_{14}O_{10}F_6S_2Eu^+$ *m/z* = 1413.2705 $[EuL_2(CF_3SO_3)_2]^+$. Found *m/z* = 1413.2681; δ_H (400 MHz, CD_3CN): 1.61 (d, *J* = 9.7 Hz), 1.76 (d, *J* = 7.1 Hz), 3.73–3.87 (m), 4.64 (d, *J* = 7.8 Hz), 4.95 (d, *J* = 7.9 Hz), 5.37 (q, *J* = 6.9 Hz), 5.81 (q, *J* = 7.9 Hz), 6.35 (t, *J* = 7.9 Hz), 6.63 (t, *J* = 7.9 Hz), 6.79 (d, *J* = 8.5 Hz), 6.87 (d, *J*= 8.5 Hz), 7.05 (d, *J* = 8.72 Hz), 7.16 (t, *J* = 8.7 Hz), 7.27 (s); FT-IR (ATR, cm^{-1}): 3503, 3101, 2981, 1612, 1588, 1514, 1466, 1245, 1158, 1119, 1053, 1027, 835, 815, 791, 752, 663.

$[Tb·(99a)_3](CF_3SO_3)_3$

HRMS (*m/z*) (MALDI+): Calculated for $C_{83}H_{81}N_{21}O_{12}F_6S_2Tb^+$ *m/z* = 1900.4973 $[TbL_3(CF_3SO_3)_2]^+$. Found *m/z* = 1900.5034; Calculated for $C_{56}H_{54}N_{14}O_{10}F_6S_2Tb^+$ *m/z* = 1419.2746 $[TbL_2(CF_3SO_3)_2]^+$. Found *m/z* = 1419.2734; δ_H (400 MHz, CD_3OD): −2.49 (br s), −0.59 (br s), 1.27 (s), 1.97 (s), 2.76 (br s), 3.11 (s), 3.19 (s), 3.61 (s), 3.77 (s), 4.55 (s),

5.23 (m), 5.91 (s), 6.23 (s), 6.93 (d), 7.30 (d), 7.92 (br s), 8.58 (br s); FT-IR (ATR, cm^{-1}): 3112, 2981, 1613, 1587, 1514, 1467, 1248, 1158, 1052, 1027, 814, 792, 752, 664.

$[Tb{\cdot}(99b)_3](CF_3SO_3)_3$

HRMS (*m/z*) (MALDI+): Calculated for $C_{83}H_{81}N_{21}O_{12}F_6S_2Tb^+$ *m/z* = 1900.4973 $[TbL_3(CF_3SO_3)_2]^+$. Found *m/z* = 1900.4973; Calculated for $C_{56}H_{54}N_{14}O_{10}F_6S_2Tb^+$ *m/z* = 1419.2746 $[TbL_2(CF_3SO_3)_2]^+$. Found *m/z* = 1419.2717; δ_H (400 MHz, CD_3OD): −2.50 (br s), −0.59 (br s), 1.26 (s), 1.98 (s), 2.76 (br s), 3.11 (s), 3.18 (s), 3.61 (s), 3.77 (s), 4.56 (s), 5.22 (m), 5.90 (s), 6.22 (s), 7.91 (d), 7.31 (d), 7.91 (br s), 8.57 (br s); FT-IR (ATR, cm^{-1}): 3112, 2981, 1613, 1587, 1515, 1467, 1249, 1155, 1052, 1028, 815, 792, 752, 664.

$[Eu{\cdot}(100a)_3](CF_3SO_3)_3$

Product decomposed over 180° C. HRMS (*m/z*) (ESI+): Calculated for $C_{100}H_{81}N_{21}O_3F_3SEu^{2+}$ *m/z* = 933.2875 $[EuL_3(CF_3SO_3)]^{2+}$. Found *m/z* = 933.2800; δ_H (4000 MHz, CD_3CN): 4.12 (s), 4.36 (s), 5.96 (s), 6.15 (s), 6.48 (s), 6.87 (s), 7.08 (m), 7.18 (m), 7.38 (m), 7.54 (m), 7.79 (s), 7.97 (m); FT-IR (ATR, cm^{-1}): 3426, 3090, 2981, 1617, 1586, 1512, 1466, 1250, 1155, 1067, 1028, 969, 852, 804, 778.

$[Eu{\cdot}(100b)_3](CF_3SO_3)_3$

Product decomposed over 180° C. HRMS (*m/z*) (ESI+): Calculated for $C_{100}H_{81}N_{21}O_3F_3SEu^{2+}$ *m/z* = 933.2875 $[EuL_3(CF_3SO_3)]^{2+}$. Found *m/z* = 933.2887; δ_H (400 MHz, CD_3CN): 1.62 (s), 4.10 (s), 4.34 (s), 5.19 (s), 5.36 (m), 5.73 (s), 5.95 (s), 6.14 (s), 6.46 (s), 6.85 (m), 7.09 (m), 7.18 (m), 7.38 (m), 7.55 (m), 7.77 (m), 7.96 (m); FT-IR (ATR, cm^{-1}): 3500, 3256, 3110, 2990, 1616, 1590, 1513, 1467, 1248, 1159, 1067, 1029, 973, 852, 803, 778.

6. References

1. Lehn, J.-M., *Science* **2002**, *295*, 2400-2403.
2. Gunnlaugsson, T.; Stomeo, F., *Org. Biomol. Chem.* **2007**, *5*, 1999-2009.
3. Mobian, P.; Kern, J.-M.; Sauvage, J.-P., *Helv. Chim. Acta* **2003**, *86*, 4195-4213.
4. Leonard, J. P.; Jensen, P.; McCabe, T.; O'Brien, J. E.; Peacock, R. D.; Kruger, P. E.; Gunnlaugsson, T., *J. Am. Chem. Soc.* **2007**, *129*, 10986-10987.
5. Lincheneau, C.; Peacock, R. D.; Gunnlaugsson, T., *Chem. Asian J.* **2010**, *5*, 500-504.
6. Lincheneau, C.; Destribats, C.; Barry, D. E.; Kitchen, J. A.; Peacock, R. D.; Gunnlaugsson, T., *Dalton Trans.* **2011**, *40*, 12056-12059.
7. Lincheneau, C.; Jean-Denis, B.; Gunnlaugsson, T., *Chem. Commun.* **2014**, *50*, 2857-2860.
8. Barry, D. E.; Kitchen, J. A.; Albrecht, M.; Faulkner, S.; Gunnlaugsson, T., *Langmuir* **2013**, *29*, 11506-11515.
9. Kitchen, J. A.; Barry, D. E.; Mercs, L.; Albrecht, M.; Peacock, R. D.; Gunnlaugsson, T., *Angew. Chem. Int. Ed.* **2012**, *51*, 704-708.
10. McMahon, B. K.; Gunnlaugsson, T., *Tetrahedron Lett.* **2010**, *51*, 5406-5410.
11. Faulkner, S.; Pope, S. J. A.; Burton-Pye, B. P., *Appl. Spectrosc. Rev.* **2005**, *40*, 1-31.
12. McMahon, B. K.; Mauer, P.; McCoy, C. P.; Lee, T. C.; Gunnlaugsson, T., *Aust. J. Chem.* **2011**, *64*, 600-603.
13. Pan, L.; Adams, K. M.; Hernandez, H. E.; Wang, X.; Zheng, C.; Hattori, Y.; Kaneko, K., *J. Am. Chem. Soc.* **2003**, *125*, 3062-3067.
14. Brayshaw, P. A.; Bünzli, J.-C. G.; Froidevaux, P.; Harrowfield, J. M.; Kim, Y.; Sobolev, A. N., *Inorg. Chem.* **1995**, *34*, 2068-2076.
15. Renaud, F.; Piguet, C.; Bernardinelli, G.; Bünzli, J.-C. G.; Hopfgartner, G., *J. Am. Chem. Soc.* **1999**, *121*, 9326-9342.
16. Platas-Iglesias, C.; Piguet, C.; Andre, N.; Bunzli, J.-C. G., *J. Chem. Soc., Dalton Trans.* **2001**, 3084-3091.
17. Ouali, N.; Bocquet, B.; Rigault, S.; Morgantini, P.-Y.; Weber, J.; Piguet, C., *Inorg. Chem.* **2002**, *41*, 1436-1445.
18. Senegas, J.-M.; Bernardinelli, G.; Imbert, D.; Bünzli, J.-C. G.; Morgantini, P.-Y.; Weber, J.; Piguet, C., *Inorg. Chem.* **2003**, *42*, 4680-4695.

19. Gassner, A.-L.; Duhot, C. l.; G. Bünzli, J.-C.; Chauvin, A.-S., *Inorg. Chem.* **2008**, *47*, 7802-7812.
20. Aebischer, A.; Gumy, F.; Bunzli, J.-C. G., *Phys. Chem. Chem. Phys.* **2009**, *11*, 1346-1353.
21. Chauvin, A. S.; Gumy, F.; Imbert, D.; Bünzli, J. C. G., *Spectrosc. Lett.* **2004**, *37*, 517-532.
22. Chauvin, A.-S.; Gumy, F.; Imbert, D.; Bünzli, J.-C. G., *Spectrosc. Lett.* **2007**, *40*, 193-193.
23. Mistri, S.; Zangrando, E.; Manna, S. C., *Inorg. Chim. Acta* **2013**, *405*, 331-338.
24. Leigh, D. A.; Lusby, P. J.; Slawin, A. M. Z.; Walker, D. B., *Angew. Chem. Int. Ed.* **2005**, *44*, 4557-4564.
25. Fuller, A.-M. L.; Leigh, D. A.; Lusby, P. J.; Slawin, A. M. Z.; Walker, D. B., *J. Am. Chem. Soc.* **2005**, *127*, 12612-12619.
26. Fuller, A.-M. L.; Leigh, D. A.; Lusby, P. J., *Angew. Chem. Int. Ed.* **2007**, *46*, 5015-5019.
27. Halvagar, M. R.; Tolman, W. B., *Inorg. Chem.* **2013**, *52*, 8306-8308.
28. Tanase, S.; Gallego, P. M.; de Gelder, R.; Fu, W. T., *Inorg. Chim. Acta* **2007**, *360*, 102-108.
29. Hua, K. T.; Xu, J.; Quiroz, E. E.; Lopez, S.; Ingram, A. J.; Johnson, V. A.; Tisch, A. R.; de Bettencourt-Dias, A.; Straus, D. A.; Muller, G., *Inorg. Chem.* **2011**, *51*, 647-660.
30. Desimoni, G.; Faita, G.; Quadrelli, P., *Chem. Rev.* **2003**, *103*, 3119-3154.
31. de Bettencourt-Dias, A.; Viswanathan, S.; Rollett, A., *J. Am. Chem. Soc.* **2007**, *129*, 15436-15437.
32. Matsumoto, K.; Suzuki, K.; Tsukuda, T.; Tsubomura, T., *Inorg. Chem.* **2010**, *49*, 4717-4719.
33. de Bettencourt-Dias, A.; Barber, P. S.; Viswanathan, S.; de Lill, D. T.; Rollett, A.; Ling, G.; Altun, S., *Inorg. Chem.* **2010**, *49*, 8848-8861.
34. de Bettencourt-Dias, A.; Barber, P. S.; Bauer, S., *J. Am. Chem. Soc.* **2012**, *134*, 6987-6994.
35. Jameson, D. L.; Blaho, J. K.; Kruger, K. T.; Goldsby, K. A., *Inorg. Chem.* **1989**, *28*, 4312-4314.
36. Halcrow, M. A., *Coord. Chem. Rev.* **2005**, *249*, 2880-2908.
37. Halcrow, M. A., *New J. Chem.* **2014**, *38*, 1868-1882.

38. Sugiyarto, K. H.; Craig, D. C.; Rae, A. D.; Goodwin, H. A., *Aust. J. Chem.* **1993**, *46*, 1269-1290.
39. Duati, M.; Fanni, S.; Vos, J. G., *Inorg. Chem. Commun.* **2000**, *3*, 68-70.
40. Duati, M.; Tasca, S.; Lynch, F. C.; Bohlen, H.; Vos, J. G.; Stagni, S.; Ward, M. D., *Inorg. Chem.* **2003**, *42*, 8377-8384.
41. Mydlak, M.; Mauro, M.; Polo, F.; Felicetti, M.; Leonhardt, J.; Diener, G.; De Cola, L.; Strassert, C. A., *Chem. Mater.* **2011**, *23*, 3659-3667.
42. Mauro, M.; Aliprandi, A.; Cebrian, C.; Wang, D.; Kubel, C.; De Cola, L., *Chem. Commun.* **2014**, *50*, 7269-7272.
43. Wu, K.-L.; Ho, S.-T.; Chou, C.-C.; Chang, Y.-C.; Pan, H.-A.; Chi, Y.; Chou, P.-T., *Angew. Chem. Int. Ed.* **2012**, *51*, 5642-5646.
44. Drew, M. G. B.; Hudson, M. J.; Iveson, P. B.; Madic, C.; Russell, M. L., *J. Chem. Soc., Dalton Trans.* **1999**, 2433-2440.
45. Chapyshev, S. V., *Chem. Heterocycl. Compd.* **2001**, *37*, 861-866.
46. Chapyshev, S. V., *Mendeleev Commun.* **1999**, *9*, 164-165.
47. Chapyshev, S. V.; Walton, R.; Lahti, P. M., *Mendeleev Commun.* **2000**, *10*, 138-139.
48. Ostapowicz, T. G.; Hölscher, M.; Leitner, W., *Chem. Eur. J.* **2011**, *17*, 10329-10338.
49. Merckx, T.; Verwilst, P.; Dehaen, W., *Tetrahedron Lett.* **2013**, *54*, 4237-4240.
50. Fleming, A.; Gaire, J.; Kelleher, F.; McGinley, J.; McKee, V., *Tetrahedron* **2011**, *67*, 3260-3266.
51. Gaire, J.; McGinley, J.; Fleming, A.; Kelleher, F., *Tetrahedron* **2012**, *68*, 5935-5941.
52. Allampally, N. K.; Strassert, C. A.; De Cola, L., *Dalton Trans.* **2012**, *41*, 13132-13137.
53. Strassert, C. A.; Chien, C.-H.; Galvez Lopez, M. D.; Kourkoulos, D.; Hertel, D.; Meerholz, K.; De Cola, L., *Angew. Chem. Int. Ed.* **2011**, *50*, 946-950.
54. Wartenberg, N.; Raccurt, O.; Bourgeat-Lami, E.; Imbert, D.; Mazzanti, M., *Chem. Eur. J.* **2013**, *19*, 3477-3482.
55. Andreiadis, E. S.; Imbert, D.; Pecaut, J.; Demadrille, R.; Mazzanti, M., *Dalton Trans.* **2012**, *41*, 1268-1277.
56. Vos, J. G.; Kelly, J. M., *Dalton Trans.* **2006**, 4869-4883.

57. Sauvage, J. P.; Collin, J. P.; Chambron, J. C.; Guillerez, S.; Coudret, C.; Balzani, V.; Barigelletti, F.; De Cola, L.; Flamigni, L., *Chem. Rev.* **1994**, *94*, 993-1019.
58. Andres, P. R.; Schubert, U. S., *Adv. Mater.* **2004**, *16*, 1043-1068.
59. Kinoshita, T.; Dy, J. T.; Uchida, S.; Kubo, T.; Segawa, H., *Nature Photon.* **2013**, *7*, 535-539.
60. Sakamoto, R.; Katagiri, S.; Maeda, H.; Nishihara, H., *Coord. Chem. Rev.* **2013**, *257*, 1493-1506.
61. Banerjee, S.; Kitchen, J. A.; Bright, S.; O'Brien, J. E.; Williams, D. C.; Kelly, J. M.; Gunnlaugsson, T., *Chem. Commun.* **2013**, *49*, 8522-8524.
62. Hannon, M. J.; Green, P. S.; Fisher, D. M.; Derrick, P. J.; Beck, J. L.; Watt, S. J.; Ralph, S. F.; Sheil, M. M.; Barker, P. R.; Alcock, N. W.; Price, R. J.; Sanders, K. J.; Pither, R.; Davis, J.; Rodger, A., *Chem. Eur. J.* **2006**, *12*, 8000-8013.
63. Han, F. S.; Higuchi, M.; Ikeda, T.; Negishi, Y.; Tsukuda, T.; Kurth, D. G., *J. Mater. Chem.* **2008**, *18*, 4555-4560.
64. Kotova, O.; Daly, R.; dos Santos, C. M. G.; Boese, M.; Kruger, P. E.; Boland, J. J.; Gunnlaugsson, T., *Angew. Chem. Int. Ed.* **2012**, *51*, 7208-7212.
65. Kitchen, J. A.; Boyle, E. M.; Gunnlaugsson, T., *Inorg. Chim. Acta* **2012**, *381*, 236-242.
66. Wang, P.; Li, Z.; Lv, G.-C.; Zhou, H.-P.; Hou, C.; Sun, W.-Y.; Tian, Y.-P., *Inorg. Chem. Commun.* **2012**, *18*, 87-91.
67. Nonat, A. M.; Harte, A. J.; Senechal-David, K.; Leonard, J. P.; Gunnlaugsson, T., *Dalton Trans.* **2009**, 4703-4711.
68. Nonat, A. M.; Quinn, S. J.; Gunnlaugsson, T., *Inorg. Chem.* **2009**, *48*, 4646-4648.
69. Byrne, J. P.; Kitchen, J. A.; Gunnlaugsson, T., *Chem. Soc. Rev.* **2014**, *43*, 5302-5325.
70. Li, Y.; Huffman, J. C.; Flood, A. H., *Chem. Commun.* **2007**, 2692-2694.
71. Zhang, C.; Shen, X.; Sakai, R.; Gottschaldt, M.; Schubert, U. S.; Hirohara, S.; Tanihara, M.; Yano, S.; Obata, M.; Xiao, N.; Satoh, T.; Kakuchi, T., *J. Polym. Sci., Part A: Polym. Chem.* **2011**, *49*, 746-753.
72. Byrne, J. P.; Kitchen, J. A.; Kotova, O.; Leigh, V.; Bell, A.; Boland, J. J.; Albrecht, M.; Gunnlaugsson, T., *Dalton Trans.* **2014**, *43*, 196-209.
73. Schulze, B.; Schubert, U. S., *Chem. Soc. Rev.* **2014**, *43*, 2522-2571.
74. Lashgari, K.; Kritikos, M.; Norrestam, R.; Norrby, T., *Acta Crystallogr. Sect. C* **1999**, *55*, 64-67.

75. Struthers, H.; Mindt, T. L.; Schibli, R., *Dalton Trans.* **2010**, *39*, 675-696.
76. Kolb, H. C.; Finn, M. G.; Sharpless, K. B., *Angew. Chem. Int. Ed.* **2001**, *40*, 2004-2021.
77. Rostovtsev, V. V.; Green, L. G.; Fokin, V. V.; Sharpless, K. B., *Angew. Chem. Int. Ed.* **2002**, *41*, 2596-2599.
78. Huisgen, R., 1,3-Dipolar cycloadditioans - Introduction, survey, mechanism. In *1,3-Dipolar Cycloaddition Chemistry*, Padwa, A., Ed. Wiley: New York, 1984; pp 1-176.
79. Michael, A., *J. Prakt. Chem.* **1893**, *48*, 94-95.
80. Tornøe, C. W.; Christensen, C.; Meldal, M., *J. Org. Chem.* **2002**, *67*, 3057-3064.
81. Crowley, J. D.; Bandeen, P. H., *Dalton Trans.* **2010**, *39*, 612-623.
82. Meudtner, R. M.; Ostermeier, M.; Goddard, R.; Limberg, C.; Hecht, S., *Chem. Eur. J.* **2007**, *13*, 9834-9840.
83. Finn, M. G.; Fokin, V. V., *Chem. Soc. Rev.* **2010**, *39*, 1231-1232.
84. Tropiano, M.; Kilah, N. L.; Morten, M.; Rahman, H.; Davis, J. J.; Beer, P. D.; Faulkner, S., *J. Am. Chem. Soc.* **2011**, *133*, 11847-11849.
85. Milne, M.; Chicas, K.; Li, A.; Bartha, R.; Hudson, R. H. E., *Org. Biomol. Chem.* **2012**, *10*, 287-292.
86. Molloy, J. K.; Kotova, O.; Peacock, R. D.; Gunnlaugsson, T., *Org. Biomol. Chem.* **2012**, *10*, 314-322.
87. Goldup, S. M.; Leigh, D. A.; Long, T.; McGonigal, P. R.; Symes, M. D.; Wu, J., *J. Am. Chem. Soc.* **2009**, *131*, 15924-15929.
88. Lahlali, H.; Jobe, K.; Watkinson, M.; Goldup, S. M., *Angew. Chem. Int. Ed.* **2011**, *50*, 4151-4155.
89. Winn, J.; Pinczewska, A.; Goldup, S. M., *J. Am. Chem. Soc.* **2013**, *135*, 13318-13321.
90. Bordoli, R. J.; Goldup, S. M., *J. Am. Chem. Soc.* **2014**, *136*, 4817-4820.
91. Teyssot, M.-L.; Nauton, L.; Canet, J.-L.; Cisnetti, F.; Chevry, A.; Gautier, A., *Eur. J. Org. Chem.* **2010**, *2010*, 3507-3515.
92. Chamas, Z. E. A.; Guo, X.; Canet, J.-L.; Gautier, A.; Boyer, D.; Mahiou, R., *Dalton Trans.* **2010**, *39*, 7091-7097.
93. Guo, X.; Canet, J.-L.; Boyer, D.; Gautier, A.; Mahiou, R., *J. Mater. Chem.* **2012**, *22*, 6117-6122.

94. Johnson, J. A.; Finn, M. G.; Koberstein, J. T.; Turro, N. J., *Macromol. Rapid Commun.* **2008**, *29*, 1052-1072.
95. Holub, J. M.; Kirshenbaum, K., *Chem. Soc. Rev.* **2010**, *39*, 1325-1337.
96. Hanni, K. D.; Leigh, D. A., *Chem. Soc. Rev.* **2010**, *39*, 1240-1251.
97. Mindt, T. L.; Struthers, H.; Brans, L.; Anguelov, T.; Schweinsberg, C.; Maes, V.; Tourwé, D.; Schibli, R., *J. Am. Chem. Soc.* **2006**, *128*, 15096-15097.
98. Bock, V. D.; Hiemstra, H.; van Maarseveen, J. H., *Eur. J. Org. Chem.* **2006**, *2006*, 51-68.
99. Hua, Y.; Flood, A. H., *Chem. Soc. Rev.* **2010**, *39*, 1262-1271.
100. Schweinfurth, D.; Deibel, N.; Weisser, F.; Sarkar, B., *Nachr. Chem.* **2011**, *59*, 937-941.
101. Crowley, J. D.; McMorran, D. A., "Click-Triazole" Coordination Chemistry: Exploiting 1,4-Disubstituted-1,2,3-Triazoles as Ligands. In *Click Triazoles*, Košmrlj, J., Ed. Springer Berlin Heidelberg: 2012; Vol. 28, pp 31-83.
102. Li, Y.; Pink, M.; Karty, J. A.; Flood, A. H., *J. Am. Chem. Soc.* **2008**, *130*, 17293-17295.
103. Meudtner, R. M.; Hecht, S., *Angew. Chem. Int. Ed.* **2008**, *47*, 4926-4930.
104. Chan, T. R.; Hilgraf, R.; Sharpless, K. B.; Fokin, V. V., *Org. Lett.* **2004**, *6*, 2853-2855.
105. Abarca, B.; Ballesteros, R.; Chadlaoui, M., *Tetrahedron* **2004**, *60*, 5785-5792.
106. Fletcher, J. T.; Bumgarner, B. J.; Engels, N. D.; Skoglund, D. A., *Organomet.* **2008**, *27*, 5430-5433.
107. Crowley, J. D.; Bandeen, P. H.; Hanton, L. R., *Polyhedron* **2010**, *29*, 70-83.
108. Brown, D. G.; Schauer, P. A.; Borau-Garcia, J.; Fancy, B. R.; Berlinguette, C. P., *J. Am. Chem. Soc.* **2013**, *135*, 1692-1695.
109. Brunet, E.; Juanes, O.; Jiménez, L.; Rodríguez-Ubis, J. C., *Tetrahedron Lett.* **2009**, *50*, 5361-5363.
110. Schulze, B.; Friebe, C.; Hoeppener, S.; Pavlov, G. M.; Winter, A.; Hager, M. D.; Schubert, U. S., *Macromol. Rapid Commun.* **2012**, *33*, 597-602.
111. Danielraj, P.; Varghese, B.; Sankararaman, S., *Acta Crystallogr. Sect. C* **2010**, *66*, m366-m370.
112. Schulze, B.; Escudero, D.; Friebe, C.; Siebert, R.; Görls, H.; Köhn, U.; Altuntas, E.; Baumgaertel, A.; Hager, M. D.; Winter, A.; Dietzek, B.; Popp, J.; González, L.; Schubert, U. S., *Chem. Eur. J.* **2011**, *17*, 5494-5498.

113. Schulze, B.; Friebe, C.; Hager, M. D.; Winter, A.; Hoogenboom, R.; Gorls, H.; Schubert, U. S., *Dalton Trans.* **2009**, 787-794.
114. Karthikeyan, T.; Sankararaman, S., *Tetrahedron: Asymmetry* **2008**, *19*, 2741-2745.
115. Schulze, B.; Friebe, C.; Hager, M. D.; Winter, A.; Hoogenboom, R.; Görls, H.; Schubert, U. S., *Polym. Prepr.* **2009**, *50*, 252.
116. Meudtner, R. M.; Hecht, S., *Macromol. Rapid Commun.* **2008**, *29*, 347-351.
117. Chandrasekhar, N.; Chandrasekar, R., *J. Org. Chem.* **2010**, *75*, 4852-4855.
118. Amb, C. M.; Rasmussen, S. C., *J. Org. Chem.* **2006**, *71*, 4696-4699.
119. Nettekoven, M.; Jenny, C., *Org. Process Res. Dev.* **2002**, *7*, 38-43.
120. Schulze, B.; Friebe, C.; Hager, M. D.; Winter, A.; Schubert, U. S., *Polym. Prepr.* **2009**, *50*, 576.
121. Schulze, B.; Friebe, C.; Hoeppener, S.; Pavlov, G. M.; Hager, M. D.; Winter, A.; Schubert, U. S., *Polym. Prepr.* **2011**, *52*, 917-918.
122. Ballesteros-Garrido, R.; Abarca, B.; Ballesteros, R.; Ramirez de Arellano, C.; Leroux, F. R.; Colobert, F.; Garcia-Espana, E., *New J. Chem.* **2009**, *33*, 2102-2106.
123. Ballesteros-Garrido, R.; Delgado-Pinar, E.; Abarca, B.; Ballesteros, R.; Leroux, F. R.; Colobert, F.; Zaragozá, R. J.; García-España, E., *Tetrahedron* **2012**, *68*, 3701-3707.
124. Zornik, D.; Meudtner, R. M.; El Malah, T.; Thiele, C. M.; Hecht, S., *Chem. Eur. J.* **2011**, *17*, 1473-1484.
125. Chandrasekhar, N.; Chandrasekar, R., *Angew. Chem. Int. Ed.* **2012**, *51*, 3556-3561.
126. Ostermeier, M.; Berlin, M.-A.; Meudtner, R. M.; Demeshko, S.; Meyer, F.; Limberg, C.; Hecht, S., *Chem. Eur. J.* **2010**, *16*, 10202-10213.
127. El Malah, T.; Ciesielski, A.; Piot, L.; Troyanov, S. I.; Mueller, U.; Weidner, S.; Samori, P.; Hecht, S., *Nanoscale* **2012**, *4*, 467-472.
128. Henke, W.; Kremer, S.; Reinen, D., *Inorg. Chem.* **1983**, *22*, 2858-2863.
129. Ramirez de Arellano, C.; Escriva, E.; Gomez-Garcia, C. J.; Minguez Espallargas, G.; Ballesteros, R.; Abarca, B., *CrystEngComm* **2013**, *15*, 1836-1839.
130. Younes, A. H.; Clark, R. J.; Zhu, L., *Supramol. Chem.* **2012**, *24*, 696-706.
131. Midya, G. C.; Paladhi, S.; Bhowmik, S.; Saha, S.; Dash, J., *Org. Biomol. Chem.* **2013**, *11*, 3057-3063.
132. Yuan, J.; Fang, X.; Zhang, L.; Hong, G.; Lin, Y.; Zheng, Q.; Xu, Y.; Ruan, Y.; Weng, W.; Xia, H.; Chen, G., *J. Mater. Chem.* **2012**, *22*, 11515-11522.

133. Yang, B.; Zhang, H.; Peng, H.; Xu, Y.; Wu, B.; Weng, W.; Li, L., *Polym. Chem.* **2014**, *5*, 1945-1953.
134. Yuan, J.; Zhang, H.; Hong, G.; Chen, Y.; Chen, G.; Xu, Y.; Weng, W., *J. Mater. Chem. B* **2013**, *1*, 4809-4818.
135. Jobe, K.; Brennan, C. H.; Motevalli, M.; Goldup, S. M.; Watkinson, M., *Chem. Commun.* **2011**, *47*, 6036-6038.
136. Li, Y.; Zhao, L.; Tam, A. Y.-Y.; Wong, K. M.-C.; Wu, L.; Yam, V. W.-W., *Chem. Eur. J.* **2013**, *19*, 14496-14505.
137. Lang, C.; Pahnke, K.; Kiefer, C.; Goldmann, A. S.; Roesky, P. W.; Barner-Kowollik, C., *Polym. Chem.* **2013**, *4*, 5456-5462.
138. Kitchen, J. A.; Olguín, J.; Kulmaczewski, R.; White, N. G.; Milway, V. A.; Jameson, G. N. L.; Tallon, J. L.; Brooker, S., *Inorg. Chem.* **2013**, *52*, 11185-11199.
139. Noble, A.; Olguín, J.; Clérac, R.; Brooker, S., *Inorg. Chem.* **2010**, *49*, 4560-4569.
140. Olguín, J.; Brooker, S., *Coord. Chem. Rev.* **2011**, *255*, 203-240.
141. Halcrow, M. A., *Coord. Chem. Rev.* **2009**, *253*, 2493-2514.
142. Schulze, B.; Escudero, D.; Friebe, C.; Siebert, R.; Görls, H.; Sinn, S.; Thomas, M.; Mai, S.; Popp, J.; Dietzek, B.; González, L.; Schubert, U. S., *Chem. Eur. J.* **2012**, *18*, 4010-4025.
143. Munuera, L.; O'Reilly, R. K., *Dalton Trans.* **2010**, *39*, 388-391.
144. Collin, J.-P.; Guillerez, S.; Sauvage, J.-P., *J. Chem. Soc., Chem. Commun.* **1989**, 776-778.
145. Thummel, R. P.; Hegde, V.; Jahng, Y., *Inorg. Chem.* **1989**, *28*, 3264-3267.
146. Hammett, L. P., *J. Am. Chem. Soc.* **1937**, *59*, 96-103.
147. Xiao, N.; Chen, Y.; Shen, X.; Zhang, C.; Yano, S.; Gottschaldt, M.; Schubert, U. S.; Kakuchi, T.; Satoh, T., *Polym J* **2013**, *45*, 216-225.
148. Bünzli, J.-C. G., *Acc. Chem. Res.* **2006**, *39*, 53-61.
149. Bünzli, J.-C. G.; Piguet, C., *Chem. Soc. Rev.* **2005**, *34*, 1048-1077.
150. dos Santos, C. M. G.; Harte, A. J.; Quinn, S. J.; Gunnlaugsson, T., *Coord. Chem. Rev.* **2008**, *252*, 2512-2527.
151. Leonard, J. P.; Nolan, C. B.; Stomeo, F.; Gunnlaugsson, T., *Top. Curr. Chem.* **2007**, *281*, 1-43.
152. Kotova, O.; Kitchen, J. A.; Lincheneau, C.; Peacock, R. D.; Gunnlaugsson, T., *Chem. Eur. J.* **2013**, *19*, 16181-16186.

153. Lincheneau, C.; Leonard, J. P.; McCabe, T.; Gunnlaugsson, T., *Chem. Commun.* **2011**, *47*, 7119-7121.
154. Stomeo, F.; Lincheneau, C.; Leonard, J. P.; O'Brien, J. E.; Peacock, R. D.; McCoy, C. P.; Gunnlaugsson, T., *J. Am. Chem. Soc.* **2009**, *131*, 9636-9637.
155. Comby, S.; Stomeo, F.; McCoy, C. P.; Gunnlaugsson, T., *Helv. Chim. Acta* **2009**, *92*, 2461-2473.
156. McMahon, B.; Mauer, P.; McCoy, C. P.; Lee, T. C.; Gunnlaugsson, T., *J. Am. Chem. Soc.* **2009**, *131*, 17542-17543.
157. Frost, G. H.; Hart, F. A.; Heath, C.; Hursthouse, M. B., *J. Chem. Soc. D, Chem. Commun.* **1969**, 1421-1422.
158. Indapurkar, A.; Henriksen, B.; Tolman, J.; Fletcher, J., *J. Pharm. Sci.* **2013**, *102*, 2589-2598.
159. Brunet, E.; Jiménez, L.; de Victoria-Rodriguez, M.; Luu, V.; Muller, G.; Juanes, O.; Rodríguez-Ubis, J. C., *Microporous Mesoporous Mater.* **2013**, *169*, 222-234.
160. Picot, S. C.; Mullaney, B. R.; Beer, P. D., *Chem. Eur. J.* **2012**, *18*, 6230-6237.
161. White, N. G.; Beer, P. D., *Chem. Commun.* **2012**, *48*, 8499-8501.
162. Vickers, M. S.; Beer, P. D., *Chem. Soc. Rev.* **2007**, *36*, 211-225.
163. Li, Y.; Flood, A. H., *Angew. Chem. Int. Ed.* **2008**, *47*, 2649-2652.
164. Li, Y.; Flood, A. H., *J. Am. Chem. Soc.* **2008**, *130*, 12111-12122.
165. Zahran, E. M.; Hua, Y.; Lee, S.; Flood, A. H.; Bachas, L. G., *Anal. Chem.* **2011**, *83*, 3455-3461.
166. Sinn, S.; Schulze, B.; Friebe, C.; Brown, D. G.; Jäger, M.; Altuntaş, E.; Kübel, J.; Guntner, O.; Berlinguette, C. P.; Dietzek, B.; Schubert, U. S., *Inorg. Chem.* **2014**, *53*, 2083-2095.
167. Sinn, S.; Schulze, B.; Friebe, C.; Brown, D. G.; Jäger, M.; Kübel, J.; Dietzek, B.; Berlinguette, C. P.; Schubert, U. S., *Inorg. Chem.* **2014**, *53*, 1637-1645.
168. Wang, S.; Cuesta-Seijo, J. A.; Lafont, D.; Palcic, M. M.; Vidal, S., *Chem. Eur. J.* **2013**, *19*, 15346-15357.
169. de Silva, A. P.; Gunaratne, H. Q. N.; McCoy, C. P., *Nature* **1993**, *364*, 42-44.
170. de Silva, A. P.; Gunaratne, H. Q. N.; Gunnlaugsson, T.; Huxley, A. J. M.; McCoy, C. P.; Rademacher, J. T.; Rice, T. E., *Chem. Rev.* **1997**, *97*, 1515-1566.
171. de Silva, A. P., *Molecular Logic-based Computation*. The Royal Society of Chemistry: Cambridge, 2012; p P001-397.
172. Hui, P.; Chandrasekar, R., *Adv. Mater.* **2013**, *25*, 2963-2967.

173. Piot, L.; Meudtner, R. M.; El Malah, T.; Hecht, S.; Samorì, P., *Chem. Eur. J.* **2009**, *15*, 4788-4792.
174. El Malah, T.; Rolf, S.; Weidner, S. M.; Thünemann, A. F.; Hecht, S., *Chem. Eur. J.* **2012**, *18*, 5837-5842.
175. Brunet, E.; Alhendawi, H. M. H.; Juanes, O.; Jimenez, L.; Rodriguez-Ubis, J. C., *J. Mater. Chem.* **2009**, *19*, 2494-2502.
176. Hong, G.; Zhang, H.; Lin, Y.; Chen, Y.; Xu, Y.; Weng, W.; Xia, H., *Macromolecules* **2013**, *46*, 8649-8656.
177. Weng, W.; Fang, X.; Zhang, H.; Peng, H.; Lin, Y.; Chen, Y., *Eur. Polym. J.* **2013**, *49*, 4062-4071.
178. Bünzli, J.-C. G.; Chauvin, A.-S.; Vandevyver, C. D. B.; Bo, S.; Comby, S., *Ann. N.Y. Acad. Sci.* **2008**, *1130*, 97-105.
179. Murray, N. S.; Jarvis, S. P.; Gunnlaugsson, T., *Chem. Commun.* **2009**, 4959-4961.
180. Bradberry, S. J.; Savyasachi, A. J.; Martinez-Calvo, M.; Gunnlaugsson, T., *Coord. Chem. Rev.* **2014**, *273-274*, 226-241.
181. Kotova, O.; Blasco, S.; Twamley, B.; O'Brien, J. E.; Peacock, R.; Kitchen, J. A.; Martinez-Calvo, M.; Gunnlaugsson, T., *Chem. Sci.* **2014**.
182. Murray, N. S. Lanthanide Luminescent Self-Assembly Complexes: From Solution Studies to Mechanical Sensing with Gold Surfaces. Ph.D. Thesis, University of Dublin, Trinity College, Dublin, 2008.
183. Caffrey, D. F. Chiral Lanthanide-Directed Self-Assembly: Ligand Substitution as a Path to Functionally Diverse Supramolecular Complexes. Ph. D. Thesis, University of Dublin, Trinity College, Dublin, 2014.
184. Barry, D. E. Lanthanide-Directed Self-Assembly Formation from Novel Dipicolinic Acid Derivatives. Ph.D. Thesis, University of Dublin, Trinity College, Dublin, 2014.
185. Lincheneau, C. Synthesis and Physical Studies of Luminescent Lanthanide and Colorimetric Chemosensors for Ions and Molecules. Ph.D. Thesis, University of Dublin, Trinity College, Dublin, 2011.
186. Elmes, R. B. P.; Erby, M.; Bright, S. A.; Williams, D. C.; Gunnlaugsson, T., *Chem. Commun.* **2012**, *48*, 2588-2590.
187. Elmes, R. B. P.; Orange, K. N.; Cloonan, S. M.; Williams, D. C.; Gunnlaugsson, T., *J. Am. Chem. Soc.* **2011**, *133*, 15862-15865.

188. Elmes, R. B. P.; Kitchen, J. A.; Williams, D. C.; Gunnlaugsson, T., *Dalton Trans.* **2012**, *41*, 6607-6610.
189. Ryan, G. J.; Quinn, S.; Gunnlaugsson, T., *Inorg. Chem.* **2007**, *47*, 401-403.
190. Wojdyla, M.; Smith, J. A.; Vasudevan, S.; Quinn, S. J.; Kelly, J. M., *Photochem. Photobiol. Sci.* **2010**, *9*, 1196-1202.
191. Alshehri, A.; Beale, P.; Yu, J. Q.; Huq, F., *Anticancer Res.* **2010**, *30*, 4547-4553.
192. Williams, J. A. G.; Wilkinson, A. J.; Whittle, V. L., *Dalton Trans.* **2008**, 2081-2099.
193. Wong, K. M.-C.; Yam, V. W.-W., *Coord. Chem. Rev.* **2007**, *251*, 2477-2488.
194. Bailey, J. A.; Hill, M. G.; Marsh, R. E.; Miskowski, V. M.; Schaefer, W. P.; Gray, H. B., *Inorg. Chem.* **1995**, *34*, 4591-4599.
195. Fletcher, J. T.; Walz, S. E.; Keeney, M. E., *Tetrahedron Lett.* **2008**, *49*, 7030-7032.
196. Collin, J.-P.; Dixon, I. M.; Sauvage, J.-P.; Williams, J. A. G.; Barigelletti, F.; Flamigni, L., *J. Am. Chem. Soc.* **1999**, *121*, 5009-5016.
197. Baker, A. T.; Craig, D. C.; Rae, A. D., *Aust. J. Chem.* **1995**, *48*, 1373-1378.
198. Nelson, J.; McKee, V.; Morgan, G., Coordination Chemistry of Azacryptands. In *Prog. Inorg. Chem.*, John Wiley & Sons, Inc.: 2007; pp 167-316.
199. Ziessel, R.; Grosshenny, V.; Hissler, M.; Stroh, C., *Inorg. Chem.* **2004**, *43*, 4262-4271.
200. Dobroschke, M.; Geldmacher, Y.; Ott, I.; Harlos, M.; Kater, L.; Wagner, L.; Gust, R.; Sheldrick, W. S.; Prokop, A., *ChemMedChem* **2009**, *4*, 177-187.
201. Brammer, L.; Bruton, E. A.; Sherwood, P., *Cryst. Growth Des.* **2001**, *1*, 277-290.
202. Zhang, J.; Su, C.-Y., *Coord. Chem. Rev.* **2013**, *257*, 1373-1408.
203. Tam, A. Y.-Y.; Yam, V. W.-W., *Chem. Soc. Rev.* **2013**, *42*, 1540-1567.
204. Piepenbrock, M.-O. M.; Lloyd, G. O.; Clarke, N.; Steed, J. W., *Chem. Rev.* **2009**, *110*, 1960-2004.
205. Daly, R.; Kotova, O.; Boese, M.; Gunnlaugsson, T.; Boland, J. J., *ACS Nano* **2013**, *7*, 4838-4845.
206. Burnworth, M.; Tang, L.; Kumpfer, J. R.; Duncan, A. J.; Beyer, F. L.; Fiore, G. L.; Rowan, S. J.; Weder, C., *Nature* **2011**, *472*, 334-337.
207. Sambri, L.; Cucinotta, F.; Paoli, G. D.; Stagni, S.; Cola, L. D., *New J. Chem.* **2010**, *34*, 2093-2096.
208. Tam, A. Y.-Y.; Wong, K. M.-C.; Yam, V. W.-W., *J. Am. Chem. Soc.* **2009**, *131*, 6253-6260.

209. Dinda, J.; Liatard, S.; Chauvin, J.; Jouvenot, D.; Loiseau, F., *Dalton Trans.* **2011**, *40*, 3683-3688.
210. Yoshikawa, N.; Matsumura-Inoue, T., *Anal. Sci.* **2003**, *19*, 761-765.
211. Norrby, T.; Börje, A.; Åkermark, B.; Hammarström, L.; Alsins, J.; Lashgari, K.; Norrestam, R.; Mårtensson, J.; Stenhagen, G., *Inorg. Chem.* **1997**, *36*, 5850-5858.
212. Eliseeva, S. V.; Bunzli, J.-C. G., *Chem. Soc. Rev.* **2010**, *39*, 189-227.
213. Yaroshevsky, A. A., *Geochem. Int.* **2006**, *44*, 48-55.
214. Bünzli, J. C. G., Luminescent Lanthanide Probes as Diagnostic and Therapeutic Tools. In *Met. Ions Biol. Syst.*, Sigel, A.; Sigel, H., Eds. Marcel Dekker Inc.: New York, 2004; Vol. 42, p 4239.
215. Matsumoto, K.; Yuan, J., *Metal ions in biological systems*. Marcel Dekker Inc.: New York, 2003; Vol. 40.
216. Stomeo, F. Design, Synthesis and Physical Evaluation of Luminescent Lanthanide-based Supramolecular Systems. Ph.D. Thesis, University of Dublin, Trinity College, Dublin, 2006.
217. de Bettencourt-Dias, A., *Dalton Trans.* **2007**, 2229-2241.
218. Plush, S. E.; Gunnlaugsson, T., *Dalton Trans.* **2008**, 3801-3804.
219. Binnemans, K., *Chem. Rev.* **2009**, *109*, 4283-4374.
220. Parker, D., *Coord. Chem. Rev.* **2000**, *205*, 109-130.
221. Montgomery, C. P.; Murray, B. S.; New, E. J.; Pal, R.; Parker, D., *Acc. Chem. Res.* **2009**, *42*, 925-937.
222. Forster, T., Discuss J. Chem. Phys. Faraday Soc. **1959**, 27.
223. Dexter, D. L., *J. Chem. Phys.* **1953**, *21*, 836-850.
224. Horrocks, W. D.; Sudnick, D. R., *Acc. Chem. Res.* **1981**, *14*, 384-392.
225. Supkowski, R. M.; Horrocks Jr, W. D., *Inorg. Chim. Acta* **2002**, *340*, 44-48.
226. Beeby, A.; M. Clarkson, I.; S. Dickins, R.; Faulkner, S.; Parker, D.; Royle, L.; S. de Sousa, A.; A. Gareth Williams, J.; Woods, M., *J. Chem. Soc., Perk. Trans. 2* **1999**, 493-504.
227. Plush, S. E.; Clear, N. A.; Leonard, J. P.; Fanning, A.-M.; Gunnlaugsson, T., *Dalton Trans.* **2010**, *39*, 3644-3652.
228. Lincheneau, C.; Stomeo, F.; Comby, S.; Gunnlaugsson, T., *Aust. J. Chem.* **2011**, *64*, 1315-1326.
229. dos Santos, C. M. G.; Fernandez, P. B.; Plush, S. E.; Leonard, J. P.; Gunnlaugsson, T., *Chem. Commun.* **2007**, 3389-3391.

230. Kotova, O.; Comby, S.; Gunnlaugsson, T., *Chem. Commun.* **2011**, *47*, 6810-6812.
231. Moore, E. G.; Xu, J.; Jocher, C. J.; Werner, E. J.; Raymond, K. N., *J. Am. Chem. Soc.* **2006**, *128*, 10648-10649.
232. Hamacek, J., *J. Alloys Compd.* **2008**, *451*, 347-351.
233. Andres, J.; Chauvin, A.-S., Lanthanides: Luminescence Applications. In *The Rare Earth Elements: Fundamentals and Applications*, Atwood, D. A., Ed. Wiley: 2013; pp 135-154.
234. Dieke, G. H.; Crosswhite, H. M.; Crosswhite, H., *Spectra and energy levels of rare earth ions in crystals*. Interscience Publishers: 1968.
235. Bonnet, C. S.; Gunnlaugsson, T., *New J. Chem.* **2009**, *33*, 1025-1030.
236. Crosby, G. A.; Demas, J. N., *J. Phys. Chem.* **1971**, *75*, 991-1024.
237. Jplus Consulting Pty Ltd, *ReactLab Equilibria*. http://jplusconsulting.com/products/reactlab-equilibria/ (Last accessed 5 November 2014).
238. Muller, G.; Schmidt, B.; Jiricek, J.; Hopfgartner, G.; Riehl, J. P.; Bunzli, J.-C. G.; Piguet, C., *J. Chem. Soc., Dalton Trans.* **2001**, 2655-2662.
239. Le Borgne, T.; Benech, J.-M.; Floquet, S.; Bernardinelli, G.; Aliprandini, C.; Bettens, P.; Piguet, C., *Dalton Trans.* **2003**, 3856-3868.
240. Ayme, J.-F.; Gil-Ramírez, G.; Leigh, D. A.; Lemonnier, J.-F.; Markevicius, A.; Muryn, C. A.; Zhang, G., *J. Am. Chem. Soc.* **2014**, *136*, 13142-13145.
241. Goldup, S. M.; Leigh, D. A.; Lusby, P. J.; McBurney, R. T.; Slawin, A. M. Z., *Angew. Chem. Int. Ed.* **2008**, *47*, 6999-7003.
242. Leigh, D. A.; Lusby, P. J.; McBurney, R. T.; Morelli, A.; Slawin, A. M. Z.; Thomson, A. R.; Walker, D. B., *J. Am. Chem. Soc.* **2009**, *131*, 3762-3771.
243. Grubbs, R. H.; Chang, S., *Tetrahedron* **1998**, *54*, 4413-4450.
244. Aarons, R. J.; Notta, J. K.; Meloni, M. M.; Feng, J.; Vidyasagar, R.; Narvainen, J.; Allan, S.; Spencer, N.; Kauppinen, R. A.; Snaith, J. S.; Faulkner, S., *Chem. Commun.* **2006**, 909-911.
245. Nitz, M.; Franz, K. J.; Maglathlin, R. L.; Imperiali, B., *ChemBioChem* **2003**, *4*, 272-276.
246. MacManus, J. P.; Hogue, C. W.; Marsden, B. J.; Sikorska, M.; Szabo, A. G., *J. Biol. Chem.* **1990**, *265*, 10358-10366.
247. Carr, R.; Evans, N. H.; Parker, D., *Chem. Soc. Rev.* **2012**, *41*, 7673-7686.

248. Muller, G.; Maupin, Christine L.; Riehl, James P.; Birkedal, H.; Piguet, C.; Bünzli, J.-Claude G., *Eur. J. Inorg. Chem.* **2003**, *2003*, 4065-4072.
249. Dickins, R. S.; Howard, J. A. K.; Maupin, C. L.; Moloney, J. M.; Parker, D.; Riehl, J. P.; Siligardi, G.; Williams, J. A. G., *Chem. Eur. J.* **1999**, *5*, 1095-1105.
250. Dickens, R. S.; Howard, J. A. K.; Maupin, C. L.; Moloney, J. M.; Parker, D.; Peacock, R. D.; Riehl, J. P.; Siligardi, G., *New J. Chem.* **1998**, *22*, 891-899.
251. Smith, D. G.; McMahon, B. K.; Pal, R.; Parker, D., *Chem. Commun.* **2012**, *48*, 8520-8522.
252. Bünzli, J.-C. G., *Chem. Rev.* **2010**, *110*, 2729-2755.
253. Gampp, H.; Maeder, M.; Meyer, C. J.; Zuberbühler, A. D., *Talanta* **1985**, *32*, 95-101.
254. Gampp, H.; Maeder, M.; Meyer, C. J.; Zuberbühler, A. D., *Talanta* **1986**, *33*, 943-951.
255. Chuprakov, S.; Chernyak, N.; Dudnik, A. S.; Gevorgyan, V., *Org. Lett.* **2007**, *9*, 2333-2336.
256. Jeong, B.; Bae, Y. H., *Nature* **1997**, *388*, 860.
257. Miyata, T.; Asami, N.; Uragami, T., *Nature* **1999**, *399*, 766-769.
258. Qiao, Y.; Lin, Y.; Zhang, S.; Huang, J., *Chem. Eur. J.* **2011**, *17*, 5180-5187.
259. Bekiari, V.; Lianos, P., *Langmuir* **2006**, *22*, 8602-8606.
260. Gunnlaugsson, T.; McCoy, C. P.; Stomeo, F., *Tetrahedron Lett.* **2004**, *45*, 8403-8407.
261. McCoy, C. P.; Stomeo, F.; Plush, S. E.; Gunnlaugsson, T., *Chem. Mater.* **2006**, *18*, 4336-4343.
262. Bradberry, S. J.; Byrne, J. P.; Peacock, R. D.; Gunnlaugsson, T., *Unpublished work* **2014**.
263. Di Pietro, S.; Imbert, D.; Mazzanti, M., *Chem. Commun.* **2014**, *50*, 10323-10326.
264. Pescitelli, G.; Di Bari, L.; Berova, N., *Chem. Soc. Rev.* **2014**, *43*, 5211-5233.
265. Albrecht, M.; Osetska, O.; Abel, T.; Haberhauer, G.; Ziegler, E., *Beilstein J. Org. Chem.* **2009**, *5*, 78.
266. Crassous, J., *Chem. Soc. Rev.* **2009**, *38*, 830-845.
267. Satyanarayana, S.; Dabrowiak, J. C.; Chaires, J. B., *Biochemistry* **1993**, *32*, 2573-2584.
268. Nilsson, K. P. R.; Rydberg, J.; Baltzer, L.; Inganäs, O., *Proc. Nat. Acad. Sci.* **2003**, *100*, 10170-10174.

269. Kelly, S. M.; Jess, T. J.; Price, N. C., *BBA-Proteins Proteom.* **2005**, *1751*, 119-139.
270. Lin, C.-C.; Morís-Varas, F.; Weitz-Schmidt, G.; Wong, C.-H., *Biorg. Med. Chem.* **1999**, *7*, 425-433.
271. Gigg, J.; Gigg, R.; Payne, S.; Conant, R., *Carbohydr. Res.* **1985**, *141*, 91-97.
272. Constable, E. C.; Housecroft, C. E.; Neuburger, M.; Rosel, P., *Chem. Commun.* **2010**, *46*, 1628-1630.
273. Paulsen, H.; Györgydeák, Z.; Friedmann, M., *Chem. Ber.* **1974**, *107*, 1568-1578.
274. Jones, J. E.; Kitchen, J. A.; Byrne, J. P.; Gunnlaugsson, T., *Manuscript under preparation* **2014**.
275. Angelo, N. G.; Arora, P. S., *J. Am. Chem. Soc.* **2005**, *127*, 17134-17135.
276. Beckmann, H. S. G.; Wittmann, V., *Org. Lett.* **2006**, *9*, 1-4.
277. Goddard-Borger, E. D.; Stick, R. V., *Org. Lett.* **2007**, *9*, 3797-3800.
278. Smith, N. M.; Greaves, M. J.; Jewell, R.; Perry, M. W. D.; Stocks, M. J.; Stonehouse, J. P., *Synlett* **2009**, *2009*, 1391-1394.
279. Maisonneuve, S.; Xie, J., *Synlett* **2009**, *2009*, 2977-2981.
280. Goddard-Borger, E. D.; Stick, R. V., *Org. Lett.* **2011**, *13*, 2514-2514.
281. Pandiakumar, A. K.; Sarma, S. P.; Samuelson, A. G., *Tetrahedron Lett.* **2014**, *55*, 2917-2920.
282. Berova, N.; Bari, L. D.; Pescitelli, G., *Chem. Soc. Rev.* **2007**, *36*, 914-931.
283. Muller, G., *Dalton Trans.* **2009**, 9692-9707.
284. Hubschle, C. B.; Sheldrick, G. M.; Dittrich, B., *J. Appl. Crystallogr.* **2011**, *44*, 1281-1284.
285. Sheldrick, G., *Acta Crystallogr. Sect. A* **2008**, *64*, 112-122.
286. Connelly, N. G.; Geiger, W. E., *Chem. Rev.* **1996**, *96*, 877-910.
287. Dana, B. H.; Robinson, B. H.; Simpson, J., *J. Organomet. Chem.* **2002**, *648*, 251-269.
288. Shin, Y.; Fryxell, G. E.; Johnson Ii, C. A.; Haley, M. M., *Chem. Mater.* **2007**, *20*, 981-986.
289. Heemstra, J. M.; Moore, J. S., *Org. Lett.* **2004**, *6*, 659-662.
290. Harvey, A.; Draganjac, M.; Chui, S.; Snell, R.; Benjamin, E., *J. Ark. Acad. Sci.* **2009**, *63*, 185.
291. Flamigni, L.; Collin, J.-P.; Sauvage, J.-P., *Acc. Chem. Res.* **2008**, *41*, 857-871.
292. Cini, R.; Donati, A.; Giannettoni, R., *Inorg. Chim. Acta* **2001**, *315*, 73-80.